

Decoding Active Sites and Mechanistic Insights for Efficient Electrochemical Water Splitting and Fuel Cell using Transition Metal-based Catalysts

A Thesis Submitted for the Degree of

Doctor of Philosophy

As a part of

Ph.D. Programme (Chemical Science)

by

Ms. Soumi Mondal



New Chemistry Unit

Jawaharlal Nehru Centre for Advanced Scientific Research

(A Deemed University)

Bangalore-560064 (INDIA)

July 2024

“Not all of us can do great things. But we can do small things with great love.”

— **Mother Teresa**

“We are what our thoughts have made us; so, take care about what you think. Words are secondary. Thoughts live; they travel far.”

— **Swami Vivekananda**

“We must believe that we are gifted for something, and that this thing, at whatever cost, must be attained.”

— **Marie Curie**

“Excellence is a continuous process and not an accident.”

— **A.P.J. Abdul Kalam**

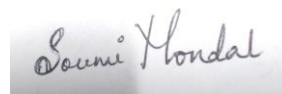
*Dedicated to Maa, Baba and All my
Teachers*

Declaration

I hereby declare that the matter embodied in the thesis entitled ***“Decoding Active Sites and Mechanistic Insights for Efficient Electrochemical Water Splitting and Fuel Cell using Transition Metal-based Catalysts”*** is the result of investigations carried out by me at the New Chemistry Unit, Jawaharlal Nehru Centre for Advanced Scientific Research, Bengaluru, India under the supervision of Prof. Sebastian C. Peter and that it has not been submitted elsewhere for the award of any degree or diploma. In keeping with the general practice in reporting scientific investigations, due acknowledgement has been made wherever the work described is based on findings of other investigators. Any omission that might have occurred by oversight or error of judgement is regretted.

Date: 30th July, 2024

Bengaluru, India



Soumi Mondal

Certificate

I hereby declare that the matter embodied in the thesis entitled “*Decoding Active Sites and Mechanistic Insights for Efficient Electrochemical Water Splitting and Fuel Cell using Transition Metal-based Catalysts*” has been carried out by Ms. Soumi Mondal at the New Chemistry Unit, Jawaharlal Nehru Centre for Advanced Scientific Research, Bengaluru, India under my supervision and that it has not been submitted elsewhere for the award of any degree or diploma.



Prof. Sebastian C. Peter

Professor

New Chemistry Unit, JNCASR

(Research Supervisor)

Date: 30th July, 2024

Bengaluru, India

Acknowledgement

I would like to thank all the people who helped me on this journey towards the successful accomplishment of my Ph.D. I firmly believe their constant help, support and enthusiasm have been the most important reasons why I have been able to finish this doctoral thesis work.

Firstly, I want to express my sincere gratitude to my research advisor, ***Prof. Sebastian C. Peter*** for encouraging and motivating me to dive into this challenging and exciting research area. His invaluable support, motivation and guidance inspired me to carry on challenging projects, independently. I am deeply appreciative of the time and effort he has invested in reviewing my work and providing insightful suggestions. I am grateful for the opportunities he has given me to carry out different advanced experiments and demonstrations in different parts of the country, where I've learned a lot and advanced myself with scientific experience.

I would like to express my sincere thanks to **Prof. C. N. R. Rao, Bharat Ratna**, for being the embodiment of the inspiration, motivation and encouragement in the scientific research in JNCASR. I also thank him for providing the wonderful infrastructure and necessary facilities to perform my research work.

I would like to thank **Prof. Subi J. George**, the Chairman, **New Chemistry Unit, Jawaharlal Nehru Centre for Advanced Scientific Research** for an excellent and world class research environment provided in the centre.

I would like to express my thanks to all my course instructors Prof. Sebastian C. Peter, Prof. Chandrabhas Narayana, Prof. Kanishka Biswas, Prof. A. Sundaresan, Prof. Ranjani Viswanatha, Prof. Bani Kanta Sarma, Prof. M. Eswaramoorthy, Prof. Sarit S. Agasti and Prof. Premkumar Senguttuvan for their excellent courses.

I would also take the opportunity to thank my collaborators: Dr. Sudip Chakraborty (HRI Allahabad), Dr. Tisita Das (HRI Allahabad), Prof. Abhishek K. Singh (IISc), Arko Parui (IISc), Manoj Dey (IISc), Dr. C. P. Vinod (NCL Pune).

My sincere thanks to all the technical staff of JNCASR: Usha Ma'am, Mr. Vasu, Mr. Anil, Mrs. Remya, Mr. Kannan, Ms. Meenakhsi, Mr. Arun and Mr. Sreehari for their help with the various characterization techniques. I would like to thank Geetanjali, Melissa, Naveen, JNCASR Administration and Academic Sections, Complab, Students' Residence, Library, Dhanvantari and Security.

I would like to thank Council of Scientific and Industrial Research (CSIR) for research fellowship. I would like to thank JNCASR, DST, DESY-Germany and KEK Japan for various fundings.

I would like to express my gratitude to my Lab Family to whom I will always remain indebted:

Present members: Dr. Veenu Mishra, Dr. Bitan Ray, Dr. Siddhi Kediya, Dr. Sandhya Saini, Dr. Amir Mehtab, Dr. Harishankar Kopperi, Devender, Subhajit, Nilutpal, Geetansh, Saurav, Diku, Sayan, Jagmeet, Saikat, Meera, Debmalya, Madhurima, Anu, Sanjay, Arnold, Sreelakshmi, Poornima, Shadhiya, Monica, Tanushree, Shreya, Yasaash, Swarnava, Gopika, Immanuel.

Breathe Members: Mekhna, Haritha, Rahul, Neehar, Manjunath and Shan.

Past members: Dr. Shreya Sarkar, Dr. Saurav Chandra Sarma, Dr. Arjun Cherevotan House, Dr. Debabrata Bagchi, Dr. Risov Das, Dr. Ashutosh Singh, Dr. Sathyapal Churipard, Dr. Kousik Das, Dr. Mohd Riyaz, Dr. Raghu Maligal Ganesh, Dr. Bharath Velaga, Dr. Suman Das, Dr. Rimzhim Gupta, Dr. Nithi Phukan, Dr. Seethiraju D. Ramarao, Dr. Ananya Chattaraj, Merin, Jithu, Kajol, Manami, Upasha, Vinay, Gouri, Ranjana, Asish, Sayanee, Chinthu, Anish, Abhishek, Shubhankar, Sandeep, Jyoti, Chanchal and Ragina.

I extend my gratitude to Dr. Ashly P. C. for being an overwhelming host and for constant enthusiasm for lab trips and parties. She has always been encouraging and positive. I extend my love and affection to Caitlyn and Angelyn whose presence made all our activities more fun filled and memorable.

I express my thanks to all my JNCASR friends and batchmates: Dipanjana Patra, Sanchita Karmakar, Surishi Vashishth, Diksha Padhi, Darshana Deb, Adrija Ghosh, Debasree Borah, Koyendrila Debnath, Aditi Saraswat, Nandini Saha, Sneha Raj.

I extend my heartfelt gratitude and love to friends outside JNCASR: Shreyashi Chowdhry, Sucheta Ganguly, Antara Chakraborty, Mouli Sarkar, Sumana Ghosh, Titin Samui, for their love and support throughout my life.

I am grateful to my Alma Mater St. Teresa's School, East West Model School, Vivekananda Mahavidyalaya, Visva-Bharati University.

I am really indebted and fortunate to have all my teachers from my school, college, and university.

Most importantly, I am grateful to my Parents, my sister, and all my family members for their love, affection, and support.

Soumi

Preface

The thesis is majorly divided into eight chapters.

Chapter 1 introduces the major environmental concern, global warming, which needs to dwindle in near future. The main source of CO₂ emission comes from fossil fuel combustion which can be sustainably substituted by green technology like fuel cells. The main fuels of fuel cell are oxygen at cathode and hydrogen, ethanol, methanol in anode. The cathodic reaction, oxygen reduction reaction has a very sluggish kinetics with a challenge for 4e⁻ transfer process, whereas the best anodic fuel is H₂ which needs to be obtained from a green source instead of grey sources like burning lignite and steam reforming of methane which release huge CO₂. The only green source of H₂ is from the electrolysis of water using renewable electricity from solar and wind power. Other anodic fuel, like ethanol is non-toxic with high-specific energy which can be oxidized with 12e⁻ transfer and that gives a high-power density from the fuel cell operation. But the major challenge of ethanol oxidation is C-C bond breaking, 12e⁻ transfer, CO-, and CH_x poisoning on the catalyst surface, which make this process difficult to be commercialized. Green hydrogen generation from water electrolysis faces the major difficulty of increased potential for water splitting from poor activity for anodic reaction of oxygen evolution. In my thesis, I have worked on designing different materials which has shown high activity in these electrochemical processes. The best catalytic activity is based on Volcano plot for each reaction which is obtained from Sabatier principle, which suggests that an optimum energy of intermediate adsorption is required to get the best activity. For achieving best active electrocatalyst for all these four reactions oxygen reduction reaction (ORR), hydrogen evolution reaction (HER), oxygen evolution reaction (OER), and ethanol oxidation reaction (EOR), I have tuned variegated materials using various design strategies like intermetallic synthesis with proper active site selection, tuning neighbouring group and ensemble effect using doping, lower metal loading with enhanced uniform distribution using different support based systems and morphology controlled studies. I have also tuned synthetic conditions from high-temperature long-duration solution phase synthesis to room temperature, ambient condition, and instantaneous synthesis via electrodeposition. Besides material design and catalytic applications, I have also dedicated my work for understanding the reactive sites, dynamics of the phase and mechanistic pathway via *in-situ* spectroscopic and analytical techniques for

understanding the reaction kinetics which can help in better enhancement in the field of electrocatalysis.

Chapter 2 demonstrates the well-known oxygen reduction reaction (ORR) and its limitation of slow kinetics of the cathodic half-cell reaction, Platinum, being the most active ORR catalyst, is still facing challenges due to its corrosive nature, and sluggish kinetics. Many novel approaches of substituting Pt have been reported, which suffer from stability issue even after mighty modifications. Designing an extremely stable, but unexplored ordered intermetallic structure, Pd₂Ge, and tuning the electronic environment of the active sites, by site-selective Pt-substitution, to crossover the hurdle of alkaline ORR is the main motive of this chapter. Platinum atoms substituting at specific Pd position leads to Pt_{0.2}Pd_{1.8}Ge demonstrated half-wave potential ($E_{1/2}$) of 0.95 V vs RHE which outperforms state-of-the-art catalyst 20% Pt/C. The mass activity (MA) of Pt_{0.2}Pd_{1.8}Ge is 320 mA/mg_{Pt}, which is almost 3.2 times better than Pt/C. $E_{1/2}$ and MA remained unaltered even after 50,000 accelerated degradation test (ADT) cycles which makes it a promising stable catalyst with its activity better than the state-of-the-art Pt/C. The undesired 2e⁻ transfer ORR forming hydrogen peroxide (H₂O₂) is diminished in Pt_{0.2}Pd_{1.8}Ge as visible from rotating-ring disk electrode (RRDE) experiment, spectroscopically visualized by *in-situ* Fourier transform infrared (FT-IR) spectroscopy and supported by computational studies. The effect of Pt substitution on Pd has been properly manifested by X-ray absorption spectroscopy (XAS) and X-ray photoelectron spectroscopy (XPS). The swinging of oxidation state of atomic sites of Pt_{0.2}Pd_{1.8}Ge during reaction is probed by *in-situ* XAS which efficiently enhances 4e⁻ transfer producing extremely low percentage of H₂O₂.

Chapter 3 discusses about atomic cobalt (Co) incorporation into the Pd₂Ge intermetallic lattice facilitates *operando* generation of a thin layer of CoO over Co substituted Pd₂Ge, with Co in the CoO surface layer functioning as single metal sites. Hence the catalyst has been titled Co₁-CoO-Pd₂Ge. High-resolution transmission electron microscopy (HR-TEM), X-ray photoelectron spectroscopy (XPS) and X-ray absorption spectroscopy (XAS) confirm the existence of CoO, with some of the Co bonded to Ge by substitution of Pd sites in the Pd₂Ge lattice. The role of the CoO layer in OER has been verified by its selective removal using argon sputtering and conducting OER on the etched catalyst. *In-situ* X-ray absorption near edge structure (XANES) and extended X-ray absorption fine structure spectroscopy (EXAFS) demonstrate that CoO gets transformed to CoOOH (Co³⁺) in *operando* condition with faster charge transfer through Pd atoms in the core Pd₂Ge lattice. *In-situ* Raman spectroscopy depicts

the emergence of a CoOOH phase on applying potential and that the phase is stable with increasing potential and time without getting converted to CoO₂. Density functional theory (DFT) calculations indicate that the Pd₂Ge lattice induces distortion in the CoO phase and generates unpaired spins in non-magnetic CoOOH system resulting in an increase in OER activity and durability. The existence of spin density even after electrocatalysis is verified from electron paramagnetic resonance spectroscopy (EPR). We have thus newly and successfully synthesized intermetallic supported CoO during synthesis and rigorously verified the role played by an intermetallic Pd₂Ge core in enhancing charge transfer, generating spin-density, improving electrochemical durability, and imparting mechanical stability to a thin CoOOH overlayer. Differential electrochemical mass spectrometry (DEMS) has been explored to visualize the instantaneous generation of oxygen gas during the onset of the reaction.

Chapter 4 describes about synthetic conditions for solution phase nanoparticles synthesis via solvothermal and colloidal synthesis at high temperature and pressure, which is being replaced with electrodeposition at room temperature, within 5-10 minutes under ambient conditions. I electrodeposited transition metals Ni, Co, Cu and Fe, amongst which Co gave a highly symmetrical hexagonal flower-like morphology for the first time. The formation mechanism for these hexagonal flowers have been explored via different controlled experiments and this material was tested for electrochemical oxygen evolution reaction (OER) with a very low overpotential of only 170 mV for 100 mA/cm². These Co-flowers were deposited on different substrates like Ni foil, Cu foil, Ni foam, stainless steel, and carbon paper which reveals the promising flexibility of these highly efficient Co nanoflowers to be commercialized due to being deposited on in-expensive versatile substrates which can be a low-cost candidate of water oxidation reaction.

Chapter 5 describes about the solution of using lesser cobalt and attaining higher OER activity due to the toxicity and expensive property of Co is becoming a concern, and hence decreasing its loading and substitution with non-toxic element like Fe forming CoFe ordered intermetallic structure has been studied in this work. Multi-walled carbon nanotubes (MWCNTs) with N-doping have been used as a conducting support where Co and Fe is initially forming their nitrides CoN/FeN and finally forming ordered intermetallic CoFe via nitride formation. It has been explored without N-doped MWCNTs, CoFe is not being formed. Nanometric uniform distribution of CoFe intermetallic NPs displayed a very high OER activity. The activity is further increased with just 1% Pt loading on CoFe which generated

compressional strain on CoFe IM lattice which enhanced feasible conversion from Co/Fe to CoOOH/FeOOH which is reflected in decreased overpotential for the reaction.

Chapter 6 discloses the discovery of novel materials for industrial standard hydrogen production which is the present need considering the global energy infrastructure. We introduce a novel electrocatalyst, Pt₃Ge, engineered with a desired crystallographic facet (202) accelerates hydrogen production by water electrolysis and records industrially desired operational stability compared to the commercial catalyst platinum. Pt₃Ge-(202) exhibits low overpotential of 21.7 mV (24.6 mV for Pt/C) and 92 mV for 10 mA/cm² and 200 mA/cm² current density, respectively in 0.5M H₂SO₄. It also exhibits remarkable stability of 15,000 accelerated degradation tests cycles (5000 for Pt/C) and exceptional durability of 500 h (@10 mA/cm²) in acidic media. Pt₃Ge-(202) also displayed low overpotential of 96 mV for 10 mA/cm² current density in the alkaline medium, rationalizing its hydrogen production ability over a wide pH range required commercial operations. Long-term durability (>75 h in alkaline media) with the industrial level current density (>500 mA/cm²) has been demonstrated by utilizing the electrochemical flow reactor. The driving force behind this stupendous performance of Pt₃Ge-(202) has been envisaged by mapping the reaction mechanism, active sites and charge transfer kinetics via controlled electrochemical experiments, ex-situ X-ray photoelectron spectroscopy, *in-situ* infrared spectroscopy and *in-situ* X-ray absorption spectroscopy further corroborated by first principles calculations.

Chapter 7 discusses one of the important criteria for an electrocatalyst is its economic viability. Volcano plot for HER suggests that Pt is the best catalyst with commercially used catalyst being 20% Pt on carbon support. This work has further reduced Pt loading to 10% with non-expensive support of CeO₂. The speciality of CeO₂ is its versatile morphology, switchable Ce(IV)-Ce(III) valency, and inexpensive. This work deals with designing cube and rod CeO₂ morphologies and incorporating Pt metal *in-situ* (during CeO₂ formation) and ex-situ (after CeO₂ formation) with different loading percentage which gave the best HER activity for *in-situ* incorporation of only 10% Pt in CeO₂ cube morphology. This is observed that Pt incorporation with enhanced Pt-CeO₂ is obtained for *in-situ* in cube and higher interface has provided higher HER. This can be correlated to the H-spillover mechanism during electrochemical HER from Pt to CeO₂ which is highest for cube morphology

Chapter 8 talks about designing a multifunctional electrocatalyst which is of surging demand. This work deals with successful solution phase synthesis of an ordered compound of Pd and Ni, Pd₃Ni, which is assumed to be difficult as almost no adjacent elements in a same

group form intermetallic compound. Pd₃Ni is a highly efficient and electrochemically stable material for tetra-functional activity, as in, hydrogen evolution reaction (HER), oxygen evolution reaction (OER), oxygen reduction reaction (ORR), and ethanol oxidation reaction (EOR) which constitutes both fuel cell and water electrolyser. Extensive ex-situ and *in-situ* characterization has disclosed the robustness of this material and reaction mechanism in different. This material has shown promising activity in proton exchange membrane water electrolyser and high temperature fuel cell. Tuned surface of the intermetallic has enhanced C-C cleavage in ethanol molecules allowing the sluggish 12e⁻ transfer process and have shown very high stability of >80k cycles of alkaline HER. Role of pH and potential has been explored in retaining the ordered phase of the intermetallic. Tetra functionality and its extensive exploration under different reaction conditions have been done in this work.

List of Abbreviations

ADT	Accelerated degradability test
AFM	Atomic force microscopy
AR	Analytical grade
ATR-FTIR	Attenuated Total Reflection Fourier-Transform Infrared Spectroscopy
BE	Binding energy
BM	Bimetallic
CA	Chronoamperometry
CE	Counter electrode
EOR	Ethanol oxidation reaction
CV	Cyclic voltammetry
DFT	Density functional theory
DMSO	Dimethyl sulfoxide
DOS	Density of states
ECO ₂ RR	Electrochemical CO ₂ Reduction Reaction
ECSA	Electrochemically active surface area
EDAX (EDS)	Energy Dispersive X-ray Spectroscopy
EDLC	Electric double layer capacitance
EIS	Electrochemical impedance spectroscopy
EXAFS	Extended X-ray absorption fine structure spectroscopy
FCC	Face-Centred cubic
FE	Faradaic efficiency
FESEM	Field emission scanning electron microscopy
FT-IR	Fourier Transform Infrared Spectroscopy
GC (E)	Glassy carbon (electrode)
GC	Gas chromatography
GDE	Gas Diffusion Electrode
GC-MS	Gas chromatography – Mass spectrometry
GGA	Generalized gradient approximation
HAADF	High-Angle Annular Dark Field
HER	Hydrogen evolution reaction
HPLC	High Performance Liquid Chromatography
HRTEM	High resolution transmission electron microscopy
ICP	Inductive coupled plasma
IF	Infrared spectroscopy
IM	Intermetallic
IPA	Isopropyl alcohol
Ir-MMO	Iridium Mixed Metal Oxide
LSV	Linear sweep voltammetry

LUMO	Lowest unoccupied molecular orbital
MFC	Mass flow controller
NGC	N-doped Graphitic Carbon
NHE	Normal hydrogen electrode
NMR	Nuclear magnetic resonance
NP	Nanoparticles
OER	Oxygen evolution reaction
ORR	Oxygen reduction reaction
PBE	Perdew-Burke-Ernzerhof
PDOS	Partial density of states
PGM	Platinum group metals
PXRD	Powder X-ray diffraction
RDE	Rotating disk electrode
rds	Rate determining step
RE	Reference electrode
RHE	Reversible hydrogen electrode
RRDE	Rotating ring disk electrode
SAED	Selected area electron diffraction
SCE	Saturated calomel electrode
SEM	Scanning Electron Microscopy
STEM	Scanning Transmission Electron Microscopy
TCD	Thermal conductivity detector
TEM	Transmission electron microscopy
TGA	Thermogravimetric analysis
TM	Transition metal
TOF	Turn over frequency
UHP	Ultrahigh pure
UV	Ultraviolet
WE	Working electrode
XAFS	X-ray absorption fine structure spectroscopy
XANES	X-ray absorption near edge spectroscopy
XAS	X-ray absorption spectroscopy
XPS	X-ray photoelectron spectroscopy
XRD	X-ray diffraction

Table of Contents

Declaration.....	v
Certificate.....	vii
Acknowledgment.....	ix
Preface.....	xii
List of Abbreviation.....	xviii
Table of contents.....	xxi

Chapter 1. Introduction.....	1
-------------------------------------	----------

1	Table of Contents	2
1.1	Background	4
1.2	Electrocatalytic Energy Conversion Reactions	5
1.2.1	Electrochemical Hydrogen Evolution Reaction (HER)	5
1.2.2	Electrochemical Oxygen Evolution Reaction (OER)	8
1.2.3	Electrochemical Oxygen Reduction Reaction (ORR)	9
1.2.4	Electrochemical Ethanol Oxidation Reaction (EOR)	10
1.3	Understanding reaction mechanism	10
1.4	Catalyst design for water splitting and fuel cell reactions	11
1.4.1	Morphology-controlled synthesis of catalyst	12
1.4.2	Single-atom or atomically dispersed catalysts	13
1.4.3	Hybrid phase or hetero-phase catalysts	13
1.4.4	Doping	15
1.4.5	Ordered and disordered catalysts	15
1.5	Variegated synthesis procedures for nanoparticles	15
1.5.1	Solvothermal/hydrothermal synthesis	16
1.5.2	Colloidal synthesis	16
1.5.3	Annealing under H ₂ atmosphere	16
1.5.4	Electrodeposition	17
1.6	Fundamental terms and Parameters to screen various electrocatalysts	17

1.6.1	Onset potential	17
1.6.2	Overpotential	17
1.6.3	Tafel slope	17
1.6.4	Electrochemically active surface area (ECSA)	18
1.6.5	Activity	18
1.6.6	Stability	18
1.6.7	Selectivity	18
1.7	Experimental and characterization tools for evaluating an electrocatalyst	19
1.7.1	Cyclic voltammetry (CV)	19
1.7.2	Linear sweep voltammetry (LSV)	19
1.7.3	Chronoamperometry (CA)	19
1.7.4	EIS spectroscopy (AC impedance)	19
1.7.5	Rotating disk electrode (RDE)	19
1.7.6	Powder X-ray diffraction (PXRD)	20
1.7.7	X-ray photoelectron spectroscopy (XPS) and argon sputtering	20
1.7.8	X-ray absorption spectroscopy (XAS)	21
1.7.9	Electron Microscopy	22
1.7.10	Inductively coupled plasma atomic emission spectroscopy (ICP-OES)	22
1.8	Electrochemical reactor for water splitting and fuel cell	23
1.8.1	Three-electrode two-compartment setup: MicroFlow cell	23
1.8.2	Two-electrode full cell water electrolyser using fabricated MEA	24
1.8.3	RDE setup	25
1.9	Spectroscopic and analytical techniques for <i>in-situ</i> mechanistic studies	25
1.9.1	<i>In-situ</i> Electrochemical Attenuated Total Reflection Fourier Transform Infrared Spectroscopy (ATR-FTIR)	25
1.9.2	<i>In-situ</i> X-ray absorption Spectroscopic studies	26
1.9.3	<i>In-situ</i> Raman Spectroscopic studies	26
1.9.4	Differential electrochemical mass spectrometry (DEMS)	27
1.10	Density Functional Theory (DFT)	28
1.11	References	31

Chapter 2. <i>In-Situ</i> Mechanistic Insights for Oxygen Reduction Reaction in Chemically Modulated Ordered Intermetallic Catalyst Promoting Complete Electron Transfer.....	38
2.1 Introduction	41
2.2 Experimental Details	43
2.2.1 Chemicals and reagents	43
2.2.2 Synthesis of Pd ₂ Ge, Pd _{1.8} Ge and Pt _{0.2} Pd _{1.8} Ge	43
2.3 Characterization	43
2.3.1 Powder X-ray Diffraction (PXRD)	43
2.3.2 Scanning electron microscopy (SEM) and Energy Dispersive Spectrum	43
2.3.3 Transmission Electron Microscope (TEM)	44
2.3.4 Inductively coupled plasma atomic emission spectroscopy (ICP-OES)	44
2.3.5 X-ray Photoelectron Spectroscopy (XPS)	44
2.3.6 X-ray Absorption Spectroscopy	44
2.3.7 In situ XANES and quick EXAFS during electrochemistry	45
2.3.8 In situ attenuated total reflection Fourier transformed infra-red) ATR-FTIR)	
Spectroscopy	45
2.3.9 Electrochemical Oxygen Reduction Reaction (ORR)	45
2.3.10 Rotating ring disk electrode experiment (RRDE)	46
2.3.11 Theoretical calculations	46
2.4 Results & Discussion	47
2.4.1 Structural insights and microscopic probing	47
2.4.2 Electrochemical Oxygen reduction (ORR)	50
2.4.3 Oxidation state and local structure by XAS	54
2.4.4 Surface oxidation state by XPS	56
2.4.5 Structural changes via operando XAS and post-ORR XPS	58
2.4.6 Deciphering reaction kinetics from operando FT-IR spectroscopy	
and computational studies	60
2.5 Conclusion	71
2.6 References	72

Chapter 3. Distortion-Induced Interfacial Charge Transfer at Single Cobalt Atom Secured on Ordered Intermetallic Surface Enhances Pure Oxygen Production	78
3.1 Introduction	81
3.2 Experimental Details	83
3.2.1 Chemicals and reagents	83
3.2.2 Synthesis of Pd ₂ Ge and Co ₁ -CoO-Pd ₂ Ge	83
3.3 Characterization	84
3.3.1 Powder X-ray Diffraction (PXRD)	84
3.3.2 Scanning electron microscopy (SEM) and Energy Dispersive Spectrum (EDS)	84
3.3.3 Transmission electron microscopy (TEM)	84
3.3.4 High-angle annular dark-field imaging Scanning Transmission electron microscopy (HAADF-STEM)	84
3.3.5 Inductively coupled plasma atomic emission spectroscopy (ICP-OES)	85
3.3.6 X-ray Photoelectron Spectroscopy (XPS)	85
3.3.7 X-ray absorption near edge spectroscopy (XANES) and Extended X-ray Absorption Fine Structure (EXAFS):	85
3.3.8 Electrochemical oxygen evolution Reaction (OER)	85
3.3.9 Rotating ring disk electrode experiment (RRDE)	86
3.3.10 <i>In-situ</i> X-ray absorption spectroscopy (XAS)	86
3.3.11 Differential electrochemical mass spectrometry (DEMS)	86
3.3.12 Computational Details	87
3.4 Results & Discussion	87
3.4.1 Phase analysis and microscopic visualization	87
3.4.2 Electrochemical oxygen evolution reduction (OER)	91
3.4.3 Local coordination and oxidation state analysis of Co ₁ -CoO-Pd ₂ Ge	95
3.4.4 Presence of oxide layer: Argon sputtered XPS and SEM analysis	95
3.4.5 Probing charge transfer during OER via operando methods	100
3.4.6 Visualizing structural evolution and stabilization: Potential-dependent Raman spectroscopy and theoretical calculations	103
3.4.7 Spectrometric analysis of oxygen generation triggered by oxidation potential – A DEMS study	107

3.5	Conclusion	108
3.6	References	111

Chapter 4. Electrochemically Sculpted Symmetrical Flowers Generating Oxygen.....119

4.1	Introduction	122
4.2	Experimental Details	123
	4.2.1 Chemicals and reagents	123
	4.2.2 Synthesis of electrodeposited catalysts	123
4.3	Characterization	123
	4.3.1 Powder X-ray Diffraction (PXRD)	123
	4.3.2 Transmission Electron Microscope (TEM)	124
	4.3.3 Scanning electron microscopy (SEM) and Energy Dispersive Spectrum	124
	4.3.4 X-ray Photoelectron Spectroscopy (XPS)	124
	4.3.5 X-ray Absorption Spectroscopy	124
	4.3.6 Electrochemical Oxygen Evolution Reaction (OER)	125
4.4	Results & Discussion	125
	4.4.1 Structural insights and microscopic probing	125
	4.4.2. Understanding the role of boric acid	129
	4.4.3. Analysis of chemical state of electrodeposited Co	131
	4.4.4 Complexing property of boric acid	134
	4.4.5. Electrochemical OER activity	138
	4.4.6. Electrodeposition of bi-metallic systems	141
4.5	Conclusion	141
4.6	References	143

Chapter 5. Non-Metal Anchored Strain-Tuned CoFe Intermetallic Formation via Nitride Formation Facilitates Oxygen Generation.....146

5.1	Introduction	149
5.2	Experimental Details	150
	5.2.1 Chemicals and reagents	150
	5.2.2 Synthesis of Co-Fe-based catalysts	151
5.3	Characterization	151

5.3.1	Powder X-ray Diffraction (PXRD)	151
5.3.2	Transmission Electron Microscope (TEM)	151
5.3.3	Scanning electron microscopy (SEM) and Energy Dispersive Spectrum	151
5.3.4	X-ray Photoelectron Spectroscopy (XPS)	152
5.3.5	X-ray Absorption Spectroscopy (XAS)	152
5.3.6	Electrochemical Oxygen Evolution Reaction (OER)	152
5.4	Results & Discussion	153
5.4.1	Structural insights and microscopic probing	153
5.4.2	Oxidation state and local structure analysis	156
5.4.3	Electrochemical OER activity	162
5.5	Conclusion	163
5.6	References	164

Chapter 6. Morphology Tuned Pt₃Ge Accelerates Water Dissociation to Industrial Standard Hydrogen Production over a wide pH Range.....167

6.1	Introduction	170
6.2	Experimental Details	172
6.2.1	Chemicals and reagents	172
6.2.2	Synthesis of Pt ₃ Ge-(110) and Pt ₃ Ge-(202)	172
6.3	Characterization	172
6.3.1	Powder X-ray Diffraction (PXRD)	172
6.3.2	Transmission Electron Microscope (TEM)	172
6.3.3	Inductively coupled plasma atomic emission spectroscopy (ICP-OES)	172
6.3.4	X-ray Photoelectron Spectroscopy (XPS)	173
6.3.5	High-angle annular dark field scanning transmission electron microscopy (HAADF-STEM)	173
6.3.6	Scanning electron microscopy (SEM) and Energy Dispersive Spectrum	173
6.3.7	X-ray Absorption Spectroscopy (XAS)	173
6.3.8	Electrochemical Hydrogen Evolution Reaction (HER)	174
6.3.9	In situ Electrochemical Attenuated Total Reflection Fourier Transform Infrared Spectroscopy (ATR-FTIR)	175
6.3.10	<i>In-situ</i> X-ray absorption spectroscopy (XAS)	175

6.3.11 Methodology of computational study	175
6.4 Results & Discussion	175
6.4.1 Hydrogen production	180
6.4.2 Driving forces for accelerated HER	187
6.5 Conclusion	198
6.6 References	198

Chapter 7. Reductant-free Sub-nm Pt NPs Anchored on Ceria Support Exploring H-spillover Mechanism in H₂ Generation.....209

7.1 Introduction	212
7.2 Experimental Details	213
7.2.1 Chemicals and reagents	213
7.2.2 Synthesis of CeO ₂ cubes (CeO ₂ -C) and CeO ₂ rods (CeO ₂ -R)	213
7.2.3 Synthesis of Pt incorporated CeO ₂ nano-rods (CeO ₂ -R) and nano-cubes (CeO ₂ -C) in the <i>in-situ</i> and <i>ex-situ</i> procedures	213
7.3 Characterization	214
7.3.1 Powder X-ray Diffraction (PXRD)	214
7.3.2 Transmission Electron Microscope (TEM)	214
7.3.3 X-ray Photoelectron Spectroscopy (XPS)	214
7.3.4 Scanning electron microscopy (SEM) and Energy Dispersive Spectrum	214
7.3.5 X-ray Absorption Spectroscopy (XAS)	214
7.3.6 Electrochemical Hydrogen Evolution Reaction (HER)	215
7.4 Results & Discussion	215
7.5 Conclusion	236
7.6 References	237

Chapter 8. Unravelling Growth Mechanism of Local Entropy Tailored Intermetallic Pd₃Ni Exhibiting Tetrafunctional Activity in Electrolyser and Fuel Cell.....242

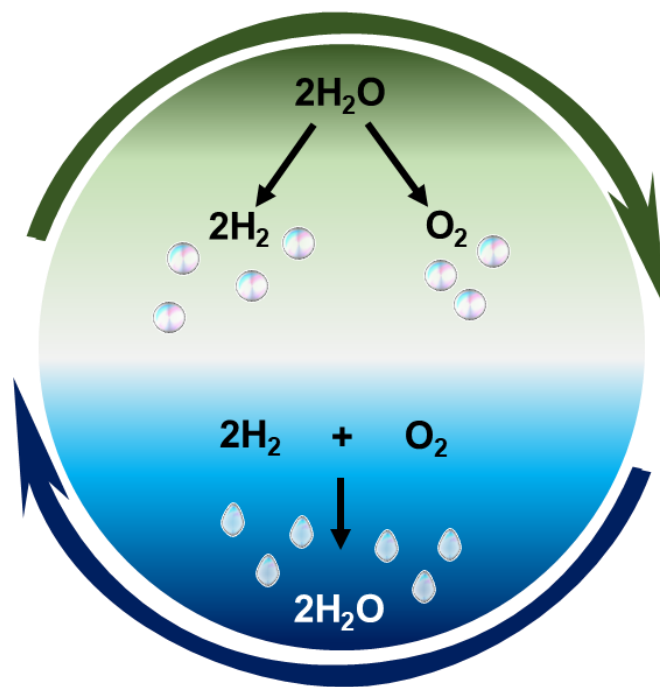
8.1 Introduction	245
8.2 Experimental Details	247
8.2.1 Chemicals and reagents	247

8.2.2	Synthesis of Pd ₃ Ni-IM and Pd ₃ Ni-Al	248
8.3	Characterization	248
8.3.1	Powder X-ray Diffraction (PXRD)	248
8.3.2	Scanning electron microscopy (SEM) and Energy Dispersive Spectrum	248
8.3.3	Transmission electron microscopy (TEM)	248
8.3.4	Inductively coupled plasma atomic emission spectroscopy (ICP-OES)	248
8.3.5	X-ray Photoelectron Spectroscopy (XPS)	249
8.3.6	X-ray absorption near edge spectroscopy (XANES) and Extended X-ray Absorption Fine Structure (EXAFS)	249
8.3.7	Differential scanning calorimetry (DSC)	249
8.3.8	Electrochemical oxygen evolution Reaction (OER)	249
8.3.9	Electrochemical oxygen reduction reaction (ORR)	250
8.3.10	Electrochemical hydrogen evolution reaction (HER)	250
8.3.11	Electrochemical ethanol oxidation reaction (EOR)	251
8.3.12	Membrane electrode assembly (MEA) fabrication	251
8.3.13	Proton exchange membrane water electrolyser	251
8.3.14	<i>In-situ</i> X-ray absorption spectroscopy (XAS)	251
8.3.15	<i>In-situ</i> Electrochemical Fourier Transform Infrared Spectroscopy (FT-IR)	251
8.3.16	<i>In-situ</i> Raman spectroscopy	252
8.3.17	Differential electrochemical mass spectrometry (DEMS)	252
8.3.18	Computational studies	252
8.4	Results & Discussion	253
8.4.1	Phase confirmation and growth mechanism	253
8.4.2	Electrochemical results	259
8.4.3	Structural insights and oxidation state analysis	265
8.4.4	Operando analysis of active species generation	266
8.4.5	Operando analysis of reaction mechanism and phase transformation	271
8.5	Conclusion	277
8.6	References	281
Summary and Future Outlook.....		288

List of Publications.....	293
Biography.....	296

Chapter 1

Introduction



1 Table of Contents

1 Table of Contents	2
1.1 Background	4
1.2 Electrocatalytic Energy Conversion Reactions	5
1.2.1 Electrochemical Hydrogen Evolution Reaction (HER)	5
1.2.2 Electrochemical Oxygen Evolution Reaction (OER)	7
1.2.3 Electrochemical Oxygen Reduction Reaction (ORR)	9
1.2.4 Electrochemical Ethanol Oxidation Reaction (EOR)	10
1.3 Understanding reaction mechanism	10
1.4 Catalyst design for water splitting and fuel cell reactions	11
1.4.1 Morphology-controlled synthesis of catalyst	12
1.4.2 Single-atom or atomically dispersed catalysts	13
1.4.3 Hybrid phase or hetero-phase catalysts	13
1.4.4 Doping	15
1.4.5 Ordered and disordered catalysts	15
1.5 Variegated synthesis procedures for nanoparticles	15
1.5.1 Solvothermal/hydrothermal synthesis	16
1.5.2 Colloidal synthesis	16
1.5.3 Annealing under H ₂ atmosphere	16
1.5.4 Electrodeposition	17
1.6 Fundamental terms and Parameters to screen various electrocatalysts	17
1.6.1 Onset potential	17
1.6.2 Overpotential	17
1.6.3 Tafel slope	17
1.6.4 Electrochemically active surface area (ECSA)	18
1.6.5 Activity	18
1.6.6 Stability	18
1.6.7 Selectivity	18
1.7 Experimental and characterization tools for evaluating an electrocatalyst	19
1.7.1 Cyclic voltammetry (CV)	19
1.7.2 Linear sweep voltammetry (LSV)	19
1.7.3 Chronoamperometry (CA)	19
1.7.4 EIS spectroscopy (AC impedance)	19
1.7.5 Rotating disk electrode (RDE)	19
1.7.6 Powder X-ray diffraction (PXRD)	20
1.7.7 X-ray photoelectron spectroscopy (XPS) and argon sputtering	20
1.7.8 X-ray absorption spectroscopy (XAS)	21
1.7.9 Electron Microscopy	22
1.7.10 Inductively coupled plasma atomic emission spectroscopy (ICP-OES)	22
1.8 Electrochemical reactor for water splitting and fuel cell	23
1.8.1 Three-electrode two-compartment setup: MicroFlow cell	23
1.8.2 Two-electrode full cell water electrolyser using fabricated MEA	24
1.8.3 RDE setup	25
1.9 Spectroscopic and analytical techniques for in situ mechanistic studies	25

Decoding Active Sites and Mechanistic Insights for Efficient Electrochemical Water Splitting and Fuel Cell using Transition Metal-based Catalysts

1.9.1	In situ Electrochemical Attenuated Total Reflection Fourier Transform Infrared Spectroscopy (ATR-FTIR).....	25
1.9.2	In situ X-ray absorption Spectroscopic studies.....	25
1.9.3	In situ Raman Spectroscopic studies.....	26
1.9.4	Differential electrochemical mass spectrometry (DEMS).....	28
1.10	Density Functional Theory (DFT).....	28
1.11	References.....	31

1.1 Background

The ultimate dream of the humankind in the current scenario is to use the terms ‘fuel’ and ‘combustion’ without having to encounter any carbon dioxide (CO_2) or carbonaceous compounds. To date, the utilization of non-renewable energy resources (like coal, petroleum and natural gas) is exceeding the use of renewable ones like wind, water, biopower and solar. The enormous growth of population has led to extensive consumption of these fossil fuels¹ and release of noxious CO_2 gas that has caused global warming, hiking the temperature at an alarming rate. This notorious gas is increasing the global temperature affecting the quality of life significantly. Increased CO_2 into the atmosphere leads to following consequences:

- a. Melting of ice caps, glaciers increasing the sea water level.
- b. Natural extremities like heavy rainfall, heatwaves, wildfire.
- c. Damages of aqua-life and wildlife severely.
- d. Increased animal and human death rate due to hike in temperature, increase in spreading diseases.

The major environmental concern, global warming, needs to dwindle in near future. The main source of CO_2 emission comes from fossil fuel combustion which can be sustainably substituted by green technology like fuel cells. The main fuels of fuel cell are oxygen at cathode and hydrogen, ethanol, methanol at anode. The cathodic reaction, oxygen reduction reaction has a very sluggish kinetics with a challenge for $4e^-$ transfer process, whereas the green anodic fuel is H_2 which needs to be obtained from a green source instead of grey sources like burning lignite and steam reforming of methane which release huge CO_2 . The only green source of H_2 is from the electrolysis of water using renewable electricity from solar and wind power. Other anodic fuel, like ethanol is non-toxic with high-specific energy which can be oxidized with $12e^-$ transfer and that gives a high-power density from the fuel cell operation. But the major challenge of ethanol oxidation is C-C bond breaking, $12e^-$ transfer, and CO, and CH_x poisoning on the catalyst surface, which make this process difficult to be commercialized.

Green hydrogen generation from water electrolysis faces the major difficulty of increased potential for water splitting from poor activity for anodic reaction of oxygen evolution. This entire thesis includes works on designing different materials which has shown high activity in these electrochemical processes. The best catalytic activity is based on Volcano plot for each reaction which is obtained from Sabatier principle, which suggests that an optimum energy of intermediate adsorption is required to get the best activity. For achieving best active

electrocatalyst for all these four reactions of fuel cell and water splitting, oxygen reduction reaction (ORR), hydrogen evolution reaction (HER), oxygen evolution reaction (OER), and ethanol oxidation reaction (EOR), variegated materials are being synthesized using various design strategies like intermetallic synthesis with proper active site selection, tuning neighboring and ensemble effect using doping, lower metal loading with enhanced uniform distribution using different support based systems and morphology controlled studies. Tuning of synthetic conditions from high-temperature long-duration solution phase synthesis to room temperature, ambient condition, and instantaneous synthesis via electrodeposition have been also conducted. Besides material design and catalytic applications, this thesis is dedicated for decoding the reactive sites, dynamics of the phase and mechanistic pathway via in-situ spectroscopic and analytical techniques for understanding the reaction kinetics which can help in better enhancement in the field of electrocatalysis.

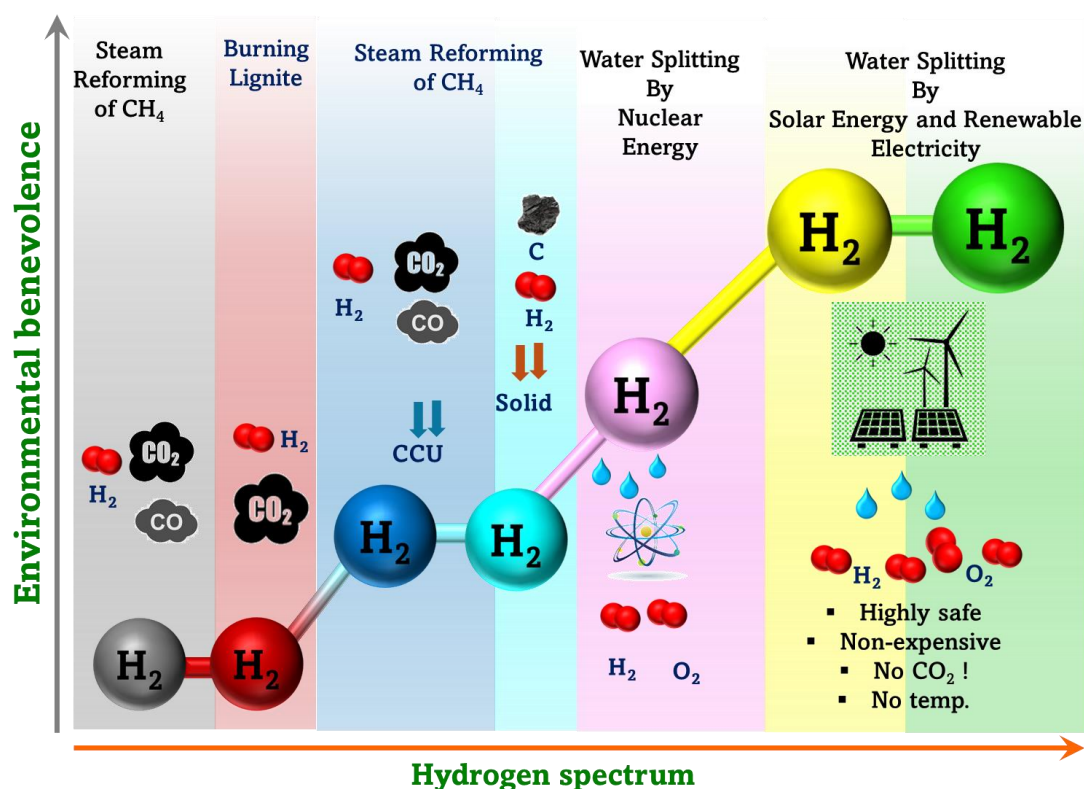


Figure 1.1 The hydrogen spectrum which represents the sources of hydrogen of different color codes.

1.2 Electrocatalytic energy conversion reactions

1.2.1 Electrochemical hydrogen evolution reaction (HER)

The mystery is that such a massive energy is pocketed inside a tiny molecule, H_2 ! The world is in desperate need of huge amounts of energy to meet the surging demands of huge population and the massive share of this energy is generated with release of enormous amounts

of carbon dioxide. Hydrogen (H_2) gas, in its molecular form, is the cleanest fuel known to date because its only combusted product is benevolent water.² Hydrogen can be used as a fuel in Proton Exchange Membrane Fuel Cells (PEMFCs) for various routine applications,³ as a reductant in the utilization of greenhouse gas CO_2 ,⁴ as a raw material in the production of several chemicals using hydrogenation processes (e.g., ammonia synthesis,⁵ methanol production⁶), as a direct fuel (e.g., in rocket⁷), in metallurgical industries,⁸ semiconductor manufacturing,⁹ pharmaceuticals,⁸ and any other sectors having concerns related to energy and environment. The hydrogen spectrum (**Figure 1.1**) shows the origin of hydrogen of different color codes. H_2 from steam reforming of methane and burning of coal is coded as grey and brown H_2 , respectively. Steam reforming of methane followed by capture of emitted CO_2 and storage of solid carbon generates the blue and turquoise H_2 , respectively. Water splitting by nuclear energy and solar energy generates pink and yellow hydrogen, respectively. Environmentally most green process, water electrolysis using renewable electricity needs an exponential growth for the development of a powerful H_2 generator.

However, large-scale H_2 production is majorly dependent on steam reforming of fossil fuels (about 96%),¹⁰ and the rest 4% by water electrolysis.¹¹⁻¹⁷ The worldwide market demand of hydrogen is skyrocketing and due to immense research and technology developments all over the world the overall price of H_2 production and setting fuel stations is also expected to decrease substantially in next 40-50 years. This is well represented in the **Figure 1.2**.

Noble metals (platinum, palladium and ruthenium¹⁸), especially platinum, are highly electroactive for hydrogen generation via water splitting attributed to their favourable electronic structure and optimum energy for hydrogen adsorption and desorption processes.

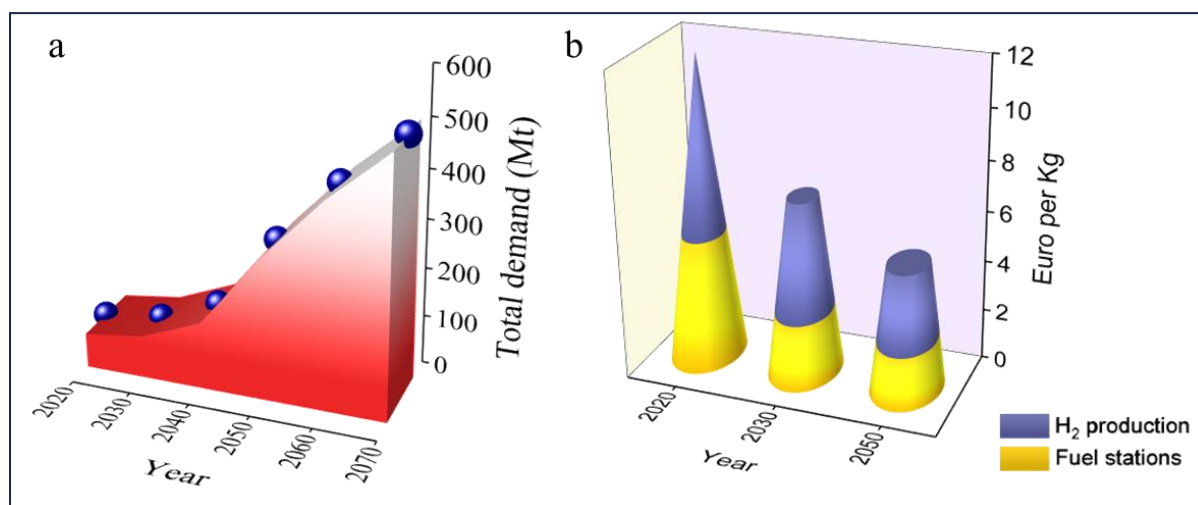


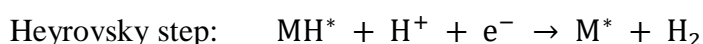
Figure 1.2. (a) Surging demand of H_2 in next 50 years and (b) Corresponding decrease in overall price in upcoming 30-40 years.

But, extensive commercialization of water electrolysis process is not yet completely achieved owing to high cost of Pt. These commercialization hurdles of water electrolysis process can be overcome either by reducing the cost of the catalyst or improving the performance or combining both. Even after a long scientific journey of synthesizing non-Pt based electrocatalysts, none of them could set foot in the performance region of Pt.

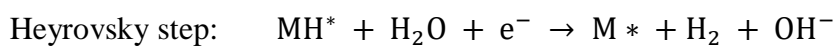
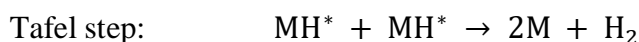
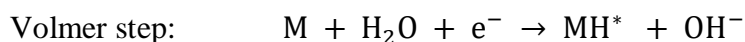
There are five critical parameters that dictate HER activity of a catalyst: (1) onset potential, (2) current density, (3) Tafel slope, (4) stability in wide pH range and (5) industrial standard durability. However, discovering a material holding all these parameters together is a challenging task. There are several strategies used to develop materials, for example, combining Pt with 3d transition metals (TMs) or p block elements. This can alter the 5d electron occupancy of Pt and Pt-Pt interatomic distance, tuning d-band center and modifying the electronic structure.¹⁹ The electronic structure modification improves the charge transfer kinetics and intermediate stability on the surface thereby lowering the activation barrier of the reaction.

Electrolysers are of two types, proton exchange membrane (PEM) water electrolyser and anion exchange membrane (AEM) water electrolyser. Designing electrocatalysts active in acidic and alkaline water is challenging hence the first step for HER is different for both cases. The reaction mechanism is given as below:

Acidic medium:



Alkaline or neutral medium:

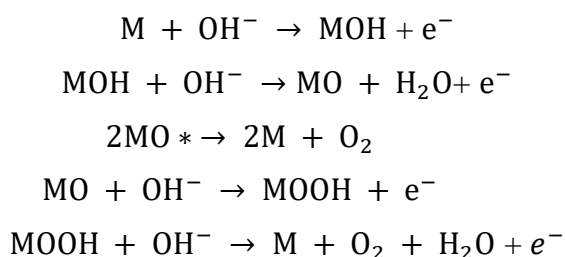


Hence, two important parameters for a best HER catalyst is optimum hydrogen adsorption and H₂O dissociation for both acid and alkali mediated HER.

1.2.2 Electrochemical oxygen evolution reaction (OER)

As discussed in the previous section, electrochemistry is the green path of generating hydrogen from water splitting via the water reduction process at the cathode.^{20, 21} The lesser

energy requirement for water splitting is ruled by the overall potential window of both the cathodic and anodic reactions.²² Even after achieving an efficient cathode material for hydrogen evolution reaction (HER), there may be increased cell potential for the water splitting due to high overpotential requirement for anodic process of oxygen evolution reaction (OER) as shown in **Figure 1.3a**.²³ Keeping a highly HER active catalyst, if the OER catalyst is varied there is significant change in the overall energy consumption for water splitting. Hence, achieving an efficient OER catalyst is an integral part of green H₂ economy. OER takes place more feasibly in alkaline media with abundance of OH⁻ which is the reactive species. The OER mechanism in alkaline media is given as:



The slower kinetics of OER is majorly due to the conversion of singlet state species OH⁻ (or H₂O) to triplet state O₂ which necessitates a higher overpotential increasing the full cell potential of an electrolyser.²⁴ Hence, an efficient OER active catalyst is also required to generate green hydrogen providing least electric potential.

Expensive metal oxides like IrO₂ or RuO₂ are being considered the state-of-the-art OER catalysts and they lack the superior activity and high durability during the long runs of OER alkaline harsh conditions due to the dissolution of Ir or Ru in reaction conditions of high pH and high oxidation potential.²⁵

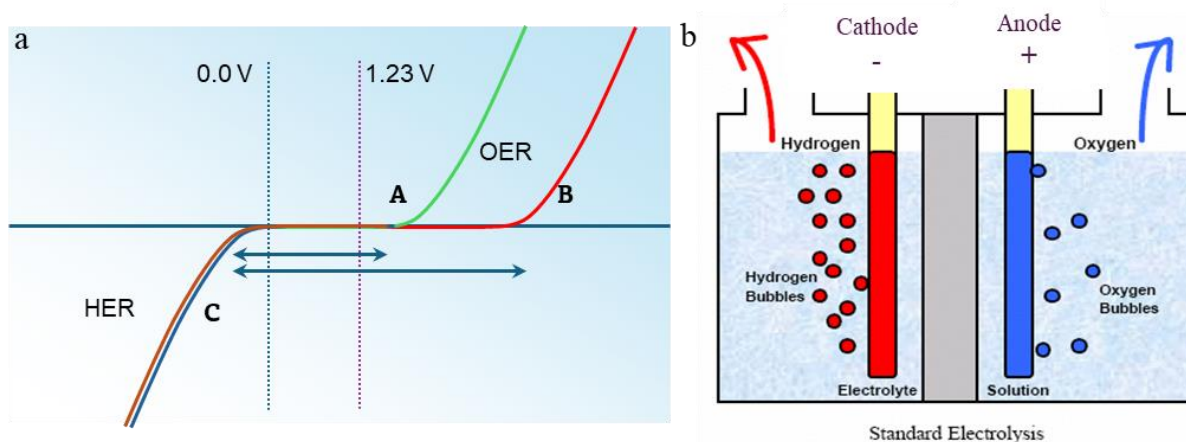


Figure 1.3. (a) Electrochemical linear sweep voltammogram (LSV) comparison of full water splitting by two different OER catalysts A and B using a same HER catalyst C. (b) Schematic representation of a proton exchange membrane fuel cell (PEMFC).

The difference between the adsorption energies of O^* and OH^* , $\Delta G_{O^*} - \Delta G_{OH^*}$, is the major descriptor for OER which decides whether the catalyst will provide faster OER kinetics. This energy difference is mainly governed by number of electrons in the d-orbital and electronic configuration (e_g) of the transition metals in their oxides.²⁶ Presence of a unpaired electron (metals with higher spin) can stabilize the O^* radical and hence making $\Delta G_{O^*} - \Delta G_{OH^*}$ more negative facilitating the overall OER kinetics. Designing an efficient material with high efficiency and durability is very necessary for making the green hydrogen generation process more economically viable.

1.2.3 Electrochemical oxygen reduction reaction (ORR)

Fuel cells, especially the proton exchange membrane fuel cells (PEMFCs) are the solution to drive automobiles without generating carbonaceous biproducts. Fuel cells have oxygen reduction (cathode) and hydrogen oxidation reaction (anode) (**Figure 1.3b**). The basic drawback of ORR is its sluggish kinetics which decreases the overall rate of fuel cell operations. The reaction mechanism of ORR in alkaline medium is:



One of the challenges for ORR is high amount of hydrogen peroxide production. ORR mechanism proceeds via incomplete ($2e^-$) transfer and complete ($4e^-$) transfer forming H_2O_2 and H_2O as the final products, respectively. Four electron transfer mechanism is the most desired one in fuel cell applications since that involves higher electron transfer and generating higher power. This reaction mechanism selectivity is dictated by the different ORR intermediate binding on the active sites of the catalyst.^{27, 28} If OOH^* intermediate is strongly adsorbed, peroxide desorption is not allowed, and O-O bond is made weaker. Thus, O-O bond cleavage occurs leading to OH desorption and adsorbed O atom further gets protonated followed by further electron transfer. Whether the OH adsorbed intermediate will desorb or protonate to form water, or it gets strongly adsorbed on the surface, dictates the stability of the catalyst in long-term reaction. Platinum is the most active and stable electrocatalyst for ORR till date, the only disadvantages being its high price, less abundance, and increased poisoning. Intermetallic compounds exhibit enhanced performance and stability. Blocking of the active sites by strongly adsorbed OH is very common in Pt and Pd sites which decreases their stability.²⁹⁻³¹ By tuning the active sites electronically using other heteroatoms in coordination (ligand effect), the adsorption energy of OH^* can be decreased, which in turn reduces the poisoning effect.

Decreasing the poisoning effect increases the number of active sites exposed to the reactant species, hence the ORR and overall fuel cell activity persists for a longer period of time.

1.2.4 Electrochemical ethanol oxidation reaction (EOR)

As H_2 is used as anodic fuel in proton exchange membrane fuel cell (PEMFC), small molecule alcohols are used as fuels in direct alcohol fuel cells (DAFCs). Amongst ethanol and methanol, ethanol is an environment-friendly fuel with a very high theoretical energy density of 8030 Wh/Kg and hence can be used as a fuel for transportation and delivery purposes.³² EOR occurs via two mechanism, $4e^-$ transfer incomplete oxidation producing CH_3COOH (or CH_3COO^-) and $12e^-$ transfer complete oxidation forming CO_2 (or CO_3^{2-}).³³ More number electrons transferred will generate more power in DAFCs.³³ Pd is considered as an EOR active state-of-the-art catalyst for generating acetic acid and carbon dioxide, whereas it is associated with notorious CO poisoning which blocks its active sites.^{34, 35} Attempts are highly required to achieve selectivity of products (majorly CO_2 formation) and to get rid of the CO poisoning effect.³⁶ Efforts have been made to diminish active-site poisoning, product selectivity, and enhanced current density.

1.3 Understanding reaction mechanism

The above discussed four electrocatalytic processes have different reaction mechanisms with different reactants and intermediates formed. **Figure 1.4a** schematically shows the reactants, intermediates and products formed during EOR, OER, ORR, and HER. The effects of conditions like the types of electrocatalysts (composition, size, shape, oxidation state, and crystal structure), electrolytes (cation, anion, concentration), pH, temperature, pressure, and applied potential gets superimposed onto the thermodynamic and kinetic considerations. A good catalyst, in general, should entail on the one hand, optimal adsorption (reactants & intermediates) and desorption energies (products) for a preferred pathway, and on the other should provide catalytic sites transferring electrons that are close to sites providing protons. As per the Sabatier principle, for attaining faster reaction kinetics, the adsorption energies (E_{ads}) for all intermediates must be optimum for easy adsorption of reactants and desorption of products. This is represented by a volcano plot of catalytic activity vs. Gibbs' free energy of different intermediates in **Figure 1.4b**.

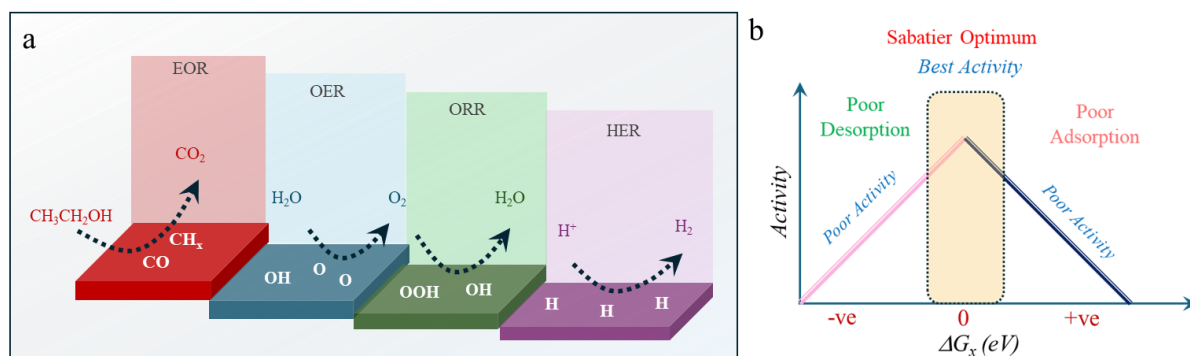


Figure 1.4. (a) Schematic representation of all electrochemical processes of EOR, OER, ORR, and HER. (b) Volcano plot of activity vs. Gibbs' free energy.

1.4 Catalyst design for water splitting and fuel cell reactions

The central part of the electrocatalysis research is to design suitable, robust catalyst materials which would be able to convert different reactants to corresponding products for all reactions shown in **Figure 1.4a** at a minimum applied potential producing higher current in the process with faster electron transfer. **Figure 1.5** summarizes some of the important classes/families, examples, and strategies of electrocatalyst designs explored in fuel cell and water splitting electrocatalysis. Catalysts design strategies for fuel cell and water splitting can be classified as few major types viz. modification of active metal site, and morphology, role of catalyst support material, single-atom catalyst, atom selective doping, tuning of ordering of catalyst, tuning of oxygen vacancies of different oxide materials, interfacial tuning of core-shell type materials, and ultimate motive is to achieve a catalyst with high efficiency and low cost for the better commercialization of the material in electrocatalysis.

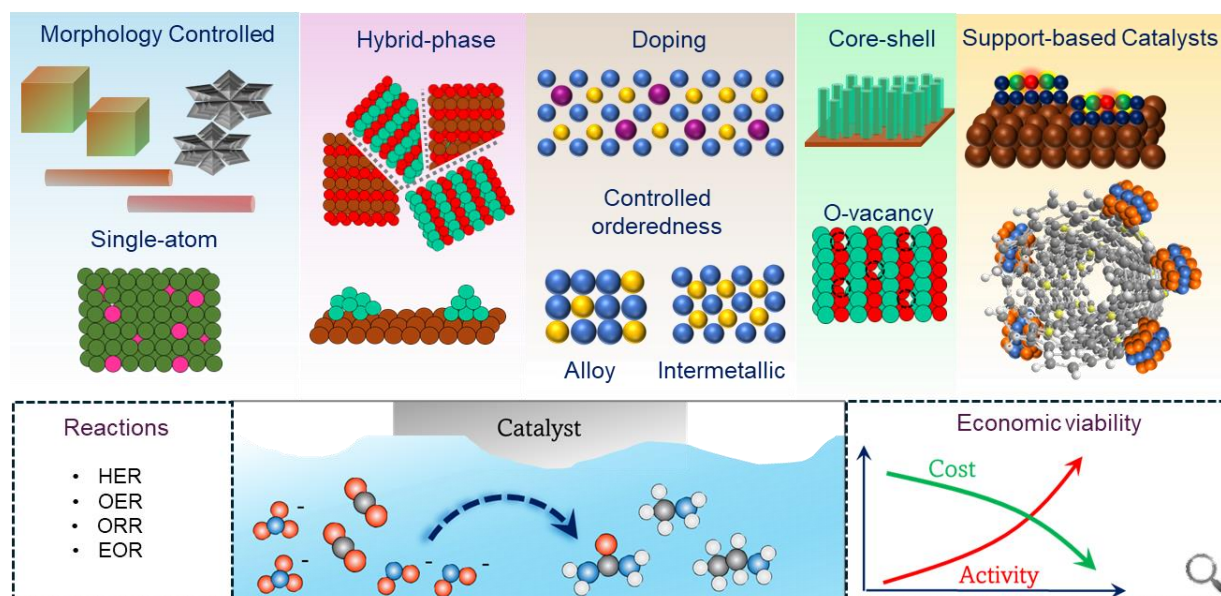


Figure 1.5. Overall schematic representation of catalyst design for electrochemical reactions of water splitting and fuel cell.

Although there are many catalyst design strategies for water splitting and fuel cell, all those strategies which have been extensively used in the working chapters of this thesis have been discussed below (**Figure 1.5**).

1.4.1 Morphology-controlled synthesis of catalyst

Catalysis is a surface phenomenon which indicates higher surface area of a catalyst will have higher catalytic activity. One of the interesting features of nanoparticles synthesis is that at the nanoscale and microscale the morphology of a material can be tuned and varied to ultimately give different unique shapes to the similar compound (**Figure 1.5**). The morphology of a nanoparticle is dictated by the type of crystal facets exposed during the growth of the particle. Shape engineering of the nanoparticle can be opted by careful synthesis, which would expose the preferred plane and give rise to proper shape and morphology.^{37, 38} The exposed crystallographic facet has a strong role in controlling the intermediate adsorption during the electrochemical reaction and determining the electrocatalytic performance.³⁹ For example, it is expected that if (100) facets of a particular phase are majorly formed, the expected morphology will be a cube, whereas if (111) facets of the similar compound are majorly formed, the expected morphology is octahedra or sometimes sphere if (111) facets are also accompanied by (100) or (110) facets.⁴⁰ When analyzed at the atomic level, different facets of a compound have different atomic arrangements, and catalysis will strongly depend on the atomic arrangements and indirectly it is related to the type of exposed facet and the overall morphology.

Porosity of a catalyst helps in increasing the surface area and hence reactive intermediates are adsorbed more feasibly and that increases the rate of the reaction. 2D thin film-like morphologies provide high surface and extended exposure of active sites on both sides of the layers, and ion-intercalation inside the layers can enhance the overall electron transfer rate during the electrocatalysis.⁴¹ Whereas 3D spherical morphology has higher curvature and exposing huge surface area that again enhances the rate of the reaction.⁴² Sharp-edged nanoparticles exhibit higher surface area, and most-importantly they have higher charge density at the tip and sharp edges of the nanoparticles, due to which more facile charge transfer takes place at those regions, instead of the flat smooth surfaces where the charge is distributed over a wide area.⁴³ In some morphologies like icosahedron, dodecahedron the high-index facets are obtained which have high-energy and dangling bonds due to coordinatively unsaturated atoms which lead to higher reactivity of the catalyst.⁴⁴ This strategy has been used in **chapters 4, 6, and 7**.

1.4.2 Single-atom or atomically dispersed catalysts

Single-atom catalysts (SACs) are commonly atomically dispersed transition metal atoms on 2D support and connected with a heteroatom (like N, C, P, O, or S).⁴⁵ SACs refer to embedding atomic sites of the active metal on an organic or inorganic support using very less loading of the atoms which actively participate in the catalytic process. SACs provide the benefit of high catalytic efficiency which indicates using the active catalyst at ultra-low concentrations and utilizing the efficiency of each atom by making the atoms dispersed on the substrate without any clustering of the active metal.

The electronic and geometric environments of single atoms can be finely tuned by modifying the type of substrates being used which can be highly crucial for achieving the Sabatier optimum for any kind of electrocatalytic process.⁴⁶ The support must help to anchor the single atoms stably to prevent the change of dynamic state of weakly anchored single atoms which leads to clustering to form small nanoclusters of the metal, losing the property of the single atoms. The support material itself should be stable in the harsh reaction conditions of electrocatalysis.⁴⁷

The major benefit of single atom catalysis is implementable for HER and ORR since the major discrepancy for their commercialization is the expensive Pt/C catalyst which is the state-of-the-art catalyst for both HER and ORR.^{48, 49} Efficient catalysts of single atomic Pt or other non-noble metals can promise an economically feasible future for green hydrogen and fuel cell research. This mode of material design has been utilized in **chapter 3**.

1.4.3 Hybrid phase or hetero-phase catalysts

Hybrid-phase or hetero-phase catalysts refer to the exposure of two different phases in a single compound. For example, a hetero phase of $\text{CoS}_x/\text{FeS}_x$ exhibited very high OER activity when compared with pure CoS_x or FeS_x nanoparticles.⁵⁰ Hetero phase intermetallic compounds of Ru_2Ge_3 and RuGe have exhibited very high current density in alkaline HER with enhanced charge transfer between the two phases at the interface which facilitated water dissociation for alkaline HER.⁵¹ Hetero-phases have an interface between them which enhances the charge transfer kinetics allowing the facile reaction. The synergistic property in a hybrid phase comes from the complementary property of each phase which enhances the property of the overall material. The number of active sites also increase when different phases are present together at the exposed surface. Different types of hetero phase or hybrid phase systems are discussed below.

1.4.3.1 Core-shell morphology

The existence of two phases with an internal core and a surface shell like layer forms the core-shell morphology as a hybrid phase catalyst. There exists an interface between the core and the shell which leads to enhanced charge transfer at the interface. Whereas the core component cannot directly participate in the catalysis and shell is usually made with the active species for the catalysis. Hence, the core can constitute of a relatively less active species yet facilitating the electron transfer at the interface. The major benefit of this process is that for the best efficiency of active species with lesser loading, a very ultra-thin layer of the active species can be used with fully exposed for the catalytic process. Au@Pd bimetallic core-shell nanorods have shown that Au core has enhanced the efficiency of Pd shell more than bulk Pd, since there is expansion in Pd lattice due to lattice mismatch at the Pd-Au interface and such lattice expansion has enhanced -OH binding on Pd reducing the energy barrier of EOR rate determining step and reduce the Pd-poisoning by carbonaceous intermediates.⁵² Many reports have successfully observed that increased efficiency of Pt metal in PEMFCs due to (i) tuned electronic structure at the Pt shell, (ii) decreased Pt loading with non-Pt core and ultra-thin Pt layer, (iii) Pt shell is preventing the dissolution of the easily oxidizable core which has increased the stability and efficiency of the low-Pt loaded fuel cell catalysts.⁵³ This strategy is exhibited in **chapter 3**.

1.4.3.2 Oxygen vacancy tuned catalysts

Oxides of metals which are capable of switchable oxidation states usually show the presence of O-vacancies in their lattice, majorly on the surface, for example, oxides of Ce, Ti, In, Zr, and many other spinels and perovskite based oxides.⁵⁴⁻⁵⁷ It has been observed that presence of O-vacancies on N doping in LaMnO₃ has helped in enhancing OER and ORR due to tuned oxidation state on Mn-species than in pristine LaMnO₃.⁵⁷ O-vacancies in CeO₂ or TiO₂ can thermodynamically stabilize the O-bound adsorption of O₂, CO, or CO₂ which reduces the energy barrier of the reaction.⁵⁸⁻⁶⁰ This strategy is utilized in **chapter 7**.

1.4.3.3 Support-based catalysts

Dynamic aggregation of nano-electrocatalysts can be avoided by using suitable support materials which have good conductivity and surface area for the electron transfer and diffusion of reactant, respectively. The physical and chemical property like porosity, toughness of support has also been investigated towards water splitting and fuel cell applications, the synergic effect between support and active metal play a very important role in monitoring electrochemical performance. This strategy is used in **chapters 3, 5 and 7**.

1.4.4 Doping

The introduction of a foreign element at the site of the host element changes the electronic structure and coordination environment of the host metal due to doping. Depending on the electronegativity, atomic size, the effect of doping can be tuned to get enhanced electrocatalytic activity. Doping can be metallic or non-metallic doping, which tunes the electronic structure of the host-lattice. Either the doped atom can participate in catalysis, or it can make the host-metal more efficient for the catalysis.⁶¹ Lattice charge distribution, vacancy concentrations, surface wettability (hydrophilicity), tuned adsorption of intermediates, modulated band-structure are attained via doping. This overall affects the catalytic property significantly.⁶² This concept is being explored in **chapters 2, 3 and 7**.

1.4.5 Ordered and disordered catalysts

The formation of an intermetallic compound (IMC) is a challenge as compared to a disordered alloy phase between two different elements.⁶³ Sometimes, it takes many days for an IM to form, whereas in some cases, it never forms.⁶⁴ The major disadvantages of disordered alloy compounds are the stability of the materials in harsh reaction conditions and non-periodicity of the active sites in the lattice preventing further tuning of the catalyst for a desired reaction.^{65, 66} IMCs are thermodynamically more stable, and all elements are ordered periodically in almost all facets which assures the availability of catalytically active sites more than the randomly oriented alloys.^{67, 68} Due to enhanced stability of IMs, the surface vulnerability of IM is lesser than alloys.⁶⁶ This can be enhanced by modifying the system by structurally ordering atoms, which in another way can be interpreted as tuning entropy of the system. The optimum tuning of structural order and entropy can induce the enhancement of catalytic activity towards a selected reaction.⁶⁹ This concept is being used in **chapters 2, 3, 5, 6, and 8**.

1.5 Variegated synthesis procedures for nanoparticles

Designing appropriate catalysts for water splitting and fuel cell is one of the most crucial parts of the entire process as it has an important role in controlling current density, and stability, and selectivity of the catalyst. All the above discussed catalyst tuning strategies are mainly dictated by the mode of synthesis being used for the nanoparticle formation. The nanoparticle synthesis formation varies from long-duration to very instantaneous synthesis, high-temperature to room-temperature conditions, from high-pressure to ambient pressure synthesis conditions along with the use of various other chemicals during the growth process of the nanoparticles. Here, in my thesis, I have tried to enhance the sustainability of the entire research by gradually

moving from high-temperature, high-pressure, chemical involved synthesis process to room-temperature, ambient-pressure and very instantaneous synthesis process using simple and harmless chemicals. Following are the different synthesis processes which have been used for all the working chapters in this thesis.

1.5.1 Solvothermal/hydrothermal synthesis

It is one of the most used techniques for producing thin films, single crystals and nanocrystals. The technique involves growing of crystals from an aqueous (for hydrothermal) or a non-aqueous solvent (for solvothermal) along with stoichiometric ratios of the desired metal salts/ precursors by thermal treatment in an autoclave, where solvents can be brought to temperatures above their boiling points to behave as supercritical fluids. Using this technique, the properties, morphology, size, and structure of nanomaterials can be tailored easily by varying the different reaction parameters, such as reaction time, temperature, reaction medium, pressure, pH, and concentration of the reactants and filled volume of autoclave. The electrocatalysts like Pd₂Ge intermetallic compound, Pt₃Ge intermetallic compounds, CeO₂ nanoparticles with different morphology, Pd₃Ni intermetallic catalysts are synthesized for chapters 2, 3, 6, 7, and 8 in this thesis.

1.5.2 Colloidal synthesis

This is a traditional chemical approach of heating organic solvents with stoichiometric ratios of salts/precursors at high temperature and ambient pressure to produce nanoparticles having a precise control over the specific morphology, shape and size of the nanoparticles. This synthesis involves the formation of a suspension of the reactant particles and continuous stirring of the solution. Inert atmosphere can be generated by creating vacuum and filling with N₂ or Ar gas in the reaction setup. Synthesis of Co-Fe mixed nitrides embedded on carbon-based support has been done via this process in **chapter 5** of this thesis.

1.5.3 Annealing under H₂ atmosphere

Annealing refers to the post-synthesis treatment of the nanoparticles synthesized via colloidal or solvothermal synthesis under high temperature for a certain period (few hours) under H₂ atmosphere (for reduction) or under N₂ or Ar atmosphere (for preventing oxidation). Here, CoFe-mixed nitrides formed from colloidal synthesis have been post-treated via annealing under H₂ gas presence at high temperature for few hours to successfully achieve CoFe intermetallic nanoparticles which are highly stable, in **chapter 5** of this thesis.

1.5.4 Electrodeposition

Electrodeposition refers to the deposition of metal nanoparticles on a conducting substrate from the electrolyte solution containing the metal ions. This deposition is due to the electric current (direct current, DC) which is applied to the substrate. This process has huge benefits of uniform coating, under very less time, at room temperature and ambient pressure and using safe chemicals. This strategy can give interesting versatile morphologies to the nanoparticles, and this has been used in **chapter 4** of my thesis.

1.6 Fundamental terms and Parameters to screen various electrocatalysts

1.6.1 Onset potential

It is defined as the least negative (for cathodic reaction) or positive potential (for anodic reaction) in which a reaction product or faradaic current is detected.

1.6.2 Overpotential

It is defined as the potential difference between the thermodynamically determined reduction/oxidation potential (E_{eq}) for a particular half-cell reaction and the experimentally observed potential (E) for the same redox event. It is related to cell's voltage efficiency. The overpotential (η) of an electrode reaction is defined as:

$$\eta = E - E_{eq} \quad (\text{Eqn. 1.1})$$

1.6.3 Tafel slope

Under high anodic overpotential the Butler-Volmer equation reduces to

$$\begin{aligned} j &= j_0 e^{-\alpha f \eta} = j_0 e^{-\alpha \eta / RT} \\ \text{hence, } \ln j &= \ln j_0 - \alpha \eta / RT \\ \text{therefore, } \eta &= a + b \log j \quad (\text{Eqn. 1.2}) \end{aligned}$$

Equation (1.2) is known as Tafel equation where a and b are constants, b is known as the Tafel slope given by:

$$b = \frac{\partial \eta}{\partial \log j} = 2.303 RT / \alpha F \quad (\text{Eqn. 1.3})$$

A smaller Tafel slope indicates a larger increase in current with small change in overpotential, which is efficient for electrocatalytic activity. The smaller b means that less overpotential is needed to achieve the same increase in current density, indicating faster electron-transfer kinetics. An efficient electrocatalyst should have a high j_0 and a small b .

1.6.4 Electrochemically active surface area (ECSA)

It is defined as the active area of the electrode material that is accessible to the electrolyte for charge transfer. The ECSA will facilitate quantification of the reacting interface area and hence, provide more accurate performance comparison of catalysts. For Pt-based catalysts ECSA can be calculated from the charge associated with one monolayer of under-deposited hydrogen desorption in cyclic voltammetry (CV) while for other catalysts it is calculated by running CVs at high scan rate.

1.6.5 Activity

The activity of an electrocatalyst is defined as its ability to speed up the electrochemical reaction. According to Sabatier principle an optimal level of intermediate adsorption and desorption is needed to enhance the performance of the catalyst. Requirement of lesser potential (overpotential) to start a reaction or achieving 1 mA/cm^2 indicates the higher activity of the catalyst. The usual practice comparing the electrocatalytic activity of catalysts are considered with respect to the potential required to attain 10 mA/cm^2 current density for HER, OER, and EOR, which is known as η_{10} value. For ORR, the potential for attaining half of the diffusion limited current density, known as half-wave potential ($E_{1/2}$) is considered.

1.6.6 Stability

The stability of a catalyst is one of the most pivotal factors, which defines the potential of a catalyst. Technical targets of the US Department of Energy (DoE) demand production of 1500 kg/day of hydrogen from electrochemical water splitting device for over a period of 10 years. Similarly, for the polymer electrolyte membrane fuel cells (PEMFCs) DOE have defined fuel cell stack durability of 30000 cycles as their technical target. Comparison of several techniques like cyclic voltammetry (CV), linear sweep voltammetry (LSV), electrochemical impedance spectroscopy (EIS), double-layer capacitance before and after the durability is utilized for long-term assessment of the catalyst.

1.6.7 Selectivity

Catalytic activity and selectivity of a material is dependent on the material's property and on the applied potential for certain chemical reactions. For example, in ORR it appears predominantly that noble metal-based catalysts prefer the direct $4e^-$ reduction of oxygen to water in comparison to the indirect $2e^-$ reduction to peroxide. In the case of EOR catalyst, it is desired to achieve $12e^-$ transfer oxidation of ethanol to CO_2 formation with C-C bond cleavage. A potentially good electrocatalyst is one which has high selectivity towards one product over a

wide pH range. Another important parameter is to avoid catalyst poisoning via fine tuning of catalyst surface.

1.7 Experimental and characterization tools for evaluating an electrocatalyst

1.7.1 Cyclic voltammetry (CV)

CV is the most used electrochemical technique that measures the current developed in an electrochemical cell when voltage is applied under specific conditions. The characteristic electrochemical response of a catalyst is determined from the oxidation and reduction potentials that can be qualitatively obtained from CV. During the CV experiment the potential is linearly ramped and after attaining the final potential, the potential is reverted to the initial potential.

1.7.2 Linear sweep voltammetry (LSV)

Using this technique working electrode potential is scanned in a particular range at a constant scan rate with fixed directionality which is dependent on the reaction that is being performed.

1.7.3 Chronoamperometry (CA)

CA is another electrochemical technique that can help in determining the reaction kinetics and mechanism. At the beginning of the experiment the potential is maintained at a fixed potential (E_i) which is then stepped up to a new potential (E_1) at $t = 0$ and the corresponding current response as a function of time is recorded.

1.7.4 EIS spectroscopy (AC impedance)

In this technique, the base potential is held constant at a constant potential. A sine waveform is superimposed onto the base potential, and its frequency is scanned from high to low with 12 components per decade. Current and potential are sampled and analyzed to obtain the real and imaginary parts of the impedance. During the experiment, you can switch between a Bode plot and a Nyquist plot by right-clicking. After the experiment, impedance data can be presented in various forms.

1.7.5 Rotating disk electrode (RDE)

A rotating disk electrode (RDE) and a rotating ring disk electrode (RRDE) are used to determine the intermediates formed during ORR. The ring current determines the amount of H_2O_2 formed while disc current determines the number of electrons transferred during ORR. During rotation H_2O_2 generated at the disc reaches the Pt ring where applied potential helps the formed H_2O_2 to oxidize back to O_2 . A potential of +1.2V is applied at the ring for driving the oxidation process under diffusion limitation to collect maximum amount of peroxide. In a RDE

oxidation (positive bias) or reduction (negative bias) takes place due to the convection process when the molecule or ion diffuses to the electrode surface. Mass transport limitations are known to occur when a reaction is constrained by the rate of analyte diffusion to the electrode surface. In both RDE and RRDE the increase in rotation speed of the electrode enhances the mass transport.

1.7.6 Powder X-ray diffraction (PXRD)

The most used characterization technique for crystal structure determination is PXRD. This technique not only provides an insight to the crystal structure, but information related to crystallite size, residual strain and preferential orientation can also be obtained. The Miller planes are formed due to the periodic arrangement of atoms in a crystalline solid. Since in a crystal structure the interatomic and interplanar distance between atoms and layers are in the order of 0.1 nm X-rays have the characteristic wavelength of 0.01-10 nm and hence is appropriate to interact with the atoms in solid materials. Interference between X-rays diffracted by layers with different depths is an integral multiple of the X-ray wavelength (λ) the signal received by the detector is termed as constructive interference. However, non-integral multiple of wavelength λ results in destructive interference with no signal. This forms the basis of Bragg's law which is defined as follows:

$$n\lambda = 2d \sin \theta \quad (\text{Eqn. 1.4})$$

where, n is the integral multiple of wavelength, λ is the wavelength of incident radiation, d is the interplanar distance and θ is the angle of diffraction. With respect to the sample surface at specific θ a miller plane is diffracted in a crystal structure.

1.7.7 X-ray photoelectron spectroscopy (XPS) and argon sputtering

XPS is an analytical technique that uses X-ray under ultra-high vacuum to examine the presence of a particular element both qualitatively and quantitatively. Using photoelectric effect the binding energy (B. E.) of the electrons corresponding to a particular element in a sample can be evaluated. With the sample being exposed to X-rays that have a defined energy ($h\nu$) electrons are knocked out from the sample and their kinetic energy (E_{kin}). Hence, binding energy (B. E.) can be calculated as follows:

$$\text{B.E.} = h\nu - E_{\text{kin}} - \phi \quad (\text{Eqn. 1.5})$$

where, ϕ is the work function of the sample surface. Binding energy values can help in the qualitative determination of the elemental composition and chemical environment.

Ar⁺ sputtering was done for 10 secs each layer for an energy of 2 KeV and high-resolution spectra of Pd 3d, Ge 3d, and Co 2p were performed after each layer etching.

1.7.8 X-ray absorption spectroscopy (XAS)

In this technique high intensity X-rays typically generated by a synchrotron light source excites the core-level electrons (K, L or M shell) of a particular element from the ground state to an excited electronic state. This process of excitation leaves an empty core, which within a short span of 10^{-15} secs is filled by an electron from the higher energy shell. Fluorescence is known to occur when this electron returns to a lower energy state from the higher one. The energy released is equal to the energy difference between the two orbitals and hence, the absorption energy is specific for each element. The incident X-ray is partly absorbed by the sample while the remaining is transmitted by the sample and the probability of X-ray absorption is defined by the X-ray absorption coefficient. This absorption coefficient being element specific increases with binding energy of the core-level electrons and hence is directly proportional to the atomic number of the elements. In a XAS measurement incident X-ray beam passes through an ionization chamber which measures the initial intensity (I_0). The fluorescence detector kept at angle of 45° from the sample detects the photoelectrons that are produced upon interaction of the incident radiation with the sample surface. The remaining radiation enters a second ionization chamber where the transmitted radiation (I_t) is measured. A reference foil is placed after the second ionization chamber and intensity of the transmitted X-rays through the reference material is determined in a third ionization chamber (I_r). The X-ray absorption coefficient can be determined based on measured intensity of incident and transmitted radiation. When the incident radiation has an energy equal to that of the energy required to excite a core-level electron a sharp increase of μ is expected which is defined as the absorption edge in a typical XAS spectrum. This absorption edge is element specific.

A typical XAS spectra comprises of two regions: X-ray near edge structure (XANES) and Extended X-ray absorption fine structure (EXAFS). XANES gives information about the oxidation state of the absorbing atoms. EXAFS gives important information about the local structure of the element i.e. bonding environment and coordination number. XANES region ranges from -50 to +100 eV of the absorption edge whereas EXAFS region begins after 50 eV from the absorption edge. A Fourier transform of the data expressed in k-space (momentum space) leads to expression of data in R-space where R is the radial distance of the neighboring atom from the absorbing atom.

1.7.9 Electron microscopy

Scanning electronic microscopy (SEM) and transmission electron microscopy (TEM) play an inevitable role in the characterization of catalysts. EM uses electron beams generated from the cathode (a tungsten filament or lanthanum hexaboride). When the beams are focused on the sample, the primary beam interacts with the atoms of the material causing scattering with various emissions, including secondary electrons (SE), backscattered electrons (BSE), and characteristic X-rays.⁷⁰ All these three radiations are usually significant for SEM analysis. These signals are associated with various types of information from microscopy. The volume of electron beams interacting with the material depends on the energy of the incident beam, the type of material, and the atomic number of the elements.⁷¹ The secondary electrons are very important in SEM while TEM uses the transmitted electrons. The number of secondary electrons emitted depends on other factors, like the acceleration and the characteristic voltage of the material (e.g., topography of the sample). These signals are responsible for information about the surface of the sample like morphology and topography. The basic distinction between SEM and TEM is closely related to the intensity of the beam and how it is controlled and optimized by optical electronic column. The inelastic scattered electrons, secondary electrons are excluded from analysis through the lens objective. In addition, the speed with which the electrons pass through the electron optic column in TEM is typically much larger compared to SEM. Here the SEM is employed to understand the morphology of solid materials and characterize them in nanoscale. SEM technique commonly offers the image on the nanometer (nm) to micrometer (μm) scale and were specially employed in non-crystalline catalysts to observe distribution and sizes of mesopores. Similarly, TEM is also employed to understand the active metal nanoparticle distribution over the mesoporous solids. For TEM, a grid laden with samples was prepared before measurements. A small amount of each powder sample was dispersed into 500 μL ethanol and sonicated for 30 minutes. 5 to 10 μL from the dispersion was dropped on a carbon-coated grid and dried at for 8 hours before imaging. TEM images and selected area electron diffraction (SAED) patterns were collected using a JEOL JEM-2010 TEM instrument.

High-angle annular dark-field imaging Scanning Transmission electron microscopy (HAADF-STEM) images were taken using FEI/TITAN THEMIS 3391 (80–300) electron microscope.

1.7.10 Inductively coupled plasma atomic emission spectroscopy (ICP-OES)

ICP-OES was performed using a Perkin Elmer Optima 7000 DV instrument. The samples were digested in concentrated aqua regia, followed by dilution with distilled water. In

a typical experiment, 2 mg of the sample was dissolved in 1 ml aqua regia and left overnight (12 hrs) for digestion. The digested sample was then diluted to 10 ml volume with deionized water. The solid particles were separated by thorough centrifugation before measurements. We have also performed the ICP-OES for the electrolyte after the running the electrochemical reactions to understand leaching of metals during reaction.

1.8 Electrochemical reactor for water splitting and fuel cell

1.8.1 Three-electrode two-compartment setup: MicroFlow cell

To achieve the industrial level current density, the HER experiments were carried out in a filter-press type Micro Flow Cell (Electrocell A/S), where a Ti sheet coated with Ir-MMO (iridium-mixed metal oxide) has been used as an Anode plate (Electrocell S/A). An anionic exchange membrane (Fumasep FAB-PK-130) was employed in the case of HER in 1M KOH medium to separate the cathode and anode compartment

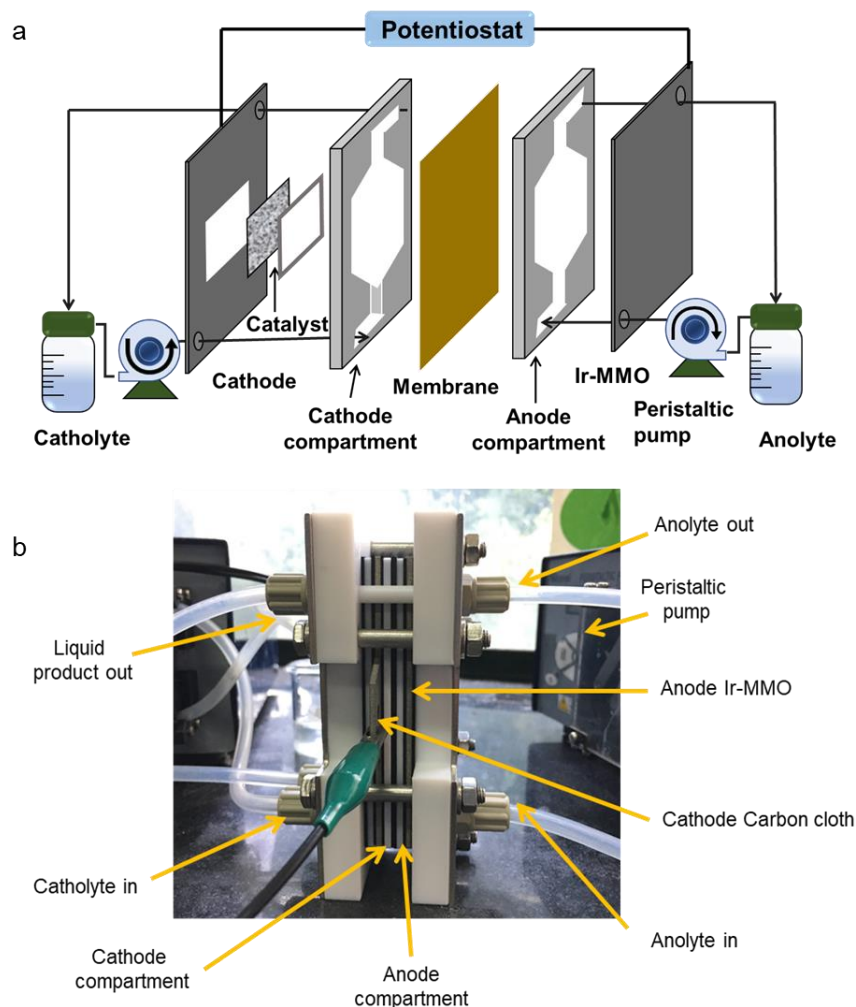


Figure 1.6. (a) Schematic illustration of flow-cell used in the electrochemical HER. (b) Optical photograph of the micro-flow cell used for performing full-cell water splitting activity in flow-cell configuration.

The electrolyte was recirculated continuously into the cell (both in cathode and anode) by two separate peristaltic pumps (Ravel, RH-P100L-100). The catalyst material was coated on the Toray carbon paper electrode and evaluated the high current density experiment for long-term HER process in the flow cell (**Figures 1.6a, 1.6b**). The reference electrode has been calibrated with respect to standard hydrogen electrode and its calibration potential has been calculated from the average potential with respect to zero current in the hydrogen reduction/oxidation region as mentioned. Saturated calomel electrode (SCE) has been used as reference electrode for electrochemical study in 0.5M H₂SO₄ and Mercury/Mercury Oxide (MMO) in 0.5 M KOH in one compartment cell. Ag/AgCl has been employed in case of 1 M KOH electrolyte in case flow cell configuration.

1.8.2 Two-electrode full cell water electrolyser using fabricated MEA

For fabricating the membrane electrode assembly (MEA), the proton conducting membrane was fabricated by using Nafion 212 membrane. The pre-treatment of the membrane was performed in 5% H₂O₂ solution at 80 for 45 minutes followed by 1M H₂SO₄ and DI water and at 80 °C. The pre-treated membrane was stored in DI water for further use while assembling the MEA. The electrode was prepared by brush coating of catalyst slurry on the top surface of a carbon gas diffusion layer (GDL) (carbon cloth). For the cathode, catalyst ink was applied onto the GDL. For the anode, Pt/C (40 wt.%) was used as the catalyst. The MEA was prepared by using the pre-treated Nafion membrane between the anode and cathode electrodes by maintaining an active area of 9 cm². The assembly was hot pressed with a pressure of 1000 psi for 3 min at temperature of 140 °C.

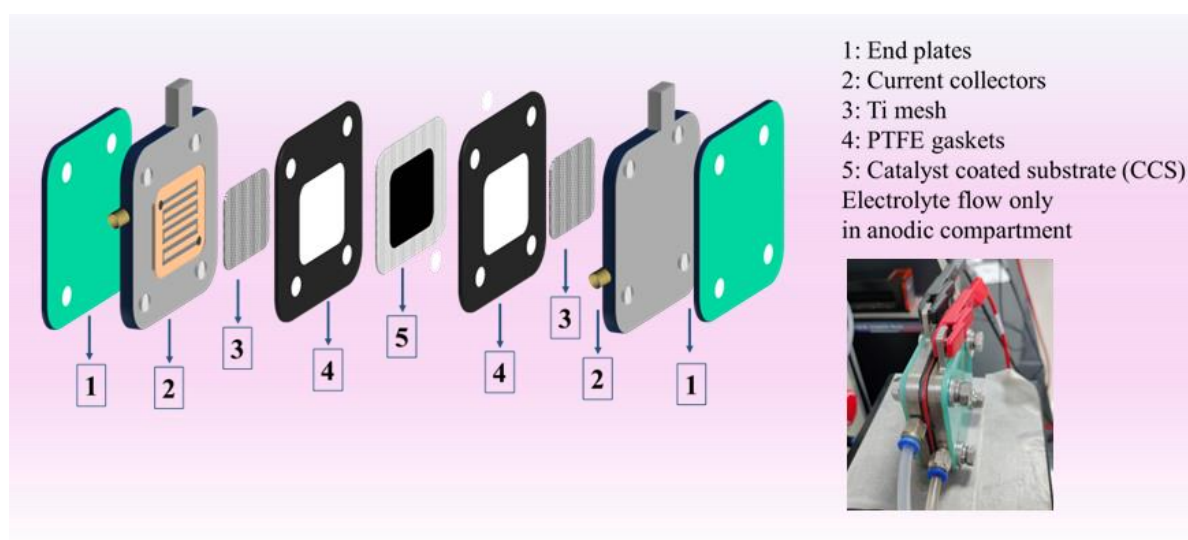


Figure 1.7: Schematic representation of the fixture of water electrolyser. And real image of the setup in the inset figure at right bottom.

The catalyst coated substrate (CCS) is then tested in proton exchange membrane water electrolyser (RSI-AEM-300, Research Supporters India Pvt. Ltd.) using DI water continuous flow only at the anodic chamber and no electrolyte flow was given in the hydrogen generation side (**Figure 1.7**).

1.8.3 RDE setup

All the electrochemical measurements for ORR were done in a 3-electrode set-up comprising of a rotating disk electrode (RDE) as the working electrode, graphite rod counter electrode, and mercury/mercuric oxide electrode (MMO) (for basic media). The catalyst ink was prepared and was drop casted on the commercial 3 mm RDE. Commercial Pt/C (20 wt.%, Sigma Aldrich) were used for comparison of activity since it is the state-of-the-art electrocatalyst. Polarization curves were the anodic sweep of the cyclic voltammograms (CVs) recorded for ORR at a scan rate of 5 mV s^{-1} at 25°C in potential range of 0.4 V to 1.0 V vs. RHE rotating the RDE at 100, 225, 400, 625, 900, 1225, 1600, 2025, and 2500 rpm. Accelerated degradation tests of 50,000 cycles were conducted in the ORR potential range with scan rate of 50 mV/sec. The reference electrode MMO was calibrated with respect to the reversible hydrogen electrode (RHE), using Pt as working and counter electrodes in 0.1 M KOH solution.

1.9 Spectroscopic and analytical techniques for in situ mechanistic studies

1.9.1 In situ electrochemical attenuated total reflection Fourier transform infrared spectroscopy (ATR-FTIR).

In situ electrochemical FT-IR spectroscopic studies were performed using a purged VERTEX FT-IR spectrometer equipped with the A530/P accessory and a mid-band MCT detector. A CaF_2 hemispherical window was used with the working electrode placed 1 mm above the window for the FTIR study. The in situ experimental setups is depicted in **Figure 1.8**. The measurement parameters were 4 cm^{-1} resolution and 100 scans. This setup enabled the detection of ORR intermediate formation and change of adsorption of various intermediates on the electrode surface and within the thin-layer electrolyte.

1.9.2 In situ x-ray absorption Spectroscopic studies

In situ XAS study has been performed in PETRA-III beamline, DESY, Germany. Both potential and time dependent XAS study were carried out. The representation of the in situ XAS set-up with its real-time photograph have been depicted in **Figure 1.9**. The spectra have been detected in the fluorescence mode as seen in **Figure 1.9**.

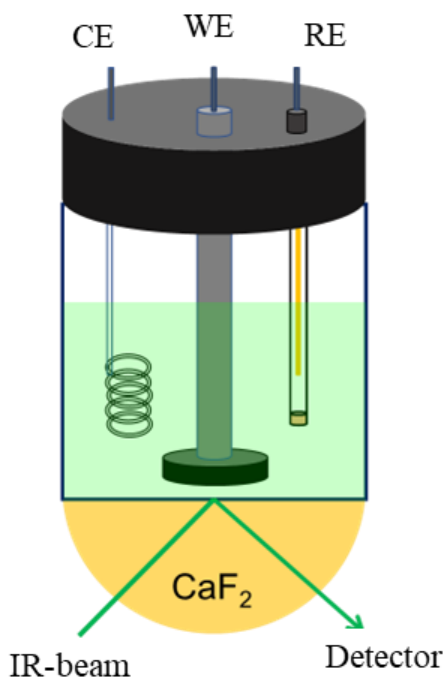


Figure 1.8. Schematic for In-situ IR set up during ORR study performed in 0.1 M KOH. CE, WE, and RE are counter, working and reference electrodes.

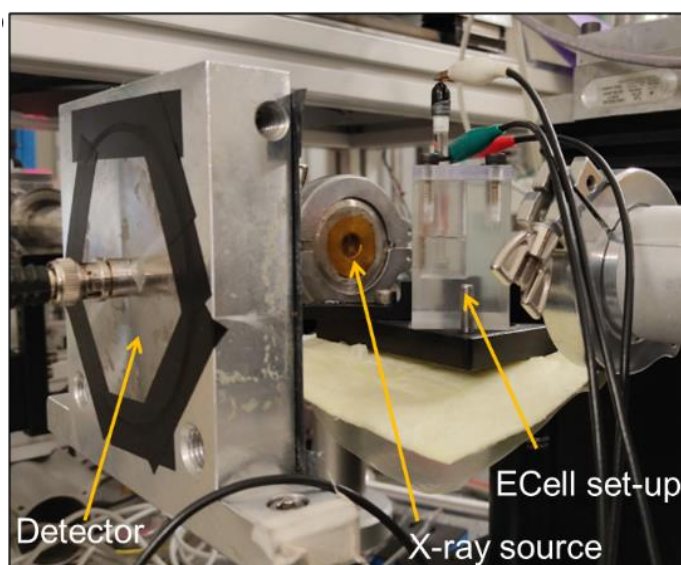


Figure 1.9. Photograph of different components of in situ XAS experiment in the CO_2RR condition.

1.9.3 In situ Raman spectroscopic studies

In situ electrochemical Raman spectroscopic studies were performed using inVia Raman microscope using both 532 nm and 785 nm lasers with 50x magnification. Since better results were observed with 532 nm laser corresponding to electrochemically active site for OER, Ni/Co-oxyhydroxides, we continued all our in-situ Raman experiments using this laser.

We have home-customized a cell where 2 ml 1M KOH was taken so that a thin film of electrolyte covers on the carbon paper having the catalyst coated on it. Pt coil and Ag/AgCl were used as counter and reference electrodes, respectively.

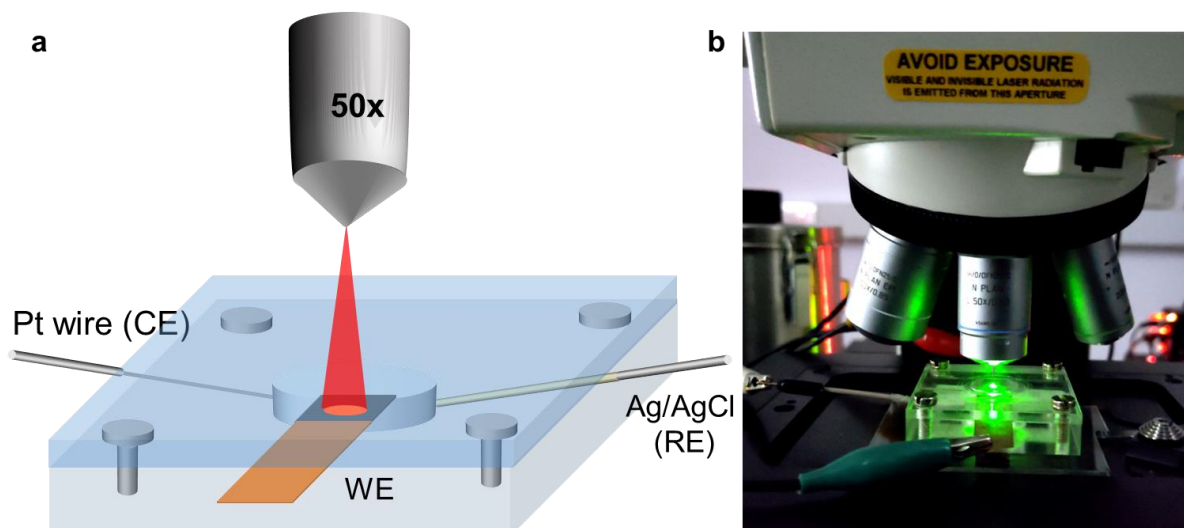


Figure 1.10. (a) Schematic illustration of in-situ Raman spectroscopic study. (b) Photograph of the in-situ Raman spectroscopy set up.

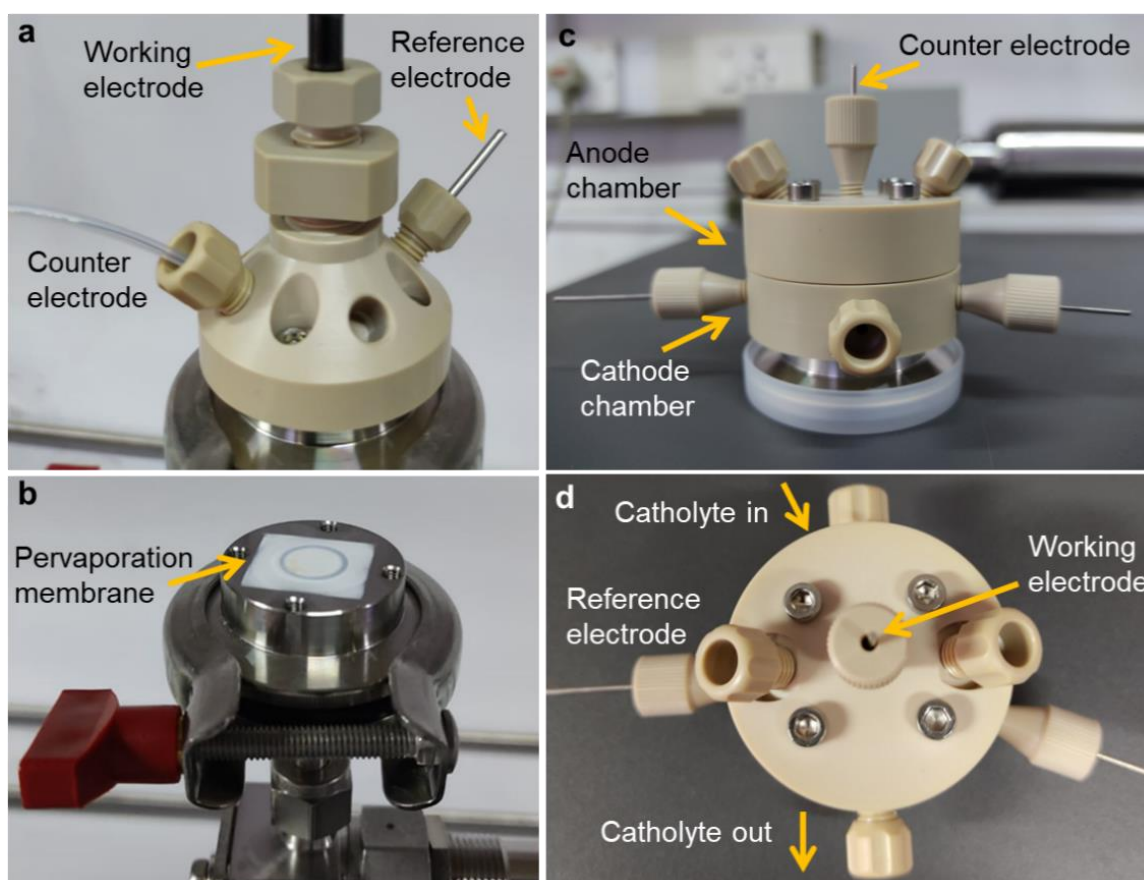


Figure 1.11. Photograph of the (a) DEMS Type-A cell (one compartment), (b) Pervaporation membrane (c-d) DEMS Type-B-cell (two compartments).

CA was conducted for 15-20 mins and Raman data was taken at 2 mins each with data acquisition time of 10 secs and using 0.1 % of the power of the laser. Background data was taken with the complete cell setup with electrolyte and without giving the electrode potential. **Figure 1.10** shows the cell setup during in-situ Raman measurements.

1.9.4 Differential electrochemical mass spectrometry (DEMS)

This analytical technique combines electrochemical half-cell setup with mass spectrometer and helps in the instantaneous detection of volatile or gaseous reactants, intermediates, or products. and used HIDEN Analytical HPR-40 DEMS system with Type A and Type B cells for electrochemical reactions. **Figure 1.11a** and **b** show the images of type A and type B cells, respectively. Type A cell is a single compartments cell whereas type B cell is more advanced. Two compartment cells with electrolyte flow in both chambers are controlled by a dual-syringe pump. Ag/AgCl and Pt wire are used as reference and counter electrodes, respectively. Quadrupole mass spectrometer from RGA series is used with mass range up to 200 amu. Before starting eCO₂RR, the pressure inside the mass spectrometer should be in 10⁻⁶ mbar range. Electrolyte solutions were taken in dual-syringe pump and continuously with 1 ml/min flow rate and CA was conducted at different potentials and mass spectrometry data have continuously been taken with QGA software and we obtained a plot of mass ion current for each constituent with respect to time. Different m/z values corresponding to different intermediate, or product species gave their individual mass ion currents at different times.

1.10 Density functional theory (DFT)

DFT has been used to calculate the formation energies, adsorption energy and strains generated in the system. The calculations have been performed on systems containing many atoms which required the optimization of the electronic/geometric structures prior to any property calculations.

Electronic optimization: It is a single-point energy calculation in which atoms are kept in a fixed position and its corresponding energy at that configuration is obtained.

Geometry optimization: This calculation facilitates perceiving the most stable configuration since the system goes through several configurations driven by minimum energy and investigating the most stable ground state configuration.

Adsorption energy: The first step in any catalytic reaction involves the adsorption of reactant molecules on the catalyst surface. The binding energies for the systems under consideration can be obtained as follows:

$$E_b = E_{(\text{ads/slab})} - E_{(\text{slab})} - E_{(\text{ads})} \quad \text{Eqn. 1.6}$$

where, $E_{(ads/slab)}$ is the energy of the final optimized adsorption configuration on the slab, $E_{(ads)}$ is the energy of the adsorbed molecule and $E_{(slab)}$ is the energy of the catalyst surface.

Descriptors: A descriptor can be defined as an experimentally determined or theoretically calculated catalytic property that can be directly correlated to the reaction thermodynamics or kinetics.

d-band centre is one such descriptor commonly used in catalysis which predicts the chemical reactivity of a metal catalyst in terms of a d-band model. Interaction of the adsorbate molecule with the metal results in bonding and anti-bonding states. The valence state of the adsorbate couples with the metal s states, which then turns to the metal d-states for coupling. The adsorbate interaction with the metal d states separates the metal d-band into bonding and anti-bonding states. Electronic modulation of the catalyst surface will cause either an upward or downward shift of the *d*-band with respect to the Fermi level. Filled bonding states and unfilled anti-bonding states will strengthen adsorbate binding to the catalyst surface hence, metals with higher *d*-band centre relative to the Fermi level will have unfilled antibonding orbitals and have a higher tendency of adsorption in comparison to the metals with lower *d*-band centre.

Adsorption free energy: Gibbs's free energy can indicate the reaction pathways. For example, in HER, hydrogen binding energy (ΔG_{H^*}) is a pivotal factor in determining the activity and kinetics of an electrocatalyst. $\Delta G_{H^*} > 0$ indicates weak hydrogen binding strength and hence, the activation of reactant/intermediate on the catalyst surface is difficult. Hydrogen binding strength is strong when $\Delta G_{H^*} < 0$ and may lead to poisoning since H_2 desorption is not facile and the intermediates will be occupied at the active sites. A maximum value is achievable when $\Delta G_{H^*} = 0$. Not only for HER adsorption energy like oxygen adsorption energy for OER and ORR, CO adsorption energy for eCO_2RR can be used as an activity descriptor for electrocatalysts. Adsorption energy (ΔG) can be calculated as follows:

$$\Delta G = \Delta E + \Delta ZPE - T\Delta S + \Delta G_U + \Delta G(pH) + \Delta G_{field} \quad \text{Eqn. 1.7}$$

where, ΔE is the ground-state energy, ΔZPE is the zero point correction, $T\Delta S$ is the entropy term, ΔG_U is related to the electrode potential, $\Delta G(pH)$ is related to the pH value of the electrolyte and ΔG_{field} is associated with the electrical double layer effect.

Free-energy diagram: The adsorption free energy can only provide information regarding the thermodynamics of the reaction intermediates without considering the kinetics. Free-energy diagram can impart the extra reaction-rate limiting steps that cannot be considered in adsorption free energy calculations. It considers the kinetic barrier between each step in addition to the thermodynamics associated with the adsorption energy of each intermediate.

Since overall reaction rate is dependent on the kinetic barrier between two intermediates, combination of both thermodynamics and kinetics is essential in determining the activity of electrocatalyst. The foundation of the free-energy diagram lies in the adsorption energy (ΔG) calculation.

Work function (ϕ) refers to the minimum work required to extract an electron from the Fermi level of a metal to the outside. The shift of Fermi level with respect to the equilibrium ϕ is dependent on the energy of the electrons in the Fermi level. Increase in ϕ of a metal can be related to higher exchange currents due to enhancement in activation of free energy. It has major implications in the electron and proton transfer rates. When the work function increases the adsorption energy becomes more endergonic.

The above-mentioned experimental techniques have been employed in summarizing our work in **Chapter 2-8**. A combination of both experimental and theoretical techniques has been utilized in comprehending some of our works like **Chapters 2, 3, 4, 6, and 8**. In this thesis we have tried to provide a perception of the structure-property relations combining both experimental and theoretical techniques.

The overall goal of the work consists of the unification of the most important mechanistic understanding of the all the cathodic and anodic reactions of electrochemical water splitting and fuel cell, which includes hydrogen and oxygen evolution reactions, oxygen reduction and ethanol oxidation reactions. The mechanistic understanding is visualized from a perspective of catalyst engineering, identification of appropriate electrocatalytic conditions, and its effect on the reaction mechanism. We have tuned variegated materials using various design strategies like intermetallic synthesis with proper active site selection, tuning neighboring and ensemble effect using doping, lower metal loading with enhanced uniform distribution using different support-based systems and morphology-controlled studies. We have also tuned synthetic conditions from high-temperature long-duration solution phase synthesis to room temperature, ambient condition, and instantaneous synthesis via electrodeposition. Besides material design and catalytic applications, this thesis is also dedicated for understanding the reactive sites, dynamics of the phase and mechanistic pathway via in-situ spectroscopic and analytical techniques for understanding the reaction kinetics which can help in better enhancement in the field of electrocatalysis.

1.11 References

1. Adams, J. A. S.; Mantovani, M. S. M.; Lundell, L. L., Wood versus fossil fuel as a source of excess carbon dioxide in the atmosphere: a preliminary report. *Science* **1977**, *196*, 54.
2. Balat, M., Potential importance of hydrogen as a future solution to environmental and transportation problems. *Int. J. Hydrog. Energy* **2008**, *33*, 4013-4029.
3. Wu, B.; Matian, M.; Offer, G. J., Hydrogen PEMFC system for automotive applications. *Int. J. Low-Carbon Technol.* **2012**, *7*, 28-37.
4. Roy, S.; Cherevotan, A.; Peter, S. C., Thermochemical CO₂ hydrogenation to single carbon products: scientific and technological challenges. *ACS Energy Lett.* **2018**, *3*, 1938-1966.
5. Hattori, M.; Iijima, S.; Nakao, T.; Hosono, H.; Hara, M., Solid solution for catalytic ammonia synthesis from nitrogen and hydrogen gases at 50 °C. *Nat. Commun.* **2020**, *11*, 2001.
6. Bellotti, D.; Rivarolo, M.; Magistri, L.; Massardo, A. F., Feasibility study of methanol production plant from hydrogen and captured carbon dioxide. *J. CO₂ Util.* **2017**, *21*, 132-138.
7. Tucker, W. C.; Chowdhury, P.; Abbott, L. J.; Haskins, J. B., Toward an in-depth material model for cermet nuclear thermal rocket fuel elements. *Nucl. Technol.* **2021**, 1-11.
8. Okolie, J. A.; Patra, B. R.; Mukherjee, A.; Nanda, S.; Dalai, A. K.; Kozinski, J. A., Futuristic applications of hydrogen in energy, biorefining, aerospace, pharmaceuticals and metallurgy. *Int. J. Hydrog. Energy* **2021**, *46*, 8885-8905.
9. Rochlitz, L.; Steinberger, M.; Oechsner, R.; Weber, A.; Schmitz, S.; Schillinger, K.; Wolff, M.; Bayler, A., Second use or recycling of hydrogen waste gas from the semiconductor industry - Economic analysis and technical demonstration of possible pathways. *Int. J. Hydrog. Energy* **2019**, *44*, 17168-17184.
10. Yu, K. M. K.; Tong, W.; West, A.; Cheung, K.; Li, T.; Smith, G.; Guo, Y.; Tsang, S. C. E., Non-syngas direct steam reforming of methanol to hydrogen and carbon dioxide at low temperature. *Nat. Commun.* **2012**, *3*, 1230.
11. Yang, J.; Mohmad, A. R.; Wang, Y.; Fullon, R.; Song, X.; Zhao, F.; Bozkurt, I.; Augustin, M.; Santos, E. J. G.; Shin, H. S.; Zhang, W.; Voiry, D.; Jeong, H. Y.;

- Chhowalla, M., Ultrahigh-current-density niobium disulfide catalysts for hydrogen evolution. *Nat. Mater.* **2019**, *18*, 1309-1314.
12. King, L. A.; Hubert, M. A.; Capuano, C.; Manco, J.; Danilovic, N.; Valle, E.; Hellstern, T. R.; Ayers, K.; Jaramillo, T. F., A non-precious metal hydrogen catalyst in a commercial polymer electrolyte membrane electrolyser. *Nat. Nanotechnol.* **2019**, *14*, 1071-1074.
13. Mo, J.; Wu, S.; Lau, T. H. M.; Kato, R.; Suenaga, K.; Wu, T. S.; Soo, Y. L.; Foord, J. S.; Tsang, S. C. E., Transition metal atom-doped monolayer MoS₂ in a proton-exchange membrane electrolyzer. *Mater. Today Adv.* **2020**, *6*, 100020.
14. Ma, L.; Sui, S.; Zhai, Y., Investigations on high performance proton exchange membrane water electrolyzer. *Int. J. Hydrog. Energy* **2009**, *34*, 678-684.
15. Görgün, H., Dynamic modelling of a proton exchange membrane (PEM) electrolyzer. *Int. J. Hydrog. Energy* **2006**, *31*, 29-38.
16. Tiwari, J. N.; Sultan, S.; Myung, C. W.; Yoon, T.; Li, N.; Ha, M.; Harzandi, A. M.; Park, H. J.; Kim, D. Y.; Chandrasekaran, S. S.; Lee, W. G.; Vij, V.; Kang, H.; Shin, T. J.; Shin, H. S.; Lee, G.; Lee, Z.; Kim, K. S., Multicomponent electrocatalyst with ultralow Pt loading and high hydrogen evolution activity. *Nat. Energy* **2018**, *3*, 773-782.
17. Dotan, H.; Landman, A.; Sheehan, S. W.; Malviya, K. D.; Shter, G. E.; Grave, D. A.; Arzi, Z.; Yehudai, N.; Halabi, M.; Gal, N.; Hadari, N.; Cohen, C.; Rothschild, A.; Grader, G. S., Decoupled hydrogen and oxygen evolution by a two-step electrochemical-chemical cycle for efficient overall water splitting. *Nat. Energy* **2019**, *4*, 786-795.
18. Su, J.; Yang, Y.; Xia, G.; Chen, J.; Jiang, P.; Chen, Q., Ruthenium-cobalt nanoalloys encapsulated in nitrogen-doped graphene as active electrocatalysts for producing hydrogen in alkaline media. *Nat. Commun.* **2017**, *8*, 14969.
19. Xu, Q.; Li, G.; Zhang, Y.; Yang, Q.; Sun, Y.; Felser, C., Descriptor for Hydrogen Evolution Catalysts Based on the Bulk Band Structure Effect. *ACS Catal.* **2020**, *10*, 5042-5048.
20. Slobodkin, I.; Davydova, E.; Sananis, M.; Breytus, A.; Rothschild, A., Electrochemical and chemical cycle for high-efficiency decoupled water splitting in a near-neutral electrolyte. *Nat. Mater.* **2024**, *23*, 398-405.
21. Guo, J.; Zhang, Y.; Zavabeti, A.; Chen, K.; Guo, Y.; Hu, G.; Fan, X.; Li, G. K., Hydrogen production from the air. *Nat. Commun.* **2022**, *13*, 5046.

22. Suryanto, B. H. R.; Wang, Y.; Hocking, R. K.; Adamson, W.; Zhao, C., Overall electrochemical splitting of water at the heterogeneous interface of nickel and iron oxide. *Nat. Commun.* **2019**, *10*, 5599.
23. Wu, D.; Kusada, K.; Yoshioka, S.; Yamamoto, T.; Toriyama, T.; Matsumura, S.; Chen, Y.; Seo, O.; Kim, J.; Song, C.; Hiroi, S.; Sakata, O.; Ina, T.; Kawaguchi, S.; Kubota, Y.; Kobayashi, H.; Kitagawa, H., Efficient overall water splitting in acid with anisotropic metal nanosheets. *Nat. Commun.* **2021**, *12*, 1145.
24. Ren, X.; Wu, T.; Sun, Y.; Li, Y.; Xian, G.; Liu, X.; Shen, C.; Gracia, J.; Gao, H.-J.; Yang, H.; Xu, Z. J., Spin-polarized oxygen evolution reaction under magnetic field. *Nat. Commun.* **2021**, *12*, 2608.
25. Knöppel, J.; Möckl, M.; Escalera-López, D.; Stojanovski, K.; Bierling, M.; Böhm, T.; Thiele, S.; Rzepka, M.; Cherevko, S., On the limitations in assessing stability of oxygen evolution catalysts using aqueous model electrochemical cells. *Nat. Commun.* **2021**, *12*, 2231.
26. Görlin, M.; Halldin Stenlid, J.; Koroidov, S.; Wang, H.-Y.; Börner, M.; Shipilin, M.; Kalinko, A.; Murzin, V.; Safonova, O. V.; Nachtegaal, M.; Uheida, A.; Dutta, J.; Bauer, M.; Nilsson, A.; Diaz-Morales, O., Key activity descriptors of nickel-iron oxygen evolution electrocatalysts in the presence of alkali metal cations. *Nat. Commun.* **2020**, *11*, 6181.
27. Ma, R.; Lin, G.; Zhou, Y.; Liu, Q.; Zhang, T.; Shan, G.; Yang, M.; Wang, J., A review of oxygen reduction mechanisms for metal-free carbon-based electrocatalysts. *Npj Comput. Mater.* **2019**, *5*, 78.
28. Stamenkovic, V. R.; Mun, B. S.; Arenz, M.; Mayrhofer, K. J. J.; Lucas, C. A.; Wang, G.; Ross, P. N.; Markovic, N. M., Trends in electrocatalysis on extended and nanoscale Pt-bimetallic alloy surfaces. *Nat. Mater.* **2007**, *6*, 241-247.
29. Nørskov, J. K.; Rossmeisl, J.; Logadottir, A.; Lindqvist, L.; Kitchin, J. R.; Bligaard, T.; Jónsson, H., Origin of the overpotential for oxygen reduction at a fuel-cell cathode. *The J. Phys. Chem. B* **2004**, *108*, 17886-17892.
30. Zhang, J.; Zhao, Z.; Xia, Z.; Dai, L., A metal-free bifunctional electrocatalyst for oxygen reduction and oxygen evolution reactions. *Nat. Nanotechnol.* **2015**, *10*, 444-452.
31. Liu, J.; Jiao, M.; Lu, L.; Barkholtz, H. M.; Li, Y.; Wang, Y.; Jiang, L.; Wu, Z.; Liu, D.-j.; Zhuang, L.; Ma, C.; Zeng, J.; Zhang, B.; Su, D.; Song, P.; Xing, W.; Xu, W.;

- Wang, Y.; Jiang, Z.; Sun, G., High performance platinum single atom electrocatalyst for oxygen reduction reaction. *Nat. Commun.* **2017**, *8*, 15938.
32. Jiang, R.; Tran, D. T.; McClure, J. P.; Chu, D., A Class of (Pd–Ni–P) Electrocatalysts for the ethanol oxidation reaction in alkaline media. *ACS Catal.* **2014**, *4*, 2577-2586.
33. Rizo, R.; Arán-Ais, R. M.; Padgett, E.; Muller, D. A.; Lázaro, M. J.; Solla-Gullón, J.; Feliu, J. M.; Pastor, E.; Abruña, H. D., Pt-Richcore/Sn-Richsubsurface/Ptskin nanocubes as highly active and stable electrocatalysts for the ethanol oxidation reaction. *J. Am. Chem. Soc.* **2018**, *140*, 3791-3797.
34. Seh, Z. W.; Kibsgaard, J.; Dickens, C. F.; Chorkendorff, I.; Nørskov, J. K.; Jaramillo, T. F., Combining theory and experiment in electrocatalysis: Insights into materials design. *Science* **2017**, *355*, eaad4998.
35. Ashly, P. C.; Sarkar, S.; Sarma, S. C.; Kaur, K.; Gautam, U. K.; Peter, S. C., Compressive strain induced by multiple phase distribution and atomic ordering in PdCu nanoparticles to enhanced ethanol oxidation reaction performance. *J. Power Sources* **2021**, *506*, 230168.
36. Zhou, X.; Ma, Y.; Ge, Y.; Zhu, S.; Cui, Y.; Chen, B.; Liao, L.; Yun, Q.; He, Z.; Long, H.; Li, L.; Huang, B.; Luo, Q.; Zhai, L.; Wang, X.; Bai, L.; Wang, G.; Guan, Z.; Chen, Y.; Lee, C.-S.; Wang, J.; Ling, C.; Shao, M.; Fan, Z.; Zhang, H., Preparation of Au@Pd core-shell nanorods with fcc-2H-fcc heterophase for highly efficient electrocatalytic alcohol oxidation. *J. Am. Chem. Soc.* **2022**, *144*, 547-555.
37. Huang, J.; Buonsanti, R., Colloidal nanocrystals as heterogeneous catalysts for electrochemical CO₂ conversion. *Chem. Mater.* **2019**, *31*, 13-25.
38. Yang, Y.; Yue, T.; Wang, Y.; Yang, Z.; Jin, X., Effects of morphology on electrocatalytic activity of CeO₂ nanomaterials. *Microchem. J.* **2019**, *148*, 42-50.
39. Choi, C.; Kwon, S.; Cheng, T.; Xu, M.; Tieu, P.; Lee, C.; Cai, J.; Lee, H. M.; Pan, X.; Duan, X.; Goddard, W. A.; Huang, Y., Highly active and stable stepped Cu surface for enhanced electrochemical CO₂ reduction to C₂H₄. *Nat. Catal.* **2020**, *3*, 804-812.
40. Mi, R.; Li, D.; Hu, Z.; Yang, R. T., Morphology effects of CeO₂ nanomaterials on the catalytic combustion of toluene: a combined kinetics and diffuse reflectance infrared Fourier transform spectroscopy study. *ACS Catal.* **2021**, *11*, 7876-7889.
41. Li, Z.; Zhang, X.; Cheng, H.; Liu, J.; Shao, M.; Wei, M.; Evans, D. G.; Zhang, H.; Duan, X., Confined synthesis of 2D nanostructured materials toward electrocatalysis. *Adv. Energy Mater.* **2020**, *10*, 1900486.

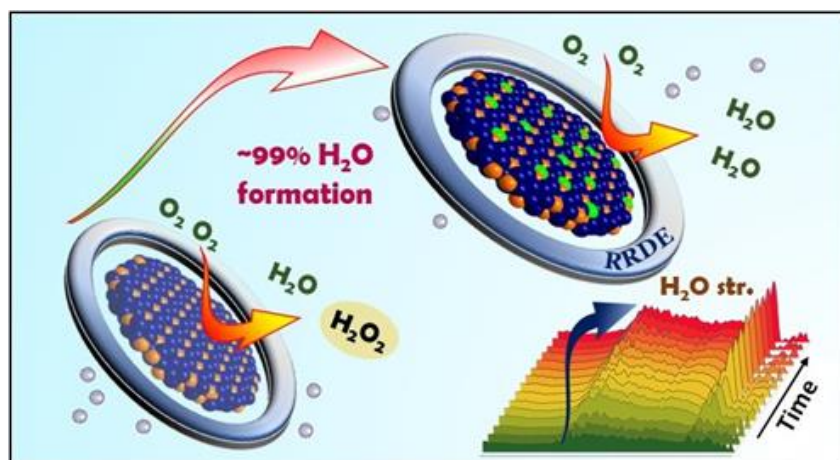
42. Liang, W.; Wang, Y.; Zhao, L.; Guo, W.; Li, D.; Qin, W.; Wu, H.; Sun, Y.; Jiang, L., 3D Anisotropic Au@Pt–Pd hemispherical nanostructures as efficient electrocatalysts for methanol, ethanol, and formic acid oxidation reaction. *Adv. Mater.* **2021**, *33*, 2100713.
43. Wang, H.; Li, X.-B.; Gao, L.; Wu, H.-L.; Yang, J.; Cai, L.; Ma, T.-B.; Tung, C.-H.; Wu, L.-Z.; Yu, G., Three-dimensional graphene networks with abundant sharp edge sites for efficient electrocatalytic hydrogen evolution. *Angew. Chem. Int. Ed.* **2018**, *57*, 192-197.
44. Tian, N.; Zhou, Z.-Y.; Sun, S.-G.; Ding, Y.; Wang, Z. L., Synthesis of tetrahedral platinum nanocrystals with high-index facets and high electro-oxidation activity. *Science* **2007**, *316*, 732-735.
45. Xiao, M.; Zhu, J.; Li, G.; Li, N.; Li, S.; Cano, Z. P.; Ma, L.; Cui, P.; Xu, P.; Jiang, G.; Jin, H.; Wang, S.; Wu, T.; Lu, J.; Yu, A.; Su, D.; Chen, Z., A single-atom iridium heterogeneous catalyst in oxygen reduction reaction. *Angew. Chem. Int. Ed.* **2019**, *58*, 9640-9645.
46. Bagchi, D.; Phukan, N.; Sarkar, S.; Das, R.; Ray, B.; Bellare, P.; Ravishankar, N.; Peter, S. C., Ultralow non-noble metal loaded MOF derived bi-functional electrocatalysts for the oxygen evolution and reduction reactions. *J. Mater. Chem. A* **2021**, *9*, 9319-9326.
47. Bagchi, D.; Riyaz, M.; Raj, J.; Roy, S.; Singh, A. K.; Cherevotan, A.; Vinod, C. P.; Peter, S. C., Unraveling the cooperative mechanisms in ultralow copper-loaded WC@NGC for enhanced CO₂ electroreduction to acetic acid. *Chem. Mater.* **2024**, *36*, 3464-3476.
48. Zhang, J.; Yang, H.; Liu, B., Coordination engineering of single-atom catalysts for the oxygen reduction reaction: a review. *Adv. Energy Mater.* **2021**, *11*, 2002473.
49. Wan, X.; Shui, J., Exploring durable single-atom catalysts for proton exchange membrane fuel cells. *ACS Energy Lett.* **2022**, *7*, 1696-1705.
50. Wang, M.; Dong, C.-L.; Huang, Y.-C.; Shen, S., Operando spectral and electrochemical investigation into the heterophase simulated active species transformation in transition-metal sulfides for efficient electrocatalytic oxygen evolution. *ACS Catal.* **2020**, *10*, 1855-1864.
51. Ma, X.; Ma, C.; Xia, J.; Han, S.; Zhang, H.; He, C.; Feng, F.; Lin, G.; Cao, W.; Meng, X.; Zhu, L.; Zhu, X.; Wang, A.-L.; Yin, H.; Lu, Q., Heterophase intermetallic

- compounds for electrocatalytic hydrogen production at industrial-scale current densities. *J. Am. Chem. Soc.* **2024**.
52. Zhou, X.; Ma, Y.; Ge, Y.; Zhu, S.; Cui, Y.; Chen, B.; Liao, L.; Yun, Q.; He, Z.; Long, H.; Li, L.; Huang, B.; Luo, Q.; Zhai, L.; Wang, X.; Bai, L.; Wang, G.; Guan, Z.; Chen, Y.; Lee, C.-S.; Wang, J.; Ling, C.; Shao, M.; Fan, Z.; Zhang, H., Preparation of Au@Pd core-shell nanorods with fcc-2H-fcc heterophase for highly efficient electrocatalytic alcohol oxidation. *J. Am. Chem. Soc.* **2022**, *144*, 547-555.
53. Zhao, X.; Sasaki, K., Advanced Pt-Based core-shell electrocatalysts for fuel cell cathodes. *Acc. Chem. Res.* **2022**, *55*, 1226-1236.
54. Tian, Z.; Du, S.; Cheng, X.; Zhang, J.; Li, F.; Chen, Z.; Lv, Y.; Zhu, Y.; Liu, G., The role of oxygen vacancy in anatase to rutile transformation of TiO₂. *Cryst. Growth Des.* **2022**, *22*, 6852-6856.
55. Liu, X.; Zhou, K.; Wang, L.; Wang, B.; Li, Y., Oxygen vacancy clusters promoting reducibility and activity of ceria nanorods. *J. Am. Chem. Soc.* **2009**, *131*, 3140-3141.
56. Liu, L.; He, C.-C.; Zeng, J.; Peng, Y.-H.; Chen, W.-Y.; Zhao, Y.-J.; Yang, X.-B., Theoretical study of oxygen-vacancy distribution in In₂O₃. *J. Phys. Chem. C* **2021**, *125*, 7077-7085.
57. Mondal, S.; Sarkar, S.; Riyaz, M.; Kar, M.; Fortuin, A. C.; Vashishth, S.; Das, R.; Eswaramoorthy, M.; Kramer, D.; Peter, S. C., Nitrogen doping-induced structural distortion in LaMnO₃ enhances oxygen reduction and oxygen evolution reactions. *ACS Energy Lett.* **2024**, *9*, 3440-3447.
58. Juntian NIU, C. Z., Haiyu LIU, Yan JIN, Riguan ZHANG, Enhanced performance of oxygen vacancies on CO₂ adsorption and activation over different phases of ZrO₂. **2023**, *17*, 545-554.
59. Wang, M.; Shen, M.; Jin, X.; Tian, J.; Li, M.; Zhou, Y.; Zhang, L.; Li, Y.; Shi, J., Oxygen vacancy generation and stabilization in CeO_{2-x} by Cu introduction with improved CO₂ photocatalytic reduction activity. *ACS Catal.* **2019**, *9*, 4573-4581.
60. Liu, L.-M.; Crawford, P.; Hu, P., The interaction between adsorbed OH and O₂ on TiO₂ surfaces. *Prog. Surf. Sci.* **2009**, *84*, 155-176.
61. Zhao, X.; Xi, C.; Zhang, R.; Song, L.; Wang, C.; Spendelow, J. S.; Frenkel, A. I.; Yang, J.; Xin, H. L.; Sasaki, K., High-performance nitrogen-doped intermetallic PtNi catalyst for the oxygen reduction reaction. *ACS Catal.* **2020**, *10*, 10637-10645.
62. Zhang, A.; Liang, Y.; Zhang, H.; Geng, Z.; Zeng, J., Doping regulation in transition metal compounds for electrocatalysis. *Chem. Soc. Rev.* **2021**, *50*, 9817-9844.

63. Gumeniuk, R., Chapter 304 - Structural and physical properties of remeika phases. In *Handbook on the Physics and Chemistry of Rare Earths*, Bünzli, J.-C. G.; Pecharsky, V. K., Eds. Elsevier: 2018; Vol. 54, pp 43-143.
64. Nash, A.; Nash, P., The Ni-Pd (nickel-palladium) system. *Bull. alloy phase diagr.* **1984**, 5, 446-450.
65. Gamler, J. T. L.; Ashberry, H. M.; Skrabalak, S. E.; Koczkur, K. M., Random alloyed versus intermetallic nanoparticles: a comparison of electrocatalytic performance. *Adv. Mater.* **2018**, 30, 1801563.
66. Antolini, E., Alloy vs. intermetallic compounds: Effect of the ordering on the electrocatalytic activity for oxygen reduction and the stability of low temperature fuel cell catalysts. *Appl. Catal. B: Environ.* **2017**, 217, 201-213.
67. Yan, Y.; Du, J. S.; Gilroy, K. D.; Yang, D.; Xia, Y.; Zhang, H., Intermetallic nanocrystals: syntheses and catalytic applications. *Adv. Mater.* **2017**, 29, 1605997.
68. Luo, M.; Sun, Y.; Wang, L.; Guo, S., Tuning multimetallic ordered intermetallic nanocrystals for efficient energy electrocatalysis. *Adv. Energy Mater.* **2017**, 7, 1602073.
69. Ma, Y.; Chen, M.; Geng, H.; Dong, H.; Wu, P.; Li, X.; Guan, G.; Wang, T., Synergistically tuning electronic structure of porous β -Mo₂C Spheres by Co doping and Mo-vacancies defect engineering for optimizing hydrogen evolution reaction activity. *Adv. Funct. Mater.* **2020**, 30, 2000561.
70. Schmal, M.; Moya, S., Nanostructured catalysts. in *heterogeneous catalysis and its industrial applications*, Springer: 2016; pp 285-327.
71. Bond, G. C.; Keane, M. A.; Kral, H.; Lercher, J. A. J. C. R., Compensation phenomena in heterogeneous catalysis: general principles and a possible explanation. *J. Catal. Rev.* **2000**, 42, 323-383.

Chapter 2

***In-Situ* Mechanistic Insights for Oxygen Reduction Reaction in Chemically Modulated Ordered Intermetallic Catalyst Promoting Complete Electron Transfer**



Soumi Mondal; Debabrata Bagchi; Mohd Riyaz; Shreya Sarkar; Ashutosh Kumar Singh; Vinod C Prabhakaran; Sebastian C. Peter, *J. Am. Chem. Soc.*, **2022**, *144*, 11859–11869

Summary

The well-known limitation of alkaline fuel cells is relying on slack kinetics of the cathodic half-cell reaction, oxygen reduction reaction (ORR). Platinum, being the most active ORR catalyst, is still facing challenges due to its corrosive nature, and sluggish kinetics. Many novel approaches of substituting Pt have been reported, which suffer from stability issue even after mighty modifications. Designing an extremely stable, but unexplored ordered intermetallic structure, Pd₂Ge, and tuning the electronic environment of the active sites, by site-selective Pt-substitution, to crossover the hurdle of alkaline ORR is the main motive of this paper. Platinum atoms substituting at specific Pd position leads to Pt_{0.2}Pd_{1.8}Ge demonstrated half-wave potential ($E_{1/2}$) of 0.95 V vs RHE which outperforms state-of-the-art catalyst 20% Pt/C. The mass activity (MA) of Pt_{0.2}Pd_{1.8}Ge is 320 mA/mg_{Pt}, which is almost 3.2 times better than Pt/C. $E_{1/2}$ and MA remained unaltered even after 50,000 accelerated degradation test (ADT) cycles which makes it a promising stable catalyst with its activity better than the state-of-the-art Pt/C. The undesired 2e⁻ transfer ORR forming hydrogen peroxide (H₂O₂) is diminished in Pt_{0.2}Pd_{1.8}Ge as visible from rotating-ring disk electrode (RRDE) experiment, spectroscopically visualized by *in-situ* Fourier transform infrared (FT-IR) spectroscopy and supported by computational studies. The effect of Pt substitution on Pd has been properly manifested by X-ray absorption spectroscopy (XAS) and X-ray photoelectron spectroscopy (XPS). The swinging of oxidation state of atomic sites of Pt_{0.2}Pd_{1.8}Ge during reaction is probed by *in-situ* XAS which efficiently enhances 4e⁻ transfer producing extremely low percentage of H₂O₂.

Table of Contents

2.1	Introduction.....	41
2.2	Experimental Details	43
2.2.1	Chemicals and reagents	43
2.2.2	Synthesis of Pd ₂ Ge, Pd _{1.8} Ge and Pt _{0.2} Pd _{1.8} Ge	43
2.3	Characterization.....	43
2.3.1	Powder X-ray Diffraction (PXRD)	43
2.3.2	Scanning electron microscopy (SEM) and Energy Dispersive Spectrum (EDS)	43
2.3.3	Transmission Electron Microscope (TEM)	44
2.3.4	Inductively coupled plasma atomic emission spectroscopy (ICP-OES)	44
2.3.5	X-ray Photoelectron Spectroscopy (XPS)	44
2.3.6	X-ray Absorption Spectroscopy (XAS)	44
2.3.7	In situ XANES and EXAFS during electrochemistry	45
2.3.8	In situ attenuated total reflection Fourier transformed infra-red) ATR-FTIR) spectroscopy	45
2.3.9	Electrochemical Oxygen Reduction Reaction (ORR)	45
2.3.10	Rotating ring disk electrode experiment (RRDE)	46
2.3.11	Theoretical calculations	46
2.4	Results & Discussion	47
2.4.1	Structural insights and microscopic probing	47
2.4.2	Electrochemical Oxygen reduction (ORR)	50
2.4.3	Oxidation state and local structure by XAS	54
2.4.4	Surface oxidation state by XPS	56
2.4.5	Structural changes via operando XAS and post-ORR XPS	58
2.4.6	Deciphering reaction kinetics from operando FT-IR spectroscopy and computational studies.....	60
2.5	Conclusion.....	71
2.6	References	72

2.1 Introduction

The demographic expansion has led to an enormous consumption of fossil fuels, and gushing in toxic gases like carbon dioxide, to the environment, causing global warming.¹ Such a crisis has led to proliferating scientific research and success erupted in the form of fuel cells,² carbon dioxide reduction³ and metal air batteries⁴ for decreasing fossil fuel usage and eating up the greenhouse gas, and power storage, respectively. Oxygen reduction reaction (ORR) is the cathodic part for fuel cells and metal air batteries which is a slow process and research is being carried out to enhance ORR kinetics. For doing so, the mechanism of ORR needs to be deciphered which requires operando probing of ORR by different spectroscopic techniques. Despite being the most active ORR electrocatalyst, commercially available Pt/C and Pd/C catalysts are well-known for ORR catalysis but faces challenges of exorbitant price, less availability, and short-term stability due to OH poisoning.⁵ Recent advances are made in catalyst synthesis such as alloy formation,⁶⁻⁸ intermetallic synthesis,⁹ core@shell structures,¹⁰ and shape and size control of nanoparticles,¹¹ to enhance the stability up to long cycles in harsh fuel-cell conditions.⁷

Combining d-block or p-block elements changes the d-electron occupancy of the noble metals, the metal-metal interatomic distance, leading to down- or up-shift of d-band center modifying the electronic structure, which improves the intermediate binding on active sites and changes the activation barrier of the reaction. The first step of ORR is O-O double bond cleavage which is having bond energy of 498 kJ/mol.¹² The O-O bond cleavage is easier when the surface is having charge separation which polarizes the neutral O₂ molecule.^{12, 13} Many attempts were employed to develop Pt- or Pd-based catalysts for ORR.¹⁴ Shape-controlled octahedral Pt-Ni alloy¹⁵ where annealing enhanced performance due to surface Pt enrichment, architecture control Pt-Ni nano-frames,¹⁶ strengthening vertex of PtCu nano frames by adding Co and forming ternary alloy PtCuCo with large stability,¹⁷ are notable morphology controlled highly active ORR catalysts with stability up to 10,000 ADT cycles. Interface engineering between noble metal on metal carbide, Pd/Mo₂C has tuned electronic state to provide very high mass activity and onset potential, but ended by having a stability of 5,000 ADT cycles.¹⁸ Ordered intermetallic PtFe has shown very high mass activity but with poor stability.¹⁹ Various MOF and COF-based systems are reported with active metal are atomically dispersed with good activity.^{20, 21} It is necessary to not only increase the activity of the catalyst, but also focusing on its stability in harsh alkaline conditions without hampering highly selective reaction mechanisms.

ORR mechanism proceeds via incomplete ($2e^-$) transfer and complete ($4e^-$) transfer forming H_2O_2 and H_2O as the final products, respectively. Four electron transfer mechanism is the most desired one in fuel cell applications since that involves higher electron transfer and generating higher power. This reaction mechanism selectivity is dictated by the different ORR intermediate binding on the active sites of the catalyst.^{12, 22} If OOH^* intermediate is strongly adsorbed, peroxide desorption is not allowed, and O-O bond is made weaker. Thus, O-O bond cleavage occurs leading to OH desorption and adsorbed O atom further gets protonated followed by further electron transfer. Whether the OH adsorbed intermediate will desorb or protonate to form water, or it gets strongly adsorbed on the surface, dictates the stability of the catalyst in long-term reaction. Blocking of the active sites by strongly adsorbed OH is very common in Pt and Pd sites which decreases their stability.²³⁻²⁵ By tuning the active sites electronically using other heteroatoms in coordination (ligand effect), the adsorption energy of OH^* can be decreased, which in turn reduces the poisoning effect. However, the mechanistic insight of ORR pathway and the role of each metal sites are still not clear since exploration of reaction mechanism by operando techniques is still not extensively achieved. In this work, two operando spectroscopic techniques (in situ infra-red (IR) and in situ X-ray absorption spectroscopy (XAS)) explicitly demonstrate the mechanism, identify the active sites, and charge transfer of the reaction.

It has been found previously that Ge modified the electronic structure and oxophilic nature of the intermetallic catalyst.^{26,27} It is reported that Ge is stable in alkaline conditions and under reduction potentials of ORR as well.^{28, 29} The intermetallic Pd_2Ge has been studied for ORR with site selective substitution of only 10% of Pd atoms by Pt atoms which showed a dramatic improvement of half-wave potential to 0.95 V vs. RHE with negligible amount of hydrogen peroxide (1.4%) formation for a very high durability up to 50,000 cycles. We have conducted bulk, local and surface structural characterizations by powder X-ray diffraction (PXRD), x-ray absorption spectroscopy (XAS), and x-ray photoelectron spectroscopy (XPS) analyses, respectively. We have performed real-time monitoring by in-situ spectroscopic studies like operando FT-IR spectroscopy, in-situ X-ray absorption near edge structure (XANES) and X-ray absorption fine structure (XAFS) analysis. In-situ XAS and FTIR techniques have explored the reaction kinetics followed by ex-situ ORR characterizations such as post-electrochemical XPS and XRD are also performed to analyze the structural evolution under alkaline ORR conditions. The driving force for the exceptional ORR activity studied from various experiments are correlated with the theoretical calculations.

2.2 Experimental Details

2.2.1 Chemicals and reagents

Potassium tetrachloropalladate (K_2PdCl_4) and germanium tetrachloride ($GeCl_4$) were purchased from Alfa-Aesar. Nafion binder (5 wt.%) were purchased from Sigma-Aldrich, and tri-ethylene glycol (TEG) were purchased from Merck. All the chemicals (more than 99% purity) were used as purchased without any further purification. Millipore water of conductivity 18.2 $M\Omega cm$ was used for the synthesis and all electrochemical studies.

2.2.2 Synthesis of Pd_2Ge , $Pd_{1.8}Ge$ and $Pt_{0.2}Pd_{1.8}Ge$

In a typical solvothermal reaction, 0.2 mmol of potassium tetrachloropalladate (K_2PdCl_4), and 0.1 mmol of germanium(IV) chloride ($GeCl_4$) for Pd_2Ge , and 0.8 mL of superhydride solution (reducing agent) were mixed in 16 mL of TEG. Similarly, 0.18 mmol of K_2PdCl_4 with taken in second and third autoclaves, along with 0.02 mmol of K_2PtCl_4 as dopant in the third autoclave. In three autoclaves, solid crystalline K_2PdCl_4 salt (along with K_2PtCl_4 salt in third autoclave) is first granulated in mortar pestle for good dissolution, and then dissolved in 16 ml TEG and magnetically stirred until dissolved completely. After complete dissolution, 11.4 mL of $GeCl_4$ is added using a micropipette in all three autoclaves. The mixture is continuously stirred for 30 mins. After that, 0.8 mL superhydride solution ($Li(C_2H_5)_3BH$) is added using a syringe and again stirred in an orbital shaker for 30-45 mins. The autoclaves were kept at 220 °C for 24 hours. The final product was washed and centrifuged several times with ethanol, and the obtained product was dried and used for further characterizations.

2.3 Characterization

2.3.1 Powder x-ray diffraction (PXRD)

PXRD measurements were done at room temperature on a Rigaku Miniflex X-ray diffractometer with Cu- K_α X-ray source ($\lambda = 1.5406 \text{ \AA}$), equipped with a position sensitive detector in the angular range $20^\circ \leq 2\theta \leq 90^\circ$ with the step size 0.02° and scan rate of 0.5 s/step calibrated against corundum standards. The experimental XRD patterns were compared to the patterns simulated from the data reported in the literature.

2.3.2 Scanning electron microscopy (SEM) and energy dispersive spectrum (EDS)

The SEM measurement was performed using Leica scanning electron microscopy equipped with an energy-dispersive X-ray spectroscopy (EDAX) instrument (Bruker 120 eV EDAX instrument). Data were acquired by using an accelerating voltage of 15 kV, and the typical time taken for data accumulation is 100 s. The elemental analyses were performed using

the P/B-ZAF standardless method (where P/B = peak to background model, Z = atomic no. correction factor, A = absorption correction factor, and F = fluorescence factor) for Cu, Ga at multiple areas on the sample coated Si wafer.

2.3.3 Transmission electron microscope (TEM)

Transmission electron microscope (TEM), high-resolution TEM (HRTEM) images and selected area electron diffraction (SAED) patterns were collected using TECNAI and JEOL 200 kV TEMs. TEM samples for these measurements were prepared by sonicating the nanocrystalline powders in ethanol and dropping a small volume onto a carbon-coated copper grid.

2.3.4 Inductively coupled plasma atomic emission spectroscopy (ICP-OES)

ICP-OES was performed using a Perkin Elmer Optima 7000 DV instrument. The samples were digested in concentrated aqua regia, followed by dilution with distilled water. In a typical experiment, 2 mg of the sample was dissolved in 1 ml aqua regia and left overnight (12 hrs) for digestion. The digested sample was then diluted to 10 ml volume with deionized water. The solid particles were separated by thorough centrifugation before measurements.

2.3.5 X-ray photoelectron spectroscopy (XPS)

XPS measurements were carried out using Thermo K-alpha+ spectrometer using micro focused and monochromated Al K α radiation with energy 1486.6 eV. The pass energy for the spectral acquisition was kept at 50 eV for individual core-levels. The electron flood gun was utilized for providing charge compensation during data acquisition. Further, the individual core-level spectra were checked for charging using C1s at 284.6 eV as standard and corrected if needed. The peak fitting of the individual core-levels was done using CASA XPS software with a Shirley type background.

2.3.6 X-ray absorption spectroscopy (XAS)

X-ray absorption near-edge spectroscopy (XANES) and quick-Extended X-ray Absorption Fine Structure (quick-EXAFS) experiments at 300 K were performed at PETRA III, beamline P64, of DESY, Germany. Measurements of Pd-K and In-K at ambient pressure were performed in fluorescence as well as transmission mode using gas ionization chambers to monitor the incident and transmitted X-ray intensities. Monochromatic X-rays were obtained using a Si (111) double crystal monochromator, which was calibrated by defining the inflection point (first derivative maxima) of Cu foil as 8980.5 eV. The beam was focused by employing a Kirkpatrick-Baez (K-B) mirror optic. A rhodium-coated X-ray mirror was used to suppress

higher-order harmonics. A CCD detector was used to record the transmitted signals. Pellets for the ex-situ measurements were made by homogeneously mixing the sample with an inert cellulose matrix to obtain an X-ray absorption edge jump close to one.

2.3.7 In situ XANES and EXAFS during electrochemistry

In situ XAS was measured using home-made customized cell set up as shown in **Figure 2.1a** under ORR conditions.

2.3.8 In situ attenuated total reflection Fourier transformed infra-red (ATR-FTIR) spectroscopy

In situ electrochemical FT-IR spectroscopic studies were performed using a purged VERTEX FT-IR spectrometer equipped with the A530/P accessory and a mid-band MCT detector. A CaF_2 hemispherical window was used with the working electrode placed 1 mm above the window for the FTIR study. The in situ experimental setups is depicted in **Figure 2.1b**. The measurement parameters were 4 cm^{-1} resolution and 100 scans. This setup enabled the detection of ORR intermediate formation and change of adsorption of various intermediates on the electrode surface and within the thin-layer electrolyte.

2.3.9 Electrochemical oxygen reduction reaction (ORR)

All the electrochemical measurements were done in a 3-electrode set-up comprising of a rotating disk electrode (RDE) as the working electrode, graphite rod counter electrode, and mercury/mercuric oxide electrode (MMO) (for basic media).

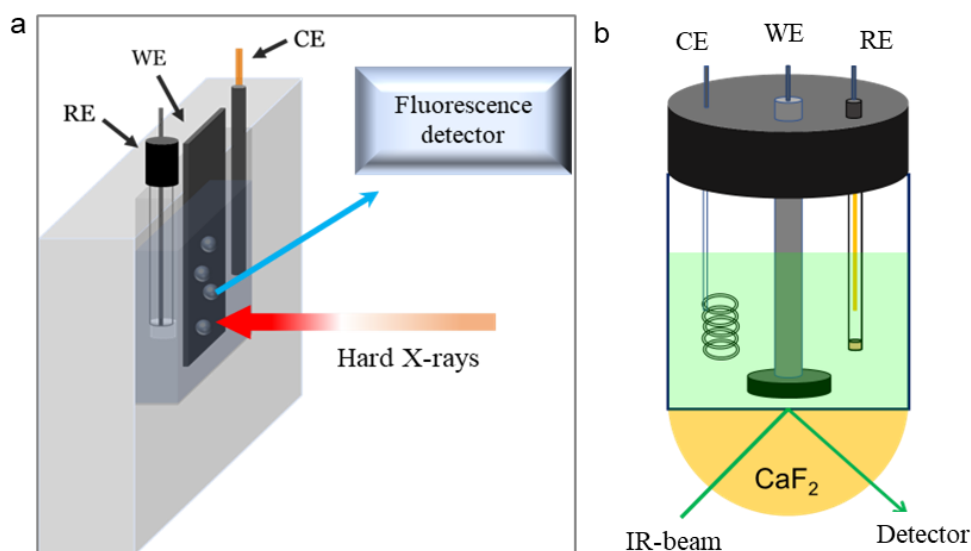


Figure 2.1. (a) Schematic of in-situ XAS set up for ORR study performed in 0.1M KOH. (b) Schematic for In-situ IR set up during ORR study performed in 0.1M KOH. CE, WE, and RE are counter, working and reference electrodes.

The catalyst ink was prepared using 1.6 mg catalyst + 0.4 mg Vulcan in 450 ml of mixed solvent (IPA: water = 1:1) + 50 μL of 1 wt.% Nafion used as binder. 5 μL of the catalyst ink was drop casted on the commercial 3 mm RDE. Commercial Pt/C (20 wt.%, Sigma Aldrich) were used for comparison of activity since it is the state-of-the-art electrocatalyst. Polarization curves were the anodic sweep of the cyclic voltammograms (CVs) recorded for ORR at a scan rate of 5 mV s^{-1} at 25 $^{\circ}\text{C}$ in potential range of 0.4 V to 1.0 V vs. RHE rotating the RDE at 100, 225, 400, 625, 900, 1225, 1600, 2025, and 2500 rpm. The electrolyte solution was deaerated by purging nitrogen gas into the solution at least for 30 min before each experiment and then N_2 saturated CV was conducted, after which O_2 is being purged for an hour to start taking CVs in ORR conditions. The polarization curves in N_2 and O_2 saturated solutions are taken in 1600 rpm rotating speed of RDE. Accelerated degradation tests of 50,000 cycles were conducted in the potential range of 0.7 V to 1.0 V vs. RHE with scan rate of 50 mV/sec. The reference electrode MMO was calibrated with respect to the reversible hydrogen electrode (RHE), using Pt as working and counter electrodes in 0.1 M KOH solution. The value obtained is as follows: for 0.1M KOH alkaline medium, $E_{\text{RHE}} = E_{\text{MMO}} + 0.911 \text{ V}$.

2.3.10 Rotating ring disk electrode experiment (RRDE)

Selectivity towards H_2O was checked using rotating ring disk electrode (RRDE) where ring as platinum and disk as glassy carbon with 4 mm diameter and keeping all other experimental conditions similar, graphite rod as the counter electrode and Hg/HgO as the reference electrode. RDE was carried out from 0.2 to 1.0 V (vs. RHE) at a rotation rate ranging from 100 to 3600 rpm in O_2 saturated 0.1 M KOH. In the RRDE experiment, the percentage of H_2O_2 produced ($X_{\text{H}_2\text{O}_2}$) and the corresponding electron transfer numbers during ORR (n) can be determined from the following equations, respectively:

$$\text{H}_2\text{O}_2 \% = 200 \times \frac{\text{Ir}/\text{N}}{\text{Id} + \text{Ir}/\text{N}} \quad (\text{Eqn. 2.1})$$

2.3.11 Theoretical calculations

DFT calculations were performed using PWSCF v.5.1 code embedded in Quantum Espresso suite for quantum simulation of materials³⁰. The PWSCF calculations were performed using generalized gradient approximation (GGA) with PBE³¹ exchange-correlation functional and ultrasoft pseudopotential. Kinetic energy (E_k) cut-off for the wavefunctions of 60.0 Ry was used to truncate the plane-wave basis. Furthermore, Gaussian smearing was used with a degauss value of 0.005 Ry. Systems were relaxed until the Hellmann–Feynman forces on

each atom are in the order of 10^{-2} - 10^{-3} eV/Å. The calculated Fermi energy (E_f) was set to zero for all the DOS plots. A vacuum of 14 Å was used to avoid any interaction among the slabs. The free energies were approximated using the computational hydrogen electrode (CHE) model proposed by Norskov et al.³ and the change in free energies (ΔG) was calculated as:

$$\Delta G = \Delta E + \Delta ZPE - T\Delta S \quad (\text{Eqn. 2.2})$$

Where ΔE is the DFT calculated change in reaction energy, ΔZPE is the zero-point energy change, and $T\Delta S$ is the entropy change at 300 K. The ZPE correction and the vibrational entropy contribution are taken from ref. 3.

2.4 Results & Discussion

2.4.1 Structural insights and microscopic probing

With the motive of obtaining Pt-like ORR activity with high stability, a less explored ordered intermetallic compound, Pd_2Ge crystallizing in hexagonal structure (space group: $P\bar{6}2m$) has been synthesized via solvothermal synthesis. Although there are several binary compounds of Pd (ordered,⁹ disordered³² and heterostructures¹⁸) reported for ORR, Pd_2Ge ordered intermetallic has been investigated for ORR for the first time in this work. By varying the Pd precursor content, a Pd deficient system, $\text{Pd}_{1.8}\text{Ge}$, and selective substitution by Pt atoms, as in $\text{Pt}_{0.2}\text{Pd}_{1.8}\text{Ge}$ are synthesized. **Figure 2.2** is the schematic showing the synthetic strategy for Pd deficient and Pt substituted Pd_2Ge system. **Figure 2.3a** and **2.3b** show the PXRD pattern comparison of different Pd_2Ge systems with Pd deficiencies created, and different percentages of Pt substituted. To discard the concept of inherent Pd vacancy in Pd_2Ge , we synthesized $\text{Pd}_{2.2}\text{Ge}$ to check if any shift in 2 θ is observed and there appears to be no difference in peak-positions in Pd_2Ge and $\text{Pd}_{2.2}\text{Ge}$. We also tested for Pt substitution both with and without creating Pd vacancies, as in $\text{Pt}_{0.2}\text{Pd}_{1.8}\text{Ge}$ and $\text{Pt}_{0.2}\text{Pd}_2\text{Ge}$, respectively. No difference among them clarifies that Pt having higher reduction potential reduces faster than Pd and occupies Pd positions even though Pd is present in excess.

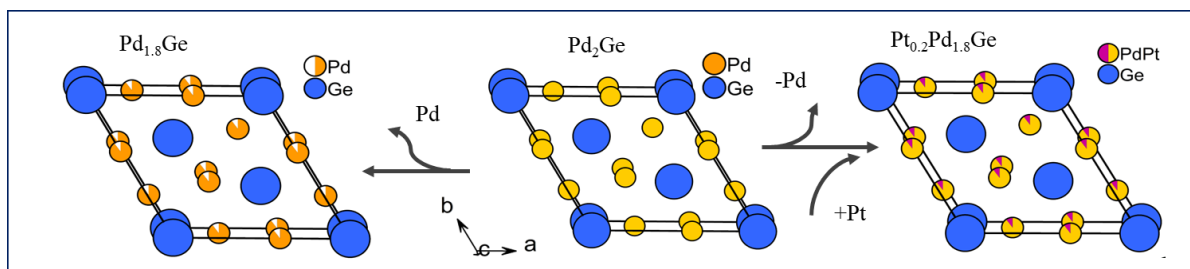


Figure 2.2. Schematic for the synthetic strategy for Pt substituted Pd_2Ge systems via deficiency formation at Pd sites.

The attempt to increase the Pt substitution resulted in the formation of a minor peak at $2\theta = 40^\circ$ corresponding to Pt nanoparticle formation. The PXRD pattern, as in **Figure 2.3c**, shows the right shift of major peak corresponding to (111) plane signifying lattice contraction due to Pd atom vacancies created in $\text{Pd}_{1.8}\text{Ge}$ and the left shift of the peak after Pt substitution signifies the lattice expansion due to larger Pt atoms substituting Pd atoms.³³

The crystallographic plane (111) is terminated by both Pt and Ge atoms, whereas (210) planes are terminated by mainly Ge atoms, with some Pt atoms which partially occupy the facet (210), as shown in **Figure 2.3d**. It is expected that if Pt atoms are substituting selectively the Pd atoms, not only the peak positions will change but peak intensity will also increase due to higher electron-dense Pt atoms. Such changes are not expected in the plane (210) which has only Ge atoms. This hypothesis gained success when relative peak intensity ratio (111):(210) was calculated for Pd_2Ge , $\text{Pd}_{1.8}\text{Ge}$, and $\text{Pt}_{0.2}\text{Pd}_{1.8}\text{Ge}$. In **Figure 2.3e**, it is observed that with Pd deficiency the (111):(210) ratio jumps down due to intensity loss of (111) facet, and just after substituting with Pt atoms, the ratio increased with a sharp rise.

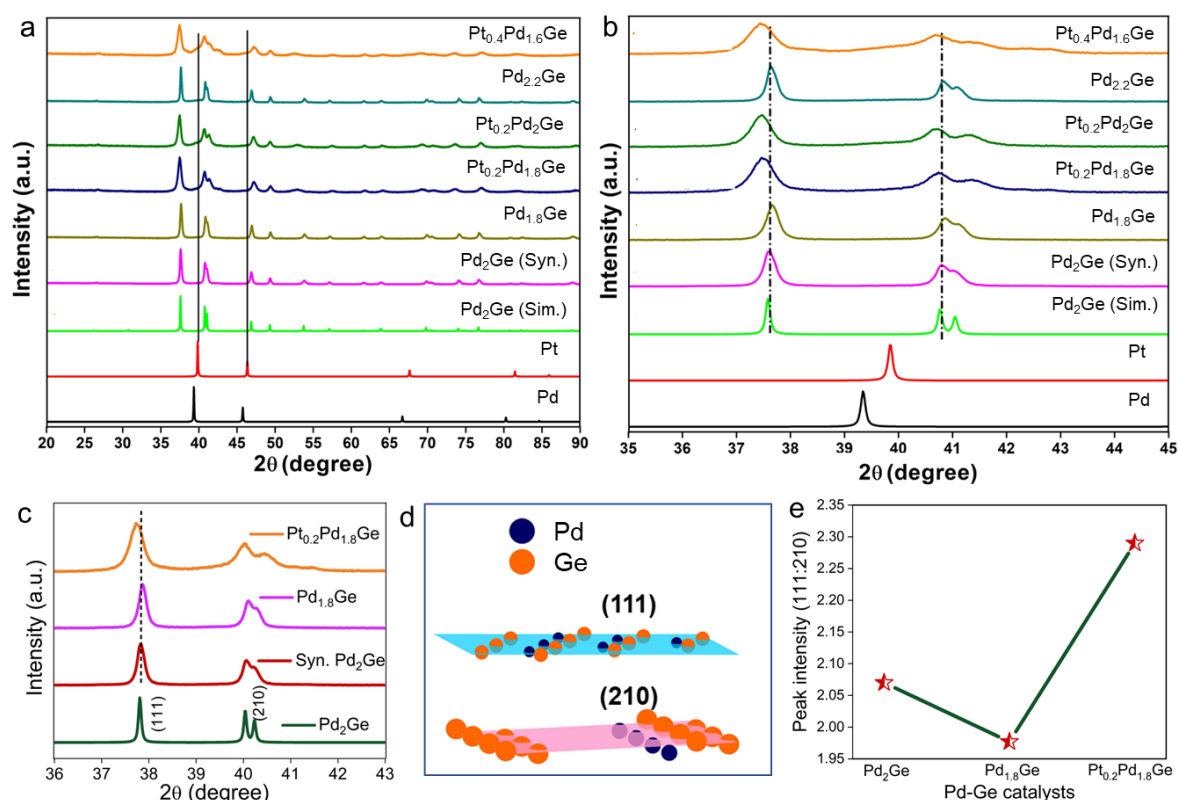


Figure 2.3. (a) Powder XRD pattern comparison of all Pd-Ge based catalysts. (b) PXRD zoomed part of first few major peaks. (c) PXRD patterns for synthesized Pd_2Ge , $\text{Pd}_{1.8}\text{Ge}$, and $\text{Pt}_{0.2}\text{Pd}_{1.8}\text{Ge}$ compared with simulated pattern of Pd_2Ge . (d) Crystallographic planes (111) and (210) drawn to show which elements are terminated. (e) Relative peak intensity ratio (111):(210) for Pd_2Ge , $\text{Pd}_{1.8}\text{Ge}$, and $\text{Pt}_{0.2}\text{Pd}_{1.8}\text{Ge}$.

This indicates that Pt is selectively occupying at the Pd sites and highly electron-rich Pt atoms increase the peak intensity due to the high atomic scattering factor of Pt. Pd₂Ge displays a morphology of nano coral-like connected nanospheres of diameter ~20nm as observed in scanning (SEM) and transmission electron microscopy (TEM) images in **Figure 2.4a** and **2.4b**, respectively. From **Figure 2.4b** showing the high-resolution TEM (HR-TEM) image for the catalyst, it is observed that in high-resolution atomic level, the most exposed facet is (111) and some places (110) are also present at d-spacing of 0.25 nm and 0.340 nm, respectively (**figure 2.4c**). **Figure 2.4d** shows the elemental distribution by color-mapping of different constituent elements like Pd, Ge and Pt. It is seen that difference in brightness (intensity) of the spots is reflected due to presence of different atoms of different atomic number. **Figure 2.5a** attached is the intensity profile for the line drawn along the atoms. **Figure 2.5b** show the ordered arrangements of the atoms in the HRTEM image. The selected area electron diffraction (SAED) pattern of the catalyst shows the presence of major crystallographic planes like (111), (210), (300) and (211) of Pd₂Ge (**Figures 2.5c**). It is noteworthy to mention that Pd and Ge are uniformly distributed on the surface as it is the main building block of the intermetallic catalyst (Pd₂Ge) whereas the presence of substituent Pt is much less compared to others.

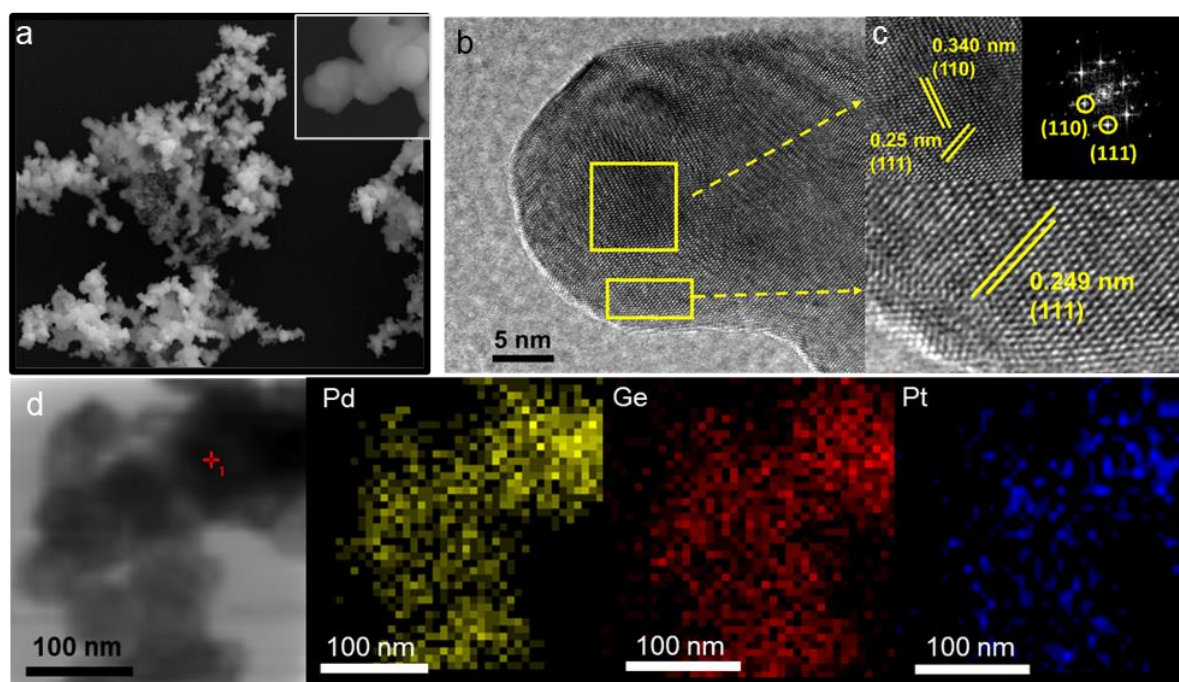


Figure 2.4. (a) Nano coral-like morphologies of Pt_{0.2}Pd_{1.8}Ge seen in SEM image. Inset is zoomed SEM image. (b) HRTEM image of Pt_{0.2}Pd_{1.8}Ge, (c) zoomed image and FFT showing prominent facets exposure. (d) TEM EDX-mapping of Pt_{0.2}Pd_{1.8}Ge. (i) HRTEM image at atomic resolution.

The SEM morphological analysis and the EDX elemental mapping of the constituent elements of Pd_2Ge , $\text{Pt}_{0.2}\text{Pd}_{1.8}\text{Ge}$ have been depicted in **Figures 2.6** and **2.7**, respectively.

2.4.2 Electrochemical Oxygen reduction (ORR)

ORR activity was carried out in alkaline media (0.1M KOH) for Pd_2Ge , the deficient ($\text{Pd}_{1.8}\text{Ge}$) and Pt substituted ($\text{Pt}_{0.2}\text{Pd}_{1.8}\text{Ge}$) compounds and their performance was compared with the state-of-the-art catalyst, commercially available 20% Pt/C (**Figure 2.8a**). From the linear sweep voltammograms (LSVs), it is observed that after creating Pd deficiencies there is a drop in current density as well as in the onset and half-wave potentials indicating Pd sites determine the activity of the ORR process. Interestingly, after substituting some Pd sites by Pt, the overpotential decreases and half-wave potential increases to 0.946 V vs. RHE, though there is no change in current density as compared to pristine Pd_2Ge catalyst.

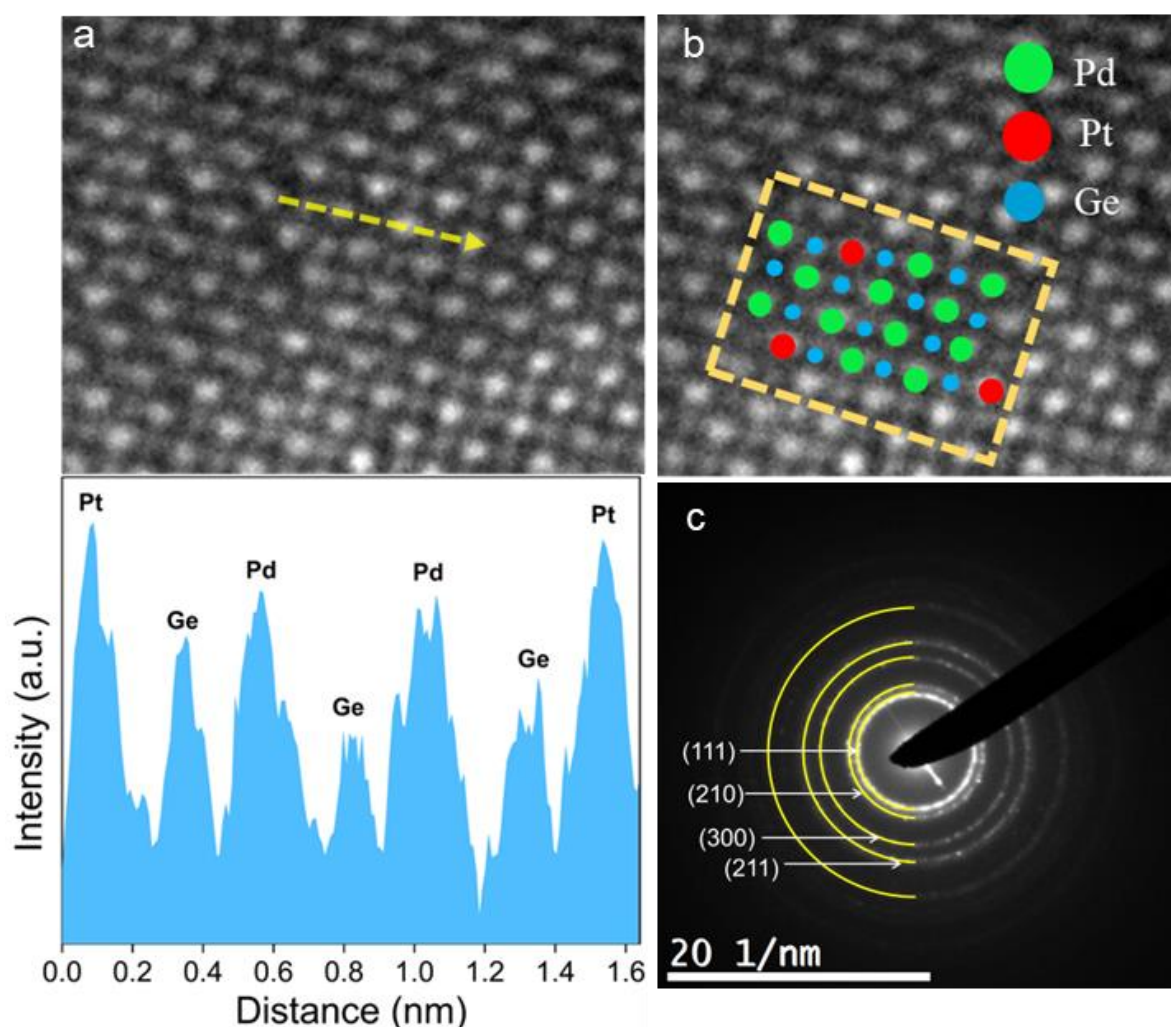


Figure 2.5. (a) Intensity profile along the line drawn across atomic sites in the HRTEM image. (b) Atomic positions designated in the atomic level resolution. (c) The selected area electron diffraction (SAED) pattern of the catalyst shows the presence of major crystallographic planes like (111), (210), (300) and (211) of Pd_2Ge .

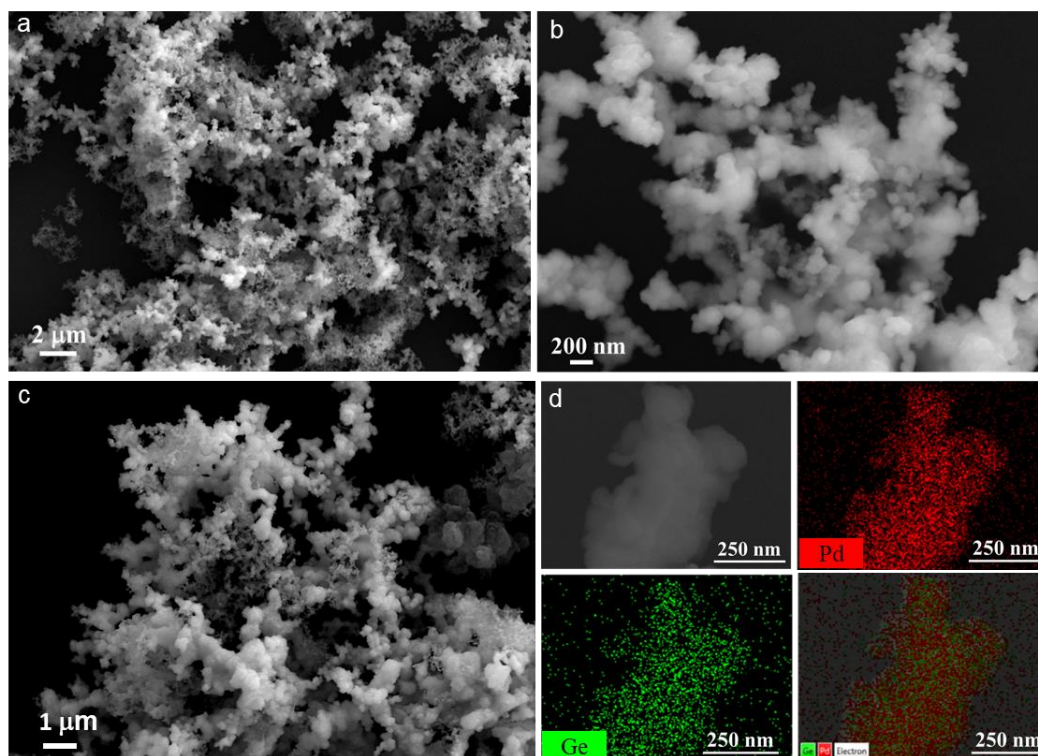


Figure 2.6. (a), (b), and (c) SEM images of Pd₂Ge. (d) EDX-mapping showing elemental distribution of Pd and Ge.

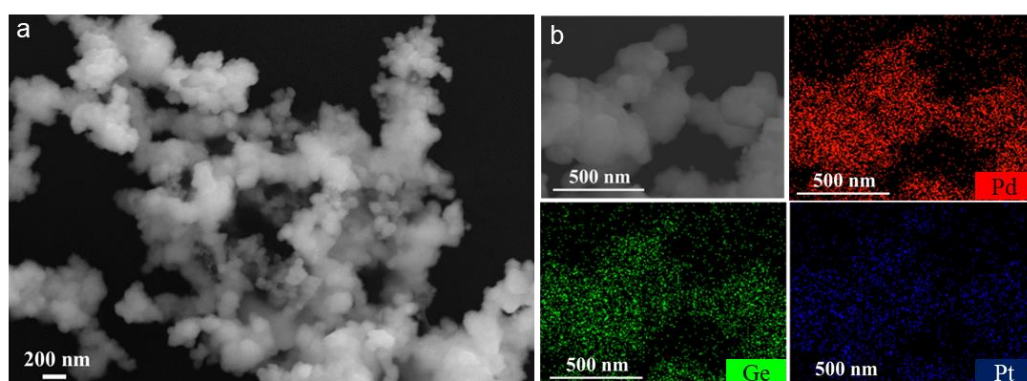


Figure 2.7. (a) SEM images of Pt_{0.2}Pd_{1.8}Ge. (b) EDX-mapping showing elemental distribution of Pd, Ge and Pt.

This strongly supports that upon substitution there is a modification in the electronic structure of Pd sites (the active sites) which drives the ORR kinetics faster and more feasible which is reflected in the higher half-wave potential. Furthermore, the Pt substituted catalyst exhibits excellent stability of 50,000 ADT cycles (**Figure 2.8b**) with minimum degradation in the $E_{1/2}$ value of about 5 mV only. The Tafel-slope for Pt_{0.2}Pd_{1.8}Ge is the lowest for both the onset potential region and half-wave potential region, which are 41.3 and 111.09 mV/dec, respectively (**Figure 2.8c**) than the other two catalysts. The lowest Tafel-slope value signifies faster charge transfer from active sites to intermediate species (O_2 to form superoxide ($O_2^{\cdot-}$) radical) with optimum adsorption and easy desorption of intermediates.³⁴

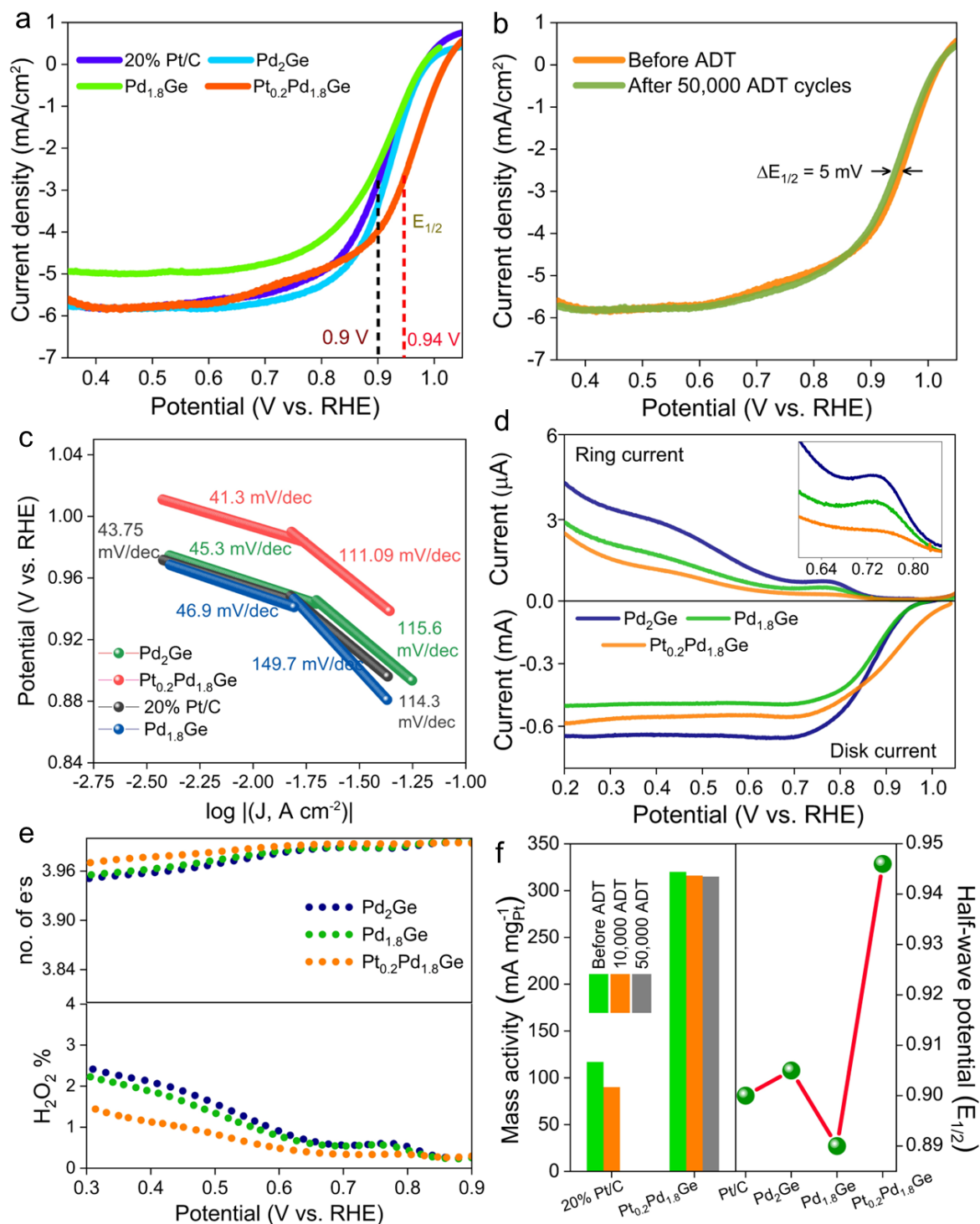


Figure 2.8. (a) LSVs for Pd₂Ge, Pd_{1.8}Ge, and Pt_{0.2}Pd_{1.8}Ge, compared with 20% Pt/C, are conducted in 0.1M KOH in potential range 0.3 to 1.0 V vs. RHE. (b) LSVs for Pt_{0.2}Pd_{1.8}Ge before and after 50,000 ADT cycles. (c) Tafel plots drawn at the onset and half-wave potential range. (d) RRDE experiment LSVs with both ring and disk currents. (e) Quantification of hydrogen peroxide and number of electron transfers during ORR, derived from the ring current experiment. (f) Mass activity and half-wave potential comparison for the catalysts.

The rotating ring disk electrode (RRDE) experiment for detection and quantification of hydrogen peroxide formation via 2e⁻ transfer mechanism of ORR is conducted, and it is

observed that $\text{Pt}_{0.2}\text{Pd}_{1.8}\text{Ge}$ shows the least ring current (see **Figure 2.8d**), with only 1.4% of H_2O_2 formation. The number of electron transfers calculated from RRDE experiment is 3.97 to 4 in the entire potential range for $\text{Pt}_{0.2}\text{Pd}_{1.8}\text{Ge}$, as shown in **Figure 2.8e** (Equation 2.1). **Figure 2.8f** shows the comparison of half-wave potential for all Pd-Ge-based catalysts and Pt/C where $\text{Pt}_{0.2}\text{Pd}_{1.8}\text{Ge}$ has the lowest half-wave potential. Along with RRDE experiment, number of electron transfers is also determined from Koutecky-Levich equation (K-L plot in **Figure 2.9**). As shown in **Figure 2.10a**, the best catalyst as per K-L plot, with the highest selectivity of $4e^-$ transfer is $\text{Pt}_{0.2}\text{Pd}_{1.8}\text{Ge}$.

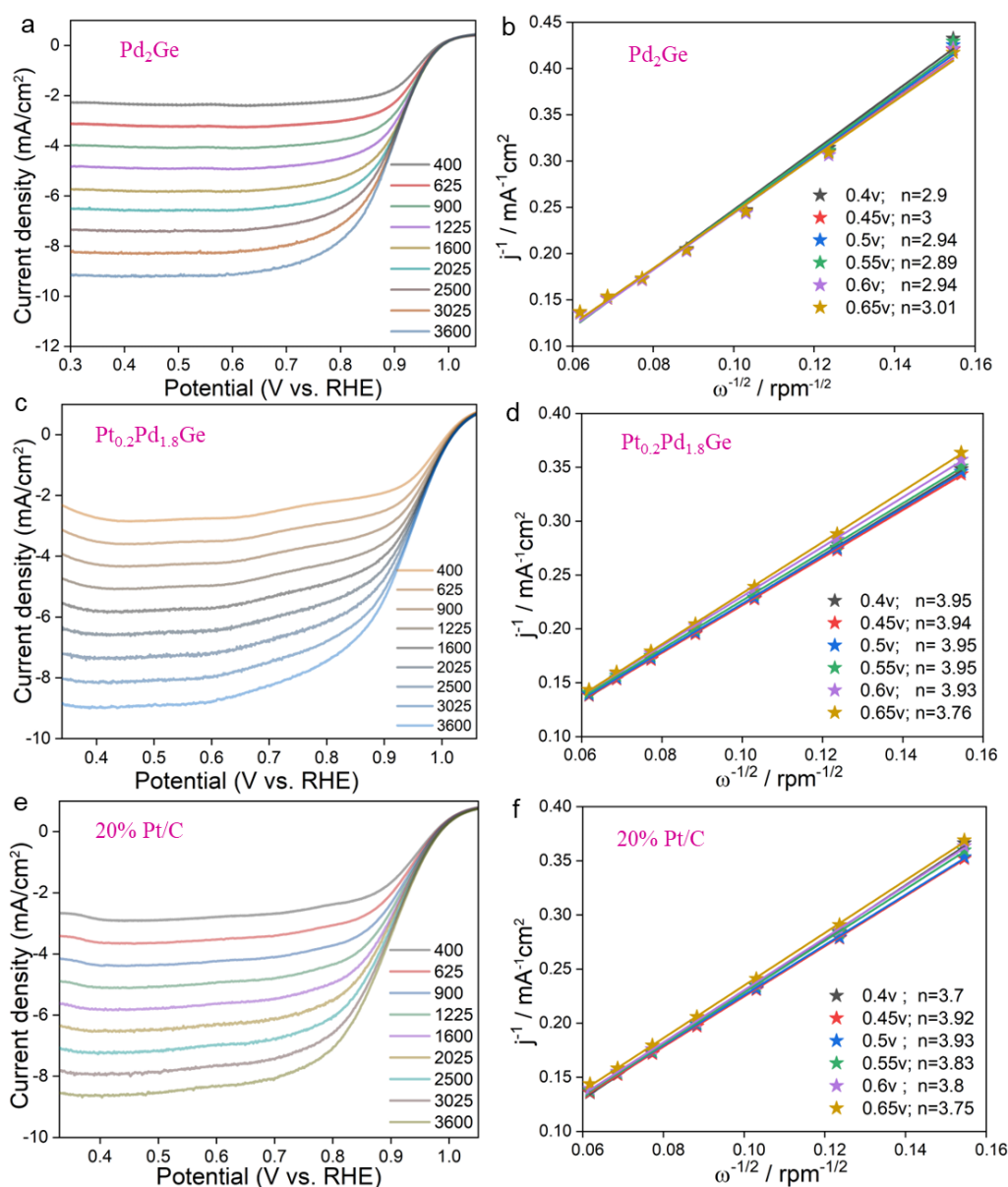


Figure 2.9. (a), (c), (e) LSVs of Pd_2Ge , $\text{Pt}_{0.2}\text{Pd}_{1.8}\text{Ge}$ and 20% Pt/C, respectively at 400, 625, 900, 1225, 1600, 2025, 2500, 3025, and 3600 rpm rotation rates of disk electrode. (b), (d) and (f) Koutecky-Levich plots obtained from LSVs at different potentials in the diffusion limited regions during ORR performed in 0.1M KOH.

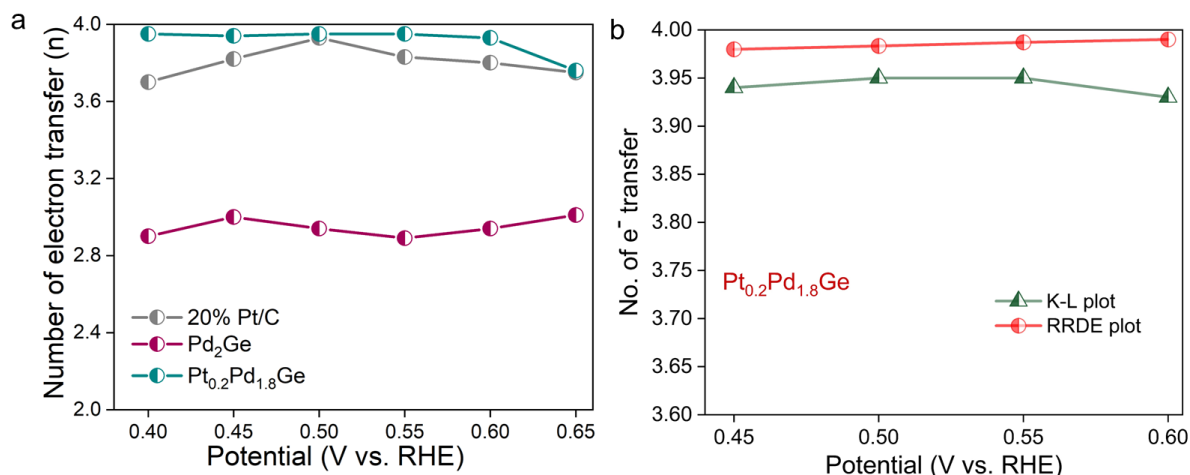


Figure 2.10. (a) Comparison of number of electrons (n) calculated for Pd₂Ge, Pt_{0.2}Pd_{1.8}Ge and 20% Pt/C from K-L plots. (b) Comparison of number of electrons (n) calculated for Pt_{0.2}Pd_{1.8}Ge from K-L plots and RRDE experiments during ORR performed in 0.1M KOH.

The results obtained from RRDE, and K-L plots are almost similar as depicted in **Figure 2.10b**. The mass activity of the best Pd-Ge-based catalyst Pt_{0.2}Pd_{1.8}Ge is 322 mA mg⁻¹ Pt which is almost 3 times higher than commercial catalyst 20% Pt/C. Also, after 50,000 ADT cycles there is only 0.01% decrement in mass activity value (see **Figure 2.8f**). **Figure 2.11** shows methanol crossover experiment using 20% Pt/C and Pt_{0.2}Pd_{1.8}Ge exhibits how the designed catalyst Pt_{0.2}Pd_{1.8}Ge remains nonchalant even after injecting methanol, whereas 20% Pt/C shows a drastic degradation in activity. This stability in methanol crossover experiment indicates that Pt_{0.2}Pd_{1.8}Ge is a promising catalyst for direct methanol fuel cells (DMFCs).³⁵

2.4.3 Oxidation state and local structure by XAS

The substitution of Pt at the Pd site can induce local structure distortion and charge polarization, which were mapped by both XANES and XAFS analyses. As seen in **Figures 2.12a** and **2.12b**, the Pd atom in Pd₂Ge was found to be in slightly higher oxidation state, where the charge is balanced by Ge atoms which are in a slightly negative oxidation state. Interestingly, after substituting some Pd atoms by Pt atoms (Pt_{0.2}Pd_{1.8}Ge), the oxidation state of Pd atoms decreases than the pristine Pd₂Ge, whereas shows that Pt is at higher oxidation state (**Figure 2.12c**). This signifies that charge (electron) transfer takes place from Pt atom to Pd atoms in Pt_{0.2}Pd_{1.8}Ge. **Figure 2.12d** shows the Fourier Transformed R-space data of Pd edge for the unsubstituted and Pt-substituted catalysts, where it is observed that there are two peaks around 2.45 and 2.8 Å corresponding to Pd-Ge and Pt-Pd/Pd-Pd bonds, respectively. **Figures 2.12e**, and **2.12f** show the wavelet transformed k -space data of Pd K -edge of Pt_{0.2}Pd_{1.8}Ge, and Pt L_3 -edge of Pt_{0.2}Pd_{1.8}Ge, respectively.

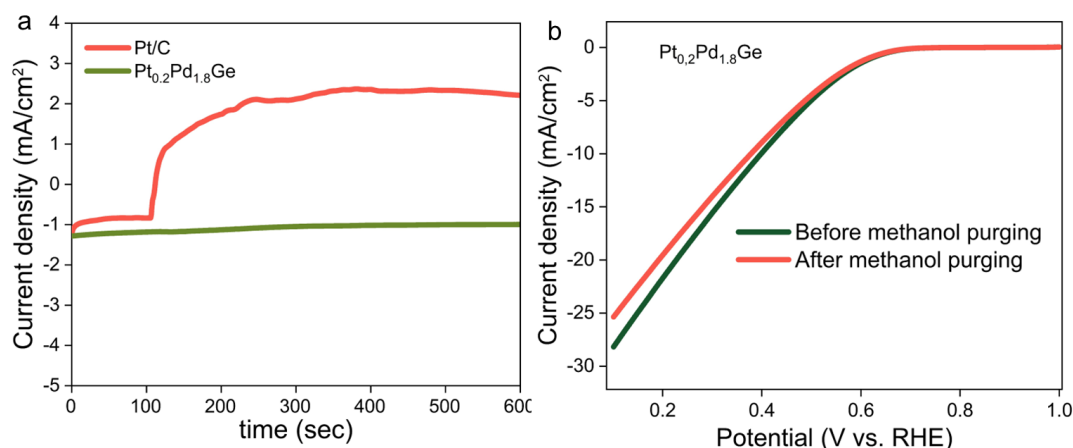


Figure 2.11. Methanol crossover experiment (a) CA compared with Pt/C and (b) LSV compared before and after methanol purging into O₂ purged solution.

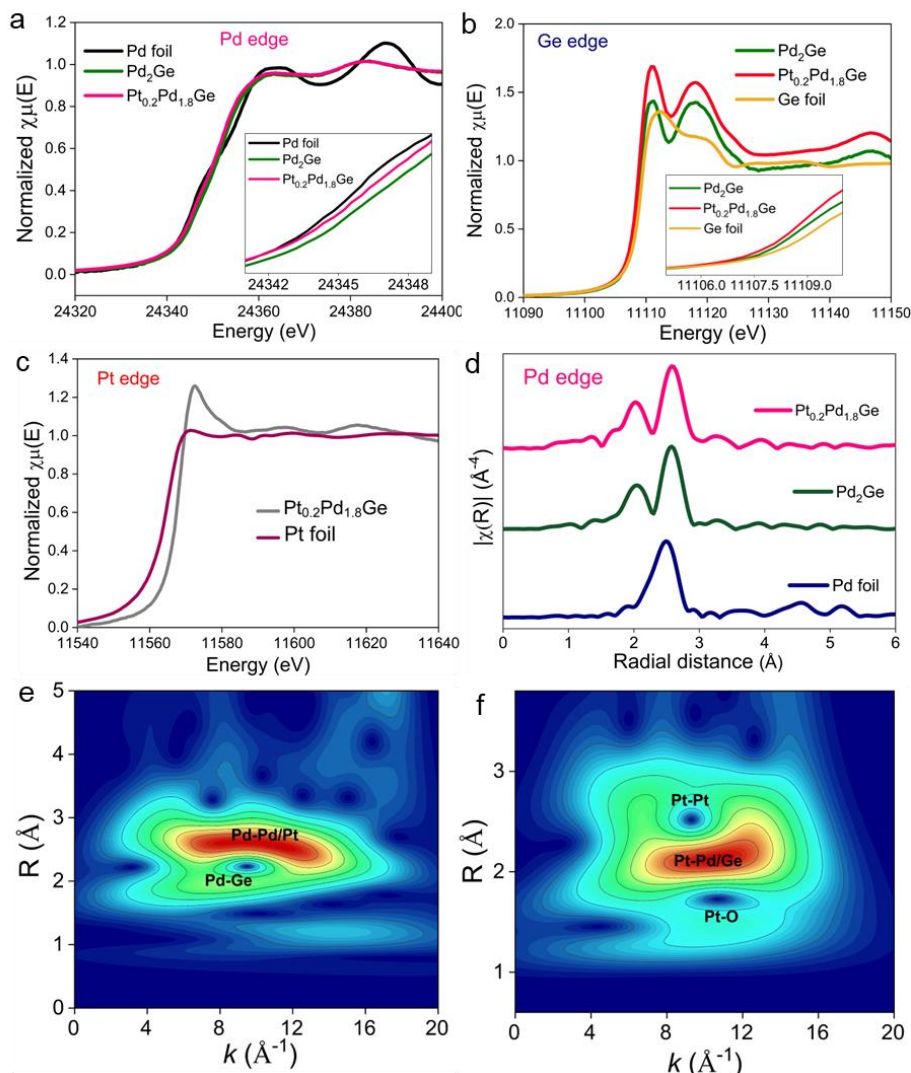


Figure 2.12. XANES spectra for (a) Pd-*K* edge (b) Ge-*K* edge and (c) Pt-*L*₃ edge for Pd₂Ge and Pt_{0.2}Pd_{1.8}Ge compared with the corresponding metal foils. (d) Fourier Transformed R-space data of Pd edge for Pd₂Ge and Pt_{0.2}Pd_{1.8}Ge. Wavelet transformed *k*-space spectra for (e) Pd *K*-edge of Pt_{0.2}Pd_{1.8}Ge, and (f) Pt *L*₃-edge of Pt_{0.2}Pd_{1.8}Ge.

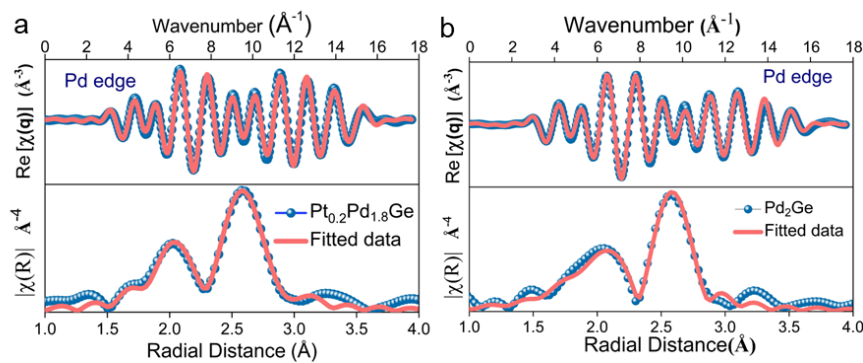


Figure 2.13. Fitted R-space and q-space data for Pd K-edge of (a) $\text{Pt}_{0.2}\text{Pd}_{1.8}\text{Ge}$ and of (b) Pd_2Ge .

These images give clear visualizations of the existence of Pd-Ge bonds in $\text{Pt}_{0.2}\text{Pd}_{1.8}\text{Ge}$ and Pt-O bonds along with Pt-Pt and Pt-Pd/Ge bonds. The Pd-Ge and Pd-Pd bond distances are found to increase after the Pt-substitution which is due to lattice expansion (as seen in PXRD, in **Figure 2.3c**), and decrease in the oxidation state of Pd refers to an increase in its electron density, which may lead to electronic repulsions causing bond expansion. **Table 2.1** gives the fitting parameters considering Pd as the central atom for both Pd_2Ge and $\text{Pt}_{0.2}\text{Pd}_{1.8}\text{Ge}$. **Figures 2.13a** and **2.13b** show the fitted R-space and q-space data of Pd edge of $\text{Pt}_{0.2}\text{Pd}_{1.8}\text{Ge}$ and Pd_2Ge , respectively.

Table 2.1. Ex-situ EXAFS fitting parameters of Pd edge of $\text{Pt}_{0.2}\text{Pd}_{1.8}\text{Ge}$

Shell	CN	$\sigma^2/(\text{\AA}^2)$	E_0 (eV)	$R/\text{\AA}$
Pd1-Ge2	3.5	0.005(8)	3.673	2.48(1)
Pd1-Pt2	1.6	0.003(6)	3.673	2.83(7)
Pd1-Pd2	3.2	0.003(9)	3.673	2.9
Pd1-Pd1	1.5	0.009(4)	3.673	3.09(2)

2.4.4 Surface oxidation state by XPS

X-ray photoelectron spectroscopy provides the oxidation state and chemical composition of the surface exposed species which helps in analyzing the charge transfer due to hetero-atom substitution. In addition to the observation obtained from XANES, XPS also confirms that Pd is in a higher oxidation state in pristine Pd_2Ge , but the oxidation state decreases after Pt substitution on Pd sites (see **Figure 2.14a**). **Figures 2.14b, 2.14c** and **2.14d** show the fitted XPS plots for Pd 3d, Ge 3d, and Pt 4f edges, respectively of $\text{Pt}_{0.2}\text{Pd}_{1.8}\text{Ge}$. It validates the existence of Pd, Ge and Pt in metallic states at binding energy 335.46 eV, 28.92 eV, and 71.49 eV with a slight presence of PdO, GeO and GeO_2 and Pt oxides, respectively, on the surface due to surface oxidation.²⁹

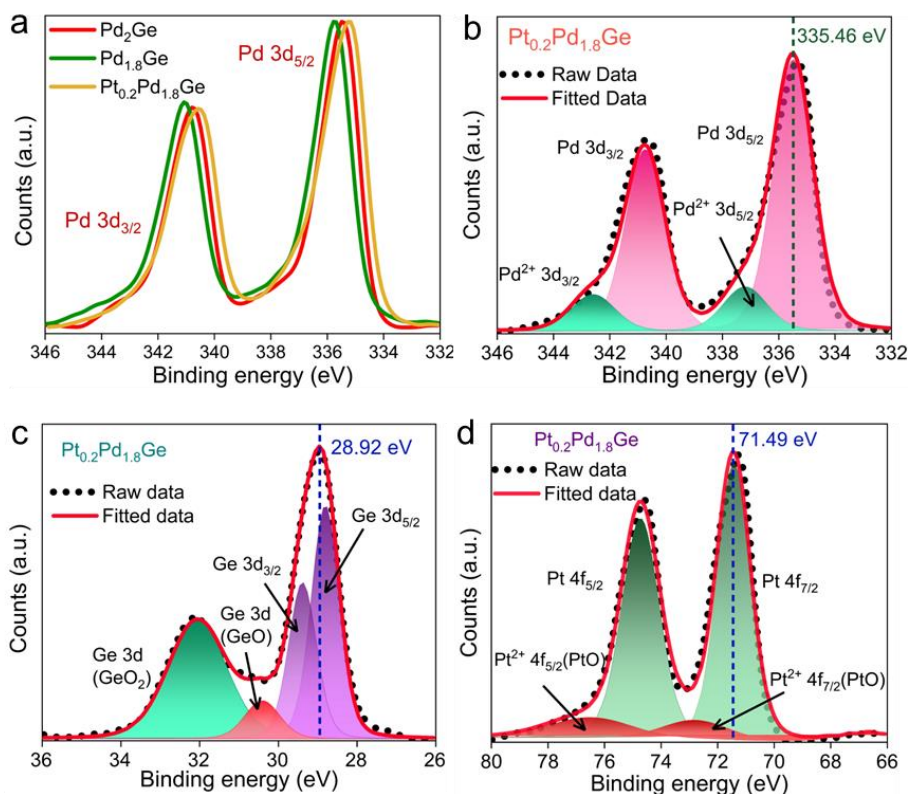


Figure 2.14. (a) Pd 3d XPS spectra comparison for all catalysts. XPS fitted spectra of (b) Pd 3d, (c) Ge 3d, and (d) Pt 4f, of $\text{Pt}_{0.2}\text{Pd}_{1.8}\text{Ge}$.

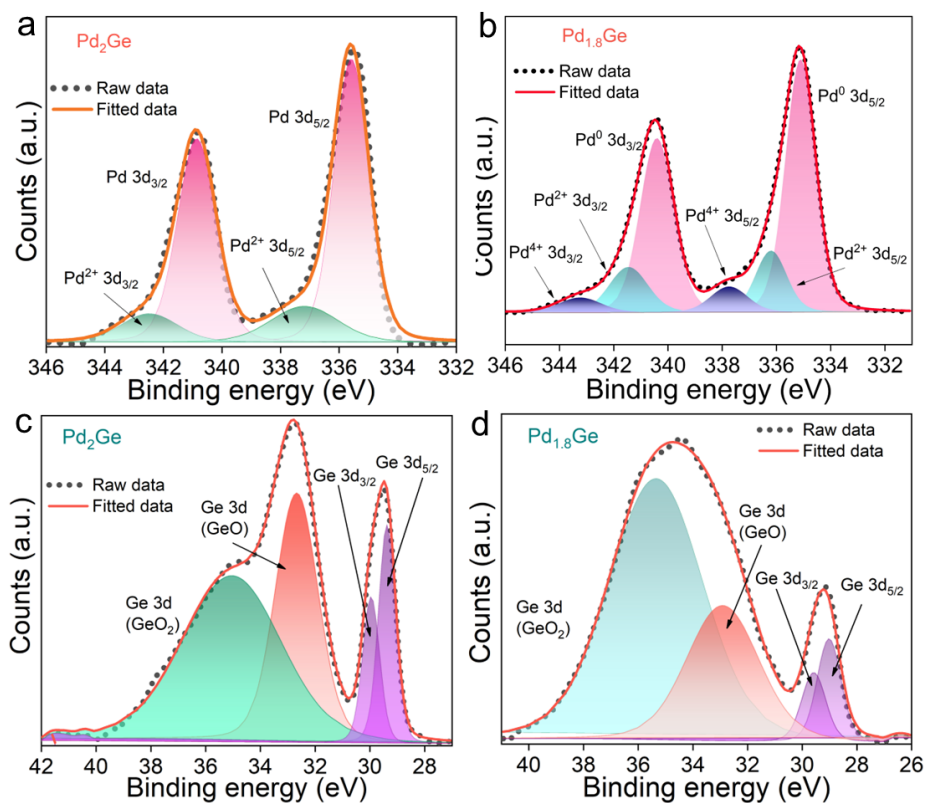


Figure 2.15. Fitted XPS spectra of Pd edges of (a) Pd_2Ge and (b) $\text{Pd}_{1.8}\text{Ge}$ and Ge edges of (c) Pd_2Ge and (d) $\text{Pd}_{1.8}\text{Ge}$.

It can be concluded that after substitution Pt stays in a slightly higher oxidation state with a decrease in Pd oxidation state. This signifies that charge transfer from Pt to Pd takes place which backs up the observation obtained from XANES analysis. **Figure 2.15** presents the fitted XPS spectra of Pd and Ge edges of Pd₂Ge and Pd_{1.8}Ge. Ge edge shows a highly broad and intense GeO₂ peak (**Figure 2.15d**) in Pd_{1.8}Ge which is because of more Ge being surface oxidized in Pd deficient system with the surface having more dangling uncoordinated bonds prone to get oxidized. Defected systems are prone to contain less coordinated highly active atomic species on the surface.

2.4.5 Structural changes via operando XAS and post-ORR XPS

Figure 2.1a shows the real image of the customized operando-XAS electrochemical cell set-up. **Figure 2.16** (**2.16a** and **2.16b**) shows that during ORR, the oxidation state of Pd in Pd₂Ge changes slightly towards higher value and the increase in oxidation state is more prominent in case of Pd edge of Pt_{0.2}Pd_{1.8}Ge as visible in **Figure 2.17a**.

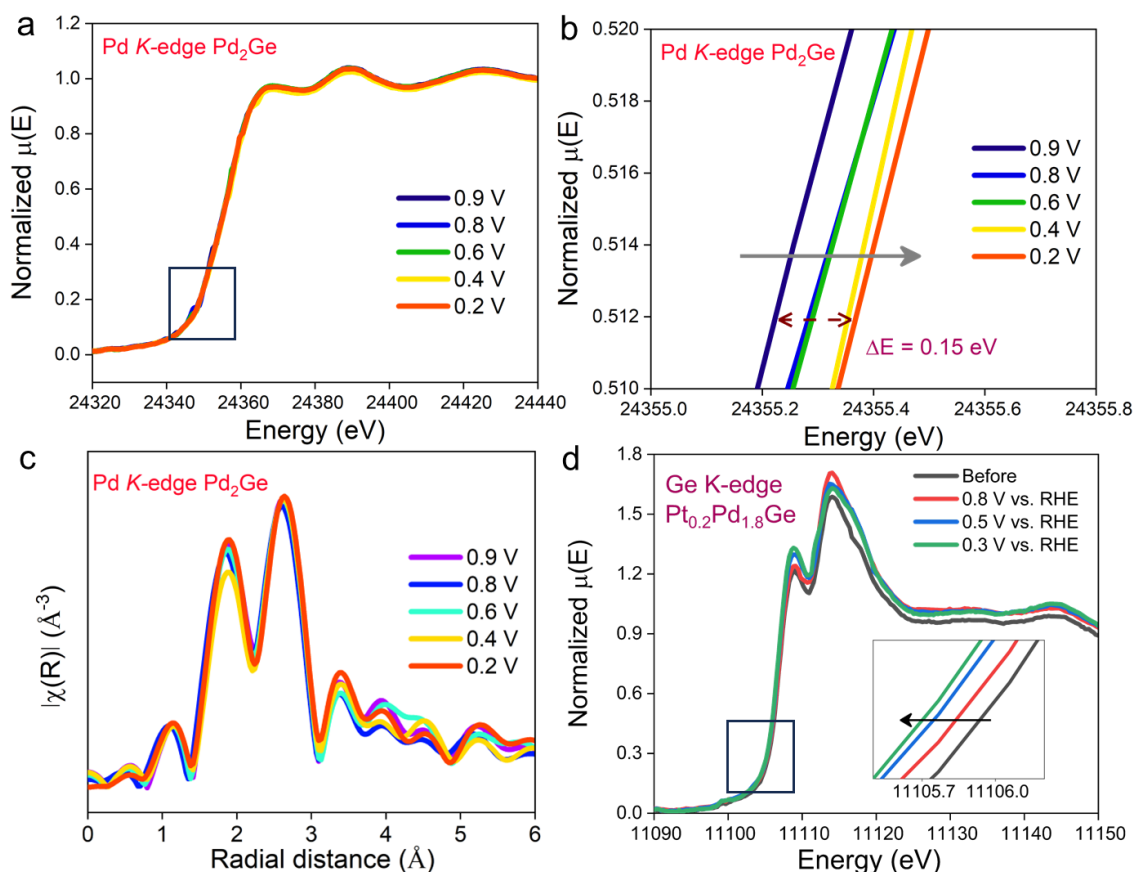


Figure 2.16. (a) Potential dependent XANES spectra for Pd *k*-edge of Pd₂Ge (b) zoomed in image of the absorption edge (c) Fourier transformed R-space data for Pd edge of Pd₂Ge during ORR performed in 0.1M KOH. (d) Potential dependent XANES spectra for Ge *k*-edge of Pt_{0.2}Pd_{1.8}Ge.

Figure 2.16d shows the Ge K-edge XANES spectra at different potential during ORR. As a result of increased oxidation state on Pd, bonds for Pd-Pd/Pt and Pd-Ge are showing contraction (**Figures 2.17b**) and not much change for Pd₂Ge (**Figure 2.16c**). **Figure 2.17c** shows Pt *L*₃-edge XANES spectra where Pt undergoes an increase in electron density during ORR. **Figure 2.17d** shows that there is an interesting correlation of bond distances between the experimental real-time observation via EXAFS analysis and computationally optimized structure analysis.³⁶ **Figure 2.17e** shows the data comparison of Pd 3d XPS for Pt_{0.2}Pd_{1.8}Ge before and after 50,000 ADT cycles of ORR. It is clearly observed that the binding energy of Pd 3d_{5/2} peak shifts from 334.9 to 335.4 eV which signifies that due to Pd being the active site, electrons are continuously channeled to molecular oxygen to form superoxide radical via Pd atoms. Due to continuous electron transfer, there develops a mild positive oxidation state of Pd atoms. At the same time, there is a broad hump around 337 eV (**Figure 2.17e**) indicating the presence of more PdO species after the ORR, which can be due to surface oxidation tendency being exposed to ORR reaction conditions. On the other hand, after ADT cycles, Pt 4f_{7/2} peak experiences a very meagre shift in lower binding energy value (see **Figure 2.17f**). The change in binding energy for Pd 3d and Pt 4f edges are much less that strongly confirms that catalyst degradation has not happened even after 50,000 ADT cycles as reflected in current density and half-wave potential in **Figure 2.8b**. As in **Figure 2.8c**, decreasing the Tafel slope value from pristine to the substituted one supports the fact that Pt substitution increases the electron density on Pd atom and makes the system strained which also modify the metal-metal bond distance of catalyst surface and active metal-O bond strength is also modified due to change in Pd coordination environment. This post-electrochemical surface analysis by XPS is strongly supported by in situ XAS study. **Figure 2.18a** shows the fitted EXAFS data acquired during ORR at different potentials. **Table 2.2** gives the fitting parameters of the EXAFS data after different potentials, **Figure 2.18b** depicts the decrease in the Pd-Pd bond with increasing reduction potential. The decrease is more prominent during the kinetic region of ORR, whereas in the diffusion limited region, the change is not that sharp. Such a decrease in electron density over Pd atom signifies continue charge transfer from Pd atom to O₂ molecule. Slight positive charge will facilitate adsorption of electron dense species like O₂, H₂O, OH which will increase the reaction kinetics. Accumulation of electron density on Pt atom during ORR also confirms that Pt is directly not the active site for ORR. Even though such modification in the oxidation state and bond distance are taking place, there is no change in the structure of Pd₂Ge which is clearly visible from the post-electrochemical PXRD as in **Figure 2.19**.

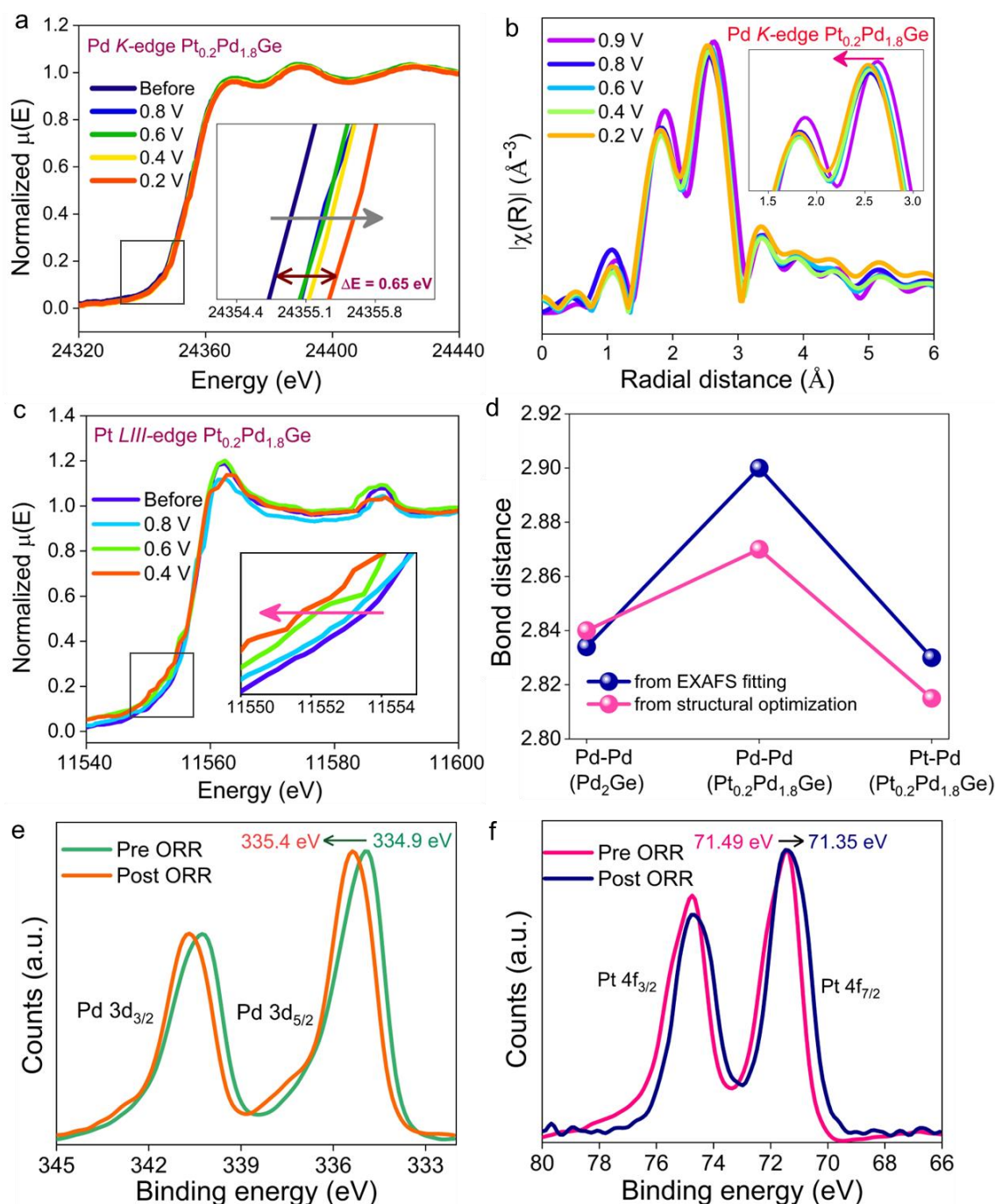


Figure 2.17. (a) In situ XANES spectra for Pd K-edge of $\text{Pt}_{0.2}\text{Pd}_{1.8}\text{Ge}$ during ORR in 0.1 M KOH. Inset shows zoomed image of absorption edge. (b) R-space data during ORR. (c) XANES spectra for Pt L_{3} -edge of $\text{Pt}_{0.2}\text{Pd}_{1.8}\text{Ge}$ during ORR. Inset shows zoomed image of absorption edge. (d) Comparison of metal-metal bond length obtained from EXAFS fitting and calculated from theoretically optimized structures. (e) XPS spectra of Pd 3d edge before and after of ORR. (f) XPS spectra of Pt 4f edge before and after ORR.

2.4.6 Deciphering reaction kinetics from operando FT-IR spectroscopy and computational studies

Despite the discovery of efficient catalysts for ORR, the main challenge remains the selectivity of reaction mechanism proceeding via $4e^-$ transfer forming water. The formation of

water from molecular O_2 depends on the feasibility of O-O bond cleavage which can be facilitated by strong adsorption on the active site and charge polarization¹³ on the catalyst surface that will easily polarize the electron cloud of the stable and neutral molecule. If the O-O cleavage occurs less, the ORR proceeds via $2e^-$ pathway forming hydrogen peroxide.^{37, 38} The RRDE experiment (**Figure 2.8d** and **2.8e**) produced too low ring current corresponding to H_2O_2 oxidation with only 1.4% of H_2O_2 formed, which triggered us to deliver mechanistic insights to bring into light the catalytic phenomena. We have performed operando FT-IR spectroscopy (**Figure 2.1b**) to recognize the stretching frequency corresponding to different intermediates formed during ORR.^{39, 40} **Figure 2.20a** shows that there is no prominent peak in IR region in absence of oxygen purging which clearly indicates that all the peaks have arisen from ORR reaction intermediates and products. **Figure 2.20b** shows the potential dependent in-situ IR spectra during ORR. **Figure 2.21a** expresses that there are peaks which corresponds to O-O stretching mode of adsorbed O_2 molecule and O_2^- adsorbed⁴² on catalyst surface around 1429 and 1080 cm^{-1} , and peak at 1270 cm^{-1} emerges slowly with increasing time indicating the bending mode vibrations of adsorbed OOH^* on catalyst surface.⁴³ **Figures 2.21b** and **2.21c** show that with increasing time there is a shift observed in the peak position corresponding to O-O stretching mode of adsorbed O_2 indicating that O-O bond strength is varying during ORR reaction.

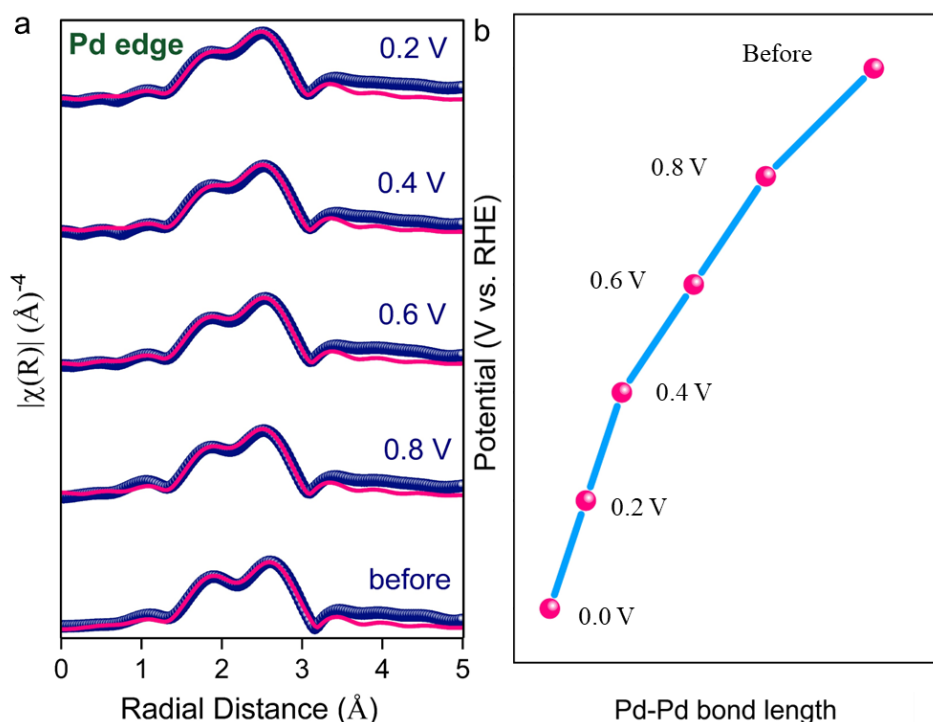


Figure 2.18. (a) Fitted R-space data of Pd *K*-edge at different potentials. (b) Comparison of Pd-Pd bond length varying at different potentials.

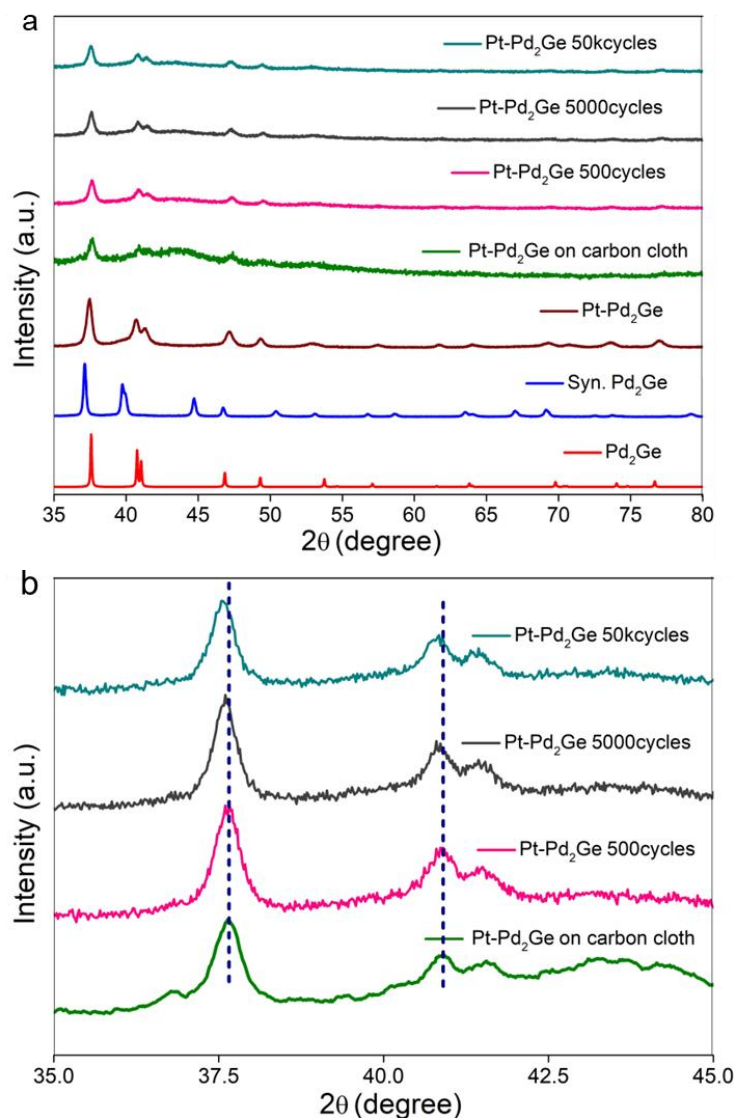


Figure 2.19. (a) PXRd pattern of Pt_{0.2}Pd_{1.8}Ge before electrochemistry and after different ADT cycles. (b) Zoomed in PXRd pattern.

Electron backdonation from Pd to O₂ active site will weaken O-O bond as reflected in decreased wavenumber at 200 secs of the reaction. The weaker O-O bond will be the easier O-O cleavage facilitating 4e⁻ transfer mechanism for ORR. Optimum M-O bond is also observed as after some time fresh O₂ molecule adsorbs on metal surface, and we observe same wavenumber after 250 secs. In addition to these ORR intermediates peak, there is H-O-H bending⁴⁴ mode arising around 1580 cm⁻¹ (**Figure 2.21a**) which gives a hint of water production during the reaction. Formation of water is strongly verified by the emergence of broad hump at 3000 cm⁻¹ due to O-H stretching frequency (**Figure 2.21d**).⁴⁴ The presence of heteroatom (Pt) in the coordination environment of Pd active sites induces the charge separation, which can facilitate the O-O cleavage. Partial density of states (PDOS) for Pd 3d orbitals has been calculated for Pd₂Ge, Pd_{1.8}Ge, and Pt_{0.2}Pd_{1.8}Ge systems.

Table 2.2. In-situ EXAFS fitting parameters of Pd edge of Pt_{0.2}Pd_{1.8}Ge before ORR and during CA at different potentials.

Potential (vs. RHE)	Path	C.N.	σ^2	R (Å)	ΔE (eV)	R-factor
Before reaction	Pd-Ge	1.99	0.00145	2.518	4.495±2.7	0.017
	Pd-Pt	2.95	0.00145	2.933		
	Pd-Pd	3.05	0.00145	2.835		
@ 0.8 V	Pd-Ge	1.84	0.00038	2.51	- 1.012±0.5	0.016
	Pd-Pt	3.13	0.00038	2.92		
	Pd-Pd	2.98	0.00038	2.832		
@ 0.6 V	Pd-Ge	1.75	0.00044	2.506	- 0.985±0.5	0.014
	Pd-Pt	2.88	0.00044	2.9167		
	Pd-Pd	3.71	0.00044	2.8301		
@ 0.4 V	Pd-Ge	1.95	0.00235	2.504	- 2.086±0.6	0.021
	Pd-Pt	2.53	0.00235	2.914		
	Pd-Pd	3.45	0.00235	2.828		
@ 0.2 V	Pd-Ge	1.88	0.00104	2.507	- 3.269±0.7	0.021
	Pd-Pt	2.83	0.00104	2.919		
	Pd-Pd	3.16	0.00104	2.827		
@ 0.0 V	Pd-Ge	1.88	0.00286	2.494	-0.213	0.02
	Pd-Pt	2.3	0.00286	2.891		
	Pd-Pd	3.67	0.00286	2.826		

Comparing the total-DOS for 111 slabs of Pd₂Ge, Pd_{1.8}Ge, and Pt_{0.2}Pd_{1.8}Ge, it is observed that after substituting there is an overall increase in the electron density near the Fermi level (**Figure 2.22**). As seen in **Figure 2.23a**, the electron density of Pd 3d orbitals is closer to the Fermi level in Pt_{0.2}Pd_{1.8}Ge as compared to the pristine and deficient system, which results in strong interaction between catalyst active site (Pd atoms) and the adsorbate molecules.⁴⁵ The electron accumulation on Pd sites will help in enhancing the ORR kinetics. **Figure 2.23b** shows the PDOS for Pd 3d for Pd₂Ge and Pt_{0.2}Pd_{1.8}Ge with d-band centres. **Table 2.3** shows the d-band centres values. From the d-band centre values of Pd and Pt sites of Pt_{0.2}Pd_{1.8}Ge, it is observed that Pd is the active site since the d-band centre corresponding to Pd 3d orbitals is closer to Fermi level than Pt.

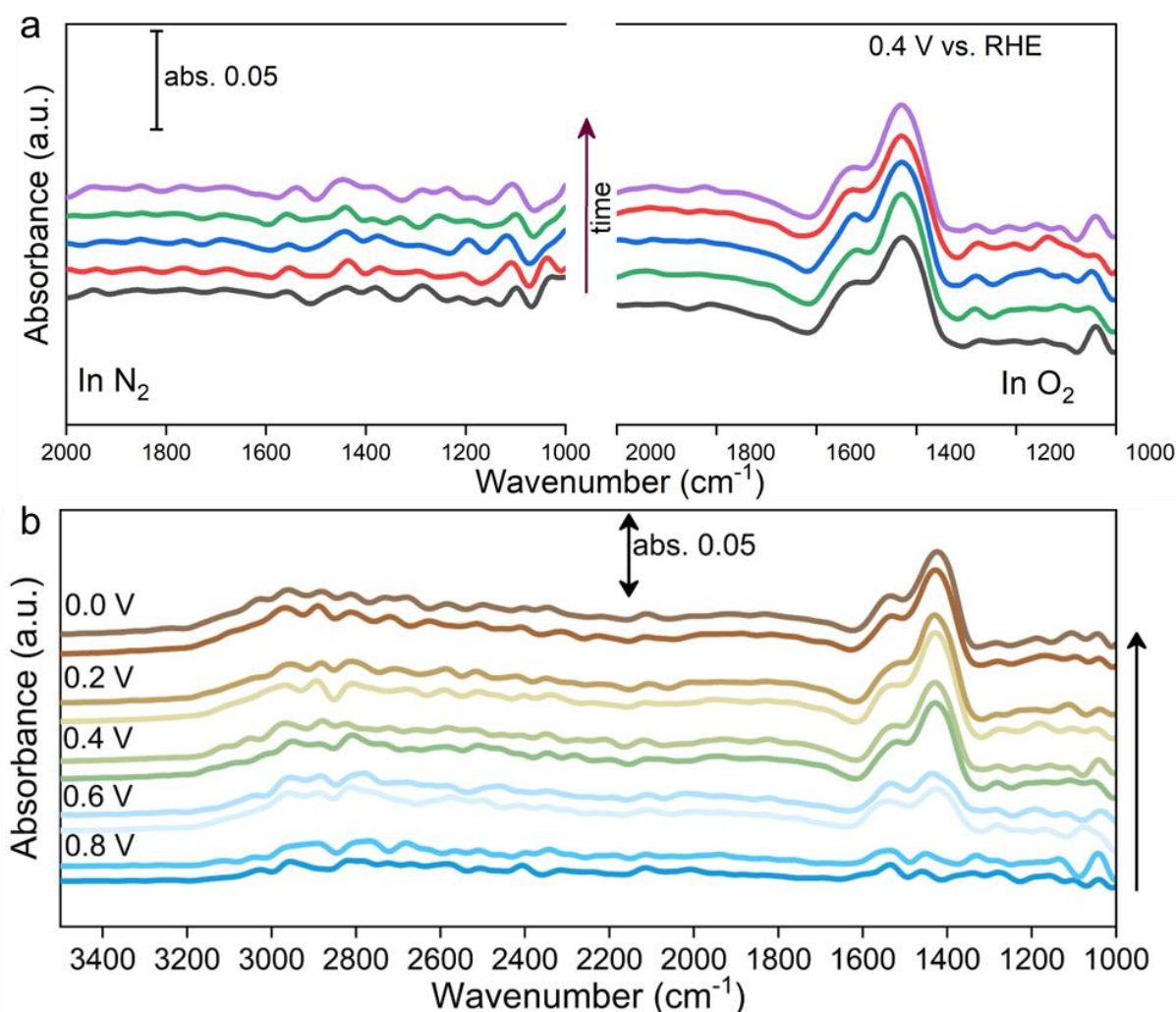


Figure 2.20. In situ FT-IR spectra during ORR in (a) presence and absence of O₂ gas. (b) at different reduction potential.

From d-band center calculation we could further confirm why Pt_{0.2}Pd_{1.8}Ge is the best catalyst and we could confirm that Pd is the active site and not Pt. The charge accumulation on the O atoms of differently adsorbed intermediate species on different sites has been quantified (Table 2.4) and we have succeeded in achieving the theoretical predictions satisfying the experimental observations. From the above table, it is observed that the negative charge accumulation on middle O atom in *OOH moiety is highest when it is adsorbed on Pd site of Pt_{0.2}Pd_{1.8}Ge which shows that this O atom will have the maximum tendency to get protonated and form water leaving behind O atom on the metal site. Simultaneously, the negative charge in O atom of *OH is also highest for Pd site of Pt_{0.2}Pd_{1.8}Ge which again confirms that adsorbed *OH will have highest tendency to abstract proton from water molecule and itself desorb from metal site as H₂O. Thus, least OH-poisoning will be observed on Pd sites of Pt_{0.2}Pd_{1.8}Ge. Models of the slabs are given in Figure 2.24 and 2.25. Higher electron density on the catalyst

surface triggers reaction kinetics. Various structural models are simulated where different ORR intermediates are adsorbed on Pd, and Pt sites present on (111) facet of Pd_2Ge and $\text{Pt}_{0.2}\text{Pd}_{1.8}\text{Ge}$.

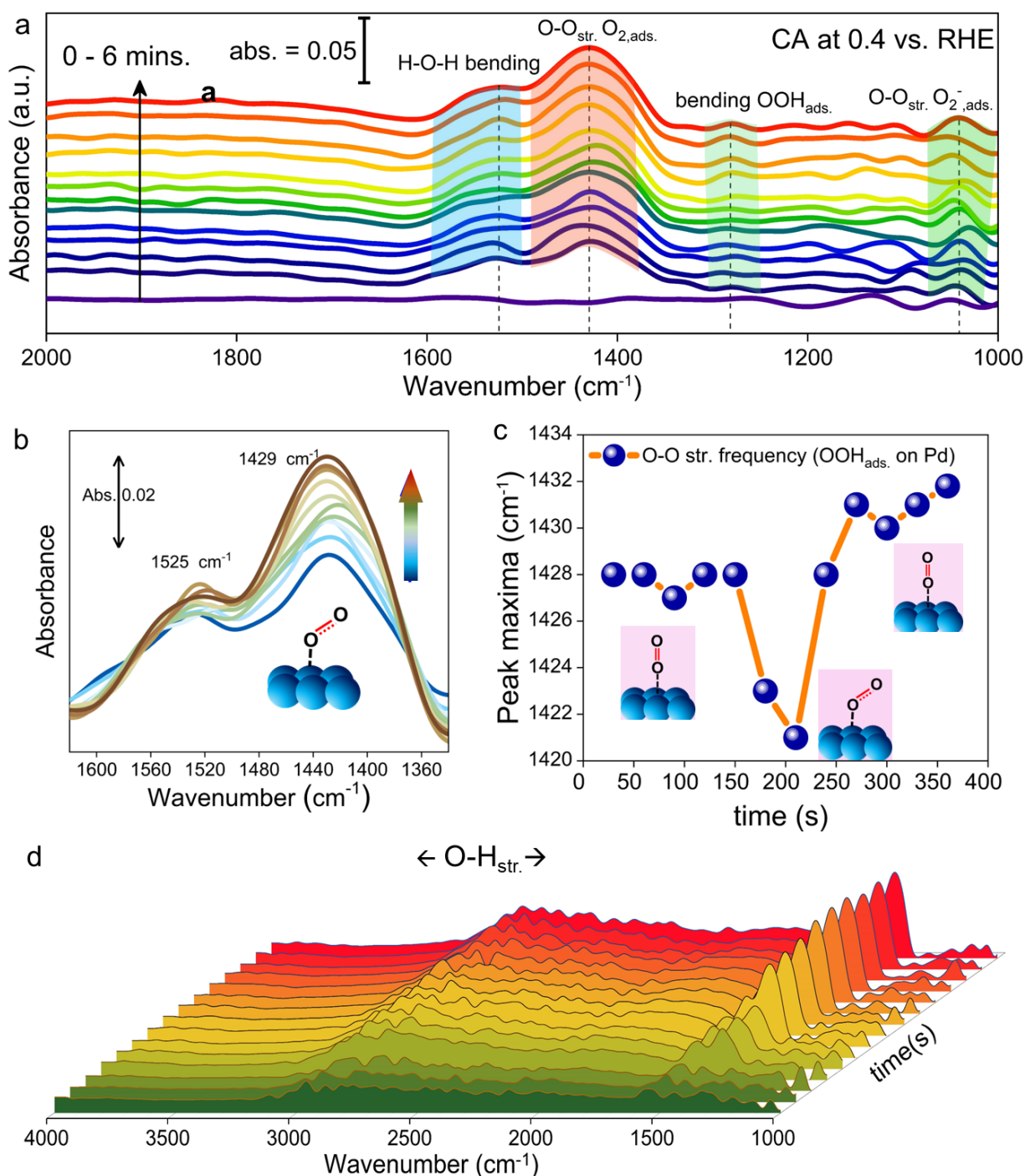


Figure 2.21. (a) In situ FT-IR spectra for $\text{Pt}_{0.2}\text{Pd}_{1.8}\text{Ge}$ during ORR CA at 0.4 V vs. RHE in 0.1M KOH. (b) Peaks around 1400 cm^{-1} are zoomed. (c) Comparison of peak maxima position shifting with time. (d) In situ IR spectra showing water formation during ORR.

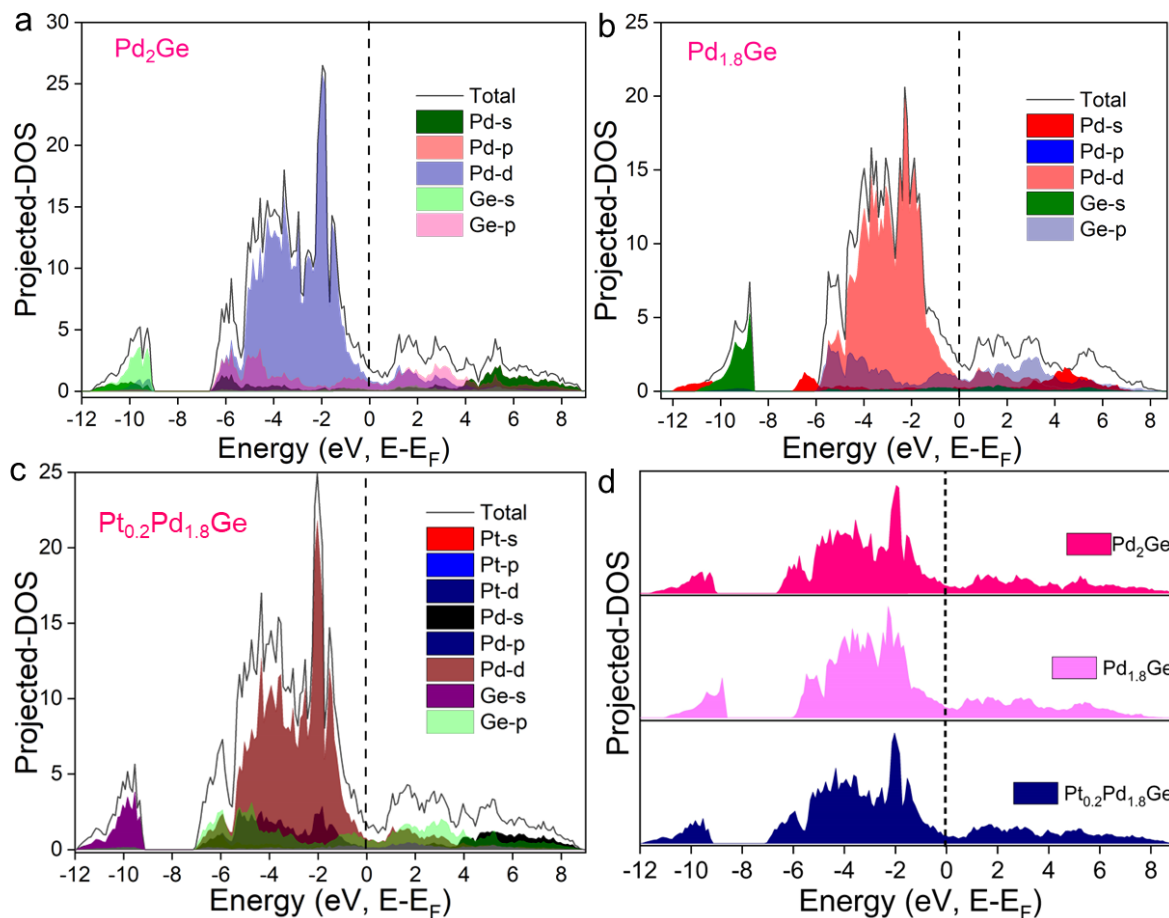


Figure 2.22. Total DOS of unit cells of (a) Pd_2Ge , (b) $\text{Pd}_{1.8}\text{Ge}$, and (c) $\text{Pt}_{0.2}\text{Pd}_{1.8}\text{Ge}$. (d) Total DOS of three catalysts compared together.

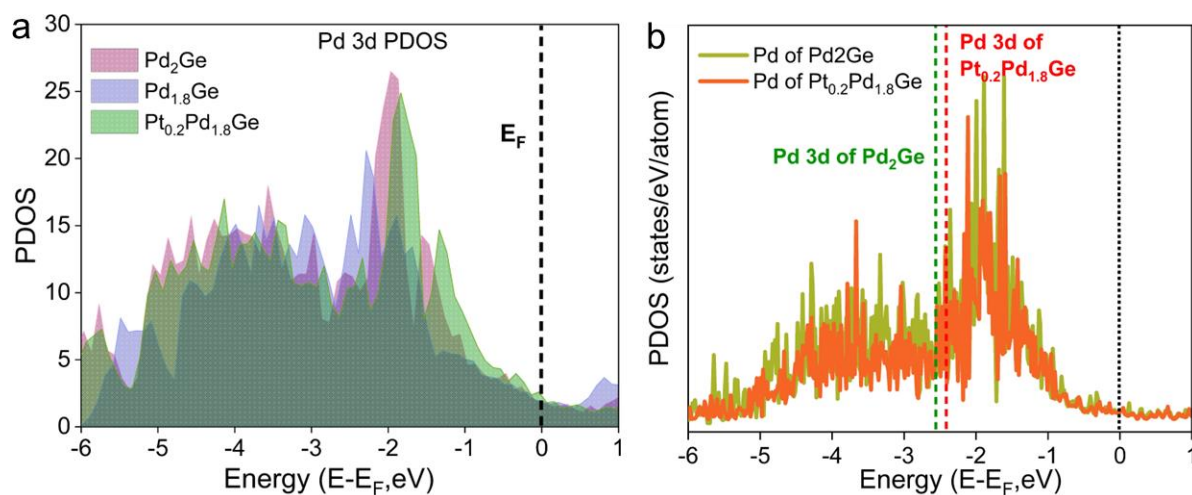


Figure 2.23. Projected density of states (PDOS) of (a) Pd 3d orbitals for Pd_2Ge , $\text{Pd}_{1.8}\text{Ge}$ and $\text{Pt}_{0.2}\text{Pd}_{1.8}\text{Ge}$, and (b) of (111) slab of Pd_2Ge and $\text{Pt}_{0.2}\text{Pd}_{1.8}\text{Ge}$ and calculation of d-band center.

Table 2.3. d-band centers for Pd and Pt atoms in Pd₂Ge and Pt_{0.2}Pd_{1.8}Ge.

Sites	d-band center (eV)
Pd of Pd ₂ Ge	-2.42
Pd of Pt _{0.2} Pd _{1.8} Ge	-2.38
Pt of Pt _{0.2} Pd _{1.8} Ge	-2.73

Table 2.4. Bader charge analysis of O atoms on different intermediate species adsorbed on Pd and Pt atoms in Pd₂Ge and Pt_{0.2}Pd_{1.8}Ge.

System	-OOH	-OOH	-OH
Pd ₂ Ge	-0.48	-0.61	-1.08
Pt _{0.2} Pd _{1.8} Ge	-0.48	-0.64	-1.48
Pt _{0.2} Pd _{1.8} Ge	-0.46	-0.59	-1.03

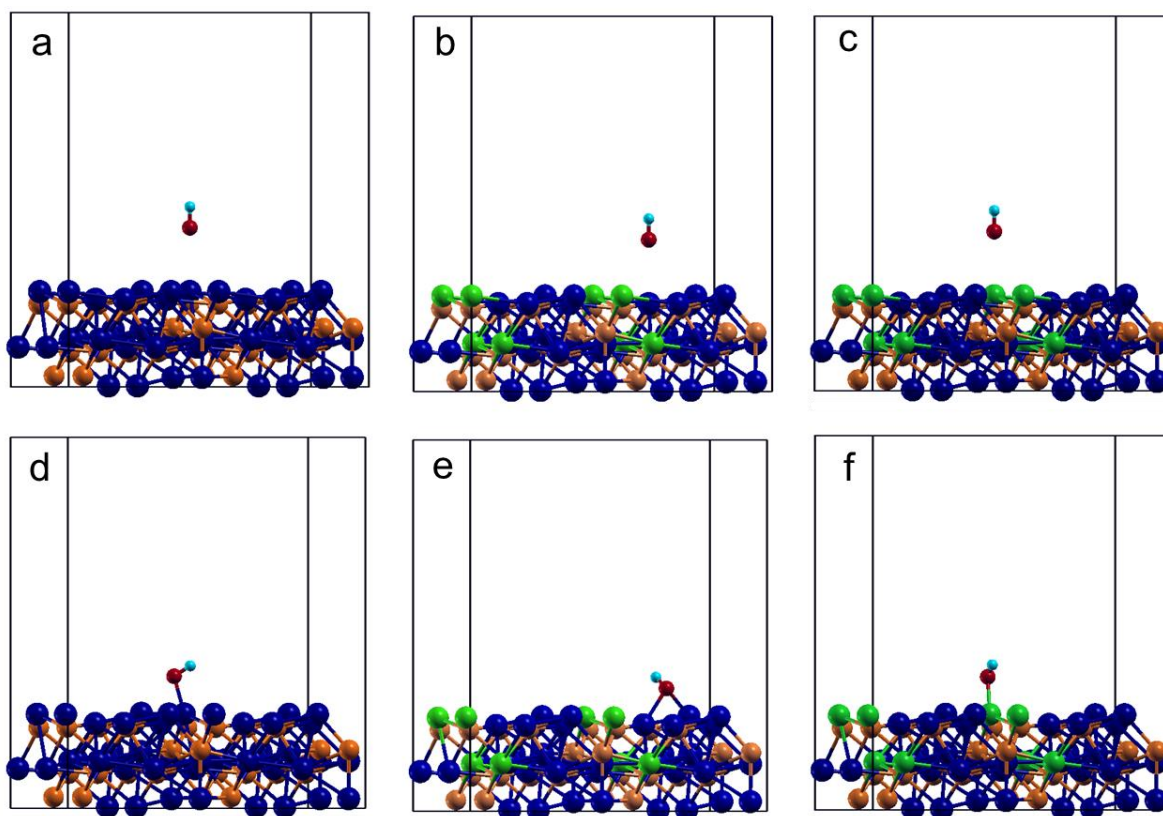


Figure 2.24. OH* moiety before getting adsorbed on Pd sites of Pd₂Ge (a), Pt_{0.2}Pd_{1.8}Ge (b), and on Pt sites of Pt_{0.2}Pd_{1.8}Ge (c). OH* moiety after getting adsorbed on Pd sites of Pd₂Ge (d), Pt_{0.2}Pd_{1.8}Ge (e), and on Pt sites of Pt_{0.2}Pd_{1.8}Ge (f).

In **Figure 2.25e** it is seen that OH* is adsorbed in bridged mode on Pd site and Pd-O bond is longer than in **Figure 2.25f**, which is due to an increase in Pd-Pd bond distance after substitution.⁴⁶ The energy for adsorption for ORR species like OH* and OOH* is calculated using the equation^{47, 48}:

$$\Delta E_{\text{ads}} = E_{\text{slab+species}} - E_{\text{slab}} - E_{\text{species}} \quad (2.3)$$

After adsorbing the species OH* on Pd and Pt atoms for both the catalysts, the PDOS for O 2p orbitals is simulated, as in **Figure 2.26a**. The 2p orbital electrons are closer to the Fermi level for those OH* which are bound to Pd or Pt atoms of Pt_{0.2}Pd_{1.8}Ge than on pristine Pd₂Ge. The more the 2p orbital electrons close to the Fermi level, the more the tendency for the electron cloud to attract a proton forming water¹³ and then desorb from the catalyst surface. Electron density on O atom of OH* species is higher in Pt substituted species than the pristine because of the decreased oxidation state of Pd in Pt_{0.2}Pd_{1.8}Ge for charge transfer from Pt to Pd atoms. The metal M-O (M= Pd, Pt) bond distance has increased after doping due to electron-dense Pd atom and large-sized Pt atoms. Thus, it is indicated that weaker M-O bond helps to get rid of the OH species and protect the surface from OH-poisoning and give a highly stable catalyst.^{49, 50} **Figure 2.26b** shows the trend of decreasing OH* poisoning with increasing metal-O bond distance of OH* species on the catalyst surface.

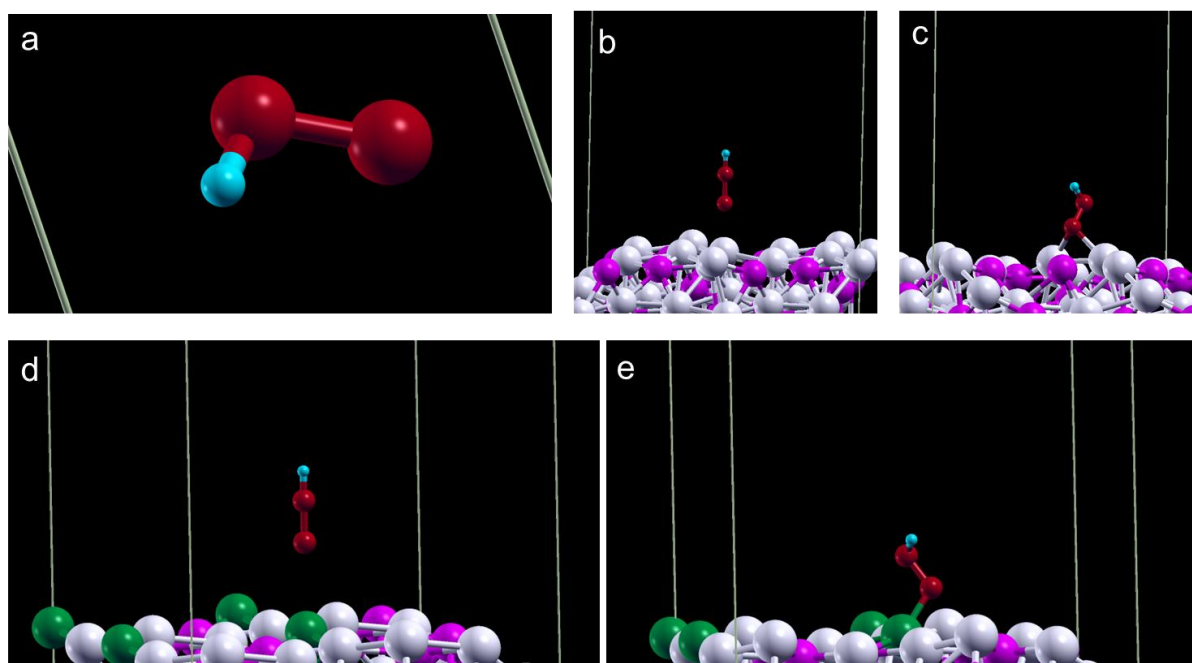


Figure 2.25. OOH* moiety before getting adsorbed on Pd sites of Pd₂Ge (a), Pt_{0.2}Pd_{1.8}Ge (b), and on Pt sites of Pt_{0.2}Pd_{1.8}Ge (c).

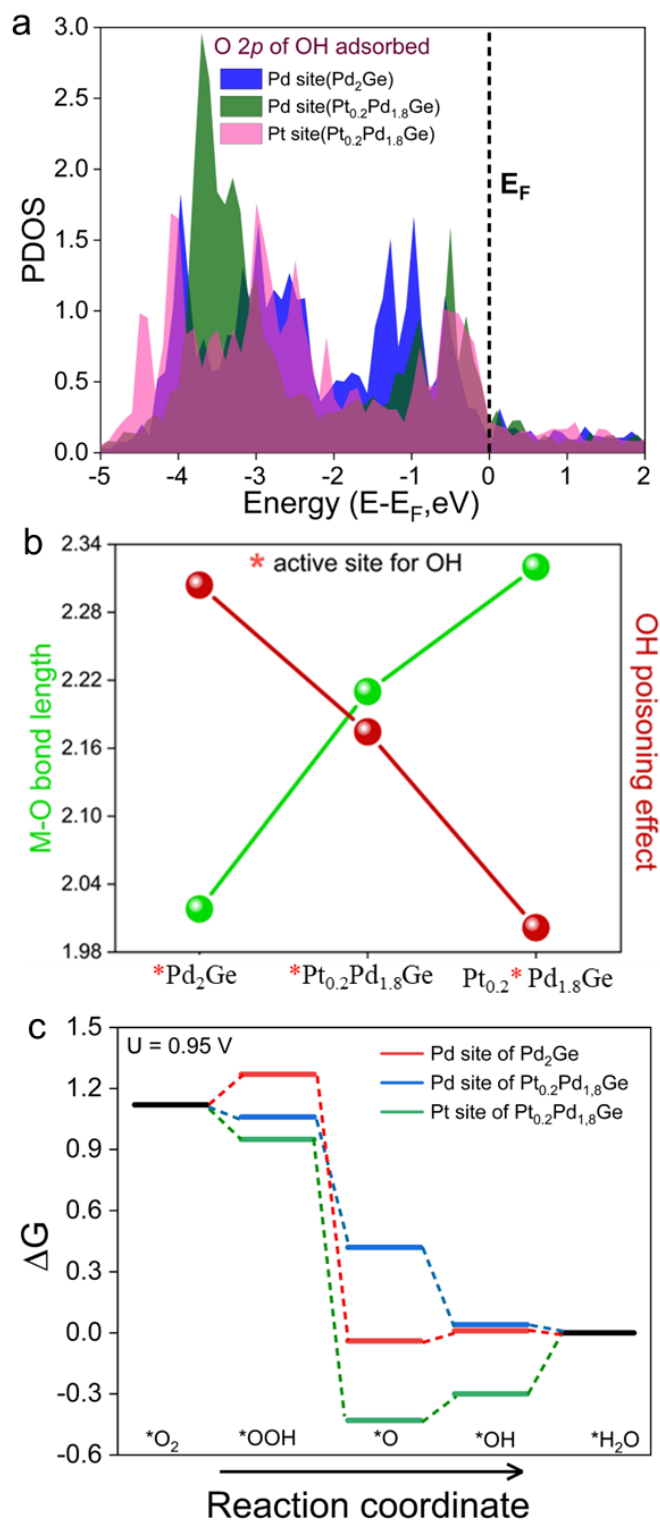


Figure 2.26. (a) PDOS of O 2p orbitals of OH* adsorbed on Pd and Pt sites of Pd₂Ge and Pt_{0.2}Pd_{1.8}Ge. (b) Comparison of metal-O bond length of adsorbed OH* species on different sites with OH poisoning effect. (c) Free energy profile for ORR reaction mechanism for both Pd₂Ge and Pt_{0.2}Pd_{1.8}Ge.

The free energy profile for ORR on various active sites for the catalysts are calculated and plotted in **Figure 2.26c**. From the energy profile diagram, it is clearly observed that *OOH

adsorption is stronger on Pt and Pd sites of $\text{Pt}_{0.2}\text{Pd}_{1.8}\text{Ge}$ and weaker on Pd sites of Pd_2Ge . This shows why the OOH desorption as peroxide ion is least in case of the best catalyst $\text{Pt}_{0.2}\text{Pd}_{1.8}\text{Ge}$. At the same time, the stronger the *OOH adsorption, the more will be O-O cleavage and hence H_2O formation tendency will be more.

While the *OH adsorption is indicative of OH-poisoning of the active sites. From the energy profile, it is observed that *OH is most strongly adsorbed on Pt sites of $\text{Pt}_{0.2}\text{Pd}_{1.8}\text{Ge}$. This means OH-poisoning will be more on Pt sites than on Pd sites. Although *OH adsorption energy is least on Pd sites of $\text{Pt}_{0.2}\text{Pd}_{1.8}\text{Ge}$. Had Pt been the active sites, this strong *OH adsorption would have been reflected in poor ORR long term activity and stability. This shows that Pd atoms of $\text{Pt}_{0.2}\text{Pd}_{1.8}\text{Ge}$ are the only active sites which not only decreases peroxide formation, but also diminishes OH-poisoning which indirectly is reflected in the extremely high stability of the catalyst $\text{Pt}_{0.2}\text{Pd}_{1.8}\text{Ge}$. It is seen that OH^* is weakly adsorbed on Pd sites of $\text{Pt}_{0.2}\text{Pd}_{1.8}\text{Ge}$ as compared to that on Pd_2Ge , which means $\text{Pt}_{0.2}\text{Pd}_{1.8}\text{Ge}$ catalyst is least poisoned. This strong binding of OOH^* on active sites is also evident from peak in in-situ IR spectra in **Figure 2.21a**. The weaker binding of OOH^* on surface sites is a bane for $4e^-$ transfer ORR mechanism⁴⁶ leading to the formation of majorly H_2O . If OOH^* is strongly bound, the tendency of peroxide anion release from catalyst surface will be less, and further $2e^-$ transfer will take place on absorbed OOH species to give water, instead of hydrogen peroxide. **Figure 2.27** schematically shows the reaction mechanism of ORR following $4e^-$ transfer generating H_2O molecule.

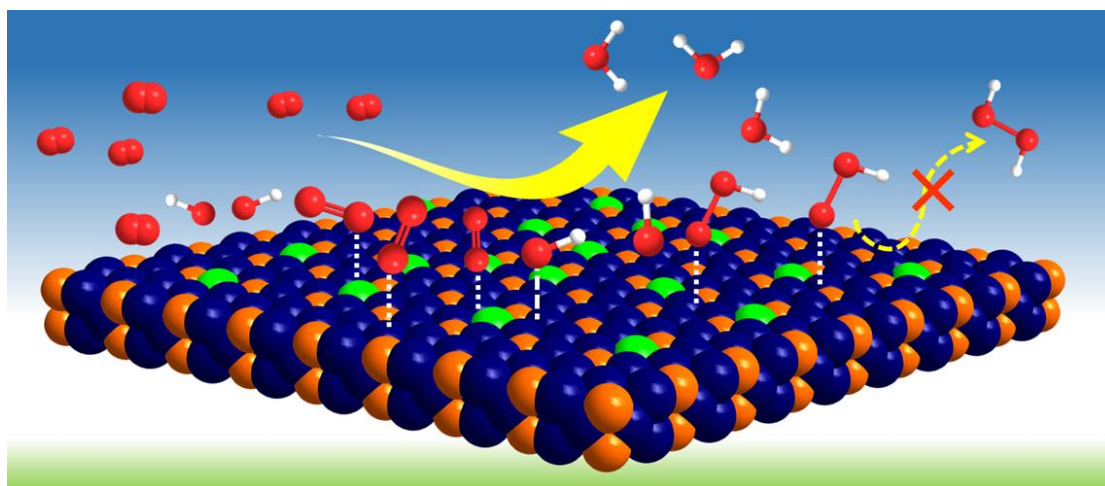


Figure 2.27. Schematic showing the ORR reaction mechanism obtained from in situ IR and computational studies.

Table 2.4 shows all recently reported Pd- or Pt- based electrocatalysts for ORR which expresses that our catalyst is having the least % of H₂O₂ produced and very high stability and excellent E_{1/2} values.

Table 2.4. Comparison of ORR activity for Pd- and Pt- based electro-catalysts at different electrochemical conditions.

Sr. No.	Catalyst	Medium	Half-wave potential (E _{1/2} , V)	H ₂ O ₂ %	Stability (ADT cycles)	References
1.	Pt _{0.2} Pd _{1.8} Ge	0.1 M KOH	0.946	1.4	50,000	This work
2.	AL-Pd/Mo ₂ C	0.1 M KOH	0.935	<5	5000	<i>J. Am. Chem. Soc.</i> 2021, 143, 6933-6941
3.	A-CoPt-NC	0.1 M KOH	0.96	>12	8000	<i>J. Am. Chem. Soc.</i> 2018, 140, 10757-10763
4.	Au/Cu ₄₀ Pd ₆₀	0.1 M KOH	-0.1 V vs Ag/AgCl	NA	-	<i>J. Am. Chem. Soc.</i> 2014, 136, 15026-15033
5.	PdCu/C	1 M KOH	0.886	NA	20,000	<i>ChemElectroChem</i> 2018, 5, 2571-2576
6.	2H-Pd ₇₁ Cu ₂₂ Pt ₇ NPs	0.1 M KOH	0.927	NA	10,000	<i>J. Am. Chem. Soc.</i> 2021, 143, 17292-17299
7.	Pt ₁ -Fe/Fe ₂ O ₃ (012)	0.1 M KOH	1.05	2.1	50,000	<i>Nat. Energy</i> 2021, 6, 614-623
8.	Co@Pd-Pt/CNT	0.1 M KOH	0.944	NA	3,10,000	<i>Nat. Commun.</i> 2019, 10, 440

2.5 Conclusion

The work has demonstrated the investigation of a less explored ordered intermetallic compound Pd₂Ge and modified the lattice site occupations by creating Pd vacancies and substituting some Pd atoms with Pt atoms which ended up in modulating the chemical and electronic environment of the Pd active sites. Selective substitution of Pd atoms with Pt atoms induced charge polarization, which reflected in the extended and contracted bond distances and altered electronic structure. These are comprehensively characterized by PXRD, XAS, XPS and supported by the simulated Pd PDOS. Changes in catalyst structure and reaction kinetics are probed real-time by operando XAS and for the first time via in-situ FT-IR spectroscopy as well. It is observed that Pt substituted counterpart, Pt_{0.2}Pd_{1.8}Ge shows higher half-wave potential and lower Tafel slope value than pristine Pd₂Ge which indicates faster charge transfer and highly active reaction sites. Interestingly, a very meagre amount of H₂O₂ (1.4%) is formed

for Pt_{0.2}Pd_{1.8}Ge which makes it a highly promising catalyst for ORR with excellent selectivity towards 4e⁻ transfer. From adsorption energy calculation, it is observed that in Pt_{0.2}Pd_{1.8}Ge the weaker OH* and stronger OOH* adsorptions are responsible for no OH poisoning with 50,000 ADT cycles stability and very less H₂O₂ formation.

2.6 References

1. Shindell, D.; Smith, C. J., Climate and air-quality benefits of a realistic phase-out of fossil fuels. *Nature* **2019**, *573*, 408-411.
2. Kordesch, K. V.; Simader, G. R., Environmental Impact of Fuel Cell Technology. *Chem. Rev.* **1995**, *95*, 191-207.
3. Zhu, D. D.; Liu, J. L.; Qiao, S. Z., Recent Advances in Inorganic Heterogeneous Electrocatalysts for Reduction of Carbon Dioxide. *Adv. Mater.* **2016**, *28*, 3423-3452.
4. Suntivich, J.; Gasteiger, H. A.; Yabuuchi, N.; Nakanishi, H.; Goodenough, J. B.; Shao-Horn, Y., Design principles for oxygen-reduction activity on perovskite oxide catalysts for fuel cells and metal–air batteries. *Nat. Chem.* **2011**, *3*, 546-550.
5. Lin, R.; Cai, X.; Zeng, H.; Yu, Z., Stability of High-Performance Pt-Based Catalysts for Oxygen Reduction Reactions. *Adv. Mater.* **2018**, *30*, 1705332.
6. Hernandez-Fernandez, P.; Masini, F.; McCarthy, D. N.; Strebel, C. E.; Friebel, D.; Deiana, D.; Malacrida, P.; Nierhoff, A.; Bodin, A.; Wise, A. M.; Nielsen, J. H.; Hansen, T. W.; Nilsson, A.; Stephens, I. E. L.; Chorkendorff, I., Mass-selected nanoparticles of Pt_xY as model catalysts for oxygen electroreduction. *Nat. Chem.* **2014**, *6*, 732-738.
7. Sarkar, S.; Peter, S. C., An Overview on Pt₃X Electrocatalysts for Oxygen Reduction Reaction. *Chem. Asian J.* **2021**, *16*, 1184-1197.
8. Sarkar, S.; Varghese, M.; Vinod, C. P.; Peter, S. C., Conductive interface promoted bifunctional oxygen reduction/evolution activity in an ultra-low precious metal based hybrid catalyst. *Chem. Commun.* **2021**, *57*, 1951-1954.
9. Kuttiyiel, K. A.; Sasaki, K.; Su, D.; Wu, L.; Zhu, Y.; Adzic, R. R., Gold-promoted structurally ordered intermetallic palladium cobalt nanoparticles for the oxygen reduction reaction. *Nat. Commun.* **2014**, *5*, 5185.
10. Su, J.; Yang, Y.; Xia, G.; Chen, J.; Jiang, P.; Chen, Q., Ruthenium-cobalt nanoalloys encapsulated in nitrogen-doped graphene as active electrocatalysts for producing hydrogen in alkaline media. *Nat. Commun.* **2017**, *8*, 14969.

11. Jana, N. R.; Gearheart, L.; Murphy, C. J., Seed-Mediated Growth Approach for Shape-Controlled Synthesis of Spheroidal and Rod-like Gold Nanoparticles Using a Surfactant Template. *Adv. Mater.* **2001**, *13*, 1389-1393.
12. Ma, R.; Lin, G.; Zhou, Y.; Liu, Q.; Zhang, T.; Shan, G.; Yang, M.; Wang, J., A review of oxygen reduction mechanisms for metal-free carbon-based electrocatalysts. *Npj Comput. Mater.* **2019**, *5*, 78.
13. Zhang, L.; Fischer, J. M. T. A.; Jia, Y.; Yan, X.; Xu, W.; Wang, X.; Chen, J.; Yang, D.; Liu, H.; Zhuang, L.; Hankel, M.; Searles, D. J.; Huang, K.; Feng, S.; Brown, C. L.; Yao, X., Coordination of Atomic Co–Pt Coupling Species at Carbon Defects as Active Sites for Oxygen Reduction Reaction. *J. Am. Chem. Soc.* **2018**, *140*, 10757-10763.
14. Sarma, S. C.; Vemuri, V.; Mishra, V.; Peter, S. C., “Sacrificial protection in action!”: ultra-high stability of palladesite mineral towards the oxygen reduction reaction. *J. Mater. Chem. A* **2019**, *7*, 979-984.
15. Beermann, V.; Gocyla, M.; Kühn, S.; Padgett, E.; Schmies, H.; Goerlin, M.; Erini, N.; Shviro, M.; Heggen, M.; Dunin-Borkowski, R. E.; Muller, D. A.; Strasser, P., Tuning the Electrocatalytic Oxygen Reduction Reaction Activity and Stability of Shape-Controlled Pt–Ni Nanoparticles by Thermal Annealing – Elucidating the Surface Atomic Structural and Compositional Changes. *J. Am. Chem. Soc.* **2017**, *139*, 16536-16547.
16. Becknell, N.; Son, Y.; Kim, D.; Li, D.; Yu, Y.; Niu, Z.; Lei, T.; Sneed, B. T.; More, K. L.; Markovic, N. M.; Stamenkovic, V. R.; Yang, P., Control of Architecture in Rhombic Dodecahedral Pt–Ni Nanoframe Electrocatalysts. *J. Am. Chem. Soc.* **2017**, *139*, 11678-11681.
17. Kwon, T.; Jun, M.; Kim, H. Y.; Oh, A.; Park, J.; Baik, H.; Joo, S. H.; Lee, K., Vertex-Reinforced PtCuCo Ternary Nanoframes as Efficient and Stable Electrocatalysts for the Oxygen Reduction Reaction and the Methanol Oxidation Reaction. *Adv. Funct. Mater.* **2018**, *28*, 1706440.
18. Huang, L.; Zheng, X.; Gao, G.; Zhang, H.; Rong, K.; Chen, J.; Liu, Y.; Zhu, X.; Wu, W.; Wang, Y.; Wang, J.; Dong, S., Interfacial Electron Engineering of Palladium and Molybdenum Carbide for Highly Efficient Oxygen Reduction. *J. Am. Chem. Soc.* **2021**, *143*, 6933-6941.

19. Du, X. X.; He, Y.; Wang, X. X.; Wang, J. N., Fine-grained and fully ordered intermetallic PtFe catalysts with largely enhanced catalytic activity and durability. *Energy Environ. Sci.* **2016**, *9*, 2623-2632.
20. Kamiya, K.; Kamai, R.; Hashimoto, K.; Nakanishi, S., Platinum-modified covalent triazine frameworks hybridized with carbon nanoparticles as methanol-tolerant oxygen reduction electrocatalysts. *Nat. Commun.* **2014**, *5*, 5040.
21. Bagchi, D.; Phukan, N.; Sarkar, S.; Das, R.; Ray, B.; Bellare, P.; Ravishankar, N.; Peter, S. C., Ultralow non-noble metal loaded MOF derived bi-functional electrocatalysts for the oxygen evolution and reduction reactions. *J. Mater. Chem. A* **2021**, *9*, 9319-9326.
22. Stamenkovic, V. R.; Mun, B. S.; Arenz, M.; Mayrhofer, K. J. J.; Lucas, C. A.; Wang, G.; Ross, P. N.; Markovic, N. M., Trends in electrocatalysis on extended and nanoscale Pt-bimetallic alloy surfaces. *Nat. Mater.* **2007**, *6*, 241-247.
23. Nørskov, J. K.; Rossmeisl, J.; Logadottir, A.; Lindqvist, L.; Kitchin, J. R.; Bligaard, T.; Jónsson, H., Origin of the Overpotential for Oxygen Reduction at a Fuel-Cell Cathode. *J. Phys. Chem. B* **2004**, *108*, 17886-17892.
24. Zhang, J.; Zhao, Z.; Xia, Z.; Dai, L., A metal-free bifunctional electrocatalyst for oxygen reduction and oxygen evolution reactions. *Nat. Nanotechnol.* **2015**, *10*, 444-452.
25. Liu, J.; Jiao, M.; Lu, L.; Barkholtz, H. M.; Li, Y.; Wang, Y.; Jiang, L.; Wu, Z.; Liu, D.-j.; Zhuang, L.; Ma, C.; Zeng, J.; Zhang, B.; Su, D.; Song, P.; Xing, W.; Xu, W.; Wang, Y.; Jiang, Z.; Sun, G., High performance platinum single atom electrocatalyst for oxygen reduction reaction. *Nat. Commun.* **2017**, *8*, 15938.
26. Sarkar, S.; Jana, R.; Suchitra; Waghmare, U. V.; Kuppan, B.; Sampath, S.; Peter, S. C., Ordered Pd₂Ge Intermetallic Nanoparticles as Highly Efficient and Robust Catalyst for Ethanol Oxidation. *Chem. Mater.* **2015**, *27*, 7459-7467.
27. Rajamani, A. R.; Ashly, P. C.; Dheer, L.; Sarma, S. C.; Sarkar, S.; Bagchi, D.; Waghmare, U. V.; Peter, S. C., Synergetic Effect of Ni-Substituted Pd₂Ge Ordered Intermetallic Nanocomposites for Efficient Electrooxidation of Ethanol in Alkaline Media. *ACS Appl. Energy Mater.* **2019**, *2*, 7132-7141.
28. Li, Q.; Yuan, F.; Yan, C.; Zhu, J.; Sun, J.; Wang, Y.; Ren, J.; She, X., Germanium and phosphorus co-doped carbon nanotubes with high electrocatalytic activity for oxygen reduction reaction. *RSC Adv.* **2016**, *6*, 33205-33211.

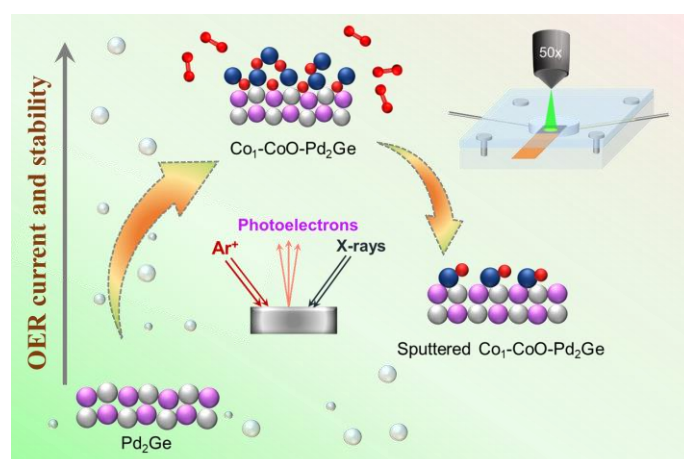
29. Xu, W.; Yan, L.; Teich, L.; Liaw, S.; Zhou, M.; Luo, H., Polymer-assisted chemical solution synthesis of $\text{La}_{0.8}\text{Sr}_{0.2}\text{MnO}_3$ -based perovskite with A-site deficiency and cobalt-doping for bifunctional oxygen catalyst in alkaline media. *Electrochim. Acta* **2018**, *273*, 80-87.
30. Giannozzi, P.; Baroni, S.; Bonini, N.; Calandra, M.; Car, R.; Cavazzoni, C.; Ceresoli, D.; Chiarotti, G. L.; Cococcioni, M.; Dabo, I.; Dal Corso, A.; de Gironcoli, S.; Fabris, S.; Fratesi, G.; Gebauer, R.; Gerstmann, U.; Gougoussis, C.; Kokalj, A.; Lazzeri, M.; Martin-Samos, L.; Marzari, N.; Mauri, F.; Mazzarello, R.; Paolini, S.; Pasquarello, A.; Paulatto, L.; Sbraccia, C.; Scandolo, S.; Sclauzero, G.; Seitsonen, A. P.; Smogunov, A.; Umari, P.; Wentzcovitch, R. M., QUANTUM ESPRESSO: a modular and open-source software project for quantum simulations of materials. *J. phys. Cond. matter : an Institute Phys. j.* **2009**, *21*, 395502.
31. Perdew, J. P.; Burke, K.; Ernzerhof, M., Generalized Gradient Approximation Made Simple. *Phys. Rev. Lett.* **1996**, *77*, 3865-3868.
32. Wang, T.; Chutia, A.; Brett, D. J. L.; Shearing, P. R.; He, G.; Chai, G.; Parkin, I. P., Palladium alloys used as electrocatalysts for the oxygen reduction reaction. *Energy Environ. Sci.* **2021**, *14*, 2639-2669.
33. Goetze, J.; Yarulina, I.; Gascon, J.; Kapteijn, F.; Weckhuysen, B. M., Revealing Lattice Expansion of Small-Pore Zeolite Catalysts during the Methanol-to-Olefins Process Using Combined Operando X-ray Diffraction and UV-vis Spectroscopy. *ACS Catal.* **2018**, *8*, 2060-2070.
34. Shinagawa, T.; Garcia-Esparza, A. T.; Takanabe, K., Insight on Tafel slopes from a microkinetic analysis of aqueous electrocatalysis for energy conversion. *Sci. Rep.* **2015**, *5*, 13801.
35. Sarkar, S.; Ramarao, S. D.; Das, T.; Das, R.; Vinod, C. P.; Chakraborty, S.; Peter, S. C., Unveiling the Roles of Lattice Strain and Descriptor Species on Pt-Like Oxygen Reduction Activity in Pd-Bi Catalysts. *ACS Catal.* **2021**, *11*, 800-808.
36. Bagchi, D.; Raj, J.; Singh, A. K.; Cherevotan, A.; Roy, S.; Manoj, K. S.; Vinod, C. P.; Peter, S. C., Structure-Tailored Surface Oxide on Cu-Ga Intermetallics Enhances CO_2 Reduction Selectivity to Methanol at Ultralow Potential. *Adv. Mater.* **2022**, *n/a*, 2109426.

37. Yang, S.; Tak, Y. J.; Kim, J.; Soon, A.; Lee, H., Support Effects in Single-Atom Platinum Catalysts for Electrochemical Oxygen Reduction. *ACS Catal.* **2017**, *7*, 1301-1307.
38. Choi, C. H.; Kim, M.; Kwon, H. C.; Cho, S. J.; Yun, S.; Kim, H.-T.; Mayrhofer, K. J. J.; Kim, H.; Choi, M., Tuning selectivity of electrochemical reactions by atomically dispersed platinum catalyst. *Nat. Commun.* **2016**, *7*, 10922.
39. Nayak, S.; McPherson, I. J.; Vincent, K. A., Adsorbed Intermediates in Oxygen Reduction on Platinum Nanoparticles Observed by In Situ IR Spectroscopy. *Angew. Chem. Int. Ed.* **2018**, *57*, 12855-12858.
40. Bagchi, D.; Sarkar, S.; Singh, A. K.; Vinod, C. P.; Peter, S. C., Potential- and Time-Dependent Dynamic Nature of an Oxide-Derived PdIn Nanocatalyst during Electrochemical CO₂ Reduction. *ACS Nano* **2022**, *16*, 6185-6196.
41. Kunimatsu, K.; Yoda, T.; Tryk, D. A.; Uchida, H.; Watanabe, M., In situ ATR-FTIR study of oxygen reduction at the Pt/Nafion interface. *Phys. Chem. Chem. Phys.* **2010**, *12*, 621-629.
42. Briega-Martos, V.; Cheuquepán, W.; Feliu, J. M., Detection of Superoxide Anion Oxygen Reduction Reaction Intermediate on Pt(111) by Infrared Reflection Absorption Spectroscopy in Neutral pH Conditions. *J. Phys. Chem. Lett.* **2021**, *12*, 1588-1592.
43. Xu, Z.; Liang, Z.; Guo, W.; Zou, R., In situ/operando vibrational spectroscopy for the investigation of advanced nanostructured electrocatalysts. *Coord. Chem. Rev.* **2021**, *436*, 213824.
44. Li, M. W.; Fu, M. H.; Cao, Y.; Wang, H.; Yu, H.; Qiao, Z.; Liang, H.; Peng, F., Mn₃O₄@C Nanoparticles Supported on Porous Carbon as Bifunctional Oxygen Electrodes and their Electrocatalytic Mechanism. *ChemElectroChem* **2019**, *6*, 359-368.
45. Hammer, B.; Nørskov, J. K., Theoretical surface science and catalysis—calculations and concepts. In *Adv. Catal.*, Academic Press: 2000; Vol. 45, pp 71-129.
46. Li, H.; Wen, P.; Itanze, D. S.; Hood, Z. D.; Adhikari, S.; Lu, C.; Ma, X.; Dun, C.; Jiang, L.; Carroll, D. L.; Qiu, Y.; Geyer, S. M., Scalable neutral H₂O₂ electrosynthesis by platinum diphosphide nanocrystals by regulating oxygen reduction reaction pathways. *Nat. Commun.* **2020**, *11*, 3928.
47. Chowdhury, A. J.; Yang, W.; Walker, E.; Mamun, O.; Heyden, A.; Terejanu, G. A., Prediction of Adsorption Energies for Chemical Species on Metal Catalyst Surfaces Using Machine Learning. *J. Phys. Chem. C* **2018**, *122*, 28142-28150.

48. Rao, D.-M.; Sun, T.; Yang, Y.-S.; Yin, P.; Pu, M.; Yan, H.; Wei, M., Theoretical study on the reaction mechanism and selectivity of acetylene semi-hydrogenation on Ni–Sn intermetallic catalysts. *Phys. Chem. Chem. Phys.* **2019**, *21*, 1384-1392.
49. Chen, C.; Zhu, X.; Wen, X.; Zhou, Y.; Zhou, L.; Li, H.; Tao, L.; Li, Q.; Du, S.; Liu, T.; Yan, D.; Xie, C.; Zou, Y.; Wang, Y.; Chen, R.; Huo, J.; Li, Y.; Cheng, J.; Su, H.; Zhao, X.; Cheng, W.; Liu, Q.; Lin, H.; Luo, J.; Chen, J.; Dong, M.; Cheng, K.; Li, C.; Wang, S., Coupling N₂ and CO₂ in H₂O to synthesize urea under ambient conditions. *Nat. Chem.* **2020**, *12*, 717-724.
50. Yang, X.; Xia, D.; Kang, Y.; Du, H.; Kang, F.; Gan, L.; Li, J., Unveiling the Axial Hydroxyl Ligand on FeN₄C Electrocatalysts and Its Impact on the pH-Dependent Oxygen Reduction Activities and Poisoning Kinetics. *Adv. Sci.* **2020**, *7*, 2000176.

Chapter 3

Distortion-Induced Interfacial Charge Transfer at Single Cobalt Atom Secured on Ordered Intermetallic Surface Enhances Pure Oxygen Production



Soumi Mondal; Mohd Riyaz; Debabrata Bagchi; Nilutpal Dutta; Ashutosh Kumar Singh; Vinod C Prabhakaran; Sebastian C. Peter, *ACS Nano* **2023**, 17, 23169–23180.

Summary

In this work, atomic cobalt (Co) incorporation into the Pd₂Ge intermetallic lattice facilitates *operando* generation of a thin layer of CoO over Co substituted Pd₂Ge, with Co in the CoO surface layer functioning as single metal sites. Hence the catalyst has been titled Co₁-CoO-Pd₂Ge. High-resolution transmission electron microscopy (HR-TEM), X-ray photoelectron spectroscopy (XPS) and X-ray absorption spectroscopy (XAS) confirm the existence of CoO, with some of the Co bonded to Ge by substitution of Pd sites in the Pd₂Ge lattice. The role of the CoO layer in OER has been verified by its selective removal using argon sputtering and conducting OER on the etched catalyst. In-situ X-ray absorption near edge structure (XANES) and extended X-ray absorption fine structure spectroscopy (EXAFS) demonstrate that CoO gets transformed to CoOOH (Co³⁺) in *operando* condition with faster charge transfer through Pd atoms in the core Pd₂Ge lattice. In-situ Raman spectroscopy depicts the emergence of a CoOOH phase on applying potential and that the phase is stable with increasing potential and time without getting converted to CoO₂. Density functional theory (DFT) calculations indicate that the Pd₂Ge lattice induces distortion in the CoO phase and generates unpaired spins in non-magnetic CoOOH system resulting in an increase in OER activity and durability. The existence of spin density even after electrocatalysis is verified from electron paramagnetic resonance spectroscopy (EPR). We have thus successfully synthesized intermetallic supported CoO during synthesis and rigorously verified the role played by an intermetallic Pd₂Ge core in enhancing charge transfer, generating spin-density, improving electrochemical durability, and imparting mechanical stability to a thin CoOOH overlayer. Differential electrochemical mass spectrometry (DEMS) has been explored to visualize the instantaneous generation of oxygen gas during the onset of the reaction.

Table of Contents

3.1	Introduction.....	81
3.2	Experimental Details	83
3.2.1	Chemicals and reagents	83
3.2.2	Synthesis of Pd ₂ Ge and Co ₁ -CoO-Pd ₂ Ge	83
3.3	Characterization.....	84
3.3.1	Powder X-ray Diffraction (PXRD)	84
3.3.2	Scanning electron microscopy (SEM) and Energy Dispersive Spectrum (EDS).....	84
3.3.3	Transmission electron microscopy (TEM)	84
3.3.4	High-angle annular dark-field imaging Scanning Transmission electron microscopy (HAADF-STEM)	84
3.3.5	Inductively coupled plasma atomic emission spectroscopy (ICP-OES)	85
3.3.6	X-ray Photoelectron Spectroscopy (XPS)	85
3.3.7	X-ray absorption near edge spectroscopy (XANES) and Extended X-ray Absorption Fine Structure (EXAFS):.....	85
3.3.8	Electrochemical oxygen evolution Reaction (OER)	85
3.3.9	Rotating ring disk electrode experiment (RRDE)	86
3.3.10	In-situ X-ray absorption spectroscopy (XAS)	86
3.3.11	Differential electrochemical mass spectrometry (DEMS).....	86
3.3.12	Computational Details.....	87
3.4	Results & Discussion	87
3.4.1	Phase analysis and microscopic visualization	87
3.4.2	Electrochemical oxygen evolution reduction (OER)	91
3.4.3	Local coordination and oxidation state analysis of Co ₁ -CoO-Pd ₂ Ge.....	95
3.4.4	Presence of oxide layer: Argon sputtered XPS and SEM analysis	95
3.4.5	Probing charge transfer during OER via operando methods	100
3.4.6	Visualizing structural evolution and stabilization: Potential-dependent Raman spectroscopy and theoretical calculations	103
3.4.7	Spectrometric analysis of oxygen generation triggered by oxidation potential – A DEMS study	107
3.5	Conclusion	108
3.6	References.....	112

3.1 Introduction

Oxygen evolution reaction (OER)¹ is the counter electrochemical reaction of water splitting via green means.¹ Enhancing the rate of OER can fasten the HER kinetics in the green mode of hydrogen generation.² The major challenge for OER is four electrons transfer process for oxidation of singlet state species OH⁻ (or H₂O) to triplet state O₂ molecules which makes it sluggish requiring high overpotential.^{3, 4} Till date, best reported OER electrocatalysts are mainly noble metal-based oxides like RuO₂ and IrO₂ which are non-magnetic in nature and this magnetic property plays a crucial role in OER mechanism.⁵⁻⁷ The real motive of the electrochemists is to generate non-noble metal-based earth-abundant catalysts which will satisfy the general descriptors for OER performance. The difference between the adsorption energies of O* and OH*, $\Delta G_{O^*} - \Delta G_{OH^*}$, is the major descriptor for OER which decides whether the catalyst will provide faster OER kinetics. This energy difference is mainly governed by number of electrons in the d-orbital and electronic configuration (e_g) of the transition metals in their oxides.⁸

The first-transition metal oxides like Ni-, Co-, and Fe-based oxides are earth abundant, low-cost, and magnetic, which have shown promising OER activity.^{9, 10} There are doped RuO₂ based catalysts delivering enhanced OER activity and stability than pristine RuO₂¹¹. Despite Co being an excellent member amongst TMs showing OER activity, the major concern is its stability.^{12, 13} To overcome this, various approaches include decreased loading of Co and generating OER-active catalysts. There are Co based polyoxometalates,¹⁴ mesoporous cobalt oxides,¹⁵ Co-based MOFs,¹⁶ and oxides like, like spinels, perovskites,¹⁷ and others like Co₃O₄,^{7, 18} Zn_xCo_{3-x}O₄,⁸ Mn-Co oxide,¹⁹ Ni_xCo_{3-x}O₄,²⁰ inverse spinel oxide LiCoVO₄, single atom catalysts²¹ have shown excellent OER activity.^{16, 22, 23} Different experimental results have pointed out that the spin state of the active site affects the OER activity directly. The singlet reactant species OH⁻ have all paired electrons, whereas triplet oxygen molecule has two electrons in two π^* orbitals with parallel alignment.^{3, 24, 25} This demands magnetically active sites with unpaired spin species on the catalyst surface which favors the spin alignment in the intermediate adsorbed species (like O*³). To facilitate this process, presence of unpaired electrons in valence orbitals is absolute necessary.

Co-based oxides are well-known catalysts with high activity due to the formation of CoOOH species providing higher current density at lower overpotentials. The Co³⁺ ion in oxides is mostly expected to be in the t_{2g}^6 state (LS state), but a favourable crystal structure can generate unpaired electron with $t_{2g}^5 e_g^1$ state (HS state).^{26, 27} Different approaches have been

proposed to generate this HS state in d^6 configuration, like, synthesizing extremely thin films of CoOOH gives rise to unpairing of electron as compared to bulk CoOOH,²⁸ incorporation of single atoms in CoOOH surface,²⁹ and doping heteroatom in ABO_3 type perovskite oxides.³⁰ Besides, the major drawback of these oxides is their poor stability in harsh alkaline OER conditions due to which current density drops after some time. This is due to agglomeration and amorphization of these oxide species under OER conditions.³¹ Different approaches to retain catalytic activity for long durations such as doping with other transition metals, creating oxygen vacancies, and including a conductive support have been reported.⁵ Conductive supports like N-doped graphitic carbon have been reportedly used with Co-oxides like CoO/NGHSs provide high ECSA and electrical conductivity,³² Fe_3O_4/CoO CNTs has high durability and increased number of active sites,³³ and so on. Constructing synergistic interfaces of cobalt oxides and highly active metals like Pt, Pd and Au/Ag can provide conductivity and stability due to enhanced charge transfer at longer periods of electrocatalysis.^{34, 35} There are reports where a dual-phase system of Co-oxides with active metals enhanced stability, like, $Ag_2O-Co_3O_4$ framework obtained from Ag-Co bimetallic,³⁶ Pd/ CoO_x for enhanced CO oxidation,³⁷ MOF templated Pd/ $PdO-Co_3O_4$,³⁸ N-doped C-nanofiber-Co/ CoO_x -Pd nanoparticles for enhanced HER and OER,³⁹ and CoO/Pd(100) derived from Pd-Co bimetallic compound has provided high conductivity due to electron tunneling from the active metal to the Co-oxide species.⁴⁰ Also, in CeO_x/CoO_x , the Ce atoms promote facile formation of CoOOH and optimizes binding energies of the OER intermediates.⁴¹ All these examples show how the bimetallic and monometallic supports themselves converted to their oxides and helped in facilitating OER kinetics. An intermetallic support is expected not to get easily converted to the oxides of the constituent elements due to highly stable and conductive structure. Keeping these observations in mind, we designed a catalyst with a stable intermetallic base surfaced with a very thin layer of Co-oxide.

This work unveils the enhanced OER activity of an unexplored intermetallic Pd_2Ge after the incorporation of Co atoms into the Pd sites, which resulted in the generation of ultra-thin layer of CoO species over Co substituted Pd_2Ge lattice. Previous reports show that Ge based systems exhibit high stability in alkaline medium.⁴² The compound Pd_2Ge has never been tested for OER and only single report on HER for the reduction counterpart of water splitting.⁴³ The major concern of OER catalysts is their mechanical and electronic stability and durability in harsh alkaline and oxidation environment. All the previous reports deal with either carbon-based or metallic supports. Extensive studies have been done on CoO anchored on

different metallic or metallic oxide or bimetallic supports. CoO has been studied on TiO_2 ,⁴⁴ Mn_3O_4 ,⁴⁵ Au metal,⁴⁶ Ag metal,³⁶ $\text{Cu}_2\text{O}@ \text{Cu}$ interface,⁴⁷ Pd-Co bimetallic system,⁴⁰ Fe_3O_4 ,³³ and so on. These approaches have succeeded in achieving facile charge transfer which has reduced overpotential and Tafel slope value, whereas the stability is still the concern. Our system is a stable intermetallic on which a CoO thin layer is secured. This is a promising strategy to provide enhanced electron tunneling and mechanical stability at the synergistic interface of CoO and Co incorporated Pd_2Ge . It has been reported that noble metals (except Ir and Ru) are not showing good activity for OER which evidently indicates that the high activity and stability of $\text{Co}_1\text{-CoO-Pd}_2\text{Ge}$ comes from the synergistic effect between Co doped Pd_2Ge core and thin layer of CoO. $\text{Co}_1\text{-CoO-Pd}_2\text{Ge}$ shows very low overpotential of 264 mV for current density of 10 mA/cm^2 , stability of 5000 cycles and durable up to 80 hours with Tafel slope value of 72 mV/dec, which are better than the state-of-the-art OER catalysts.^{5, 25} In-situ XANES show that CoO layer is the active species with electron transfer observed from Pd atoms in the core. Conversion of Co^{2+} to Co^{3+} (cobalt oxyhydroxide) has been mapped by in-situ XANES and post-electrochemical XPS techniques. In-situ Raman spectroscopy visualized the generation of CoOOH phase on giving potential and found to be stable even upon increasing potential and time. The density functional theory (DFT) calculations exhibit that Pd_2Ge phase imparts distortion in the CoO phase and generates unpaired electron density in non-magnetic CoOOH system which ultimately increases the OER activity and durability. Finally, differential electrochemical mass spectrometry (DEMS) has been explored to visualize the instantaneous generation of oxygen gas during the onset of the reaction.

3.2 Experimental Details

3.2.1 Chemicals and reagents

Potassium tetrachloropalladate (K_2PdCl_4) and Nafion binder (5 wt.%) were purchased from Sigma-Aldrich, germanium tetrachloride (GeCl_4) and cobalt(II) chloride hexahydrate ($\text{CoCl}_2.6\text{H}_2\text{O}$) were purchased from Alfa-Aesar, and tri-ethylene glycol (TEG) were purchased from Merck. All the chemicals (more than 99% purity) were used as purchased without any further purification. Millipore water of conductivity $18.2 \text{ M}\Omega\text{cm}$ was used for the synthesis and all electrochemical studies.

3.2.2 Synthesis of Pd_2Ge and $\text{Co}_1\text{-CoO-Pd}_2\text{Ge}$

In a typical solvothermal reaction, 0.2 mmol of potassium tetra chloropalladate (K_2PdCl_4), 0.1 of germanium (IV) chloride (GeCl_4) for Pd_2Ge and 0.01 mmol of $\text{CoCl}_2.6\text{H}_2\text{O}$ was added along with other Pd (0.19 mmol) and Ge (0.1 mmol) salts to synthesize $\text{Co}_1\text{-CoO-}$

Pd₂Ge and 0.8 mL of superhydride solution (reducing agent) were mixed in 18 mL of TEG. In two autoclaves, solid K₂PdCl₄ and CoCl₂·6H₂O salts were dissolved in 18 ml TEG and magnetically stirred until dissolved completely. After complete dissolution, GeCl₄ was added using a micropipette as 11.4 mL. The mixture is continuously stirred for 30 mins. After that, 0.8 mL superhydride solution (Li(C₂H₅)₃BH) was added using a syringe and again stirred in an orbital shaker for 30-45 mins. The autoclave was kept at 220 °C for 24 h. The final product was washed several times with ethanol, and the obtained product was dried and used for further characterization.

3.3 Characterization

3.3.1 Powder x-ray diffraction (PXRD)

PXRD measurements were done at room temperature on a Rigaku Miniflex X-ray diffractometer with a Cu-K_α X-ray source ($\lambda = 1.5406 \text{ \AA}$), equipped with a position-sensitive detector in the angular range of $10^\circ \leq 2\theta \leq 90^\circ$ with the step size 0.02° and a scan rate of 0.5 s/step calibrated against corundum standards. The experimental XRD patterns were compared to the patterns simulated from the data reported in the literature.

3.3.2 Scanning electron microscopy (SEM) and energy dispersive spectrum (EDS)

The SEM measurement was performed using Leica scanning electron microscopy equipped with an energy-dispersive X-ray spectroscopy (EDAX) instrument (Bruker 120 eV EDAX instrument). Data were acquired by using an accelerating voltage of 15 kV, and the typical time taken for data accumulation is 100 s. The elemental analyses were performed using the P/B-ZAF standardless method (where P/B = peak to background model, Z = atomic no. correction factor, A = absorption correction factor, and F = fluorescence factor) for Cu, Ga at multiple areas on the sample coated Si wafer.

3.3.3 Transmission electron microscopy (TEM)

TEM and high-resolution TEM (HRTEM) images, selected area electron diffraction (SAED) patterns were collected using a JEOL 200 TEM instrument. Samples for these measurements were prepared by dropping a small volume of sonicated nanocrystalline powders in ethanol onto a carbon-coated copper grid.

3.3.4 High-angle annular dark-field imaging scanning transmission electron microscopy (HAADF-STEM)

HAADF-STEM images were taken using FEI/TITAN THEMIS 3391 (80–300) electron microscope.

3.3.5 Inductively coupled plasma atomic emission spectroscopy (ICP-OES)

ICP-OES was performed using a Perkin Elmer Optima 7000 DV instrument. The samples were digested in concentrated aqua regia, followed by dilution with distilled water. In a typical experiment, 2 mg of the sample was dissolved in 1 ml aqua regia and left overnight (12 hrs) for digestion. The digested sample was then diluted to 10 ml volume with deionized water. The solid particles were separated by thorough centrifugation before measurements. We have also performed the ICP-OES for the electrolyte after the running the OER reaction.

3.3.6 X-ray photoelectron spectroscopy (XPS)

XPS measurements were carried out using Thermo K-alpha+ spectrometer using micro focused and monochromated Al K α radiation with energy 1486.6 eV. The pass energy for spectral acquisition was kept at 50 eV for individual core-levels. The electron flood gun was utilized for providing charge compensation during data acquisition. Further, the individual core-level spectra were checked for charging using C1s at 284.6 eV as standard and corrected if needed. The peak fitting of the individual core-levels was done using XPSpeak 41 software with a Shirley type background. XPS spectra were measured to study the valence state, chemical composition, and electronic interactions. Ar⁺ sputtering was done for 10 secs each layer for an energy of 2 KeV and high-resolution spectra of Pd 3d, Ge 3d, and Co 2p were performed after each layer etching.

3.3.7 X-ray absorption near edge spectroscopy (XANES) and extended x-ray absorption fine structure (EXAFS):

XANES and EXAFS experiments at 300 K were performed at PETRA III, beamline P64, of DESY, Germany. Measurements of Pt-L edges at ambient pressure were performed in fluorescence as well as transmission mode using gas ionization chambers to monitor the incident and transmitted X-ray intensities. Monochromatic X-rays were obtained using a Si (111) double crystal monochromator. Pellets for the ex-situ measurements were made by homogeneously mixing the sample with an inert cellulose matrix to obtain an X-ray absorption edge jump close to one. Background subtraction, normalization, and alignment of the EXAFS data were performed by ATHENA software. Theoretical XAFS models were constructed and fitted to the experimental data in ARTEMIS.

3.3.8 Electrochemical oxygen evolution Reaction (OER)

All the electrochemical measurements were done in a 3-electrode set-up comprising of a glassy carbon as the working electrode (GCE), graphite rod counter electrode, and mercury/mercuric oxide electrode (MMO) (for basic media). The catalyst ink was prepared

using 1.6 mg catalyst + 0.4 mg Vulcan in 200 μ l of mixed solvent (IPA:H₂O = 1:1) + 20 μ L of 1 wt.% Nafion used as binder. Five μ L of the catalyst ink was drop-casted on the commercial 3 mm GCE. Commercial IrO₂ (Sigma Aldrich) was used for comparison of activity with the reported electrocatalysts. Linear sweep voltammetry (LSV) was recorded for OER at a scan rate of 5 mV s⁻¹ at 25 °C. Electrochemical impedance studies were performed in the frequency range from 10 mHz to 100 kHz at different applied DC potentials for different reactions depending on their onset potential values. The electrolyte solution was deaerated by purging N₂ gas into the solution at least for 30 min before each experiment. All the reference electrodes were calibrated with respect to the reversible hydrogen electrode (RHE), using Pt as working and counter electrodes in the respective electrolytes. The values obtained are as follows: alkaline medium, ERHE = EMMO + 0.911 V.

3.3.9 Rotating ring disk electrode experiment (RRDE)

O₂ formation via 4-electron transfer was checked using rotating ring disk electrode (RRDE) where ring as platinum and disk as glassy carbon with 4 mm diameter and keeping all other experimental conditions similar, graphite rod as the counter electrode and Hg/HgO as the reference electrode. A linear sweep potential was given to the disk electrode from 1.2V to 1.6 V (vs. RHE) at a rotation rate of 1600 rpm in 0.5 M KOH. Ring potential was fixed at 1.5 V vs. RHE which allows the further oxidation of H₂O₂ oxidation to O₂. In the RRDE experiment, the percentage of H₂O₂ produced ($X_{H_2O_2}$) and the corresponding electron transfer numbers during ORR (n) can be determined from the following equations, respectively:

$$H_2O_2 \% = 200 \times \frac{I_r/N}{I_d + I_r/N} \quad (\text{Equation 3.1})$$

3.3.10 In-situ x-ray absorption spectroscopy (XAS)

In-situ XAS was measured using home-made customized cell set up under OER conditions. Details of this setup are provided in our previous papers where in-situ XAS has been explored in ORR, HER, CO₂RR and so on.

3.3.11 Differential electrochemical mass spectrometry (DEMS)

Hidden H-40 analytical is used for measuring mass spectra of instantly produced volatile components due to electrochemical reactions. Here we have performed oxygen evolution reaction and probed the instantaneous formation of oxygen gas. We have used Type-A cell which is a one-compartment cell with a glassy carbon rod where the catalyst in needed to be coated. Ag/AgCl electrode and Pt-wire have been used as reference and counter electrodes. We have used PTFE membrane as the pervaporation layer to allow the volatile products to pass

through the electrochemical cell to the mass chamber. We have used a dual-syringe pump to keep a continuous flow of electrolyte into the electrochemical cell.

3.3.12 Computational details

The electronic structure calculations were done using DFT implemented in Viana Ab-initio Simulation Package (VASP). The exchange-correlation functional was approximated using Perdew-Becke Ernzerhof (PBE) in combination with plane-wave augmented pseudopotential. A kinetic energy cutoff of 450 eV is applied to truncate the plane-wave basis used to describe the Kohn-Sham orbitals, and a convergence threshold of 0.03 eV/Å is accounted for forces on the atoms for ionic minimization. The slab models of the heterostructures were generated using VASPKIT with less than 3% lattice mismatch. A $(3 \times 3 \times 1)$ and $(2 \times 3 \times 1)$ Monkhorst-Pack k-points grid was used for the surface slab of CoOOH@Pd₂Ge and CoO@Pd₂Ge respectively. The slab model of CoO@Pd₂Ge contains three layers of Pd₂Ge and two layers of CoO with a vacuum thickness of 15 Å. The atoms in the bottom two layers were fixed at the bulk equilibrium and the remaining were allowed to relax. After relaxing the geometry, a tetrahedron occupation scheme with Blöchl corrections was used to calculate the electronic structure.

3.4 Results & Discussion

3.4.1 Phase analysis and microscopic visualization

We have synthesized a Pd₂Ge intermetallic compound which stabilizes in the hexagonal structure of space group $P\bar{6}2m$ (synthesis details are given in the SI and in our previous works).⁴⁸⁻⁵⁰ From literature surveyed for OER, no reports exist using this particular intermetallic compound as the OER electrocatalyst. In a previous report we explored the generation of Pd vacancies in Pd₂Ge for the controlled substitution of Pt for electronic structure modulation that resulted in enhanced ORR performance.⁵⁰ Utilizing that successful strategy, here we aimed at substituting Pd atoms with Co, and interestingly obtained a Co substituted Pd₂Ge with a nano-coral morphology with a very thin layer of CoO well distributed at the surface. **Figure 3.1a** shows the PXRD pattern of Pd₂Ge, Pd_{1.9}Ge, and Co₁-CoO-Pd₂Ge, expressing that after Pd deficiency there is lattice contraction, whereas after Co incorporation there is again lattice expansion (left shift of peak as compared to pristine Pd₂Ge). **Figure 3.1b** clearly shows the shift in PXRD peak corresponding to (111) facet of Pd₂Ge. **Figures 3.2a, b** and **3.2c, d** show the transmission electron microscopy (TEM) images of Pd₂Ge and of Co₁-CoO-Pd₂Ge, respectively. It is clearly observed that there is a thin layer surrounding the nano-networks in Co₁-CoO-Pd₂Ge which is absent in the case of pristine Pd₂Ge.⁵⁰

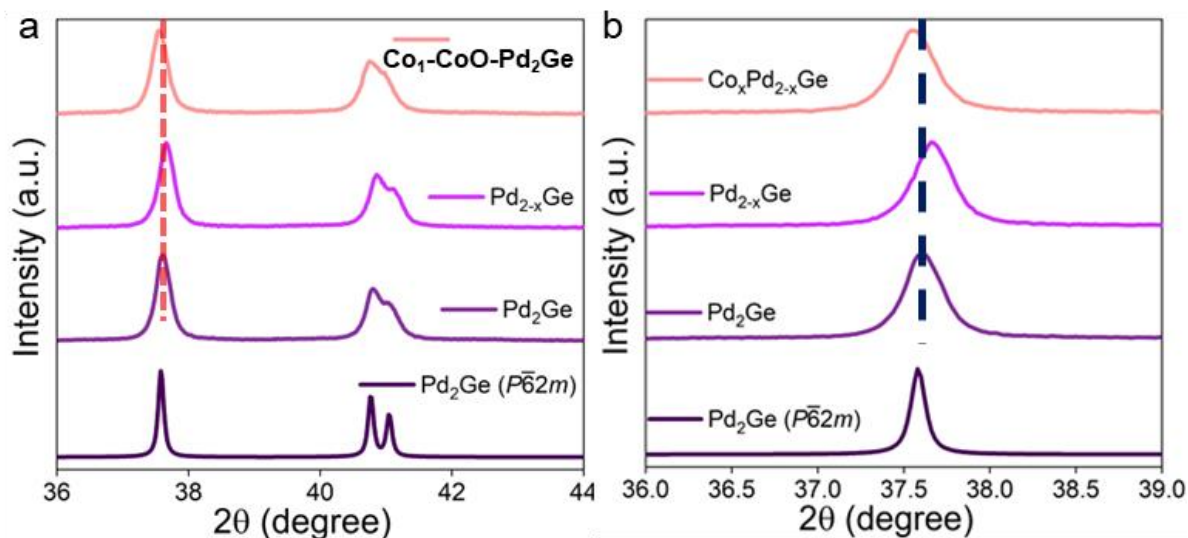


Figure 3.1. (a) PXRD patterns of Pd_2Ge , Pd_{2-x}Ge , and $\text{Co}_1\text{-CoO-Pd}_2\text{Ge}$. (b) Zoomed in peak corresponding to (111) facet of Pd_2Ge showing the peak shift with creating Pd deficiency and Co incorporation.

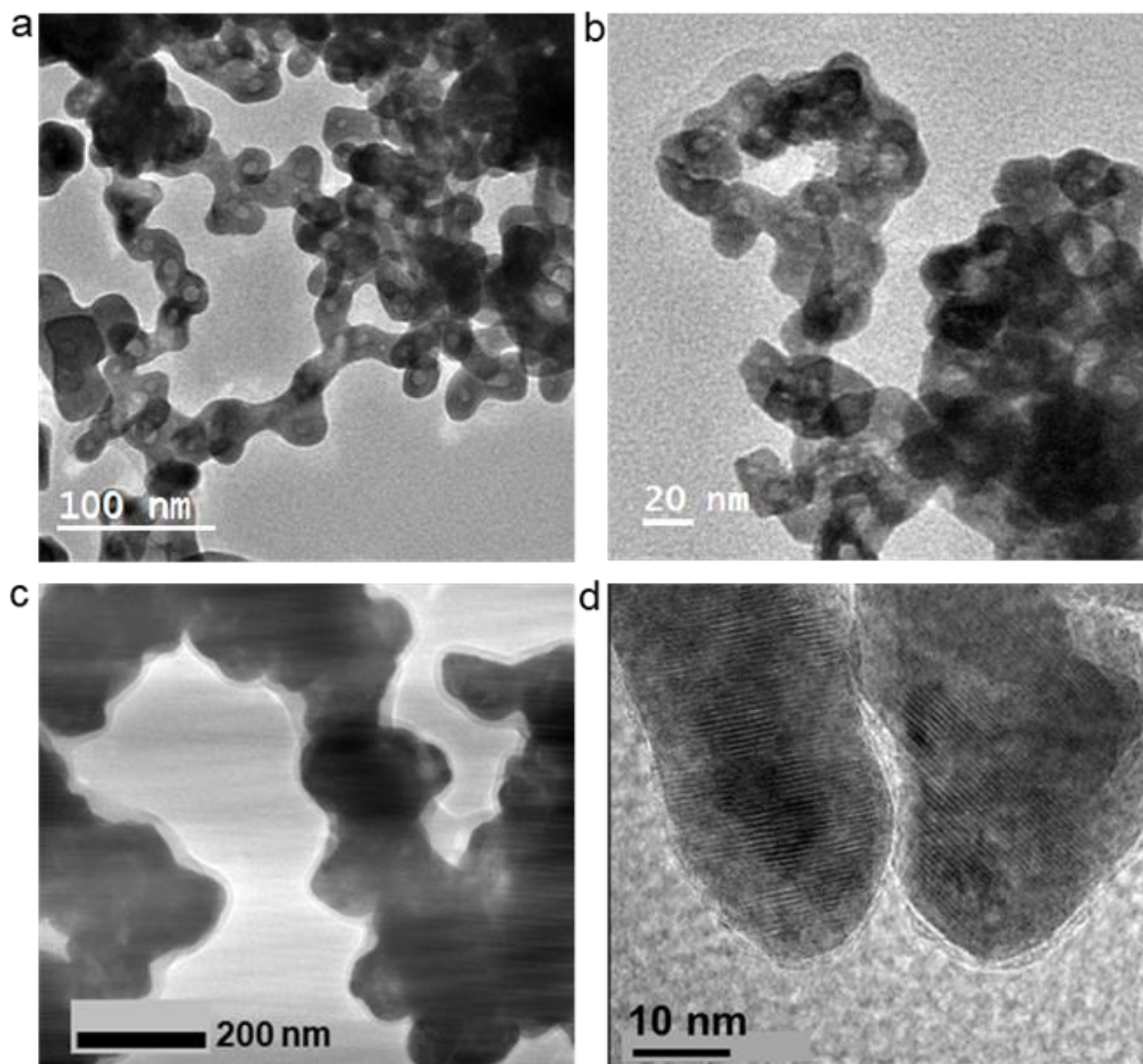


Figure 3.2. TEM images of (a,b) pristine Pd_2Ge and (c,d) $\text{Co}_1\text{-CoO-Pd}_2\text{Ge}$.

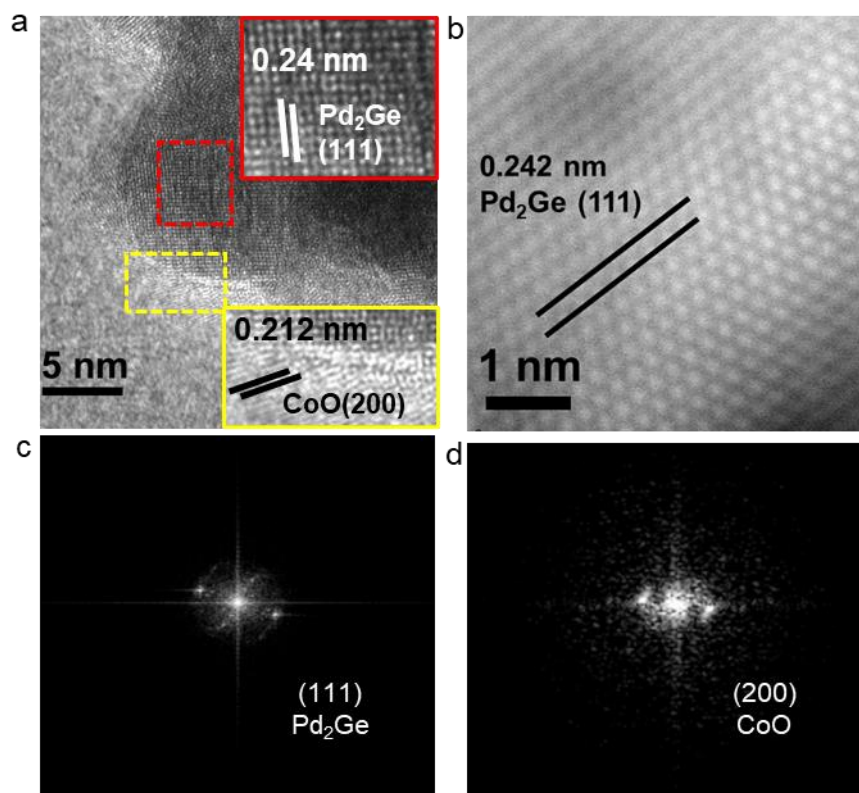


Figure 3.3. (a) HR-TEM image of Co₁-CoO-Pd₂Ge and inset images show the zoomed-in images of surface and central fringes. (b) High-angle annular dark-field imaging scanning transmission electron microscopic (HAADF-STEM) image at very high resolution. Fast Fourier Transform (FFT) pattern of d-spacing corresponding to (c) (111) facet of Co substituted Pd₂Ge lattice. (d) (200) facet of CoO thin layer from **Figure 3.3a**. The red box indicate (111) facet of Pd₂Ge and (200) facet of CoO.

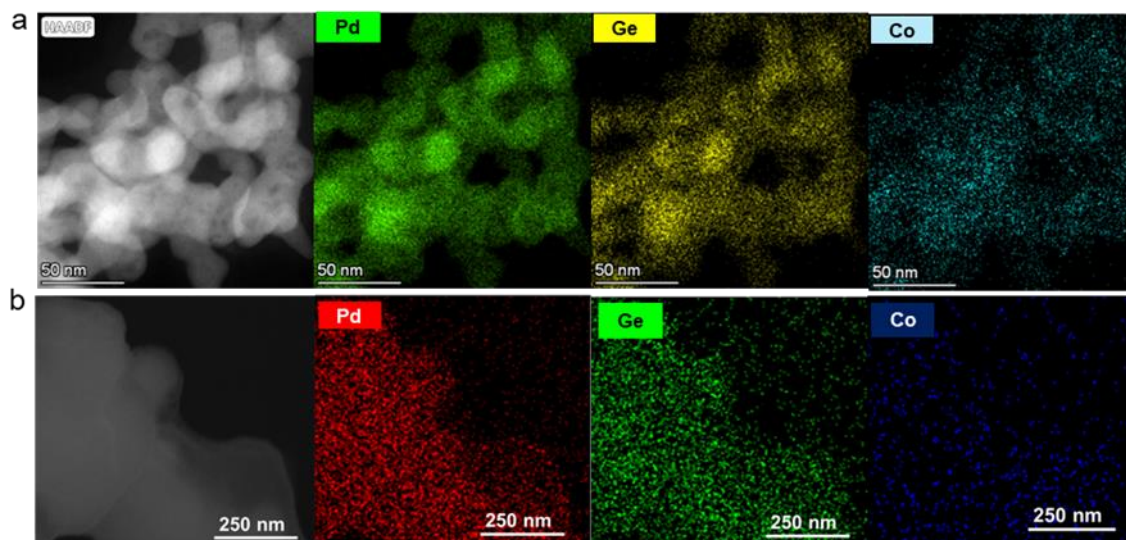


Figure 3.4. (a) HAADF-STEM color mapping and (b) SEM-EDX elemental mapping of Co₁-CoO-Pd₂Ge.

Figures 3.3a shows the prominent layer and HR-TEM image with clear fringes corresponding to (111) facet of Pd₂Ge in the internal core and (200) facets of CoO in the layer and **Figure 3.3b** shows the HAADF-STEM image of Co₁-CoO-Pd₂Ge at the atomic resolution.

Figures 3.3c and **3.3d** represents the Fast Fourier Transform (FFT) pattern of d-spacing corresponding to (a) (111) facet of Co substituted Pd_2Ge lattice and (b) (200) facet of CoO thin layer. Elemental distribution of $\text{Co}_1\text{-CoO-Pd}_2\text{Ge}$ has been shown via HAADF-STEM and SEM-EDX elemental mapping in **Figure 3.4a** and **3.4b**, respectively. **Figure 3.5** shows the schematic of formation of CoO layer on Co substituted Pd_2Ge lattice during one step solvothermal synthesis. The schematic represents exactly what is being observed from SEM and TEM images. **Table 3.1** shows the elemental composition of $\text{Co}_1\text{-CoO-Pd}_2\text{Ge}$ after Argon sputtering. Inductively coupled plasma-optical emission spectroscopy (ICP-OES) has been used to estimate the amount of Co substituted in Pd_2Ge . **Figure 3.6** and **Table 3.2** show the calibration plots for Pd, Co, and Ge and the atomic % of each element. The overall existence of Co is found to be 5% only.

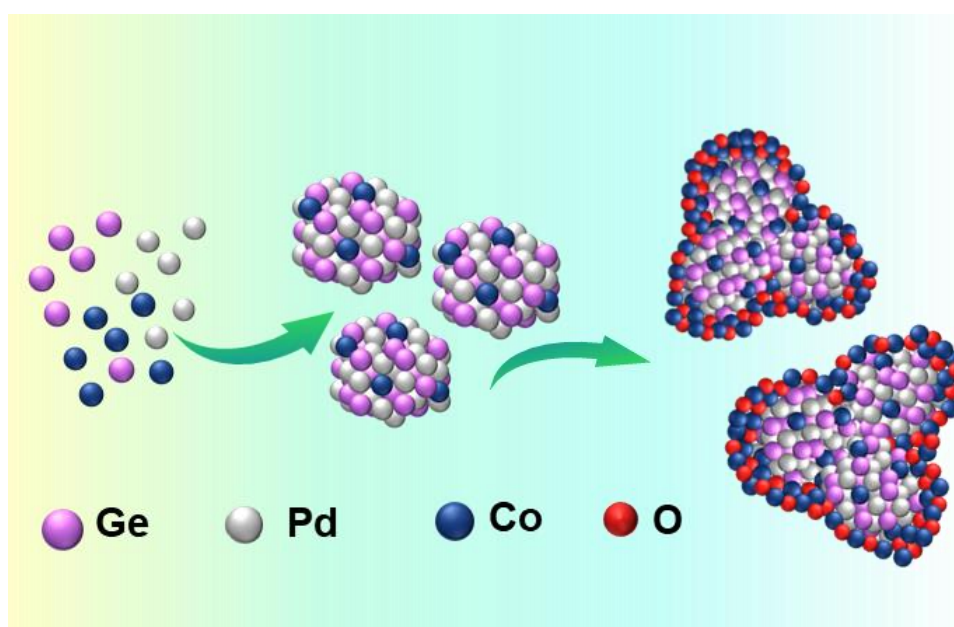


Figure 3.5. Schematic of synthesis of $\text{Co}_1\text{-CoO-Pd}_2\text{Ge}$ with CoO thin layer on the Co substituted Pd_2Ge .

Table 3.1. Atomic percentage of each element $\text{Co}_1\text{-CoO-Pd}_2\text{Ge}$ by SEM/EDX analysis after Argon sputtering as shown in **Figure S14**.

Elements	Pd	Ge	Co	O
At. %	59.33	36.87	3.80	0.00

Table 3.2. Atomic percentage of each element for $\text{Co}_1\text{-CoO-Pd}_2\text{Ge}$ by ICP analysis.

Elements	Pd	Ge	Co
At. %	61.3	33.5	5.2

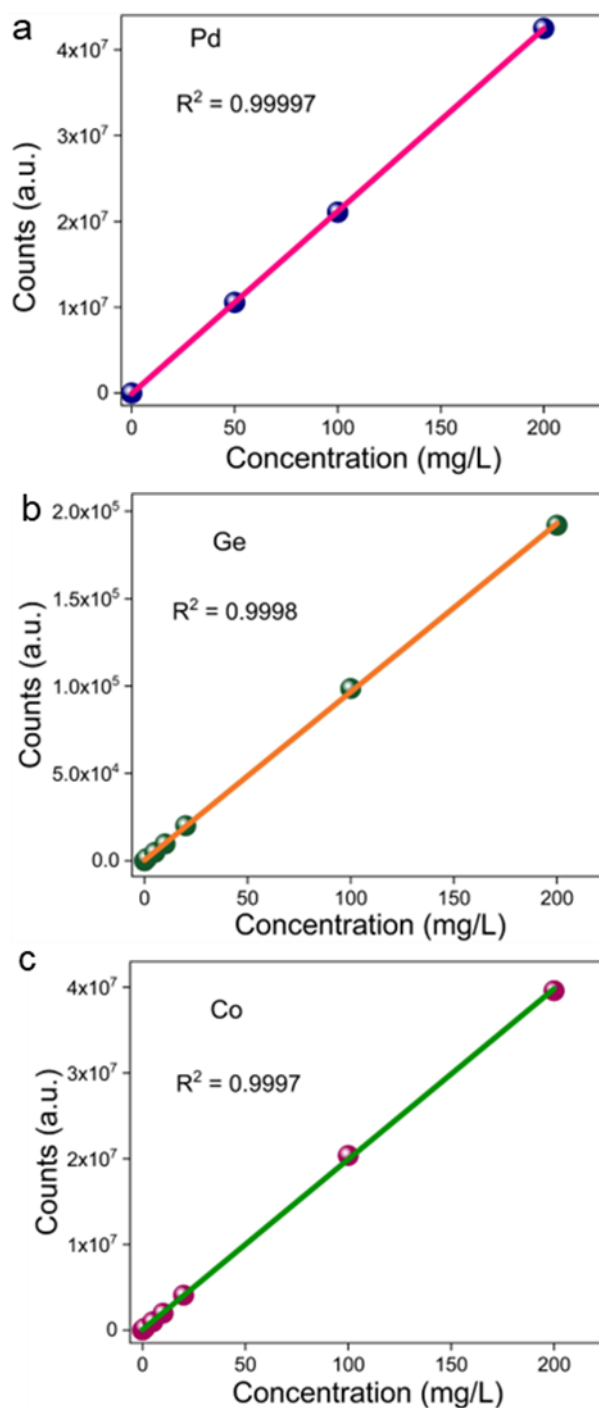


Figure 3.6. ICP-OES calibration plots for (a) Pd, (b) Ge, and (c) Co for elemental quantification of Co₁-CoO-Pd₂Ge.

3.4.2 Electrochemical oxygen evolution reduction (OER)

The catalyst Co₁-CoO-Pd₂Ge has been tested for electrochemical OER. It is observed that with the progress of the reaction, the activity is seen to increase gradually, as shown in **Figure 3.7a**. To probe this enhancement, first two LSVs of Co₁-CoO-Pd₂Ge have been compared as shown in **Figure 3.7b**.

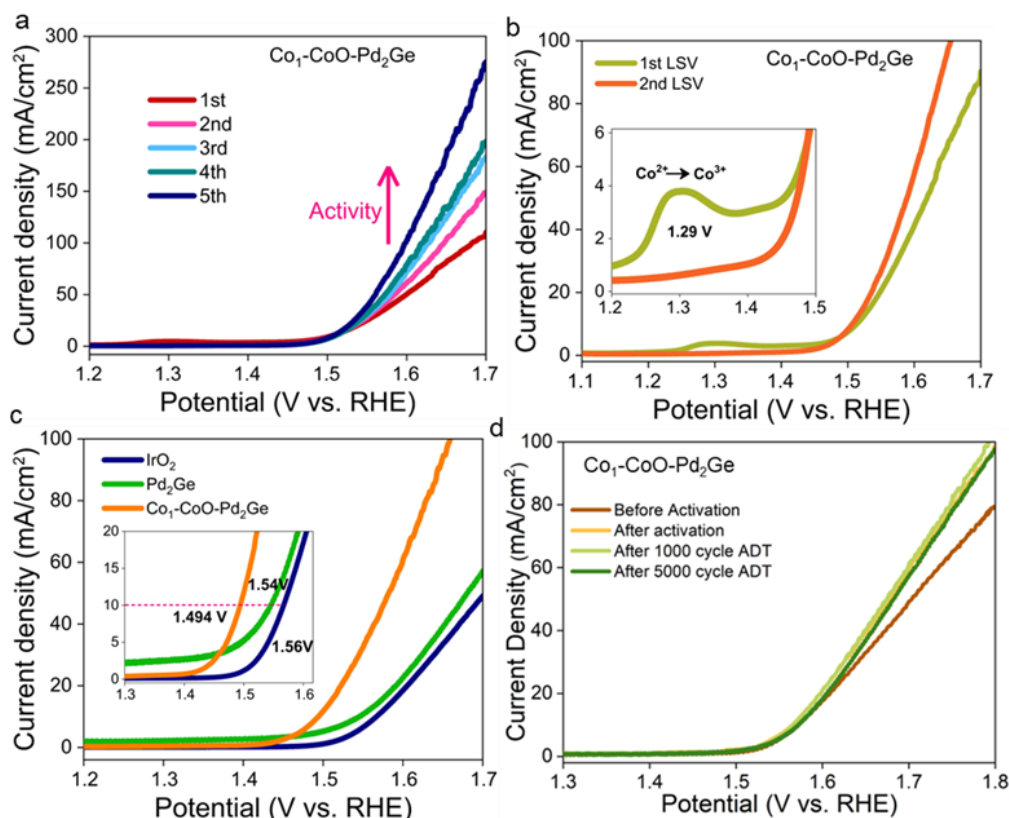


Figure 3.7. (a) Linear sweep voltammograms (LSVs) of OER for $\text{Co}_1\text{-CoO-Pd}_2\text{Ge}$ in 0.5 M KOH medium. (b) LSVs of OER for $\text{Co}_x\text{Pd}_{2-x}\text{Ge}$ with time. (c) LSVs for OER compared for Pd_2Ge , $\text{Co}_1\text{-CoO-Pd}_2\text{Ge}$, and IrO_2 . (d) LSVs of OER for $\text{Co}_1\text{-CoO-Pd}_2\text{Ge}$ before and after 5000 ADT cycles.

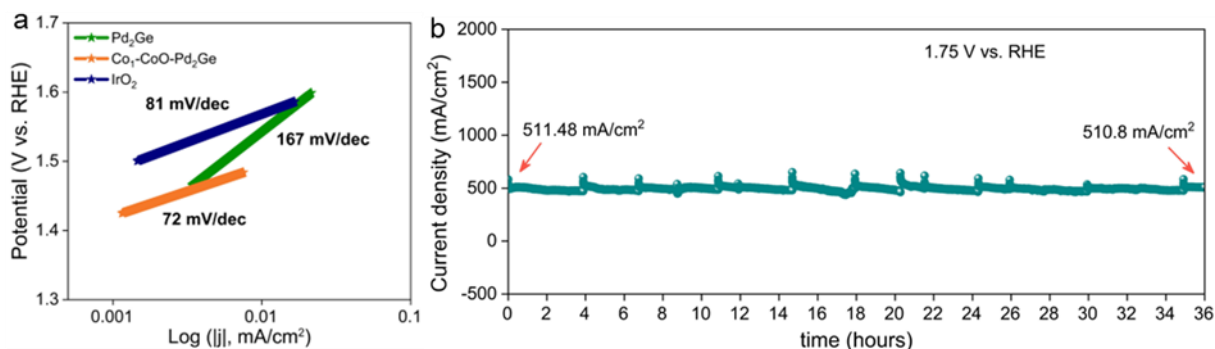


Figure 3.8. (a) Tafel slopes for Pd_2Ge , $\text{Co}_1\text{-CoO-Pd}_2\text{Ge}$ and IrO_2 . (e) Chronoamperometry (CA) for $\text{Co}_1\text{-CoO-Pd}_2\text{Ge}$ during OER in 0.5 M KOH at 500 mA/cm^2 current density.

It is clearly observed that there is an oxidative hump at 1.29 V indicating the conversion of Co^{2+} to Co^{3+} which depicts the conversion of CoO to CoOOH .⁵¹ And there is no oxidative hump corresponding to Co^{4+} formation. **Figure 3.7c** shows the comparison in OER activity between Pd_2Ge , $\text{Co}_1\text{-CoO-Pd}_2\text{Ge}$, and IrO_2 in 0.5 M KOH medium. The activity of $\text{Co}_1\text{-CoO-Pd}_2\text{Ge}$ is much better than both IrO_2 and pristine Pd_2Ge where overpotential for 10 mA/cm^2 is only 264 mV for $\text{Co}_1\text{-CoO-Pd}_2\text{Ge}$ whereas it is 310 and 330 mV for Pd_2Ge and IrO_2 , respectively.

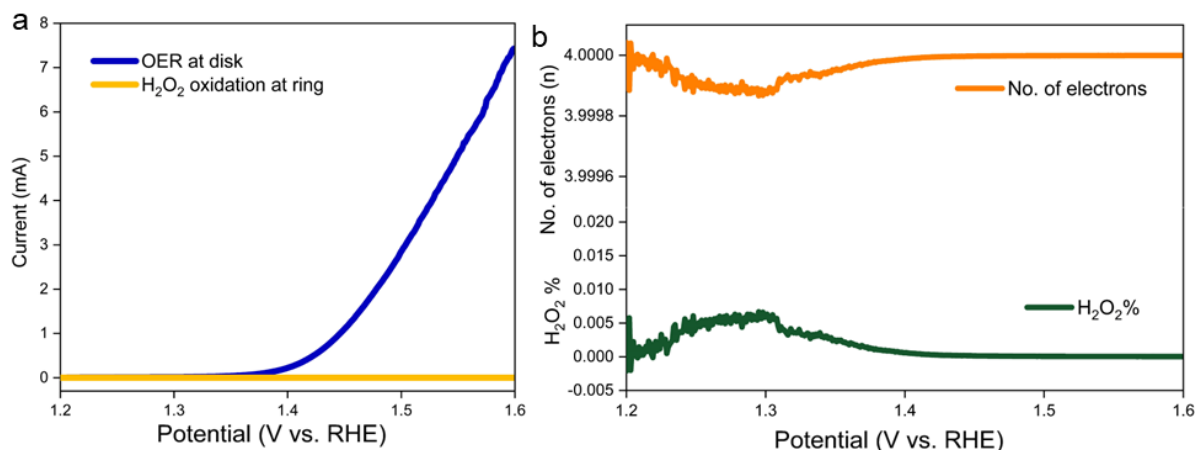


Figure 3.9. (a) LSVs for the RRDE experiment showing the disk current corresponding to the OER and ring current corresponding to the conversion of H₂O₂ to O₂. (b) Number of electron transfer and H₂O₂ % formation during the OER reaction.

Even after 5000 ADT cycles, Co₁-CoO-Pd₂Ge shows increased OER activity manifesting the enhanced stability of the catalyst (**Figure 3.7d**). **Figures 3.8a** shows the decreased Tafel slope value of Co₁-CoO-Pd₂Ge as compared to pristine Pd₂Ge and IrO₂ indicating faster kinetics of OER. **Figures 3.8b** shows the chronoamperometry plots of Co₁-CoO-Pd₂Ge at current density 500 mA/cm² for 36 hours with no degradation of current density. Such an incredible enhancement in stability and durability of Co₁-CoO-Pd₂Ge is a result of stable support (Pd₂Ge) solving the major disadvantage of instability of most of the Co based oxides reported for OER.^{28, 47, 52} It has been observed that there is almost no current at the ring which means no formation of H₂O₂ due to partial water oxidation (**Figure 3.9a**). After the calculation, it is observed that 4 electron transfer process took place with almost 0.001-0.002% of H₂O₂ formation (**Figure 3.9b**). **Table 3.3** lists the comparison of different catalysts with the state-of-the-art catalyst. To further illustrate the role of the thin CoO layer we have performed OER after removing the CoO layer at various intervals of Ar⁺ sputtering, followed by OER activity test (**Figures 3.10**).

Table 3.3. Comparison of electrochemical OER activity of different catalysts with the state-of-the-art catalysts:

Sl. No.	Catalyst	Potential (10 mA/cm ²)	Stability
1	Co ₁ -CoO-Pd ₂ Ge	1.494 V	80 h (5000 cycles)
2	Pd ₂ Ge	1.54 V	< 10 hours
3	CoOOH@Pd _{2-x} Ge	1.52 V	< 3 hours
4	IrO ₂	1.56 V	1000 cycles

It has been observed that with increased levels of sputtering there is gradual decrease in activity (**Figure 3.10a**). The activity of fully sputtered catalyst is slightly higher than

compared to pristine Pd_2Ge (**Figure 3.10b**) which can be attributed due to the presence of Co atoms in the Pd_2Ge lattice which also contributes to the OER activity. Thus, it is electrochemically also verified that Co has not only formed CoO layer, but also incorporated into the Pd_2Ge lattice.

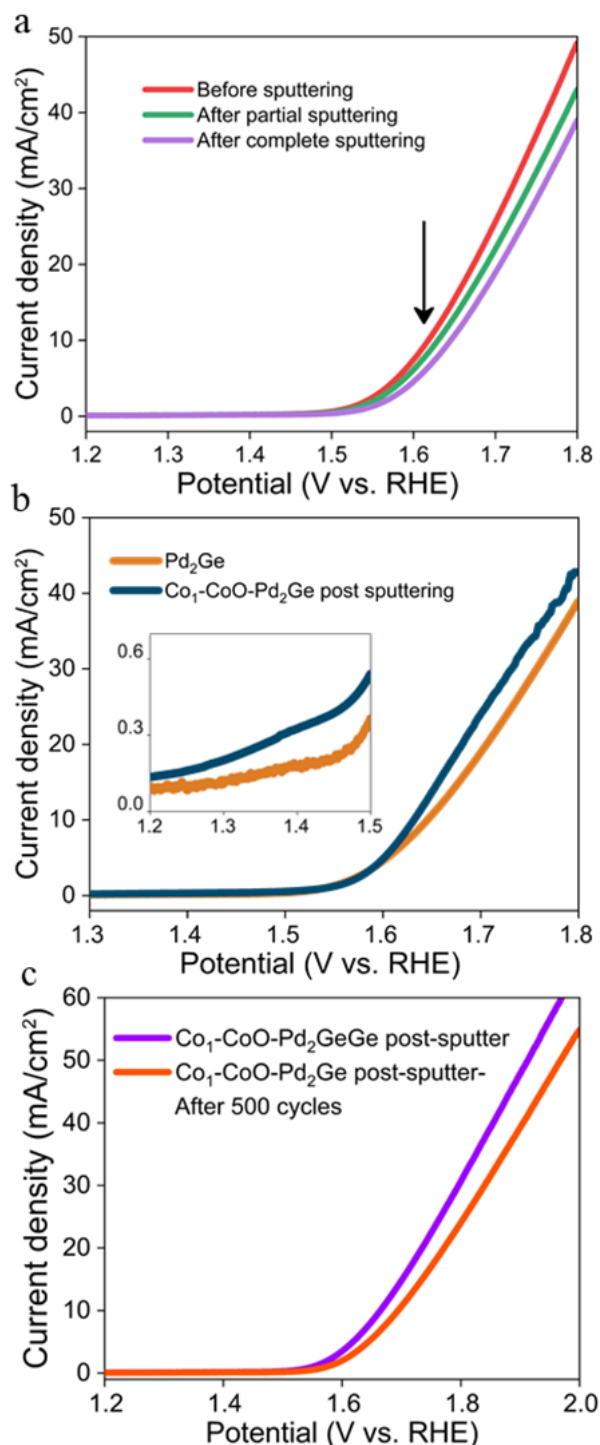


Figure 3.10. LSVs of OER (a) for $\text{Co}_1\text{-CoO-Pd}_2\text{Ge}$ before and after partial and full Ar^+ sputtering (b) the comparison between the samples $\text{Co}_1\text{-CoO-Pd}_2\text{Ge}$ and pristine Pd_2Ge after complete sputtering. (c) LSVs of OER for $\text{Co}_1\text{-CoO-Pd}_2\text{Ge}$ after full Ar^+ sputtering before and after 500 ADT cycles.

Figures 3.10c shows that upon removal of CoO layer, the stability and durability of the catalyst is degraded within short period of operation (after 500 ADT cycles). The removal of CoO layer has been verified by post-sputtering characterizations like XPS, SEM imaging, and SEM-EDS which will be discussed in the later section.

3.4.3 Local coordination and oxidation state analysis of Co₁-CoO-Pd₂Ge

The XANES spectra for Co-*K* edge as in **Figure 3.11a** shows that Co is in higher oxidation state which matches with Co-oxide species, CoO.^{17, 53} Whereas XANES spectra for Pd-*K* and Ge-*K* edges as in **Figures 3.11b** and **3.11c** show that both Pd and Ge are in metallic state in Pd₂Ge intermetallic compound with partial positive charge on Pd and partial negative charge accumulation on Ge atoms. It has been observed that with Co incorporation into Pd₂Ge lattice, there is very less increase in oxidation state of Pd and Ge which is due to less amount of Co has been incorporated into the Pd₂Ge lattice while remaining has settled on the surface as thin layer of CoO. From the Fourier transformed R-space EXAFS data shown in **Figure 3.11d**, it is observed that Co-Co metallic bonds are absent in Co₁-CoO-Pd₂Ge which triggered the naming as Co₁-CoO-Pd₂Ge.

Figures 3.11e and **3.11f** show the wavelet transformed EXAFS data for Co foil and Co edge of Co₁-CoO-Pd₂Ge. It is seen that most intense peak corresponds to Co-O bonds at 1.54 Å with a very less intense Co-Ge bonds at 2.17 Å. **Figure 3.12a, b** represent the EXAFS R-space data for Pd and Ge-*K* edges of Co₁-CoO-Pd₂Ge. **Figure 3.12a** shows the presence of Pd-Ge and Pd-Pd bonds from Pd *K*-edge XAS. Pd-Ge and Pd-Pd bonds are present in pristine Pd₂Ge at 2.05 and 2.6 Å. Whereas Pd-Ge and Pd-Pd bonds are at 2.02 and 2.6 Å in Co₁-CoO-Pd₂Ge. **Figure 3.12b** shows Ge-Ge and Ge-Pd bonds in Co₁-CoO-Pd₂Ge from Ge *K*-edge XAS data. **Figure 3.12c, d** show the fitted EXAFS data for Co *K*-edge of Co₁-CoO-Pd₂Ge, and it is observed that the data is well fitted considering Co-O and Co-Ge bonds (**Figure 3.12c**) and **Table 3.4** shows the fitting parameters. This is confirming the existence of CoO with Co incorporated in Pd₂Ge lattice which generates peak for Co-Ge bonds (**Figure 3.12d**). In summarizing all these findings, XAFS comprehensively confirms the formation of Co₁-CoO-Pd₂Ge with Co predominantly existing as single-atoms in the thin CoO layer, while a small fraction of Co exists in the metallic state and substitutes Pd sites in Pd₂Ge.

3.4.4 Presence of oxide layer: argon sputtered XPS and SEM analysis

Figures 3.13a and **3.13b** show the fitted Pd 3*d* and Ge 3*d* XPS spectra of Co₁-CoO-Pd₂Ge. It is seen that both Pd and Ge exists in elemental state with some trace amounts of PdO, GeO and GeO₂ on the surface due to aerial oxidation. To verify the existence of Co metallic

state underneath the oxide layer, XPS measurement has been performed after Ar^+ sputtering at different time duration. Co $2p$ XPS after Ar^+ etching shows emergence of Co^0 state from Co^{2+} state, as in **Figure 3.13c**, which keeps on increasing after each layer removal.

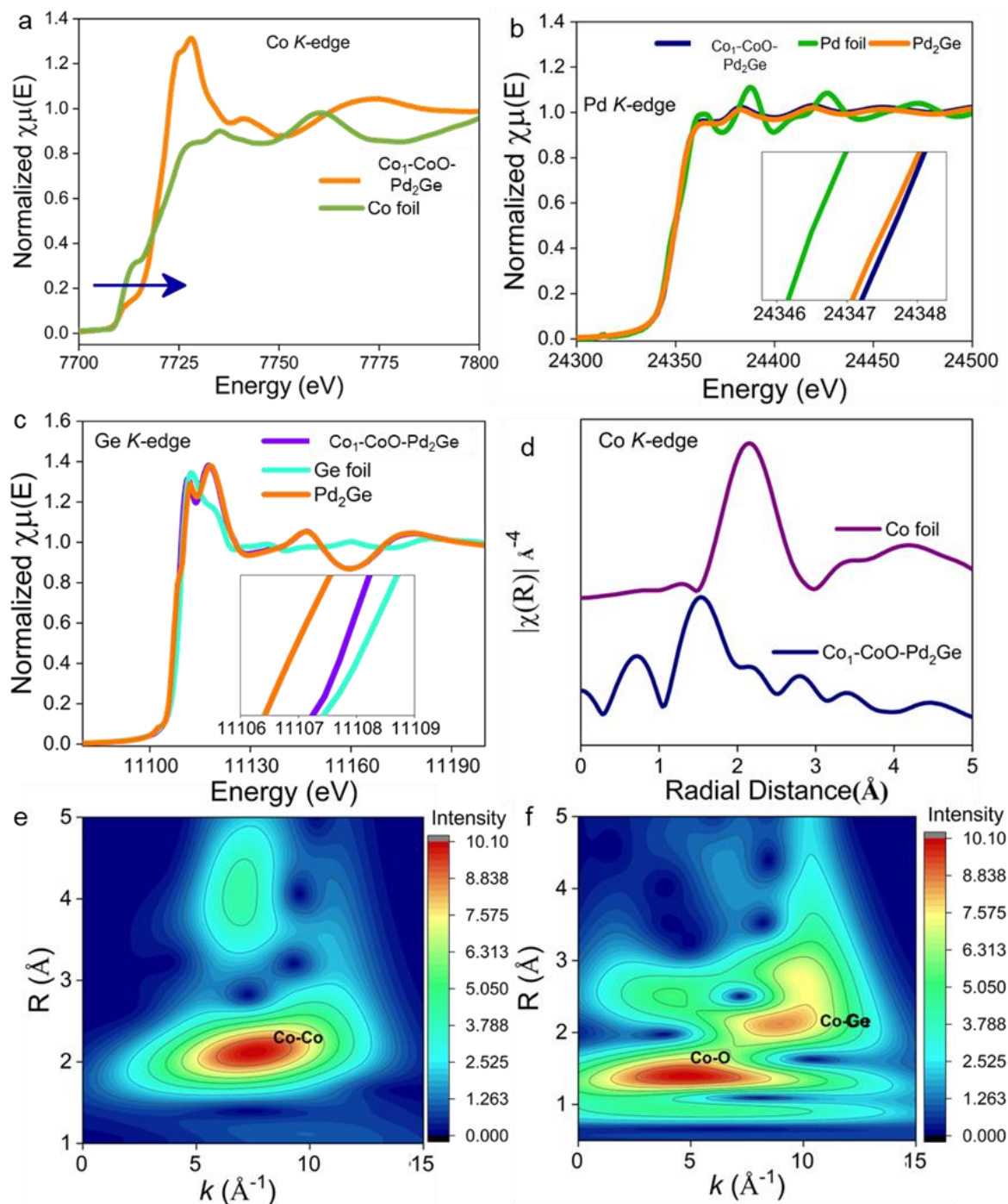


Figure 3.11. (a) XANES spectra of Co K -edge for $\text{Co}_1\text{-CoO-Pd}_2\text{Ge}$. (b) XANES spectra of Pd K -edge for Pd_2Ge , $\text{Co}_1\text{-CoO-Pd}_2\text{Ge}$ and Pd foil. (c) XANES spectra of Ge K -edge for Pd_2Ge , $\text{Co}_1\text{-CoO-Pd}_2\text{Ge}$ and Ge foil. (d) Fourier transformed R-space data for Co K -edge for $\text{Co}_1\text{-CoO-Pd}_2\text{Ge}$. Wavelet transformed EXAFS data of Co K -edge of (e) Co foil and (f) $\text{Co}_1\text{-CoO-Pd}_2\text{Ge}$.

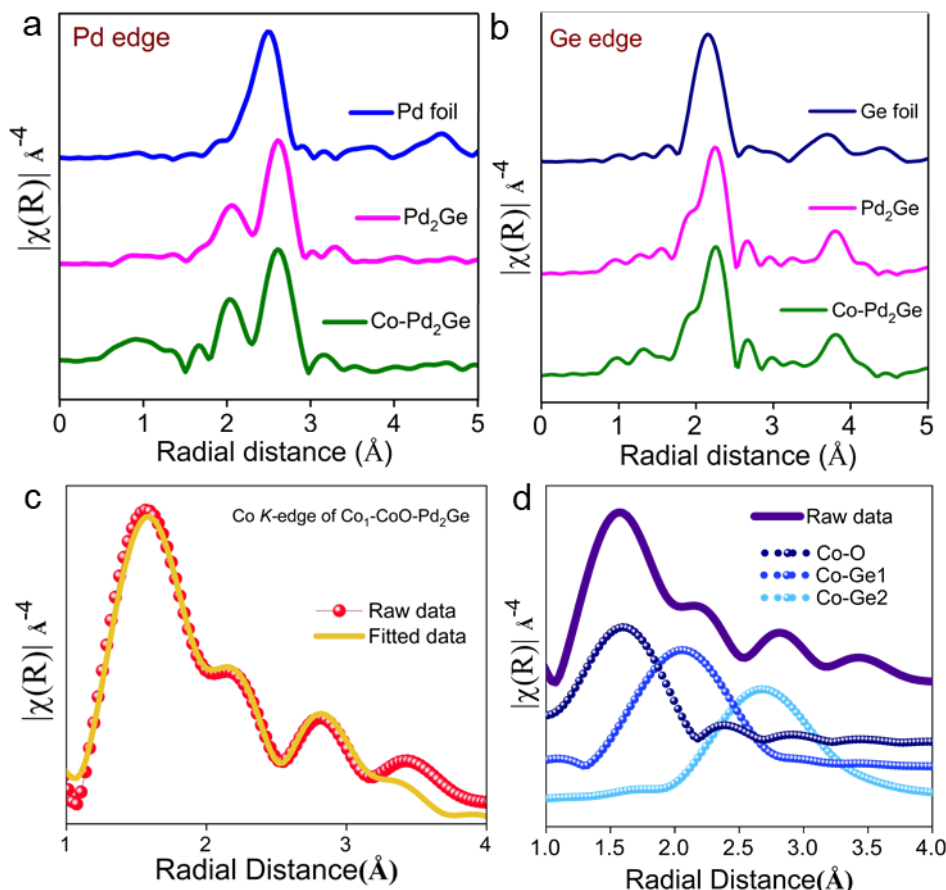


Figure 3.12. Fourier transform data for (a) Pd *K*-edge and (b) Ge *K*-edge of Co₁-CoO-Pd₂Ge. (c) Fitted R-space data for Co *K*-edge of Co₁-CoO-Pd₂Ge. (d) All the paths taken for fitting which are Co-O and two types of Co-Ge bonds.

This confirms the removal of CoO layer and exposing elemental cobalt in Co incorporated Pd₂Ge lattice.⁵⁴ **Figure 3.14** show the XPS spectra of Pd 3d and Ge 3d after different layers of etching. **Figures 3.15a** and **3.15b** show the magnetization curve and EPR spectra of Co₁-CoO-Pd₂Ge, which depict the presence of unpaired electrons which is due to the presence of Co²⁺ centers on the surface and thus this unpaired electron will facilitate the stabilization of O^{*} species on active sites. Presence of unpaired electrons also help in spin cross-over from singlet to triplet species during OER and reducing the energy barrier for conversion of OH^{*} to O^{*} species.⁵⁵ Additionally, SEM images and EDX mapping were done to visualize and quantify the morphology and atomic composition after sputtering. **Figure 3.16** shows the SEM images of Co₁-CoO-Pd₂Ge after argon sputtering where the layer is no more visible as was observed in **Figure 3.5** clearly confirms the presence of CoO at the surface of Co₁-CoO-Pd₂Ge. **Table 3.1** shows the elemental composition showing no O amount present which confirms the removal of O atom from the surface layer of the nanoparticles. This confirms further the absence of CoO on the surface after the sputtering.

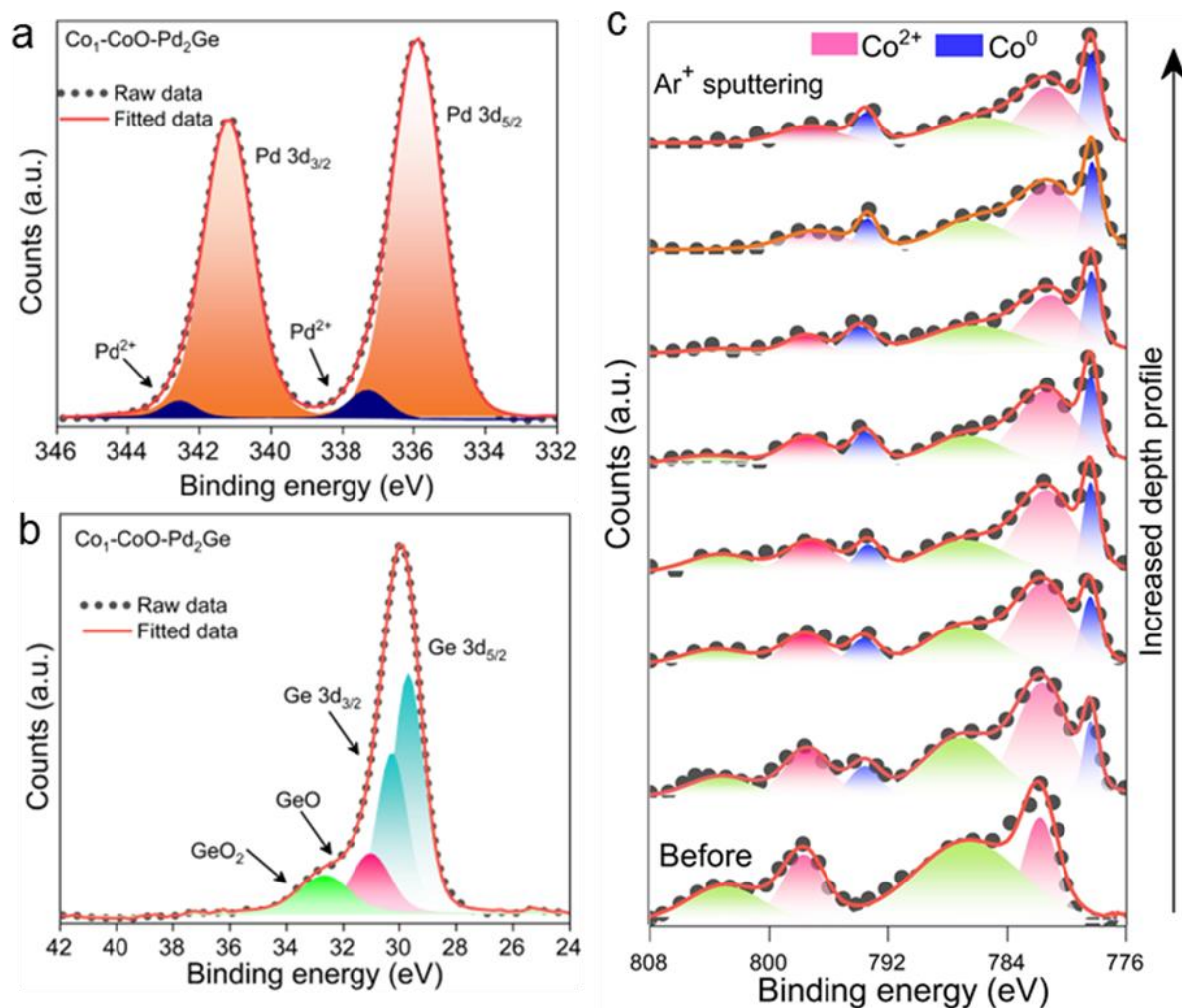


Figure 3.13. (a) Pd 3d, (b) Ge 3d XPS spectra of Co₁-CoO-Pd₂Ge and (c) Co 2p XPS spectra of Co₁-CoO-Pd₂Ge during stepwise removal of CoO layer upon argon sputtering.

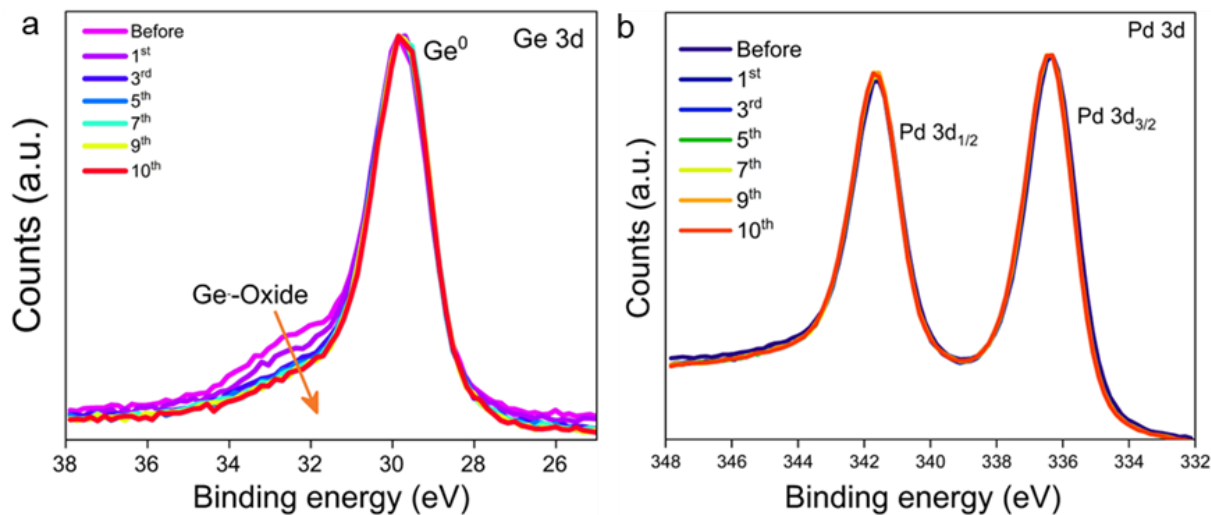


Figure 3.14. (a) Pd 3d and (b) Ge 3d XPS spectra of Co₁-CoO-Pd₂Ge during stepwise removal of CoO layer upon argon sputtering.

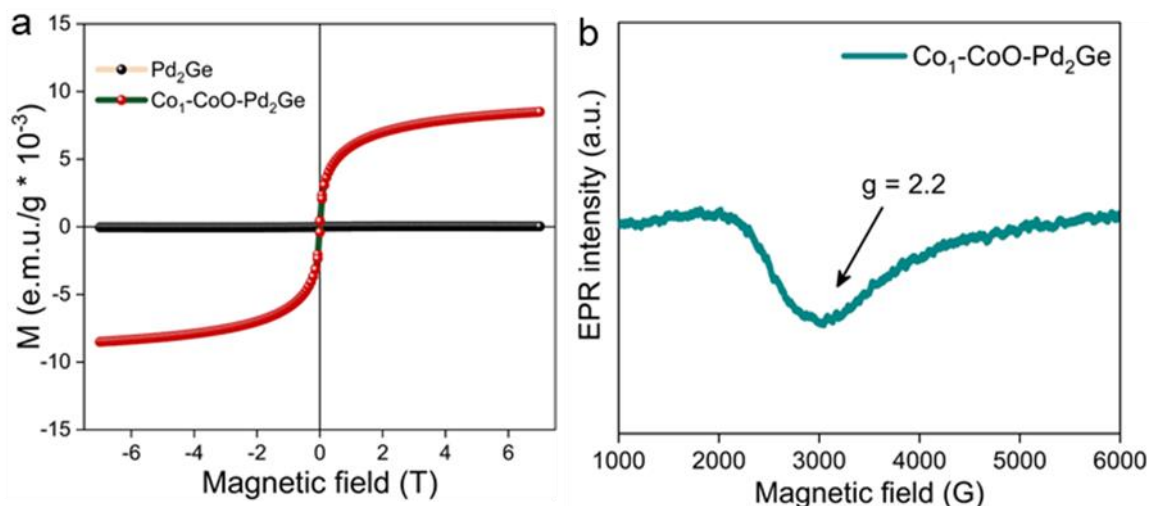


Figure 3.15. (a) Isothermal magnetization curves (M-H curves) at 2 K for Pd_2Ge and $\text{Co}_1\text{-CoO-Pd}_2\text{Ge}$. (b) EPR spectra of $\text{Co}_1\text{-CoO-Pd}_2\text{Ge}$.

Table 3.4. EXAFS fitting parameters.

Path	C.N.	R (Å)	$\sigma^2(\text{\AA}^2)$
Co-O	4.89	2.13	0.009
Co-Ge1	6.4	2.31	0.016
Co-Ge2	1.6	2.51	0.003

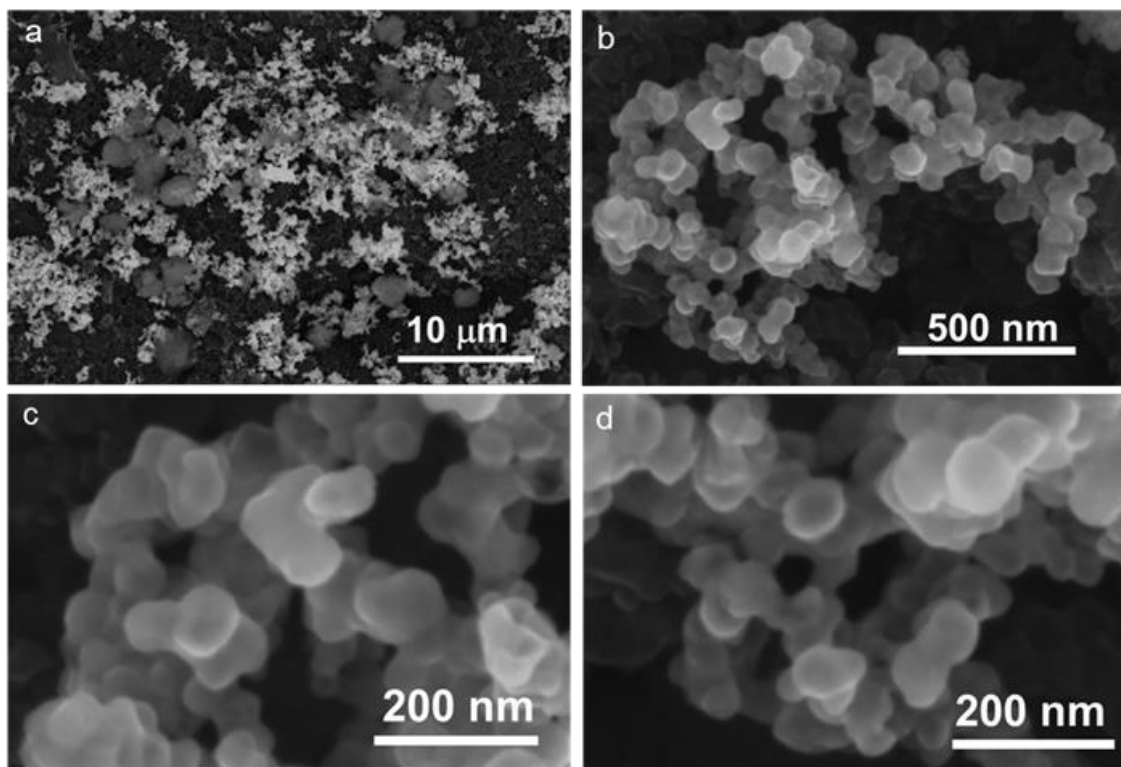


Figure 3.16. SEM images taken after Ar^+ sputtering on $\text{Co}_1\text{-CoO-Pd}_2\text{Ge}$ for 14 layers etching.

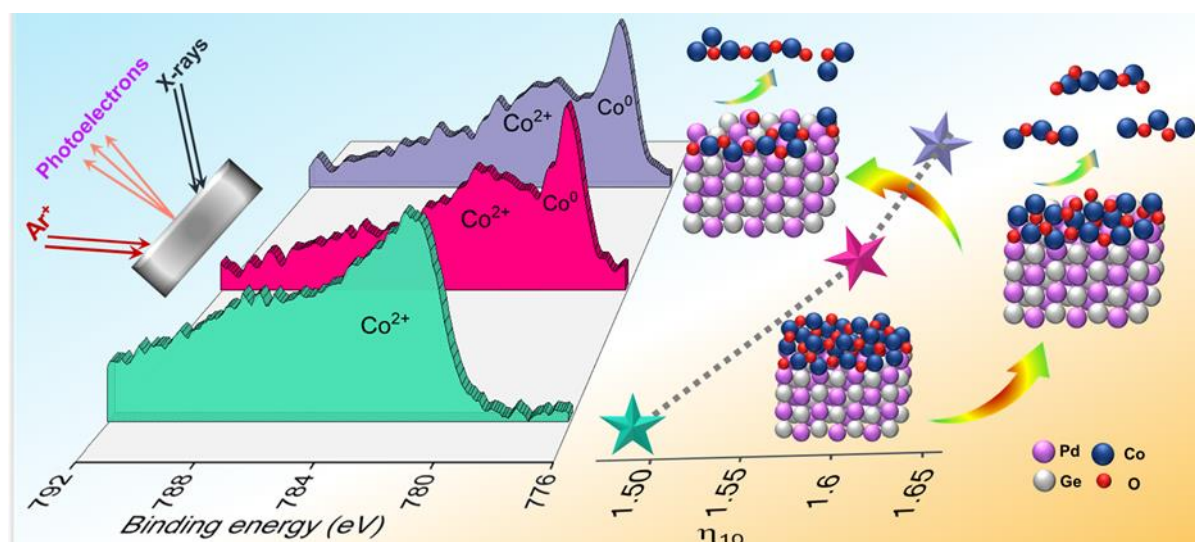


Figure 3.17. Schematic of XPS spectra for CoO controlled surface-etching by Ar^+ sputtering and the trend in its OER activity after different levels of etching.

Figure 3.17 shows a schematic where the XPS spectra of CoO surface on Pd_2Ge lattice after different layers of Ar^+ sputtering and the trend in the OER activity and its overpotential for 10 mA/cm^2 current density are plotted with structural models of different etching level.

3.4.5 Probing charge transfer during OER via operando methods

An electrochemical cell is customized for operating real-time XAS during OER (**Figure 3.18a**). **Figure 3.18b** shows the in-situ XANES spectra of Co K -edge of $\text{Co}_1\text{-CoO-Pd}_2\text{Ge}$, which depicts a sharp increase in the adsorption energy just at 1.5 V vs. RHE. This increment in energy is no more observed when potential is varied from 1.7 to 1.9 V . This is a clear indication that Co oxidation state changes (Co^{2+} to Co^{3+}) occurring within 1.5 V vs. RHE. As observed from the Pd- K edge XANES (**Figure 3.18c**), the oxidation state of Pd is increasing with increasing oxidation potential since there is a shift of absorption edge towards higher photon energy.^{56, 57} R-space EXAFS data for Pd K -edge during OER shows that there is contraction in both lengths corresponding to both Pd-Pd and Pd-Ge bonds at 2 and 2.7 \AA , respectively (**Figure 3.18d**).⁵⁸⁻⁶⁰ This bond contraction reflects the increase in oxidation state of Pd centers. This observation is further supported by post-OER XPS spectra for Co $2p$ orbitals. **Figure 3.18e** shows the prominent difference in XPS spectra before and after OER. **Figure 3.18f** shows the fitted XPS spectra where it is observed that Co^{2+} gets almost converted to Co^{3+} during OER. CoO is getting converted to CoOOH which ultimately drives the overall OER activity of the catalyst. Further, operando XANES show that after some potential (till 1.5 V vs. RHE) the XANES spectra is stabilized for both Co and Pd K -edges which indicate a stability achieved on the catalyst surface.

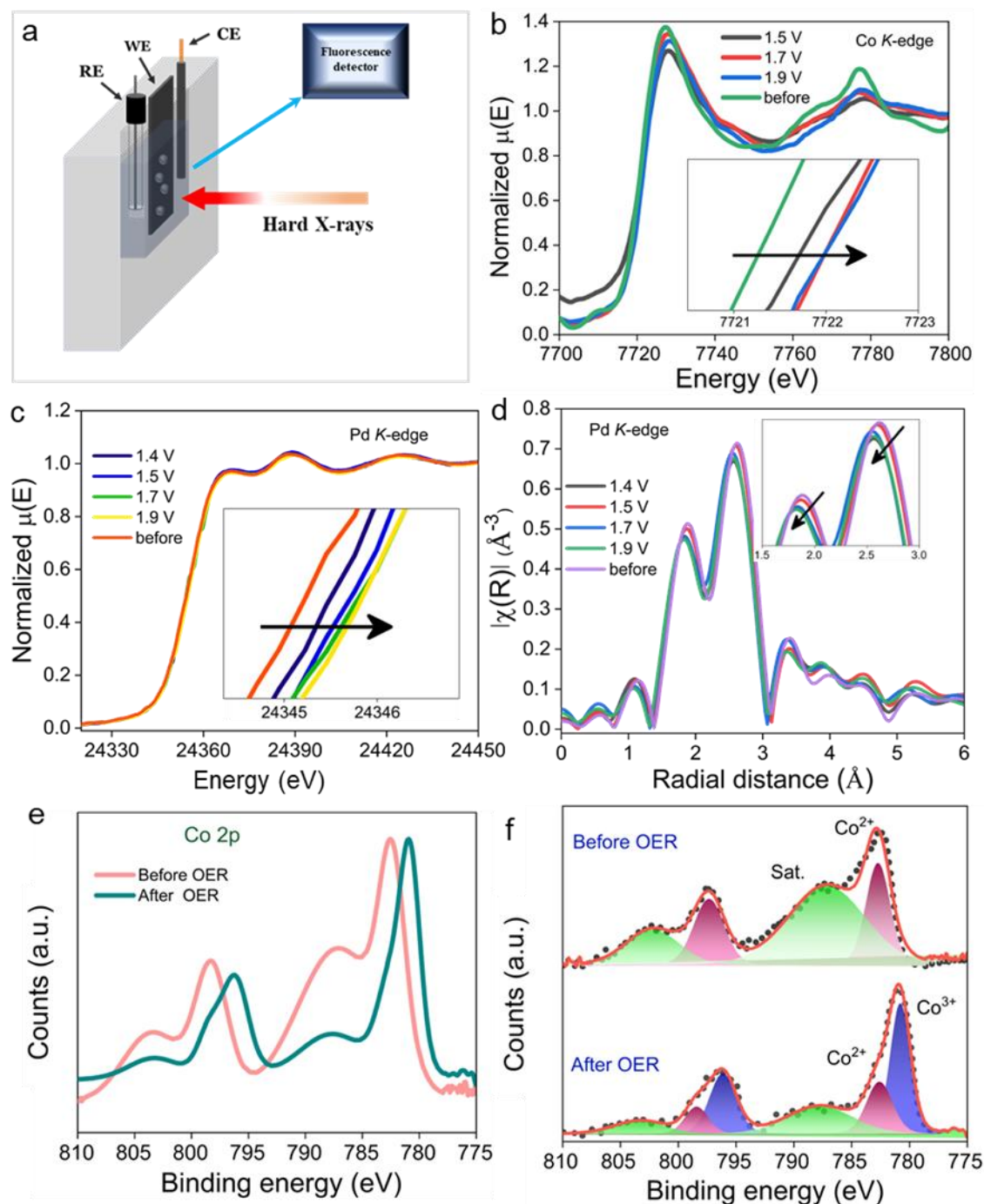


Figure 3.18. (a) Schematic of cell setup for in-situ XAS measurements. (b) Co K-, and (c) Pd K-edge XANES spectra for Co₁-CoO-Pd₂Ge during OER at different potentials. (d) Pd K-edge R-space data during OER at different potentials. (e) Co 2p XPS spectra before and after OER. (f) Fitted XPS spectra for Co 2p before and after OER.

Post-electrochemical SEM and TEM images are taken for Co₁-CoO-Pd₂Ge to confirm the phase transformation, which is accounted for charge transfer. **Figure 3.19** shows the SEM images after OER where the CoO is converted to CoOOH oxide which is intact after the electrocatalysis. **Figure 3.20** shows the TEM and HRTEM images after OER strongly confirms the existence of CoOOH after OER which was not present before reaction.

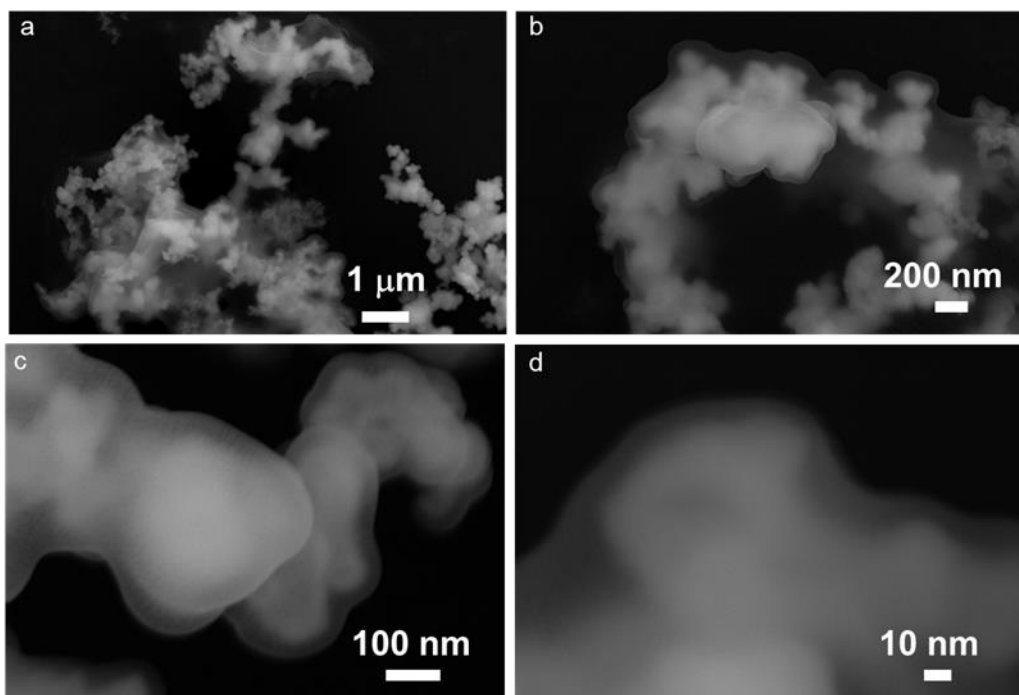


Figure 3.19. SEM images of Co₁-CoO-Pd₂Ge after electrochemical oxygen evolution reaction (a-d) at different scale bars and different locations.

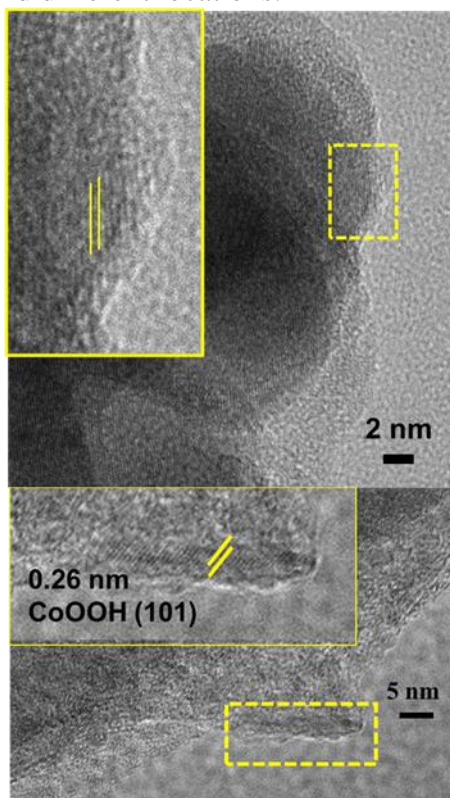


Figure 3.20. TEM images of Co₁-CoO-Pd₂Ge after electrochemical oxygen evolution reaction. These images show that the nanoparticles are surrounded by a thin layer of CoOOH which is verified by d-spacing.

All these in situ and post-electrochemical characterizations jointly supports that further oxidation of Co from (III) to (IV) oxidation state has not taken place which is also reflected

from the LSV shown in **Figure 3.7b**. Although Co is highly prone to get oxidized to Co(III) and Co(IV) under OER oxidations, sometimes this Co(IV) species hinders OER kinetics.³⁸ Pd₂Ge lattice is acting as a support to control the higher oxidation of Co species of the CoO surface layer.

3.4.6 Visualizing structural evolution and stabilization: Potential-dependent Raman spectroscopy and theoretical calculations

Figure 3.21a shows the schematic of lab-customized cell setup for in-situ Raman spectroscopy during OER for catalyst Co₁-CoO-Pd₂Ge. **Figures 3.21b** and **3.21c** show the potential- and time-dependent Raman spectra for Co₁-CoO-Pd₂Ge.

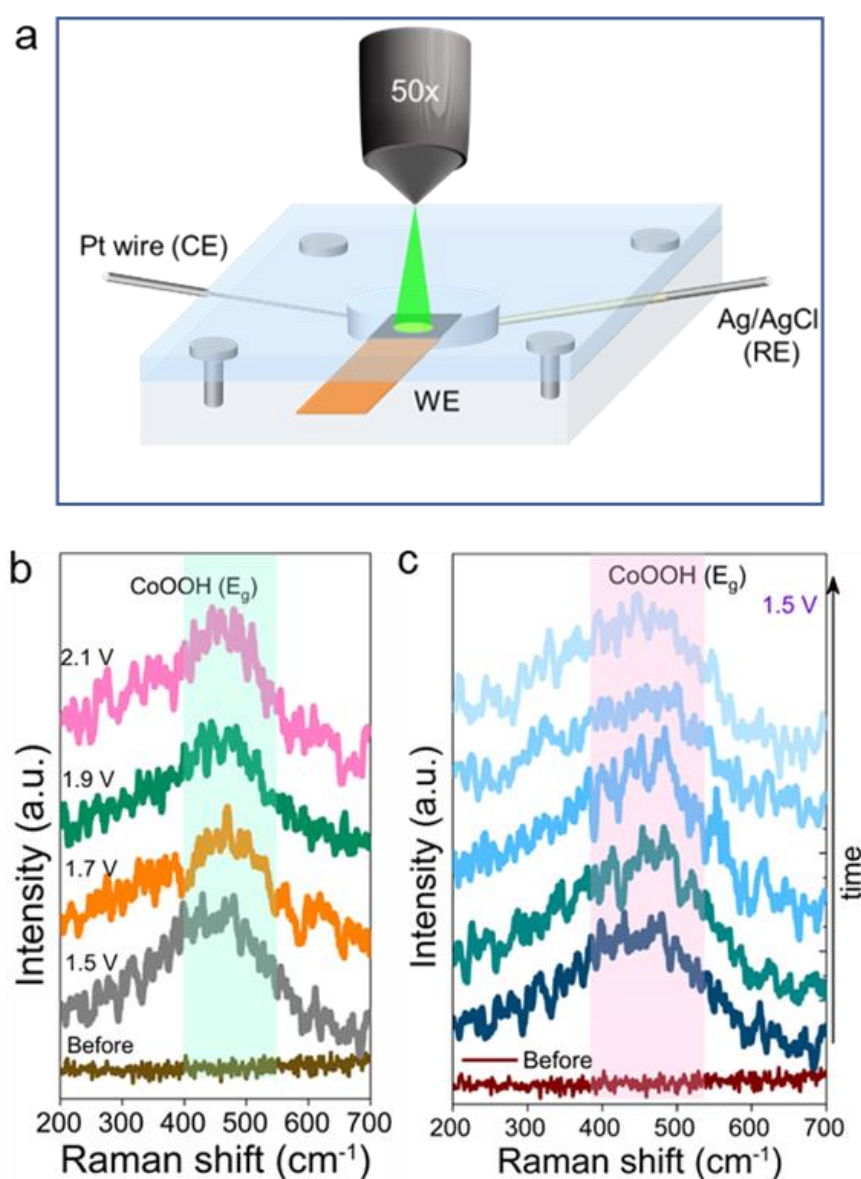


Figure 3.21. (a) Schematic of electrochemical cell setup for in-situ Raman spectroscopy measurements. (b) Potential-dependent and (c) time dependent in-situ Raman spectroscopy for Co₁-CoO-Pd₂Ge.

It is observed that Raman peak corresponding to E_g mode of CoOOH phase after giving potential which is stable even in higher potential.^{29, 52} Thus, operando Raman spectroscopy firmly confirms the observation of CoOOH formation during reaction kinetics which supports the post-electrochemical XPS and HRTEM analysis (**Figures 3.18e, 3.18f**). No peak corresponding to CoO₂ is observed even at higher potential in Raman spectroscopy. After theoretical optimization of pure CoO, pure CoOOH, CoO@Pd₂Ge and CoOOH@Pd₂Ge, it has been observed that the fcc structure of CoO gets deformed and distorted on being supported on hexagonal Pd₂Ge lattice (**Figures 3.22a and 3.22b**). This distortion led to non-uniform bond distance of Co-O as compared to pure CoO where all the Co-O bonds are uniform (**Figures 3.22b(i) and 3.22b(ii)**). The optimized structure showed a significant change in Co-O bond length due to the lattice strain which is from 2.12 to 1.77 Å when supported on Pd₂Ge lattice, but the overall structure remained intact.

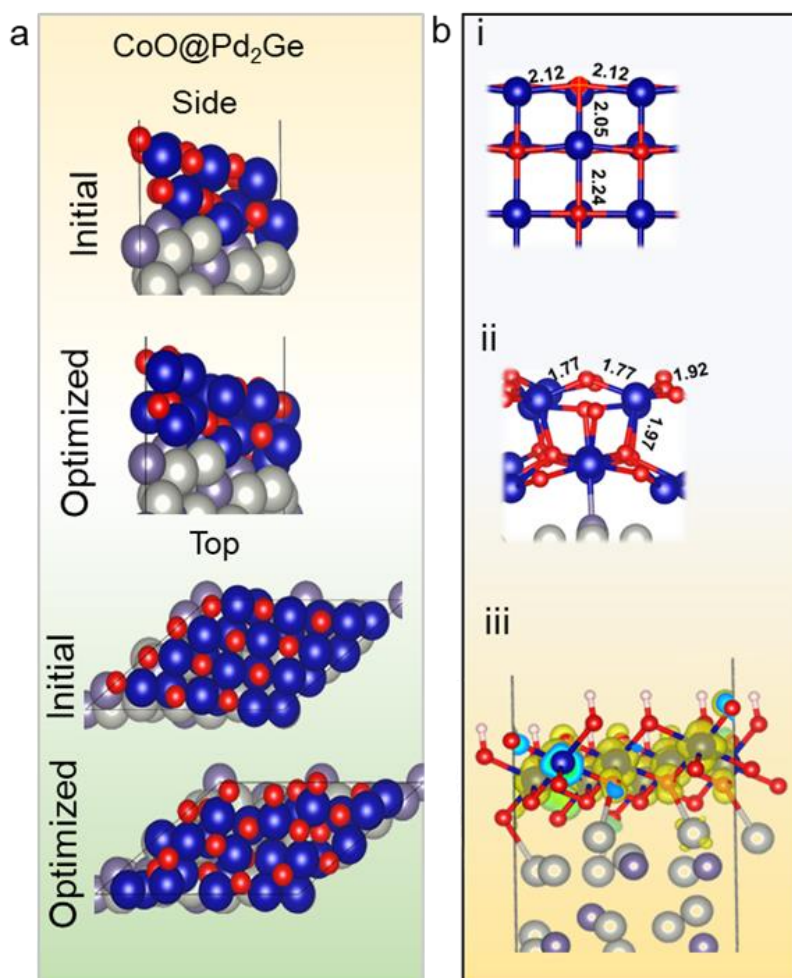


Figure 3.22. (a) Simulated structural models of CoO on Pd₂Ge before and after structure optimization from top view and side view. (b) it represents (i) zoomed portion of Co atoms surrounded by neighboring O atoms in bulk CoO and (ii) In CoO on Pd₂Ge heterostructure, and (iii) Spin density on CoOOH supported on Pd₂Ge lattice.

The decrease of Co-O bond lengths of CoO supported on Pd₂Ge can be attributed to the increased oxidation state on Co centers due to being incorporated on Pd₂Ge. **Figure 3.23** also shows that after incorporation of CoO on Pd₂Ge, there is an accumulation of electronic charge near the interface of CoO and Pd₂Ge with slight deficient electronic density in CoO lattice and bulk Pd₂Ge. This observation from theoretical studies have been completely supported by experimental Pd 3d XPS spectra of Co₁-CoO-Pd₂Ge before and after different layers of etching by Ar⁺ sputtering. **Figure 3.23** shows schematically that before etching Pd was in lower oxidized state which indicates the interface between CoO and Pd₂Ge. Whereas, while digging the Pd₂Ge surface more, higher oxidized state of Pd is being exposed which again is supporting the theoretical observation of lower electron density in the internal layers of Pd₂Ge. Such an electron transfer from bulk layers to interfacial layers is the reflection of electron transfer from the Co atoms of the surface CoO to the surface of Pd₂Ge species, which creates a surface charge accumulation.

In **Figure 3.22b(i)** and **3.22b(ii)**, it is shown how Pd₂Ge lattice created a more oxidized state of cobalt in CoO than pure CoO with contracted Co-O bond length. This strongly supports electron transfer from Co atoms to surface Pd/Ge atoms enriched the surface with higher electron density. Dissipation of electron on CoO will further enhance adsorption of OH⁻ species and conversion of Co²⁺ to Co³⁺ will be facilitated. Such a bond distortion will lead to loss of Co 3d orbital degeneracy which will modify the density of states of Co 3d orbitals.^{30, 61} **Figure 3.24a** shows the significant change in DOS for Co 3d orbitals for pure CoO and CoO on Pd₂Ge lattice. The electronic states near the fermi level is highly increased when CoO is layered on Pd₂Ge lattice which enhances the charge transfer kinetics during the OER reaction, as compared to pure CoO.⁶² It has been reported that with inducing distortion in octahedral geometry of transition metals in their oxides, there is loss of degeneracy in electronic states creating more number of energy levels which is evident in DOS.^{30, 63}

In this work, the distortion is induced by a highly stable and exclusive intermetallic lattice, Pd₂Ge. The d⁶ configuration of Co³⁺ in CoOOH is expected to be in low spin state where all the electrons are paired and CoOOH is non-magnetic. But Pd₂Ge induces electronic lifting to e_g level and gave rise to unpaired spin density in CoOOH which ultimately facilitated the rate determining step of OER kinetics. This firmly confirms the contribution of Pd₂Ge incorporated CoO drives higher activity, lower overpotential and higher stability than pure oxides.^{36, 45}

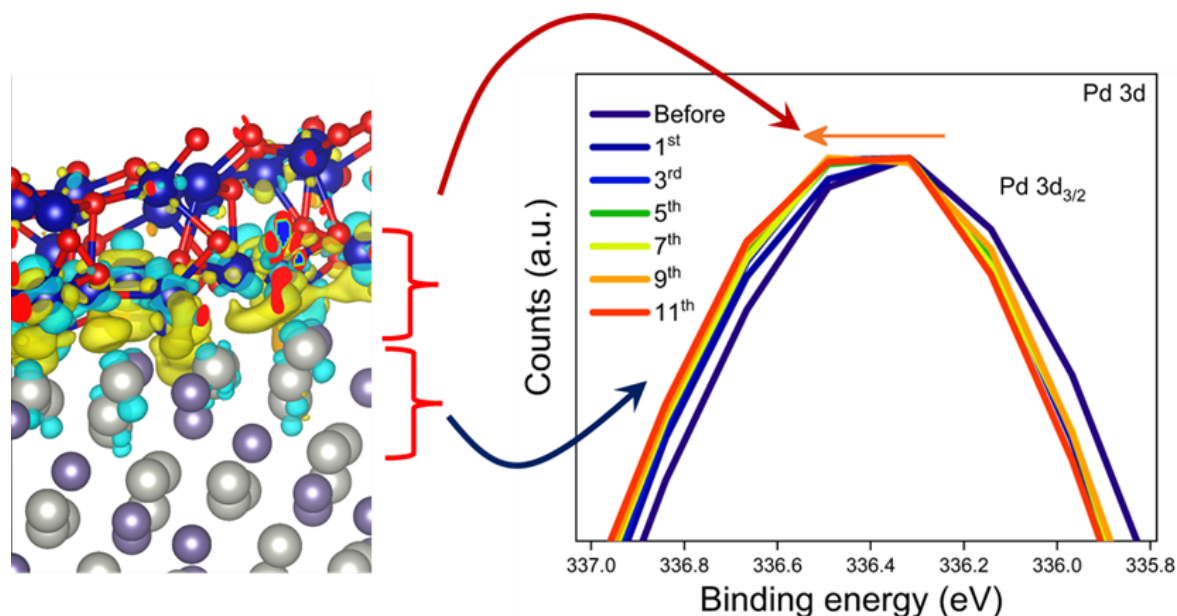


Figure 3.23. Schematic showing charge density distribution for Co₁-CoO-Pd₂Ge and Pd 3d XPS spectra after different different layers etching by Ar⁺ sputtering.

Figure 3.24b shows the EPR spectra of Co₁-CoO-Pd₂Ge catalyst before and after OER. It is observed that even after conversion of Co from (II) to (III) oxidation state, there is existence of unpaired electrons. Despite being EPR inactive, CoOOH still showed unpaired electron density which is due to presence of of unpaired electrons which strongly supports distortion induced d-orbital splitting which led to less pairing of electrons.⁶⁴ **Figure 3.24c** depicts the electronic states for Co 3d orbitals closer to Fermi level for CoOOH in heterostructure than in bulk CoOOH. **Figure 3.22b(iii)** shows that non-magnetic CoOOH attains a magnetic nature with some unpaired electron density in it after being incorporated on Pd₂Ge lattice. Unpaired spin will enhance the OER mechanism due to the unpaired electron participating in stabilization of O^{*} species which is one of the important OER descriptors.

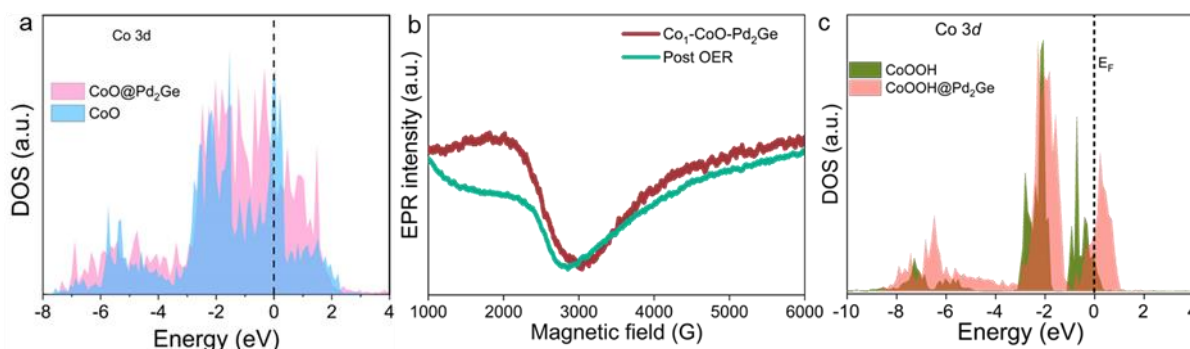


Figure 3.24. (a) DOS of 3d orbitals for pure CoO and CoO-Pd₂Ge heterostructure. (b) EPR spectra of Co₁-CoO-Pd₂Ge before and after electrochemical OER. (c) DOS for Co 3d orbitals for pure CoOOH and CoOOH@Pd₂Ge means CoOOH on Pd₂Ge stabilized heterostructurally. E_F shows the Fermi level.

Thus, Pd₂Ge lattice is not only enhancing the stability of the CoO layer and in-situ formed CoOOH by providing a stable metallic support, also it is triggering the reaction kinetics by fast transforming CoO to CoOOH and gifting CoOOH with unpaired spin density which will fasten the O* stabilization on active sites. These characterization studies demonstrated how the role of Pd₂Ge increased the OER efficiency of CoO thin layer and not the direct role of Pd₂Ge support in participating in OER.

3.4.7 Spectrometric analysis of oxygen generation triggered by oxidation potential – A DEMS study

A visual correlation of oxygen generation with input potential is made using the analytical tool of differential electrochemical mass spectrometry (DEMS). **Figure 3.25** shows the real image of the DEMS setup and its electrochemical cell components. The schematic for the DEMS cell setup is given in **Figure 3.26a**. The pervaporation membrane in **Figure 3.25d** helps in diffusion and passage of the volatile components from the electrochemical cell to the mass chamber. **Figure 3.26b** shows the mass spectra of m/z value of 16 and 32 for O₂ gas and the LSV during which the mass spectra is recorded. It is very clear that the oxygen generation started when the potential reached the onset value. When the mass spectra for oxygen is compared for blank glassy carbon electrode and catalyst Co₁-CoO-Pd₂Ge, it is prominent that no oxygen formed when blank electrode has been used (**Figure 3.26c**).

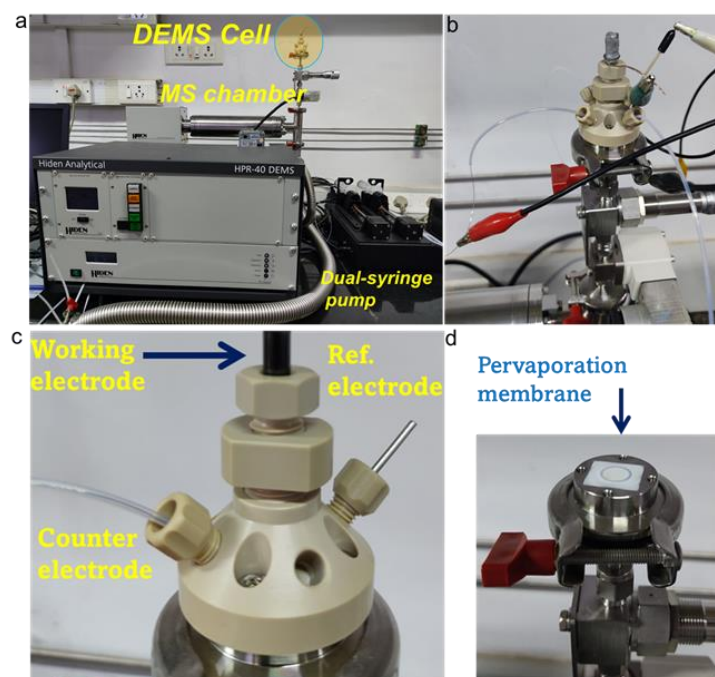


Figure 3.25. The full DEMS instrument with the electrochemical cell (a,b). (c) The electrochemical cell setup with three electrode setup. (d) The position where the formed volatile products enter the ionization chamber of the mass spectrometer.

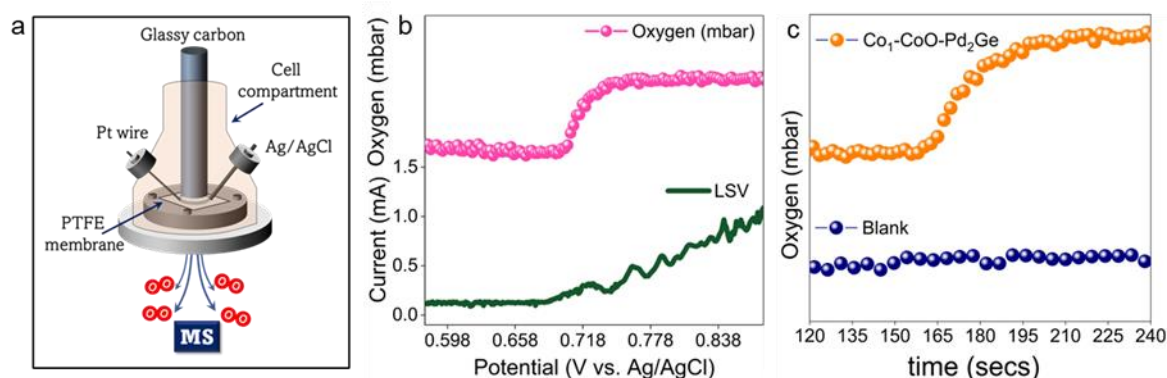


Figure 3.26. (g) Schematic of differential electrochemical mass spectrometer (DEMS) setup. (h) DEMS data with the LSV for catalyst Co₁-CoO-Pd₂Ge. (i) DEMS data during OER for Co₁-CoO-Pd₂Ge and blank glassy carbon electrode.

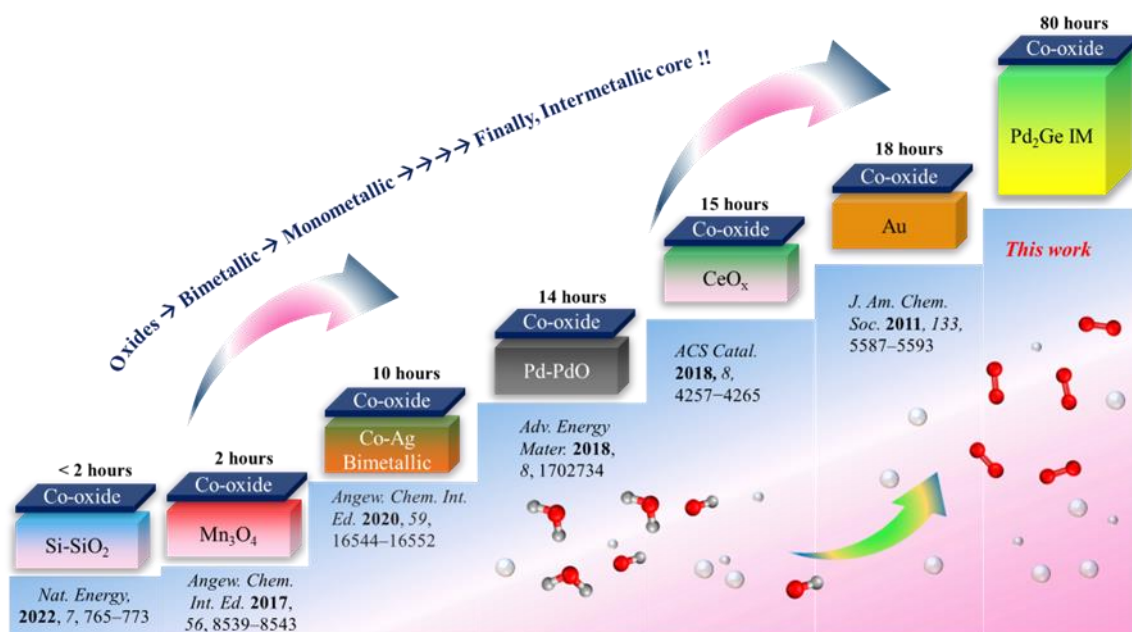


Figure 3.27. Schematic showing how the stability of OER activity of Co-oxides is increasing from different metallic, bimetallic, metal oxide supports and having an intermetallic base provides the best conductive and stable support.

3.5 Conclusion

This work introduces a rational design of an active and stable catalyst for efficient production of oxygen. This work introduces the design of an intermetallic compound as a support to stabilize OER catalyst (CoO), which structurally induce the distortion which favored chemical transformation to an active species, CoOOH, during the operando condition. The presence of the thin layer of CoO comprehensively mapped by XPS, XAS, SEM, and TEM. Selective removal of CoO layers upon argon sputtering firmly confirmed the significant role of this oxide in OER activity. In-situ XAS has been done to observe the charge transfer kinetics during the reaction which shows that Pd atoms from the support are enhancing the charge

transfer kinetics of electrons from OH⁻ to the catalyst surface. This Pd atoms also stabilizes the Co³⁺ species (CoOOH) which is one of the crucial discrepancies of alkaline media OER conditions. Post-electrochemical SEM and TEM very clearly show the presence of CoOOH after OER. In-situ Raman spectroscopic studies show the prominent existence of CoOOH phase upon giving potential. DFT calculations further demonstrates that Pd₂Ge lattice distorts CoO lattice with charge transfer from CoO to the interface which modulates the DOS of Co 3d orbitals enhancing the OER activity. The OER performance of Co₁-CoO-Pd₂Ge has been compared with all the support-based CoO systems reported in the literature (**Table 3.5** and **Figure 3.27**).

Table 3.5. List of support-based Co-oxides for alkaline OER activity.

Sl.no.	Catalysts	Electrolyte	η_{10} potential	Durability	References
1.	Co ₁ -CoO-Pd ₂ Ge	0.5 M KOH	264 mV	80 hours	This work
2.	Fe ₃ O ₄ /CoO CNTs	1 M KOH	270 mV	45 hours	<i>ACS Sustainable Chem. Eng.</i> 2020 , 8, 3336–3346
3.	CoO/hi-Mn ₃ O ₄	1 M KOH	378 mV	2 hours	<i>Angew. Chem. Int. Ed.</i> 2017 , 56, 8539–8543
4.	Co ₈ Ag oxide	1 M KOH	344 mV	10 hours	<i>Angew. Chem. Int. Ed.</i> 2020 , 59, 16544–16552
5.	Pd@PdO-Co ₃ O ₄	1 M KOH	310 mV	14 hours	<i>Adv. Energy Mater.</i> 2018 , 8, 1702734
6.	Pd-CoO	1 M KOH	274 mV	12 hours	<i>Sci Rep</i> , 2020 , 10, 14469.
7.	CoO _x /Au	0.1 M KOH	351 mV	18 hours	<i>J. Am. Chem. Soc.</i> 2011 , 133, 5587–5593.
8.	Cu ₂ O/Cu@CoO	1 M KOH	330 mV	12 hours	<i>Inorg. Chem. Front.</i> , 2019 , 6, 1660–1666.
9.	CuO _x @CoO NRs/CF	1 M KOH	254 mV	24 hours	<i>ChemCatChem.</i> , 2020 , 12, 1639.
10.	CoO@Cu ₂ S	1 M KOH	277 mV	1000 ADT cycles	<i>Appl. Sur. Sci.</i> , 2021 , 555, 149441.

Table 3.6 and **3.7** compare all the pure Co-oxide based materials reported with Co₁-CoO-Pd₂Ge and their TOFs are also compared. The design of Co₁-CoO-Pd₂Ge outperforms all of them with best activity and high stability. Post-electrochemical EPR measurements and DFT

also show how unpaired spin character is instilled in non-magnetic CoOOH lattice which further increases the OER activity and outperforms the activity and stability compared to all the support-based CoO systems reported in the literature. Finally, DEMS measurements during the reaction show the formation of oxygen starts only when the potential reaches the onset value (**Figure 3.28**). This design strategy can attract the researchers to develop efficient materials for many catalytic applications, especially water splitting, fuel cell, electrochemical CO₂ reduction and N₂ reduction.

Table 3.6. List of different types of Co-oxides for alkaline OER activity.

Sl. no.	Catalyst	Potential (at 10mA/cm ²)	Durability	Journal
1.	Co ₁ -CoO-Pd ₂ Ge	1.494 V (0.5M KOH) (264 mV)	36 h (500 mA/cm ²) 50 h, 80 h (100 & 10 mA/cm ²)	This work
2.	Li ₂ Co ₂ O ₄	1.58 V (1M KOH)	100 h (10 mA/cm ²)	<i>Nature Communications</i> https://doi.org/10.1038/s41467-020-15925-2
3.	CoO _x -4h	1.536 V (306 mV)	3 hours (5 mA/cm ²)	<i>Nano Energy</i> , 2018 , 43 110–116
4.	Co _{3-x} O ₄	1.498 V (1M KOH)	3 hours (10mA/cm ²)	<i>ACS Catal.</i> 2018, 8, 3803–3811
5.	Co(OH) ₂	1.52 V (290 mV)	24 hours (10 mA/cm ²)	<i>Appl. Sur. Sci.</i> , 2018 , 427, 253–259
6.	Co ₃ O ₄ /CoO	1.53 V (300 mV)	11 hours (10 mA/cm ²)	<i>Small</i> , 2019 , 15, 1904903
7.	Co ₃ O ₄ -CoO(40)	1.568 V (338 mV)	12 h (10 mA/cm ²)	<i>Eur. J. Inorg. Chem.</i> , 2022 , e202200065(1 of 10)
8.	electrodeposited CoO _x	1.593 V (363 mV)	25 h (at 2V)	https://doi.org/10.1007/s11696-023-02837-w
9.	SC CoO NRs	1.56 V (330 mV)	-	<i>Nat Commun</i> , 2016 , 7, 12876
10.	α-Co(OH) ₂ -Cl	1.55 V (320 mV)	16 h (10 mA/cm ²)	<i>J. Mater. Chem. A</i> , 2016 , 4, 9578-9584

Table 3.7. List of different types of Co-oxides for alkaline OER activity with their TOF values.

Catalyst	Overpotential	TOF (s ⁻¹)	Reference
Co ₁ -CoO-Pd ₂ Ge	351 mV	2.22	<i>This work</i>
P ₁ -CoO NSs	300 mV	0.0024	https://doi.org/10.1016/j.jallcom.2021.161704
CoO _x /Au	351 mV	1.8	<i>J. Am. Chem. Soc.</i> 2011 , 133, 5587–5593
CoO-300 (Co _{3-x} O ₄)	350 mV	0.39	<i>ACS Catal.</i> 2018 , 8, 3803–3811
CoO _x -4h	350 mV	0.012	<i>Nano Energy</i> , 2018 , 43 110–116
α-Co(OH) ₂ -Cl	320 mV	0.0121	<i>J. Mater. Chem. A</i> , 2016 , 4, 9578–9584
CoO _x +Fe ³⁺	350 mV	1.6	<i>ACS Catal.</i> , 2018 , 8, 807–814
CoOOH	350 mV	0.007	<i>J. Am. Chem. Soc.</i> , 2015 , 137, 10, 3638–3648
Fe ₁ Co ₁ -ONP	350 mV	0.022	<i>Adv. Mater.</i> , 2017 , 29, 1606793
Co@nCNFs	550 mV	0.14	<i>Nanoscale Adv.</i> , 2019 , 1, 1224–1231

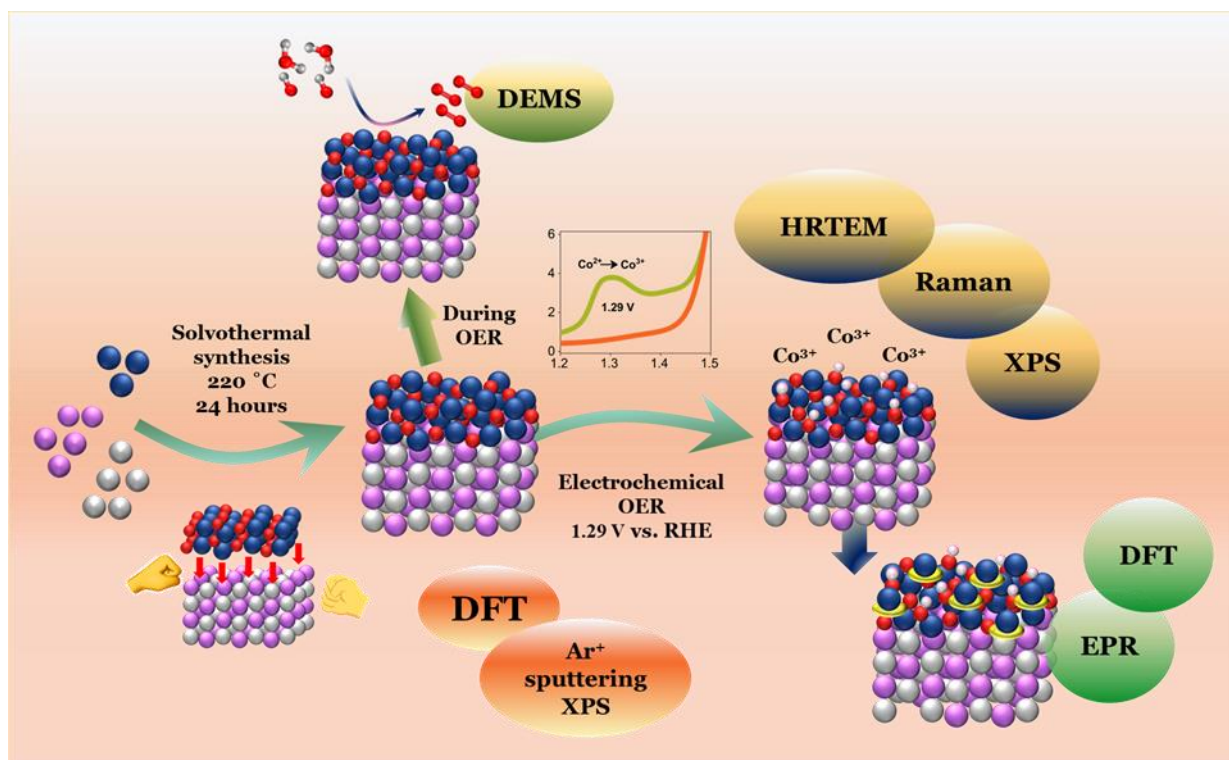


Figure 3.28. Schematic showing how different techniques have illustrated the material design has successfully provided a high OER activity and its reaction mechanism.

3.6 References

1. Wang, H.-Y.; Hsu, Y.-Y.; Chen, R.; Chan, T.-S.; Chen, H. M.; Liu, B., Ni³⁺-Induced Formation of Active NiOOH on the Spinel Ni–Co Oxide Surface for Efficient Oxygen Evolution Reaction. *Adv. Energy Mater.* **2015**, *5*, 1500091.
2. Mondal, S.; Sarkar, S.; Bagchi, D.; Das, T.; Das, R.; Singh, A. K.; Prasanna, P. K.; Vinod, C. P.; Chakraborty, S.; Peter, S. C., Morphology-Tuned Pt₃Ge Accelerates Water Dissociation to Industrial-Standard Hydrogen Production over a wide pH Range. *Adv. Mater.* **2022**, *34*, 2202294.
3. Ren, X.; Wu, T.; Sun, Y.; Li, Y.; Xian, G.; Liu, X.; Shen, C.; Gracia, J.; Gao, H.-J.; Yang, H.; Xu, Z. J., Spin-polarized oxygen evolution reaction under magnetic field. *Nat. Commun.* **2021**, *12*, 2608.
4. Du, K.; Gao, E.; Zhang, C.; Ma, Y.; Wang, P.; Yu, R.; Li, W.; Zheng, K.; Cheng, X.; Tang, D.; Deng, B.; Yin, H.; Wang, D., An iron-base oxygen-evolution electrode for high-temperature electrolyzers. *Nat. Commun.* **2023**, *14*, 253.
5. Shi, Q.; Zhu, C.; Du, D.; Lin, Y., Robust noble metal-based electrocatalysts for oxygen evolution reaction. *Chem. Soc. Rev.* **2019**, *48*, 3181-3192.
6. Lee, S.; Lee, Y.-J.; Lee, G.; Soon, A., Activated chemical bonds in nanoporous and amorphous iridium oxides favor low overpotential for oxygen evolution reaction. *Nat. Commun.* **2022**, *13*, 3171.
7. Qin, Y.; Yu, T.; Deng, S.; Zhou, X.-Y.; Lin, D.; Zhang, Q.; Jin, Z.; Zhang, D.; He, Y.-B.; Qiu, H.-J.; He, L.; Kang, F.; Li, K.; Zhang, T.-Y., RuO₂ electronic structure and lattice strain dual engineering for enhanced acidic oxygen evolution reaction performance. *Nat. Commun.* **2022**, *13*, 3784.
8. Görlin, M.; Halldin Stenlid, J.; Koroidov, S.; Wang, H.-Y.; Börner, M.; Shipilin, M.; Kalinko, A.; Murzin, V.; Safonova, O. V.; Nachttegaal, M.; Uheida, A.; Dutta, J.; Bauer, M.; Nilsson, A.; Diaz-Morales, O., Key activity descriptors of nickel-iron oxygen evolution electrocatalysts in the presence of alkali metal cations. *Nat. Commun.* **2020**, *11*, 6181.
9. Ma, L.; Chen, S.; Pei, Z.; Li, H.; Wang, Z.; Liu, Z.; Tang, Z.; Zapfen, J. A.; Zhi, C., Flexible Waterproof Rechargeable Hybrid Zinc Batteries Initiated by Multifunctional Oxygen Vacancies-Rich Cobalt Oxide. *ACS Nano* **2018**, *12*, 8597-8605.

10. Capilli, G.; Chen, Y.; Szkopek, T.; Cerruti, M., Selective Catalytic Electro-Oxidation of Water with Cobalt Oxide in Ion Impermeable Reduced Graphene Oxide Porous Electrodes. *ACS Nano* **2022**, *16*, 12488-12499.
11. Jin, H.; Liu, X.; An, P.; Tang, C.; Yu, H.; Zhang, Q.; Peng, H.-J.; Gu, L.; Zheng, Y.; Song, T.; Davey, K.; Paik, U.; Dong, J.; Qiao, S.-Z., Dynamic rhenium dopant boosts ruthenium oxide for durable oxygen evolution. *Nat. Commun.* **2023**, *14*, 354.
12. van den Brink, S.; Kleijn, R.; Sprecher, B.; Tukker, A., Identifying supply risks by mapping the cobalt supply chain. *Resour. Conserv. Recycl.* **2020**, *156*, 104743.
13. Chakraborty, S.; Marappa, S.; Agarwal, S.; Bagchi, D.; Rao, A.; Vinod, C. P.; Peter, S. C.; Singh, A.; Eswaramoorthy, M., Improvement in Oxygen Evolution Performance of NiFe Layered Double Hydroxide Grown in the Presence of 1T-Rich MoS₂. *ACS Appl. Mater. Interfaces* **2022**, *14*, 31951-31961.
14. Shimoyama, Y.; Ogiwara, N.; Weng, Z.; Uchida, S., Oxygen Evolution Reaction Driven by Charge Transfer from a Cr Complex to Co-Containing Polyoxometalate in a Porous Ionic Crystal. *J. Am. Chem. Soc.* **2022**, *144*, 2980-2986.
15. Rosen, J.; Hutchings, G. S.; Jiao, F., Ordered Mesoporous Cobalt Oxide as Highly Efficient Oxygen Evolution Catalyst. *J. Am. Chem. Soc.* **2013**, *135*, 4516-4521.
16. Bagchi, D.; Phukan, N.; Sarkar, S.; Das, R.; Ray, B.; Bellare, P.; Ravishankar, N.; Peter, S. C., Ultralow non-noble metal loaded MOF derived bi-functional electrocatalysts for the oxygen evolution and reduction reactions. *J. Mater. Chem. A* **2021**, *9*, 9319-9326.
17. Haase, F. T.; Rabe, A.; Schmidt, F.-P.; Herzog, A.; Jeon, H. S.; Frandsen, W.; Narangoda, P. V.; Spanos, I.; Friedel Ortega, K.; Timoshenko, J.; Lunkenbein, T.; Behrens, M.; Bergmann, A.; Schlögl, R.; Roldan Cuenya, B., Role of Nanoscale Inhomogeneities in Co₂FeO₄ Catalysts during the Oxygen Evolution Reaction. *J. Am. Chem. Soc.* **2022**, *144*, 12007-12019.
18. Yu, M.; Weidenthaler, C.; Wang, Y.; Budiyo, E.; Onur Sahin, E.; Chen, M.; DeBeer, S.; Rüdiger, O.; Tüysüz, H., Surface Boron Modulation on Cobalt Oxide Nanocrystals for Electrochemical Oxygen Evolution Reaction. *Angew. Chem.* **2022**, *61*, e202211543.
19. Menezes, P. W.; Indra, A.; Sahraie, N. R.; Bergmann, A.; Strasser, P.; Driess, M., Cobalt–Manganese-Based Spinel as Multifunctional Materials that Unify Catalytic Water Oxidation and Oxygen Reduction Reactions. *ChemSusChem* **2015**, *8*, 164-171.

20. Wang, H.-Y.; Hsu, Y.-Y.; Chen, R.; Chan, T.-S.; Chen, H. M.; Liu, B., Oxygen Evolution Reaction: Ni³⁺-Induced Formation of Active NiOOH on the Spinel Ni–Co Oxide Surface for Efficient Oxygen Evolution Reaction. *Adv. Energy Mater.* **2015**, *5*.
21. Zhu, Y.; Wang, J.; Koketsu, T.; Kroschel, M.; Chen, J.-M.; Hsu, S.-Y.; Henkelman, G.; Hu, Z.; Strasser, P.; Ma, J., Iridium single atoms incorporated in Co₃O₄ efficiently catalyze the oxygen evolution in acidic conditions. *Nat. Commun.* **2022**, *13*, 7754.
22. Chen, R. R.; Sun, Y.; Ong, S. J. H.; Xi, S.; Du, Y.; Liu, C.; Lev, O.; Xu, Z. J., Antiferromagnetic Inverse Spinel Oxide LiCoVO₄ with Spin-Polarized Channels for Water Oxidation. *Adv. Mater.* **2020**, *32*, 1907976.
23. Xiang, W.; Yang, N.; Li, X.; Linnemann, J.; Hagemann, U.; Ruediger, O.; Heidelmann, M.; Falk, T.; Aramini, M.; DeBeer, S.; Muhler, M.; Tschulik, K.; Li, T., 3D atomic-scale imaging of mixed Co-Fe spinel oxide nanoparticles during oxygen evolution reaction. *Nat. Commun.* **2022**, *13*, 179.
24. Chrétien, S.; Metiu, H., O₂ evolution on a clean partially reduced rutile TiO₂(110) surface and on the same surface precovered with Au₁ and Au₂: The importance of spin conservation. *J. Chem. Phys.* **2008**, *129*, 074705.
25. Torun, E.; Fang, C. M.; de Wijs, G. A.; de Groot, R. A., Role of Magnetism in Catalysis: RuO₂ (110) Surface. *J. Phys. Chem. C* **2013**, *117*, 6353-6357.
26. Sun, Y.; Ren, X.; Sun, S.; Liu, Z.; Xi, S.; Xu, Z. J., Engineering High-Spin State Cobalt Cations in Spinel Zinc Cobalt Oxide for Spin Channel Propagation and Active Site Enhancement in Water Oxidation. *Angew. Chem.* **2021**, *60*, 14536-14544.
27. Miao, X.; Zhou, S.; Wu, L.; Zhao, J.; Shi, L., Spin-State Transition Enhanced Oxygen Evolving Activity in Misfit-Layered Cobalt Oxide Nanosheets. *ACS Sus. Chem. Eng.* **2018**, *6*, 12337-12342.
28. Huang, J.; Chen, J.; Yao, T.; He, J.; Jiang, S.; Sun, Z.; Liu, Q.; Cheng, W.; Hu, F.; Jiang, Y.; Pan, Z.; Wei, S., CoOOH Nanosheets with High Mass Activity for Water Oxidation. *Angew. Chem.* **2015**, *54*, 8722-8727.
29. Zhang, Z.; Feng, C.; Wang, D.; Zhou, S.; Wang, R.; Hu, S.; Li, H.; Zuo, M.; Kong, Y.; Bao, J.; Zeng, J., Selectively anchoring single atoms on specific sites of supports for improved oxygen evolution. *Nat. Commun.* **2022**, *13*, 2473.
30. Yun, T. G.; Heo, Y.; Bin Bae, H.; Chung, S.-Y., Elucidating intrinsic contribution of d-orbital states to oxygen evolution electrocatalysis in oxides. *Nat. Commun.* **2021**, *12*, 824.

31. Guo, T.; Li, L.; Wang, Z., Recent Development and Future Perspectives of Amorphous Transition Metal-Based Electrocatalysts for Oxygen Evolution Reaction. *Adv. Energy Mater.* **2022**, *12*, 2200827.
32. Jiang, Z.-J.; Jiang, Z., Interaction Induced High Catalytic Activities of CoO Nanoparticles Grown on Nitrogen-Doped Hollow Graphene Microspheres for Oxygen Reduction and Evolution Reactions. *Sci. Rep.* **2016**, *6*, 27081.
33. Luo, Y.; Yang, H.; Ma, P.; Luo, S.; Zhao, Z.; Ma, J., Fe₃O₄/CoO Interfacial Nanostructure Supported on Carbon Nanotubes as a Highly Efficient Electrocatalyst for Oxygen Evolution Reaction. *ACS Sus. Chem. Eng.* **2020**, *8*, 3336-3346.
34. Sarkar, S.; Varghese, M.; Vinod, C. P.; Peter, S. C., Conductive interface promoted bifunctional oxygen reduction/evolution activity in an ultra-low precious metal based hybrid catalyst. *Chem. Commun.* **2021**, *57*, 1951-1954.
35. Sarkar, S.; Peter, S. C., Dealloying Induced Manipulative Disruption of Ni₂P–SnP Heterostructure Enabling Enhanced Hydrogen Evolution Reaction. *J. Phys. Chem. C* **2021**, *125*, 13225-13233.
36. Yu, M.; Moon, G.-h.; Castillo, R. G.; DeBeer, S.; Weidenthaler, C.; Tüysüz, H., Dual Role of Silver Moieties Coupled with Ordered Mesoporous Cobalt Oxide towards Electrocatalytic Oxygen Evolution Reaction. *Angew. Chem.* **2020**, *59*, 16544-16552.
37. Wu, C. H.; Liu, C.; Su, D.; Xin, H. L.; Fang, H.-T.; Eren, B.; Zhang, S.; Murray, C. B.; Salmeron, M. B., Bimetallic synergy in cobalt–palladium nanocatalysts for CO oxidation. *Nat. Catal.* **2019**, *2*, 78-85.
38. Li, H.-C.; Zhang, Y.-J.; Hu, X.; Liu, W.-J.; Chen, J.-J.; Yu, H.-Q., Metal–Organic Framework Templated Pd@PdO–Co₃O₄ Nanocubes as an Efficient Bifunctional Oxygen Electrocatalyst. *Adv. Energy Mater.* **2018**, *8*, 1702734.
39. Barhoum, A.; El-Maghrabi, H. H.; Nada, A. A.; Sayegh, S.; Roualdes, S.; Renard, A.; Iatsunskiy, I.; Coy, E.; Bechelany, M., Simultaneous hydrogen and oxygen evolution reactions using free-standing nitrogen-doped-carbon–Co/CoO_x nanofiber electrodes decorated with palladium nanoparticles. *J. Mater, Chem. A* **2021**, *9*, 17724-17739.
40. Ehsan, M. A.; Hakeem, A. S.; Rehman, A., Synergistic effects in bimetallic Pd–CoO electrocatalytic thin films for oxygen evolution reaction. *Sci. Rep.* **2020**, *10*, 14469.
41. Kim, J.-H.; Shin, K.; Kawashima, K.; Youn, D. H.; Lin, J.; Hong, T. E.; Liu, Y.; Wygant, B. R.; Wang, J.; Henkelman, G.; Mullins, C. B., Enhanced Activity Promoted

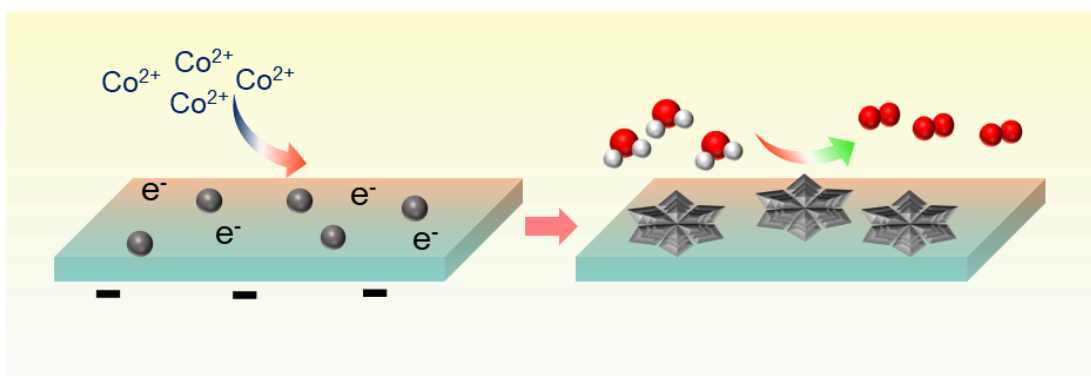
- by CeO_x on a CoO_x Electrocatalyst for the Oxygen Evolution Reaction. *ACS Catal.* **2018**, *8*, 4257-4265.
42. Xu, Z.; Li, W.; Wang, X.; Wang, B.; Shi, Z.; Dong, C.; Yan, S.; Zou, Z., Novel Cobalt Germanium Hydroxide for Electrochemical Water Oxidation. *ACS Appl. Mater. Interfaces* **2018**, *10*, 30357-30366.
43. Chen, J.-Y.; Jheng, S.-L.; Chan, C.-Y.; Tuan, H.-Y., Morphology controlled synthesis of Pd₂Ge nanostructures and their shape-dependent catalytic properties for hydrogen evolution reaction. *Int. J. Hydrog. Energy* **2019**, *44*, 12958-12970.
44. Yan, Y.; Liu, C.; Jian, H.; Cheng, X.; Hu, T.; Wang, D.; Shang, L.; Chen, G.; Schaaf, P.; Wang, X.; Kan, E.; Zhang, T., Substitutionally Dispersed High-Oxidation CoO_x Clusters in the Lattice of Rutile TiO₂ Triggering Efficient Co-Ti Cooperative Catalytic Centers for Oxygen Evolution Reactions. *Adv. Funct. Mater.* **2021**, *31*, 2009610.
45. Guo, C.; Zheng, Y.; Ran, J.; Xie, F.; Jaroniec, M.; Qiao, S.-Z., Engineering High-Energy Interfacial Structures for High-Performance Oxygen-Involving Electrocatalysis. *Angew. Chem.* **2017**, *56*, 8539-8543.
46. Yeo, B. S.; Bell, A. T., Enhanced Activity of Gold-Supported Cobalt Oxide for the Electrochemical Evolution of Oxygen. *J. Am. Chem. Soc.* **2011**, *133*, 5587-5593.
47. Zhong, X.; Zhang, Y.; Geng, Z.; Shi, F.; Jiang, M.; Sun, Y.; Wu, X.; Huang, K.; Feng, S., Engineering Cu₂O/Cu@CoO hierarchical nanospheres: synergetic effect of fast charge transfer cores and active shells for enhanced oxygen evolution reaction. *Inorg. Chem. Front.* **2019**, *6*, 1660-1666.
48. Sarkar, S.; Jana, R.; Suchitra; Waghmare, U. V.; Kuppan, B.; Sampath, S.; Peter, S. C., Ordered Pd₂Ge Intermetallic Nanoparticles as Highly Efficient and Robust Catalyst for Ethanol Oxidation. *Chem. Mater.* **2015**, *27*, 7459-7467.
49. Rajamani, A. R.; Ashly, P. C.; Dheer, L.; Sarma, S. C.; Sarkar, S.; Bagchi, D.; Waghmare, U. V.; Peter, S. C., Synergetic Effect of Ni-Substituted Pd₂Ge Ordered Intermetallic Nanocomposites for Efficient Electrooxidation of Ethanol in Alkaline Media. *ACS Appl. Energy Mater.* **2019**, *2*, 7132-7141.
50. Mondal, S.; Bagchi, D.; Riyaz, M.; Sarkar, S.; Singh, A. K.; Vinod, C. P.; Peter, S. C., In Situ Mechanistic Insights for the Oxygen Reduction Reaction in Chemically Modulated Ordered Intermetallic Catalyst Promoting Complete Electron Transfer. *J. Am. Chem. Soc.* **2022**, *144*, 11859-11869.

51. Wang, J.; Kim, S.-J.; Liu, J.; Gao, Y.; Choi, S.; Han, J.; Shin, H.; Jo, S.; Kim, J.; Ciucci, F.; Kim, H.; Li, Q.; Yang, W.; Long, X.; Yang, S.; Cho, S.-P.; Chae, K. H.; Kim, M. G.; Kim, H.; Lim, J., Redirecting dynamic surface restructuring of a layered transition metal oxide catalyst for superior water oxidation. *Nat. Catal.* **2021**, *4*, 212-222.
52. Chen, Z.; Kronawitter, C. X.; Yeh, Y.-W.; Yang, X.; Zhao, P.; Yao, N.; Koel, B. E., Activity of pure and transition metal-modified CoOOH for the oxygen evolution reaction in an alkaline medium. *J. Mater, Chem. A* **2017**, *5*, 842-850.
53. You, B.; Jiang, N.; Sheng, M.; Gul, S.; Yano, J.; Sun, Y., High-Performance Overall Water Splitting Electrocatalysts Derived from Cobalt-Based Metal–Organic Frameworks. *Chem. Mater*, **2015**, *27*, 7636-7642.
54. Luo, W.; Wang, Y.; Luo, L.; Gong, S.; Wei, M.; Li, Y.; Gan, X.; Zhao, Y.; Zhu, Z.; Li, Z., Single-Atom and Bimetallic Nanoalloy Supported on Nanotubes as a Bifunctional Electrocatalyst for Ultrahigh-Current-Density Overall Water Splitting. *ACS Catal.* **2022**, *12*, 1167-1179.
55. Li, Z.; Wang, Z.; Xi, S.; Zhao, X.; Sun, T.; Li, J.; Yu, W.; Xu, H.; Herng, T. S.; Hai, X.; Lyu, P.; Zhao, M.; Pennycook, S. J.; Ding, J.; Xiao, H.; Lu, J., Tuning the Spin Density of Cobalt Single-Atom Catalysts for Efficient Oxygen Evolution. *ACS Nano* **2021**, *15*, 7105-7113.
56. Yuan, N.; Majeed, M. H.; Bajnóczi, É. G.; Persson, A. R.; Wallenberg, L. R.; Inge, A. K.; Heidenreich, N.; Stock, N.; Zou, X.; Wendt, O. F.; Persson, I., In situ XAS study of the local structure and oxidation state evolution of palladium in a reduced graphene oxide supported Pd(II) carbene complex during an undirected C–H acetoxylation reaction. *Catal. Sci. Technol.* **2019**, *9*, 2025-2031.
57. Roy, S.; Bagchi, D.; Dheer, L.; Sarma, S. C.; Rajaji, V.; Narayana, C.; Waghmare, U. V.; Peter, S. C., Mechanistic insights into the promotional effect of Ni substitution in non-noble metal carbides for highly enhanced water splitting. *Appl. Catal, B: Environ.* **2021**, *298*, 120560.
58. Risch, M.; Morales, D. M.; Villalobos, J.; Antipin, D., What X-Ray Absorption Spectroscopy Can Tell Us About the Active State of Earth-Abundant Electrocatalysts for the Oxygen Evolution Reaction**. *Angew. Chem.* **2022**, *61*, e202211949.
59. Timoshenko, J.; Haase, F. T.; Saddeler, S.; Rüschler, M.; Jeon, H. S.; Herzog, A.; Hejral, U.; Bergmann, A.; Schulz, S.; Roldan Cuenya, B., Deciphering the Structural

- and Chemical Transformations of Oxide Catalysts during Oxygen Evolution Reaction Using Quick X-ray Absorption Spectroscopy and Machine Learning. *J. Am. Chem. Soc.* **2023**.
60. Bagchi, D.; Sarkar, S.; Singh, A. K.; Vinod, C. P.; Peter, S. C., Potential- and Time-Dependent Dynamic Nature of an Oxide-Derived PdIn Nanocatalyst during Electrochemical CO₂ Reduction. *ACS Nano* **2022**, *16*, 6185-6196.
61. Bak, J.; Bin Bae, H.; Chung, S.-Y., Atomic-scale perturbation of oxygen octahedra via surface ion exchange in perovskite nickelates boosts water oxidation. *Nat. Commun.* **2019**, *10*, 2713.
62. Wang, X.; Li, J.; Xue, Q.; Han, X.; Xing, C.; Liang, Z.; Guardia, P.; Zuo, Y.; Du, R.; Balcells, L.; Arbiol, J.; Llorca, J.; Qi, X.; Cabot, A., Sulfate-Decorated Amorphous–Crystalline Cobalt-Iron Oxide Nanosheets to Enhance O–O Coupling in the Oxygen Evolution Reaction. *ACS Nano* **2023**, *17*, 825-836.
63. Feng, C.; Zhang, Z.; Wang, D.; Kong, Y.; Wei, J.; Wang, R.; Ma, P.; Li, H.; Geng, Z.; Zuo, M.; Bao, J.; Zhou, S.; Zeng, J., Tuning the Electronic and Steric Interaction at the Atomic Interface for Enhanced Oxygen Evolution. *J. Am. Chem. Soc.* **2022**, *144*, 9271-9279.
64. McAlpin, J. G.; Surendranath, Y.; Dincă, M.; Stich, T. A.; Stoian, S. A.; Casey, W. H.; Nocera, D. G.; Britt, R. D., EPR Evidence for Co(IV) Species Produced During Water Oxidation at Neutral pH. *J. Am. Chem. Soc.* **2010**, *132*, 6882-6883.

Chapter 4

Electrochemically Sculpted Symmetrical Flowers Generating Oxygen



Soumi Mondal; Debabrata Bagchi; Arko Parui; Manoj Dey; Nilutpal Dutta;
Ashutosh Kumar Singh; Subhajit Chakraborty; Abhishek K. Singh; and
Sebastian C. Peter (*manuscript under preparation*)

Summary

Synthesis of highly symmetrical hexagonal flower-like morphology is very challenging since controlling at the nanoscale is very difficult. This work reports the first ever highly symmetrical and uniform hexagonal cobalt flowers in just few minutes under room temperature and ambient pressure. Besides Co, other similar transition metals Cu, Ni, and Fe has not given any flower-like morphology. Co flowers have successfully grown on Toray carbon, Ni and Cu metal foils, stainless-steel foils and Ni foam which exhibits the potential for economically viable material. Uniformly hexagonal morphology has been provided by boric acid which is explicitly analyzed in this work. Wulff construction models have shown how the selective formation of (101) facet of hexagonal Co has majorly given the flower-like morphology. Moreover, these flowers exhibited very stable industrial level current density for oxygen evolution reaction with only 260 mV overpotential for attaining 100 mA/cm² current density. Spectroscopic techniques like Raman, X-ray photoelectron and X-ray absorption spectroscopy and density functional theory (DFT) have helped to understand the formation mechanism of these flowers.

Table of Contents

4.1	Introduction	122
4.2	Experimental Details	123
4.2.1	Chemicals and reagents	123
4.2.2	Synthesis of electrodeposited catalysts	123
4.3	Characterization	123
4.3.1	Powder X-ray Diffraction (PXRD)	123
4.3.2	Transmission Electron Microscope (TEM)	124
4.3.3	Scanning electron microscopy (SEM) and Energy Dispersive Spectrum (EDS)	124
4.3.4	X-ray Photoelectron Spectroscopy (XPS)	124
4.3.5	X-ray Absorption Spectroscopy	124
4.3.6	Electrochemical Oxygen Evolution Reaction (OER)	125
4.4	Results & Discussion	125
4.4.1	Structural insights and microscopic probing	125
4.4.2	Understanding the role of boric acid	129
4.4.3	Analysis of chemical state of electrodeposited Co	131
4.4.4	Complexing property of boric acid	134
4.4.5	Electrochemical OER activity	138
4.4.6	Electrodeposition of bi-metallic systems	141
4.5	Conclusion	141
4.6	References	143

4.1 Introduction

Mimicking the nature's beauty in science is the most intriguing outcome of research. From understanding the mystery behind such uniform hexagonal honeycomb cells built by the special physical motions of bees,¹ to understanding the hexagonal 2D growth of snowflakes, nature has always been a huge content of immense research.² The six-fold symmetry of the growth of hexagonal snowflakes is highly dependent on the atmospheric pressure and temperature and humidity, which signifies the crystallization of water molecules in a fixed pattern is highly dependent on atmospheric components.^{3,4} Even the same water molecules can arrange in three-fold symmetry instead of having six-fold hexagonal molecular symmetry of ice crystal and this trigonal geometry formation is explained to be dependent on temperature and water-vapor supersaturation.⁵

Like slow crystallization of water molecules to form ice-crystals, metals can crystallize following a specific growth mechanism depending on its chemical and physical environments. Metals can reduce from their ionic form and gradually form a small seed which finally grows along a direction to form metal nanoparticles of a specific morphology. This type of synthesis involves use of surface directing agent and usually happens at higher temperatures or at higher pressure and takes few hours to grow up to nanometric dimension.⁶⁻⁸ To get metal clustering in a few minutes, at room temperature, under ambient pressure, and with less chemicals, electrodeposition is a feasible strategy. Metal salts are taken in the aqueous electrolyte and reductive potentials are given to the cathode for metal ion to metal reduction and deposition on the cathode substrate.⁹ Electrochemical deposition is a very instantaneous process, imparting a uniform deposition of metal. Just like the snowflake crystallization, metal electrodeposition follows the shape according to the electrolyte components and coordination environment of the metal ions in the bulk electrolyte and near the electrode-electrolyte interface.

First-row transition metals like Fe, Co, Ni, Cu have relatively closer standard reduction potential values which makes their electrodeposition more feasible and simultaneous under similar potential conditions. This work explores electrodeposition of these metals under similar reaction conditions. Interestingly, only Co metal exhibited highly uniform six-fold hexagonal flower like morphology which is first ever reported in this work. Previously, researchers have already achieved hexagonal Co phase but with sheet-like morphology using solvothermal process which takes few hours and high temperature around 160 °C and 700 °C and for 5 and 3 hours, respectively.¹⁰ Other attempts to synthesize hexagonal phase of cobalt using strong reducing agents at high-temperature synthesis have not generated any flower-like

morphology.^{11, 12} This has succeeded to achieve unique flower-like morphology using a simple molecule, H_3BO_3 which is non-toxic and inexpensive. To understand the flower formation mechanism, various control experiments have been performed to deconvolute the exact parameters which dictate the growth mechanism. Finally, these instantly flowers have been tested for electrochemical oxygen evolution reaction (OER) and industrial level catalytic activity has been achieved. As mentioned in the introduction of this thesis, OER is the bottleneck reaction for green hydrogen generation which needs to be facilitated using efficient electrocatalysts. Faster and safer synthesis, nature-like flower morphology, and high OER activity has enriched this work.

4.2 Experimental Details

4.2.1 Chemicals and reagents

Cobalt (II) sulphate heptahydrate ($\text{CoSO}_4 \cdot 7\text{H}_2\text{O}$), nickel (II) sulphate heptahydrate ($\text{NiSO}_4 \cdot 7\text{H}_2\text{O}$), iron (II) sulphate heptahydrate ($\text{FeSO}_4 \cdot 7\text{H}_2\text{O}$), copper (II) sulphate heptahydrate ($\text{CuSO}_4 \cdot 7\text{H}_2\text{O}$), and sodium sulphate (Na_2SO_4) and boric acid (H_3BO_3) (from SDFCL). All the chemicals (more than 99% purity) were used as purchased without any further purification. Millipore water of conductivity $18.2 \text{ M}\Omega\text{cm}$ was used for the synthesis and all electrochemical studies.

4.2.2 Synthesis of electrodeposited catalysts

The substrate is first dipped in diluted HCl for proper cleaning and activation and then rinsed with DI water. The substrates used here are Toray carbon paper, Ni foil, Cu foil, Ni foam, and stainless-steel foil. Electrolyte solution for electrodeposition consists of $1 \text{ M Na}_2\text{SO}_4$, 0.1 M metal sulphate salts, $0.5 \text{ M H}_3\text{BO}_3$ dissolved in DI water. Pt wire/graphite carbon rod is used as counter electrode, Ag/AgCl electrode has been used for reference electrode and $1 \times 1 \text{ cm}^2$ surface area bearing activated substrates are connected to an electrode holder and all three electrodes are dipped in the electrolyte solution prepared. The first chronoamperometry (CA) has been run at $-1.1 \text{ V vs. Ag/AgCl}$ for 300 seconds and then a second CA is run at $-1.2 \text{ V vs. Ag/AgCl}$ for 270 seconds. After the electrodeposition, the substrates are washed with running DI water and are being used for characterization and electrocatalysis.

4.3 Characterization

4.3.1 Powder x-ray diffraction (PXRD)

PXRD measurements were done at room temperature on a Rigaku Miniflex X-ray diffractometer with a Cu-K_α X-ray source ($\lambda = 1.5406 \text{ \AA}$), equipped with a position-sensitive

detector in the angular range of $10^\circ \leq 2\theta \leq 90^\circ$ with the step size 0.02° and a scan rate of 0.5 s/step calibrated against corundum standards. The experimental XRD patterns were compared to the patterns simulated from the data reported in the literature.

4.3.2 Transmission electron microscope (TEM)

TEM images and selected area electron diffraction patterns were collected using a JEOL JEM-2010 TEM instrument. The samples for these measurements were prepared by sonicating the nanocrystalline powders in ethanol and drop-casting a small volume onto a carbon-coated copper grid.

4.3.3 Scanning electron microscopy (SEM) and energy dispersive spectrum (EDS)

The SEM measurement was performed using Leica scanning electron microscopy equipped with an energy-dispersive X-ray spectroscopy (EDAX) instrument (Bruker 120 eV EDAX instrument). Data were acquired by using an accelerating voltage of 15 kV, and the typical time taken for data accumulation is 100 s. The elemental analyses were performed using the P/B-ZAF standardless method (where P/B = peak to background model, Z = atomic no. correction factor, A = absorption correction factor, and F = fluorescence factor) for Cu, Ga at multiple areas on the sample coated Si wafer.

4.3.4 X-ray photoelectron spectroscopy (XPS)

XPS measurements were carried out using Thermo K-alpha+ spectrometer using micro focused and monochromated Al K α radiation with energy 1486.6 eV. The pass energy for the spectral acquisition was kept at 50 eV for individual core-levels. The electron flood gun was utilized for providing charge compensation during data acquisition. Further, the individual core-level spectra were checked for charging using C1s at 284.6 eV as standard and corrected if needed. The peak fitting of the individual core-levels was done using CASA XPS software with a Shirley type background.

4.3.5 X-ray absorption spectroscopy

X-ray absorption near-edge spectroscopy (XANES) and quick-Extended X-ray Absorption Fine Structure (quick-EXAFS) experiments at 300 K were performed at PETRA III, beamline P64, of DESY, Germany. Measurements of Cu-K and Pd-K at ambient pressure were performed in fluorescence as well as transmission mode using gas ionization chambers to monitor the incident and transmitted X-ray intensities. Monochromatic X-rays were obtained using a Si (111) double crystal monochromator, which was calibrated by defining the inflection point (first derivative maxima) of Cu foil as 8980.5 eV. The beam was focused by employing

a Kirkpatrick-Baez (K-B) mirror optic. A rhodium-coated X-ray mirror was used to suppress higher-order harmonics. A CCD detector was used to record the transmitted signals. Pellets for the ex-situ measurements were made by homogeneously mixing the sample with an inert cellulose matrix to obtain an X-ray absorption edge jump close to one.

4.3.6 Electrochemical oxygen evolution reaction (OER)

All the electrochemical measurements were done in a 3-electrode set-up comprising of the electrodeposited catalyst as working electrode, graphite rod counter electrode, and mercury/mercuric oxide electrode (MMO) (for basic media). Commercial IrO₂/C (Sigma Aldrich) was used for comparison of activity with the reported electrocatalysts. Linear sweep voltammetry (LSV) was recorded for OER at a scan rate of 5 mV s⁻¹ at 25 °C. Electrochemical impedance studies were performed in the frequency range from 10 mHz to 100 kHz at different applied DC potentials for different reactions depending on their onset potential values. The electrolyte solution was deaerated by purging N₂ gas into the solution at least for 30 min before each experiment. All the reference electrodes were calibrated with respect to the reversible hydrogen electrode (RHE), using Pt as working and counter electrodes in the respective electrolytes.

4.4 Results & Discussion

4.4.1 Structural insights and microscopic probing

Four important transition metals, Fe, Co, Ni, and Cu have been electrochemically synthesized (**Figure 4.1a**). Same electrochemical conditions are used for all the metals since the standard reduction potential values are similar for all these metals. As shown in **Figure 4.1b, 4.1c**, two potentials are chosen from the first linear sweep voltammogram, and two consecutive chronoamperometry (CA) are run at -1.1 V vs. Ag/AgCl for 270 secs and -1.2 V vs. Ag/AgCl for 300 secs. The sample codes for different metal deposition are given in **Table 4.1**. The PXRD pattern shows that Ni and Fe have purely crystallized in FCC lattice (space group: *Fm* $\bar{3}$ *m*), (**Figure 4.2a, 4.2b**) and Cu has crystallized in FCC lattice with some trace amounts of Cu₂O (**Figure 4.2c**). On the other hand, Co is the only metal which has crystallized in the hexagonal lattice (*P6*₃/*mmc*) as shown in **Figure 4.2d**. **Figure 4.3a, 4.3b-d** show schematic and SEM images of the spherical, fern-like, non-uniform spherical floral morphologies are obtained for Ni, Cu and Fe metals. The most interesting and uniform hexagonal flower-like morphology has been achieved for only Co metal. Due to the intriguing morphology, this work majorly focuses on Co and unravels the mechanism behind the hexagonal morphology of the Co metal.

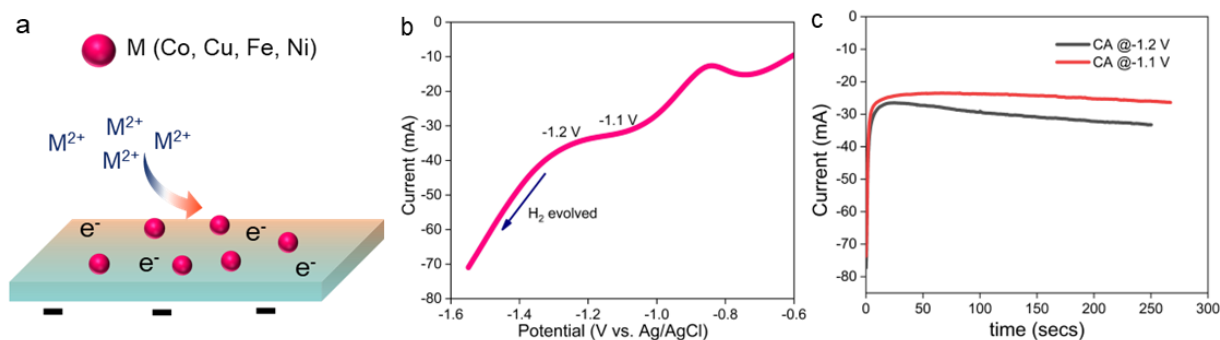


Figure 4.1. (a) Schematic representation of electrodeposition of divalent metal ions on electrode substrate with negative electrode potential. (b) LSV for understanding metal deposition potential, (c) CA at two different potentials consecutively, i.e. CA1 at -1.1 V and CA2 at -1.2 V vs. Ag/AgCl.

Table 4.1. List of sample codes for different metal-electrodeposition process with H_3BO_3 being 0.5M and Na_2SO_4 being 1M for all.

Sample code	Metal salt (0.1 M)
Co-ED	$CoSO_4 \cdot 7H_2O$
Cu-ED	$CuSO_4 \cdot 7H_2O$
Ni-ED	$NiSO_4 \cdot 7H_2O$
Fe-ED	$FeSO_4 \cdot 7H_2O$

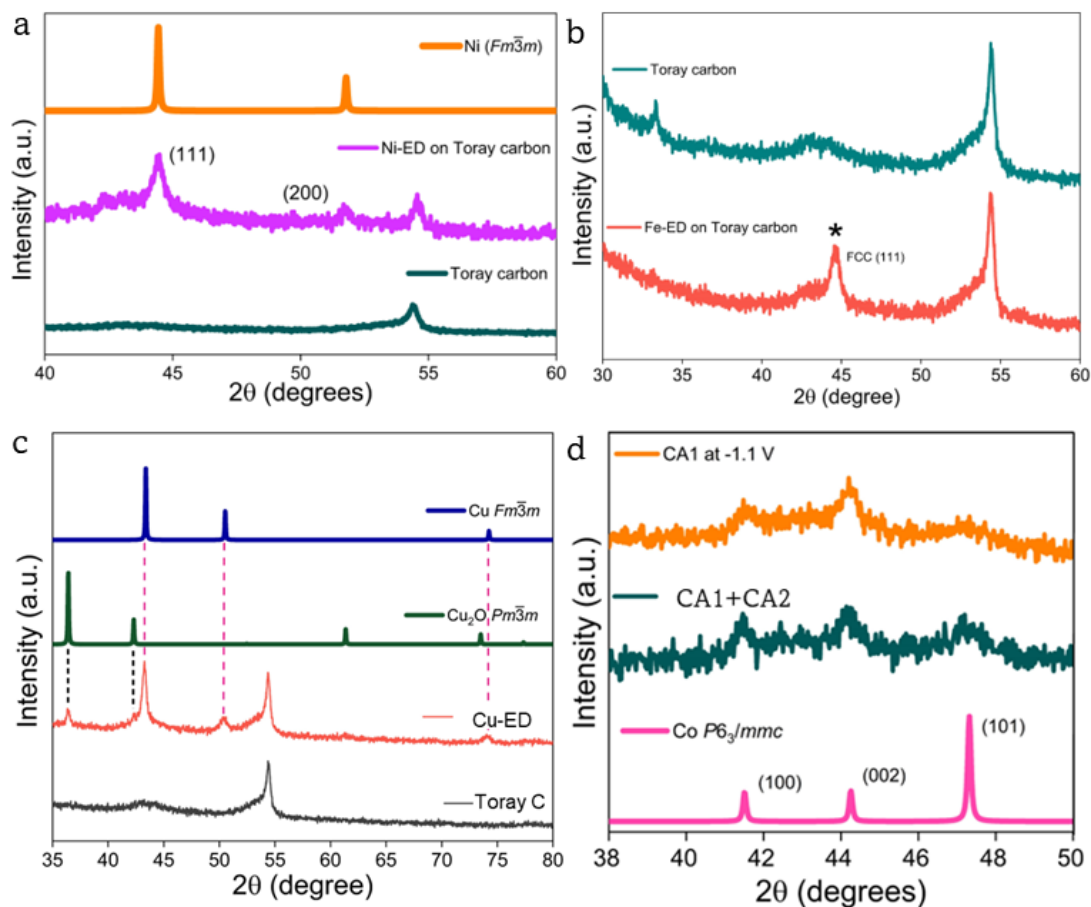


Figure 4.2. PXRD pattern of (a) Ni and (b) Fe, (c) Cu, and (d) Co electrodeposited on Toray carbon substrate.

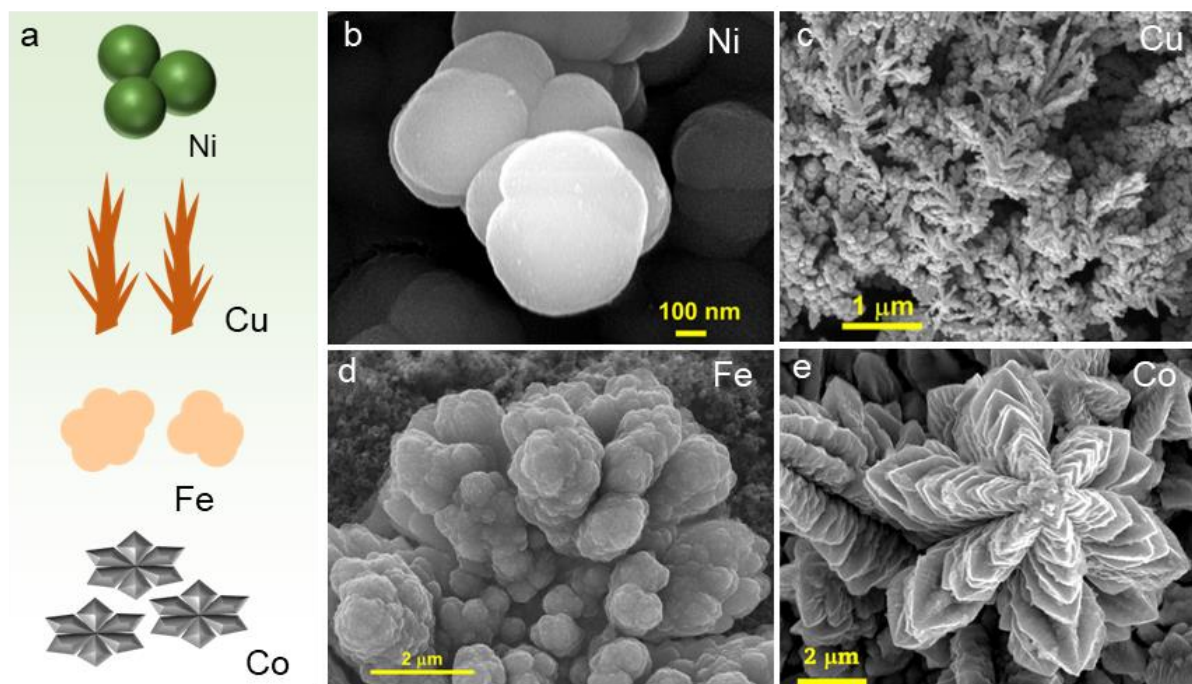


Figure 4.3. (a) Pictorial representation of different transition metal after their deposition. Scanning electron microscopy (SEM) images of (b) Ni, (c) Cu, (d) Fe, (e) Co.

Table 4.2. List of sample codes for different potential during electrodeposition with H_3BO_3 being 0.5M and Na_2SO_4 being 1M and metal sulphates being 0.1M for all. CA=chronoamperometry.

Potentials	CA1 -1.1 V vs. Ag/AgCl	CA2 -1.2 V vs. Ag/AgCl	CA1+CA2
Sample Code	Co-ED ₁	Co-ED ₂	Co-ED

Separate analysis has been done after the CA of each potential and hence the electrodeposited Co only after first CA1, only after CA2, and after CA1 followed by CA2 are being studied with codes being, Co-ED₁, Co-ED₂, and Co-ED (Table 4.2).

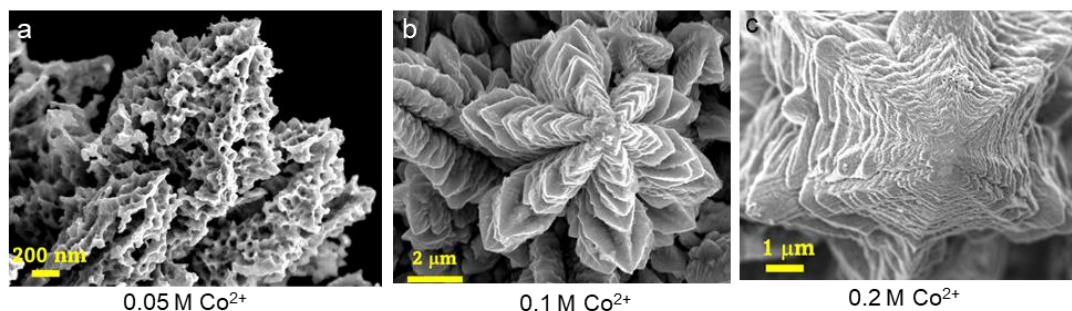


Figure 4.3. SEM images of Co ED with Co^{2+} of (a) 0.05 M, (b) 0.1 M, (c) 0.2 M.

During the electrodeposition process, sodium sulphate has been used in 1 M concentration which acts as a supporting electrolyte for providing conductivity,¹³ and H_3BO_3 has been used to create a buffer to avoid sudden increase in pH due to extensive hydrogen evolution reaction (HER) at such high negative electrode potential.¹⁴ $\text{CoSO}_4 \cdot 7\text{H}_2\text{O}$ being the precursor to supply metallic Co for building the hexagonal flower, the concentration of Co^{2+} has been varied to understand the build-up process of the perfect flower morphology. **Table 4.3** enlists different concentrations used and **Figures 4.3a**, **4.3b**, and **4.3c** visualize the morphology through SEM images. It is clearly observed that a hexagonal protruding 3D framework has been generated with 0.05 M Co^{2+} (Co-ED-0.05Co) with porous structure which is filled Co^{2+} when the concentration is increased to 0.1 M looks like a complete flower with all the edges and crests between two petals being very sharp and prominent (**Figures 4.3b** and **4.4**).

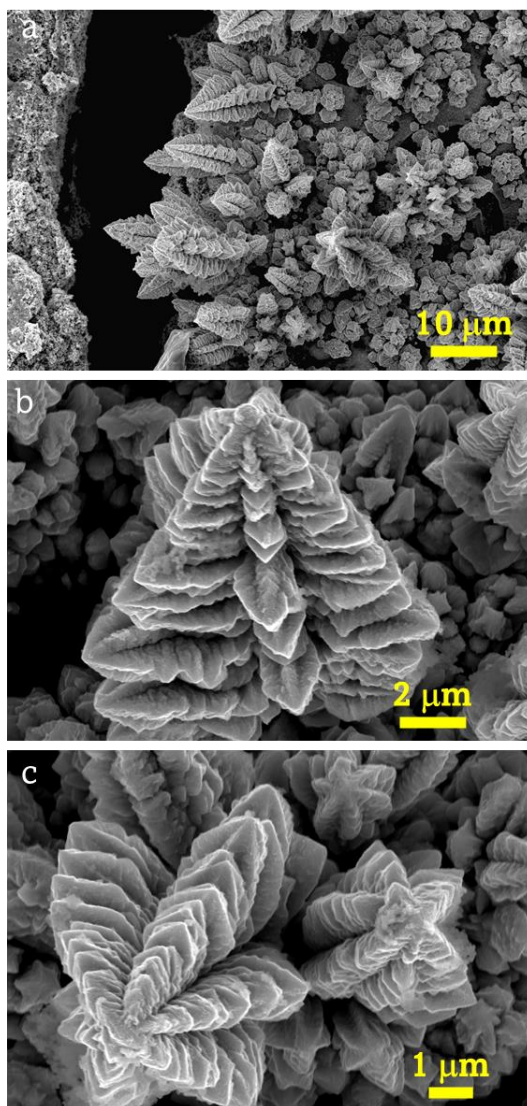


Figure 4.4. SEM images of Co-ED with 0.5 M BA, 0.1 M Co^{2+} solution.

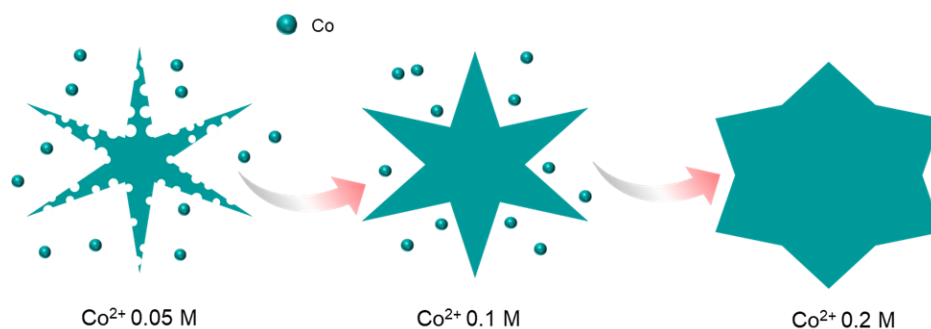


Figure 4.5. Schematic representation of Co electrodeposition at different Co^{2+} concentrations.

With further increment of Co^{2+} 0.2 M (Co-ED-0.2Co), there is further deposition of Co-atoms to the crests and makes the edges blunt with over-deposition of Co, although the overall hexagonal framework is retained. This mechanism on tuned Co^{2+} deposition has been shown schematically in **Figure 4.5**. Based on the perfection in morphology, Co-ED with 0.1 M Co^{2+} has been used to carry out experiments for understanding its formation mechanism.

4.4.2. Understanding the role of boric acid

To observe the effects of H_3BO_3 , electrodeposition of Co has been carried out at different concentrations of H_3BO_3 (**Table 4.4**). Without boric acid (BA), there is no trace of flower formation (**Figure 4.6**), and elemental mapping shows that Co-ED-0B has prominent presence of O and Co on the deposited materials which indicates formation of Co-hydroxide or oxide on the substrate (**Figure 4.6**). With 0.25 M BA, some small florets have started to form (**Figure 4.7**) and with 0.5 M BA there is clear formation of hexagonal prominent flowers with well-separated six-tips (**Figure 4.4**).

Table 4.3. List of sample codes for different concentrations of $\text{CoSO}_4 \cdot 7\text{H}_2\text{O}$ with Na_2SO_4 being 1M and H_3BO_3 being 0.5 M for all and after both CA1+CA2.

Sample code	$\text{CoSO}_4 \cdot 7\text{H}_2\text{O}$
Co-ED-0.05Co	0.05 M
Co-ED	0.1 M
Co-ED-0.2Co	0.2 M

Table 4.4. List of sample codes for different concentrations of H_3BO_3 with Na_2SO_4 being 1M and metal sulphates being 0.1M for all and after both CA1+CA2.

Sample code	H_3BO_3
Co-ED-0B	0
Co-ED-0.06B	0.06 M
Co-ED-0.125B	0.125 M
Co-ED-0.25B	0.25 M
Co-ED	0.5 M
Co-ED-1B	1 M
Co-ED-2B	2 M

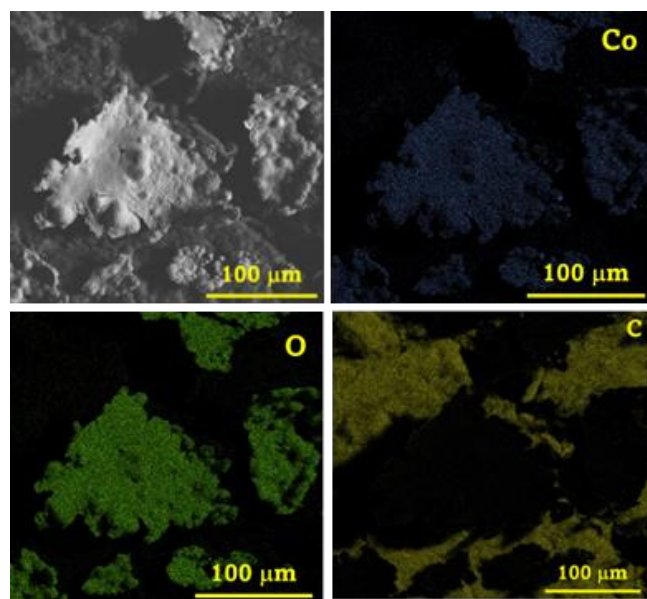


Figure 4.6. SEM image and SEM-EDX mapping of Co-ED-0B where no BA is taken during the electrodeposition and mainly $\text{Co}(\text{OH})_2$ species have formed.

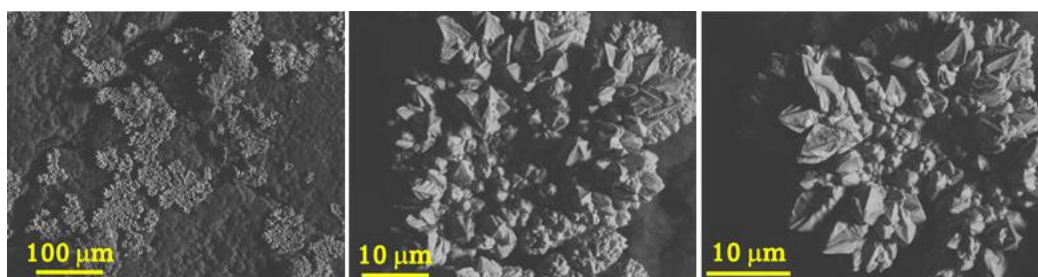


Figure 4.7. SEM images of Co-ED-0.25B where 0.25 M BA is being used for Co metal electrodeposition.

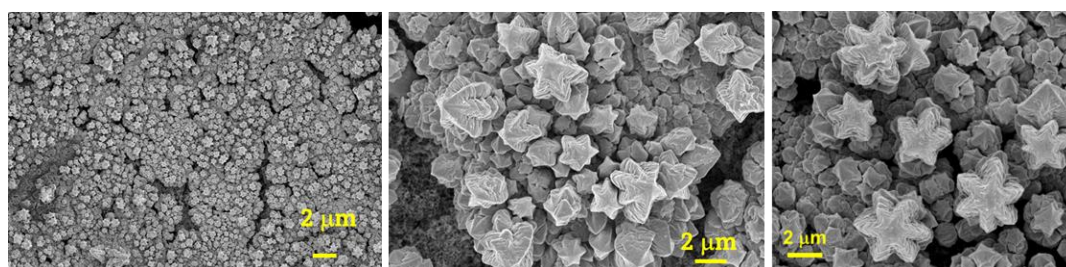


Figure 4.8. SEM images of Co-ED-1B where 1 M BA is being used for Co metal electrodeposition.

When further increased to 1 M BA, there are still uniformly distributed hexagonal Co flowers but with significant decrease in the size of the flowers (**Figure 4.8**), and when BA is taken in 2 M concentration, although the hexagonal morphology remained intact, but there is deposition of amorphous materials on the flowers and the sharpness of the flower petals decreased (**Figure 4.9a**). The trend of flower size with respect to H_3BO_3 has been shown in **Figure 4.9b**, which indicates most prominent flowers are achieved when 0.5 M BA is used.

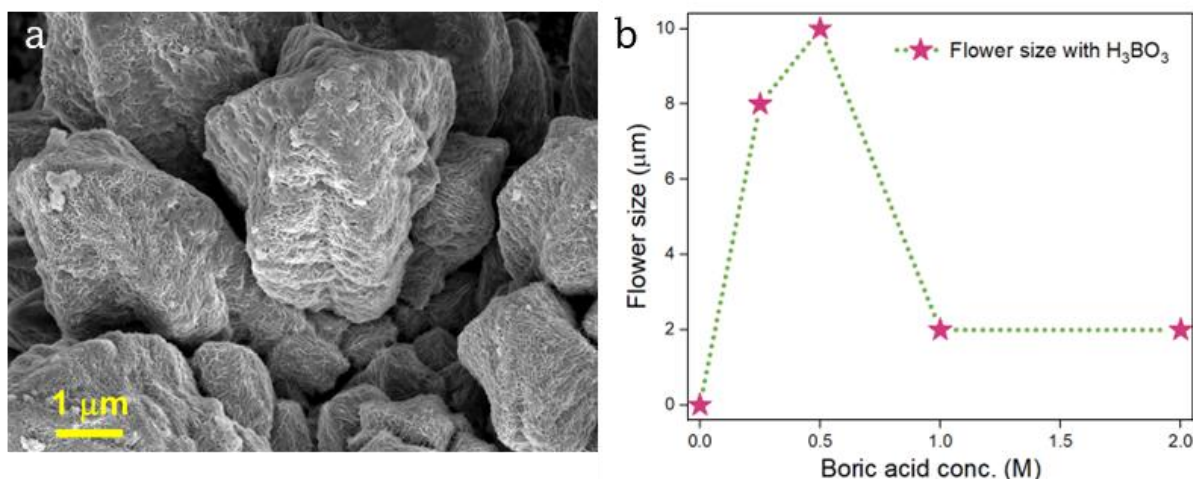


Figure 4.9. (a) SEM images of Co-ED-2B where 2 M BA is being used for Co metal electrodeposition. (b) Flower size distribution plot with respect to concentration of BA.

4.4.3. Analysis of chemical state of electrodeposited Co

To understand the surface chemical properties of the electrodeposited Co at different BA concentrations, position specific Raman spectroscopy has been conducted. **Figure 4.10a** represents the Raman spectra of two positions (Position 1 and Position 2) marked on two locations (viewed in optical microscopy image of Raman instrument) for Co-ED (with 0.5 M BA with highest prominence in morphology) where no peak is observed which means the entire surface is fully metallic with no surface oxide or hydroxide. **Figure 4.10b** schematically explains why higher BA concentration (1M BA) gives smaller flowers than 0.5 M BA. Higher boric acid contents will release more protons from dissociation of H_2O molecules following the equation: $\text{B}(\text{OH})_3 + \text{H}_2\text{O} \rightarrow \text{B}(\text{OH})_4^- + \text{H}^+$.¹⁵

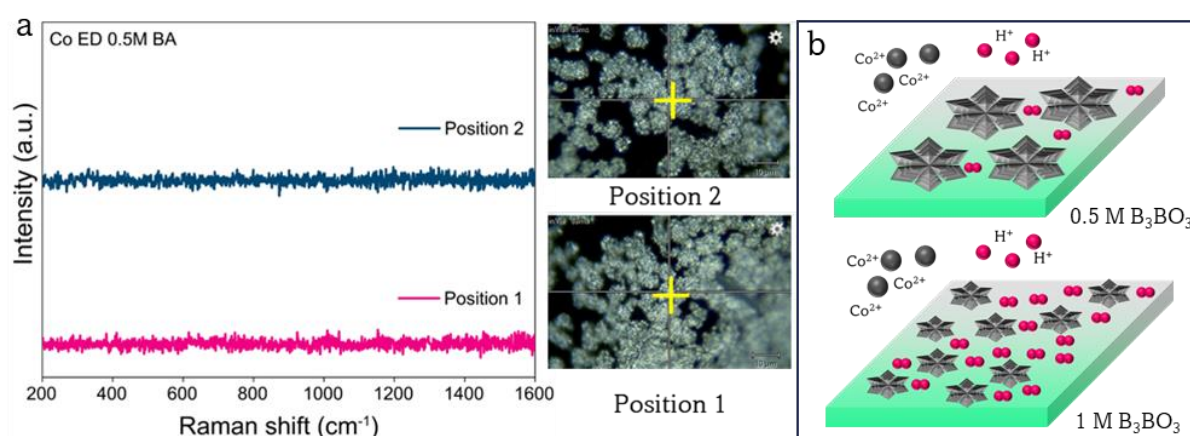


Figure 4.10. (a) Raman spectra of Co-ED with 0.5 M BA and position 1 and 2 indicates the two microscopic images with pointed mark. (b) Schematic representation of flower size decrement due to increased BA concentration.

These protons will get reduced to molecular hydrogen near the electrode surface due to the negative electrode potential.¹⁶ The negative electrode potential performs two actions: Co electro-reduction from solution Co^{2+} to metallic Co on substrate, and hydrogen evolution reaction, $2\text{H}^+ + 2\text{e}^- \rightarrow \text{H}_2$.¹⁷ More of hydrogen evolution will increase the accumulation of bubble formation near the electrode surface which will impart mechanical barrier for Co-flowers to grow big due to interruption in growth by bubbles of gaseous H_2 . To understand the loss of perfect morphology when 2M BA has been used, surface chemical analysis via position specific Raman spectroscopy is performed. **Figure 4.11** indicates that the silvery white shining regions in position 1 and 3 show no Raman peak which clearly indicate metallic Co, and the black region in the position 2 indicates the substrate Toray carbon paper, and the other chunk-like off-white-colored regions in position 4 and position 5 has peaks in Raman spectra corresponding to Co-oxides and hydroxide species.¹⁸ Furthermore, surface analysis technique, XPS, has been used for understanding the chemical state of Co in its deposition with 0.5 M boric acid (Co-ED) and in its absence (Co-ED-0B). Co 2p XPS, **Figure 4.12a** and **Figure 4.12b** represent the presence of metallic Co (Co $2p_{3/2}$ at around 778 eV) in case of Co-ED and Co^{2+} (Co $2p_{3/2}$ at around 780.1 eV) for Co-ED-0B, which means boric acid's absence has generated only hydroxide or oxide and no metallic Co. **Figure 4.13a** and **4.13b** represents the Co K-edge XANES and R-space data for Co electrodeposition in absence of BA and in presence of different concentrations of BA. From the white-line intensity it is observed that Co deposited in absence of BA has the highest peak intensity and its R-space data shows the presence of Co-O bond significantly, while all other electrodeposited Co has majorly Co-Co bonds and their XANES spectra show resemblance to the metallic Co foil. Hence, BA is necessary to deposit metallic Co.

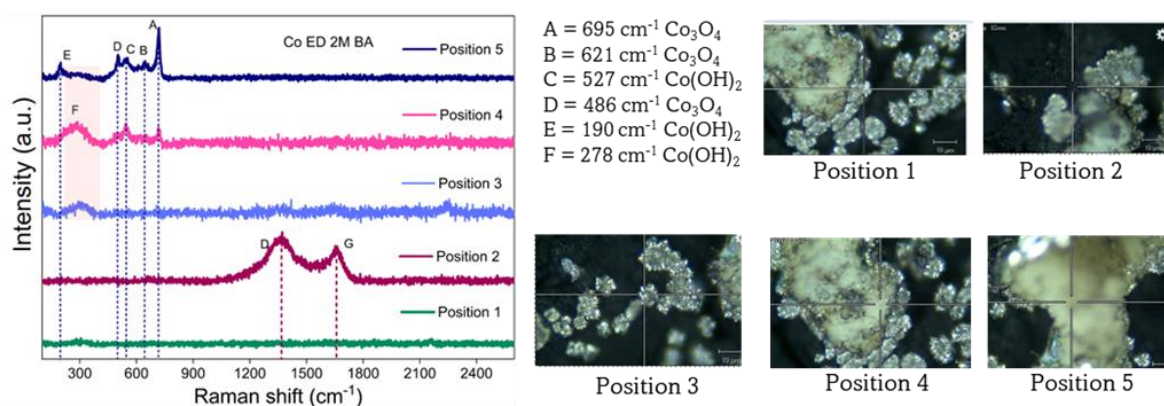


Figure 4.11. Position specific Raman spectra at each position marked in the microscopic figures attached adjacent to the Raman spectra.

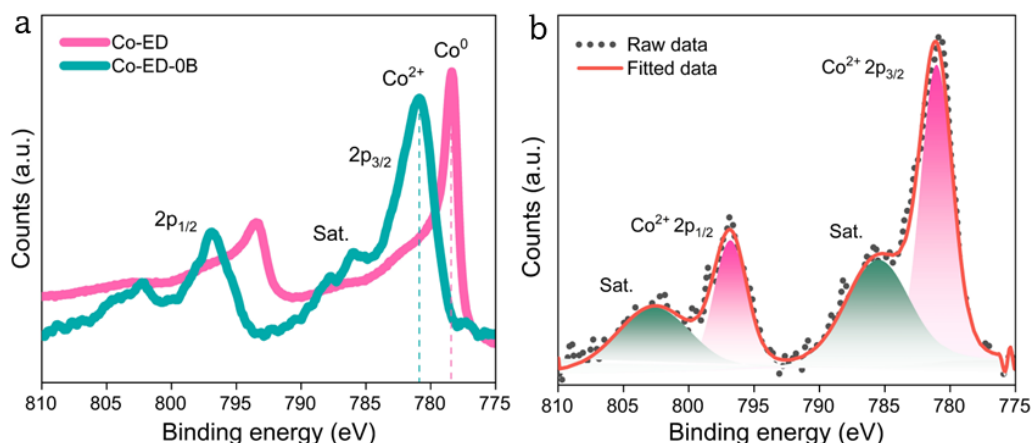


Figure 4.12. (a) X-ray photoelectron spectroscopy (XPS) of Co 2p orbital for electrodeposited Co with 0.5 M BA and with no BA. (b) Co 2p XPS of Co-ED-0B.

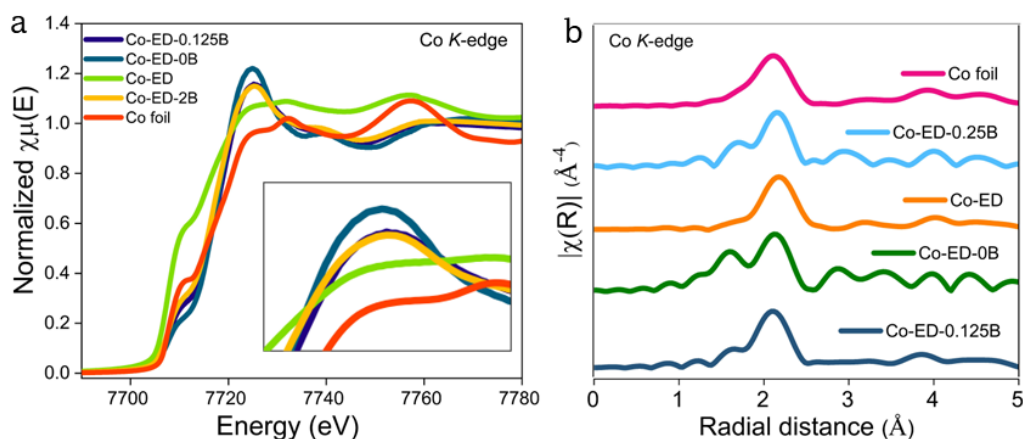


Figure 4.13. (a) X-ray absorption near edge spectra (XANES) of Co *K*-edge for Co electrodeposition without BA and different concentrations of BA (Co-ED, Co-ED-0.125B, Co-ED-0.25B, and Co-ED-0B) and Co metal foil. (b) Fourier transformed R-space data for Co-ED, Co-ED-0.125B, Co-ED-2B, and Co-ED-0B) and Co metal foil.

Figure 4.11 indicates that when a higher content of BA is used there is formation of metal hydroxide which is due to fact that with increased BA concentration, there will be more H_2O dissociation and proton reduction and hence huge OH^- generation and accumulation near the electrode surface will rapidly increase the local pH of the electrode surface. It is important to note that boric acid acts as a buffer, it is more of a Lewis acid (abstract OH^-) from water, than an Arrhenius acid and boric acid generates an increased pH when used in its larger concentration. Thus, there is a huge pH gradient generated between the local and bulk environments. This enhanced pH near electrode surface immediately helps forming $\text{Co}(\text{OH})_2$ or other oxides before it gets reduced to metallic Co and deposit on the substrate. **Figure 4.14** schematically represents this observation at the electrode-electrolyte interfacial chemistry with and without boric acid during electrodeposition.

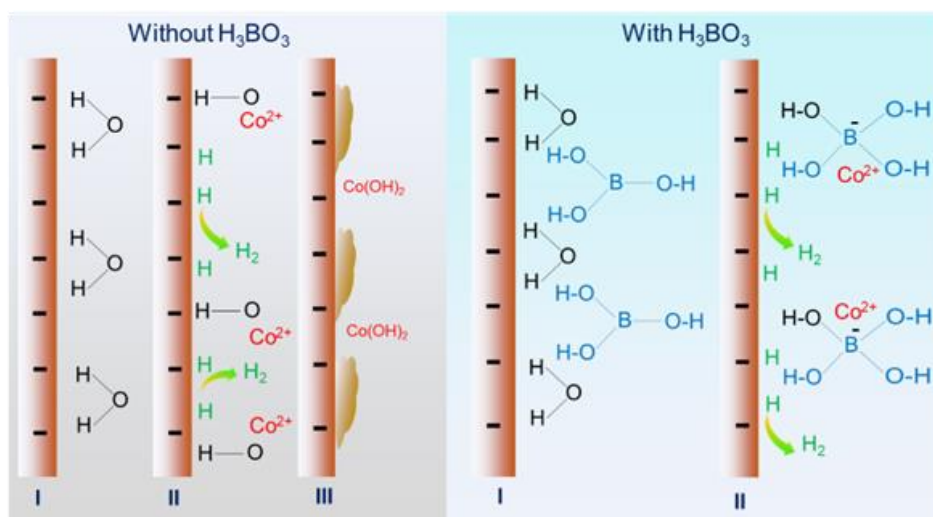


Figure 4.14. Scheme for representing the formation of Co-oxide and hydroxide when 2 M BA is used.

4.4.4 Complexing property of boric acid

With all the observations observed till now it can be concluded that boric acid is integral for the flower formation (**Figure 4.6**) and that too with Co^{2+} ions only and not the other transition metal ions (**Figures 4.3a-e**). Till today, the role of boric acid in electrodeposition has been explained only for its being a potential buffer.¹⁹ Interestingly, even with utilizing the buffer property of boric acid, no report has been observed with the generation of such highly symmetrical and uniformly distributed hexagonal flowers before.²⁰⁻²² This triggered the further control experiments to understand the exact role of boric acid in the electrolyte solution. To under the role of acidity of boric acid, other acids are being used instead of BA, which are enlisted in **Table 4.5**. As observed from the SEM images in **Figure 4.15a**, **4.15b**, **4.15c**, and **4.15d**, the hexagonal flower-like morphology is not obtained with CH_3COOH , H_2SO_4 , ascorbic acid, and H_3PO_4 , where boric acid is absent. There is no Co-deposition at all when nitric acid is being used instead of BA. This means that acidity of boric acid does not play any role in dictating the Co morphology.

Table 4.5. List of sample codes for different morphology-directing agents. Concentration of $\text{CoSO}_4 \cdot 7\text{H}_2\text{O}$ being 0.1 M with Na_2SO_4 being 1M for all and after both CA1+CA2.

Sample code	Complexing agents
Co-ED	Boric acid
Co-ED-SA	Sulfuric acid
Co-ED-NA	Nitric acid
Co-ED-PA	Phosphoric acid
Co-ED-AA	Acetic acid
Co-ED-AscA	Ascorbic acid
Co-ED-EDTA	Ethylenediaminetetracetate ions (EDTA)

Furthermore, the complexing property of boric acid is being inexplicitly analyzed. From the molecular structure of acetic acid, sulfuric acid, and phosphoric acids, it can be said that complexation of Co^{2+} by these acid anions will be weak and caging of Co^{2+} ions by these anions are not possible (Figures 4.16a, 4.16b, 4.16c). Some chelation can be feasible by di-deprotonated form of ascorbic acid (Figure 4.16d), but that is not a stable complexation, due to which random morphology of Co deposition is observed.

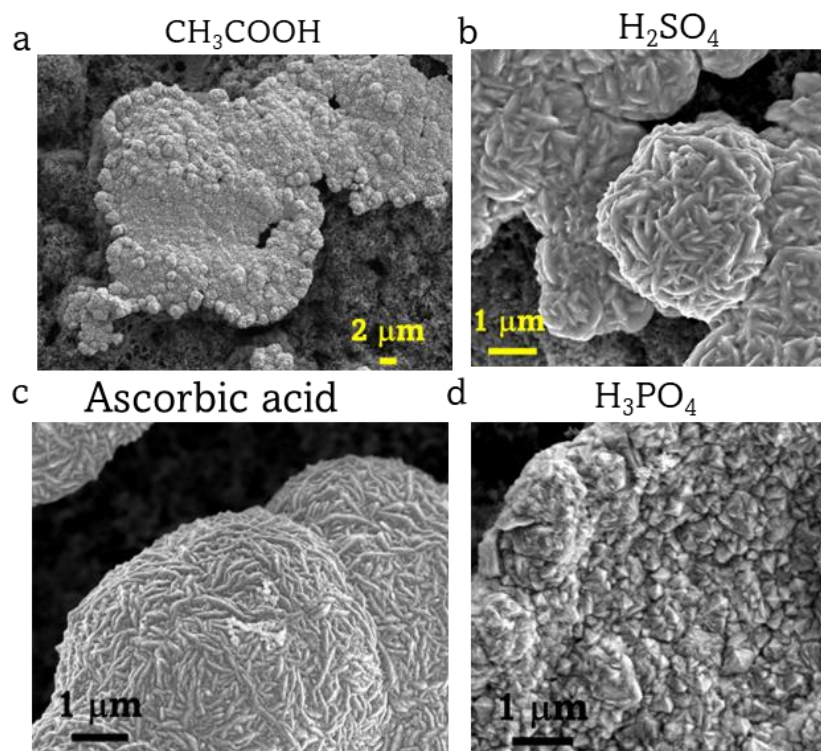


Figure 4.15. SEM image of electrodeposited Co when acids like (a) CH_3COOH , (b) H_2SO_4 , (c) $\text{C}_6\text{H}_8\text{O}_6$ (ascorbic acid), (d) H_3PO_4 are being used instead of boric acid, H_3BO_3 .

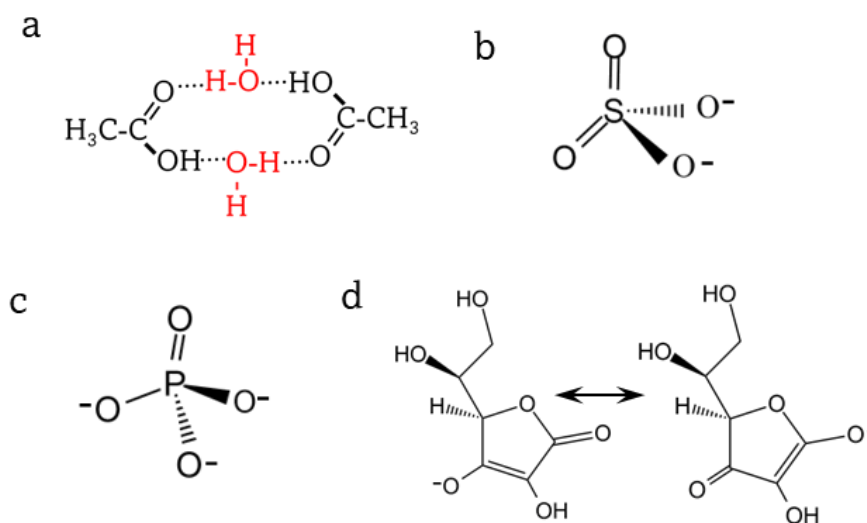


Figure 4.16. Molecular structure of (a) CH_3COOH , (b) H_2SO_4 , (c) H_3PO_4 , (d) $\text{C}_6\text{H}_8\text{O}_6$.

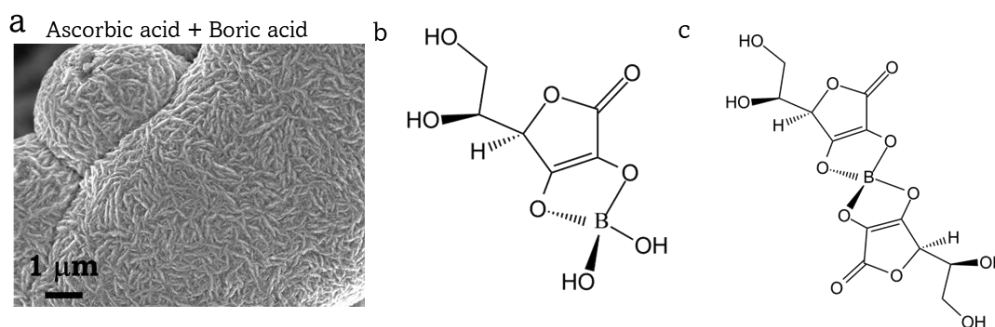


Figure 4.17. SEM image of electrodeposited Co (a) when both boric acid and ascorbic acid are taken. Molecular structure of (b) mono-borate and (c) di-borate ester of boric acid and ascorbic acid.

Interestingly when both boric acid and ascorbic acid are taken together in the electrolyte, then also the hexagonal morphology is not observed even though boric acid is still present (**Figure 4.17a**). It is well reported that there is formation of mono-borate and di-borate ester when ascorbic acid and boric acids are mixed in aqueous solutions (**Figure 4.17b** and **4.17c**). This gives a firm indication that Co^{2+} ions are complexed with boric acid which is absent when ascorbic acid is present in the solution and boric acid molecules are not free due to esterification with ascorbic acid.²³

It is well known that boric acid exists as different polymeric structure based on its tendency to bond with hydroxyl ions extracted from water dissociation.²⁰ Hence, it is obvious that different polymeric structure will have different trends of complexation with Co^{2+} and different stabilization energies for adsorption on metallic Co crystal facets. To delve deep into understanding the role of different polymeric structures of boric acid in giving a specific morphology to the deposited Co metal, surface energies have been calculated for three major facets of Co, (100), (002), and (101) with different polymeric structures of boric acid adsorbed on them. Based on these surface stabilization energies, Wulff constructed structures have been derived. **Figures 4.18a, 4.18b, 4.18c, and 4.18d** show the Wulff construction models when the respective polymeric conformation of boric acid is absorbed on the three facets of Co metal. It is found that only with the polymeric form $[\text{B}_3\text{O}_3(\text{OH})_5]^{-2}$ there is large occupancy of facet (101) giving the Wulff model a protruded sharp appearance which indicates that with increased content of facet (101) Co will have a sharp hexagonal morphology, otherwise Co will deposit as hexagonal plate-like structure. Hexagonal flake-like or plate-like morphologies are very common, but achieving a 3D hexagonal pointed flower-like morphology is being observed for the first time in this work. Further support to this observation is obtained when there is no Co metal electrodeposition at all on the substrate when ethylenediaminetetraacetate (EDTA) ions instead of boric acid in the reaction medium.

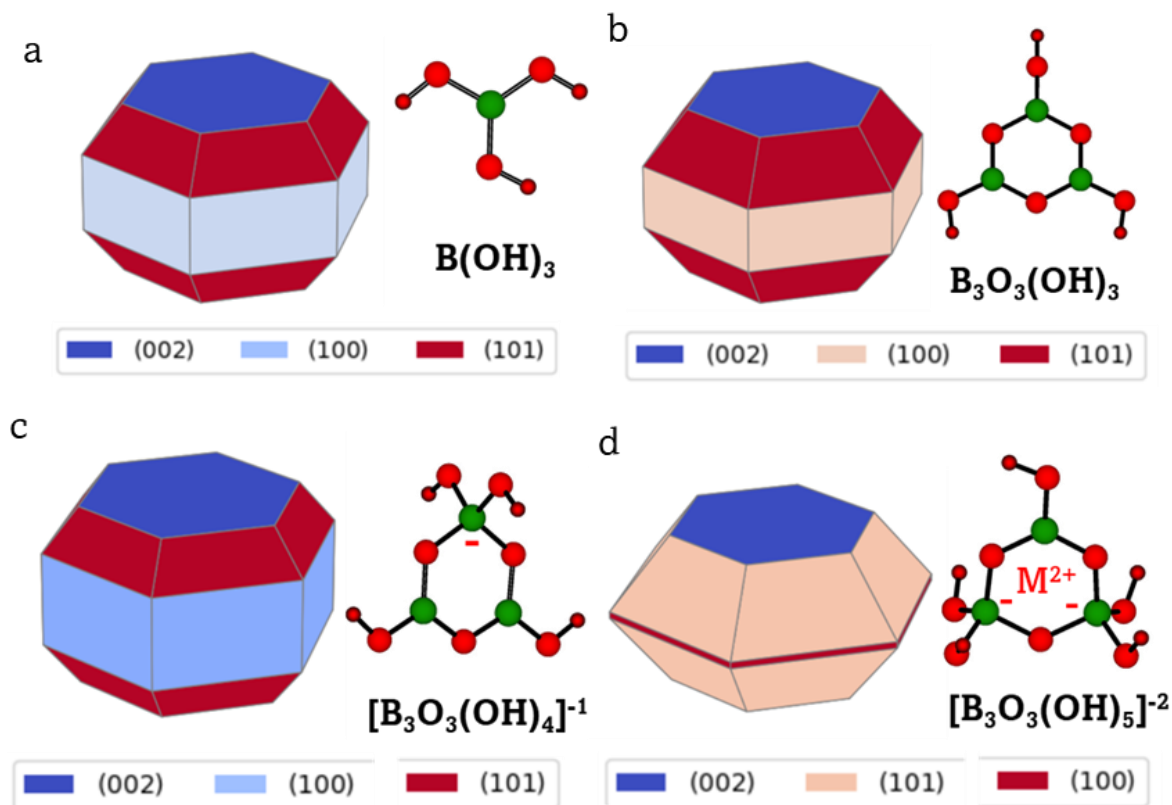


Figure 4.18. Wulff constructed structure of hexagonal Co metal when the different polymeric structure of boric acids is being considered while adsorbing on (002), (100) and (101) facets of metallic cobalt (a) $B(OH)_3$, (b) $B_3O_3(OH)_3$, (c) $[B_3O_3(OH)_4]^{-1}$, and (d) $[B_3O_3(OH)_5]^{-2}$.

This is due to the extremely stable complex formation of Co^{2+} ions with EDTA in aqueous solutions which makes no Co^{2+} ions available for deposition.²⁴ Hence, from the control experiments of ascorbic acid and EDTA, it is evident that a complexing property of boric acid is highly significant in giving that highly symmetrical 6-fold morphology. As mentioned earlier, **Figure 4.2d** shows the PXRD pattern for Co ED using first CA (Co-ED₁) and using both CA1 followed by CA2 (Co-ED). This observation indicates that presence of (101) facet is observed only after the second CA, i.e., -1.1 V followed by -1.2 V vs. Ag/AgCl. **Figure 4.19a, b** shows that just after CA1 at -1.1 V vs. Ag/AgCl, no flower like morphology is observed. **Figure 4.19c, d** shows that with only CA2 at -1.2 V vs. Ag/AgCl, flower morphology is not observed. However, both the consecutive CAs are needed to give the prominent shape of the hexagonal flower morphology. This experimental observation provides direct support to the theoretical prediction from the Wulff construction model when $[B_3O_3(OH)_5]^{-2}$ polymeric form of boric acid is being considered for being present in the electrolyte solution. Moreover, $[B_3O_3(OH)_5]^{-2}$ is a divalent polymeric form, and it can easily cage a divalent cationic species Co^{2+} which will not be stabilized by monovalent anion $[B_3O_3(OH)_4]^{-1}$ or neutral $B_3O_3(OH)_3$ species.

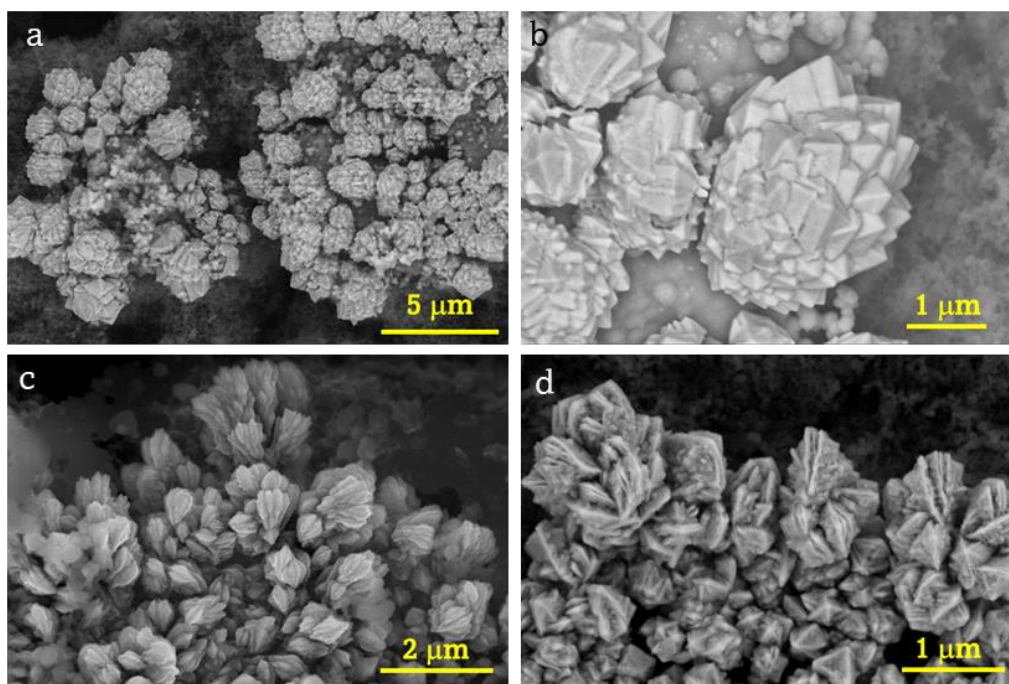


Figure 4.19. (a-b) SEM images of Co-ED₁ when Co electrodeposition is done only at the first CA at -1.1 V vs. Ag/AgCl. (c-d) SEM images of Co-ED₂ when Co electrodeposition is done only at the second CA at -1.2 V vs. Ag/AgCl.

4.4.5. Electrochemical OER activity

Finally, to realize the catalytic potential of these instantly deposited Co flowers, electrochemical OER is conducted using these electrodeposited substrates as working electrodes in 1 M KOH electrolyte. The importance of flower formation is observed when OER activity for Co-ED is more than Co-ED₁, this means both the chronoamperometry (-1.1 V vs. Ag/AgCl followed by -1.2 V vs. Ag/AgCl) is essential rather than only just one potential (Figure 4.20a).

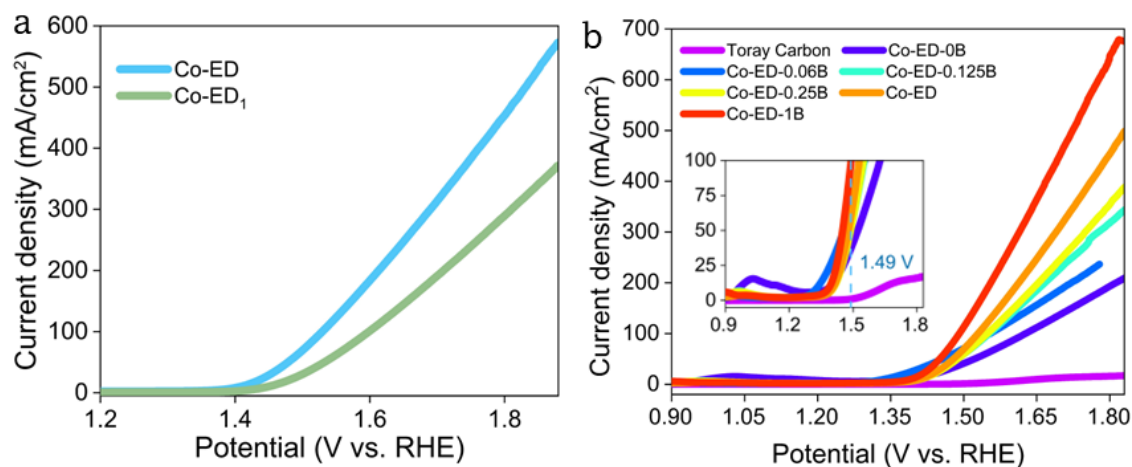


Figure 4.20. (a) Linear sweep voltammogram (LSVs) for oxygen evolution reaction (OER) for both Co-ED₁ and Co-ED. (b) LSVs for OER for all electrodeposited Co using 0 M, 0.06 M, 0.125 M, 0.25 M, 0.5 M, 1 M BA and compared with blank toray carbon paper.

OER activity has been checked for all the Co electrodeposition using different amounts of boric acid (**Figure 4.20b**). It has been observed that highest OER activity with respect to current density and overpotential has been observed for Co-ED-1B. There is a gradual increment in activity with increasing the H_3BO_3 concentration (during electrodeposition) from no BA to 1 M BA via 0.06 M, 0.125 M, 0.25 M and 0.5 M BA. The increase in activity from 0 M to 0.5 M BA can be directly related to the increase in the size of the flowers, i.e., the more the content Co metal atoms the more will be the OER activity. But the increase in activity from 0.5 M BA to 1 M BA can be related to the size of the flowers. It is well known that smaller flowers will have more surface area which indicates more exposed active sites which has provided more OER activity for smaller flowers in Co-ED-1B than larger ones Co-ED (**Figure 4.21a**). Achieving industrial level current density, the Co metals are being now deposited on less-expensive conducting supports like Ni foam, Ni foil, Cu foil, and stainless-steel foil (**Table 4.6**) to enhance the economic viability of these flowers in electrocatalysis. From the SEM images, it is clearly observed that hexagonal uniformly distributed Co-flowers are observed on all these substrates (**Figures 4.21b**).

Table 4.6. List of sample codes for different substrates with concentration of $\text{CoSO}_4 \cdot 7\text{H}_2\text{O}$ being 0.1 M with Na_2SO_4 being 1M for all and boric acid being 0.5 M and after both CA1+CA2.

Sample code	Substrates
Co-ED	Toray carbon paper
Co-ED-NF	Ni foil
Co-ED-CF	Cu foil
Co-ED-NFm	Ni foam
Co-ED-SS	Stainless-steel

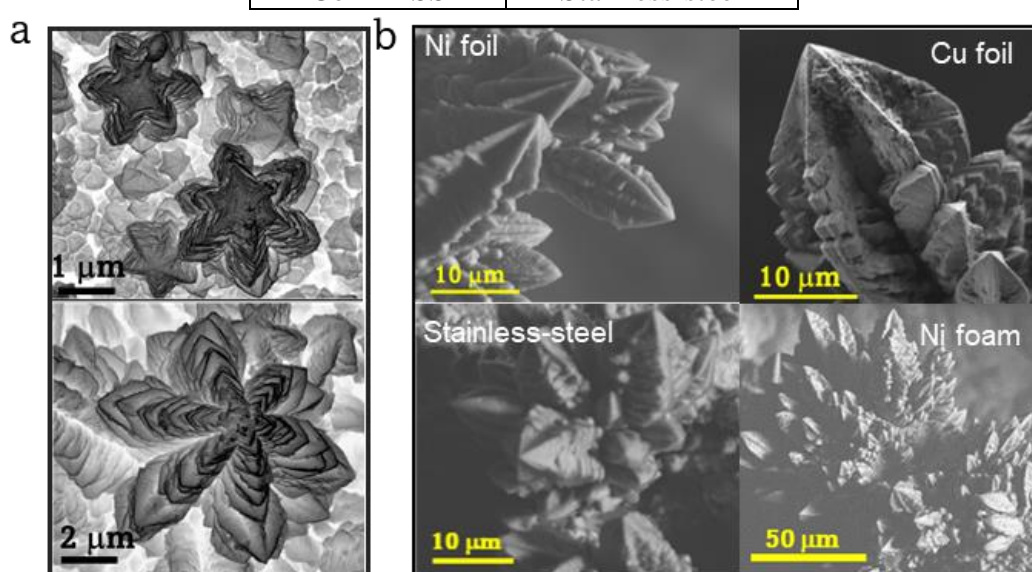


Figure 4.21. (a) SEM images of electrodeposited Co using 0.5 M (above) and 1 M BA (below). (b) SEM images of electrodeposited Co on Ni foil, Cu foil, stainless-steel foil, and Ni foam.

From the theoretical calculations, it is observed that the overall energy barrier for the (101) is lesser than (002) (**Figure 4.22a-c**) due to which the flower morphology after both CA1 and CA2 is giving better activity than only after CA1 (**Figure 4.20a**). As a future extension, electrodeposition has been done for Co, controlling other important parameters. Magnetic stirring or mechanical force has been provided during the electrodeposition process and it is seen that hexagonal flowers are not properly formed although metal deposition has taken place (**Figure 4.23**). This confirms that mechanical force can disrupt the growth process which ultimately affects the morphology.

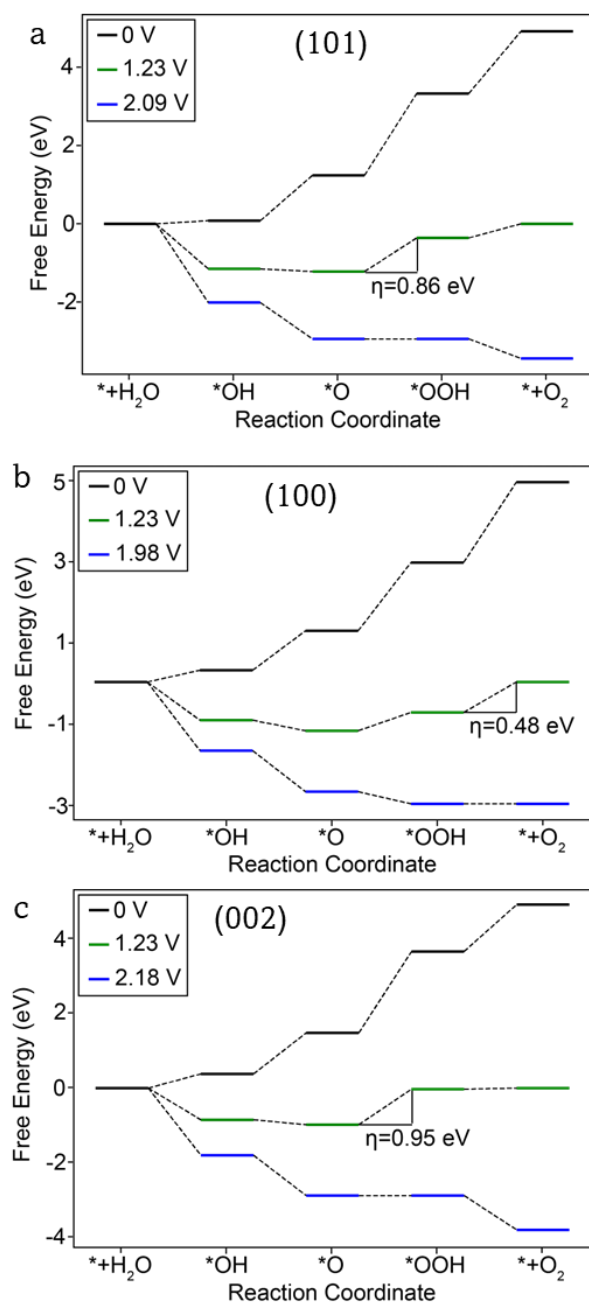


Figure 4.22. Free energy profile diagram for OER reaction on (a) (101) facet, (b) (100) and (c) (002) facets of hexagonal cobalt phase at 0 V, 1.23 V, and 2.09 V potential.

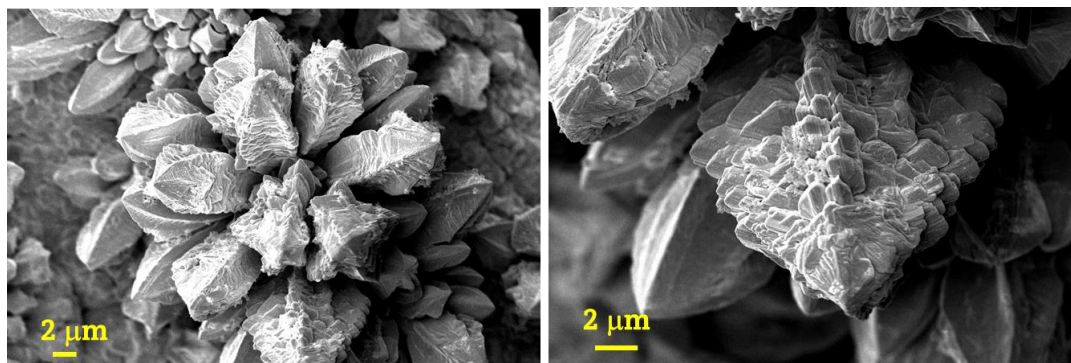


Figure 4.23. SEM images of Co-ED on Toray carbon substrate in presence of magnetic stirring during the electrodeposition.

4.4.6. Electrodeposition of bi-metallic systems

After this monometallic deposition, it is thought of using two metals together during deposition and understand how one of the metals affect the deposition of Co flowers. When Ni^{2+} ions are mixed with Co^{2+} ions during electrodeposition keeping all other parameters, it is observed that hexagonal flowers of Co are formed with some minor changes in the sharpness of the edges of the flowers, keeping the framework of Co morphology intact (**Figure 4.24**). The SEM-EDX mapping shows that Ni metal has been deposited in those regions where Co metal is also deposited (**Figure 4.25**). Whereas, when Cu^{2+} ions are taken along with Co^{2+} , interestingly the flower morphology is no more observed rather small cubes of Cu metal deposition has been found on electrodeposited Co metal (**Figure 4.26**). If no Cu^{2+} ions are taken, Co deposits as hexagonal flowers, while Cu alone deposits as fern-like branched particle, but both morphologies get affected when both type of ions are taken together.

4.5 Conclusion

This work reports for the first time a highly symmetrical, uniformly distributed six-fold symmetry cobalt metal flowers. Tuned morphologies are usually obtained by using morphology-directing chemicals during solvothermal or colloidal syntheses.

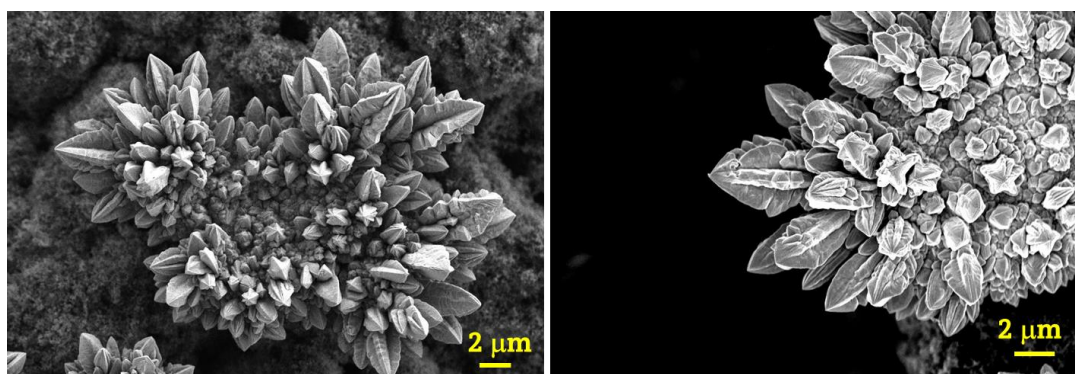


Figure 4.24. SEM images of CoNi-ED where Co^{2+} and Ni^{2+} ions are present during the electrodeposition.

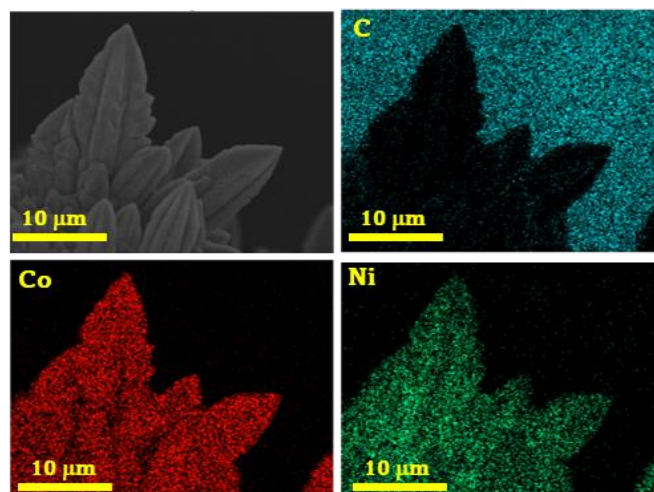


Figure 4.25. SEM-EDX mapping of CoNi-ED.

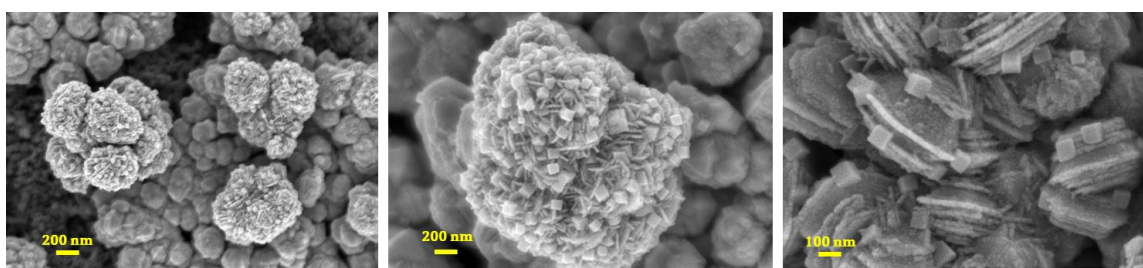
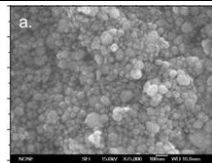
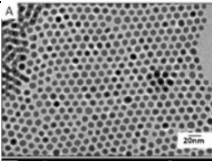
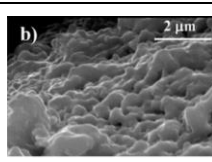
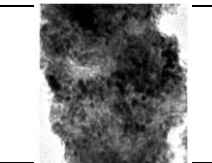
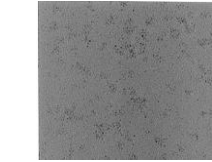
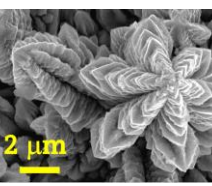


Figure 4.26. SEM images of CoCu-ED where Co^{2+} and Cu^{2+} ions are present during the electrodeposition.

Table 4.7 lists out all the hexagonal Co metal nanoparticles synthesized at harsh synthetic conditions, but they are not having any flower like morphology. Electrodeposition is an instantaneous process of nanoparticles synthesis using aqueous electrolyte with non-toxic ingredients. This work unfurls the unexplored role of boric acid during metal electrodeposition process. No other acids or chelating agents have given this hexagonal morphology and with only Co metal ions. Theoretical calculations generated Wulff models for different polymeric structures of boric acid on Co crystal facets have supported that a specific facet (101) of Co have enhanced the build-up of the flower morphology. Hexagonal room temperature stable phase of Co makes it different from the other metals Ni, Cu, or Fe which exist in cubic phase in room temperature. In presence of metal ions, Co hexagonal flower formation is disrupted which depicts that the formation an uninterrupted hexagonal cage like structure of boric acid- Co^{2+} ions is necessary to get the perfect six-fold symmetry of flowers. This protocol is successful in achieving the similar uniform morphology even after deposition on other non-expensive substrates increasing the economic viability of this strategy. Furthermore, industrial level OER activity is also achieved using these Co flowers. Instant formation, non-toxic and

non-expensive synthesis conditions, uniform deposition on various easily available and inexpensive substrates, and industrial level OER activity, have exhibited a promising strategy of designing efficient electrode materials for future.

Table 4.7. List of the publications related to this present invention of Co hcp nanoparticles synthesis via other methods which are energy-intensive and involves lots of chemicals and, they do not generate any specific morphology for the system.

Sl. No.	Medium	Reaction conditions	Morphology	References
1.	cobalt (II) chloride sodium borohydride tetraglyme oleylamine	N ₂ -H ₂ atmosphere (200-270 °C) 440 °C		https://doi.org/10.1016/j.jmmm.2015.07.051
2.	Triphenylphosphine sodium-borohydride ClCo(PPh ₃) ₃ oleylamine	190 °C 1 hour Inert atmosphere		<i>Nanoscale</i> , 2016 , 8, 18640-18645
3.	Co(NO ₃) ₂ ·6H ₂ O H ₂ O H ₂ +CO mixtures	pH at 12 80 °C 110 °C Overnight 450 °C for 4 hours		<i>Chem. Mater.</i> 2009 , 21, 23, 5637–5643
4.	cobalt (II) acetate tetrahydrate diphenyl ether Oleic acid	260 °C for 10 min 260 °C (Ar) for 15 min		10.1080/17458080.2011.563323
5.	Co(η ³ -C ₈ H ₁₃)(η ⁴ -C ₈ H ₁₂) polyvinylpyrrolidone	3 bar H ₂ 0 °C, 20 °C, 60 °C		<i>J. Phys. Chem.</i> 1996 , 100, 35, 14571–14574
6.	CoSO₄·7H₂O Na₂SO₄ H₃BO₃	Room temp. Ambient pressure -1.1V and -1.2V vs. Ag/AgCl for 270 and 300 secs		This Work

4.6 References

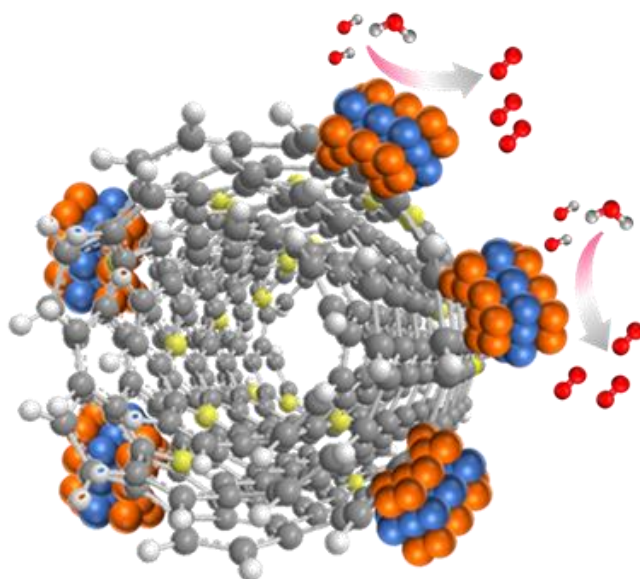
1. Nazzi, F., The hexagonal shape of the honeycomb cells depends on the construction behavior of bees. *Sci. Rep.* **2016**, 6, 28341.
2. Nichols, H. B., Snow Crystals: Natural and Artificial. Ukichiro Nakaya. Harvard Univ. Press, Cambridge, 1954. xii + 510 pp. Illus. \$10. *Science* **1954**, 120, 755-755.

3. Gravner, J.; Griffeath, D., Modeling snow-crystal growth: A three-dimensional mesoscopic approach. *Phys. Rev. E* **2009**, *79*, 011601.
4. Demange, G.; Zapolsky, H.; Patte, R.; Brunel, M., A phase field model for snow crystal growth in three dimensions. *Npj Comput. Mater.* **2017**, *3*, 15.
5. Libbrecht, K., Triangular Snowflakes: Growing Structures with Three-fold Symmetry using a Hexagonal Ice Crystal Lattice. 2021.
6. Afrooz, A. R. M. N.; Sivalapalan, S. T.; Murphy, C. J.; Hussain, S. M.; Schlager, J. J.; Saleh, N. B., Spheres vs. rods: The shape of gold nanoparticles influences aggregation and deposition behavior. *Chemosphere* **2013**, *91*, 93-98.
7. Sau, T. K.; Rogach, A. L., Nonspherical Noble Metal Nanoparticles: Colloid-Chemical Synthesis and Morphology Control. *Adv. Mater.* **2010**, *22*, 1781-1804.
8. Bronstein, L. M.; Shifrina, Z. B., Dendrimers as Encapsulating, Stabilizing, or Directing Agents for Inorganic Nanoparticles. *Chem. Rev.* **2011**, *111*, 5301-5344.
9. Zhou, M.; Dick, J. E.; Bard, A. J., Electrodeposition of Isolated Platinum Atoms and Clusters on Bismuth—Characterization and Electrocatalysis. *J. Am. Chem. Soc.* **2017**, *139*, 17677-17682.
10. Wang, D.; Chen, Z.-W.; Gu, K.; Chen, C.; Liu, Y.; Wei, X.; Singh, C. V.; Wang, S., Hexagonal Cobalt Nanosheets for High-Performance Electrocatalytic NO Reduction to NH₃. *J. Am. Chem. Soc.* **2023**, *145*, 6899-6904.
11. Abel, F. M.; Tzitzios, V.; Hadjipanayis, G. C., New approach for direct chemical synthesis of hexagonal Co nanoparticles. *J. Magn. Magn. Mater.* **2016**, *400*, 286-289.
12. de la Peña O'Shea, V. A.; de la Piscina, P. R.; Homs, N.; Aromí, G.; Fierro, J. L. G., Development of Hexagonal Closed-Packed Cobalt Nanoparticles Stable at High Temperature. *Chem. Mater.* **2009**, *21*, 5637-5643.
13. Zurita, N.; García, S. G., Comparative study of electrodeposited copper nanoparticles on different substrates for their use in the reduction of nitrate ions. *Res. Engineer.* **2023**, *17*, 100800.
14. Ji, J.; Cooper, W. C.; Dreisinger, D. B.; Peters, E., Surface pH measurements during nickel electrodeposition. *J. Appl. Electrochem.* **1995**, *25*, 642-650.
15. Kabay, N.; Güler, E.; Bryjak, M., Boron in seawater and methods for its separation — A review. *Desalination* **2010**, *261*, 212-217.
16. Popov, K. I.; Djokić, S. S.; Nikolić, N. D.; Jović, V. D., Electrodeposition of Metals with Hydrogen Evolution. In *Morphology of Electrochemically and Chemically Deposited Metals* Eds. Springer International Publishing, Cham, **2016**, pp, 171-203.

17. Nikitin, V. S.; Ostanina, T. N.; Rudoi, V. M.; Kuloshvili, T. S.; Darintseva, A. B., Features of hydrogen evolution during electrodeposition of loose deposits of copper, nickel and zinc. *J. Electroanal. Chem.* **2020**, 870, 114230.
18. Yang, J.; Liu, H.; Martens, W. N.; Frost, R. L., Synthesis and Characterization of Cobalt Hydroxide, Cobalt Oxyhydroxide, and Cobalt Oxide Nanodiscs. *J. Phys. Chem. C* **2010**, 114, 111-119.
19. Yin, K. M.; Lin, B. T., Effects of boric acid on the electrodeposition of iron, nickel and iron-nickel. *Surf. Coat. Technol.* **1996**, 78, 205-210.
20. Zech, N.; Landolt, D., The influence of boric acid and sulfate ions on the hydrogen formation in NiFe plating electrolytes. *Electrochim. Acta* **2000**, 45, 3461-3471.
21. Wu, Y.; Chang, D.; Kim, D.; Kwon, S.-C., Influence of boric acid on the electrodepositing process and structures of Ni–W alloy coating. *Surf. Coat. Technol.* **2003**, 173, 259-264.
22. Kieling, V. C., Parameters influencing the electrodeposition of Ni-Fe alloys. *Surf. Coat. Technol.* **1997**, 96, 135-139.
23. Köse, D. A.; Zümreoglu-Karan, B., Complexation of boric acid with vitamin C. *New J. Chem.* **2009**, 33, 1874-1881.
24. Blet, V., Effluent Decontamination. 2021.

Chapter 5

Non-Metal Anchored Strain-Tuned CoFe Intermetallic Formation via Nitride Formation Facilitates Oxygen Generation



Soumi Mondal; Debabrata Bagchi; Nilutpal Dutta; Subhajit Chakraborty; and
Sebastian C. Peter (*manuscript under preparation*)

Summary

Green hydrogen generation is the promising solution for global warming. One of the major challenges of green hydrogen generation via electrochemical water splitting is the sluggish counter oxidation reaction which is generation of oxygen from water oxidation at the anode during water splitting. This work explores the ordered phase formation between Co and Fe via nitride formation mechanism. It is interesting to note that presence of Co can make Fe easily reduce to metallic Fe and diffuse to form ordered intermetallic (IM) CoFe cubic lattice. Anchoring effect of N on carbon nanotube support has helped in embedding smaller nanoparticles of CoFe IM preventing the agglomeration due to sintering at high temperature synthesis. Further, ultra-low Pt incorporation has been done on CoFe leading to compressional to tensile strain which has significantly tuned the OER activity. The synergistic effects of Co and Fe in enhancing the electrochemical oxygen evolution reaction (OER) and addition of ultra-low concentrations of Pt metal has significantly enhanced the OER activity of CoFe. The lowest overpotential of only 190 mV is obtained for current density of 10 mA/cm² for only 1% Pt incorporation into CoFe lattice. The materials have been extensively characterized using techniques like powder X-ray diffraction, X-ray photoelectron spectroscopy, X-ray absorption spectroscopy, and microscopic techniques for understanding the chemical state of each element and how are the active sites playing role during OER.

Table of Contents

5.1	Introduction	149
5.2	Experimental Details	150
5.2.1	Chemicals and reagents	150
5.2.2	Synthesis of Co-Fe-based catalysts	151
5.3	Characterization	151
5.3.1	Powder X-ray Diffraction (PXRD)	151
5.3.2	Transmission Electron Microscope (TEM)	151
5.3.3	Scanning electron microscopy (SEM) and Energy Dispersive Spectrum (EDS)	151
5.3.4	X-ray Photoelectron Spectroscopy (XPS)	152
5.3.5	X-ray Absorption Spectroscopy	152
5.3.6	Electrochemical Oxygen Evolution Reaction (OER)	152
5.4	Results & Discussion	153
5.4.1	Structural insights and microscopic probing	153
5.4.2	Oxidation state and local structure analysis	156
5.4.3	Electrochemical OER activity	162
5.5	Conclusion	163
5.6	References.....	164

5.1 Introduction

Electrochemistry is playing the green role of generating hydrogen from water splitting via the water reduction process at the cathode.^{1, 2} The lesser energy requirement for water splitting is ruled by the overall potential window of both the cathodic and anodic reactions.³ Even after achieving an efficient cathode material for hydrogen evolution reaction (HER), there may be increased cell potential for the water splitting due to high overpotential requirement for anodic process of oxygen evolution reaction (OER).⁴ The slower kinetics of OER is majorly due to the conversion of singlet state species OH^- (or H_2O) to triplet state O_2 which necessitates a higher overpotential increasing the full cell potential of an electrolyser.⁵ Hence, an efficient OER active catalyst is also required to generate green hydrogen providing least electric potential. Expensive metal oxides like IrO_2 or RuO_2 are being considered the state-of-the-art OER catalysts and they lack the superior activity and high durability during the long runs of OER alkaline harsh conditions due to the dissolution of Ir or Ru in reaction conditions of high pH and high oxidation potential.⁶

Many other first-row transition metal oxides, hydroxides of Fe, Ni, and Co are being extensively used for lab-scale testing of OER.^{7, 8} Although pure Ni, Co or Fe oxide/hydroxides are not highly OER active, a mixture of these metal oxide/hydroxides have exhibited better activity due to a synergistic effect between the two elements.^{9, 10} For Co, Ni, and Fe, the active species of OER is metal oxyhydroxide ($\text{CoOOH}/\text{NiOOH}/\text{FeOOH}$) which is in-situ formed during the OER reaction around potential of 1.2-1.35 V vs. RHE under reaction conditions. Fe leads to charge transfer effects to activate CoOOH or NiOOH more for OER and stabilizes the oxidation state of Co or Ni. The spin state of the active species is playing a huge role in stabilizing O^* radical in the step before O^*-O^* coupling or $^*\text{OOH}$ formation.¹⁰ In MOOH , M^{3+} tends to stay in octahedral geometry with t_{2g} and e_g levels filled as per the high-spin or low-spin state. It is observed that Co^{3+} ions in the intermediate spin state (IS) with electronic configuration $t_{2g}^5 e_g^1$ which has the perfect e_g configuration for best OER performance.¹¹ It has been observed that with doping of Fe in CoOOH , there is more chance of Co^{3+} to stay in IS which increases the OER activity.¹¹ Even though high activity layer-double hydroxide (LDH) has been achieved but they are yet to be commercialized due to poor conductivity and stability in long run.¹² One of the important criteria of an efficient electrocatalyst is its retaining conductivity which defines its stability and long durability under real-life reaction conditions.

Oxides and hydroxides tend to have decreased conductivity under higher oxidation potential in -OH medium.¹² Whereas a metallic system is highly conducting, and an

intermetallic compound (IMC) is expected to provide the highest stability due to its intrinsic ordered arrangement of atoms. In this work, we have successfully achieved cubic lattice of CoFe ordered IMC via a unique pathway of metal nitride (CoN-FeN) formation anchored on N doped multi-walled carbon nanotubes (N-MWCNTs). Multi-walled carbon nanotubes can provide higher surface area due to presence of multiple walls. The inner walls of MWCNT provide very high electronic conductivity and facilitating the oxidation process. The MWCNTs have an inter-layer distance of 0.36 nm and N atoms can easily intercalate in between the layers and hence will lead to enhancement of conductivity in N doped MWCNTs (N-MWCNTs).¹³ N-doping has led to formation of Co and Fe nitrides (CoN/FeN) which finally forms CoFe IM upon further reduction at higher temperatures. The major disadvantage of high temperature reduction is the sintering of nanoparticles which leads to formation of larger nanoparticles and reduced surface area of the catalysts.¹⁴ N-doping not only increased the conductivity of the support, it also helped in embedding the CoFe nanoparticles retaining the smaller size of the nanoparticles. N doping also enhanced the formation of CoFe intermetallic via the metal-nitride formation pathway. Interestingly, further incorporation of Pt metal in ultra-low concentrations has enhanced the OER activity of N-MWCNTs supported CoFe. The enhancement in activity and the determination of active sites have been studied via different characterization techniques. There is a volcano trend of OER activity achieved with only 1% of Pt loading and its activity decreased when concentrations of Pt is being increased. Pt metal is not well-known for OER activity due to its inactive poor-conducting Pt-oxide formation during OER anodic scan.¹⁵ The interesting observation of enhanced OER activity up on lower loading of Pt is due to strain effect imposed by lesser Pt content on CoFe lattice which itself gets converted to metal-oxyhydroxides faster than the pristine CoFe driven by strain-relaxation.

5.2 Experimental Details

5.2.1 Chemicals and reagents

The following chemicals were used: Urea (SDFCL), multi-walled carbon nanotubes (MWCNTs, Sigma Aldrich), Cobalt(II) acetylacetonate ($\text{Co}(\text{acac})_2$, Sigma Aldrich), Iron(III) acetylacetonate ($\text{Fe}(\text{acac})_3$, Merck), potassium tetra-chloroplatinate(II) (K_2PtCl_4 , Alfa Aesar), tri-ethylene glycol (TEG, Merck), superhydride solution (Sigma Aldrich). All the chemicals used were commercially available certified reagents and used without further purifications unless mentioned.

5.2.2 Synthesis of Co-Fe-based catalysts

Urea and MWCNTs are mixed in de-ionized water and sonicated for 2 hours and then stirred under heating at 80 °C for 6 hours and then the suspension is washed with ethanol and then dried. In the next step, 15 mg of the collected N-doped MWCNTs powder is taken in 15 ml of TEG in a two-necked round bottom flask and stirred till uniform suspension and then 0.1 mmol of Fe(acac)₃ and 0.1 mmol of Co(acac)₂ (and K₂PtCl₄ in case of Pt incorporated samples) are added to the solution. Then, the mixture is connected to the Schlenk line and N₂ gas is used for making the reaction setup inert. Then 1 ml of superhydride solution is injected to the solution under 60 °C and then the temperature is raised to 200 °C and kept for 2 hours. Then the reaction mixture is cooled down, washed with ethanol, and dried. This samples are named as the pre-annealed samples. This powder is annealed under H₂ atmosphere at 600 °C for 4 hours and the collected powder catalysts are named as post-annealed samples.

5.3 Characterization

5.3.1 Powder x-ray diffraction (PXRD)

PXRD measurements were done at room temperature on a Rigaku Miniflex X-ray diffractometer with a Cu-K_α X-ray source ($\lambda = 1.5406 \text{ \AA}$), equipped with a position-sensitive detector in the angular range of $10^\circ \leq 2\theta \leq 90^\circ$ with the step size 0.02° and a scan rate of 0.5 s/step calibrated against corundum standards. The experimental XRD patterns were compared to the patterns simulated from the data reported in the literature.

5.3.2 Transmission electron microscope (TEM)

TEM images and selected area electron diffraction patterns were collected using a JEOL JEM-2010 TEM instrument. The samples for these measurements were prepared by sonicating the nanocrystalline powders in ethanol and drop-casting a small volume onto a carbon-coated copper grid.

5.3.3 Scanning electron microscopy (SEM) and energy dispersive spectrum (EDS)

The SEM measurement was performed using Leica scanning electron microscopy equipped with an energy-dispersive X-ray spectroscopy (EDAX) instrument (Bruker 120 eV EDAX instrument). Data were acquired by using an accelerating voltage of 15 kV, and the typical time taken for data accumulation is 100 s. The elemental analyses were performed using the P/B-ZAF standardless method (where P/B = peak to background model, Z = atomic no. correction factor, A = absorption correction factor, and F = fluorescence factor) for Cu, Ga at multiple areas on the sample coated Si wafer.

5.3.4 X-ray photoelectron spectroscopy (XPS)

XPS measurements were carried out using Thermo K-alpha+ spectrometer using micro focused and monochromated Al K α radiation with energy 1486.6 eV. The pass energy for the spectral acquisition was kept at 50 eV for individual core-levels. The electron flood gun was utilized for providing charge compensation during data acquisition. Further, the individual core-level spectra were checked for charging using C1s at 284.6 eV as standard and corrected if needed. The peak fitting of the individual core-levels was done using CASA XPS software with a Shirley type background.

5.3.5 X-ray absorption spectroscopy

X-ray absorption near-edge spectroscopy (XANES) and quick-Extended X-ray Absorption Fine Structure (quick-EXAFS) experiments at 300 K were performed at PETRA III, beamline P64, of DESY, Germany. Measurements of Cu-K and Pd-K at ambient pressure were performed in fluorescence as well as transmission mode using gas ionization chambers to monitor the incident and transmitted X-ray intensities. Monochromatic X-rays were obtained using a Si (111) double crystal monochromator, which was calibrated by defining the inflection point (first derivative maxima) of Cu foil as 8980.5 eV. The beam was focused by employing a Kirkpatrick-Baez (K-B) mirror optic. A rhodium-coated X-ray mirror was used to suppress higher-order harmonics. A CCD detector was used to record the transmitted signals. Pellets for the ex-situ measurements were made by homogeneously mixing the sample with an inert cellulose matrix to obtain an X-ray absorption edge jump close to one.

5.3.6 Electrochemical oxygen evolution reaction (OER)

All the electrochemical measurements were done in a 3-electrode set-up comprising of a glassy carbon as the working electrode (GCE), graphite rod counter electrode, and mercury/mercuric oxide electrode (MMO) (for basic media). The catalyst ink was prepared using 1.6 mg catalyst + 0.4 mg Vulcan in 200 μ L of mixed solvent (IPA:H₂O = 1:1) + 20 μ L of 1 wt.% Nafion used as binder. Five μ L of the catalyst ink was drop casted on the commercial 3 mm glassy carbon electrode. Commercial Pt/C (20 wt%, Sigma Aldrich) was used for comparison of activity with the reported electrocatalysts. Linear sweep voltammetry (LSV) was recorded for OER at a scan rate of 5 mV s⁻¹ at 25 °C. Electrochemical impedance studies were performed in the frequency range from 10 mHz to 100 kHz at different applied DC potentials for different reactions depending on their onset potential values. The electrolyte solution was deaerated by purging N₂ gas into the solution at least for 30 min before each experiment. All the reference electrodes were calibrated with respect to the reversible hydrogen

electrode (RHE), using Pt as working and counter electrodes in the respective electrolytes. The values obtained are as follows: alkaline medium, $E_{\text{RHE}} = E_{\text{MMO}} + 0.9 \text{ V}$.

5.4 Results & Discussion

5.4.1 Structural insights and microscopic probing

The synthesis procedure is provided in **Figure 5.1** schematic. It has been observed that after colloidal treatment of Co and Fe salts in N doped multi-walled carbon nanotubes (MWCNTs), there is formation of metal nitrides CoN and FeN and after annealing the nitrides are totally converted to CoFe intermetallic of space group $Pm\bar{3}m$, which is evident from the PXRD pattern in **Figures 5.2a** and **5.2b**. To understand which element Co or Fe initiates the nucleation, control syntheses are being done following the similar procedure (**Figure 5.1**) with considering Co or Fe precursors individually. It has been observed that after the annealing treatment under H_2 atmosphere, Co is getting converted to metallic cobalt (**Figure 5.2c**) whereas Fe is not getting reduced and stays as Fe_3O_4 even under high-temperature and reducing environment (**Figure 5.2d**). This indicates that when Fe is not accompanied by other metal Co, it is not having the tendency to get reduced at all and due to its higher oxidation tendency, it forms stable oxides at high temperature. Interestingly, in presence of Co, there is full conversion of Fe to metallic form inside the cubic lattice of CoFe intermetallic. This hints that Co can be the nucleating atom which itself gets reduced and allows the diffusion of Fe atoms and form the lattice of intermetallic compound. SEM, TEM, and HRTEM images in **Figures 5.3a** and **5.3b** (inset figure) show the random distribution of nanoparticles which shows fringes corresponding to (111) facet of CoN or FeN or may be both.

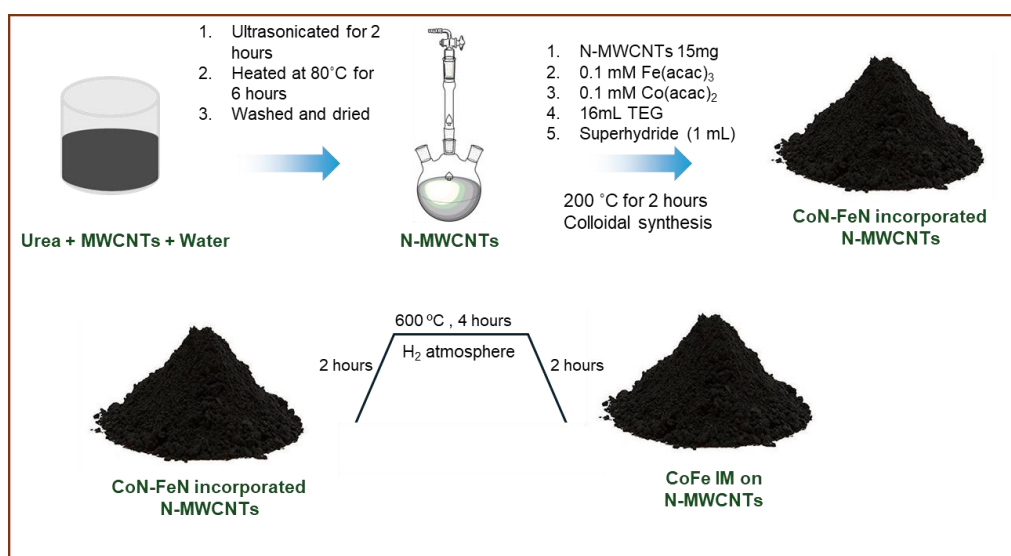


Figure 5.1. Schematic representation of synthesis procedure.

SEM, TEM, and HRTEM images in **Figures 5.3c** and **5.3d** (inset figure) show the uniformly distributed nanoparticles on the MWCNTs which show fringes corresponding to (110) facet of CoFe IM. The proper distribution of nanometric CoFe IM particles without any agglomeration even in higher temperature is majorly due to the anchoring effect of the N atoms in the MWCNTs. If no N doping is done and using pure MWCNTs, there is no formation of CoFe IM is observed. This signifies that metal nitride formation is facilitating the CoFe formation. If no anchoring effect is there, there will be sintering at higher temperatures during the annealing process, due to which, N-atom anchoring has helped to hold the CoFe nanoparticles in embedded on MWCNTs (Figures 5.3c and 5.3d) and no two particles are agglomerated with each other. Figures 5.4a, 5.4b and 5.4c, 5.4d show the embedded nanoparticles of Co metal and Fe oxide after annealing. Figure 5.5 schematically represents the formation mechanism of CoFe intermetallic which via CoN/FeN formation on N doped MWCNTs.

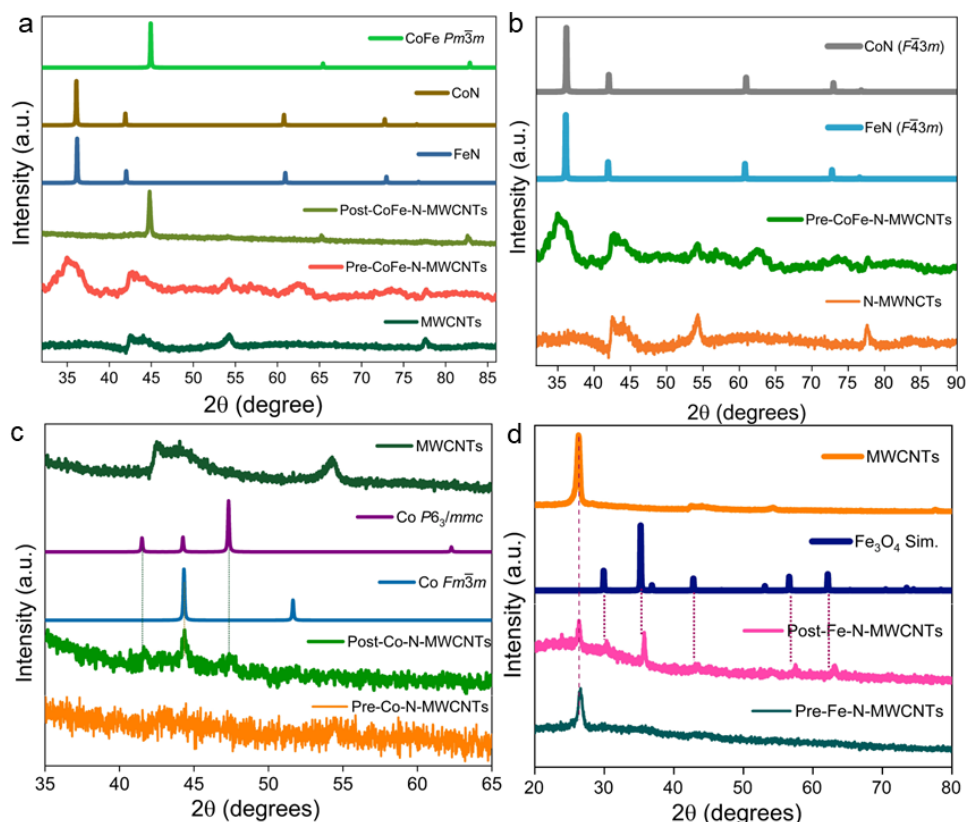


Figure 5.2. (a) Powder x-ray diffraction (PXRD) pattern of MWCNTs, Pre-CoFe-N-MWCNTs, and Post-CoFe-N-MWCNTs compared with simulated patterns of CoN, FeN, and CoFe intermetallic compound. (b) PXRD pattern of Pre-CoFe-N-MWCNTs compared with simulated patterns of CoN and FeN. PXRD patterns of (b) Pre-Co-N-MWCNTs, and (c) Pre-Fe-N-MWCNTs compared with metallic Co and Fe-oxide phases, respectively.

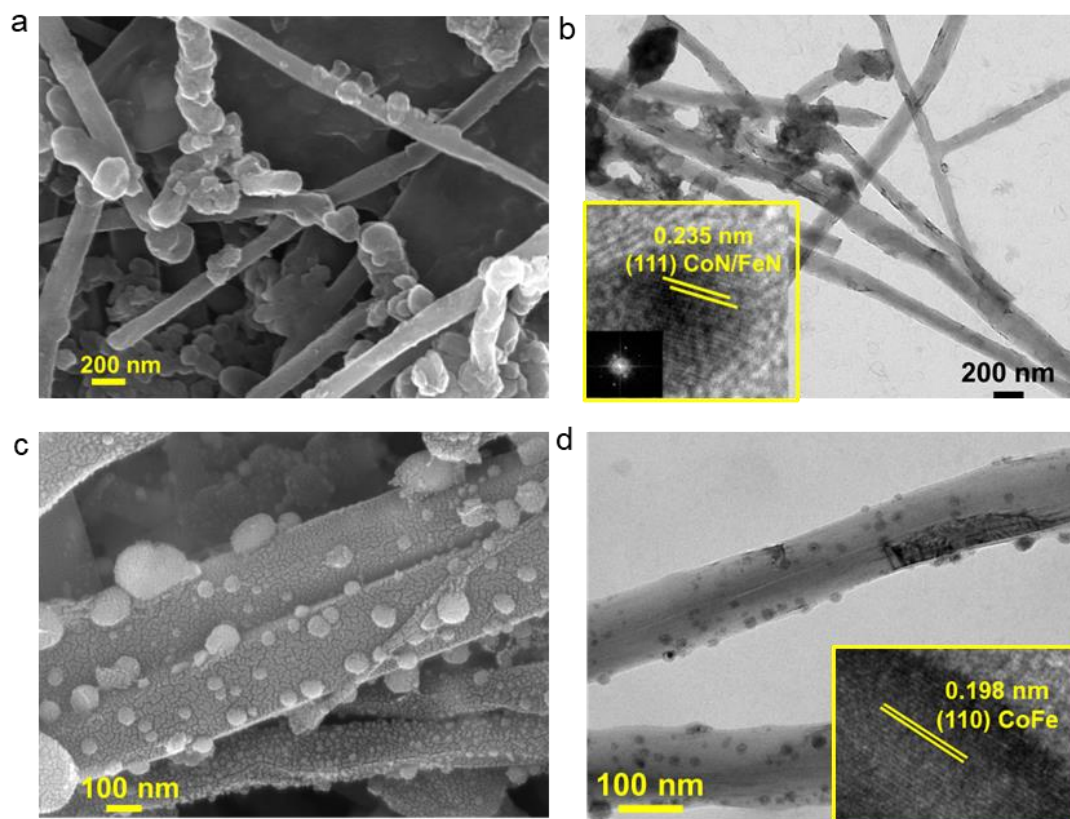


Figure 5.3. Scanning electron microscopic (SEM) image of (a) Pre-CoFe-N-MWCNTs, and (c) Post-CoFe-N-MWCNTs, Transmission electron microscopic (TEM) and High-resolution TEM (HRTEM) images of (b) Pre-CoFe-N-MWCNTs, and (d) Post-CoFe-N-MWCNTs.

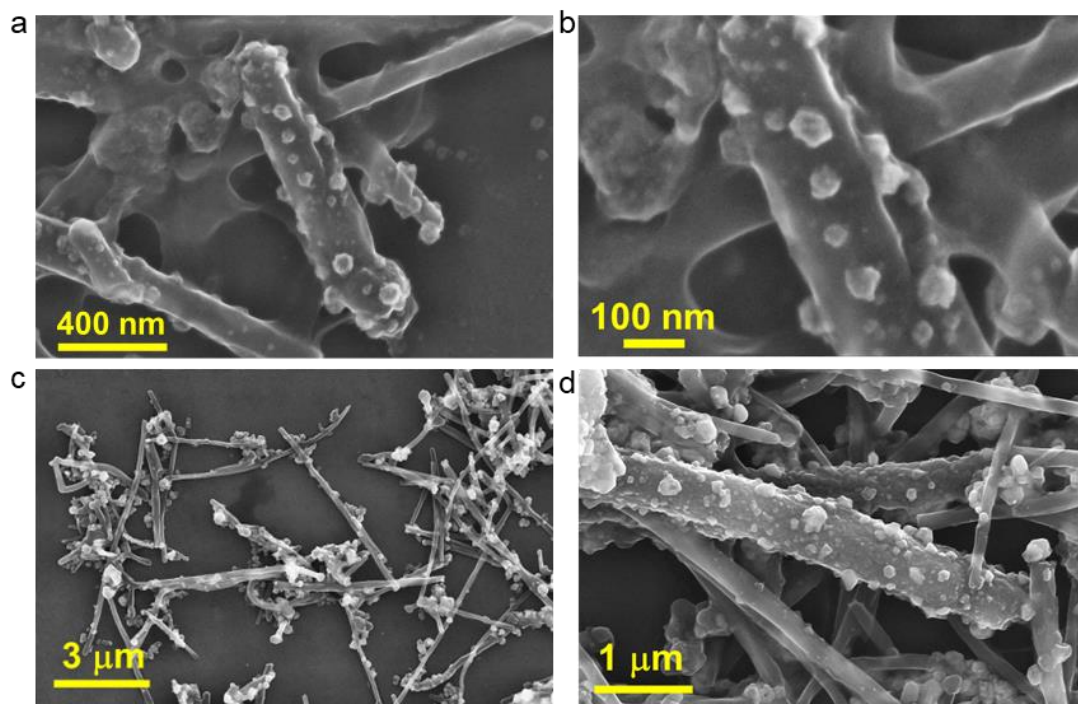


Figure 5.4. SEM images of (a), (b) Post-Co-N-MWCNTs and (c), (d) Post-Fe-N-MWCNTs.

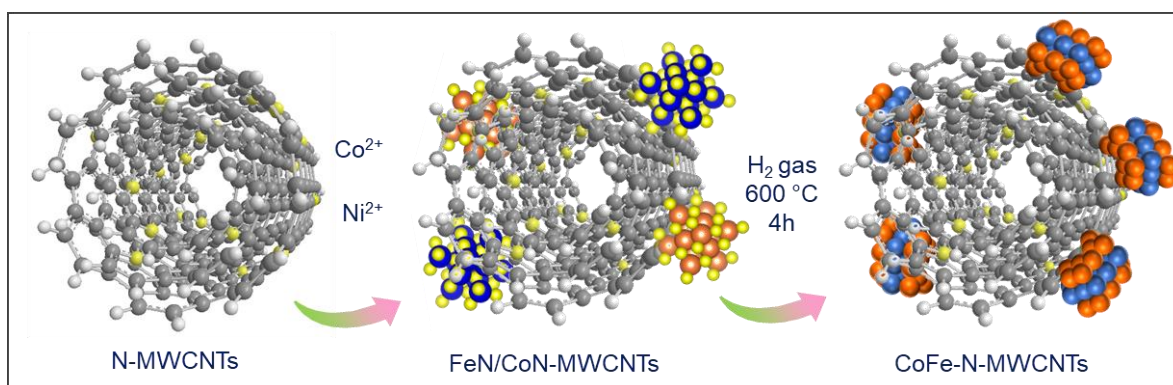


Figure 5.5. Schematic representation of CoFe intermetallic formation.

5.4.2 Oxidation state and local structure analysis

The observation from PXRD characterization is further supported by local-structure and oxidation state analysis technique, X-ray absorption spectroscopy (XAS). A sharp difference is observed in the oxidation state of Co and Fe when they are individually used during the synthesis (**Figures 5.6a** and **5.6b**). After the annealing step, the XANES spectra show that Co reaches its metallic state matching with the foil, whereas Fe stays in highly oxidized state even after the annealing process. Fourier transformed R-space data also indicates the presence of Co-Co metallic bond in case of Post-Co-N-MWCNTs, where there is similar Fe-O bonds being present even after annealing process (**Figures 5.6c** and **5.6d**). Intriguing observation is found when both Co and Fe are used together during the synthesis, both Co and Fe get converted to metallic form as CoFe IM after the annealing in H₂ atmosphere (**Figures 5.7a** and **5.7b**). From the R-space data of Co and Fe *K*-edge, it is very clear that before the annealing process, there is prominent formation of metal nitrides with strong peak around 1.5 Å for both Co and Fe which correspond to Co-N/Fe-N bonds (**Figures 5.7c** and **5.7d**). Whereas just after the annealing, both Fe and Co get converted to metallic form with presence of only metal-metal bond. This similar observation is pictorially represented via wavelet transformed Co *K*-edge R-space data (**Figures 5.8a** and **5.8b**). This spectroscopic technique gives an interpretation of the local structure of an element in a compound which ultimately supports the bulk structure analysis achieved from PXRD. The feasible oxidation tendency of Fe due to its more oxidation potential has been reflected here when pure Fe is taken, whereas the reduction potential and nucleating property of Fe is totally modulated in presence of Co ions in its neighboring environment. There is a tuning of reduction potential of Fe³⁺/Fe⁰ couple due to the presence of Co²⁺ ions in the vicinity. Furthermore, Pt is added to the similar synthesis mixture (**Figure 5.1**) as Pt²⁺ ions (from K₂PtCl₄) along with Co²⁺ and Fe³⁺ ions in different loading percentages, here used are 1%, 5% and 10%, respectively.

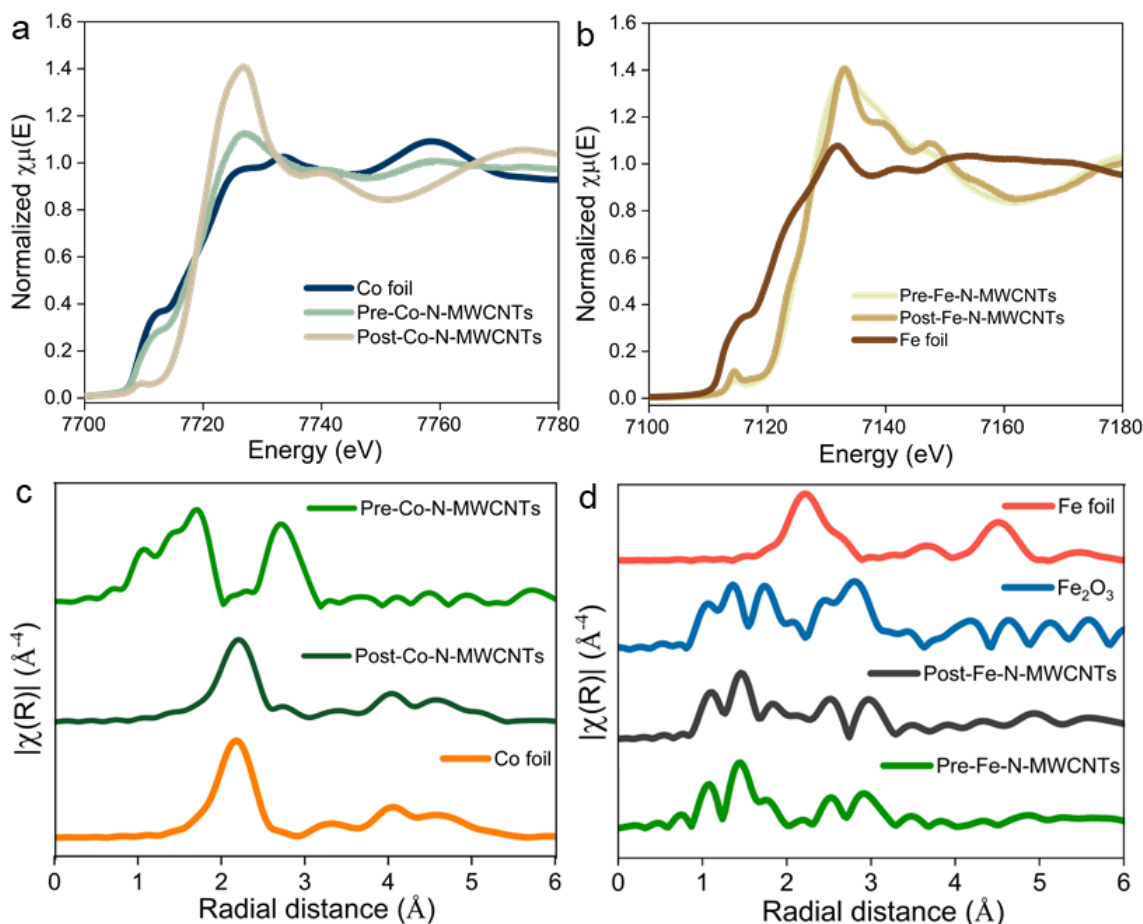


Figure 5.6. (a) Co K-edge X-ray absorption near edge spectra (XANES) of Pre-Co-N-MWCNTs and Post-Co-N-MWCNTs and compared with Co foil. (b) Fe K-edge X-ray absorption near edge spectra (XANES) of Pre-Fe-N-MWCNTs and Post-Fe-N-MWCNTs and compared with Fe foil. (c) Co K-edge Fourier transformed R-space data of Pre-Co-N-MWCNTs and Post-Co-N-MWCNTs and compared with Co foil. (d) Fourier transformed R-space data of Fe K-edge of Pre-Fe-N-MWCNTs and Post-Fe-N-MWCNTs and standards Fe_2O_3 and Fe foil.

From **Figures 5.9a** and **5.9b**, it is observed that post-annealing treatment there is no peak for Pt in case of 1% loading (1-Pt-Post-CoFe), whereas with 5% loading there is very small emergence of peak of Pt and that peak is highly prominent in case of 10% Pt loaded in CoFe (10-Pt-Post-CoFe). When observed carefully, it is seen that the peaks corresponding to CoFe intermetallic shows a right shift when 1% Pt loading is done, then gradually shows a left shift from 5% to 10% Pt loading. This indicates there is initial lattice contraction and then with larger content of Pt, there is lattice expansion.¹⁶ Interestingly, it is observed that Pt peak is shifted to the right for the 5% and 10% loaded CoFe samples, that clearly indicates that an alloy has formed between Pt and Co or Fe. Hence, in case of 5-Pt-Post-CoFe and 10-Pt-Post-CoFe, there is presence of two phases CoFe IM and Pt-Fe/Co alloy and there must be an interface between the two phases.

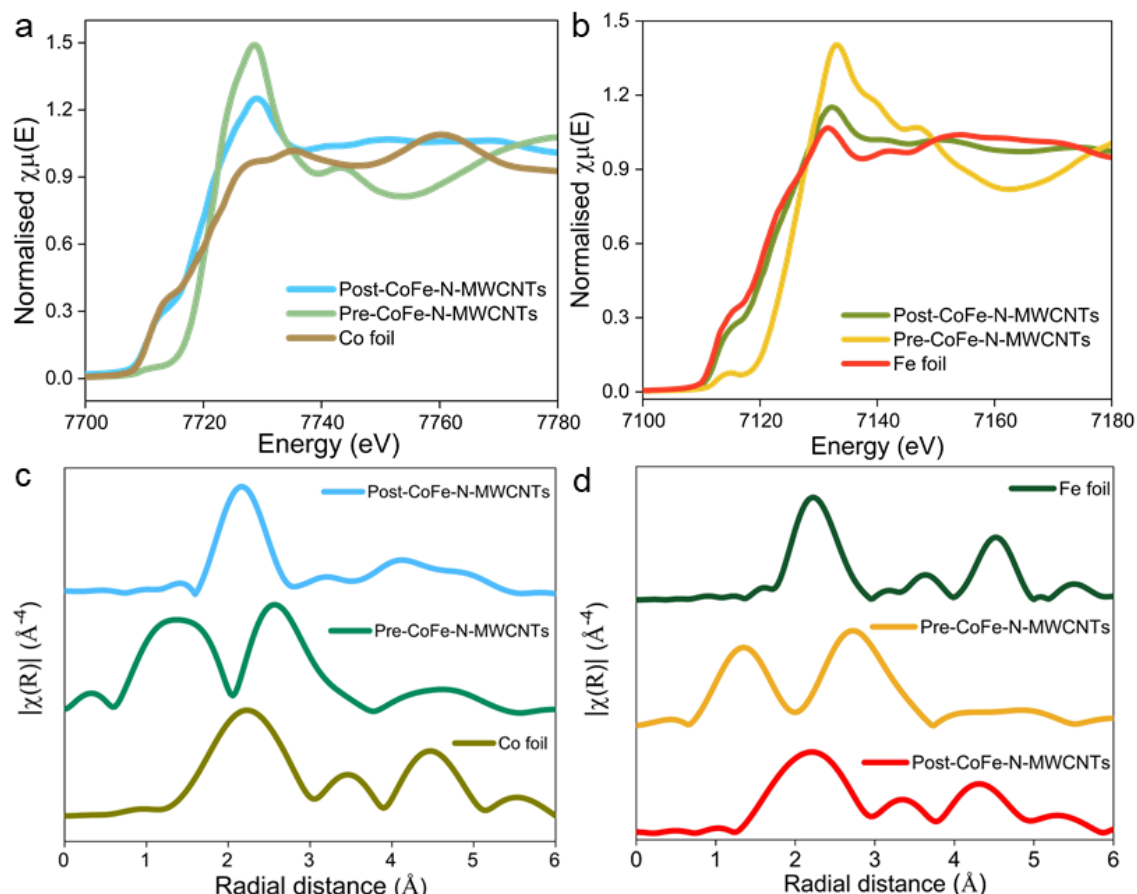


Figure 5.7. (a) Co K-edge X-ray absorption near edge spectra (XANES) of Pre-CoFe-N-MWCNTs and Post-CoFe-N-MWCNTs and compared with Co foil. (b) Fe K-edge X-ray absorption near edge spectra (XANES) of Pre-CoFe-N-MWCNTs and Post-CoFe-N-MWCNTs and compared with Co foil. (c) Co K-edge Fourier transformed R-space data of Pre-CoFe-N-MWCNTs and Post-CoFe-N-MWCNTs and compared with Co foil. (d) Fe K-edge Fourier transformed R-space data of Pre-CoFe-N-MWCNTs and Post-CoFe-N-MWCNTs and compared with Fe foil.

It is expected that the lattice constant for CoFe is smaller than Pt-based alloy due to which the CoFe lattice will undergo tensile strain to expand itself to match with the lattice constant of Pt-alloy phase, and due to that left-shift of PXRD peak is observed.¹⁷ Whereas in case of 1-Pt-Post-CoFe, there is slight right shift of CoFe peak indicating pressure inserted by Pt atoms embedded on CoFe lattice since Pt is larger atom and when it tries to form a bond it will push the CoFe lattice inserting compressive strain to the system. Before annealing under reduction atmosphere, Pt is also in higher oxidation state like Co and Fe atoms as observed from XPS, and Pt attains metallic state upon H₂-atmosphere reduction (**Figure 5.9c**) and similar thing is observed when 5% Pt is incorporated (**Figure 5.9d**). **Figures 5.10a** and **5.10b** and **5.10c** show the Fe K-edge and Co K-edge R-space data of pre- and post-annealing different percentage of Pt loading in CoFe supported on N-doped MWCNTs.

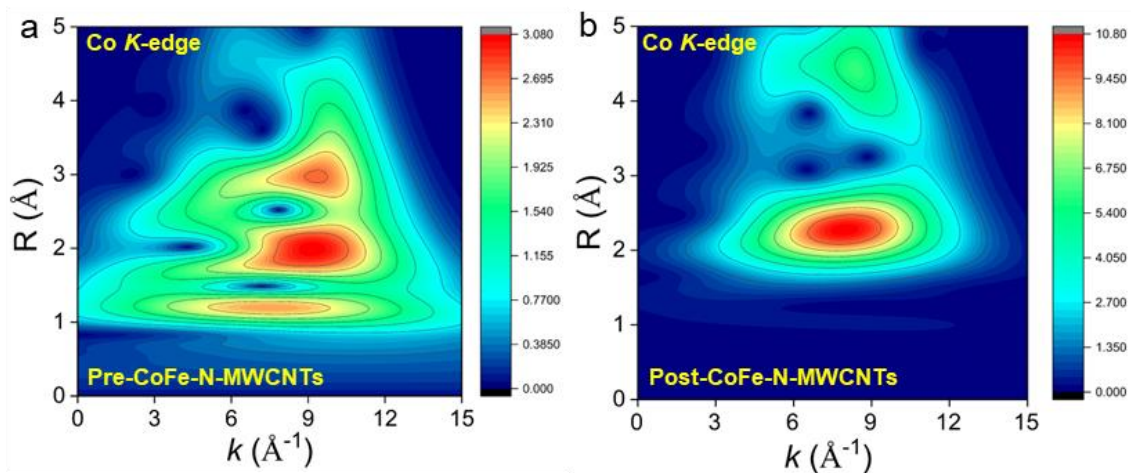


Figure 5.8. Co K-edge wavelet transformed data of (a) Pre-CoFe-N-MWCNTs and (b) Pre-CoFe-N-MWCNTs.

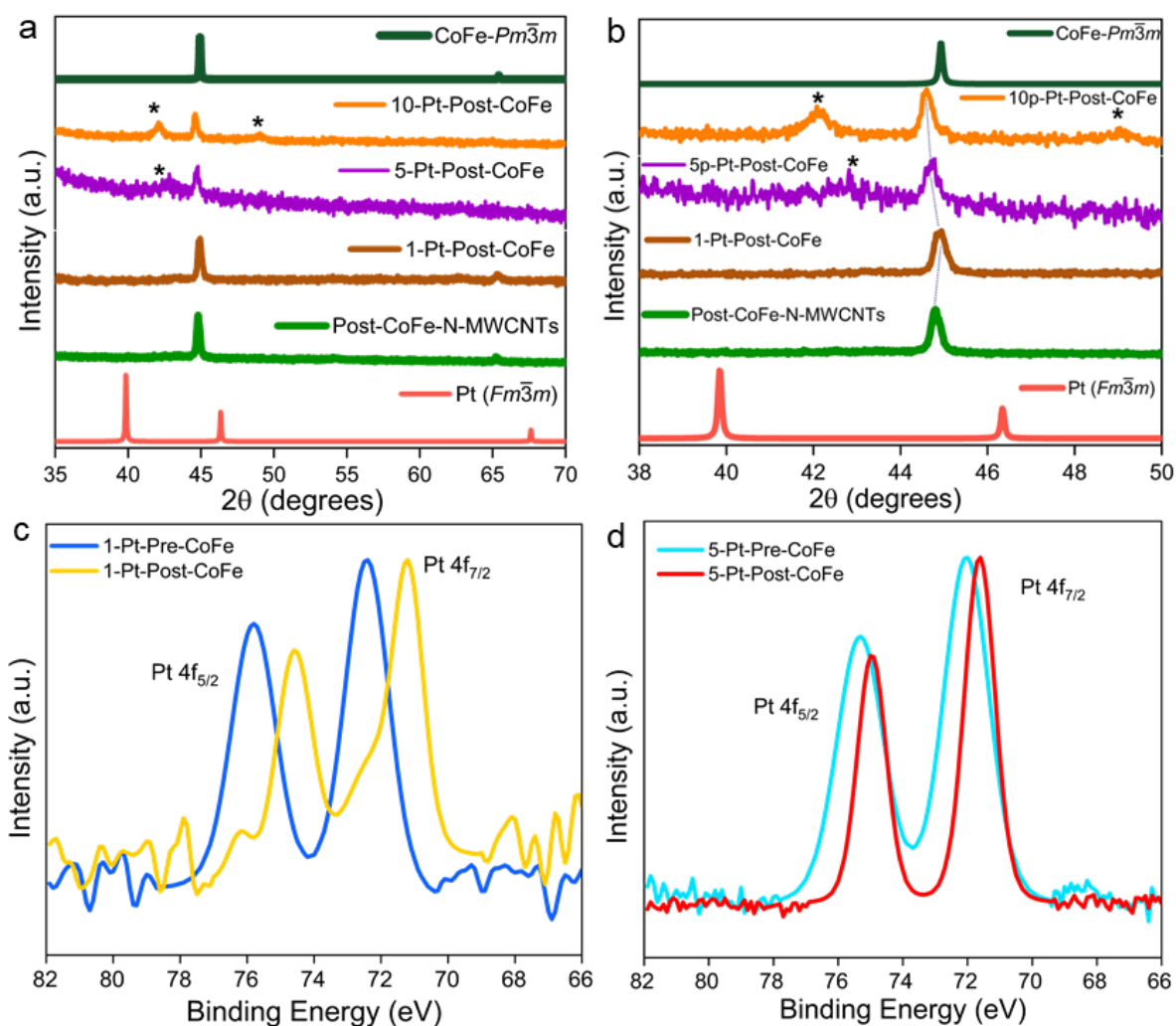


Figure 5.9. (a) and (b) PXRD pattern of 1-Pt-Post-CoFe, 5-Pt-Post-CoFe, and 10-Pt-Post-CoFe compared with simulated pattern of CoFe intermetallic and Pt metal. (c) Pt 4f XPS spectra of 1-Pt-Pre-CoFe and 1-Pt-Post-CoFe. (d) Pt 4f XPS spectra of 5-Pt-Pre-CoFe and 5-Pt-Post-CoFe.

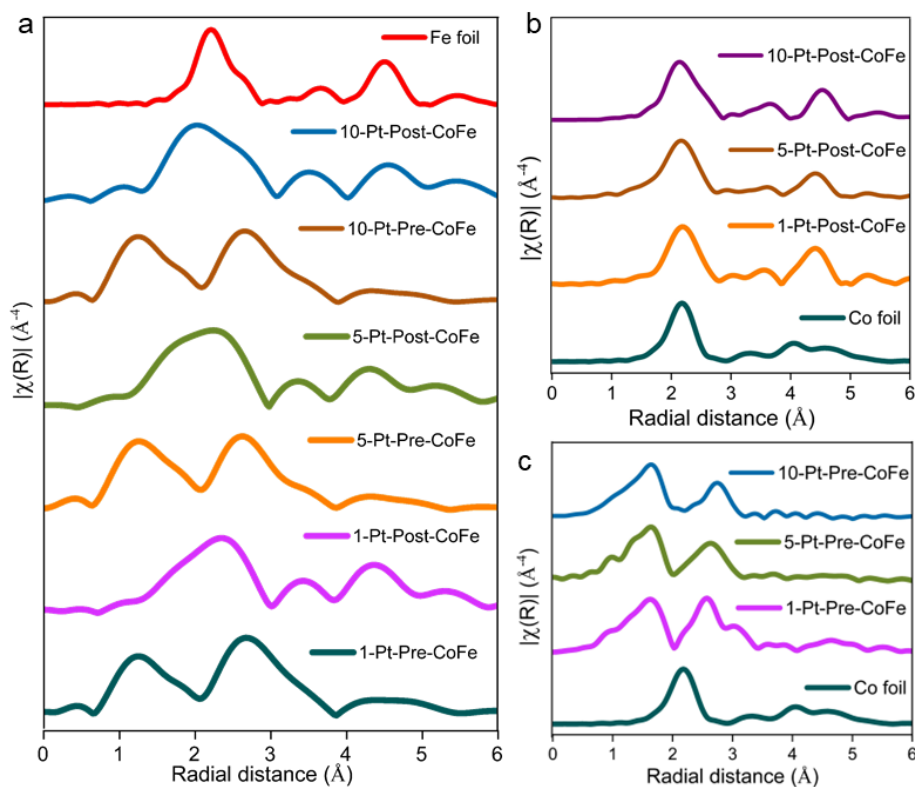


Figure 5.10. (a) Fe *K*-edge R-space data of all the Pt incorporated pre and post annealing catalysts. (b, c) Co *K*-edge R-space data of all the Pt incorporated pre and post annealing catalysts.

It is clearly observed that before annealing Co and Fe stays in higher oxidation state and after annealing, both Co and Fe are observed in their metallic state, indicating successful formation of CoFe IM after reductive treatment. **Figures 5.11a** and **5.11b** show the XANES spectra of Fe *K*-edge and Co *K*-edge for the post-annealed samples of 1%, 5%, and 10% Pt incorporated samples. It is seen that both Co and Fe stays at relatively higher partial oxidation state with higher white-line intensity in case 1% and 5% Pt loaded samples. This gives an indication that electron transfer takes place from Co and Fe to Pt atoms when Pt is loaded in 1% and 5% and when 10% Pt loading is done, the electron transfer is not prominent from Co or Fe to Pt atoms. This is possible when prominent bond formation of Pt with Co and Fe has taken place. Due to more electronegativity of Pt, it pulls the electrons from Co and Fe when it is bonded to them. From Pt *L*₃-edge XANES (**Figure 5.12a**), it is observed that Pt shows higher white-line (WL) intensity in case of the pre-annealed samples with lower WL intensities in case of post-annealed samples. When R-space data for Pt *L*₃-edge is observed for pre-annealed samples (**Figure 5.12b**), it is seen that majorly Pt-O/C/N bonds are observed and there are no peaks for Pt-Pt or Pt-Co/Fe bonds. Whereas for the post-annealed samples (**Figure 5.13a**), it is seen that clearly one peak for each has been observed at 1.9 and 2.2 Å for 1% and 5% and 10% Pt loaded samples.

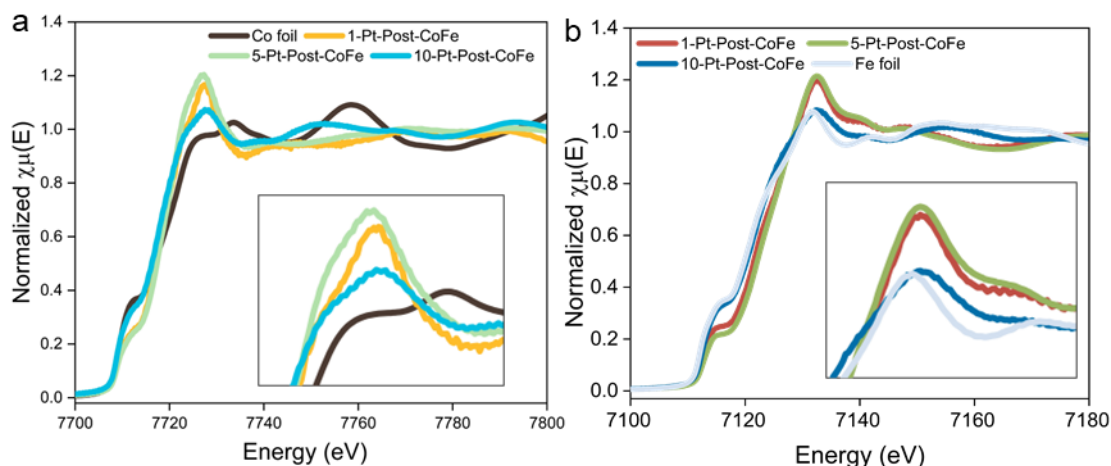


Figure 5.11. XANES spectra of (a) Co K-edge of Co foil, 1-Pt-Post-CoFe, 5-Pt-Post-CoFe, and 10-Pt-Post-CoFe, (b) Fe K-edge of Fe foil, 1-Pt-Post-CoFe, 5-Pt-Post-CoFe, and 10-Pt-Post-CoFe.

This can signify that when very low loading of Pt is taken (1%), there is formation of Pt-Fe/Co bonds on the surface of CoFe IM and no Pt nanocluster have formed (observed from bulk technique PXRD and local structure analyzing technique XAS). But when larger content of Pt is taken then Pt nanoclusters have formed with presence of Pt-Pt and Pt-Fe/Co bonds due to formation of Pt alloy. This is imposing strain into the lattice of CoFe lattice, which is causing the PXRD peak shift, since there is no option of Pt substitution into the CoFe lattice due to huge difference in size of the Co and Fe with Pt atom. This is schematically demonstrated in **Figure 5.13b**.

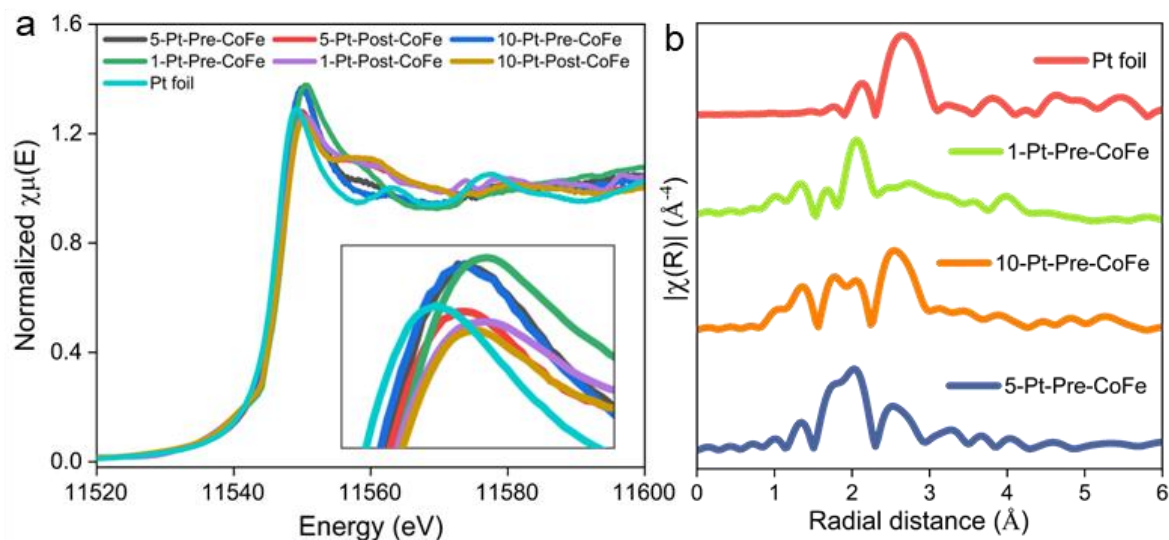


Figure 5.12. (a) XANES spectra of Pt L3-edge of 1-Pt-Pre-CoFe, 5-Pt-Pre-CoFe, and 10-Pt-Pre-CoFe, 1-Pt-Post-CoFe, 5-Pt-Post-CoFe, and 10-Pt-Post-CoFe, and Pt foil. (b) R-space data of Pt L3-edge of 1-Pt-Pre-CoFe, 5-Pt-Pre-CoFe, and 10-Pt-Pre-CoFe.

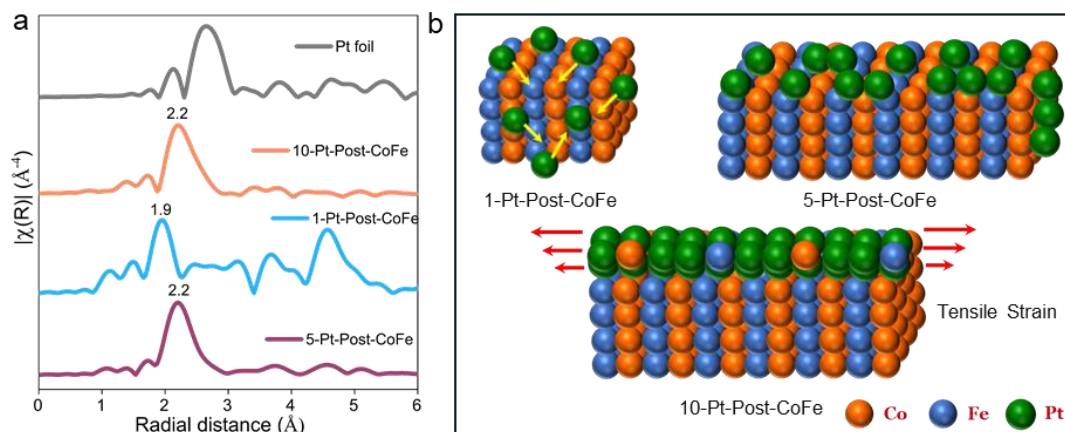


Figure 5.13. (a) R-space data of Pt L_3 -edge of 1-Pt-Post-CoFe, 5-Pt-Post-CoFe, and 10-Pt-Post-CoFe. (b) Schematic representation of Pt incorporation on CoFe IM lattice.

5.4.3 Electrochemical OER activity

These catalysts are tested for OER in alkaline media. **Figure 5.14a** shows the LSVs of OER activity in 1 M KOH electrolyte with a scan rate of 5 mV/sec for all the catalysts, Post-CoFe-N-MWCNTs, 1-Pt-Post-CoFe, 5-Pt-Post-CoFe, and 10 -Pt-Post-CoFe. It is observed that the overpotential requirement for attaining current density of 10 mA/cm² is following the trend: 1-Pt-Post-CoFe > 5-Pt-Post-CoFe > Post-CoFe-N-MWCNTs > 10-Pt-Post-CoFe (**Figure 5.14b**). The major active sites for CoFe catalyst are the formation of CoOOH/FeOOH during the OER anodic sweep. The faster kinetics of OER indicates the faster formation of metal oxyhydroxide (CoOOH/FeOOH). From the PXRD pattern and bond length it has been observed that CoFe lattice has experienced lattice contraction in 1-Pt-Post-CoFe where only 1% of Pt is incorporated.

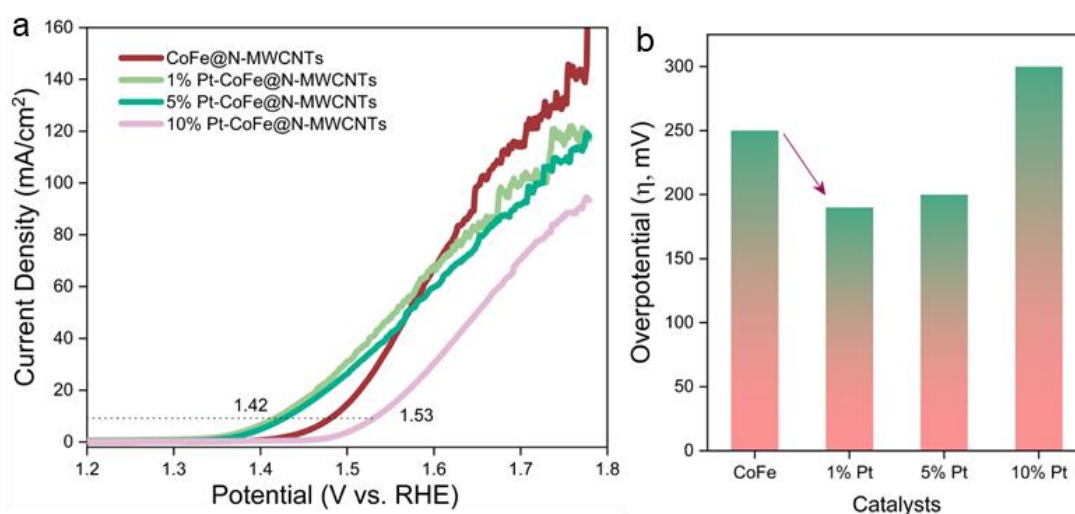


Figure 5.14. (a) Linear sweep voltammograms (LSVs) of OER for 1-Pt-Post-CoFe, 5-Pt-Post-CoFe, and 10 -Pt-Post-CoFe, and Post-CoFe-N-MWCNTs. (b) Comparison of OER overpotential for 1-Pt-Post-CoFe, 5-Pt-Post-CoFe, and 10 -Pt-Post-CoFe, and Post-CoFe-N-MWCNTs.

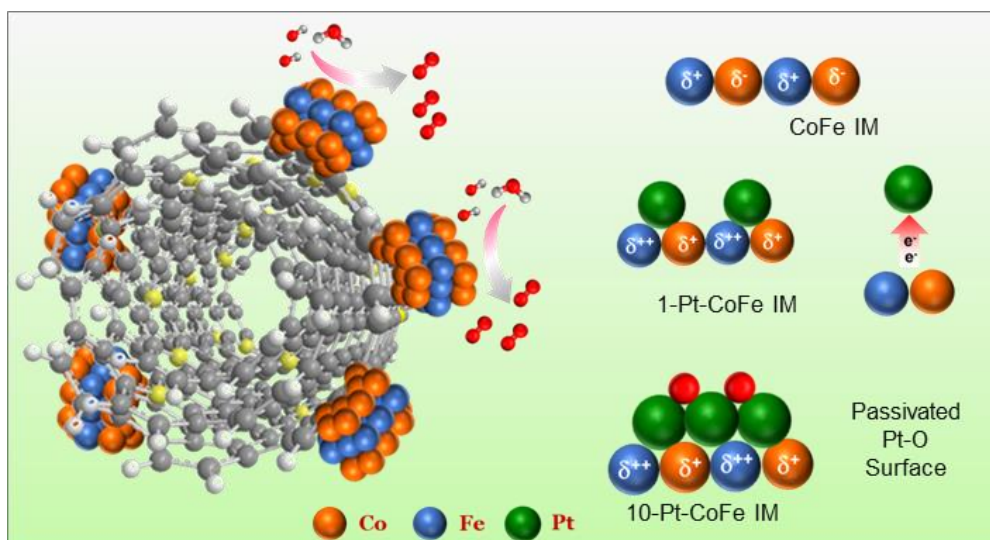


Figure 5.15. Schematic representation of plausible OER mechanism of Pt incorporated CoFe IM catalyst.

The compressional strain experienced by CoFe lattice will trigger formation of CoOOH/FeOOH faster to release the strain. On the other hand, when the amount of Pt is increased further to 10%, the OER activity drastically decreased which is due to coverage of CoFe lattice with Pt-metal or Pt-based alloys and Pt gets inactive under OER potential in alkaline media.¹⁵ Hence, a tuned presence of Pt has enhanced the activity of CoFe IM catalyst. **Figure 5.15** has schematically represented the overall phenomenon and explains why 1-Pt-Post-CoFe has given the best activity. Also, it has been observed in **Figures 5.11a** and **5.11b**, when 1 and 5% of Pt is incorporated into the CoFe system, the partial oxidation state of both Co and Fe are highest and again their oxidation state decreases when 10% Pt is loaded. This increased electron deficiency indicates electron transfer from Co/Fe to Pt atoms and higher oxidation state on Co and Fe will help the easier conversion of metallic Co and Fe to Co^{3+} and Fe^{3+} in CoOOH and FeOOH. A combined effect of synergy is achieved from strain effect and electron transfer phenomena which gives enhanced OER activity in presence of just 1% of Pt.

5.5 Conclusion

This work demonstrates the formation of stable CoFe IMC via unique nitride formation pathway. A two-step synthesis has been performed to first get the metal nitrides and then treat under reducing atmosphere at high temperatures for attaining the ordered cubic phase of CoFe. N doped MWCNTs have been used as a conducting support as well as which leads to the formation of CoN or FeN and further when annealed, the CoFe IM nanoparticles are embedded in the MWCNTs without getting agglomerated. Annealing at high temperatures usually lead to sintering of nanoparticles which form larger nanoparticles with lesser surface area. N-

anchoring effect have strongly embedded the CoFe nanoparticles which has prevented the sintering and hence smaller nanoparticles with larger electrochemical surface area is achieved. With no N-doping or without using MWCNTs, there is no formation metal nitride and hence no CoFe IM formation is achieved. It is interesting to note that without the presence of Co, Fe stays in oxide form whereas in presence of Co, Fe^{3+} ions get reduced to atomic Fe and diffuses with Co atoms to form ordered CoFe IM. Co plays a supporting role in modulating the reduction potential of $\text{Fe}^{3+}/\text{Fe}^0$ redox couple. This observation is confirmed by powerful characterization techniques like PXRD, TEM, SEM, and XAS. To further enhance the synergy of the material, Pt metal has been incorporated into the similar synthesis process in different loading percentages. It has been observed that when Pt is used in ultra-low 1%, the highest OER activity is achieved with only 190 mV overpotential to achieve 10 mA/cm^2 current density. From PXRD and EXAFS data analysis, it is confirmed that at 1% of Pt loading, there is no nanocluster of Pt and no Pt-Pt bonds are present. From R-space data analysis it is seen some Pt-Fe/Pt-Co bonds have been formed which increases when loading of Pt is increased. The Pt-M bond distance is increased which means some contribution from Pt-Pt bond is also there along with Pt-Fe/Co bonds. And PXRD confirms the formation of Pt-Fe/Pt-Co alloy along with CoFe intermetallic formation. Thus, when loading of Pt is increased there is hetero-phase formation between CoFe IM and Pt-M (M=Co or Fe) alloy. Due to the reduced surface area of CoFe IM the OER activity is seen to decrease upon increased Pt loading. Whereas increase in activity from pristine CoFe to 1% Pt CoFe is majorly due to the synergistic effect of Pt atoms on CoFe lattice, that is the compressional strain imposed on the CoFe lattice will help is faster conversion of Co and Fe to $\text{CoOOH}/\text{FeOOH}$.

5.6 References

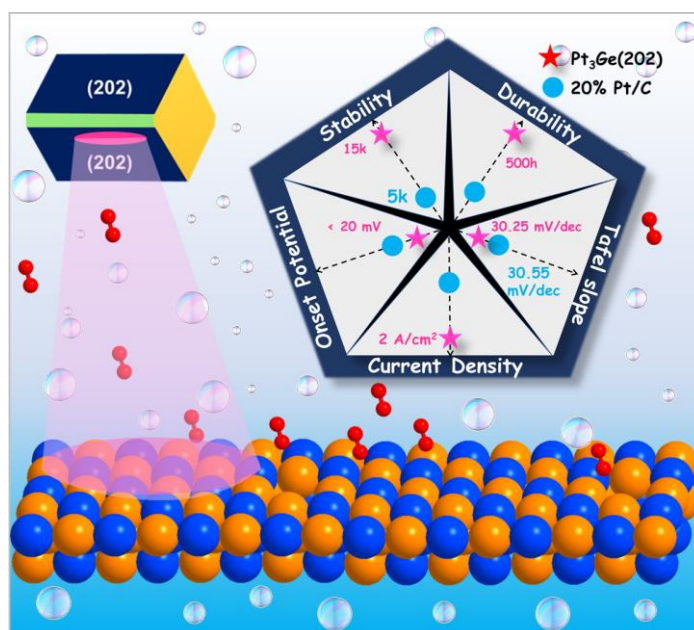
1. Slobodkin, I.; Davydova, E.; Sananis, M.; Bretyus, A.; Rothschild, A., Electrochemical and chemical cycle for high-efficiency decoupled water splitting in a near-neutral electrolyte. *Nat. Mater.* **2024**, *23*, 398-405.
2. Guo, J.; Zhang, Y.; Zavabeti, A.; Chen, K.; Guo, Y.; Hu, G.; Fan, X.; Li, G. K., Hydrogen production from the air. *Nat. Commun.* **2022**, *13*, 5046.
3. Suryanto, B. H. R.; Wang, Y.; Hocking, R. K.; Adamson, W.; Zhao, C., Overall electrochemical splitting of water at the heterogeneous interface of nickel and iron oxide. *Nat. Commun.* **2019**, *10*, 5599.
4. Wu, D.; Kusada, K.; Yoshioka, S.; Yamamoto, T.; Toriyama, T.; Matsumura, S.; Chen, Y.; Seo, O.; Kim, J.; Song, C.; Hiroi, S.; Sakata, O.; Ina, T.; Kawaguchi, S.;

- Kubota, Y.; Kobayashi, H.; Kitagawa, H., Efficient overall water splitting in acid with anisotropic metal nanosheets. *Nat. Commun.* **2021**, *12*, 1145.
5. Ren, X.; Wu, T.; Sun, Y.; Li, Y.; Xian, G.; Liu, X.; Shen, C.; Gracia, J.; Gao, H.-J.; Yang, H.; Xu, Z. J., Spin-polarized oxygen evolution reaction under magnetic field. *Nat. Commun.* **2021**, *12*, 2608.
6. Knöppel, J.; Möckl, M.; Escalera-López, D.; Stojanovski, K.; Bierling, M.; Böhm, T.; Thiele, S.; Rzepka, M.; Cherevko, S., On the limitations in assessing stability of oxygen evolution catalysts using aqueous model electrochemical cells. *Nat. Commun.* **2021**, *12*, 2231.
7. Ou, Y.; Twight, L. P.; Samanta, B.; Liu, L.; Biswas, S.; Fehrs, J. L.; Sagui, N. A.; Villalobos, J.; Morales-Santelices, J.; Antipin, D.; Risch, M.; Toroker, M. C.; Boettcher, S. W., Cooperative Fe sites on transition metal (oxy)hydroxides drive high oxygen evolution activity in base. *Nat. Commun.* **2023**, *14*, 7688.
8. Jung, H. Y.; Park, J. H.; Ro, J. C.; Suh, S. J., Fabrication of Trimetallic Fe–Co–Ni Electrocatalysts for Highly Efficient Oxygen Evolution Reaction. *ACS Omega* **2022**, *7*, 45636-45641.
9. Baek, J.; Hossain, M. D.; Mukherjee, P.; Lee, J.; Winther, K. T.; Leem, J.; Jiang, Y.; Chueh, W. C.; Bajdich, M.; Zheng, X., Synergistic effects of mixing and strain in high entropy spinel oxides for oxygen evolution reaction. *Nat. Commun.* **2023**, *14*, 5936.
10. Fang, C.; Zhou, J.; Zhang, L.; Wan, W.; Ding, Y.; Sun, X., Synergy of dual-atom catalysts deviated from the scaling relationship for oxygen evolution reaction. *Nat. Commun.* **2023**, *14*, 4449.
11. Lee, W. H.; Han, M. H.; Ko, Y.-J.; Min, B. K.; Chae, K. H.; Oh, H.-S., Electrode reconstruction strategy for oxygen evolution reaction: maintaining Fe-CoOOH phase with intermediate-spin state during electrolysis. *Nat. Commun.* **2022**, *13*, 605.
12. Xu, R.; Wang, X.; Yang, Z.; Chang, Y.; Chen, X.; Wang, J.; Li, H., Electrodeposition Fabrication of La-Doped NiFe Layered Double Hydroxide to Improve Conductivity for Efficient Overall Water Splitting. *ACS Appl. Energy Mater.* **2024**, *7*, 3866-3875.
13. Kharissova, O. V.; Kharisov, B. I., Variations of interlayer spacing in carbon nanotubes. *RSC Adv.* **2014**, *4*, 30807-30815.
14. Liu, C.; Wu, X.; Klemmer, T.; Shukla, N.; Weller, D.; Roy, A. G.; Tanase, M.; Laughlin, D., Reduction of Sintering during Annealing of FePt Nanoparticles Coated with Iron Oxide. *Chem. Mater.* **2005**, *17*, 620-625.

15. Reier, T.; Oezaslan, M.; Strasser, P., Electrocatalytic Oxygen Evolution Reaction (OER) on Ru, Ir, and Pt Catalysts: A Comparative Study of Nanoparticles and Bulk Materials. *ACS Catal.* **2012**, 2, 1765-1772.
16. Cheraghizade, M.; Jamali Sheini, F.; Yousefi, R., Optical, electrical, and photovoltaic properties of PbS thin films by anionic and cationic dopants. *Appl. Phys. A* **2017**, 123, 390.
17. Sarma, S. C.; Mishra, V.; Ann Mary, K. A.; Roy, S.; Peter, S. C., “Inverse Strain Effect in Atomic Scale”—Enhanced Hydrogen Evolution Activity and Durability in Cu-Substituted Palladseite. *ACS Energy Lett.* **2018**, 3, 3008-3014.

Chapter 6

Morphology Tuned Pt₃Ge Accelerates Water Dissociation to Industrial Standard Hydrogen Production over a wide pH Range



Soumi Mondal; Shreya Sarkar; Debabrata Bagchi; Tisita Das; Risov Das; Ashutosh Kumar Singh; Ponnappa Kechanda Prasanna; Vinod C Prabhakaran; Sudip Chakraborty; Sebastian C. Peter, *Adv. Mater.* **2022**, 34, 2202294.

Summary

The discovery of novel materials for industrial standard hydrogen production is the present need considering the global energy infrastructure. We introduce a novel electrocatalyst, Pt₃Ge, engineered with a desired crystallographic facet (202) accelerates hydrogen production by water electrolysis and records industrially desired operational stability compared to the commercial catalyst platinum. Pt₃Ge-(202) exhibits low overpotential of 21.7 mV (24.6 mV for Pt/C) and 92 mV for 10 mA/cm² and 200 mA/cm² current density, respectively in 0.5M H₂SO₄. It also exhibits remarkable stability of 15,000 accelerated degradation tests cycles (5000 for Pt/C) and exceptional durability of 500 h (@10 mA/cm²) in acidic media. Pt₃Ge-(202) also displayed low overpotential of 96 mV for 10 mA/cm² current density in the alkaline medium, rationalizing its hydrogen production ability over a wide pH range required commercial operations. Long-term durability (>75 h in alkaline media) with the industrial level current density (>500 mA/cm²) has been demonstrated by utilizing the electrochemical flow reactor. The driving force behind this stupendous performance of Pt₃Ge-(202) has been envisaged by mapping the reaction mechanism, active sites and charge transfer kinetics via controlled electrochemical experiments, ex-situ X-ray photoelectron spectroscopy, in-situ infrared spectroscopy and in-situ X-ray absorption spectroscopy further corroborated by first principles calculations.

Table of Contents

6.1	Introduction	170
6.2	Experimental Details	172
6.2.1	Chemicals and reagents	172
6.2.2	Synthesis of Pt ₃ Ge-(110) and Pt ₃ Ge-(202)	172
6.3	Characterization	172
6.3.1	Powder X-ray Diffraction (PXRD)	172
6.3.2	Transmission Electron Microscope (TEM)	172
6.3.3	Inductively coupled plasma atomic emission spectroscopy (ICP-OES)	172
6.3.4	X-ray Photoelectron Spectroscopy (XPS)	173
6.3.5	High-angle annular dark field scanning transmission electron microscopy (HAADF-STEM)	173
6.3.6	Scanning electron microscopy (SEM) and Energy Dispersive Spectrum (EDAX)	173
6.3.7	X-ray Absorption Spectroscopy (XAS)	173
6.3.8	Electrochemical Hydrogen Evolution Reaction (HER)	174
6.3.9	In situ Electrochemical Attenuated Total Reflection Fourier Transform Infrared Spectroscopy (ATR-FTIR)	175
6.3.10	In-situ X-ray absorption spectroscopy	175
6.3.11	Methodology of computational study	175
6.4	Results & Discussion	175
6.4.1	Hydrogen production	180
6.4.2	Driving forces for accelerated HER	187
6.5	Conclusion	198
6.6	References	198

6.1 Introduction

The ultimate dream of the human kind in the current scenario is to use the terms ‘fuel’ and ‘combustion’ without having to encounter any carbon dioxide (CO₂) or carbonaceous compounds. To date, the utilization of non-renewable energy resources (like coal, petroleum and natural gas) is exceeding the use of renewable ones like wind, water, biopower and solar. The enormous growth of population has led to extensive consumption of these fossil fuels¹ and release of noxious CO₂ gas that has caused global warming, hiking the temperature at an alarming rate. Hydrogen (H₂) gas, in its molecular form, is the cleanest fuel known to date because its only combusted product is benevolent water.² Hydrogen can be used as a fuel in Proton Exchange Membrane Fuel Cells (PEMFCs) for various routine applications,³ as a reductant in the utilization of greenhouse gas CO₂,⁴ as a raw material in the production of several chemicals using hydrogenation processes (e.g., ammonia synthesis,⁵ methanol production⁶), as a direct fuel (e.g., in rocket⁷), in metallurgical industries,⁸ semiconductor manufacturing,⁹ pharmaceuticals,⁸ and any other sectors having concerns related to energy and environment. However, large-scale H₂ production is majorly dependent on steam reforming of fossil fuels (about 96%),¹⁰ and the rest 4% by water electrolysis.^[11-17] Environmentally benign process, water electrolysis needs an exponential growth for the development of a powerful H₂ generator. Noble metals (platinum, palladium and ruthenium¹⁸), especially platinum, are highly electroactive for hydrogen generation via water splitting attributed to their favourable electronic structure and optimum energy for hydrogen adsorption and desorption processes. But, extensive commercialization of water electrolysis process is not yet completely achieved owing to high cost of Pt. These commercialization hurdles of water electrolysis process can be overcome either by reducing the cost of the catalyst or improving the performance or combining both. Even after a long scientific journey of synthesizing non-Pt based electrocatalysts, none of them could set foot in the performance region of Pt.

Extensive research activities are being carried out to maximize the catalytic activity of Pt along with decreased mass loading.¹⁹ The hydrogen evolution reaction (HER) activity of Pt can be tuned by alloying with other transition elements,²⁰⁻²² formation of heterostructures,²³⁻²⁵ core-shell design,²⁵⁻²⁷ substituting with carbides^{28, 29} or nitrides or phosphides³⁰ and even generation of single-atom catalysts.^{16, 31-34} Despite showing promising catalytic performance, these materials were found to be incapable of fulfilling one or the other parameters required for commercial operation. There are five critical parameters (hereafter coined as Fabulous Five (Fab-Five)) that dictate HER activity of a catalyst: (1) onset potential, (2) current density, (3)

Tafel slope, (4) stability in wide pH range and (5) industrial standard durability. However, discovering a material holding all these parameters together is a challenging task. There are several strategies used to develop materials, for example, combining Pt with 3d transition metals (TMs) or p block elements. This can alter the 5d electron occupancy of Pt and Pt-Pt interatomic distance, tuning d-band center and modifying the electronic structure.³⁵ The electronic structure modification improves the charge transfer kinetics and intermediate stability on the surface thereby lowering the activation barrier of the reaction.

Although several approaches have been explored,³⁶⁻⁴⁰ there still lacks clarity in which atomic level modifications alter the electronic structure enhancing the HER activity close to the theoretical value. One such concept is to tune the arrangement of atoms within the crystal lattice, which can be achieved by the synthesis of ordered intermetallic compounds. Nevertheless, the situation can be even more complicated as the atomic packing at different crystallographic planes may alter the HER activity. It is worth mentioning that tuning a specific surface for catalysis at the atomic level is extremely difficult. There are a few handpicked numbers of works which proposed this concept by different synthetic strategies.⁴¹⁻⁴³ In this work we have introduced a novel concept, where we selectively tuned a surface favourable for HER activity close to the theoretical target. To achieve enhancement in Fab-Five parameters exceeding that of the state-of-the-art commercial Pt, we have selected an unexplored intermetallic compound Pt₃Ge (tetragonal system and space group: *I4/mcm*) (**Figure 6.1a**). Selective exposure of facets is typically done by the use of capping agents, whereas our work eliminates surfactants from the synthesis completely classifying it as a green approach. Our work highlights the in-situ formation of a secondary phase which facilitates the exposure of an HER active facet. To the best of our knowledge, this new catalyst is the first HER electrocatalyst which surpasses all Fab-Five parameters mentioned earlier. Using several controlled experiments including synthesis, electrochemical studies, spectroscopic measurements, operando FT-IR, XAS and DFT calculations, the driving force behind the stupendous performance of this unique material is being established. The industrial level current density ($>500 \text{ mA/cm}^2$) has been achieved by the meticulous optimization of the flow reactor and long-term durability ($>75 \text{ h}$) of HER has been obtained even in the sluggish alkaline media (1M KOH) for practical utilization.

6.2 Experimental Details

6.2.1 Chemicals and reagents

Potassium tetrachloroplatinate (K₂PtCl₄) and nafion binder (5 wt.%) were purchased from Sigma-Aldrich, germanium tetrachloride (GeCl₄) was purchased from Alfa-Aesar, and tri-ethylene glycol (TEG) were purchased from Merck. All the chemicals (more than 99% purity) were used as purchased without any further purification. Millipore water of conductivity 18.2 MΩcm was used for the synthesis and all electrochemical studies.

6.2.2 Synthesis of Pt₃Ge-(110) and Pt₃Ge-(202)

In a typical solvothermal reaction, 0.3 mmol of K₂PtCl₄, 0.1, and 0.3 mmol of GeCl₄ for Pt₃Ge-(110) and Pt₃Ge-(202), and 0.8 mL of superhydride solution (reducing agent) (Li(C₂H₅)₃BH) were mixed in 18 mL of TEG. In two autoclaves, solid K₂PtCl₄ salt is dissolved in 18ml TEG and magnetically stirred until dissolved completely. After complete dissolution, GeCl₄ is added using a micropipette as 11.4 μL and 34.2 μL for Pt₃Ge-(110) and Pt₃Ge-(202), respectively. The mixture is continuously stirred for 30 mins. After that, 0.8 mL Li(C₂H₅)₃BH is added using a syringe and again stirred in an orbital shaker for 30-45 mins. The autoclave was kept at 220 °C for 36 h. The final product was washed several times with ethanol, and the obtained product was dried and used for further characterization.

6.3 Characterization

6.3.1 Powder x-ray diffraction (PXRD)

PXRD measurements were done at room temperature on a Rigaku Miniflex X-ray diffractometer with Cu-K_α X-ray source ($\lambda = 1.5406 \text{ \AA}$), equipped with a position sensitive detector in the angular range $20^\circ \leq 2\theta \leq 80^\circ$ with the step size 0.02° and scan rate of 0.5 s/step calibrated against corundum standards. The experimental XRD patterns were compared to the patterns simulated from the data reported in the literature.

6.3.2 Transmission electron microscope (TEM)

TEM images and selected area electron diffraction patterns were collected using a JEOL JEM-2010 TEM instrument and color mapping was done in TECHNAI. The samples for these measurements were prepared by sonicating the nanocrystalline powders in ethanol and drop-casting a small volume onto a carbon-coated copper grid.

6.3.3 Inductively coupled plasma atomic emission spectroscopy (ICP-OES)

ICP-OES was performed using a Perkin Elmer Optima 7000 DV instrument. The samples were digested in concentrated aqua regia, followed by dilution with distilled water. In

a typical experiment, 2 mg of the sample was dissolved in 1 ml aqua regia and left overnight (12 hrs) for digestion. The digested sample was then diluted to 10 ml volume with deionized water. The solid particles were separated by thorough centrifugation before measurements.

6.3.4 X-ray photoelectron spectroscopy (XPS)

XPS measurements were carried out using Thermo K-alpha+ spectrometer using micro focused and monochromated Al K α radiation with energy 1486.6 eV. The pass energy for the spectral acquisition was kept at 50 eV for individual core-levels. The electron flood gun was utilized for providing charge compensation during data acquisition. Further, the individual core-level spectra were checked for charging using C1s at 284.6 eV as standard and corrected if needed. The peak fitting of the individual core-levels was done using CASA XPS software with a Shirley type background.

6.3.5 High-angle annular dark field scanning transmission electron microscopy (HAADF-STEM)

Aberration corrected FEI Titan G2 60–300 kV microscope has been used to investigate the nature of the catalyst. High-Angle Annular Dark Field Scanning Transmission Electron Microscopy (HAADF STEM) imaging has been performed at an accelerating voltage of 300 kV with a probe convergence angle of 24.5 mrad using 70 μ m aperture.

6.3.6 Scanning electron microscopy (SEM) and energy dispersive spectrum (EDAX)

The FESEM measurement was performed using Leica scanning electron microscopy equipped with an energy-dispersive X-ray spectroscopy (EDX) instrument (Bruker 120 eV EDAX instrument). Data were acquired by using an accelerating voltage of 15 kV, and the typical time taken for data accumulation is 100 s. The elemental analyses were performed using the P/B-ZAF standardless method (where P/B = peak to background model, Z = atomic no. correction factor, A = absorption correction factor, and F = fluorescence factor) for Cu, Ga at multiple areas on the sample coated Si wafer.

6.3.7 X-ray absorption spectroscopy (XAS)

X-ray absorption near-edge spectroscopy (XANES) and quick-Extended X-ray Absorption Fine Structure (quick-EXAFS) experiments at 300 K were performed at PETRA III, beamline P64, of DESY, Germany. Measurements of Cu-K and Pd-K at ambient pressure were performed in fluorescence as well as transmission mode using gas ionization chambers to monitor the incident and transmitted X-ray intensities. Monochromatic X-rays were obtained using a Si (111) double crystal monochromator, which was calibrated by defining the inflection point (first derivative maxima) of Cu foil as 8980.5 eV. The beam was focused by employing

a Kirkpatrick-Baez (K-B) mirror optic. A rhodium-coated X-ray mirror was used to suppress higher-order harmonics. A CCD detector was used to record the transmitted signals. Pellets for the ex-situ measurements were made by homogeneously mixing the sample with an inert cellulose matrix to obtain an X-ray absorption edge jump close to one.

6.3.8 Electrochemical hydrogen evolution reaction (HER)

All the electrochemical measurements were done in a 3-electrode set-up comprising of a glassy carbon as the working electrode (GCE), graphite rod counter electrode, saturated calomel electrode (SCE) (for acidic media) and mercury/mercuric oxide electrode (MMO) (for basic media). The catalyst ink was prepared using 1.6 mg catalyst + 0.4 mg Vulcan in 200 μL of mixed solvent (IPA: water = 1:1) + 20 μL of 1 wt.% Nafion used as binder. 10 μL of the catalyst ink was drop casted on the commercial 3 mm glassy carbon electrode. Commercial Pt/C (20 wt%, Sigma Aldrich) were used for comparison of activity with the reported electrocatalysts. Linear sweep voltammetry (LSV) was recorded for HER at a scan rate of 5 mV s^{-1} at 25 °C. Electrochemical impedance studies were performed in the frequency range from 10 mHz to 100 kHz at different applied DC potentials for different reactions depending on their onset potential values. The electrolyte solution was deaerated by purging nitrogen gas into the solution at least for 30 min before each experiment. All the reference electrodes were calibrated with respect to the reversible hydrogen electrode (RHE), using Pt as working and counter electrodes in the respective electrolytes. The values obtained are as follows: acidic medium, $E_{\text{RHE}} = E_{\text{SCE}} + 0.265 \text{ V}$; alkaline medium, $E_{\text{RHE}} = E_{\text{MMO}} + 0.881 \text{ V}$.

To achieve the industrial level current density, the HER experiments were carried out in a filter-press type Micro Flow Cell (Electrocell A/S), where a Ti sheet coated with Ir-MMO (iridium-mixed metal oxide) has been used as an Anode plate (Electrocell S/A). An anionic exchange membrane (Fumasep FAB-PK-130) was employed in the case of HER in 1M KOH medium to separate the cathode and anode compartment. The electrolyte was recirculated continuously into the cell (both in cathode and anode) by two separate peristaltic pumps (Ravel, RH-P100L-100). The catalyst material was coated on the Toray carbon paper electrode and evaluated the high current density experiment for long-term HER process in the flow cell.

The reference electrode has been calibrated with respect to standard hydrogen electrode and its calibration potential has been calculated from the average potential with respect to zero current in the hydrogen reduction/oxidation region as mentioned. Saturated calomel electrode (SCE) has been used as reference electrode for electrochemical study in 0.5M H₂SO₄ and

Mercury/Mercury Oxide (MMO) in 0.5 M KOH in one compartment cell. Ag/AgCl has been employed in case of 1 M KOH electrolyte in case flow cell configuration.

6.3.9 In-situ electrochemical attenuated total reflection Fourier transform infrared spectroscopy (ATR-FTIR).

In-situ electrochemical FT-IR spectroscopic studies were performed using a purged VERTEX FT-IR spectrometer equipped with the A530/P accessory and a mid-band MCT detector. A silicon hemispherical window (F530-8) was used with the working electrode placed 1 mm above the window as the single reflection attenuated total reflection (ATR) accessory for the FTIR study. The in situ experimental set-up is depicted in **Figure 2.1b (Chapter 2)** The measurement parameters were 4 cm^{-1} resolution and 100 scans. This setup enabled the detection of Pt-H and Ge-H bond formation on the electrode surface, as well as within the thin-layer electrolyte. The spectra were analyzed by the OPUS software and the absorption spectra have been directly plotted at various potential and time.

6.3.10 In-situ x-ray absorption spectroscopy

In-situ XAS was measured using home-made customized cell set up as shown in **Figure 2.1a (Chapter 2)** under HER conditions.

6.3.11 Methodology of computational study

The DFT calculations are carried out using Vienna ab-initio Simulation Package (VASP) in conjunction with projector augmented plane wave (PAW) method. The exchange-correlation energy has been treated using the Perdew-Burke-Ernzerhof (PBE) type generalized gradient approximation (GGA). An energy cut-off of 450 eV has been used for the plane wave basis set for the electronic wave functions. Full ionic relaxations have been performed until the forces on the ions become smaller than 0.01 eV/Å. Energy convergence criterion for electronic converge has been set to 10^{-3} eV. For (110) plane the Brillouin zone sampling has been done using $5 \times 5 \times 1$ Monkhorst-Pack k-mesh, whereas for the (202) plane a k-mesh of size $3 \times 5 \times 1$ has been used depending on the size of the lattice. van der Waals interactions have been included via the pairwise semi-empirical interaction (DFT-D3) as proposed by Grimme. A vacuum of more than ~ 15 Å has been incorporated in the slab to avoid the spurious interaction between the images.

6.4 Results & Discussion

Noble metal-based compounds having T_3X (T = Noble Metal; X = transition metal/p-block elements) composition have been known for superior electrochemical performance.^{44, 45}

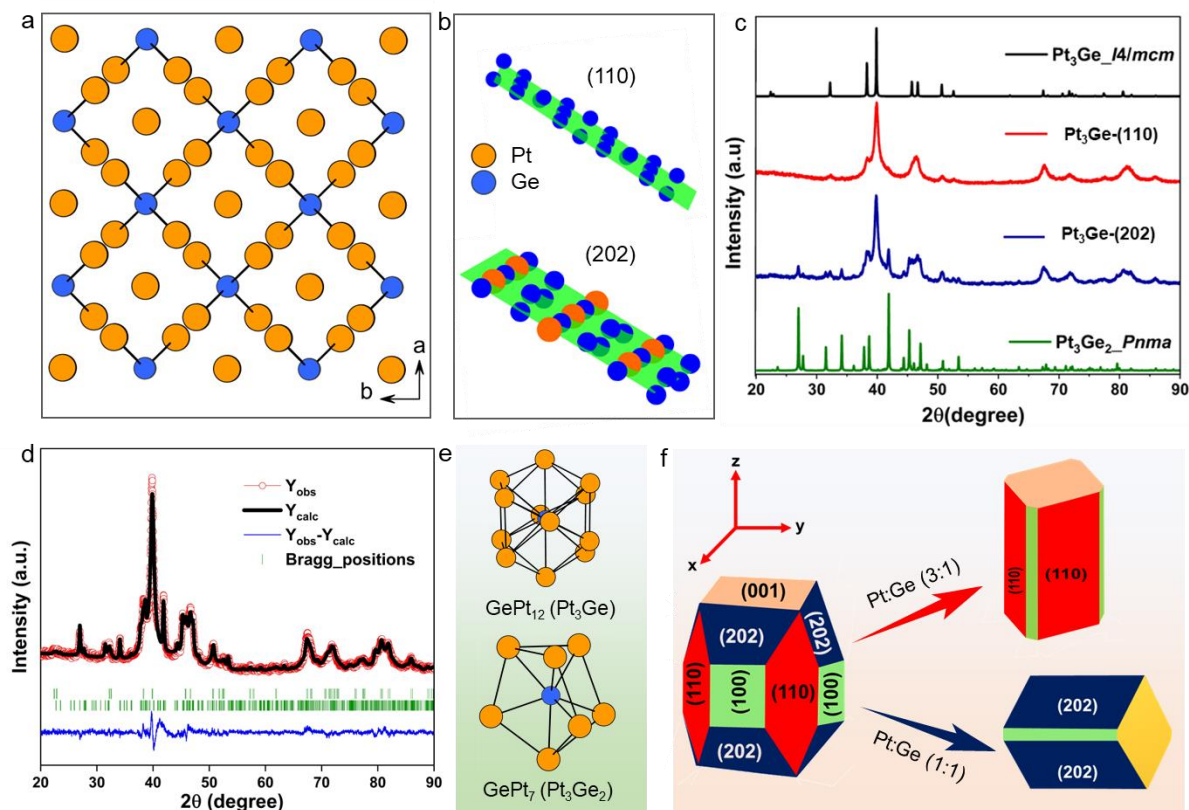


Figure 6.1. Crystal structure of (a) Pt₃Ge and (b) (110) and (202) facets of Pt₃Ge. (c) PXR D of Pt₃Ge-(110) and Pt₃Ge-(202), and (d) Rietveld refinement of Pt₃Ge-(202). (e) The coordination environment of Pt and Ge in Pt₃Ge and Pt₃Ge₂. (f) Schematic of the synthesis illustrating tuned formation of Pt₃Ge-(110) and Pt₃Ge-(202).

Partial replacement of Pt atoms by Ge is a highly cost-effective endeavour since the price of Ge is much lesser than that of Pt. Germanium is reported for its tendency to form hydrides⁴⁶ in acidic media and promote HER when incorporated with other active noble metals like ruthenium⁴⁷ and palladium.⁴⁸

Due to the stable formation of GeH⁴⁹ and GeH₂,⁵⁰ there is an expected enhancement of reaction kinetics of HER towards making it Volmer-Tafel mechanism resembling Pt. Non-similar adjacent atoms can lead to stronger heteroatomic interactions facilitating rapid charge transfer and optimal Metal-H bond strengths.⁵¹ To substantiate this, we have simulated (110) and (202) crystallographic planes of Pt₃Ge using DFT calculations. The selection of these planes has been done based on the fact that (110) has only Pt atoms (equivalent to Pt metal) and (202) has an ordered arrangement of Pt and Ge atoms (**Figure 6.1b**). The preliminary calculations including the formation energy, density of states (DOS) and free energy of H* adsorption provided a hint of (202) being the active surface for HER.⁵² We have generated different crystallographic planes in Pt₃Ge selectively using different synthetic conditions (see detailed synthetic strategies, **Figure 6.1c**, **6.1d** and **Table 6.1**).

Table 6.1. Structural parameters extracted through Rietveld refinement of the Powder XRD of Pt₃Ge-(110) and Pt₃Ge-(202) samples.

Catalyst	Phase	a (Å)	b (Å)	c (Å)	χ^2	Wt. Fraction (%)
Pt₃Ge-(110)	Pt ₃ Ge	5.5141	5.5141	7.8927	3.33	100.00
Pt₃Ge-(202)	Pt ₃ Ge ₂	12.227	7.509	6.829	2.43	21.25
	Pt ₃ Ge	5.4780	5.4780	7.9164		78.75

Figure 6.1e shows the cuboctahedron and bicapped-pentagon co-ordination environment of Ge in tetragonal Pt₃Ge and orthorhombic Pt₃Ge₂ phases, respectively. Ge is relatively less coordinated in Pt₃Ge₂ phase than in Pt₃Ge phase. Thus, it can be interpreted that Pt₃Ge is more stable phase compared to Pt₃Ge₂. The facet-selective synthetic strategy for the crystal growth of Pt₃Ge with (202) (named as Pt₃Ge-(202)) and (110) (Pt₃Ge-(110)) phases is schematically shown in **Figure 6.1f**. As mentioned in the synthesis details, lesser Pt precursor input resulted in the formation of more active facet (202) of Pt₃Ge as the exposed plane.

In order to validate the powder XRD analysis on the anisotropic crystal growth, transmission electron microscopic (TEM) images have been taken on different samples. As seen in **Figure 6.2a**, Pt₃Ge formed nanospheres (**Figures 6.2a(i)** and **6.2a(iii)**) with an approximate particle size of 2.5 nm and 3.3 nm for Pt₃Ge-(202) and Pt₃Ge-(110), respectively (**Figure 6.2b** and **6.2c**). High-resolution TEM (HR-TEM) image of Pt₃Ge-(110) nanoparticles shows the most exposed facet being (110) plane with d-spacing around 0.39 nm (**Figure 6.2a(ii)**). Whereas, HRTEM of the sample with higher Ge (**Figure 6.2a(iv)**) shows the existence of Pt₃Ge phase exposing (202) plane with d-spacing of 0.23 nm for Pt₃Ge. **Figure 6.3a** shows the HAADF-STEM images of Pt₃Ge-(110) nanoparticles. **Figure 6.3b** and **6.3c** show the HAADF-STEM images of Pt₃Ge-(202) with both exposed facets of (202) facets of Pt₃Ge and (322) facets of Pt₃Ge₂. **Figure 6.3d** and **6.3e** show wide region HRTEM images of Pt₃Ge-(202) and Pt₃Ge-(110). These figures show that facets (110) and (202) are exclusively exposed in cases of Pt₃Ge-110 and Pt₃Ge-202, respectively. The presence of the orthorhombic Pt₃Ge₂ phase disrupts the crystal growth along the (110) direction and triggers the selective formation of the facet (202) of Pt₃Ge, which is in excellent agreement with the HRTEM analysis. In this design, Pt₃Ge₂ phase can be termed as the ‘sacrificial phase’, which is later self-destroyed during the electrochemical HER process. Scanning electron microscopy (SEM) (**Figure 6.4a**, **6.4b**, and **6.4c**) depicts the morphology and point energy-dispersive X-ray spectra (EDX) (**Table 6.2**) confirm the expected elemental composition and distribution, which is in agreement with the Rietveld refinement (**Table 6.1**).

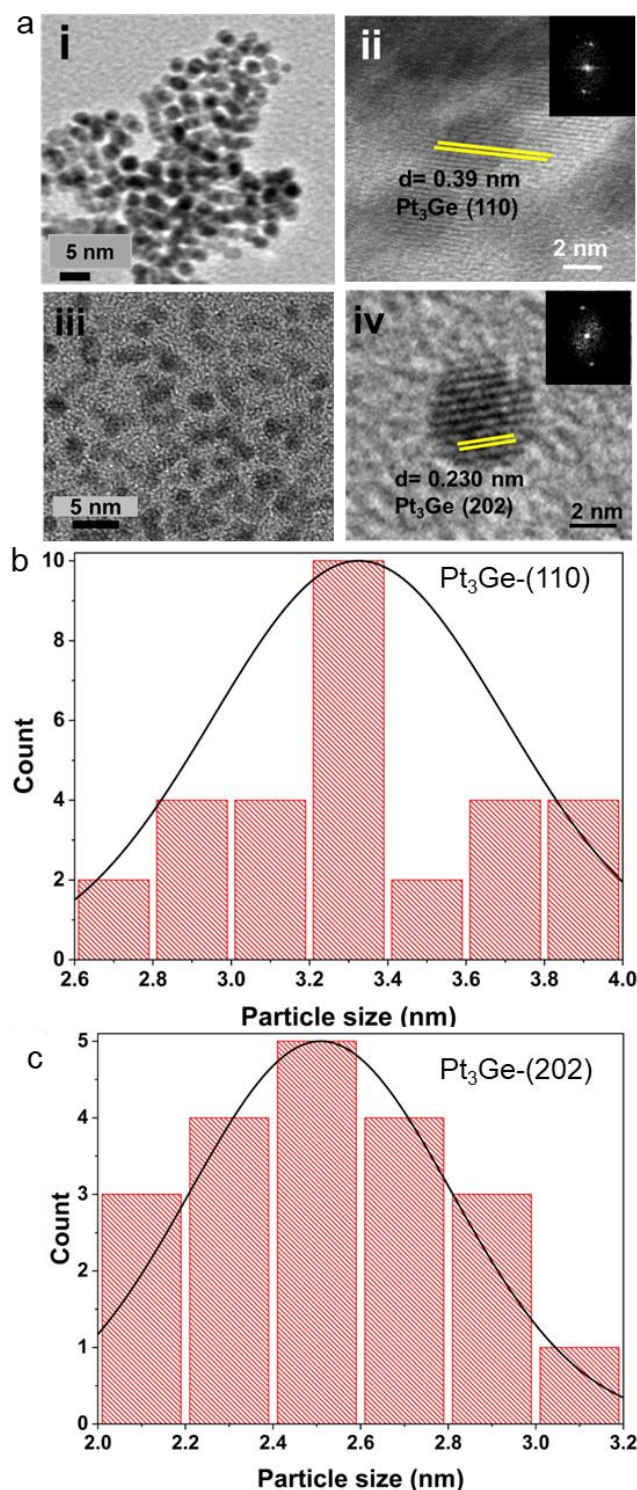


Figure 6.2. (a) Transmission Electron Microscopic (TEM) images of (i) Pt₃Ge-(110) and (iii) Pt₃Ge-(202) nanoparticles. Scale bar is 5 nm for i and iii. High-Resolution TEM (HR-TEM) images of (ii) Pt₃Ge-(110) and (iv) Pt₃Ge-(202) nanoparticles. FFT images shown as inset figures in (ii) and (iv). Histogram showing particle size distribution from TEM image of (a) Pt₃Ge-(110) catalyst being 3.3 nm. (b) Pt₃Ge-(202) catalyst being 2.5 nm.

Inductively Coupled Plasma-Optical Emission Spectrometry (ICP-OES) further confirms the bulk elemental composition (Table 6.3 and Figure 6.4d and 6.4e).

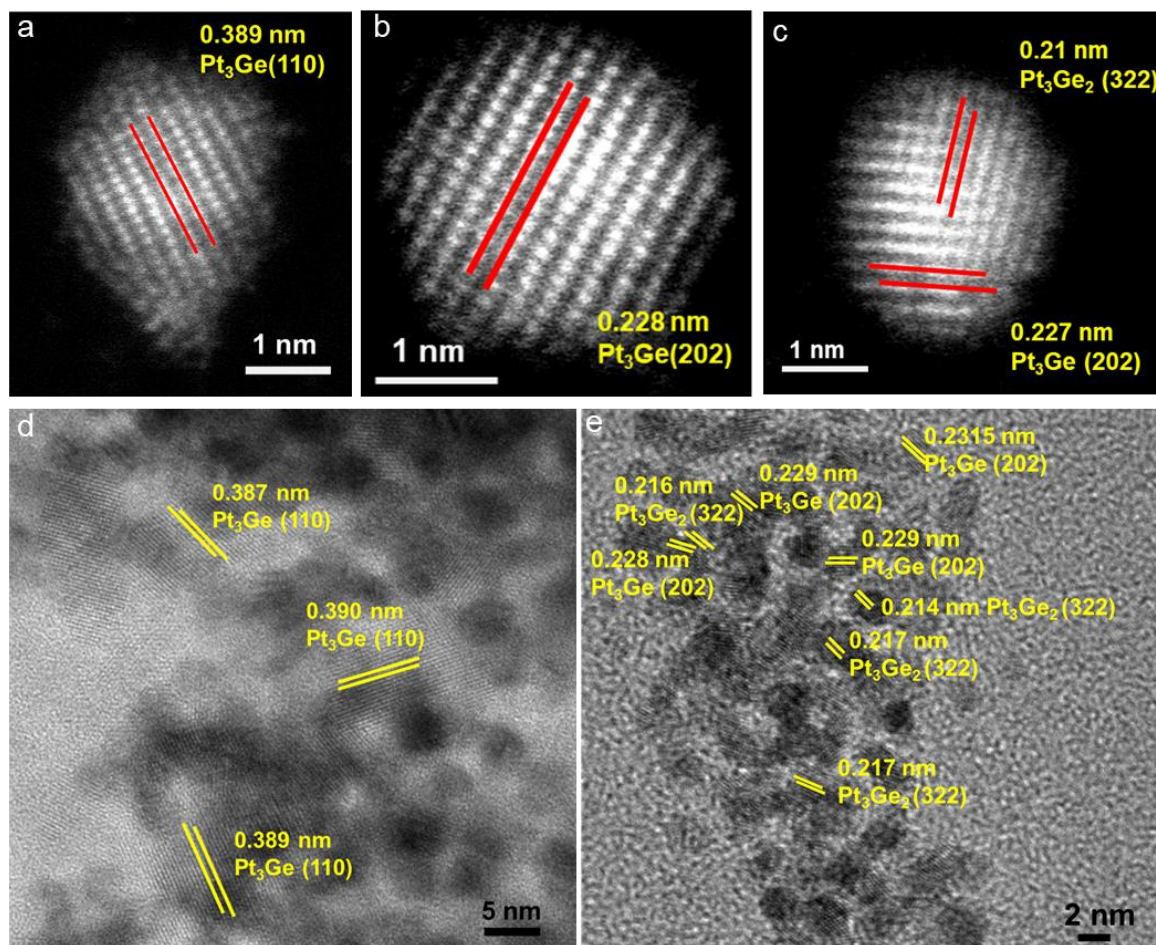


Figure 6.3. (a) HAADF-STEM image for Pt_3Ge -(110). (b-c) HAADF-STEM images of Pt_3Ge -(202). HR-TEM images for (a) Pt_3Ge -(110) and (b) Pt_3Ge -(202).

Table 6.2. SEM-EDS Atomic percentages of Pt_3Ge -(110) and Pt_3Ge -(202) before electrochemical test and after performing HER stability test.

Catalyst	Pt at %	Ge at %
Pt_3Ge -(110)	76.22	23.78
Pt_3Ge -(202)	66.36	33.64

Table 6.3. Elemental composition quantified from ICP-OES measurements.

Catalyst	Atomic percentage (%)	
	Pt	Ge
Pt_3Ge -(110)	73	27
Pt_3Ge -(202)	58.3	41.7

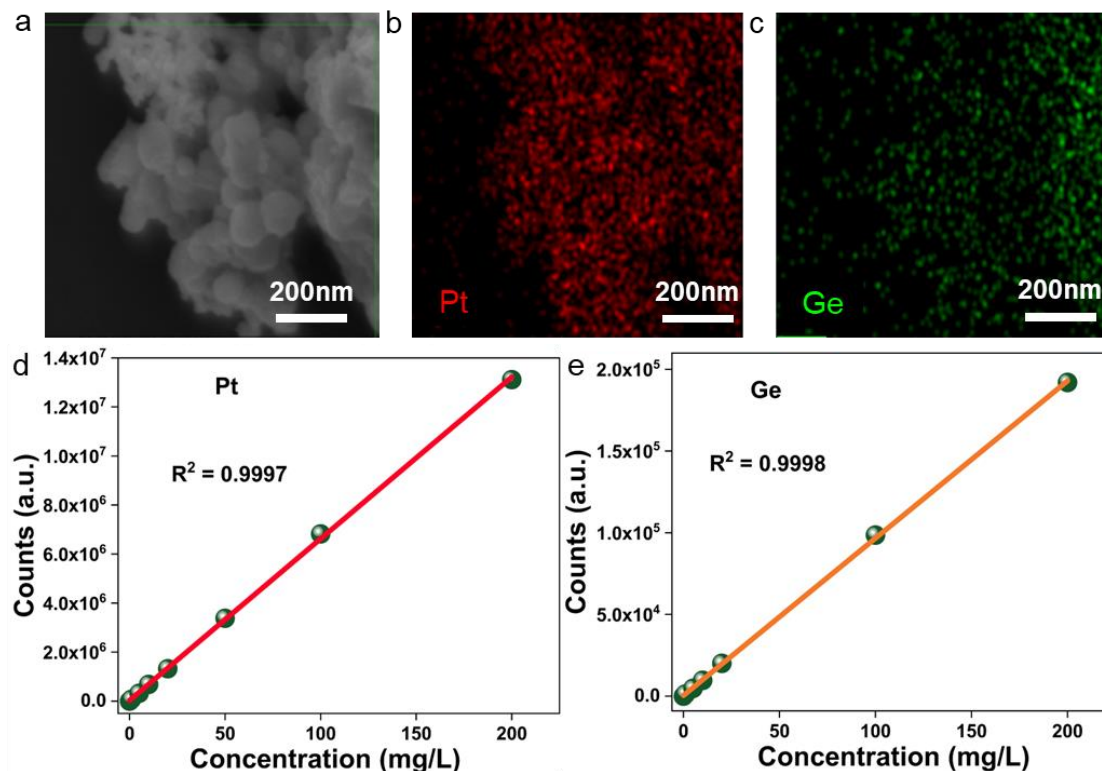


Figure 6.4. SEM images of (a) Pt₃Ge-(202) and (b) Pt and (c) Ge color mapping for showing elemental distribution. ICP-OES calibration plots for elements (d) Pt and (e) Ge.

6.4.1 Hydrogen production

In order to validate our proposed concept, we have performed HER in both acidic and alkaline media (wide pH range).⁵³ **Figure 6.5a** shows the linear sweep voltammograms (LSVs) of Pt₃Ge-(110) and Pt₃Ge-(202) in acidic condition (0.5M H₂SO₄) compared with commercial 20% Pt/C. The overpotential corresponding to 10 mA/cm² (i_{10}) current density is 34 mV, 21.7 mV and 24.6 mV, respectively, for Pt₃Ge-(110), Pt₃Ge-(202) and Pt/C (**Table 6.4**). LSV data for Pt₃Ge-(202) and 20% Pt/C taken using rotating disk electrode (RDE) shows current density up to 2000 mA/cm² at -0.6V vs. RHE (**Figure 6.5b**) with a remarkably low overpotential of 92 mV and 102 mV for 200 mA/cm² current density (inset in **Figure 6.5b**) for Pt₃Ge-(202) and 20% Pt/C, respectively.

Table 6.4. Comparison of electrochemical HER performance of Pt₃Ge-(110) and Pt₃Ge-(202) with state-of-the-art catalyst 20% Pt/C.

Catalyst	Onset (mV vs RHE)		Tafel (mV/dec)	C _{dl} mF/cm ²
	η_{10}	η_{20}		
Pt ₃ Ge-(110)	33.6	58.6	31.29	2.299
Pt ₃ Ge-(202)	21.7	30.7	30.25	16.74
20% Pt/C	24.6	32.9	31.1	12.53

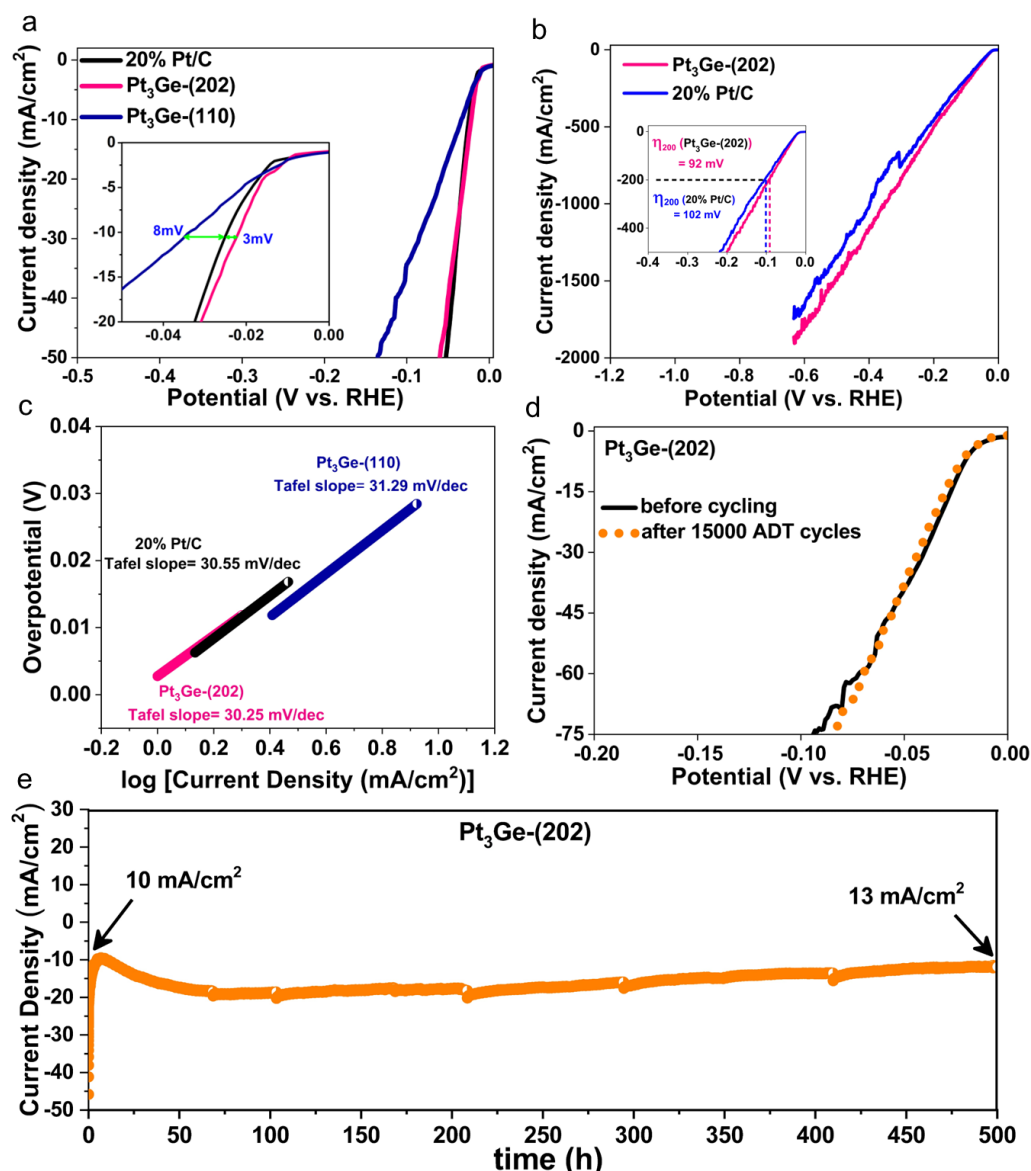


Figure 6.5. (a) Comparison of HER polarization curve (LSVs) of Pt₃Ge-(110), Pt₃Ge-(202) and 20% Pt/C, (ir-corrected) (b) LSVs of Pt₃Ge-(202) and 20% Pt/C using rotating disk electrode (RDE) at 2000 rpm in 0.5 M H₂SO₄, (ir-corrected) (c) Tafel slopes of Pt₃Ge-(110), Pt₃Ge-(202) and 20% Pt/C, (d) LSVs of Pt₃Ge-(202) before and after 15,000 ADT cycles, respectively, in 0.5 M H₂SO₄, (e) Chronoamperometric (CA) study for Pt₃Ge-(202) for 500 h at 10 mA/cm² current density in 0.5 M H₂SO₄

The Tafel slope observed is similar for all the catalysts (**Figure 6.5c**) suggesting Volmer-Tafel mechanistic pathway of HER^{54, 55} with faster reaction kinetics in the case of Pt₃Ge-(202). Pt₃Ge-(202) shows no degradation even after 15000 ADT cycles (**Figure 6.5d**), whereas Pt₃Ge-(110) degraded by 9 mV after similar duration (**Figure 6.6a**). In contrary, the activity of 20% Pt/C degraded within 5000 ADT cycles (**Figure 6.6b**). Additionally, Pt₃Ge-(202) also exhibited a remarkable durability of 500 h chronoamperometry (CA) at 10 mA/cm² (**Figure 6.5e**), which is one of the highest reported durability for any material having the onset

potential and overpotential better than Pt/C, till date.⁴⁰ Impedance studies were done for both the catalysts and compared with 20% Pt/C (Figure 6.6c).

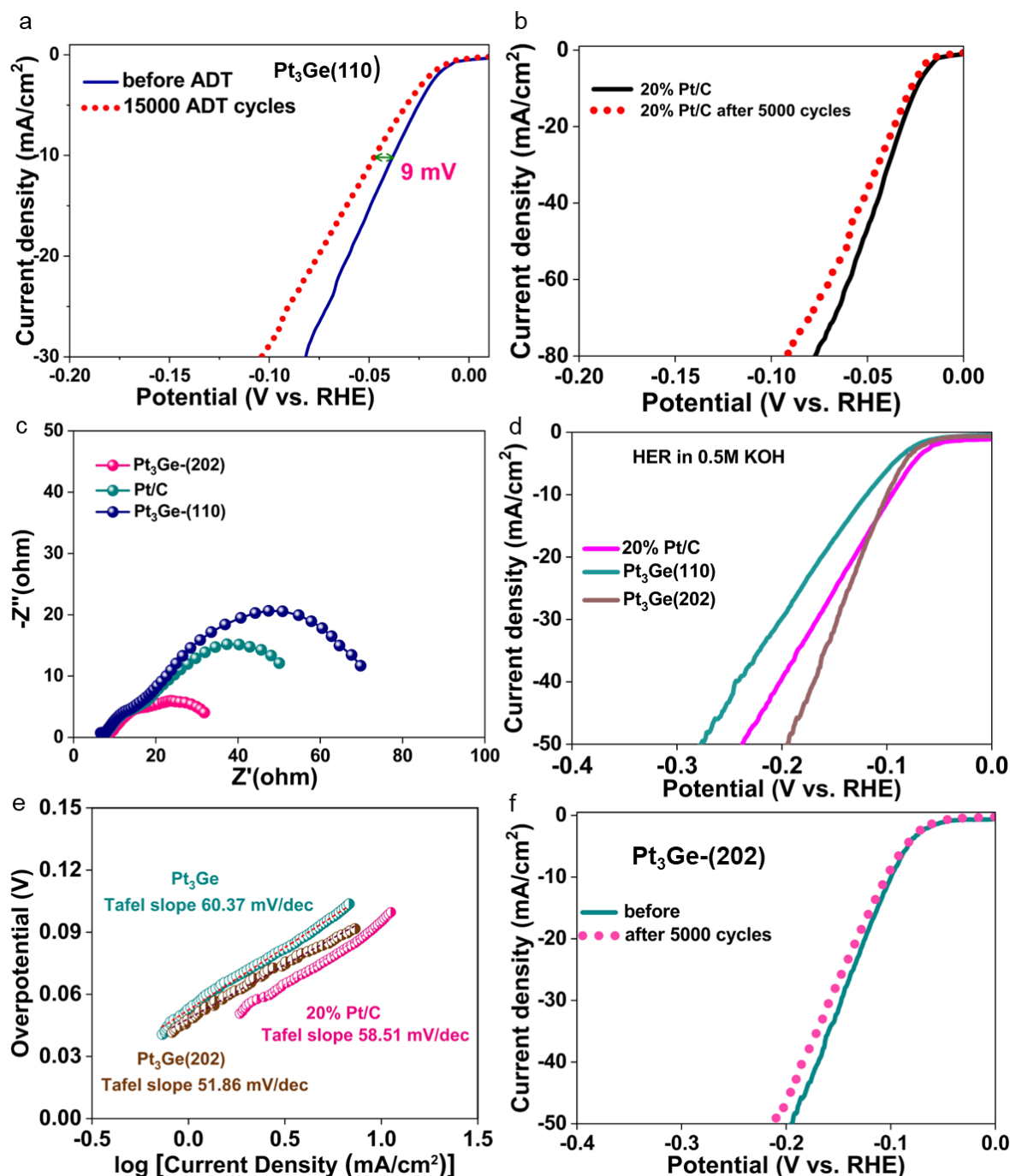


Figure 6.6. (a) Comparison of LSV polarization curve of Pt₃Ge-(110) catalyst for before and after different number of ADT cycle in 0.5M H₂SO₄ for HER. (b) LSVs before and after 5000 ADT cycles for 20% Pt/C. (c) Nyquist plots of Pt₃Ge-(202) and Pt₃Ge-(110) compared with 20% Pt/C. Z' and Z'' are real and imaginary parts of impedance with units of $\Omega \text{ cm}^2$. (d) Comparison of HER polarization curve (Linear sweep voltammograms) of Pt₃Ge-(110), Pt₃Ge-(202), and 20% Pt/C in 0.5 M KOH electrolyte. (e) Tafel slopes of Pt₃Ge-(110) and Pt₃Ge-(202). (f) LSVs of Pt₃Ge-(110) before and after 5000 ADT cycles, respectively. HER study was performed in 0.5M KOH under a scan rate of 5 mV/s using MMO as the reference and graphitic rod as the counter electrode.

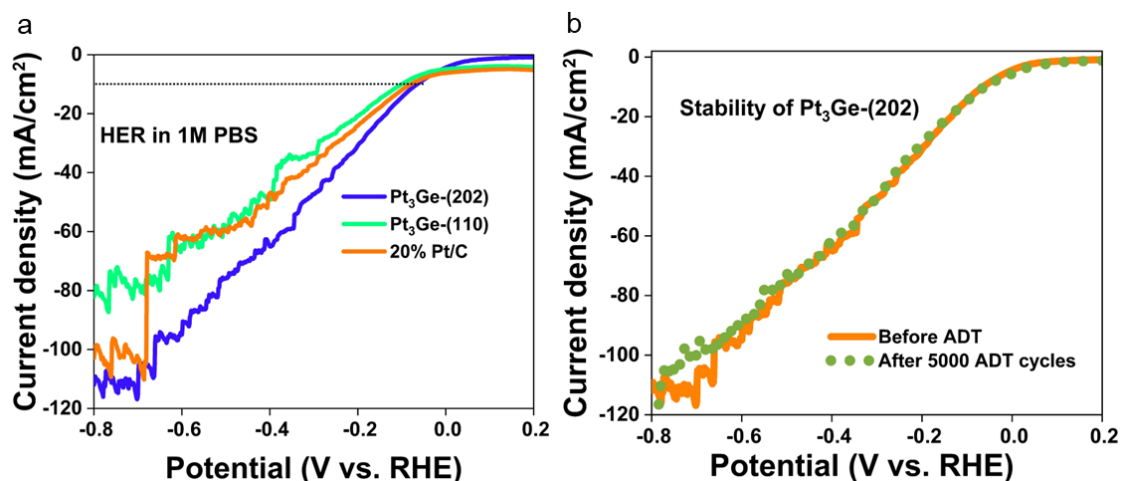


Figure 6.7. (a) (d) HER in 1 M PBS as neutral medium. (e) Stability test of 5000 ADT cycles for Pt₃Ge-(202) in neutral medium.

The charge transfer resistance for Pt₃Ge-(202) is 10 Ω which means faster charge transfer to the active sites where reactants are adsorbed. To evaluate the commercial viability of the catalysts in multiple operational conditions,⁵⁶⁻⁶⁰ the activity has been checked in the alkaline media (0.5M KOH) as well (**Figure 6.6d**). Obtained Tafel slope value of 51.86 mV/dec is even smaller than that of 20% Pt/C (**Figure 6.6e**). Pt₃Ge-(202) catalyst achieves 10 mA/cm² current density at only 96 mV which is on par with the state-of-the-art catalyst 20% Pt/C and significant stability up to 5000 cycles with no degradation in η_{10} value (**Figure 6.6f**). This signifies faster HER kinetics compared to Pt/C even in alkaline condition, which is also portrayed in the LSV where Pt₃Ge-(202) has lower overpotential compared to 20% Pt/C at the entire current density region. **Figure 6.7a** and **6.7b** show the activity of the catalysts in neutral medium (1M PBS as neutral medium) and the stability of the catalyst upto 5000 ADT cycles was achieved. The catalyst Pt₃Ge-(202) exhibited 10 mA/cm² at overpotential of 60 mV which is lesser than 20% Pt/C. Thus, the catalyst proves to be an efficient HER electrocatalyst in wide pH range.⁶¹ To achieve industrial level current density, micro flow cell setup was optimized and alkaline HER in 1 M KOH medium was conducted. The schematic of the flow cell setup during HER is shown in **Figures 6.8a** and **6.8b**. Interestingly, the catalyst Pt₃Ge-(202) shows very high durability for 75 h when done at 500 mA/cm² current density (**Figure 6.8c**).

Cyclic voltammograms in the non-Faradaic region (0.25V to 0.85V vs. RHE) during the activation process of both catalysts are presented in **Figures 6.9a** and **6.9b**, where a notable difference in Ge leaching during the oxidation sweep is observed. This can be correlated to the difference in the exposed crystallographic planes as ordered arrangement of Pt and Ge atoms are present exclusively on (202) facet of Pt₃Ge-(202) (**Figure 6.1b**).

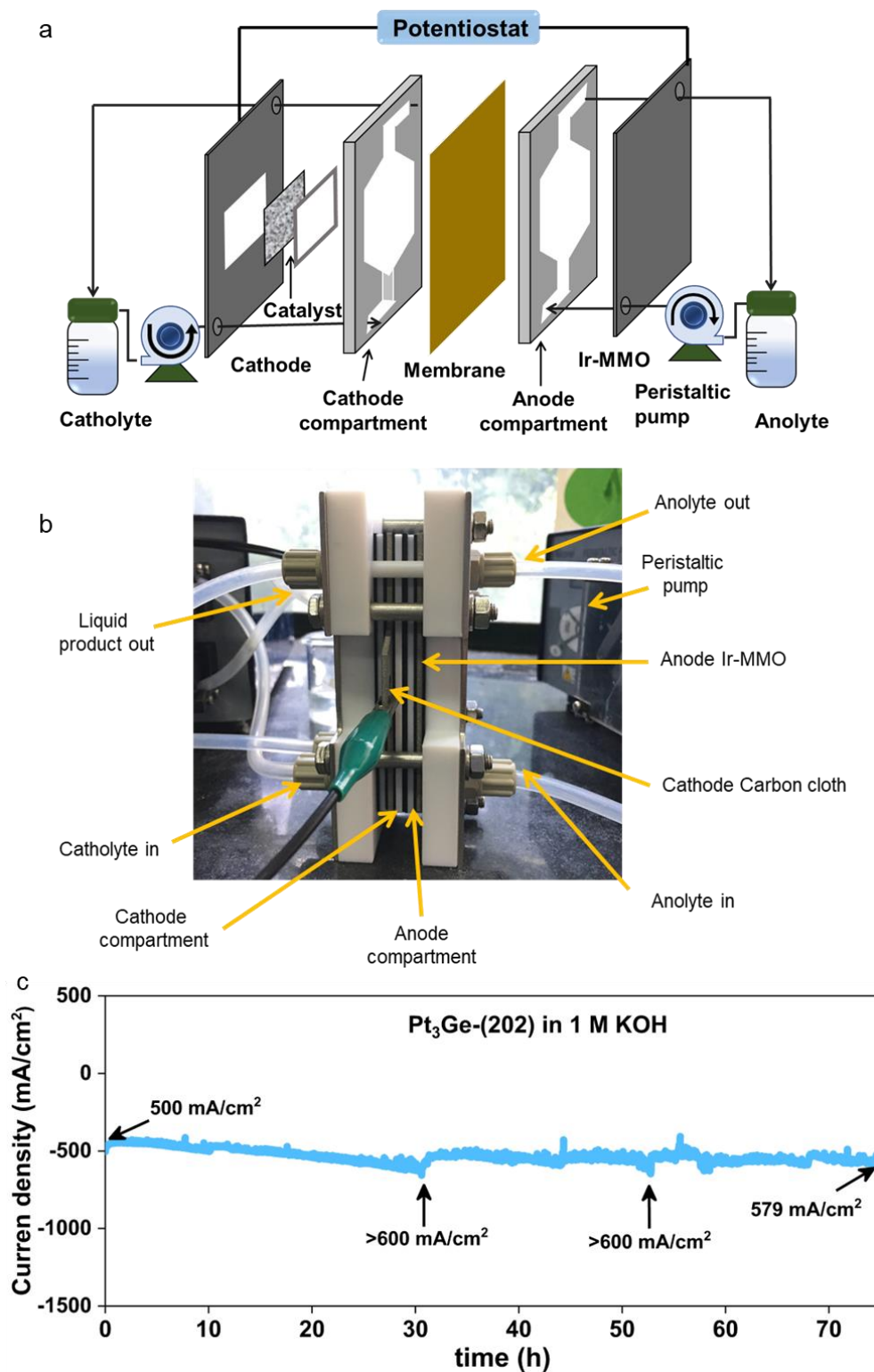


Figure 6.8. (a) Schematic of flow cell set-up for doing HER in 1 M KOH solution (b) Image of the flow-cell setup. (c) CA study for Pt₃Ge-(202) for 75 h at 500 mA/cm² current density in 1 M KOH medium.

Moreover, as shown in **Figure 6.1e**, Ge is coordinated by 12 Pt atoms in Pt₃Ge and surrounded by 7 Pt atoms in Pt₃Ge₂. Due to it being less coordinated by Pt, Ge in Pt₃Ge₂ is more prone to get leached.

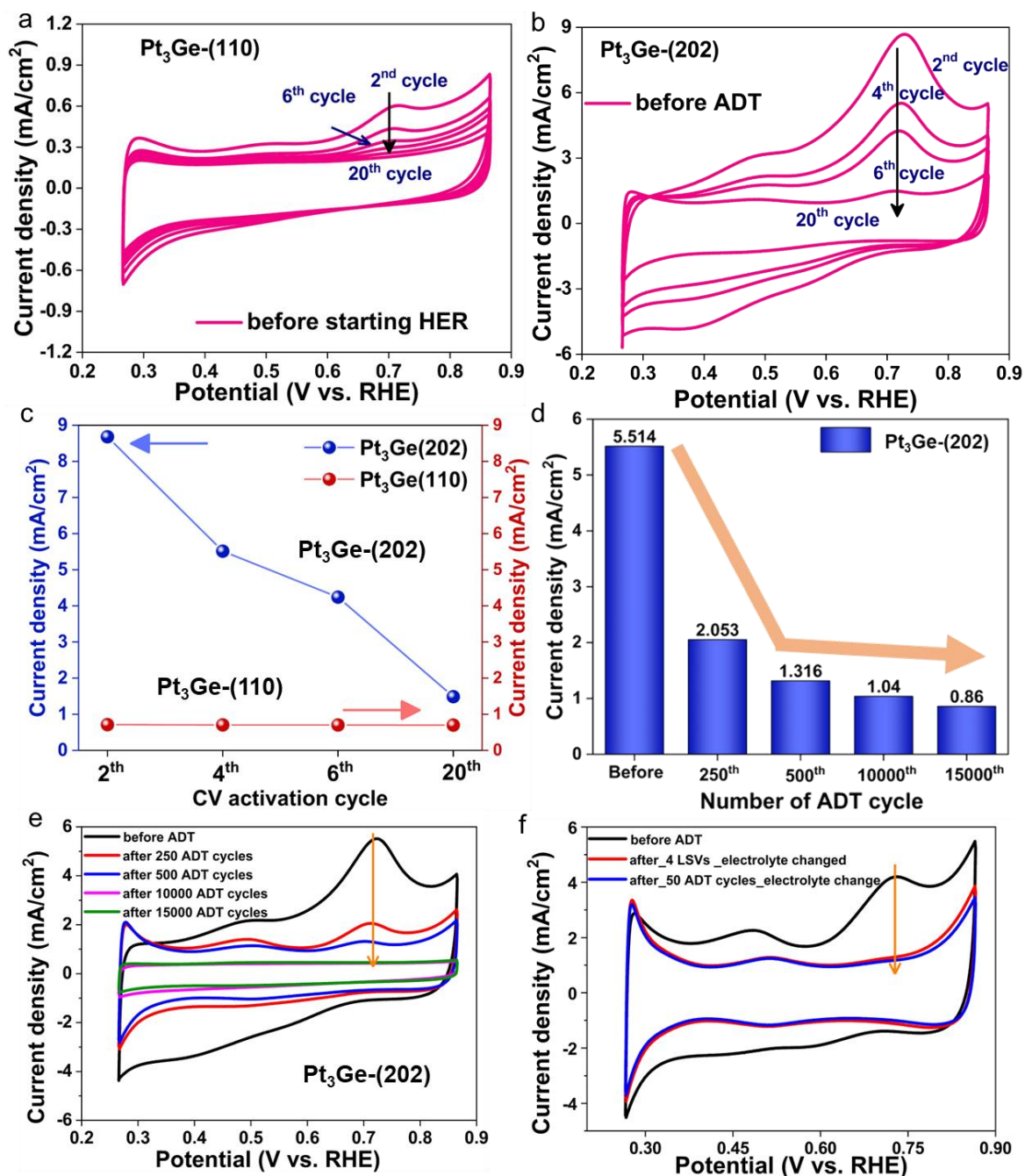


Figure 6.9. (a) Activation CVs of Pt₃Ge-(110) after each cycle. (b) Activation CVs of Pt₃Ge-(202) after each cycle. (c) Comparison of current density corresponding to Ge leaching for both catalysts during activation CVs as in fig (a) and (b) for Pt₃Ge-(202) and Pt₃Ge-(110). (d) Current density comparison for different activation CVs before and after ADT cycles in HER potential range of Pt₃Ge-(202). (e) Activation CVs (2nd CV taken) of Pt₃Ge-(202) before and after different ADT cycles. (f) Activation CVs of Pt₃Ge-(202) before and after different changing solution containing leached Ge after activation cycles.

These two factors drive the selective dissolution of Ge from the Pt₃Ge₂ phase which leads to the operando disruption of Pt₃Ge₂, leading to the formation of pure Pt₃Ge phase.

With increasing cycles, the peak intensity of CV curve corresponding to Ge oxidation decreases (**Figures 6.9a and 6.9b**), indicating majority of the Ge atoms at the surface are leached in the first few cycles. The absence of any Ge oxidation peak at the 20th cycle confirms no further dissolution of Ge. As seen in **Figure 6.9c** (derived from **Figures 6.9a and 6.9b**), Ge leaching process is predominant in the case of Pt₃Ge-(202) with a substantial drop of current density from 9 to 1 mA/cm², which is negligible in the case of Pt₃Ge-(110). However, after a prolonged period of HER CVs, leached Ge re-deposit on the surface during the reduction process. This leaching and re-depositing processes continue and finally stop completely after 15,000 cycles of ADT confirming absence of any oxidizable Ge present at the surface (**Figure 6.9d and 6.9e**). This signifies that surface reconstruction takes place during the HER conditions for first few cycles. This surface stabilizes the HER kinetics which is reflected in 500 h stability during CA. The dissolved Ge in the electrolyte was verified by ICP-OES (**Figure 6.4d and 6.4e**). There might arise confusion whether the oxidation peak corresponding to Ge cation formation or GeO/GeO₂ formation on the surface of the catalyst. To verify this, an electrochemical control experiment was conducted where just after 20 activation CVs in the non-Faradaic region, the electrolyte was taken out and fresh electrolyte was added. In the fresh electrolyte, a few LSVs were run in the reduction potential range. Then, again some activation CVs were run, where the oxidation peak was no more observed. This confirms that it the dissolution of Ge as Ge cations into the electrolyte, some of which were getting re-deposited on cathode under reduction potential of HER. **Figure 6.9f** illustrates this observation. **Figure 6.10** shows the ECSA normalized LSV of 20% Pt/C and Pt₃Ge-(202) catalysts which shows Pt₃Ge-(202) is better with respect to specific activity.

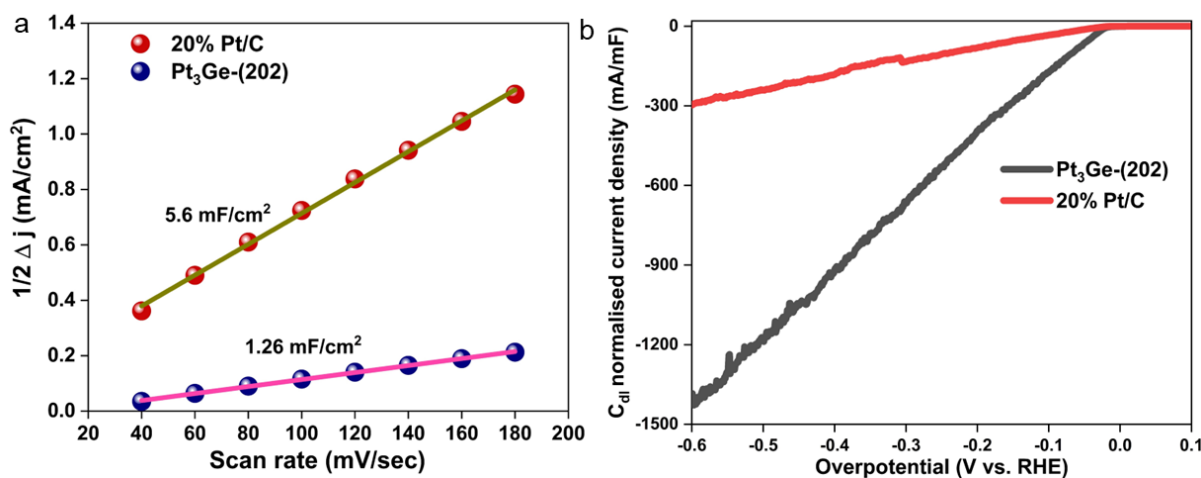


Figure 6.10. (a) C_{dl} plots for Pt₃Ge-(202) and 20% Pt/C. (b) LSV normalized by double layer capacitance value (ECSA).

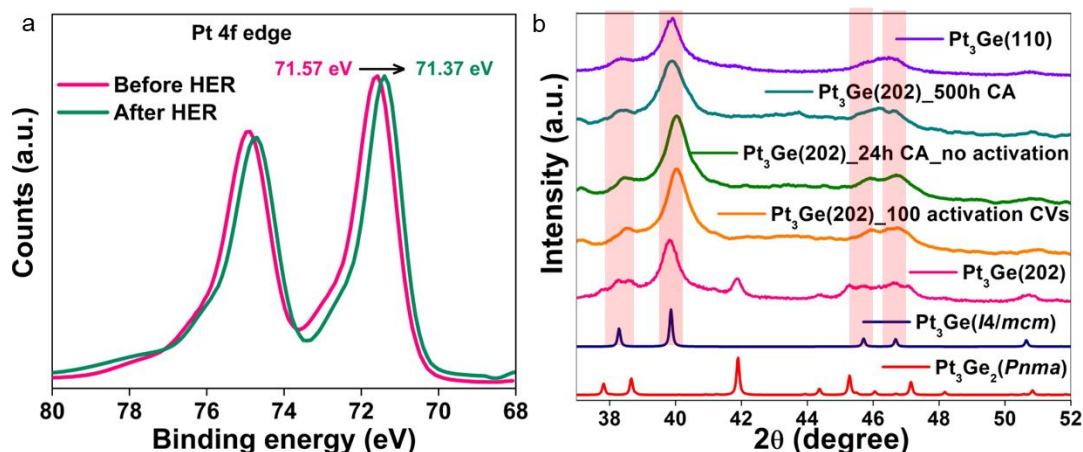


Figure 6.11. (a) Post-HER Pt 4f XPS spectra of $\text{Pt}_3\text{Ge}-(202)$. (b) Post-HER PXRD pattern comparison for $\text{Pt}_3\text{Ge}-(202)$.

Post-HER X-ray photoelectron spectroscopy (XPS) provides a downshift of binding energy of Pt 4f edge (**Figure 6.11a**), which indicates that notable charge transfer from Ge to Pt takes place leading to Ge leaching and faster electron transfer from Pt to H^+ . Further verification of conversion of dual-phase compound to single phase Pt_3Ge has been done by post-HER PXRD (**Figure 6.11b**). The control studies have been performed where the XRD data was taken on the catalyst which were exposed to a) oxidation potential for 100 activation CVs, b) 24 h CA without any activation (no oxidation potential experienced), and c) 500 h CA with activation. All these three conditions steer the catalyst to reach a similar fate, which is nothing but a total collapse of the ‘sacrificial phase’ Pt_3Ge_2 and the operando generation of Pt_3Ge single phase with (202) exposed facet. Germanium leaching was observed even in the absence of oxidation potential which confirms the inherent charge transfer from Ge to Pt during HER.

6.4.2 Driving forces for accelerated HER

6.4.2.1 Charge transfer

As mentioned in the previous section, the selective dissolution of Ge and accelerated hydrogen production have been originated through the charge transfer from Ge to Pt. To map it in depth, X-ray absorption (XAS) (**Figures 6.12a, 6.12c, 6.13** and **Table 6.5**) and XPS (**Figure 6.12b, 6.12d**) techniques have been employed. Pt L_{III} edge X-ray absorption Near Edge spectra (XANES) represented in **Figure 6.12a** provide the oxidation state of Pt in the order of Pt foil < $\text{Pt}_3\text{Ge}-(202)$ < $\text{Pt}_3\text{Ge}-(110)$. This trend is well corroborated in the Pt 4f edge XPS spectra (**Figure 6.12b**). $\text{Pt}_3\text{Ge}-(202)$ XPS fitted spectra shows Pt has slightly high binding energy due to Pt-Ge charge separation and a slight amount of PtO present as surface oxide (**Figure S18b**).⁶² Lower oxidation state of Pt in $\text{Pt}_3\text{Ge}-(202)$ depicts that the charge transfer

(electron transfer)⁶³ from Ge to Pt is significant in the case of Pt₃Ge-(202) (**Figure 6.12b**). The electron transfer from Ge to Pt is playing a crucial role in enhancing the HER kinetics because the electron-donation to H⁺ by Pt sites is significantly more than elemental Pt. The R-space data shows Pt-Pt and Pt-Ge bond lengths at relevant positions with no Pt-oxides present in the bulk.

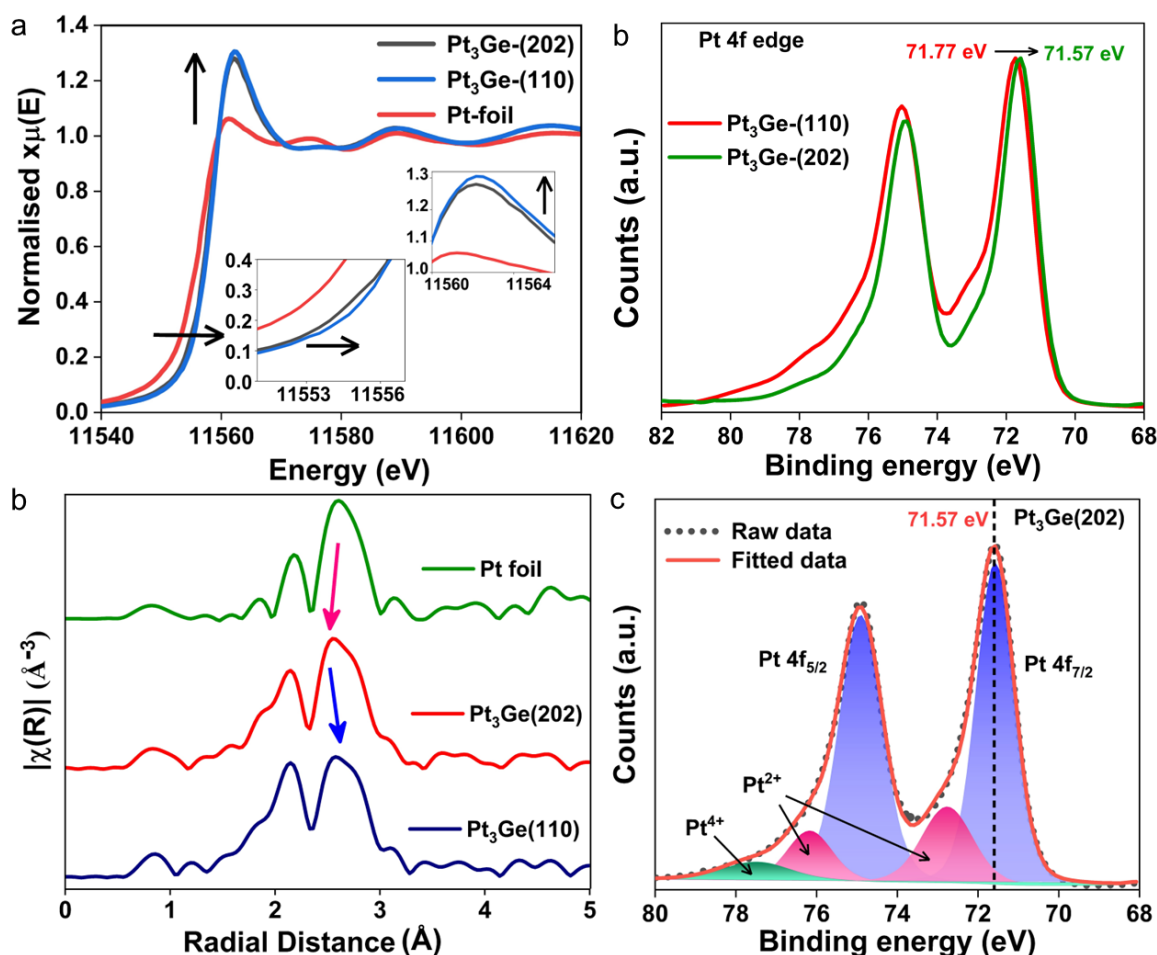


Figure 6.12. (a) The normalized Pt *L*_{III} edge XANES spectra of Pt₃Ge-(110), Pt₃Ge-(202) and Pt foil. The insets show the zoomed-in images of the white line intensity and absorption edge. (b) XPS of Pt 4f edge for Pt₃Ge-(202) and Pt₃Ge-(110). (a) The normalized Pt K-edge XANES spectra of Pt₃Ge-(110), Pt₃Ge-(202) and Pt foil. The insets show the zoomed-in images of the white line intensity and absorption edge. (b) Fitted plots of Pt 4f XPS data of both catalysts.

Table 6.5. EXAFS fitting parameters obtained from R-space data fitting for Pt k-edge for Pt₃Ge-(110) and Pt₃Ge-(202).

Catalyst	Path	CN	E ₀	ΔR	R _{eff}	R
Pt ₃ Ge-(110)	Ge.1	0.75	5.468	0.0302	2.4639	2.4941
	Pt1.1	5.75	5.468	-0.0674	2.8258	2.7583
Pt ₃ Ge-(202)	Ge.1	1.5	5.355	0.0514	2.4639	2.5153
	Pt1.1	5.025	5.355	-0.0566	2.8258	2.7691

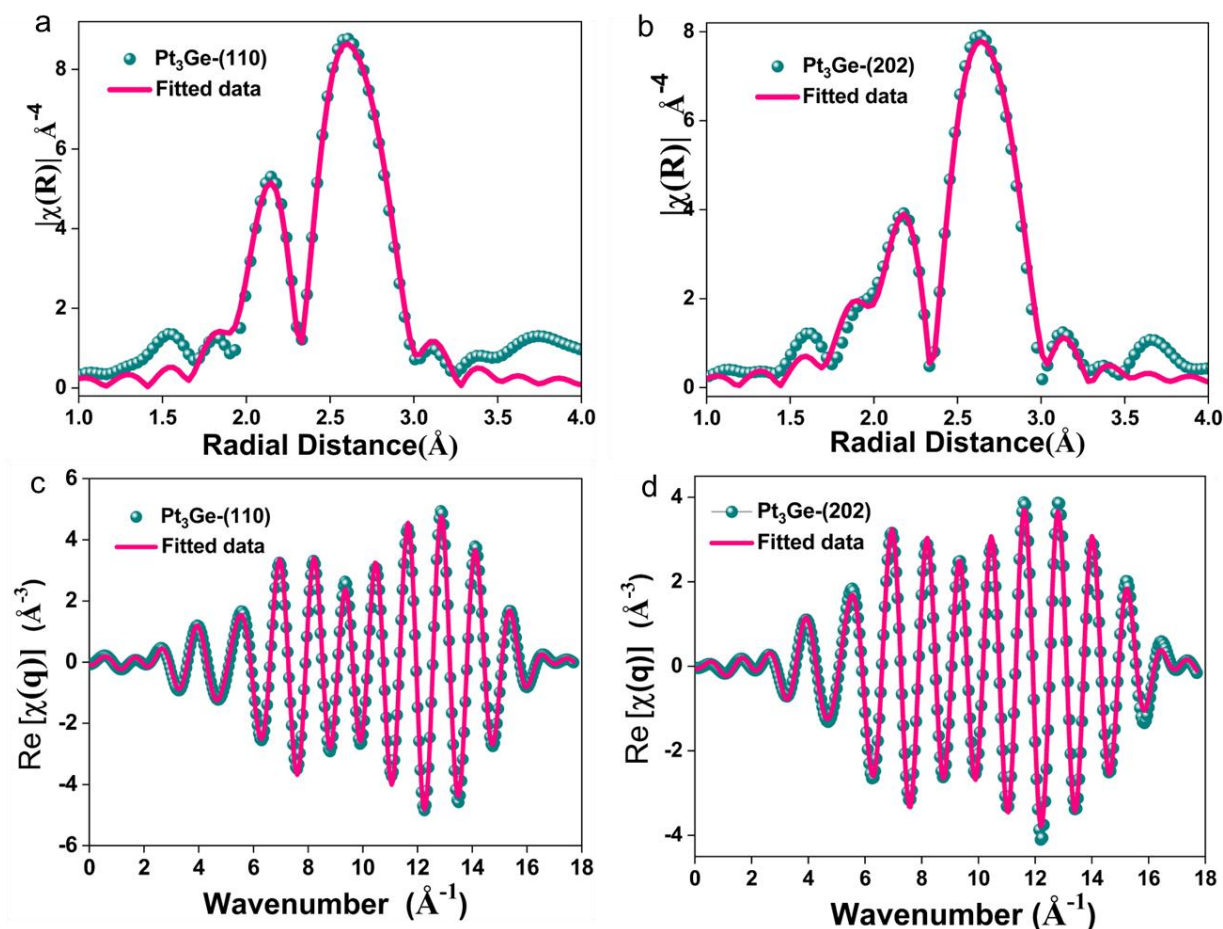


Figure 6.13. Fourier-Transformed R-space and k-space fitted data of Pt₃Ge-(110) (in a and c) and Pt₃Ge-(202) (in b and d) catalysts.

The peak corresponding to Pt-Pt bond length is slightly shifted to a smaller distance than Pt foil indicating bond contraction, which is due to the observed higher oxidation state of Pt in Pt₃Ge than elemental Pt.⁶⁴ Pt-Pt and Pt-Ge bond distances in Pt₃Ge(202) are slightly larger than that in Pt₃Ge-(110) attributed to the less oxidation state of Pt in Pt₃Ge-(202) than Pt₃Ge-(110) (Table 6.5).

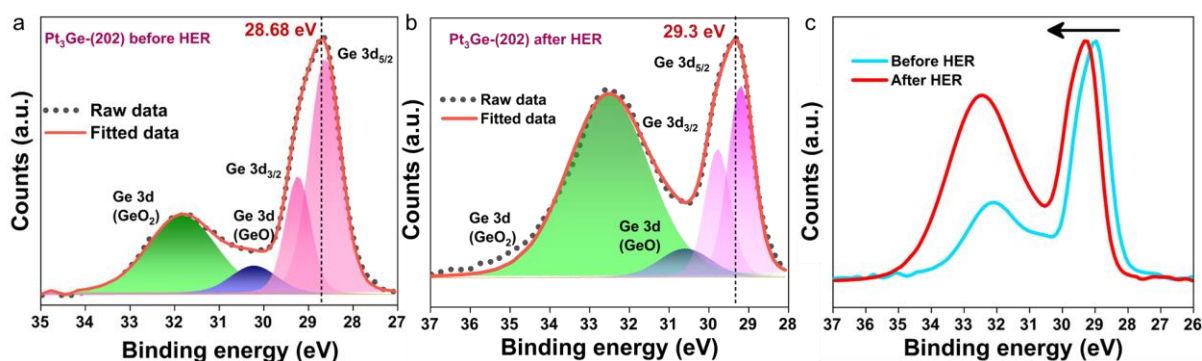


Figure 6.14. XPS fitting for Ge 3d orbitals of Pt₃Ge-(202) before and after HER.

As obtained from XAFS, the coordination number of Ge around Pt is more in Pt₃Ge-(202) compared to Pt₃Ge-(110) which is justified from the fact that (202) facet contains both Pt and Ge atoms and facet (110) has only Pt atoms (**Figure 6.1b** and **Table 6.5**). **Figure 6.14** shows the Ge 3d XPS spectra before and after HER which shows that Ge sites are undergoing oxidation during HER. This again confirms the charge transfer from Ge to Pt during HER (**Figure 6.11a** shows about Pt 4f XPS).

6.4.2.2 Electronic structure tuning

To further elucidate the detailed mechanism of one facet yielding better catalytic activity compared to other we have theoretically predicted the HER activity using first principles density functional (DFT) calculation. **Figure 6.15** depicts the optimized slab models of Pt₃Ge with exposed (110) and (202) surfaces along with adsorbed hydrogen used throughout the calculation. The (110) plane consists of four Pt₃Ge units with 12 Pt and 4 Ge atoms while 202 contains 18 Pt and 6 Ge atoms. Both the planes have mixed termination with Pt and Ge atoms residing at the surface. To check the thermodynamic stability of both the planes we have determined their formation energy (E_f) as per the following equation:

$$E_f = E(\text{Pt}_3\text{Ge}) - m\mu_{\text{Pt}} - n\mu_{\text{Ge}},$$

where $E(\text{Pt}_3\text{Ge})$ is the DFT calculated ground state energy of the corresponding plane and μ_{Pt} and μ_{Ge} denote the respective chemical potentials of Pt and Ge atoms and m , n are the numbers of the corresponding atoms present in the slab model. For calculating the chemical potentials of Pt and Ge their naturally occurring bulk states are taken as the reference states. The calculated values show, the (202) plane is thermodynamically more stable compared to (110) which in turn supports that stability of the experimentally synthesized Pt₃Ge catalyst with stable exposed (202) facet. To have a profound understanding of the electronic properties of the two facets, we have calculated their partial density of states (PDOS) along the projections on Pt and Ge sites. In order to explore the thermodynamic stability of (202) facet with some Ge atoms removed, we have considered one of the most important cases of vacancy induced defect in the Pt₃Ge surface along (202) direction, while removing the terminating Ge atom from the surface along (202) direction. After obtaining the minimum energy configuration with the lowest energy, we have determined the corresponding formation energy for the Ge vacancy induced defect in (202) facet of Pt₃Ge as 2.91 eV.

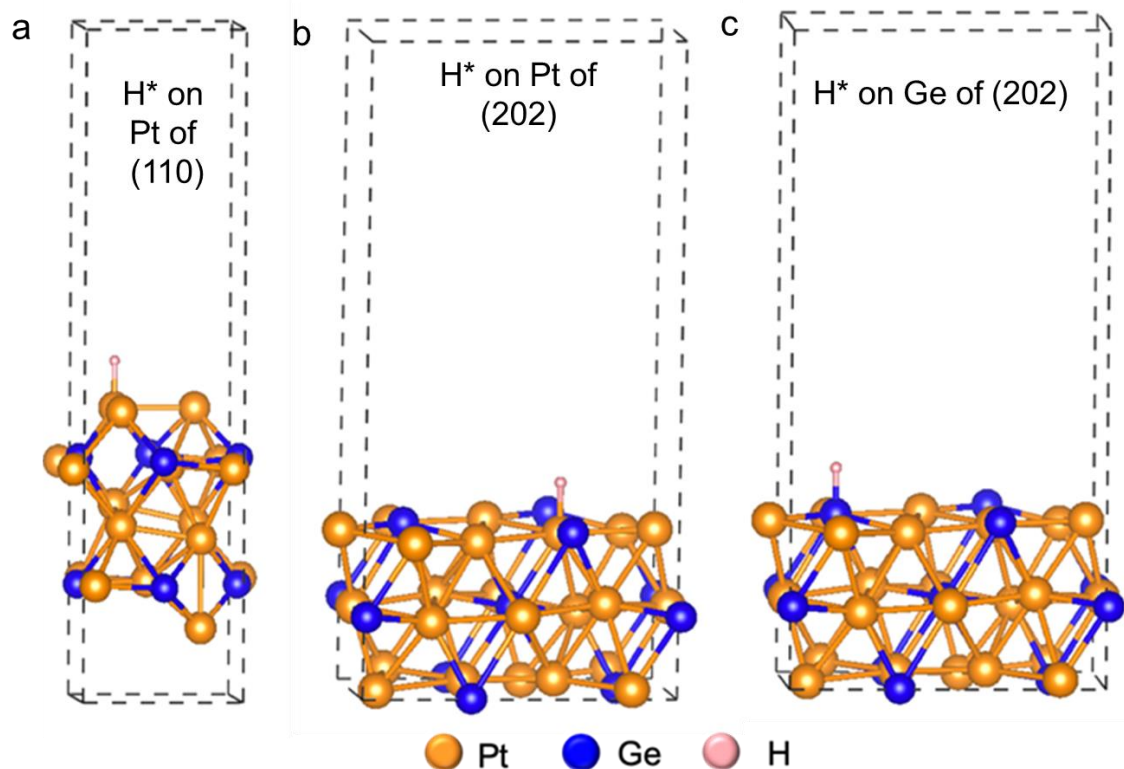


Figure 6.15. The minimum energy configurations of H atom adsorbed on top of Pt and Ge sites in (110) and (202) terminated Pt_3Ge catalyst.

Table 6.6 shows that the formation energy for (202) facet is negative value for the pristine phase where no Ge deficiency was created. This confirms that the Ge vacancy at the surface will lead to instability in the Pt_3Ge along its growth in (202) direction as compared to the pristine counterpart (without Ge deficiency) and therefore, we can theoretically support the fact that by increasing Ge content (Pt:Ge ration from 3:1 to 1:1) we get a stabilized (202) facet which is having a positive formation energy value when Ge vacancies are present in (202) facet. This confirms and establishes the formation mechanism of selective (202) facet formation during synthesis when more Ge were taken.⁶⁵ As we can observe from **Figure 6.16a** and **b**, electronic property of both the facets is mainly governed by Pt. A careful observation (as in **Figure 6.16c**) reveals that near the Fermi region the states are higher in case of (202) plane compared to (110).

Table 6.6. Formation energy (E_f), Hydrogen adsorption energy and free energy values on different crystallographic plane of Pt_3Ge catalyst.

Plane	E_f (eV)	Adsorption site	E_{ads}^H (eV)	ΔG_H
110	-4.5	Pt	-0.51	-0.27
202	-7.67	Ge	0.53	0.77
		Pt	-0.45	-0.21

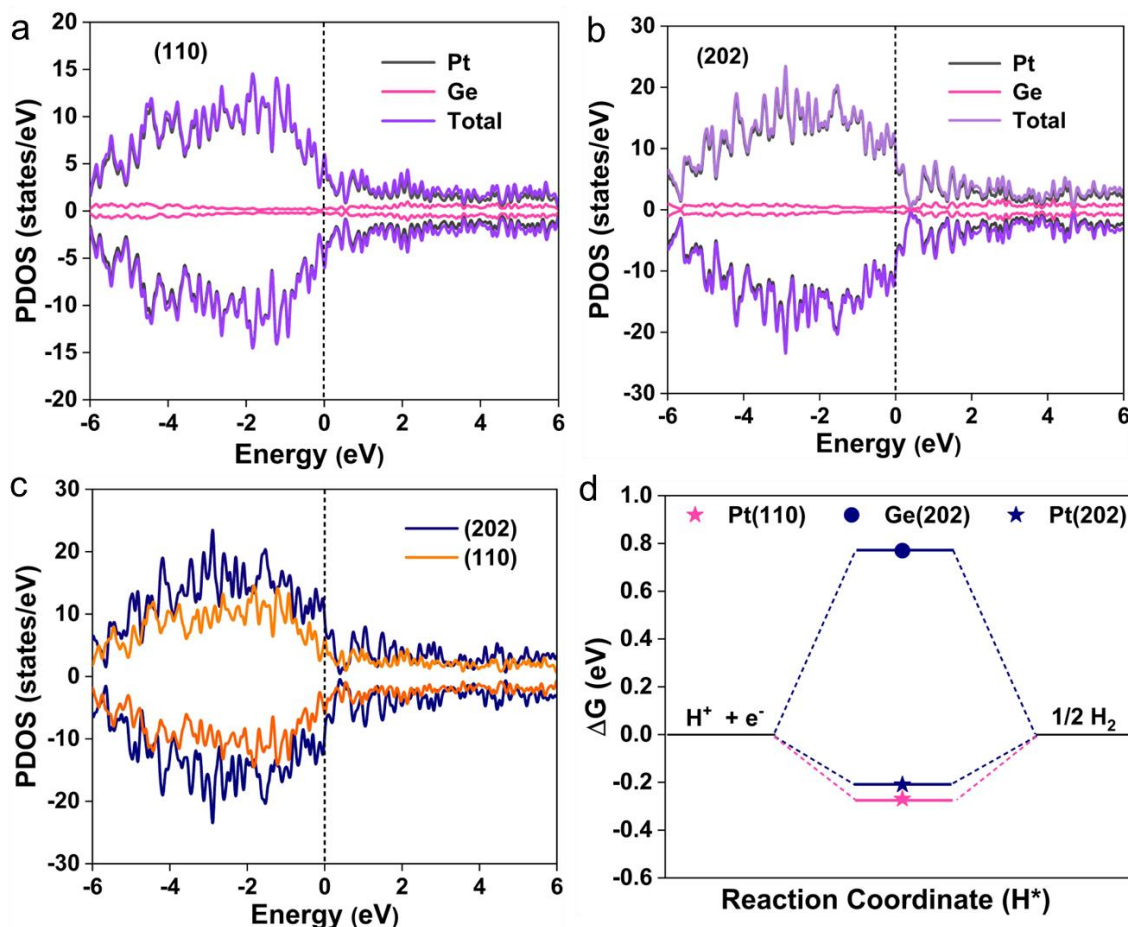


Figure 6.16. Total and partial density of states (a) for (110) and (b) (202) -terminated Pt₃Ge surface. (c) PDOS for Pt₃Ge-(202) and Pt₃Ge-(110). (d) Energy profile diagram for H* adsorption on various sites of (110) and (202) facets of Pt₃Ge.

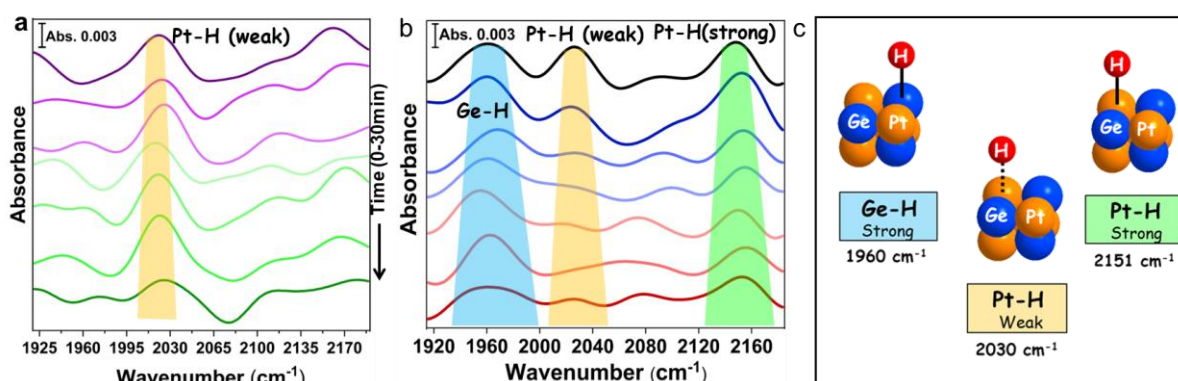


Figure 6.17. In-situ ATR FTIR for (b) Pt₃Ge-(110) and (b) Pt₃Ge-(202) during CA for 30 mins at -0.3 V vs. RHE 0.5M H₂SO₄. (f) Different binding modes of hydrogen on Pt and Ge and their respective stretching frequencies.

This indicates the probability of having a greater number of electrons in the former case which showed better HER performance. To conduct detailed analysis of facet-selective HER activity, free energy of H* adsorption on different sites of (110) and (202) facets were calculated (**Figure 6.16d** and **Table 6.6**) illustrating H* adsorption on Pt of (110) and (202)

are exothermic with ΔG_{H^*} values of -0.27 and -0.21 eV, respectively. More optimum binding is expected on Pt atoms of (202) facet due to ΔG_{H^*} close to 0 which leads to easy desorption of H_2 from the surface.⁶⁶ A ΔG_{H^*} value of 0.77 eV for Ge site on (202) facet facilitates easy breaking of Ge-H bond leading to faster kinetics.

6.4.2.3 Mechanistic pathway

The enhanced performance of Pt_3Ge -(202) compared to the commercial Pt/C can be explained if the mechanism of the HER can be mapped in *operando* condition. In-situ Attenuated Total Reflection-Fourier Transform Infrared Spectroscopy (ATR-FTIR) measurements (**Figure 2.1b, Chapter 2**) have been performed to probe Ge-H bonding⁶⁷ along with highly probable Pt-H bonding (**Figure 6.17a and 6.17b**).^{68, 69} It is already reported in the literature that Pt-H^{68, 69} and Ge-H^{49, 67} bonds show a stretching frequency at 2030-2150 cm^{-1} and 1960 cm^{-1} , respectively (**Figure 6.17c**). Pt_3Ge -(110) shows a prominent peak at 2030 cm^{-1} corresponding to Pt-H bond stretching vibration. Whereas, Pt_3Ge -(202) shows prominent peaks at 1960 cm^{-1} and 2151 cm^{-1} corresponding to stretching vibrations of Ge-H and Pt-H bonds, respectively. Notably, peaks at 1960 cm^{-1} were totally absent in case of Pt_3Ge -(110) (**Figure 6.17a**) indicating that Ge atoms are not exposed in Pt_3Ge -(110), which is in perfect agreement with the crystal structure of Pt_3Ge (**Figure 6.1b**). This exposure of Ge in Pt_3Ge -(202) is the driving force for the accelerated hydrogen production as it contributes to H-adsorption along with Pt.

6.4.2.4 Probing catalyst structure during reaction

Figure 2.1a (in Chapter 2) shows the cell set-up for in-situ XAS measurements. It is clearly observed from in-situ XANES spectra of Pt *LIII* edge that oxidation state of Pt is decreasing with increasing time during HER (**Figure 6.18a**). R-space data for Pt *LIII* edge shows an interesting trend of increment of Pt-Pt bond distance and decrease of Pt-Ge bond distance (**Figure 6.18b**). Whereas the oxidation state for Ge edge is increasing with time during CA at a reducing potential (**Figure 6.18c**). We can infer the charge transfer from Ge to Pt from the XANES spectra. From close observation of the inset images of XANES spectra for both edges, it is found that the change in oxidation state is very prominent in first few minutes, and the change stopped after some time (after approx. 12 mins for Pt and 18 mins for Ge), which indicates that the structural modifications occur at the first instant of HER, then the structural reconstruction ceases and Ge leaching also stops after attaining a stable structure. R-space data for Pt *LIII* edge (**Figure 6.18b**) supports that Pt-Ge bond contraction occurs due to increase oxidation state of Ge and Ge leaching can also shorten the bond length. The *operando* XAS

study finally confirms all other observations from electrochemical control experiments (Ge leaching, increasing activity after some time of CA), ICP-OES measurements showing no Pt leaching but only Ge leaching which stops after some time.⁷⁰

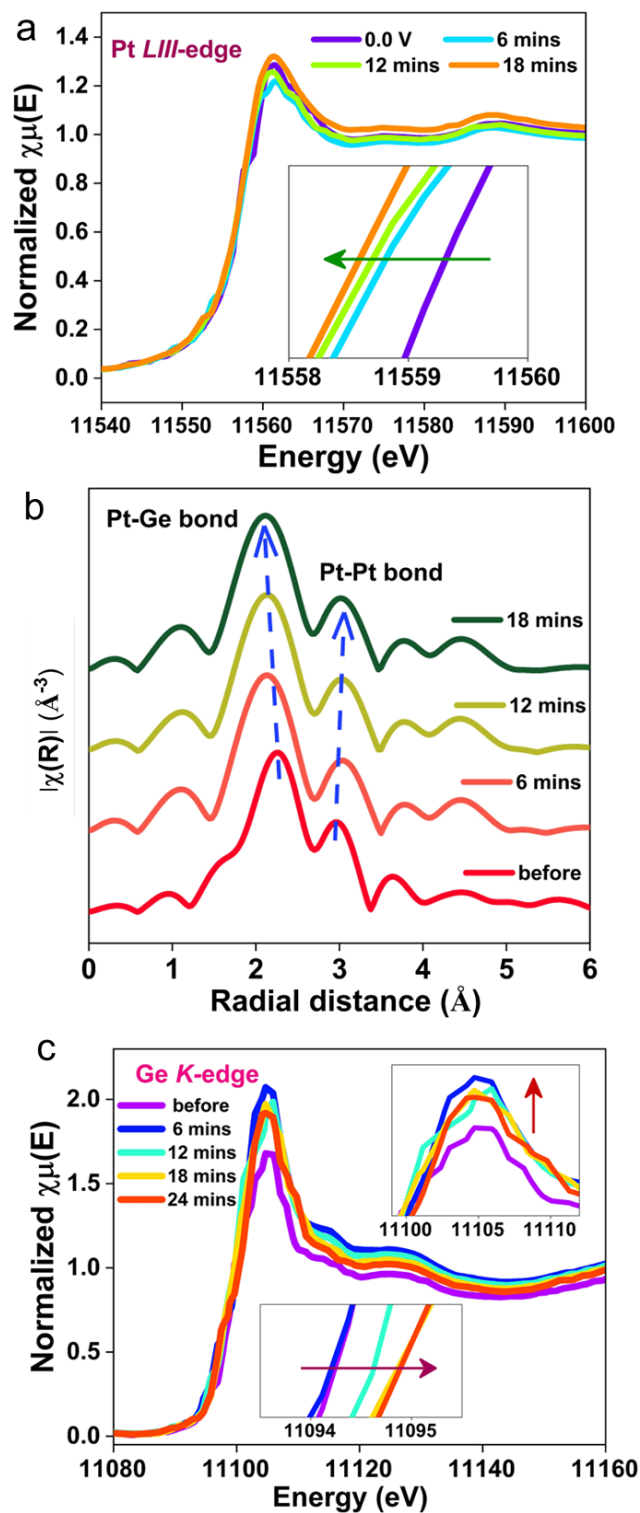


Figure 6.18. (a) Pt *LIII*-edge XANES spectra during operando HER conditions. (b) Fourier transformed R-space data for Pt edge during HER. (c) Ge *K*-edge XANES spectra measured during HER.

It is understood why the current density of our catalyst during a CA (both acidic and alkaline media) shows an enhancement of current density just after some time of CA. The schematic of the HER mechanism derived from the in-situ ATR FTIR studies is shown in **Figure 6.19**. **Figure 6.20** shows how the catalyst retains its well dispersed spherical morphology, its size and also the exposed facet (202).

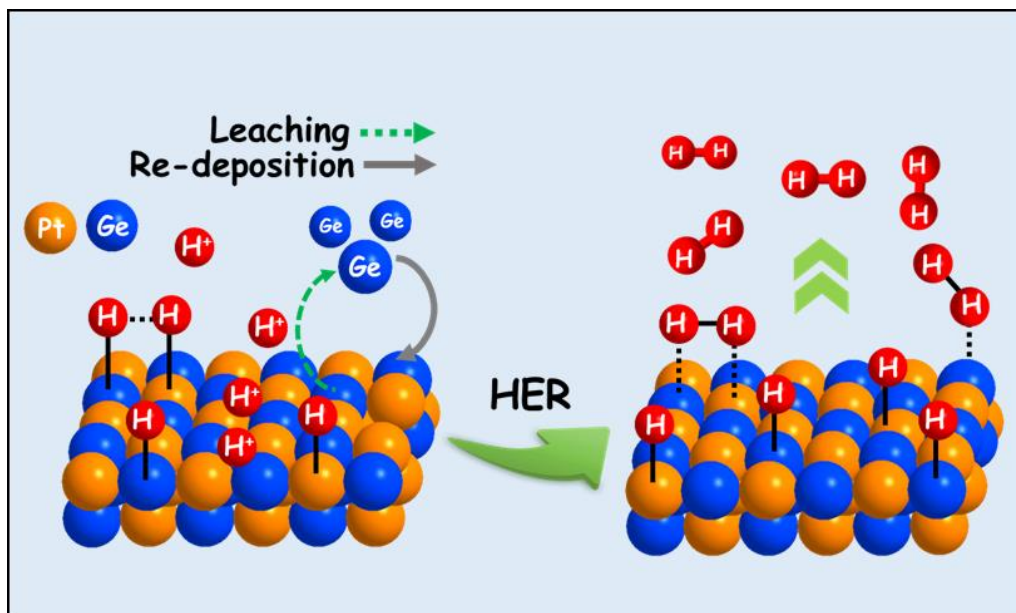


Figure 6.19. Schematic for reaction mechanism derived from in-situ IR and in-situ XAS.

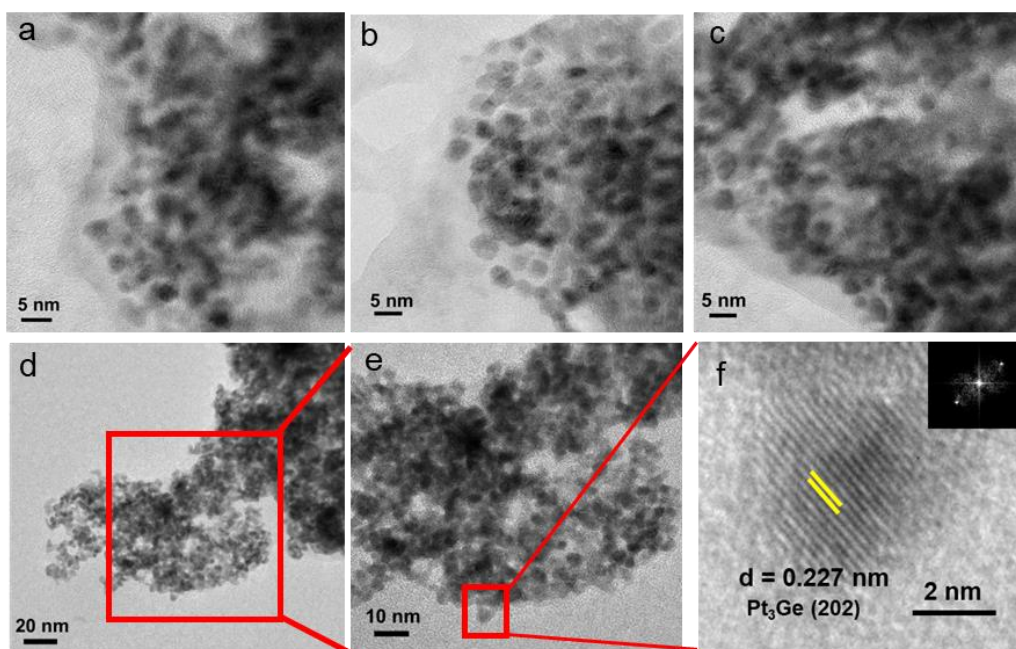


Figure 6.20. Post-activation TEM and HR-TEM images of Pt₃Ge-(202). Fig. f shows the d-spacing corresponding to the exposed lines indicate exposed (202) facet of Pt₃Ge. Inset shows the FFT pattern.

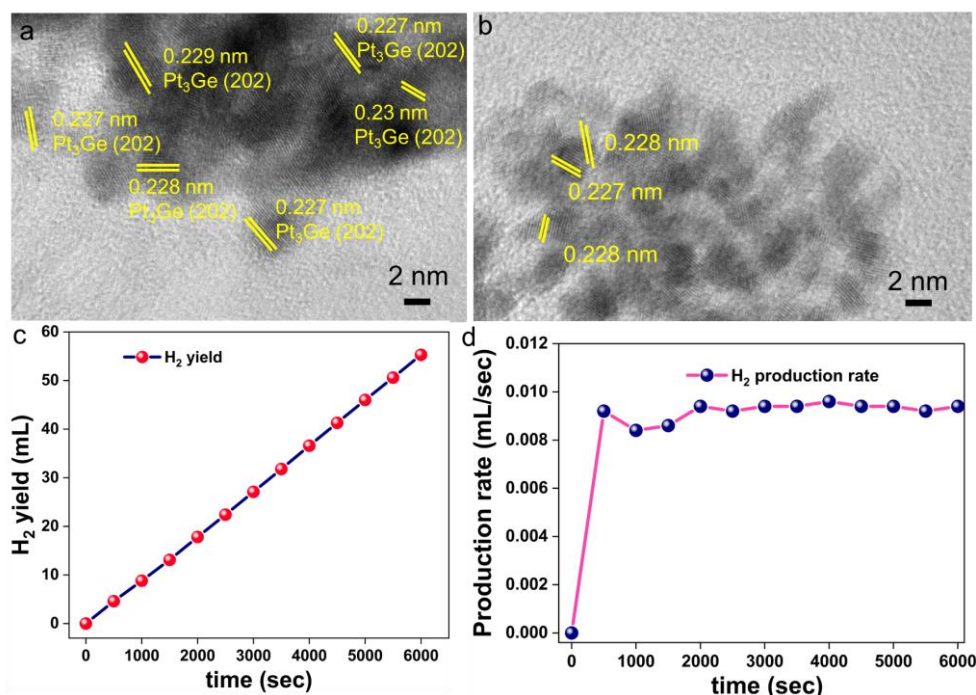


Figure 6.21. (a-b) Post-activation HR-TEM images of Pt₃Ge-(202). Hydrogen production was quantified during CA being run for 6000 secs. (c) Yield after every instant. (d) Production rate at every seconds.

This strongly suggests that the catalyst structure does not change after extensive HER and thus is highly stable. **Figure 6.21a,b** shows the wide region HRTEM image indexing after HER, showing that after HER Pt₃Ge₂ phase completely destroyed and leaving behind only (202) facets of Pt₃Ge. Hydrogen quantification performed using inverse burette method confirms the efficient production of hydrogen by Pt₃Ge-(202) (**Figure 6.21c,d**).

6.5 Conclusion

In conclusion, a new hydrogen production catalyst, Pt₃Ge-(202), has been discovered using a novel synthetic approach. To the best of our knowledge, this is the first ever material holding all Fabulous Five properties ((1) Onset potential, (2) current density, (3) Tafel slope value, (4) stability in wide pH range and (5) industrial standard durability better than the state-of-the-art commercial Pt/C for the industrial standard production of hydrogen (**Figure 6.22a**). The synthetically tuned Pt₃Ge-(202) surpasses the onset potential of Pt and excellent stability having much lower onset potential and faster kinetics compared to all other Pt-based catalysts reported in the literature (**Figure 6.22b, Table 6.7**). Finally, the industrial production of hydrogen has been demonstrating using a flow cell in alkaline media, which demonstrated that the catalyst Pt₃Ge-(202) shows long term durability for 75 h when done at 500 mA/cm² current density. A comparison provided in **Table 6.8** clearly confirm that the combination of all the Fab-Five parameters is indeed impossible in a single material and our catalyst stands out as the

near-ideal material for industrial production of hydrogen. The mechanism and charge transfer kinetics of HER on Pt₃Ge-(202) is clearly manifested by in-situ IR and XAS measurements and theoretical calculations.

Table 6.7. Comparison of the electrocatalytic HER performance of Pt₃Ge-(202) (reported here) under acidic medium with some efficient precious-metal based HER catalysts that have been recently reported in the same medium.

Catalysts	Electrolyte	η_{10} (mV)	Tafel (mV/dec)	Stability	Ref
Pt ₃ Ge-(202)	0.5 M H ₂ SO ₄	21.7	30.25	>15000, 500h	This work
IM-Pt ₂ Si-MS	0.5 M H ₂ SO ₄		30.5		81
Pt ₃ Ge	0.5 M H ₂ SO ₄	53	37		71
Pt/NPC	0.5 M H ₂ SO ₄	27	28		72
Mo ₂ C@C@Pt	1.0 M phosphate buffer	25	33		73
PteTiN NAs	0.5 M H ₂ SO ₄	39.7	38.6		74
Pt/GNs	0.5 M H ₂ SO ₄	25	33	3000	75
Pt/LSG	0.5 M H ₂ SO ₄	131	72		82
Pt-SnS ₂	0.5 M H ₂ SO ₄	117	69	2000	83
PtO PdONPs@Ti ₃ C ₂ T _x	0.5 M H ₂ SO ₄	26.5	39	1000	76
Pt@DNA	0.5 M H ₂ SO ₄	26	30		77
Pt NCs	0.5 M H ₂ SO ₄	42	101		78
Pt ₁ @Fe-N-C	0.5 M H ₂ SO ₄	60	42		84
Pd/Cu-Pt	0.5 M H ₂ SO ₄	22.8	25		79
Pt ₁ O ₂ C ₁	0.5 M H ₂ SO ₄	38	36		80
Mo ₂ TiC ₂ T _x -PtSA	0.5 M H ₂ SO ₄	30	30		28
Pt SASs/AG	0.5 M H ₂ SO ₄	12	29.33	2000	85
HCS-N-Pt	0.5 M H ₂ SO ₄	15	22	3000	86
PtCu/CB	0.5 M H ₂ SO ₄	10	29.72	1000	87
K ₂ PtCl ₄ @NC-M	0.5 M H ₂ SO ₄	11	21	40 h	34
[Ru(SA)+Ru(NP)@RuN _x @GN]/GN	0.1 M HClO ₄	31	28	10,000 cycles	33
Pt-GT-1	0.5 M H ₂ SO ₄	18	24	10000 cycles	16

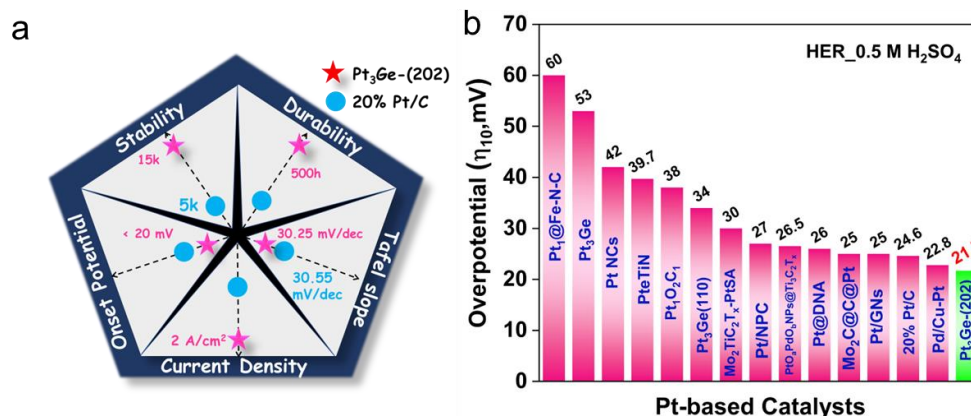


Figure 6.22. (a) The comparison of Fab-five parameters of Pt₃Ge-(202) with commercial 20% Pt/C. (b) Comparison (overpotential values at current density of 10 mA/cm²) of HER performance in acidic media of different Pt-based catalysts reported in literature with that of Pt₃Ge-(202) ^{28, 31, 71-80}.

Table 6.8. Comparison of the electrocatalytic HER performance of Pt₃Ge-(202) (reported here) under acidic medium with some efficient HER catalysts that have been recently reported in the same medium having excellent activity w.r.t some of the criteria among Fab-Five.

Sl. No.	Catalyst	Overpotential (For mA/cm ²)	Current density	Tafel slope (mV/dec)	Stability (ADT cycles)	durability	Ref.
1.	Pt-GT-1	18.4 mV(10)		24	10,000		16
2.	2H Nb _{1.35} S ₂	100 mV (onset)	1 A/cm ² (0.37 V)	40	10,000		11
3.	Pt ₁ /OLC	38 mV (10)		36	6,000	100 h	80
4.	MoS ₂ /Mo ₂ C		1 A/cm ² (0.227 V)	53	10,000	24 h	88
5.	MoS ₂ /Ni ₃ S ₂ NW-NF		1 A/cm ² (0.2 V)	58.9	2000	12 h	89
6.	NC/Ni ₃ Mo ₃ N/NF	44.6 mV (10)	1.5 A/cm ² (0.95 V)	41.5		50 h	90
7.	Mo ₂ TiC ₂ T _x -Pt _{SA}	30 mV (10)	200 mA/cm ² (0.104 V)	30	10,000	100 h	28

6.6 References

- Adams, J. A. S.; Mantovani, M. S. M.; Lundell, L. L., Wood Versus Fossil Fuel as a Source of Excess Carbon Dioxide in the Atmosphere: A Preliminary Report. *Science* **1977**, *196*, 54.
- Balat, M., Potential importance of hydrogen as a future solution to environmental and transportation problems. *Int. J. Hydrog. Energy* **2008**, *33*, 4013-4029.
- Wu, B.; Matian, M.; Offer, G. J., Hydrogen PEMFC system for automotive applications. *Inter. J. Low-Carbon Technol.* **2012**, *7*, 28-37.

4. Roy, S.; Cherevotan, A.; Peter, S. C., Thermochemical CO₂ Hydrogenation to Single Carbon Products: Scientific and Technological Challenges. *ACS Energy Lett.* **2018**, *3*, 1938-1966.
5. Hattori, M.; Iijima, S.; Nakao, T.; Hosono, H.; Hara, M., Solid solution for catalytic ammonia synthesis from nitrogen and hydrogen gases at 50 °C. *Nat. Commun.* **2020**, *11*, 2001.
6. Bellotti, D.; Rivarolo, M.; Magistri, L.; Massardo, A. F., Feasibility study of methanol production plant from hydrogen and captured carbon dioxide. *J. CO₂ Util.* **2017**, *21*, 132-138.
7. Tucker, W. C.; Chowdhury, P.; Abbott, L. J.; Haskins, J. B., Toward an In-Depth Material Model for Cermet Nuclear Thermal Rocket Fuel Elements. *Nucl. Technol.* **2021**, 1-11.
8. Okolie, J. A.; Patra, B. R.; Mukherjee, A.; Nanda, S.; Dalai, A. K.; Kozinski, J. A., Futuristic applications of hydrogen in energy, biorefining, aerospace, pharmaceuticals and metallurgy. *Int. J. Hydrog. Energy* **2021**, *46*, 8885-8905.
9. Rochlitz, L.; Steinberger, M.; Oechsner, R.; Weber, A.; Schmitz, S.; Schillinger, K.; Wolff, M.; Bayler, A., Second use or recycling of hydrogen waste gas from the semiconductor industry - Economic analysis and technical demonstration of possible pathways. *Int. J. Hydrog. Energy* **2019**, *44*, 17168-17184.
10. Yu, K. M. K.; Tong, W.; West, A.; Cheung, K.; Li, T.; Smith, G.; Guo, Y.; Tsang, S. C. E., Non-syngas direct steam reforming of methanol to hydrogen and carbon dioxide at low temperature. *Nat. Commun.* **2012**, *3*, 1230.
11. Yang, J.; Mohmad, A. R.; Wang, Y.; Fullon, R.; Song, X.; Zhao, F.; Bozkurt, I.; Augustin, M.; Santos, E. J. G.; Shin, H. S.; Zhang, W.; Voiry, D.; Jeong, H. Y.; Chhowalla, M., Ultrahigh-current-density niobium disulfide catalysts for hydrogen evolution. *Nat. Mater.* **2019**, *18*, 1309-1314.
12. King, L. A.; Hubert, M. A.; Capuano, C.; Manco, J.; Danilovic, N.; Valle, E.; Hellstern, T. R.; Ayers, K.; Jaramillo, T. F., A non-precious metal hydrogen catalyst in a commercial polymer electrolyte membrane electrolyser. *Nat. Nanotechnol.* **2019**, *14*, 1071-1074.
13. Mo, J.; Wu, S.; Lau, T. H. M.; Kato, R.; Suenaga, K.; Wu, T. S.; Soo, Y. L.; Foord, J. S.; Tsang, S. C. E., Transition metal atom-doped monolayer MoS₂ in a proton-exchange membrane electrolyzer. *Mater. Today Adv.* **2020**, *6*, 100020.

14. Ma, L.; Sui, S.; Zhai, Y., Investigations on high performance proton exchange membrane water electrolyzer. *Int. J. Hydrog. Energy* **2009**, *34*, 678-684.
15. Görgün, H., Dynamic modelling of a proton exchange membrane (PEM) electrolyzer. *Int. J. Hydrog. Energy* **2006**, *31*, 29-38.
16. Tiwari, J. N.; Sultan, S.; Myung, C. W.; Yoon, T.; Li, N.; Ha, M.; Harzandi, A. M.; Park, H. J.; Kim, D. Y.; Chandrasekaran, S. S.; Lee, W. G.; Vij, V.; Kang, H.; Shin, T. J.; Shin, H. S.; Lee, G.; Lee, Z.; Kim, K. S., Multicomponent electrocatalyst with ultralow Pt loading and high hydrogen evolution activity. *Nat. Energy* **2018**, *3*, 773-782.
17. Dotan, H.; Landman, A.; Sheehan, S. W.; Malviya, K. D.; Shter, G. E.; Grave, D. A.; Arzi, Z.; Yehudai, N.; Halabi, M.; Gal, N.; Hadari, N.; Cohen, C.; Rothschild, A.; Grader, G. S., Decoupled hydrogen and oxygen evolution by a two-step electrochemical–chemical cycle for efficient overall water splitting. *Nat. Energy* **2019**, *4*, 786-795.
18. Su, J.; Yang, Y.; Xia, G.; Chen, J.; Jiang, P.; Chen, Q., Ruthenium-cobalt nanoalloys encapsulated in nitrogen-doped graphene as active electrocatalysts for producing hydrogen in alkaline media. *Nat. Commun.* **2017**, *8*, 14969.
19. Kim, J.; Kim, H.; Lee, W.-J.; Ruqia, B.; Baik, H.; Oh, H.-S.; Paek, S.-M.; Lim, H.-K.; Choi, C. H.; Choi, S.-I., Theoretical and Experimental Understanding of Hydrogen Evolution Reaction Kinetics in Alkaline Electrolytes with Pt-Based Core–Shell Nanocrystals. *J. Am. Chem. Soc.* **2019**, *141*, 18256-18263.
20. Cao, Z.; Chen, Q.; Zhang, J.; Li, H.; Jiang, Y.; Shen, S.; Fu, G.; Lu, B.-a.; Xie, Z.; Zheng, L., Platinum-nickel alloy excavated nano-multipods with hexagonal close-packed structure and superior activity towards hydrogen evolution reaction. *Nat. Commun.* **2017**, *8*, 15131.
21. Chen, H.; Wang, G.; Gao, T.; Chen, Y.; Liao, H.; Guo, X.; Li, H.; Liu, R.; Dou, M.; Nan, S.; He, Q., Effect of Atomic Ordering Transformation of PtNi Nanoparticles on Alkaline Hydrogen Evolution: Unexpected Superior Activity of the Disordered Phase. *J. Phys. Chem. C* **2020**, *124*, 5036-5045.
22. Li, L.; Wang, S.; Xiong, L.; Wang, B.; Yang, G.; Yang, S., Surface-engineered mesoporous Pt nanodendrites with Ni dopant for highly enhanced catalytic performance in hydrogen evolution reaction. *J. Mater. Chem. A* **2019**, *7*, 12800-12807.

23. Yin, H.; Zhao, S.; Zhao, K.; Muqsit, A.; Tang, H.; Chang, L.; Zhao, H.; Gao, Y.; Tang, Z., Ultrathin platinum nanowires grown on single-layered nickel hydroxide with high hydrogen evolution activity. *Nat. Commun.* **2015**, *6*, 6430.
24. Wei, J.; Zhou, M.; Long, A.; Xue, Y.; Liao, H.; Wei, C.; Xu, Z. J., Heterostructured Electrocatalysts for Hydrogen Evolution Reaction Under Alkaline Conditions. *Nano-Micro Letters* **2018**, *10*, 75.
25. Wang, P.; Zhang, X.; Zhang, J.; Wan, S.; Guo, S.; Lu, G.; Yao, J.; Huang, X., Precise tuning in platinum-nickel/nickel sulfide interface nanowires for synergistic hydrogen evolution catalysis. *Nat. Commun.* **2017**, *8*, 14580.
26. Han, L.; Liu, H.; Cui, P.; Peng, Z.; Zhang, S.; Yang, J., Alloy Cu₃Pt nanoframes through the structure evolution in Cu-Pt nanoparticles with a core-shell construction. *Sci. Rep.* **2014**, *4*, 6414.
27. Van Dao, D.; Nguyen, T. T. D.; Le, T. D.; Kim, S.-H.; Yang, J.-K.; Lee, I.-H.; Yu, Y.-T., Plasmonically driven photocatalytic hydrogen evolution activity of a Pt-functionalized Au@CeO₂ core-shell catalyst under visible light. *J. Mater. Chem. A* **2020**, *8*, 7687-7694.
28. Zhang, J.; Zhao, Y.; Guo, X.; Chen, C.; Dong, C.-L.; Liu, R.-S.; Han, C.-P.; Li, Y.; Gogotsi, Y.; Wang, G., Single platinum atoms immobilized on an MXene as an efficient catalyst for the hydrogen evolution reaction. *Nat. Catal.* **2018**, *1*, 985-992.
29. Roy, S.; Bagchi, D.; Dheer, L.; Sarma, S. C.; Rajaji, V.; Narayana, C.; Waghmare, U. V.; Peter, S. C., Mechanistic insights into the promotional effect of Ni substitution in non-noble metal carbides for highly enhanced water splitting. *Appl. Catal. B: Environ.* **2021**, *298*, 120560.
30. Popczun, E. J.; McKone, J. R.; Read, C. G.; Biacchi, A. J.; Wiltrout, A. M.; Lewis, N. S.; Schaak, R. E., Nanostructured Nickel Phosphide as an Electrocatalyst for the Hydrogen Evolution Reaction. *J. Am. Chem. Soc.* **2013**, *135*, 9267-9270.
31. Zeng, X.; Shui, J.; Liu, X.; Liu, Q.; Li, Y.; Shang, J.; Zheng, L.; Yu, R., Single-Atom to Single-Atom Grafting of Pt₁ onto FeN₄ Center: Pt₁@FeNC Multifunctional Electrocatalyst with Significantly Enhanced Properties. *Adv. Energy Mater.* **2018**, *8*, 1701345.
32. Wang, C.; Wang, K.; Feng, Y.; Li, C.; Zhou, X.; Gan, L.; Feng, Y.; Zhou, H.; Zhang, B.; Qu, X.; Li, H.; Li, J.; Li, A.; Sun, Y.; Zhang, S.; Yang, G.; Guo, Y.; Yang, S.; Zhou, T.; Dong, F.; Zheng, K.; Wang, L.; Huang, J.; Zhang, Z.; Han, X.,

- Co and Pt Dual-Single-Atoms with Oxygen-Coordinated Co–O–Pt Dimer Sites for Ultrahigh Photocatalytic Hydrogen Evolution Efficiency. *Adv. Mater.* **2021**, *33*, 2003327.
33. Tiwari, J. N.; Harzandi, A. M.; Ha, M.; Sultan, S.; Myung, C. W.; Park, H. J.; Kim, D. Y.; Thangavel, P.; Singh, A. N.; Sharma, P.; Chandrasekaran, S. S.; Salehnia, F.; Jang, J.-W.; Shin, H. S.; Lee, Z.; Kim, K. S., High-Performance Hydrogen Evolution by Ru Single Atoms and Nitrided-Ru Nanoparticles Implanted on N-Doped Graphitic Sheet. *Advan. Energy Mater.* **2019**, *9*, 1900931.
34. Jin, H.; Sultan, S.; Ha, M.; Tiwari, J. N.; Kim, M. G.; Kim, K. S., Simple and Scalable Mechanochemical Synthesis of Noble Metal Catalysts with Single Atoms toward Highly Efficient Hydrogen Evolution. *Adv. Funct. Mater.* **2020**, *30*, 2000531.
35. Xu, Q.; Li, G.; Zhang, Y.; Yang, Q.; Sun, Y.; Felser, C., Descriptor for Hydrogen Evolution Catalysts Based on the Bulk Band Structure Effect. *ACS Catal.* **2020**, *10*, 5042-5048.
36. Chang, K.; Hai, X.; Pang, H.; Zhang, H.; Shi, L.; Liu, G.; Liu, H.; Zhao, G.; Li, M.; Ye, J., Targeted Synthesis of 2H- and 1T-Phase MoS₂ Monolayers for Catalytic Hydrogen Evolution. *Adv. Mater.* **2016**, *28*, 10033-10041.
37. Huang, Y.; Gong, Q.; Song, X.; Feng, K.; Nie, K.; Zhao, F.; Wang, Y.; Zeng, M.; Zhong, J.; Li, Y., Mo₂C Nanoparticles Dispersed on Hierarchical Carbon Microflowers for Efficient Electrocatalytic Hydrogen Evolution. *ACS Nano* **2016**, *10*, 11337-11343.
38. Jiang, N.; You, B.; Sheng, M.; Sun, Y., Electrodeposited Cobalt-Phosphorous-Derived Films as Competent Bifunctional Catalysts for Overall Water Splitting. *Angew. Chem. Int. Ed.* **2015**, *54*, 6251-6254.
39. Xie, L.; Qu, F.; Liu, Z.; Ren, X.; Hao, S.; Ge, R.; Du, G.; Asiri, A. M.; Sun, X.; Chen, L., In situ formation of a 3D core/shell structured Ni₃N@Ni–Bi nanosheet array: an efficient non-noble-metal bifunctional electrocatalyst toward full water splitting under near-neutral conditions. *J. Mater. Chem. A* **2017**, *5*, 7806-7810.
40. Zhu, J.; Hu, L.; Zhao, P.; Lee, L. Y. S.; Wong, K.-Y., Recent Advances in Electrocatalytic Hydrogen Evolution Using Nanoparticles. *Chem. Rev.* **2020**, *120*, 851-918.
41. Huang, X.; Zhao, Z.; Fan, J.; Tan, Y.; Zheng, N., Amine-Assisted Synthesis of Concave Polyhedral Platinum Nanocrystals Having {411} High-Index Facets. *J. Am. Chem. Soc.* **2011**, *133*, 4718-4721.

42. Tian, N.; Zhou, Z.-Y.; Sun, S.-G.; Ding, Y.; Wang, Z. L., Synthesis of Tetrahedral Platinum Nanocrystals with High-Index Facets and High Electro-Oxidation Activity. *Science* **2007**, *316*, 732.
43. Huang, L.; Liu, M.; Lin, H.; Xu, Y.; Wu, J.; Dravid, V. P.; Wolverton, C.; Mirkin, C. A., Shape regulation of high-index facet nanoparticles by dealloying. *Science* **2019**, *365*, 1159.
44. Sarkar, S.; Peter, S. C., An Overview on Pt₃X Electrocatalysts for Oxygen Reduction Reaction. *Chem. Asian J.* **2021**, *16*, 1184-1197.
45. Tsai, H.-C.; Yu, T. H.; Sha, Y.; Merinov, B. V.; Wu, P.-W.; Chen, S.-Y.; Goddard, W. A., Density Functional Theory Study of Pt₃M Alloy Surface Segregation with Adsorbed O/OH and Pt₃Os as Catalysts for Oxygen Reduction Reaction. *J. Phys. Chem. C* **2014**, *118*, 26703-26712.
46. Choi, K.; Buriak, J. M., Hydrogermylation of Alkenes and Alkynes on Hydride-Terminated Ge(100) Surfaces. *Langmuir* **2000**, *16*, 7737-7741.
47. Fan, M.; Zhang, B.; Wang, L.; Li, Z.; Liang, X.; Ai, X.; Zou, X., Germanium-regulated adsorption site preference on ruthenium electrocatalyst for efficient hydrogen evolution. *Chem. Commun.* **2021**.
48. Chen, J.-Y.; Jheng, S.-L.; Chan, C.-Y.; Tuan, H.-Y., Morphology controlled synthesis of Pd₂Ge nanostructures and their shape-dependent catalytic properties for hydrogen evolution reaction. *Int. J. Hydrog. Energy* **2019**, *44*, 12958-12970.
49. Maroun, F.; Ozanam, F.; Chazalviel, J. N., In situ infrared monitoring of hydrogen adsorption/desorption at a germanium electrode. *Surf. Sci.* **1999**, *427-428*, 184-189.
50. Dick, D.; Veyan, J.-F.; Longo, R. C.; McDonnell, S.; Ballard, J. B.; Qin, X.; Dong, H.; Owen, J. H. G.; Randall, J. N.; Wallace, R. M.; Cho, K.; Chabal, Y. J., Digermane Deposition on Si(100) and Ge(100): from Adsorption Mechanism to Epitaxial Growth. *J. Phys. Chem. C* **2014**, *118*, 482-493.
51. Wang, J.; Liao, T.; Wei, Z.; Sun, J.; Guo, J.; Sun, Z., Heteroatom-Doping of Non-Noble Metal-Based Catalysts for Electrocatalytic Hydrogen Evolution: An Electronic Structure Tuning Strategy. *Small Methods* **2021**, *5*, 2000988.
52. Kotmool, K.; Li, B.; Chakraborty, S.; Bovornratanaraks, T.; Luo, W.; Mao, H.-k.; Ahuja, R., High pressure-induced distortion in face-centered cubic phase of thallium. *Proc. Natl. Acad. Sci.* **2016**, *113*, 11143-11147.

53. Wang, Y.; Chen, L.; Yu, X.; Wang, Y.; Zheng, G., Superb Alkaline Hydrogen Evolution and Simultaneous Electricity Generation by Pt-Decorated Ni₃N Nanosheets. *Adv. Energy Mater.* **2017**, *7*, 1601390.
54. Bockris, J. O. M.; Ammar, I. A.; Huq, A. K. M. S., The Mechanism of the Hydrogen Evolution Reaction on Platinum, Silver and Tungsten surfaces in Acid Solutions. *J. Phys. Chem.* **1957**, *61*, 879-886.
55. Dubouis, N.; Grimaud, A., The hydrogen evolution reaction: from material to interfacial descriptors. *Chem. Sci.* **2019**, *10*, 9165-9181.
56. Tong, W.; Forster, M.; Dionigi, F.; Dresp, S.; Sadeghi Erami, R.; Strasser, P.; Cowan, A. J.; Farràs, P., Electrolysis of low-grade and saline surface water. *Nat. Energy* **2020**, *5*, 367-377.
57. Ledezma-Yanez, I.; Wallace, W. D. Z.; Sebastián-Pascual, P.; Climent, V.; Feliu, J. M.; Koper, M. T. M., Interfacial water reorganization as a pH-dependent descriptor of the hydrogen evolution rate on platinum electrodes. *Nat. Energy* **2017**, *2*, 17031.
58. Zhong, W.; Xiao, B.; Lin, Z.; Wang, Z.; Huang, L.; Shen, S.; Zhang, Q.; Gu, L., RhSe₂: A Superior 3D Electrocatalyst with Multiple Active Facets for Hydrogen Evolution Reaction in Both Acid and Alkaline Solutions. *Adv. Mater.* **2021**, *33*, 2007894.
59. Wu, Y.-L.; Li, X.; Wei, Y.-S.; Fu, Z.; Wei, W.; Wu, X.-T.; Zhu, Q.-L.; Xu, Q., Ordered Macroporous Superstructure of Nitrogen-Doped Nanoporous Carbon Implanted with Ultrafine Ru Nanoclusters for Efficient pH-Universal Hydrogen Evolution Reaction. *Adv. Mater.* **2021**, *33*, 2006965.
60. An, L.; Wei, C.; Lu, M.; Liu, H.; Chen, Y.; Scherer, G. G.; Fisher, A. C.; Xi, P.; Xu, Z. J.; Yan, C.-H., Recent Development of Oxygen Evolution Electrocatalysts in Acidic Environment. *Adv. Mater.* **2021**, *33*, 2006328.
61. An, L.; Feng, J.; Zhang, Y.; Wang, R.; Liu, H.; Wang, G.-C.; Cheng, F.; Xi, P., Epitaxial Heterogeneous Interfaces on N-NiMoO₄/NiS₂ Nanowires/Nanosheets to Boost Hydrogen and Oxygen Production for Overall Water Splitting. *Adv. Funct. Mater.* **2019**, *29*, 1805298.
62. Kim, J.; Jung, H.; Jung, S.-M.; Hwang, J.; Kim, D. Y.; Lee, N.; Kim, K.-S.; Kwon, H.; Kim, Y.-T.; Han, J. W.; Kim, J. K., Tailoring Binding Abilities by Incorporating Oxophilic Transition Metals on 3D Nanostructured Ni Arrays for Accelerated Alkaline Hydrogen Evolution Reaction. *J. Am. Chem. Soc.* **2021**, *143*, 1399-1408.

63. Yan, Q.-Q.; Wu, D.-X.; Chu, S.-Q.; Chen, Z.-Q.; Lin, Y.; Chen, M.-X.; Zhang, J.; Wu, X.-J.; Liang, H.-W., Reversing the charge transfer between platinum and sulfur-doped carbon support for electrocatalytic hydrogen evolution. *Nat. Commun.* **2019**, *10*, 4977.
64. Kaito, T.; Mitsumoto, H.; Sugawara, S.; Shinohara, K.; Uehara, H.; Ariga, H.; Takakusagi, S.; Hatakeyama, Y.; Nishikawa, K.; Asakura, K., K-Edge X-ray Absorption Fine Structure Analysis of Pt/Au Core–Shell Electrocatalyst: Evidence for Short Pt–Pt Distance. *J. Phys. Chem. C* **2014**, *118*, 8481-8490.
65. Kotmool, K.; Kaewmaraya, T.; Chakraborty, S.; Anversa, J.; Bovornratanaraks, T.; Luo, W.; Gou, H.; Piquini Paulo, C.; Kang Tae, W.; Mao, H.-k.; Ahuja, R., Revealing an unusual transparent phase of superhard iron tetraboride under high pressure. *Proc. Natl. Acad. Sci.* **2014**, *111*, 17050-17053.
66. Jaramillo Thomas, F.; Jørgensen Kristina, P.; Bonde, J.; Nielsen Jane, H.; Horch, S.; Chorkendorff, I., Identification of Active Edge Sites for Electrochemical H₂ Evolution from MoS₂ Nanocatalysts. *Science* **2007**, *317*, 100-102.
67. Nayak, S.; Erbe, A., Mechanism of the potential-triggered surface transformation of germanium in acidic medium studied by ATR-IR spectroscopy. *Phys. Chem. Chem. Phys.* **2016**, *18*, 25100-25109.
68. Dong, Y.; Hu, G.; Hu, X.; Xie, G.; Lu, J.; Luo, M., Hydrogen Adsorption and Oxidation on Pt Film: An in Situ Real-Time Attenuated Total Reflection Infrared (ATR-IR) Spectroscopic Study. *J. Phys. Chem. C* **2013**, *117*, 12537-12543.
69. Nichols, R. J.; Bewick, A., Spectroscopic identification of the adsorbed intermediate in hydrogen evolution on platinum. *J. Electroanal. Chem. Interfac. Electrochem.* **1988**, *243*, 445-453.
70. Yang, Y.; Wang, Y.; Xiong, Y.; Huang, X.; Shen, L.; Huang, R.; Wang, H.; Pastore, J. P.; Yu, S.-H.; Xiao, L.; Brock, J. D.; Zhuang, L.; Abruña, H. D., In Situ X-ray Absorption Spectroscopy of a Synergistic Co–Mn Oxide Catalyst for the Oxygen Reduction Reaction. *J. Am. Chem. Soc.* **2019**, *141*, 1463-1466.
71. Stojić, D. L.; Cekić, B. D.; Maksić, A. D.; Kaninski, M. P. M.; Miljanić, Š. S., Intermetallics as cathode materials in the electrolytic hydrogen production. *Int. J. Hydrog. Energy* **2005**, *30*, 21-28.

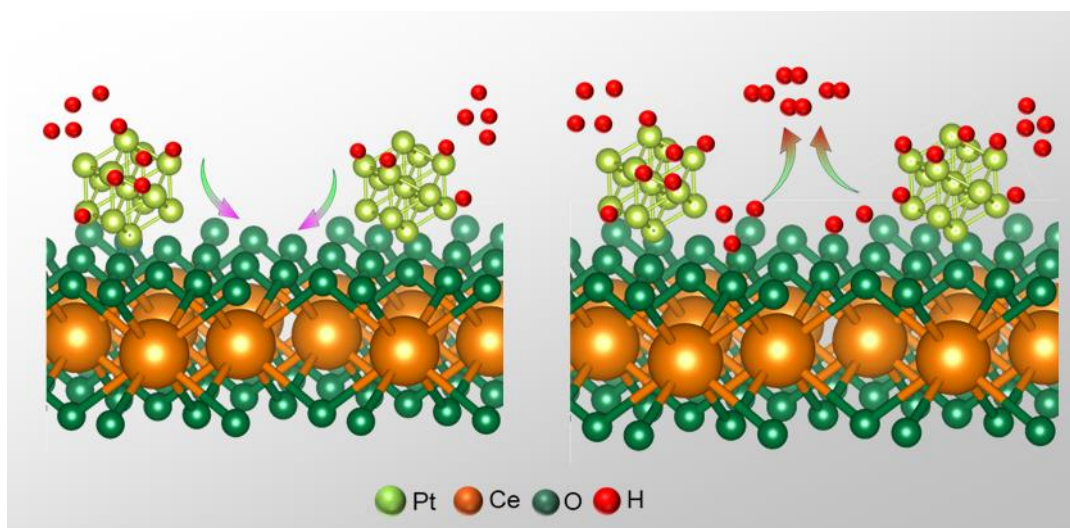
72. Wang, C.; Hu, F.; Yang, H.; Zhang, Y.; Lu, H.; Wang, Q., 1.82 wt.% Pt/N, P co-doped carbon overwhelms 20 wt.% Pt/C as a high-efficiency electrocatalyst for hydrogen evolution reaction. *Nano Research* **2017**, *10*, 238-246.
73. Chi, J.-Q.; Xie, J.-Y.; Zhang, W.-W.; Dong, B.; Qin, J.-F.; Zhang, X.-Y.; Lin, J.-H.; Chai, Y.-M.; Liu, C.-G., N-Doped Sandwich-Structured Mo₂C@C@Pt Interface with Ultralow Pt Loading for pH-Universal Hydrogen Evolution Reaction. *ACS Appl. Mater. Inter.* **2019**, *11*, 4047-4056.
74. Ajdari, F. B.; Kowsari, E.; Ehsani, A.; Schorowski, M.; Ameri, T., New synthesized ionic liquid functionalized graphene oxide: Synthesis, characterization and its nanocomposite with conjugated polymer as effective electrode materials in an energy storage device. *Electrochim. Acta* **2018**, *292*, 789-804.
75. Yan, X.; Li, H.; Sun, J.; Liu, P.; Zhang, H.; Xu, B.; Guo, J., Pt nanoparticles decorated high-defective graphene nanospheres as highly efficient catalysts for the hydrogen evolution reaction. *Carbon* **2018**, *137*, 405-410.
76. Cui, B.; Hu, B.; Liu, J.; Wang, M.; Song, Y.; Tian, K.; Zhang, Z.; He, L., Solution-Plasma-Assisted Bimetallic Oxide Alloy Nanoparticles of Pt and Pd Embedded within Two-Dimensional Ti₃C₂T_x Nanosheets as Highly Active Electrocatalysts for Overall Water Splitting. *ACS Appl. Mater. Inter.* **2018**, *10*, 23858-23873.
77. Anantharaj, S.; Karthik, P. E.; Subramanian, B.; Kundu, S., Pt Nanoparticle Anchored Molecular Self-Assemblies of DNA: An Extremely Stable and Efficient HER Electrocatalyst with Ultralow Pt Content. *ACS Catal.* **2016**, *6*, 4660-4672.
78. Tian, H.; Cui, X.; Zeng, L.; Su, L.; Song, Y.; Shi, J., Oxygen vacancy-assisted hydrogen evolution reaction of the Pt/WO₃ electrocatalyst. *J. Mater. Chem. A* **2019**, *7*, 6285-6293.
79. Chao, T.; Luo, X.; Chen, W.; Jiang, B.; Ge, J.; Lin, Y.; Wu, G.; Wang, X.; Hu, Y.; Zhuang, Z.; Wu, Y.; Hong, X.; Li, Y., Atomically Dispersed Copper–Platinum Dual Sites Alloyed with Palladium Nanorings Catalyze the Hydrogen Evolution Reaction. *Angew. Chem. Int. Ed.* **2017**, *56*, 16047-16051.
80. Liu, D.; Li, X.; Chen, S.; Yan, H.; Wang, C.; Wu, C.; Haleem, Y. A.; Duan, S.; Lu, J.; Ge, B.; Ajayan, P. M.; Luo, Y.; Jiang, J.; Song, L., Atomically dispersed platinum supported on curved carbon supports for efficient electrocatalytic hydrogen evolution. *Nat. Energy* **2019**, *4*, 512-518.

81. Zhu, Y.; Yuan, M.; Deng, L.; Ming, R.; Zhang, A.; Yang, M.; Chai, B.; Ren, Z., High-efficiency electrochemical hydrogen evolution based on the intermetallic Pt₂Si compound prepared by magnetron-sputtering. *RSC Advances* **2017**, *7*, 1553-1560.
82. Nayak, P.; Jiang, Q.; Kurra, N.; Wang, X.; Buttner, U.; Alshareef, H. N., Monolithic laser scribed graphene scaffolds with atomic layer deposited platinum for the hydrogen evolution reaction. *J. Mater. Chem. A* **2017**, *5*, 20422-20427.
83. Liu, G.; Qiu, Y.; Wang, Z.; Zhang, J.; Chen, X.; Dai, M.; Jia, D.; Zhou, Y.; Li, Z.; Hu, P., Efficiently Synergistic Hydrogen Evolution Realized by Trace Amount of Pt-Decorated Defect-Rich SnS₂ Nanosheets. *ACS Appl. Mater. Interf.* **2017**, *9*, 37750-37759.
84. Zeng, X.; Shui, J.; Liu, X.; Liu, Q.; Li, Y.; Shang, J.; Zheng, L.; Yu, R., Single-Atom to Single-Atom Grafting of Pt₁ onto FeN₄ Center: Pt₁@FeNC Multifunctional Electrocatalyst with Significantly Enhanced Properties. *Adv. Energy Mater.* **2018**, *8*, 1701345.
85. Ye, S.; Luo, F.; Zhang, Q.; Zhang, P.; Xu, T.; Wang, Q.; He, D.; Guo, L.; Zhang, Y.; He, C.; Ouyang, X.; Gu, M.; Liu, J.; Sun, X., Highly stable single Pt atomic sites anchored on aniline-stacked graphene for hydrogen evolution reaction. *Energy Environ. Sci.* **2019**, *12*, 1000-1007.
86. Shang, X.; Liu, Z.-Z.; Lu, S.-S.; Dong, B.; Chi, J.-Q.; Qin, J.-F.; Liu, X.; Chai, Y.-M.; Liu, C.-G., Pt-C Interfaces Based on Electronegativity-Functionalized Hollow Carbon Spheres for Highly Efficient Hydrogen Evolution. *ACS Appl. Mater. Inter.* **2018**, *10*, 43561-43569.
87. Tuo, Y.; Lu, Q.; Chen, C.; Liu, T.; Pan, Y.; Zhou, Y.; Zhang, J., The facile synthesis of core-shell PtCu nanoparticles with superior electrocatalytic activity and stability in the hydrogen evolution reaction. *RSC Advances* **2021**, *11*, 26326-26335.
88. Luo, Y.; Tang, L.; Khan, U.; Yu, Q.; Cheng, H.-M.; Zou, X.; Liu, B., Morphology and surface chemistry engineering toward pH-universal catalysts for hydrogen evolution at high current density. *Nat. Commun.* **2019**, *10*, 269.
89. Xue, S.; Liu, Z.; Ma, C.; Cheng, H.-M.; Ren, W., A highly active and durable electrocatalyst for large current density hydrogen evolution reaction. *Science Bulletin* **2020**, *65*, 123-130.
90. Chen, Y.; Yu, J.; Jia, J.; Liu, F.; Zhang, Y.; Xiong, G.; Zhang, R.; Yang, R.; Sun, D.; Liu, H.; Zhou, W., Metallic Ni₃Mo₃N Porous Microrods with Abundant Catalytic

Sites as Efficient Electrocatalyst for Large Current Density and Superstability of Hydrogen Evolution Reaction and Water Splitting. *Appl.Catal. B: Environ.* **2020**, 272, 118956.

Chapter 7

Reductant-free Sub-nm Pt NPs Anchored on Ceria Support Exploring H-spillover Mechanism in H₂ Generation



Soumi Mondal; Pooja Rani Dahiya; Nilutpal Dutta; Subhajit Chakroborty;
Sebastian C. Peter (*manuscript under preparation*)

Summary

Electrochemical hydrogen generation is considered as the green hydrogen generation which imparts the potential promise of combating the global warming. One of the important criteria for an electrocatalyst is its economic viability. Volcano plot for hydrogen evolution reaction (HER) suggests that Pt is the best catalyst with commercially used catalyst being 20% Pt on carbon support. This work has further reduced Pt loading to 10% with non-expensive support of CeO₂. The specialty of CeO₂ is its versatile morphology, switchable Ce(IV)-Ce(III) valency, and inexpensive nature. Both cube and rod morphologies of CeO₂ have been explored and Pt metal is incorporated *in-situ* (during CeO₂ formation) and *ex-situ* (after CeO₂ formation) with different loading percentage amongst which the best HER activity is achieved for *in-situ* incorporation of only 10% Pt in CeO₂ cube morphology. Raman spectroscopy, X-ray photoelectron spectroscopy, X-ray absorption spectroscopy have detected the presence of O_{vac} and Ce³⁺ in all the catalysts. In-situ incorporation of Pt in CeO₂-cube has shown maximum interfacial charge transfer between Pt and CeO₂. Interestingly, presence of Pt in reaction medium has modified the perfect cube-like structure and this Pt-tuned modification has generated a highly active interface which led to higher HER activity than 20% Pt/C. On the other hand, different facets of CeO₂ tune different facets of Pt, generating the highest HER activity. This role of support can be correlated to the H-spillover mechanism during electrochemical HER from Pt to CeO₂ which is highest for cube morphology.

Table of Contents

7.1	Introduction	212
7.2	Experimental Details	213
7.2.1	Chemicals and reagents	213
7.2.2	Synthesis of CeO ₂ cubes (CeO ₂ -C) and CeO ₂ rods (CeO ₂ -R)	213
7.2.3	Synthesis of Pt incorporated CeO ₂ nano-rods (CeO ₂ -R) and nano-cubes (CeO ₂ -C) in the <i>in-situ</i> and <i>ex-situ</i> procedures	213
7.3	Characterization	214
7.3.1	Powder X-ray Diffraction (PXRD)	214
7.3.2	Transmission Electron Microscope (TEM)	214
7.3.3	X-ray Photoelectron Spectroscopy (XPS)	214
7.3.4	Scanning electron microscopy (SEM) and Energy Dispersive Spectrum (EDAX).....	214
7.3.5	X-ray Absorption Spectroscopy (XAS).....	214
7.3.6	Electrochemical Hydrogen Evolution Reaction (HER).....	215
7.4	Results & Discussion	215
7.5	Conclusion	238
7.6	References.....	239

7.1 Introduction

To combat increased global warming in near future, the key technology is the use of green fuel, hydrogen, in fuel cells.¹ Green mode of hydrogen generation is achieved by electrochemical splitting of water using renewable electricity, which needs to gradually replace the industrial mode of grey hydrogen generation via steam reforming of methane which gushes out huge amounts of CO₂ into the atmosphere. As per Sabatier principle, the most optimized H-adsorption is achieved on Pt which is the state-of-the-art catalyst being commercially used for industrial level water splitting.² The large-scale water electrolysis for hydrogen generation is economically challenging due to expensive nature and scarcity of Pt metal since a high metal loading is necessary for getting efficient activity.^{3,4}

Instead on using the active metal alone, dispersing the HER active metal on a non-expensive is always desired.^{5,6} The role of support includes uniform dispersion of active metal increasing the efficient active surface area, synergistic effect of the metal and support, interfacial chemistry enhancing the efficiency of the metal, and the participation of the support actively in increasing the activity of the overall catalyst.^{7,8} Mostly commonly used oxides for metal supported catalysts which have been reported are CoO_x, TiO₂, Cu-oxides, NiO and so on.⁹ One of the very interesting lanthanum-based oxide, CeO₂, is being explored in various catalysis for its properties like switchable valency, versatile morphology formation, labile lattice oxygen with tunable oxygen-vacancy, and of course, less expensive in nature.¹⁰ Although CeO₂ is not electrically conducting, its different morphology has different band-gap and other metal incorporation can tune the electronic property of CeO₂. Most of the metal incorporated CeO₂ requires reduction conditions, either using H₂ gas during annealing or using hydride based reducing agents to get transition metals in their metallic form. Otherwise, the metals stay as metal oxide-CeO₂ heterostructure or metal doped CeO₂.

Electrochemical hydrogen evolution reaction (HER) is highly facile on Pt. Noble metal supported on CeO₂ has been explored as catalysts due to the strong metal support interaction (SMSI) effect.¹¹ To achieve increased HER activity with decreased loading of metal, using an active, non-toxic, and non-expensive support is of high significance.¹² CeO₂ is important candidate for catalysis due to its unique properties like versatile morphology formation, switchable valency of Ce⁴⁺ and Ce³⁺ and feasible formation of vacancies (O_{vac}).¹³ In this work we have tuned the synthesis of Pt incorporated CeO₂ nano cubes and rods without using any reductant and Pt exists in metallic state with an interface of Pt-O-Ce that enhances the metal attachment to the CeO₂ nanoparticles.

7.2 Experimental Details

7.2.1 Chemicals and reagents

Potassium tetrachloroplatinate (K_2PtCl_4) was purchased from Alfa-Aesar, superhydride solution ($Li(C_2H_5)_3BH$), and nafion binder (5 wt.%) were purchased from Sigma-Aldrich, and sodium hydroxide (NaOH), cerium(III) nitrate hexahydrate ($Ce(NO_3)_3 \cdot 6H_2O$, 99.999% trace metals basis), were purchased from Qualigens and Spectrochem, respectively, and tri-ethylene glycol (TEG) was purchased from Merck. All the chemicals (more than 99% purity) were used as purchased without any further purification. Millipore water of conductivity 18.2 $M\Omega cm$ was used for the synthesis and all electrochemical studies.

7.2.2 Synthesis of CeO_2 cubes (CeO_2 -C) and CeO_2 rods (CeO_2 -R)

In a typical solvothermal reaction, a mixture of $Ce(NO_3)_3 \cdot 6H_2O$ and NaOH and DI water are stirred for 30 minutes and heated at 100 °C for 24 hours in an autoclave. Then, the reaction mixture is centrifuged and washed with ethanol and then dried. This dried powder is further calcined at 400 °C for 4 hours. This is the synthesis of CeO_2 nanorods.

The similar procedure is used where the first solvothermal treatment is done at 180 °C for synthesizing the CeO_2 nano-cubes. The remaining process is the same as the synthesis of CeO_2 nanorods.

7.2.3 Synthesis of Pt incorporated CeO_2 nano-rods (CeO_2 -R) and nano-cubes (CeO_2 -C) in the *in-situ* and *ex-situ* procedures

For the *in-situ* incorporation of Pt the similar synthesis of CeO_2 nano-rods and nano-cubes is followed where along with the $Ce(NO_3)_3 \cdot 6H_2O$ and NaOH and DI water, Pt precursor salt K_2PtCl_4 is also added, and then followed the similar process of ceria cube and rod synthesis as discussed in section 7.2.2.

For the *ex-situ* incorporation of Pt loading, at first the CeO_2 -R and CeO_2 -C are synthesized as per the details in section 7.2.2, and then second step of Pt incorporation is done. 10 mg CeO_2 -R powder is taken in an autoclave and made a uniform suspension in 16 mL of ethanol and then K_2PtCl_4 is added and stirred for dissolution and then equivalent amount of superhydride solution is injected with proper care. Then the solution is stirred for 30 minutes and then put inside the oven for 18 hours under 180 °C. The similar process is used for Pt incorporation using already synthesized CeO_2 -C powder already synthesized.

Here, 3%, 5%, and 10% weight percentage loading of Pt is used for both *ex-situ* and *in-situ* mode of incorporation. The overall synthesis scheme is provided in **Figure 7.1**.

7.3 Characterization

7.3.1 Powder x-ray diffraction (PXRD)

PXRD measurements were done at room temperature on a Rigaku Miniflex X-ray diffractometer with Cu-K α X-ray source ($\lambda = 1.5406 \text{ \AA}$), equipped with a position sensitive detector in the angular range $20^\circ \leq 2\theta \leq 80^\circ$ with the step size 0.02° and scan rate of 0.5 s/step calibrated against corundum standards. The experimental XRD patterns were compared to the patterns simulated from the data reported in the literature.

7.3.2 Transmission electron microscope (TEM)

TEM images and selected area electron diffraction patterns were collected using a JEOL JEM-2010 TEM instrument and color mapping was done in TECHNAI. The samples for these measurements were prepared by sonicating the nanocrystalline powders in ethanol and drop-casting a small volume onto a carbon-coated copper grid.

7.3.3 X-ray photoelectron spectroscopy (XPS)

XPS measurements were carried out using Thermo K-alpha+ spectrometer using micro focused and monochromated Al K α radiation with energy 1486.6 eV . The pass energy for the spectral acquisition was kept at 50 eV for individual core-levels. The electron flood gun was utilized for providing charge compensation during data acquisition. Further, the individual core-level spectra were checked for charging using C1s at 284.6 eV as standard and corrected if needed. The peak fitting of the individual core-levels was done using CASA XPS software with a Shirley type background.

7.3.4 Scanning electron microscopy (SEM) and energy dispersive spectrum (EDAX)

The FESEM measurement was performed using Leica scanning electron microscopy equipped with an energy-dispersive X-ray spectroscopy (EDX) instrument (Bruker 120 eV EDAX instrument). Data were acquired by using an accelerating voltage of 15 kV , and the typical time taken for data accumulation is 100 s . The elemental analyses were performed using the P/B-ZAF standardless method (where P/B = peak to background model, Z = atomic no. correction factor, A = absorption correction factor, and F = fluorescence factor) for Cu, Ga at multiple areas on the sample coated Si wafer.

7.3.5 X-ray absorption spectroscopy (XAS)

X-ray absorption near-edge spectroscopy (XANES) and quick-Extended X-ray Absorption Fine Structure (quick-EXAFS) experiments at 300 K were performed at PETRA III, beamline P64, of DESY, Germany. Measurements of Cu-K and Pd-K at ambient pressure

were performed in fluorescence as well as transmission mode using gas ionization chambers to monitor the incident and transmitted X-ray intensities. Monochromatic X-rays were obtained using a Si (111) double crystal monochromator, which was calibrated by defining the inflection point (first derivative maxima) of Cu foil as 8980.5 eV. The beam was focused by employing a Kirkpatrick-Baez (K-B) mirror optic. A rhodium-coated X-ray mirror was used to suppress higher-order harmonics. A CCD detector was used to record the transmitted signals. Pellets for the ex-situ measurements were made by homogeneously mixing the sample with an inert cellulose matrix to obtain an X-ray absorption edge jump close to one.

7.3.6 Electrochemical hydrogen evolution reaction (HER)

All the electrochemical measurements were done in a 3-electrode set-up comprising of a glassy carbon as the working electrode (GCE), graphite rod counter electrode, saturated calomel electrode (SCE) (for acidic media). The catalyst ink was prepared using 1.6 mg catalyst + 0.4 mg Vulcan in 200 μL of mixed solvent (IPA: water = 1:1) + 20 μL of 1 wt.% Nafion used as binder. 10 μL of the catalyst ink was drop casted on the commercial 3 mm glassy carbon electrode. Commercial Pt/C (20 wt%, Sigma Aldrich) were used for comparison of activity with the reported electrocatalysts. Linear sweep voltammetry (LSV) was recorded for HER at a scan rate of 5 mV s^{-1} at 25 $^{\circ}\text{C}$. The electrolyte solution was deaerated by purging nitrogen gas into the solution at least for 30 min before each experiment. All the reference electrodes were calibrated with respect to the reversible hydrogen electrode (RHE), using Pt as working and counter electrodes in the respective electrolytes. The values obtained are as follows: acidic medium, $E_{\text{RHE}} = E_{\text{SCE}} + 0.2591 \text{ V}$.

7.4 Results & Discussion

The materials have been synthesized using solvothermal process followed by calcination. Two modes of Pt incorporation into CeO_2 have been done: *in-situ* and *ex-situ* processes which is pictorially demonstrated in **Figure 7.1**. Here, three different weight percentages of Pt loading have been done on CeO_2 (3%, 5%, and 10%) via both *in-situ* and *ex-situ* modes. The *in-situ* process deals with addition of Pt ions during the formation of CeO_2 nanoparticles (NPs) and whereas, the *ex-situ* process indicates the formation of CeO_2 NPs and then addition of Pt ions in presence of a reducing agent. Here, CeO_2 nanoparticles have been synthesized tuning their rod-like and cube-like morphologies, to check the role of morphology in HER and to understand the role of Pt ions during the formation of these morphologies. Different loading percentage of Pt has been used and the naming of the compounds are being given as: 3%, 5%, and 10% loadings for *in-situ* and *ex-situ* incorporation for rods are 3p-*in*-

situ-CeO₂-R, 5p-*in-situ*-CeO₂-R, 10p-*in-situ*-CeO₂-R, 3p-*ex-situ*-CeO₂-R, 5p-*ex-situ*-CeO₂-R, 10p-*ex-situ*-CeO₂-R, respectively. The 3%, 5%, and 10% loadings for *in-situ* and *ex-situ* incorporation for cubes are 3p-*in-situ*-CeO₂-C, 5p-*in-situ*-CeO₂-C, 10p-*in-situ*-CeO₂-C, 3p-*ex-situ*-CeO₂-C, 5p-*ex-situ*-CeO₂-C, 10p-*ex-situ*-CeO₂-C, respectively. Both CeO₂ and Pt crystallize in face-centered cubic lattice (Space group: $Fm\bar{3}m$). **Figure 7.2** shows the PXRD pattern of CeO₂-C and CeO₂-R compared with the simulated pattern of cubic CeO₂ lattice. From the FWHM, it is observed that overall size of the rods is much smaller than the cube since the growth is majorly in one direction for the rods. **Figures 7.3** and **7.4** signify that with 3%, 5%, and 10% of Pt incorporation into CeO₂ rods during its formation via *in-situ* and *ex-situ* processes, there is emergence of Pt peaks and intensity of the peaks increase with increasing loading percentage.

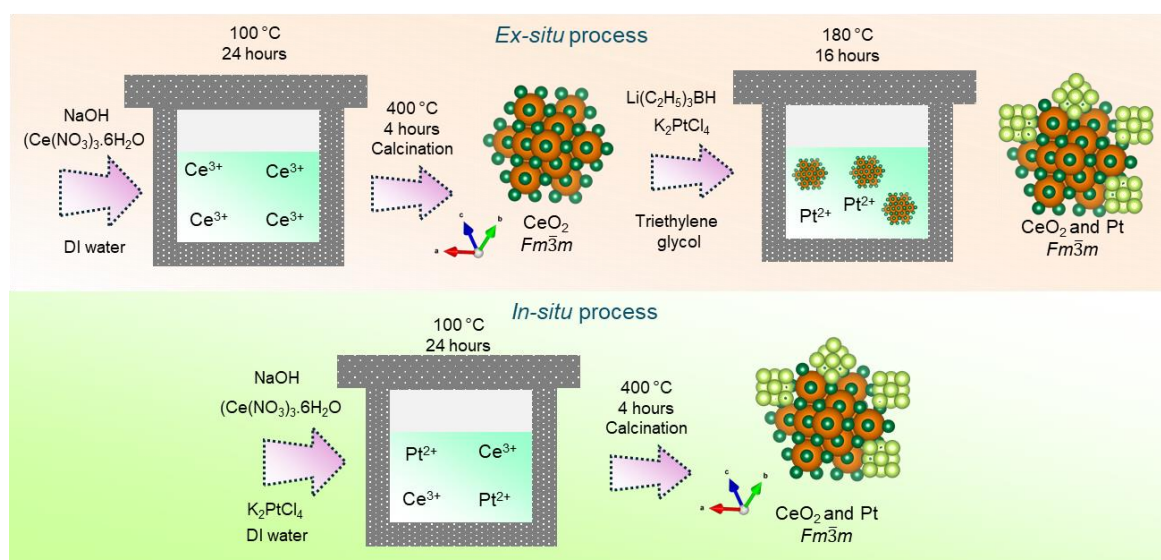


Figure 7.1. Schematic representation of the synthetic processes: *In-situ* and *Ex-situ* processes of Pt incorporation in CeO₂ support.

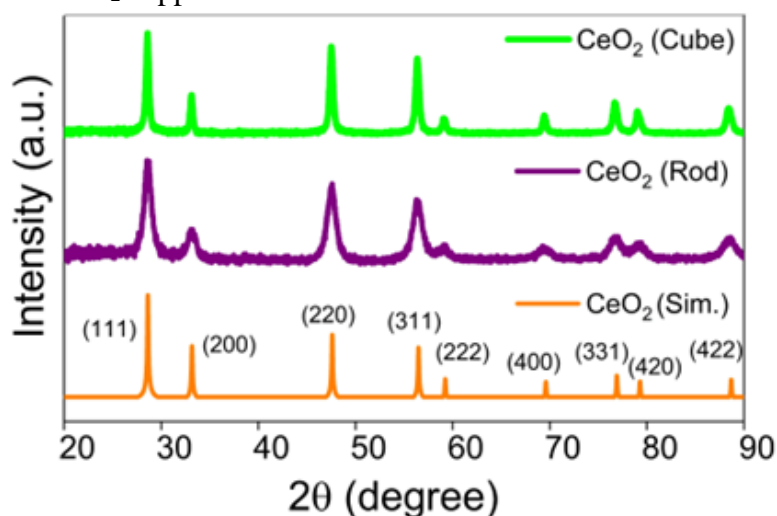


Figure 7.2. PXRD pattern of ceria rods (CeO₂-R) and ceria cubes (CeO₂-C).

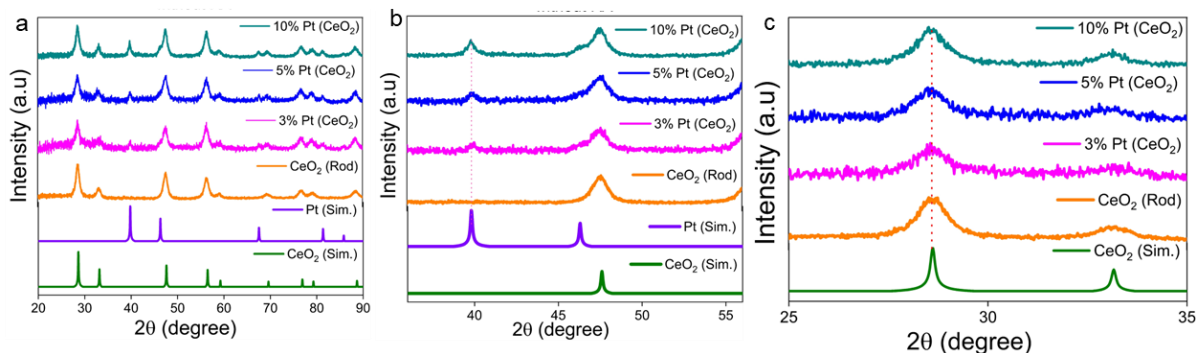


Figure 7.3. PXRD pattern of ceria rods ($\text{CeO}_2\text{-R}$) with Pt incorporation of different loading percentage without reducing agent via *in-situ* method (3p-*in-situ*- $\text{CeO}_2\text{-R}$, 5p-*in-situ*- $\text{CeO}_2\text{-R}$, 10p-*in-situ*- $\text{CeO}_2\text{-R}$).

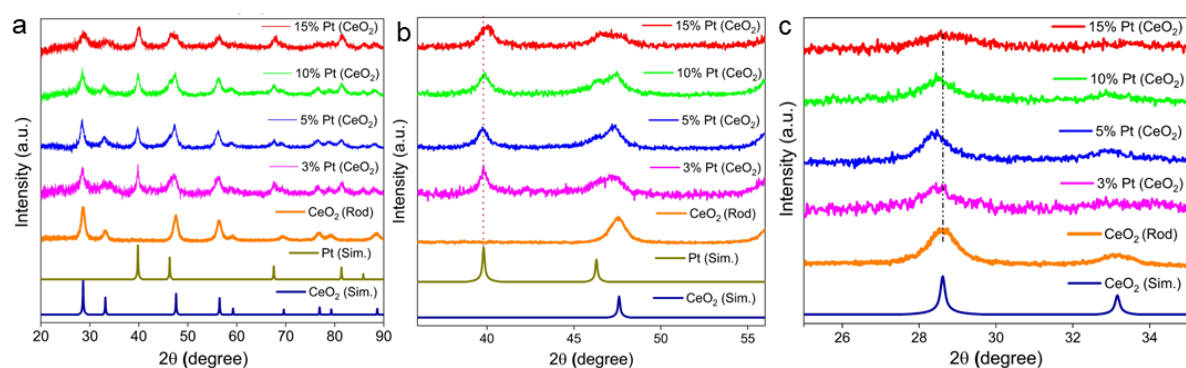


Figure 7.4. PXRD pattern of ceria rods ($\text{CeO}_2\text{-R}$) with Pt incorporation of different loading percentage without reducing agent via *ex-situ* method (3p-*ex-situ*- $\text{CeO}_2\text{-R}$, 5p-*ex-situ*- $\text{CeO}_2\text{-R}$, 10p-*ex-situ*- $\text{CeO}_2\text{-R}$, 15p-*ex-situ*- $\text{CeO}_2\text{-R}$).

But there is no significant change in the peak maxima and FWHM for both Pt and CeO_2 with incorporation of Pt during the synthesis of CeO_2 . This gives an indication that addition of Pt during CeO_2 rod formation imposes less impact and separate phases of Pt and CeO_2 nanorods form individually. **Figure 7.5** shows the PXRD pattern for 3%, 5%, 10%, and 15% Pt incorporation in CeO_2 cubes in the *ex-situ* process which shows emergence of Pt peaks with increased loading and not much peak maxima shift observed for both Pt and CeO_2 lattice. Whereas, when Pt is incorporated in CeO_2 cubes during *in-situ* process, there is a gradual right shift of the CeO_2 peaks till 5% Pt loading followed by further left shift from 10%-15% of Pt loading (**Figures 7.6a, 7.6b, 7.6c**). This indicates that there is lattice contraction upon addition of Pt up to 5% and after that lattice starts to relax itself and hence the left shift in 2θ value is observed.¹⁴ This indicates that at lesser Pt loading there is formation of Pt-oxide with substitution of Ce^{4+} with Pt^{2+} which is of smaller radius than Ce^{4+} and that leads to lattice contraction.¹⁵ But with larger Pt concentration, due to easier reducibility of Pt, it forms Pt nanoclusters instead to inserting into the lattice of CeO_2 , hence very prominent Pt peaks are observed with not much shift in PXRD peak of CeO_2 .

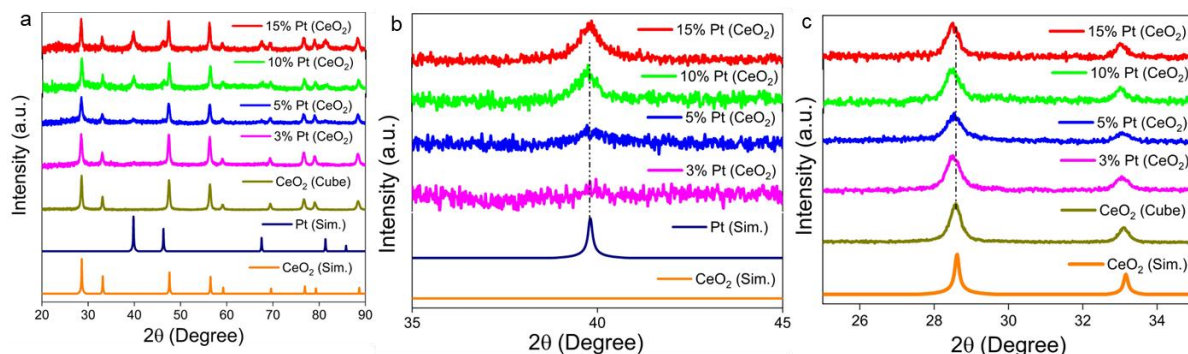


Figure 7.5. PXRD pattern of ceria cubes (CeO₂-C) with Pt incorporation of different loading percentage without reducing agent via *ex-situ* method (3p-*ex-situ*-CeO₂-C, 5p-*ex-situ*-CeO₂-C, 10p-*ex-situ*-CeO₂-C, 15p-*ex-situ*-CeO₂-C).

From the relative peak intensity ratio for peaks corresponding to (311) and (200) planes, it is observed that the ratio drastically increases upon Pt loading under *in-situ* conditions whereas there is no monotonic trend in the ratio with no significant change when Pt is loaded in *ex-situ* process (Figure 7.6d).

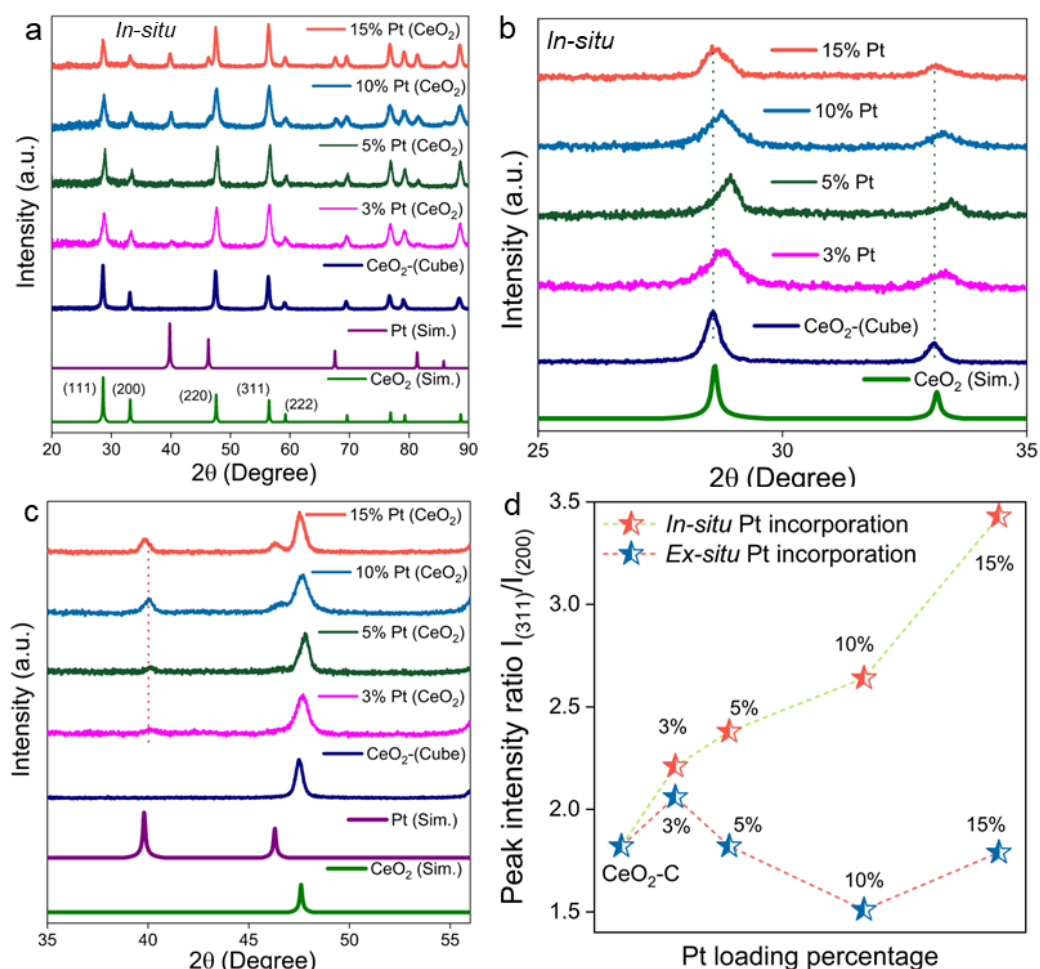


Figure 7.6. (a) Powder X-ray diffraction (PXRD) pattern of CeO₂-C and 3%, 5%, 10%, 15% loaded Pt under *in-situ* process, (b, c) zoomed-in PXRD pattern for analyzing the CeO₂ peaks. (d) relative peak intensity ratio of facets (311):(200) for CeO₂ under *in-situ* and *ex-situ* Pt incorporation for the cube morphology (CeO₂-C).

This observation gives the first indication that there is significant change in the facet exposure and morphology of CeO₂ nano-cubes when Pt guest ions are added during its formation which will be further verified by microscopic studies. SEM and TEM images (**Figures 7.7** and **7.8**) show the uniform distribution of nanorods of ceria and the majorly exposed facets are (111) of CeO₂. It has been observed from TEM images and particle size distribution in **Figure 7.9** that increment of Pt loading during the *in-situ* formation of CeO₂ nanorods (CeO₂-R) has monotonically decreased the overall length of the nanorods, with 88 nm to 73.9 nm to 21.6 nm of length of rods from 3% to 5% to 10% loading of Pt during the formation of CeO₂. This signifies that the formation of CeO₂ rods along one of the directions is hindered when more Pt²⁺ ions are present in the solution, even though phase formation is not interrupted, but growth along the length is prohibited. Whereas, when Pt incorporation is done *ex-situ* in the second step on the already formed CeO₂-nanorods, there are no change in the rods but there is presence of 2.5-3.5 nanometric sizes of Pt nanoparticles with 3% and 10% Pt loading in two-step process (**Figure 7.10**). **Figure 7.11** show the uniformly distributed CeO₂ nano-cubes (CeO₂-C) have only (100) facets exposed. When Pt is incorporated *ex-situ* on the already formed CeO₂ NCs (CeO₂-C), Pt NPs get embedded on the ceria cubes (facets (200)) with smaller size 2.87 nm for 3p-*ex-situ*-CeO₂-C and 4.15 nm for 10p-*ex-situ*-CeO₂-C (**Figures 7.12** and **7.13**).

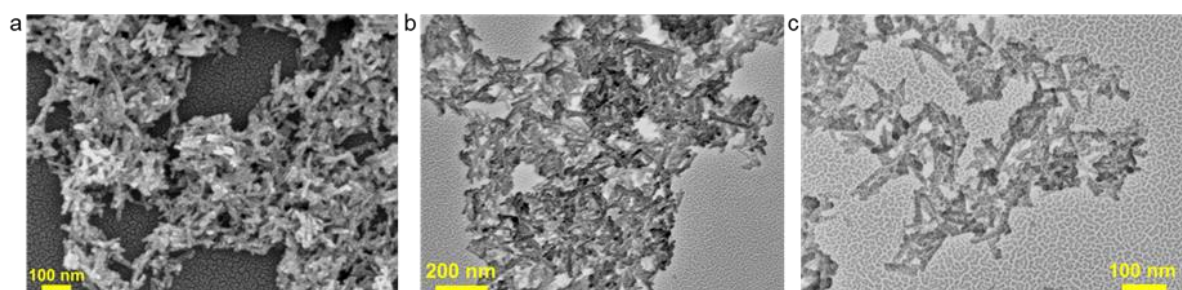


Figure 7.7. SEM images of ceria rods (CeO₂-R) at different resolution.

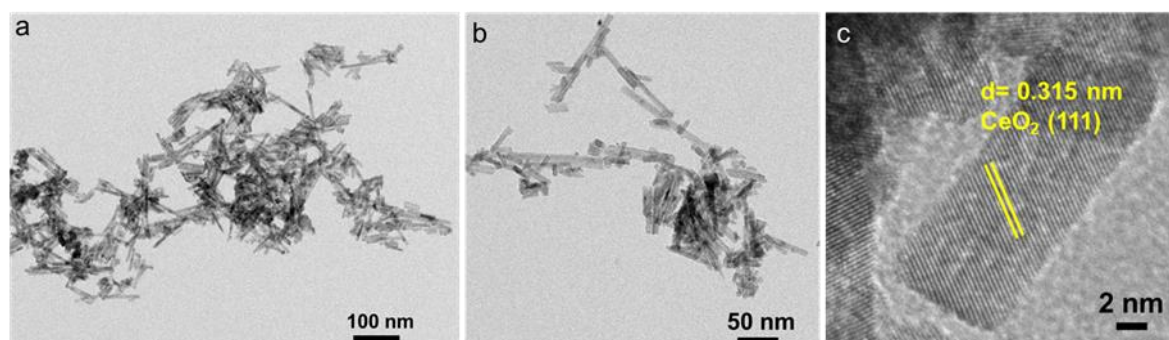


Figure 7.8. (a) and (b) TEM images and (c) HRTEM images of ceria rods (CeO₂-R) at different resolution with exposed (111) facets majorly.

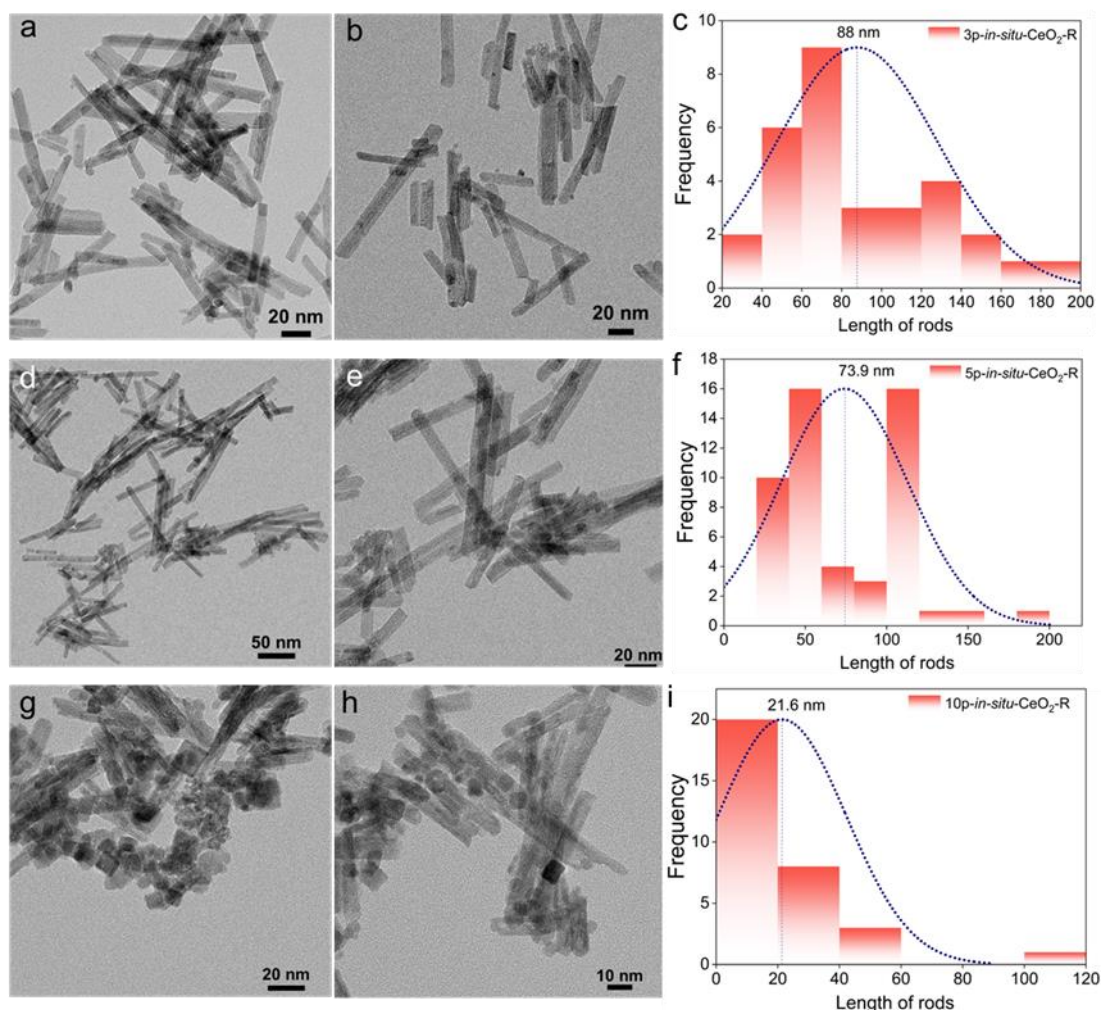


Figure 7.9. (a), (b) TEM images and (c) histogram for particle size distribution of 3% Pt incorporation in CeO₂ rods via *in-situ* process (3p-*in-situ*-CeO₂-R). TEM images of (d), (e) and (f) histogram for particle size distribution of 5% Pt incorporation in CeO₂ rods via *in-situ* process (5p-*in-situ*-CeO₂-R). TEM images of (g), (h) and (i) histogram for particle size distribution of 10% Pt incorporation in CeO₂ rods via *in-situ* process (10p-*in-situ*-CeO₂-R).

Interestingly, when Pt incorporation is done under *in-situ* conditions during the cube's formation, there is distortion in the cube morphology (**Figures 7.14** and **7.15**) and presence of Pt nanoparticles is observed in between two CeO₂ distorted cubes. In the HRTEM image, it is observed that instead of (200) facets, (111) facets of CeO₂ have been found on *in-situ* Pt loading (**Figure 7.15**). This microscopic visualization of distorted ceria NCs supports the observation from PXRD (**Figures 7.6a** and **7.6d**) that peak-intensity ratio of (311):(200) increases drastically with *in-situ* loading of Pt. With the understanding of CeO₂-C morphology under the effect of *in-situ* and *ex-situ* Pt incorporation from TEM images, HRTEM images have shown that Pt has been embedded on CeO₂-C with (111) facets exclusively on (200) facets of CeO₂ under the *ex-situ* process and Pt exposes its (200) and (220) facets when it is enclosed between two distorted CeO₂ NCs under the *in-situ* process (**Figures 7.16a** and **7.16b**). This is because

under the influence of Pt ions during ceria NC formation, CeO₂ exposes its (111) and other of its high-index facets and those facets stabilize (200) and (220) facets of Pt NPs, under the *in-situ* mode. Hence, it can be concluded that ex-situ Pt incorporation is not making any changes in either rod or cube morphology of ceria since it is already designed in the first step (**Figure 7.1**). But there is reduction in rod length and distortion of cube morphology under the *in-situ* Pt incorporation. Thus, while rod formation Pt²⁺ ions hinder the growth after certain length, although there is no intrinsic change in the crystal structure, but there is difference in facet growth observed in case of cubes.

It can be concluded that (200) facets of CeO₂ are not being permitted to grow under the influence of Pt²⁺ ions which promote the growth of (111) and other high-index facets. **Figures 7.17a, 7.17b, 7.17c, and 7.17d** show the schematic representation of Pt and CeO₂ after *in-situ* and *ex-situ* incorporation of Pt to CeO₂ rods and cubes, respectively. **Figures 7.17e and 7.17f** show the front view of (200) and (111) facets of CeO₂. It is observed that in facet (200), O atoms are bonded to two Ce atoms in bridged mode, whereas in (111) each O atom is bonded to three Ce atoms. Hence, when Pt is incorporated during CeO₂ cube formation, the tendency to form two bonds with Ce and one bond with Pt can generally give rise to formation of (111) facets instead of (200).

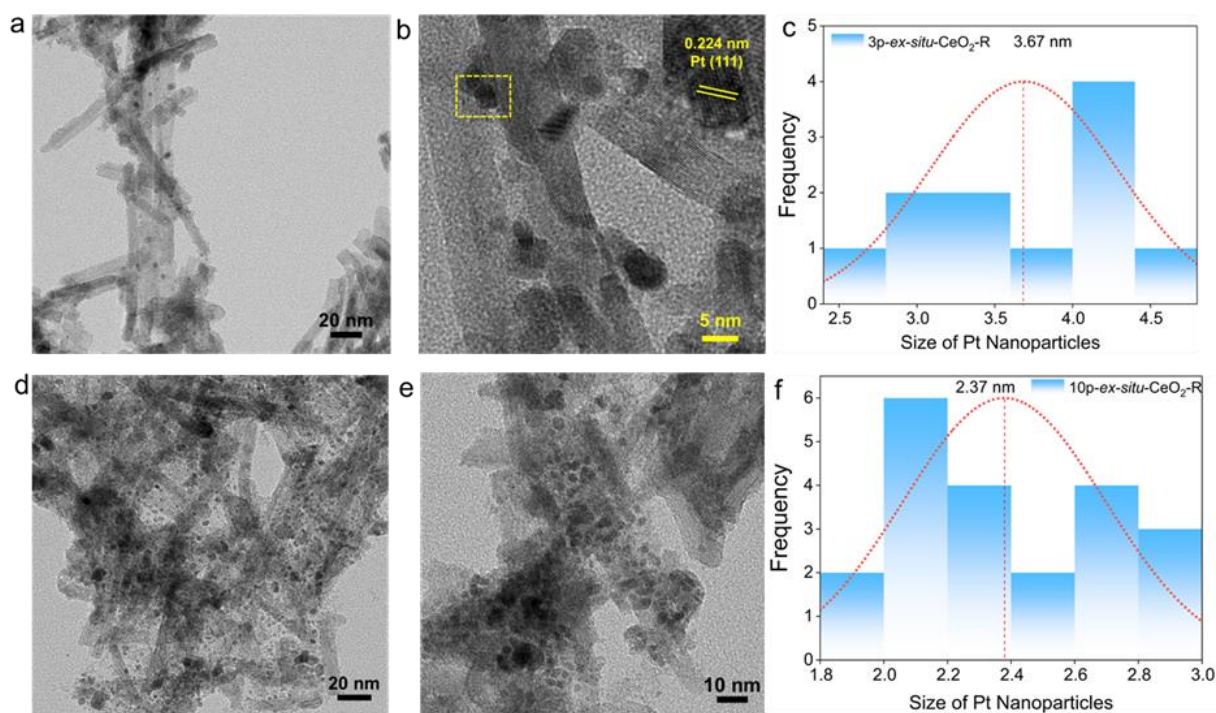


Figure 7.10. (a) TEM and (b) HRTEM images, and (c) histogram for particle size distribution of 3% Pt incorporated ceria rods *ex-situ* (3p-*ex-situ*-CeO₂-R) and (d) and (e) TEM images and (f) particle size distribution of 10% Pt incorporated ceria rods *ex-situ* (10p-*ex-situ*-CeO₂-R).

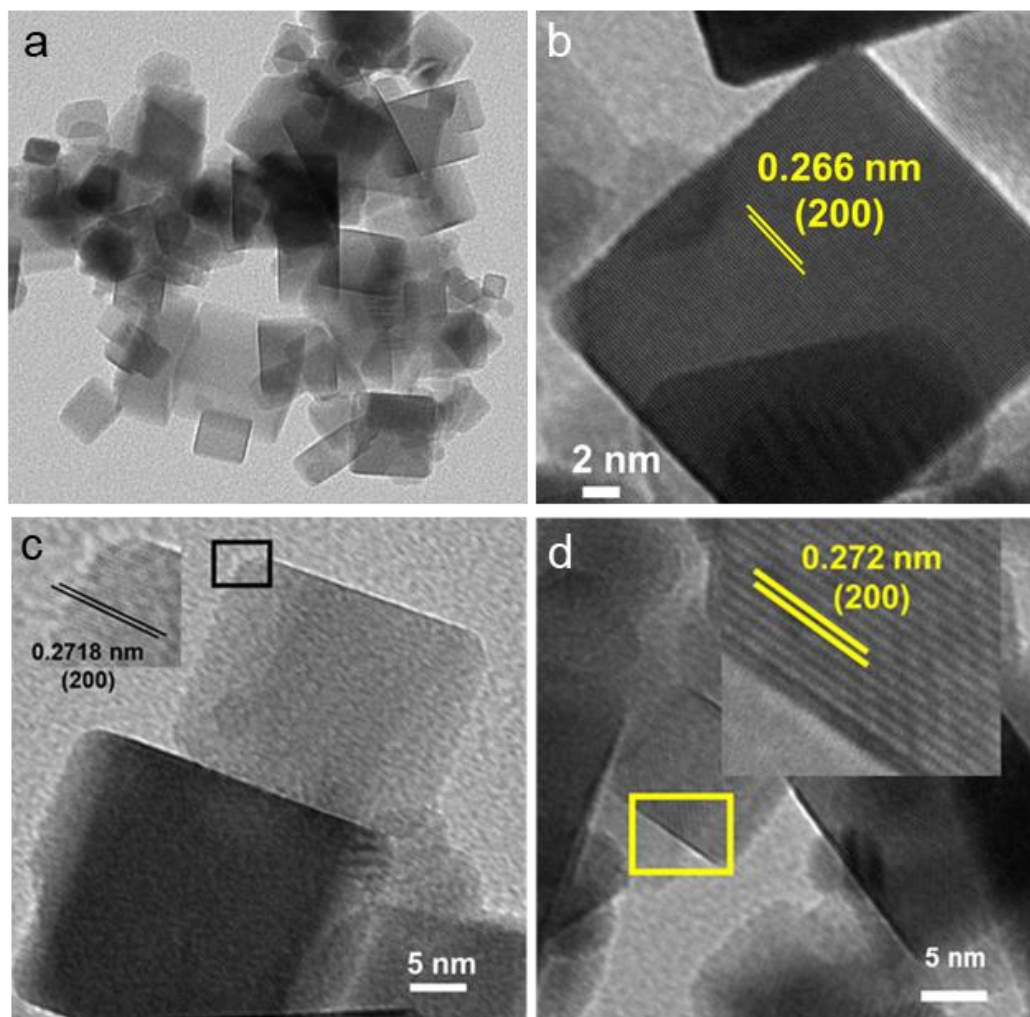


Figure 7.11. (a) TEM images and (b), (c), (d) HRTEM images of ceria cubes (CeO₂-C) at different resolution with exposed (200) facets majorly.

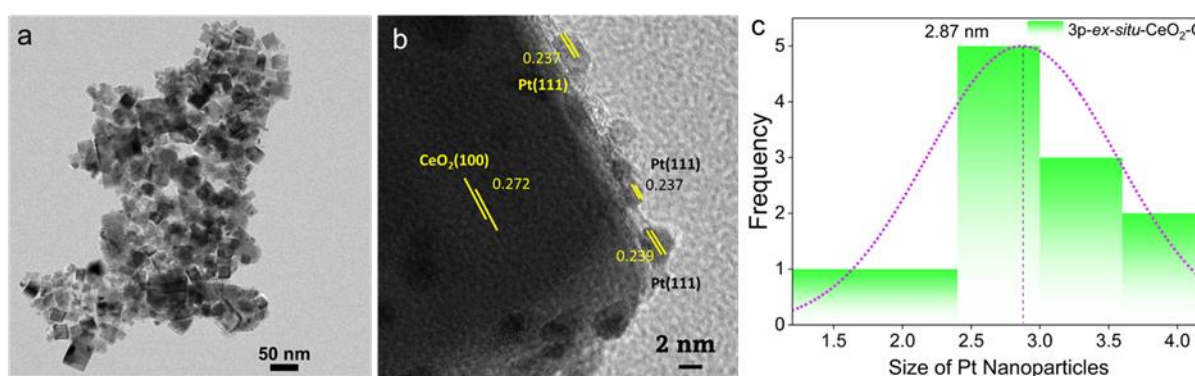


Figure 7.12. (a), (b) TEM images and (c) histogram for particle size distribution of 3% Pt incorporation in CeO₂ cubes via *ex-situ* process (3p-*ex-situ*-CeO₂-C). Major facets exposed are (100) of CeO₂ and (111) facets of Pt.

Thus, surface Pt-O bonds are expected to occur and hence the interface of CeO₂-Pt is having (111) facets instead of (200) facets when Pt²⁺ ions are added during the *in-situ* formation of CeO₂ (schematically shown in **Figure 7.17g**).

In Raman spectroscopy there is a peak at around 457 cm^{-1} corresponding to F_{2g} vibrational mode of CeO_2 .¹⁶ In addition to that, there is increase in intensity of the peak at 559.9 cm^{-1} in case of Pt incorporation in CeO_2 cubes under *in-situ* conditions which indicates an increase in oxygen vacancies O_{vac} (**Figure 7.18a**), whereas there is not much O_{vac} formation in case of *ex-situ* process for cube (**Figure 7.18b**). The similar trend in O_{vac} increment is also observed when Pt is incorporated *in-situ* in CeO_2 -rods (**Figure 7.18c**). But a huge increase in O_{vac} was observed when Pt is incorporated in ceria rods under *ex-situ* conditions with a huge increase in the peak intensity at around 560 cm^{-1} (**Figure 7.18d**). It is visible from the Raman spectra, that the amount of O_{vac} of any concentration (here 10%) follows the trend of $10\text{p-}ex\text{-situ-CeO}_2\text{-C} < 10\text{p-}in\text{-situ-CeO}_2\text{-C} = 10\text{p-}in\text{-situ-CeO}_2\text{-R} \ll 10\text{p-}ex\text{-situ-CeO}_2\text{-R}$. This observation is supported by XPS spectra where Ce^{3+} peak area is seen to be more in *in-situ* Pt incorporated in ceria nano-cubes than the *ex-situ* incorporated ones (**Figure 7.19a**).

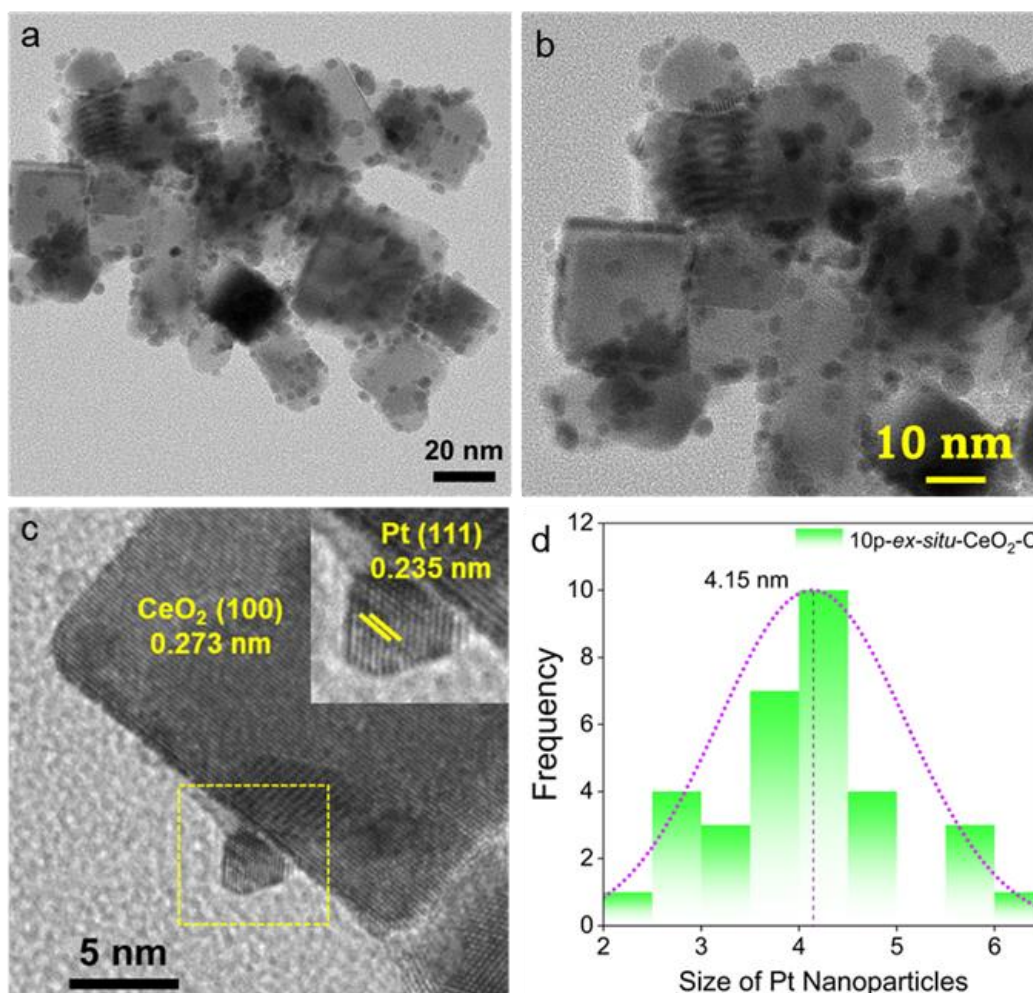


Figure 7.13. (a), (b) TEM images and (c) histogram for particle size distribution of 10% Pt incorporation in CeO_2 cubes via *ex-situ* process (10p-*ex-situ*- $\text{CeO}_2\text{-C}$). Major facets exposed are (100) of CeO_2 and (111) facets of Pt.

Similarly, *ex-situ* incorporated Pt on ceria nano-rods shows more Ce³⁺ than in-situ incorporated ones (**Figure 7.19b**) which support the higher amount of O_{vac} in *ex-situ* Pt incorporated ceria nano-rods. The trend of content of Ce³⁺ follows the order: 10p-*ex-situ*-CeO₂-C < 10p-*in-situ*-CeO₂-C = 10p-*in-situ*-CeO₂-R << 10p-*ex-situ*-CeO₂-R which is same as the amount of O_{vac} as observed from Raman spectroscopy. The content of O_{vac} was finally confirmed by EXAFS fitting of the Ce L₃ edge Fourier transformed R-space data. **Table 7.1** lists the EXAFS fitting parameters after considering the Ce-O single scattering path from the first coordination sphere. It is observed that Ce-O coordination number decreases with in-situ Pt incorporation in CeO₂-C and *ex-situ* Pt incorporation in CeO₂-R which further supports the XPS and Raman observation.

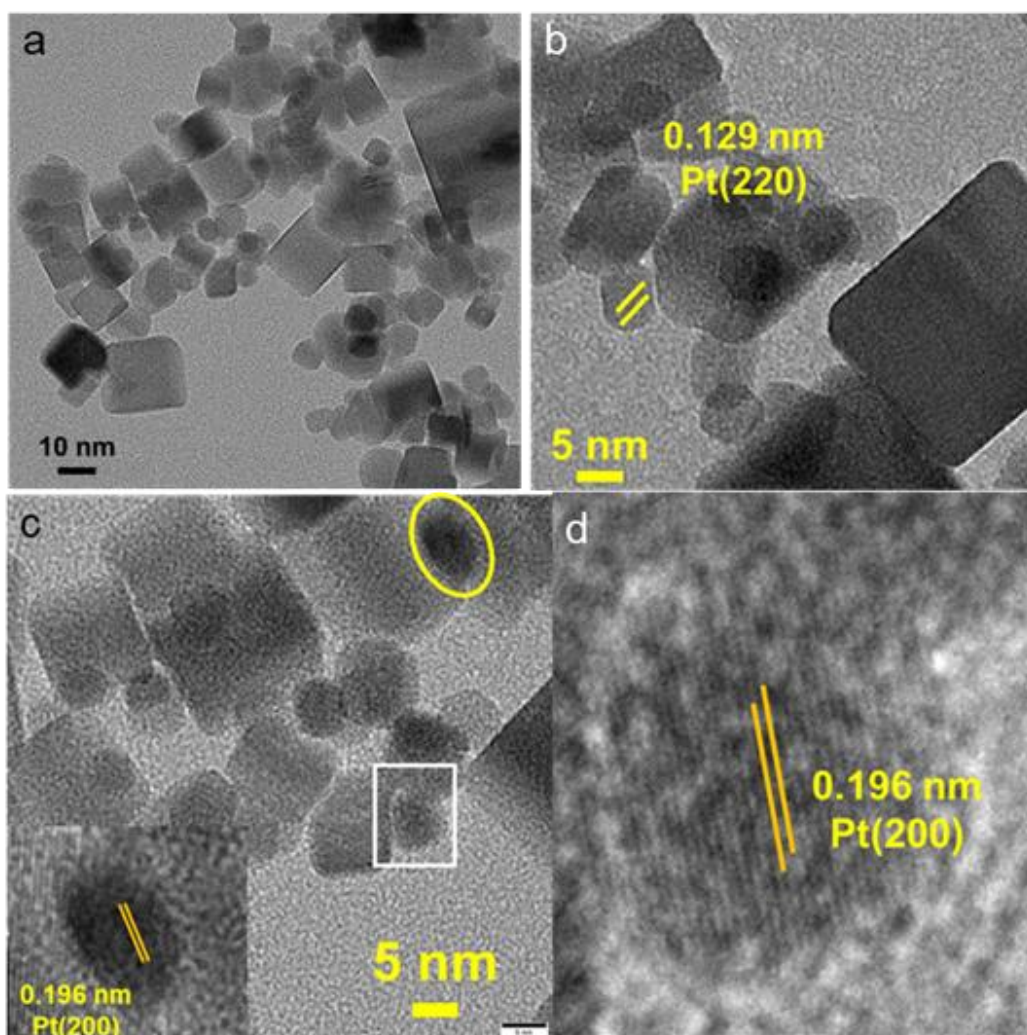


Figure 7.14. (a) TEM images and (b), (c), (d) HRTEM images of 3% Pt incorporated in ceria cubes via *in-situ* process (3p-*in-situ*-CeO₂-C) at different resolution with exposed (200) and (220) facets of Pt.

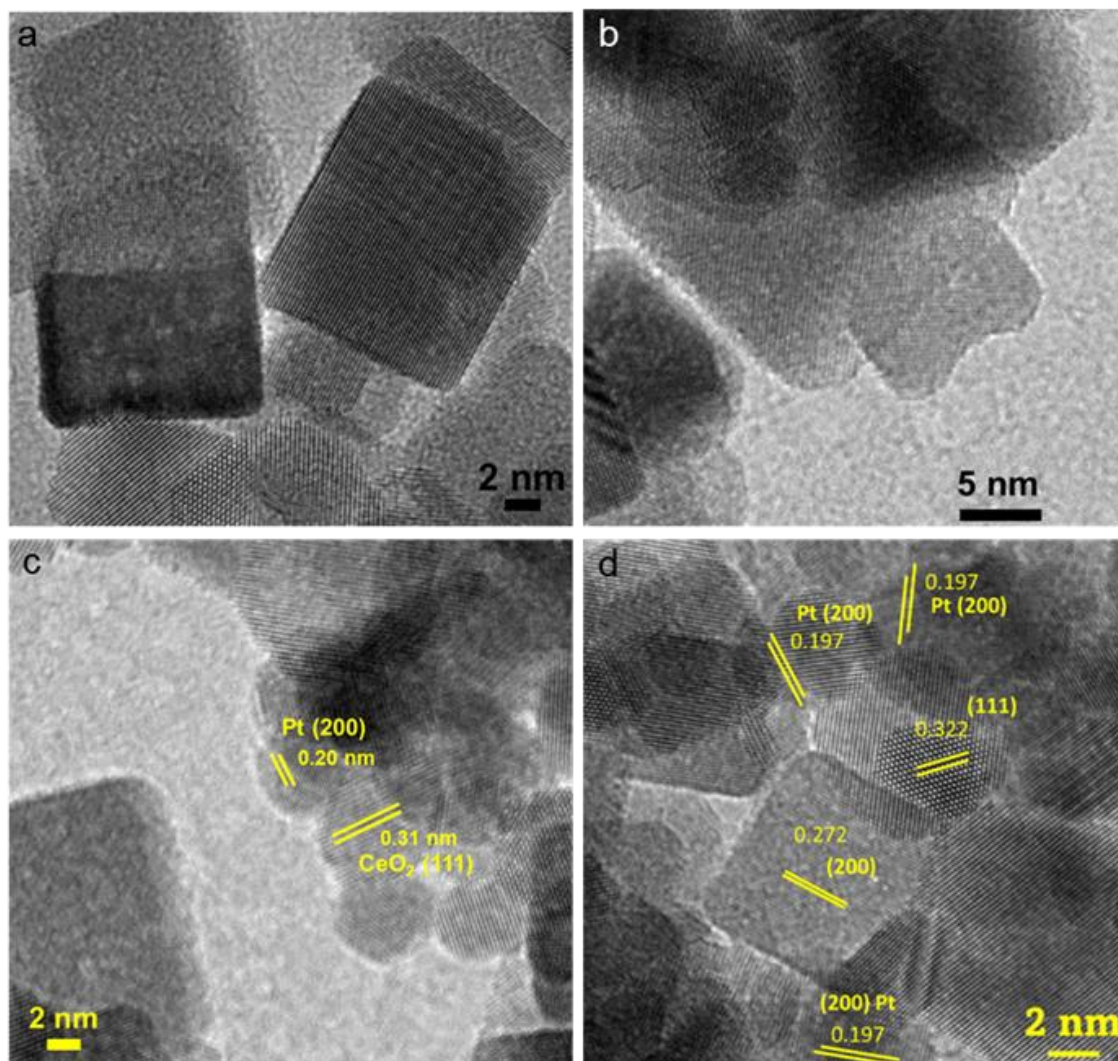


Figure 7.15. (a), (b) TEM images and (c), (d) HRTEM images of 10% Pt incorporated in ceria cubes via *in-situ* process (10p-*in-situ*-CeO₂-C) at different resolution with exposed (200) and (220) facets of Pt and (111) facets of CeO₂.

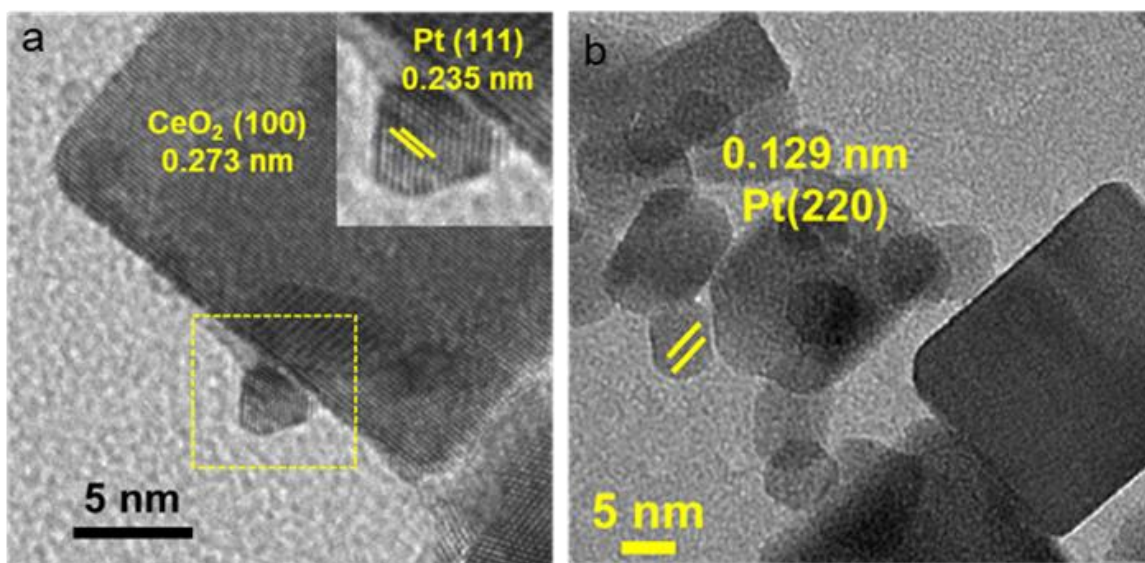


Figure 7.16. HRTEM images of (a) 10p-*ex-situ*-CeO₂-C and (b) 10p-*in-situ*-CeO₂-C.

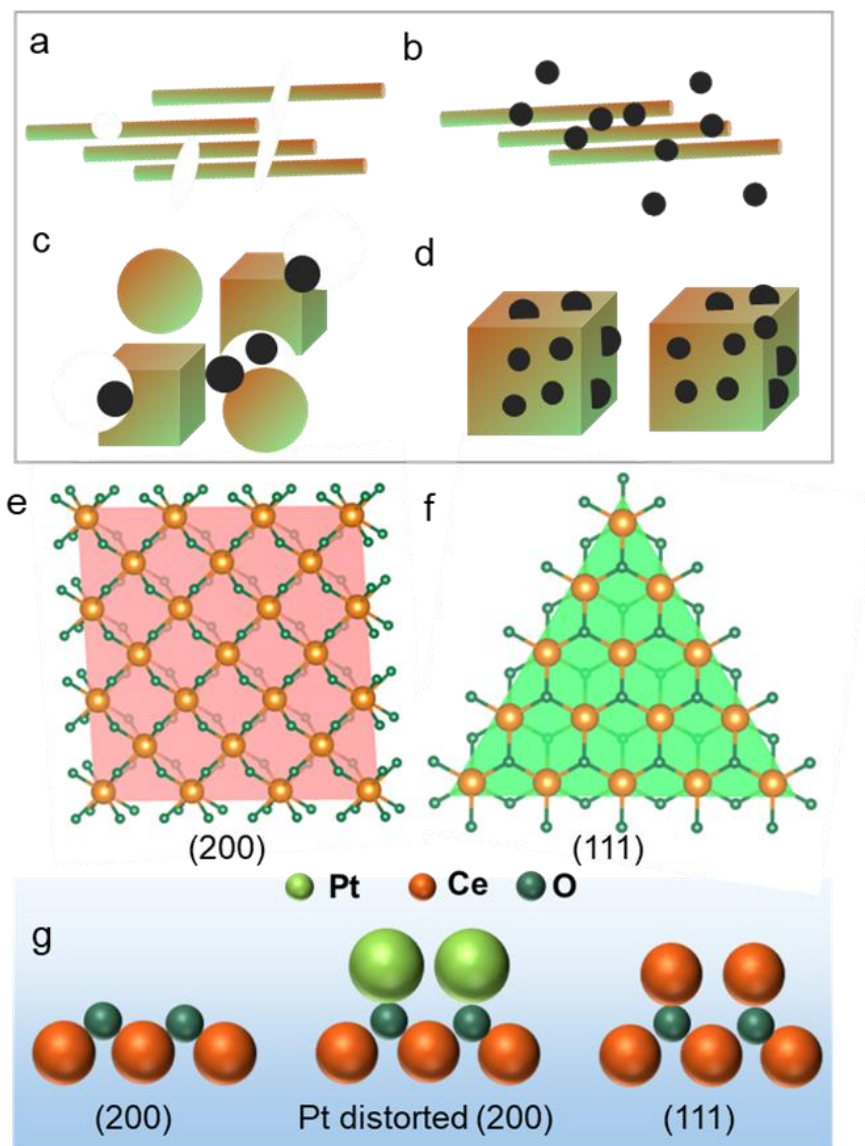


Figure 7.17. Schematic of CeO₂ rods (a) during In-situ Pt addition, (b) during ex-situ Pt addition. Schematic of CeO₂ cubes (a) during In-situ Pt addition, (b) during ex-situ Pt addition. Crystallographic representations of (e) (200) facets and (f) (111) facets of Ceria. (g) Schematic representation of influence of Pt²⁺ during *in-situ* formation of CeO₂ cubes and distortion of (200) and formation of (111) facets triggered by Pt atoms.

Table 7.1. EXAFS fitting parameters of Ce-O shell for pristine CeO₂ cube and rod with Pt loading under in-situ and ex-situ conditions of synthesis.

Sample	Shell	CN	R (Å)	σ^2	E ₀
CeO ₂ -C	Ce-O	5.701	2.34164	0.00752	15.048
3p- <i>in-situ</i> -CeO ₂ -C	Ce-O	5.025	2.30953	0.00479	6.372
10p- <i>in-situ</i> -CeO ₂ -C	Ce-O	4.6634	2.31981	0.00617	7.168

3p- <i>ex-situ</i> -CeO ₂ -C	Ce-O	4.92	2.32930	0.00378	6.831
5p- <i>in-situ</i> -CeO ₂ -C	Ce-O	4.74578	2.33189	0.00582	7.271
CeO ₂ -R	Ce-O	4.570	2.33283	0.00737	14.674
10p- <i>in-situ</i> -CeO ₂ -R	Ce-O	4.2020	2.32491	0.00526	7.856
10p- <i>ex-situ</i> -CeO ₂ -R	Ce-O	2.8898	2.29218	0.0069	3.963

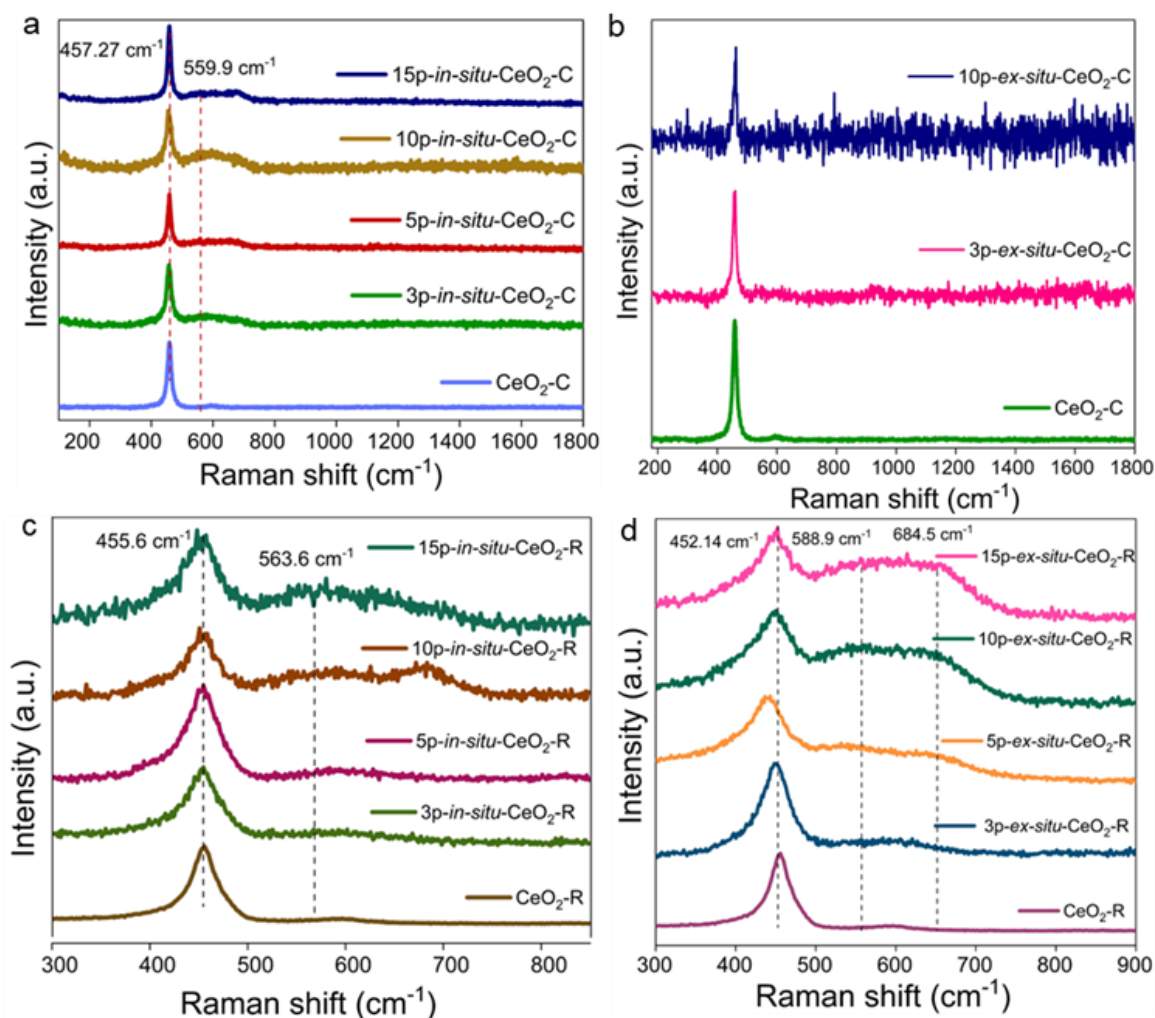


Figure 7.18. (a) Raman spectra of CeO₂-C and different loading of Pt under in-situ conditions in CeO₂-C. Raman spectra of (b) 3% and 10% Pt incorporation in CeO₂-C via *ex-situ* process and Raman spectra of CeO₂-R and 3%, 5%, 10%, and 15% Pt incorporation in CeO₂-R via (c) *in-situ* process and (d) *ex-situ* process.

Figure 7.20a and **7.20b** show the fitted EXAFS data for Ce *L*₃-edge for in-situ and ex-situ incorporated Pt in CeO₂-C and CeO₂-R, respectively. From X-ray absorption near edge spectra (XANES), it is observed that Ce³⁺ is present in significant amount for the *ex-situ* incorporated Pt on CeO₂, as compared to *in-situ* incorporated ones.^{17, 18}

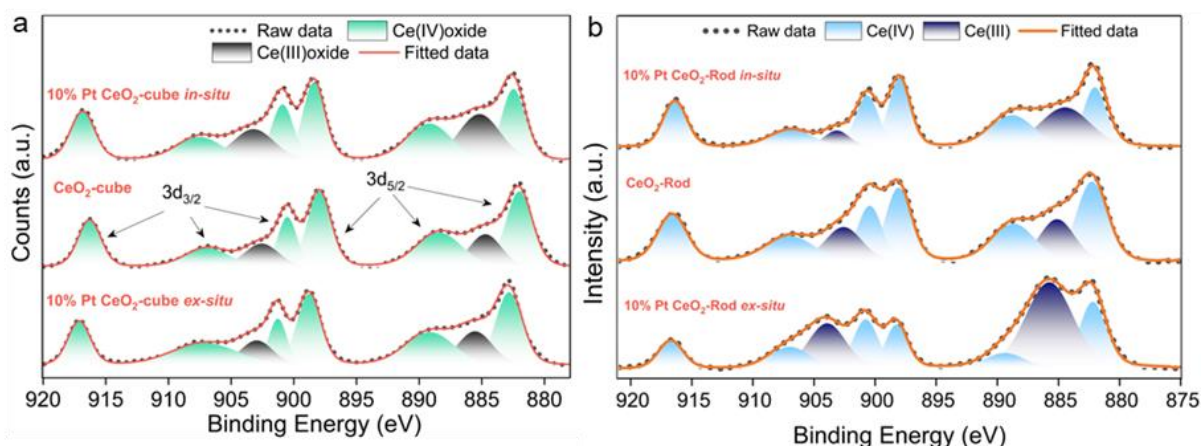


Figure 7.19. Fitted Ce 3d XPS spectra of 10% Pt loading under *ex-situ* and *in-situ* processes in (b) CeO₂-C and (c) CeO₂-R.

Figure 7.21 shows that with increased loading percentage of Pt up to 10% increases the peak for Ce³⁺ via *ex-situ* synthesis, and **Figure 7.22** shows that there is not much change in the XAS data in the *in-situ* incorporation of Pt in CeO₂-R. XAS data is thus supporting the observation achieved from Raman spectroscopy and XPS characterizations. From the inset in **Figure 7.23a**, peak corresponding to Ce³⁺ is more in 3p-*ex-situ*-CeO₂-R than both CeO₂-R and 3p-*ex-situ*-CeO₂-R. **Figure 7.23b** shows the conclusive schematic of qualitative content of O_{vac} and Ce³⁺ in all the Pt loaded rods and cubes as characterized by various spectroscopic techniques like XPS, Raman spectroscopy, and XAS. Analyzing the oxidation state of Ce from Ce L₃-edge XAS, Ce 3d XPS and Raman spectra, Pt L₃-edge XAS and Pt 4f XPS have been performed to understand the fate of Pt under *in-situ* and *ex-situ* addition to both the CeO₂ rod and cube morphologies.

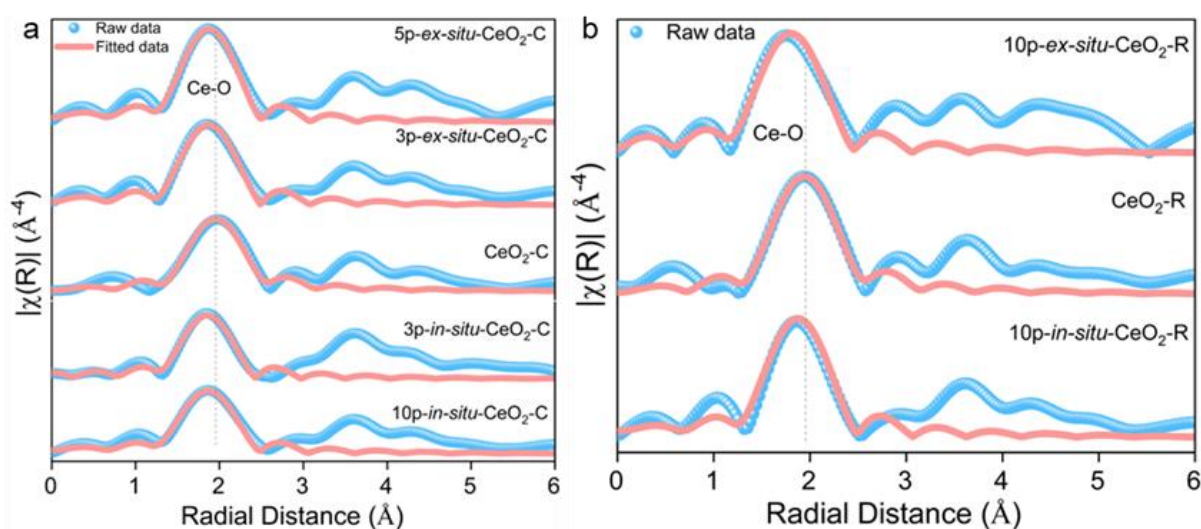


Figure 7.20. (a) Fitted EXAFS spectra for *ex-situ* and *in-situ* Pt loaded CeO₂-C. (b) Fitted EXAFS of CeO₂-R, 10p-*in-situ*-CeO₂-R, and 10p-*ex-situ*-CeO₂-R.

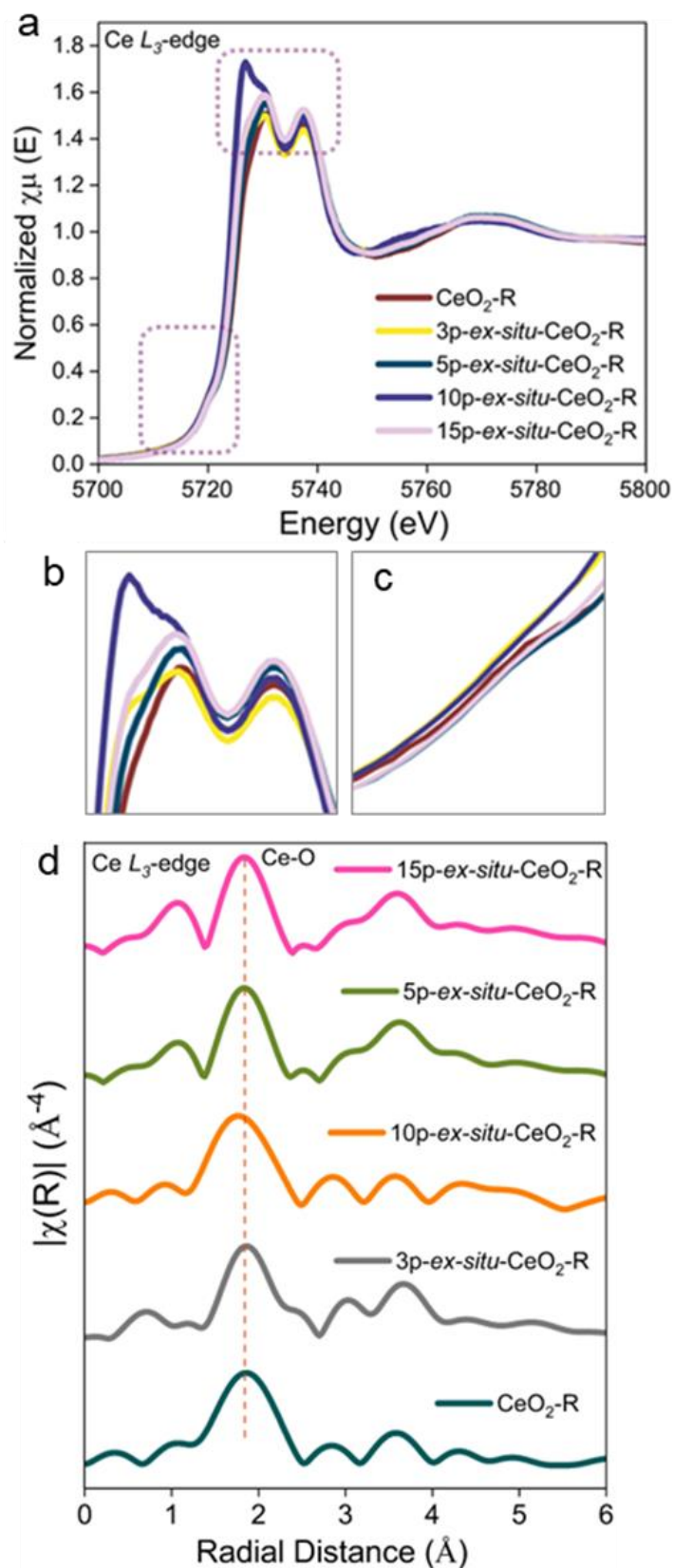


Figure 7.21. (a) XANES of CeO₂-R, 3p-ex-situ-CeO₂-R, 5p-ex-situ-CeO₂-R, 10p-ex-situ-CeO₂-R, and 15p-ex-situ-CeO₂-R (b) zoomed in white-line intensity region and (c) absorption edge of XANES spectra. (d) Fourier transformed R-space data of CeO₂-R, 3p-ex-situ-CeO₂-R, 5p-ex-situ-CeO₂-R, 10p-ex-situ-CeO₂-R, and 15p-ex-situ-CeO₂-R.

From Pt 4f XPS spectra (**Figure 7.24a**) for 10p-*in-situ*-CeO₂-R and 10p-*in-situ*-CeO₂-C, it is found that surface Pt-oxides are much more in case of 10p-*in-situ*-CeO₂-R, whereas a higher binding energy value of metallic Pt 71.51 eV for 10p-*in-situ*-CeO₂-C is observed when metallic Pt is at 71.11 eV for 10p-*in-situ*-CeO₂-R.

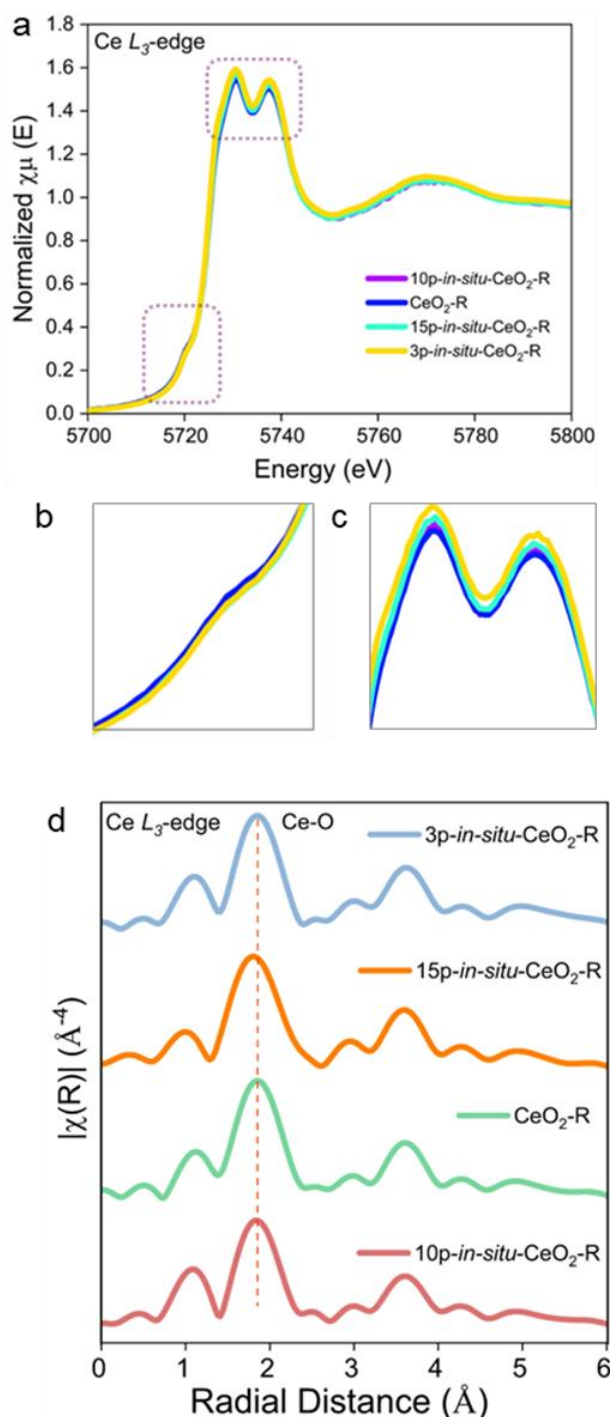


Figure 7.22. (a) XANES of CeO₂-R, 3p-*in-situ*-CeO₂-R, 10p-*in-situ*-CeO₂-R, and 15p-*in-situ*-CeO₂-R (b) zoomed in white-line intensity region and (c) absorption edge of XANES spectra. (d) Fourier transformed R-space data of CeO₂-R, 3p-*in-situ*-CeO₂-R, 10p-*in-situ*-CeO₂-R, and 15p-*in-situ*-CeO₂-R.

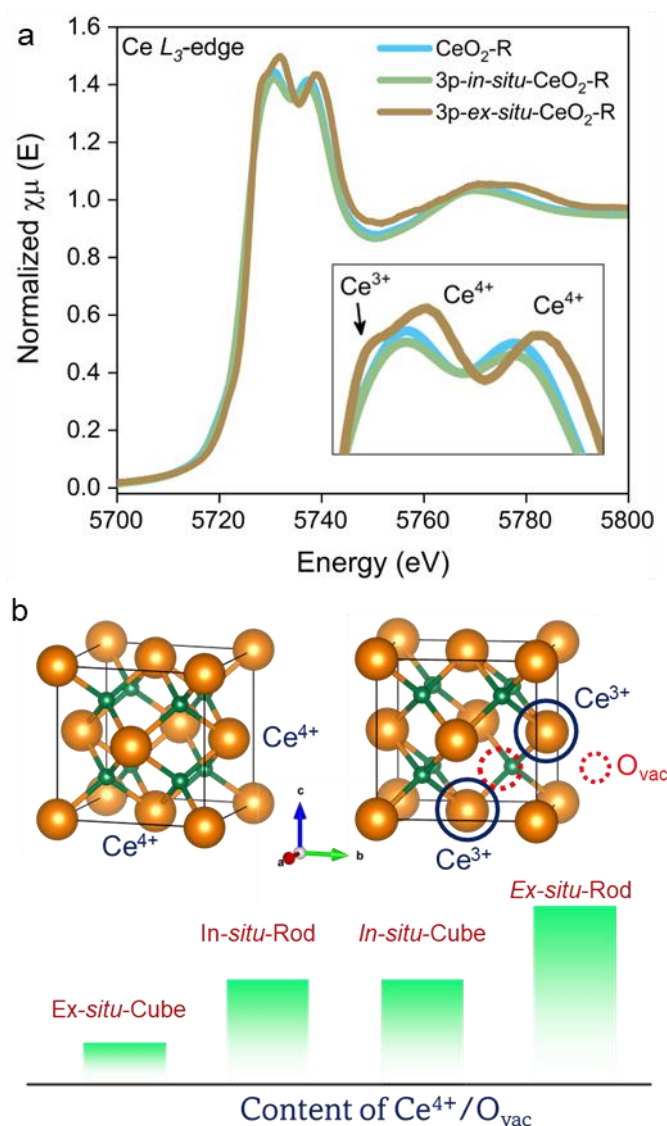


Figure 7.23. (a) XANES spectra for 3% *ex-situ* and *in-situ* Pt loaded $\text{CeO}_2\text{-R}$. (b) Schematic representation of O_{vac} and Ce^{3+} detection via XAS, XPS, and Raman spectroscopy.

This can be correlated with the TEM images where **Figure 7.9** does not show much Pt nearby the CeO_2 rods, whereas in **Figure 7.16b**, the Pt NPs are trapped in between two CeO_2 distorted nano-cubes.

Hence, Pt has formed random clusters of isolated metallic Pt NPs and traces of surface oxides for 10p-*in-situ*- $\text{CeO}_2\text{-R}$, whereas there is proper interface formation between Pt clusters and $\text{CeO}_2\text{-C}$ which leads to some interfacial Pt-O bond formation and charge transfer from Pt due to which higher binding energy is achieved for 10p-*in-situ*- $\text{CeO}_2\text{-C}$. Similar observation is obtained from Pt L_{3} -edge XANES spectra which exhibits that the white-line is observed at higher energy for 10p-*in-situ*- $\text{CeO}_2\text{-C}$ than for 10p-*in-situ*- $\text{CeO}_2\text{-R}$ (**Figure 7.24b**). **Figure 7.25a** shows the R-space data for 10% Pt loading on cube and rod using both *in-situ* and *ex-situ* process of synthesis. This indicates that mild presence of Pt-O is present in cubes for both

in-situ and ex-situ synthesis, whereas for ex-situ synthesis of Pt loading in rod is not present at all. **Figure 7.25b** shows the binding energy of Pt metallic state is relatively higher for 10p-in-situ-CeO₂-C than 10p-ex-situ-CeO₂-C which means electron transfer from Pt is more for 10p-in-situ-CeO₂-C.

This can be directly correlated to **Figures 7.16a** and **7.16b** which show that more Pt-CeO₂ interface is present in case of 10p-in-situ-CeO₂-C than 10p-ex-situ-CeO₂-C. Moreover, for 10p-in-situ-CeO₂-C, (111) facets of CeO₂ and for 10p-ex-situ-CeO₂-C, (200) facets of CeO₂ are exposed.

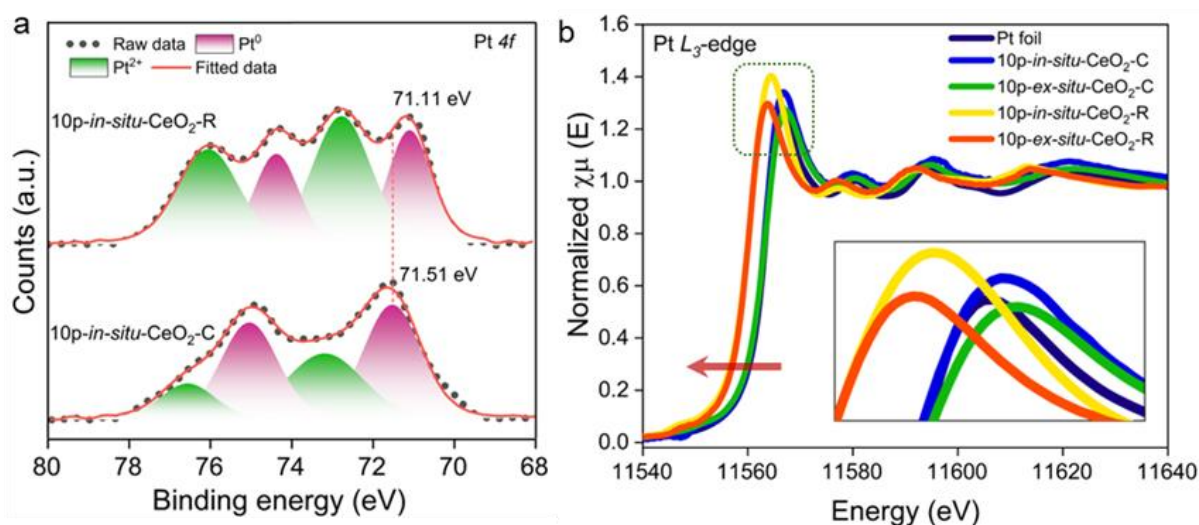


Figure 7.24. (a) Pt 4f XPS spectra of 10p-in-situ-CeO₂-C and 10p-in-situ-CeO₂-R. (b) Pt L₃-edge XANES spectra of 10p-in-situ-CeO₂-C, 10p-ex-situ-CeO₂-C, 10p-in-situ-CeO₂-R, 10p-ex-situ-CeO₂-R.

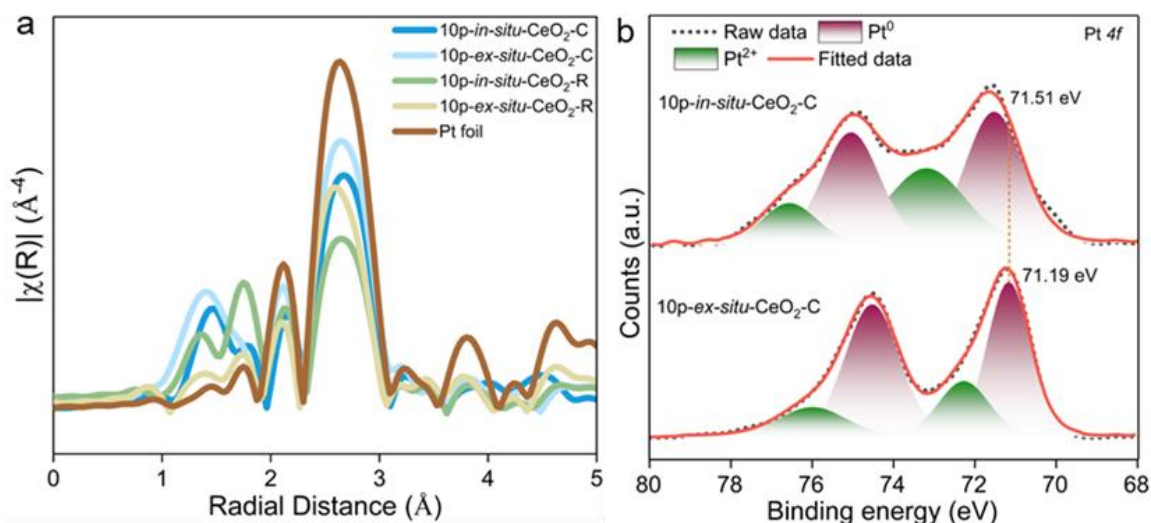


Figure 7.25. (a) R-space data for 10p-in-situ-CeO₂-R, 10p-ex-situ-CeO₂-R, 10p-in-situ-CeO₂-C, 10p-ex-situ-CeO₂-C, and Pt foil. (b) Pt 4f XPS spectra of 10p-in-situ-CeO₂-C and 10p-ex-situ-CeO₂-C.

Different facets of CeO_2 will have different Ce-O dangling bonds making Pt-O formation easier for (111) than the (200) facets, which makes Pt metal more electron deficient in 10p-in-situ- CeO_2 -C than 10p-ex-situ- CeO_2 -C.

Figures 7.26a and **7.26b** also indicates the similar observation that Pt-O bonds are present both in ex-situ and in-situ Pt loading in ceria cubes which means Pt- CeO_2 is formed in both the cases with more charge transfer from Pt in case of the in-situ samples which can be directly related to the increased Pt- CeO_2 interface and different facets of CeO_2 exposed for in-situ and ex-situ cases. It has been schematically represented that with 3% Pt loading via in-situ mode cube morphology, there is Pt substitution at Ce positions (as obtained from PXRD, **Figure 7.6b**) and further increased loading, there are prominent formation Pt nanoclusters.

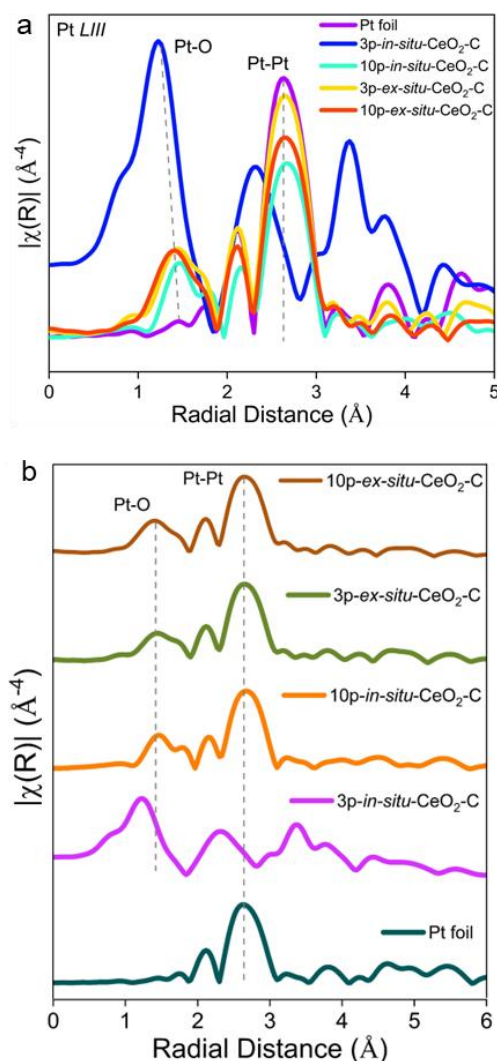


Figure 7.26. (a) Fourier transformed R-space data for 3p-in-situ- CeO_2 -C, 10p-in-situ- CeO_2 -C, 3p-ex-situ- CeO_2 -C, 10p-ex-situ- CeO_2 -C. (b) R-space data for 3p-in-situ- CeO_2 -C, 10p-in-situ- CeO_2 -C, 3p-ex-situ- CeO_2 -C, 10p-ex-situ- CeO_2 -C, and Pt foil.

It also shows with ex-situ mode of Pt loading there is no substitution of Pt at Ce positions and only Pt nanocluster formation is observed. It needs to be observed that there will be generation of O_{vac} to retain the electroneutrality when 2+ charged Pt is substituting 4+ charged Ce ions. **Figure 7.27** shows schematically the incorporation of Pt into the CeO₂ lattice during in-situ incorporation in cube morphology. When only 3% of Pt is loaded, there is presence of smaller Pt nanoclusters and along with that some Pt substitution in the CeO₂ cube lattice also which is reflected in a very small Pt PXRD peak and prominent shift in the CeO₂ PXRD peak. Whereas on *ex-situ* incorporation of Pt, there is only formation of Pt NPs on CeO₂ and there is no Pt²⁺ substituting Ce⁴⁺ in the CeO₂ lattice. Wavelet transformed **Figures 7.28a**, **7.28b**, and **7.28c** show clearly the presence of weak Pt-O bonds in both 10p-ex-situ-CeO₂-C and 10p-in-situ-CeO₂-C which is totally absent in case of Pt foil.

Electrochemical HER is being conducted using 0.5 M H₂SO₄ for the 10% Pt loaded catalysts on both cubes and rods using in-situ and ex-situ process of synthesis. **Figure 7.29a** and **b** show the CV for 10p-ex-situ-CeO₂-C and 10p-in-situ-CeO₂-C at the region of H-adsorption and desorption. **Figure 7.29c** shows the plot of peak maxima position (for H-desorption peak) vs. scan rate. It is observed that a very low slope of 2.3×10^{-6} is observed for 10p-in-situ-CeO₂-C. The lower the value of the slope, the higher the feasibility of H-spillover mechanism. **Figure 7.30a** displays the linear sweep voltammetry plots for all 10p-ex-situ-CeO₂-C, 10p-in-situ-CeO₂-C, 10p-ex-situ-CeO₂-R, 10p-in-situ-CeO₂-R, and state-of-the-art catalyst 20% Pt/C. The potential requirement for achieving 10 mA/cm² follows the trend of 10p-in-situ-CeO₂-R (41.99 mV) > 20% Pt/C (30.55 mV) > 10p-ex-situ-CeO₂-R = 10p-ex-situ-CeO₂-C > 10p-in-situ-CeO₂-C. The HER activity trend has a direct relationship with the existence of Pt NPs along with CeO₂. As already observed from all PXRD patterns (**Figures 7.6a**, **7.3**, **7.4**, and **7.5**), Pt NPs are present in all the cases of in-situ and ex-situ for both cube and rod morphologies of ceria. If the content of Pt is the major descriptor, then all the catalysts should be showing similar activity.

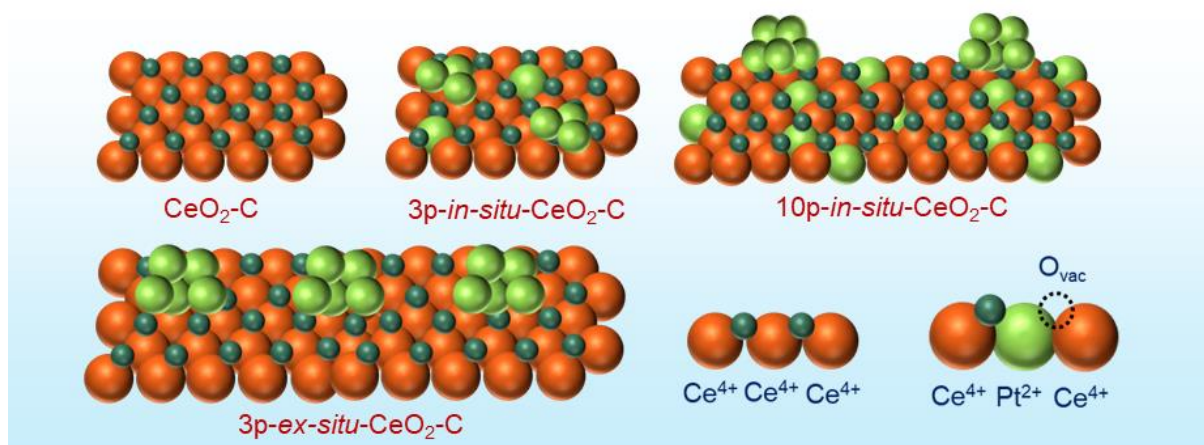


Figure 7.27. Schematic representation of Pt-Ceria interface in *in-situ* and *ex-situ* Pt incorporated CeO_2 cubes.

Interesting observations from TEM images indicate that Pt NPs are not near the CeO_2 rods under *in-situ* conditions, non-uniformity of the catalyst is being observed (**Figure 7.9**). This is the reason behind the lowest activity of $10\text{p-in-situ-CeO}_2\text{-R}$ and high amounts of surface Pt-oxides which will decrease the activity. For *ex-situ* Pt addition in rods, both the presence of Pt NPs and CeO_2 rods are observed but non-uniform interfacial interaction between the two are observed (**Figure 7.10**). Some of the Pt NPs are on the rods and some are outside the rods, hence the activity is not completely from interfacial dynamics. Whereas, for the cube morphology, Pt NPs are always embedded on the CeO_2 -cubes only (**Figures 7.12, 7.13, 7.14 and 7.15**).

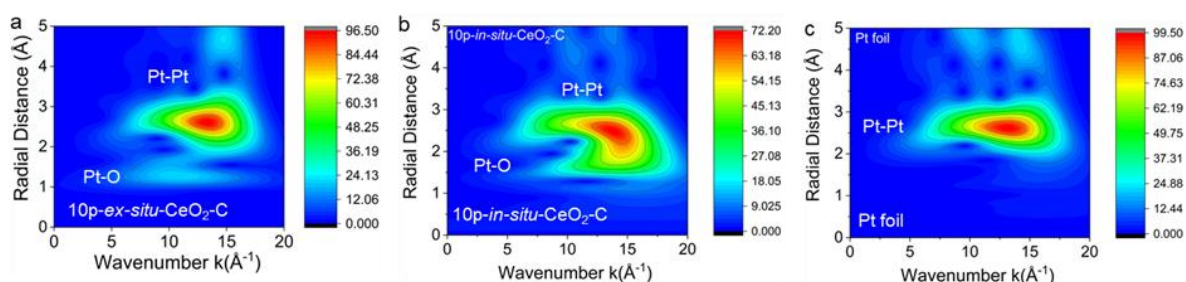


Figure 7.28. Wavelet transform of (f) $10\text{p-ex-situ-CeO}_2\text{-C}$, (g) $10\text{p-in-situ-CeO}_2\text{-C}$, and (h) Pt foil.

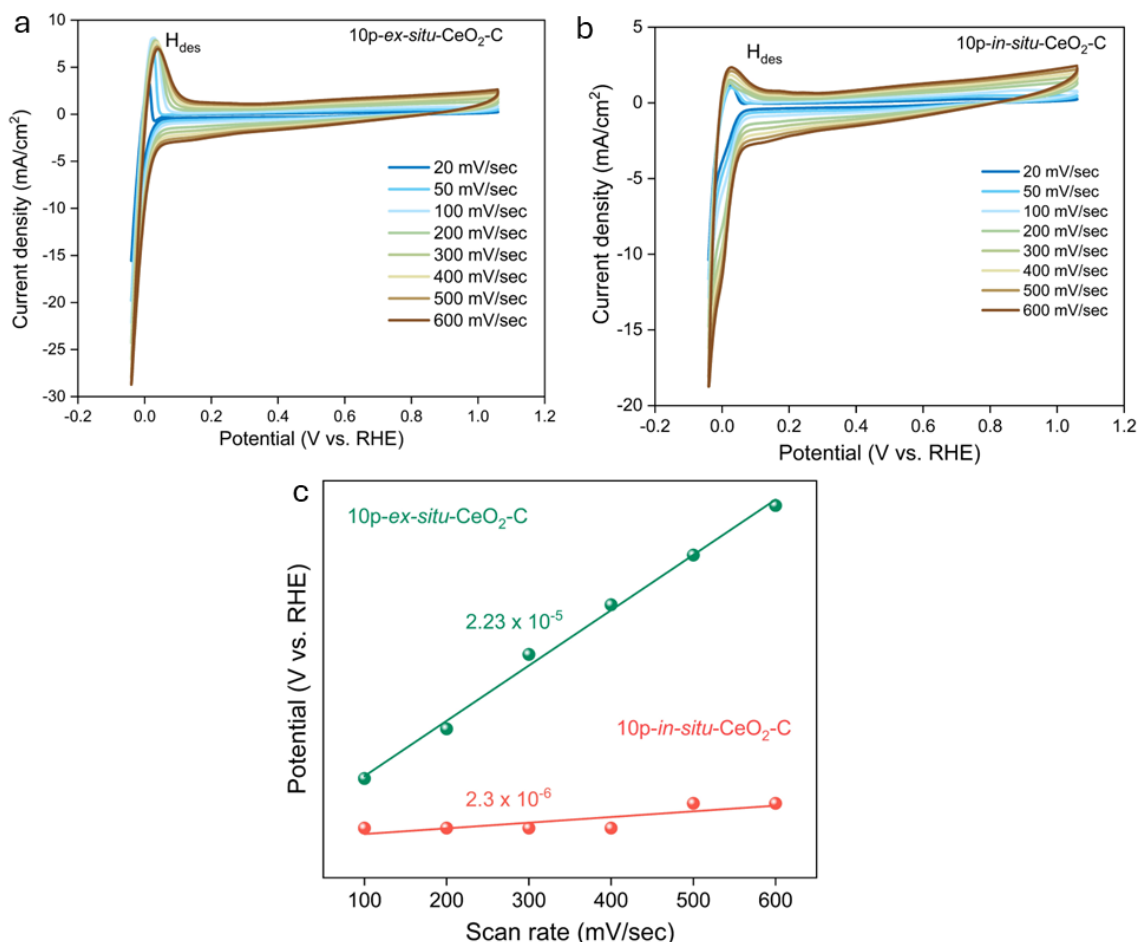


Figure 7.29. CV for H-UPD for both (a) ex-situ, (b) in-situ Pt incorporated catalysts, (c) Peak maxima vs. scan rate plot.

From **Figures 7.16a** and **7.16b**, it is interestingly observed that Pt is having more interface with CeO₂ cubes in in-situ based Pt loaded synthesis. Moreover, CeO₂ has exposed (200) facets for 10p-ex-situ-CeO₂-C and (111) facets for 10p-in-situ-CeO₂-C. On the other hand, Pt NPs have stabilized (111) facet on (200) facets of CeO₂ and (200) and (220) facets on (111) facets of CeO₂ with distorted cubelike structure. Raman spectroscopy, EXAFS fitting of Ce-O shell and XPS have confirmed that 10p-in-situ-CeO₂-C has moderate O_{vac} and Ce³⁺ content.

Overall, the enhanced HER activity of 10p-in-situ-CeO₂-C compared to its ex-situ analogue, 10p-ex-situ-CeO₂-C can be explained from the interfacial interaction of Pt and CeO₂, and the role of different facets of Pt, and finally the role of O_{vac} and Ce³⁺ in spilling over H-atoms from Pt surface to CeO₂ surface for enhanced HER stability and kinetics.

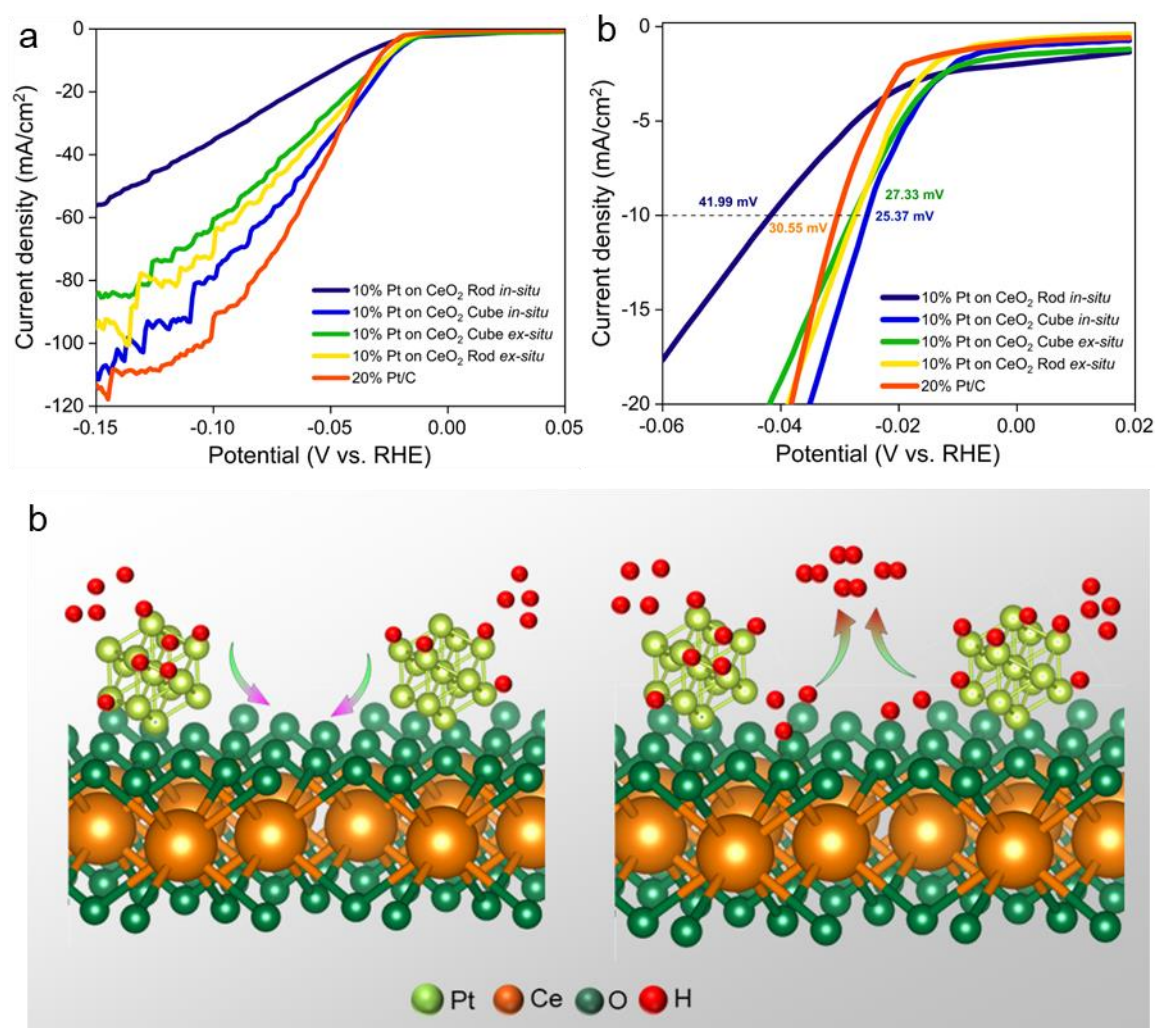


Figure 7.30. (a, b) Linear sweep voltammograms for 10% Pt loaded catalysts during HER in 0.5 M H₂SO₄ using the scan rate of 5 mV/sec. (c) Schematic representation of plausible reaction mechanism.

It has been previously reported that acid mediated HER activity on different facets of Pt follows the trend of (111) \ll (100) $<$ (110).^{19, 20} This partially answers why distorted cubes (under *in-situ* conditions of Pt loading) is exhibiting the best activity as the (110) and (100) facets of Pt are getting more exposed when it is trapped between two distorted ceria cubes. Moreover, the stabilization of H atoms on CeO₂ facets is highly essential for a successful H-spillover to take place from the adsorbed H atoms on Pt clusters.^{21, 22} More H adsorption will happen on either on labile O²⁻ ions or available Ce³⁺ ions on CeO₂ surface. The versatile switchability of Ce⁴⁺/Ce³⁺ makes electron transfer from Ce³⁺ to H atoms to activate the H-atom. Hence, with a feasible H-atom spillover, the overall kinetics and availability of Pt active sites will increase, and the HER activity will also increase. The schematic in **Figure 7.30c** shows the H-spillover mechanism with Pt cluster embedded on CeO₂ facet.

Figure 31a and **b** shows the in-situ Raman spectra for 10p-in-situ-CeO₂-C during HER. The intensity ratio of F_{2g}/O_{vac} is calculated for the spectra on increasing time at -0.7 V vs. Ag/AgCl. It is observed that on increasing time, there is an increase in O_{vac} and again with further increase in time, there is a decrease in O-vacancies. The observation is schematically represented in the **figure 31c**.

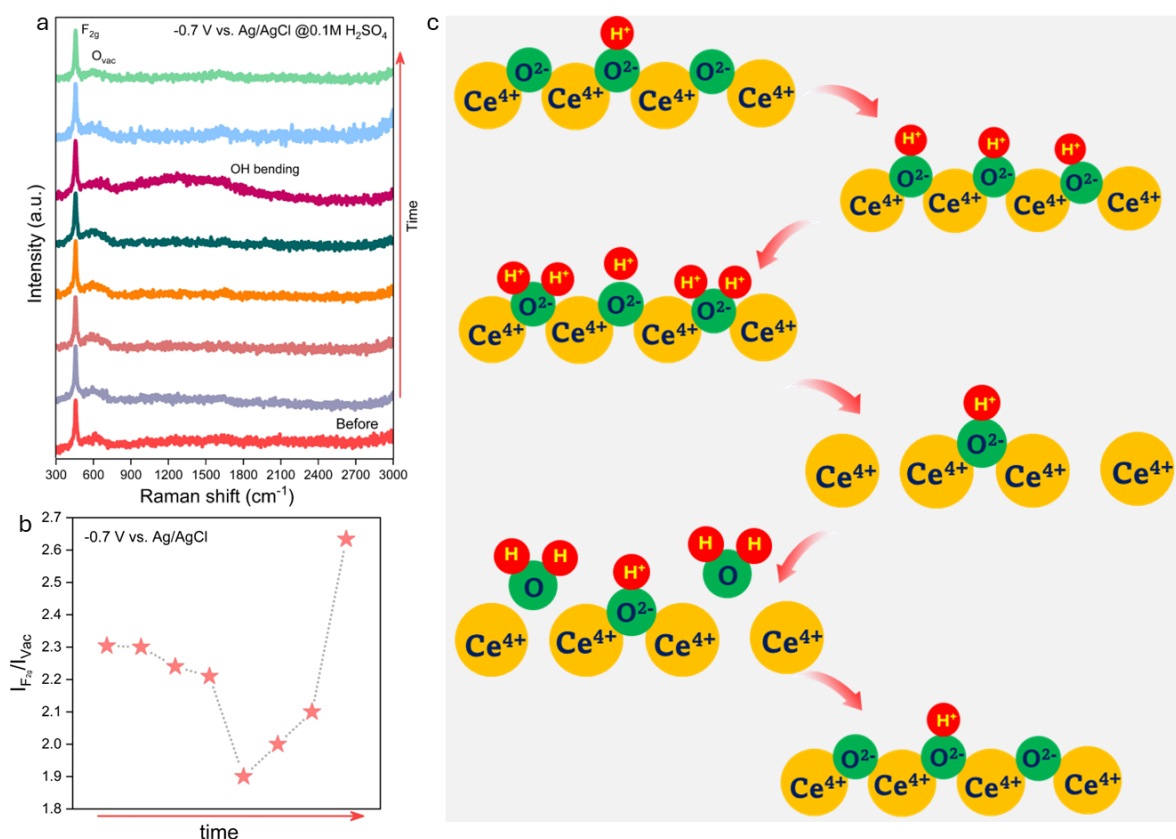


Figure 31. In-situ Raman data during HER: (a) The Raman spectra with time-dependent study, (b) Relative intensity of F_{2g} and O_{vac} with time, (c) Reaction mechanism schematic.

7.5 Conclusion

This work reports enhanced electrochemical HER activity with only 10% Pt loading on a non-expensive CeO₂ support. This catalyst has achieved better activity than the state-of-the-art catalyst 20% Pt/C. To understand the CeO₂ formation, Pt loading has been done in both in-situ and ex-situ modes to CeO₂ rods and cubes. The catalyst with 10% Pt loading in in-situ mode to the cube morphology gave the best HER activity. It has been confirmed that presence of Pt as guest ions, have tuned the CeO₂ facets different, and the presence of different CeO₂ facets have tuned different facets of Pt metal. It has been clearly observed that (200) facet of CeO₂ have exposed (111) facet of Pt, and (111) facet of CeO₂ have stabilized (200) and (220) facets of Pt. This interesting synergistic effect has given the best activity for (200) and (220)

facet of Pt when exposed on (111) facets of CeO₂. It has been clearly confirmed that a tuned content of Ce³⁺ and O_{vac} will be essential for achieving the best HER activity. H-spillover mechanism has been proposed for this of support induced enhancement in HER activity of Pt metallic nanoparticles.

7.6 References

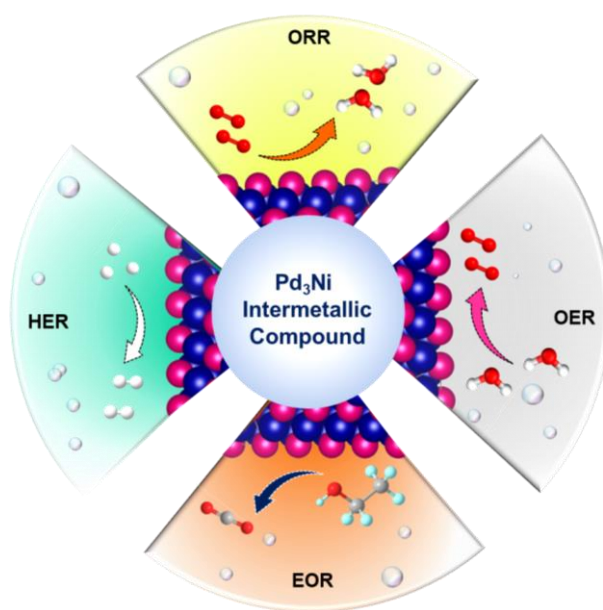
1. van Renssen, S., The hydrogen solution? *Nat. Clim. Change* **2020**, *10*, 799-801.
2. Seh, Z. W.; Kibsgaard, J.; Dickens, C. F.; Chorkendorff, I.; Nørskov, J. K.; Jaramillo, T. F., Combining theory and experiment in electrocatalysis: Insights into materials design. *Science* **2017**, *355*, eaad4998.
3. Abbas, M. A.; Bang, J. H., Rising Again: Opportunities and Challenges for Platinum-Free Electrocatalysts. *Chem. Mater.* **2015**, *27*, 7218-7235.
4. Kemppainen, E.; Bodin, A.; Sebok, B.; Pedersen, T.; Seger, B.; Mei, B.; Bae, D.; Vesborg, P. C. K.; Halme, J.; Hansen, O.; Lund, P. D.; Chorkendorff, I., Scalability and feasibility of photoelectrochemical H₂ evolution: the ultimate limit of Pt nanoparticle as an HER catalyst. *Energy Environ. Sci.* **2015**, *8*, 2991-2999.
5. Smiljanić, M.; Panić, S.; Bele, M.; Ruiz-Zepeda, F.; Pavko, L.; Gašparič, L.; Kokalj, A.; Gabersček, M.; Hodnik, N., Improving the HER Activity and Stability of Pt Nanoparticles by Titanium Oxynitride Support. *ACS Catal.* **2022**, *12*, 13021-13033.
6. Li, J.; Zhang, J.; Zhang, J.; Pan, K.; Xu, H.; Chen, H.; Liu, G.; Wu, N.; Yuan, C.; Liu, X., Tailoring supports for enhancing the electrocatalytic hydrogen evolution performance of platinum species: a review. *J. Mater. Chem. A* **2023**, *11*, 19812-19844.
7. Zheng, N.; Stucky, G. D., A General Synthetic Strategy for Oxide-Supported Metal Nanoparticle Catalysts. *J. Am. Chem. Soc.* **2006**, *128*, 14278-14280.
8. Zhang, J.; Zhang, Q.; Feng, X., Support and Interface Effects in Water-Splitting Electrocatalysts. *Adv. Mater.* **2019**, *31*, 1808167.
9. Zhou, K. L.; Wang, Z.; Han, C. B.; Ke, X.; Wang, C.; Jin, Y.; Zhang, Q.; Liu, J.; Wang, H.; Yan, H., Platinum single-atom catalyst coupled with transition metal/metal oxide heterostructure for accelerating alkaline hydrogen evolution reaction. *Nat. Commun.* **2021**, *12*, 3783.
10. Montini, T.; Melchionna, M.; Monai, M.; Fornasiero, P., Fundamentals and Catalytic Applications of CeO₂-Based Materials. *Chem. Rev.* **2016**, *116*, 5987-6041.

11. Acerbi, N.; Tsang, S. C. E.; Jones, G.; Golunski, S.; Collier, P., Rationalization of Interactions in Precious Metal/Ceria Catalysts Using the d-Band Center Model. *Angew. Chem. Int. Ed.* **2013**, *52*, 7737-7741.
12. Tiwari, J. N.; Sultan, S.; Myung, C. W.; Yoon, T.; Li, N.; Ha, M.; Harzandi, A. M.; Park, H. J.; Kim, D. Y.; Chandrasekaran, S. S.; Lee, W. G.; Vij, V.; Kang, H.; Shin, T. J.; Shin, H. S.; Lee, G.; Lee, Z.; Kim, K. S., Multicomponent electrocatalyst with ultralow Pt loading and high hydrogen evolution activity. *Nat. Energy* **2018**, *3*, 773-782.
13. Ke, J.; Xiao, J.-W.; Zhu, W.; Liu, H.; Si, R.; Zhang, Y.-W.; Yan, C.-H., Dopant-Induced Modification of Active Site Structure and Surface Bonding Mode for High-Performance Nanocatalysts: CO Oxidation on Capping-free (110)-oriented CeO₂:Ln (Ln = La–Lu) Nanowires. *J. Am. Chem. Soc.* **2013**, *135*, 15191-15200.
14. Deraz, N. M., Effect of NiO content on structural, surface and catalytic characteristics of nano-crystalline NiO/CeO₂ system. *Ceram. Int.* **2012**, *38*, 747-753.
15. Pilger, F.; Testino, A.; Carino, A.; Proff, C.; Kambolis, A.; Cervellino, A.; Ludwig, C., Size Control of Pt Clusters on CeO₂ Nanoparticles via an Incorporation–Segregation Mechanism and Study of Segregation Kinetics. *ACS Catal.* **2016**, *6*, 3688-3699.
16. Schilling, C.; Hofmann, A.; Hess, C.; Ganduglia-Pirovano, M. V., Raman Spectra of Polycrystalline CeO₂: A Density Functional Theory Study. *J. Phys. Chem. C* **2017**, *121*, 20834-20849.
17. Aragón, F. F. H.; Villegas-Lelovsky, L.; Cabral, L.; Lima, M. P.; Mesquita, A.; Coaquira, J. A. H., Tuning the magnetic properties of Sn_{1-x-y}Ce_{4+x}Ce_{3+y}O₂ nanoparticles: an experimental and theoretical approach. *Nanoscale Adv.* **2021**, *3*, 1484-1495.
18. Morgan, L. M.; Loche, D.; Corrias, A.; Hayama, S.; Mountjoy, G., Using Ex Situ and In Situ HERFD-XANES to Reveal the Superior Oxidation and Reduction Cycling of Ceria Nanocubes Dispersed in Silica Aerogel. *J. Phys. Chem. C* **2023**, *127*, 19554-19562.
19. Marković, N. M.; Grgur, B. N.; Ross, P. N., Temperature-Dependent Hydrogen Electrochemistry on Platinum Low-Index Single-Crystal Surfaces in Acid Solutions. *J. Phys. Chem. B* **1997**, *101*, 5405-5413.
20. Conway, B. E.; Barber, J.; Morin, S., Comparative evaluation of surface structure specificity of kinetics of UPD and OPD of H at single-crystal Pt electrodes1Presented

- at the Surface Electrochemistry Conference, Alicante, Spain, September 1997.1. *Electrochim. Acta* **1998**, *44*, 1109-1125.
21. Lee, J.; Tieu, P.; Finzel, J.; Zang, W.; Yan, X.; Graham, G.; Pan, X.; Christopher, P., How Pt Influences H₂ Reactions on High Surface-Area Pt/CeO₂ Powder Catalyst Surfaces. *JACS Au* **2023**, *3*, 2299-2313.
22. Dutta, G.; Waghmare, U. V.; Baidya, T.; Hegde, M. S., Hydrogen Spillover on CeO₂/Pt: Enhanced Storage of Active Hydrogen. *Chem. Mater.* **2007**, *19*, 6430-6436.

Chapter 8

Unravelling Growth Mechanism of Local Entropy Tailored Intermetallic Pd₃Ni Exhibiting Tetrafunctional Activity in Electrolyser and Fuel Cell



Soumi Mondal; Shreya Sarkar; Mohd Riyaz; Debabrata Bagchi; Ranjana Burman; Nilutpal Dutta; Ashutosh Kumar Singh; Sayan Das; Meera Radhakrishnan; Sebastian C. Peter (*manuscript under revision*)

Summary

Master of all trades! Designing a multifunctional electrocatalyst is of surging demand. This work deals with successful solution phase synthesis of an ordered compound of Pd and Ni, Pd₃Ni, which is assumed to be difficult as almost no adjacent elements in a same group form intermetallic compound. Pd₃Ni is a highly efficient and electrochemically stable material for tetra-functional activity, as in, hydrogen evolution reaction (HER), oxygen evolution reaction (OER), oxygen reduction reaction (ORR), and ethanol oxidation reaction (EOR) which constitutes both fuel cell and water electrolyser. Extensive ex-situ and in-situ characterization has disclosed the robustness of this material and reaction mechanism in different reactions. This material has shown promising activity in proton exchange membrane water electrolyser and high temperature fuel cell. Tuned surface of the intermetallic has enhanced C-C cleavage in ethanol molecules allowing the sluggish 12e⁻ transfer process and has shown very high stability of >80k cycles of alkaline HER. Role of pH and potential has been explored in retaining the ordered phase of the intermetallic. Tetra functionality and its extensive exploration under different reaction conditions have been exhaustively done in this work.

Table of Contents

8.1	Introduction.....	246
8.2	Experimental Details	248
8.2.1	Chemicals and reagents	248
8.2.2	Synthesis of Pd ₃ Ni-IM and Pd ₃ Ni-Al.....	249
8.3	Characterization.....	249
8.3.1	Powder X-ray Diffraction (PXRD).....	249
8.3.2	Scanning electron microscopy (SEM) and Energy Dispersive Spectrum (EDS)	249
8.3.3	Transmission electron microscopy (TEM).....	249
8.3.4	Inductively coupled plasma atomic emission spectroscopy (ICP-OES)	249
8.3.5	X-ray Photoelectron Spectroscopy (XPS).....	250
8.3.6	X-ray absorption near edge spectroscopy (XANES) and Extended X-ray Absorption Fine Structure (EXAFS):	250
8.3.7	Differential scanning calorimetry (DSC)	250
8.3.8	Electrochemical oxygen evolution Reaction (OER)	250
8.3.9	Electrochemical oxygen reduction reaction (ORR).....	251
8.3.10	Electrochemical hydrogen evolution reaction (HER)	251
8.3.11	Electrochemical ethanol oxidation reaction (EOR)	252
8.3.12	Membrane electrode assembly (MEA) fabrication	252
8.3.13	Proton exchange membrane water electrolyser	252
8.3.14	In-situ X-ray absorption spectroscopy (XAS).....	252
8.3.15	In-situ Electrochemical Fourier Transform Infrared Spectroscopy (FT-IR)	252
8.3.16	In-situ Raman spectroscopy	253
8.3.17	Differential electrochemical mass spectrometry (DEMS)	253
8.3.18	Computational studies.....	253
8.4	Results & Discussion	254
8.4.1	Phase confirmation and growth mechanism.....	254
8.4.2	Electrochemical results	260
8.4.3	Structural insights and oxidation state analysis	266
8.4.4	Operando analysis of active species generation	267
8.4.5	Operando analysis of reaction mechanism and phase transformation	272
8.5	Conclusion	278
8.6	References.....	282

8.1 Introduction

The formation of an intermetallic compound (IMC) is a challenge as compared to a disordered alloy phase between two different elements.¹ Sometimes, it takes many days for an IM to form, whereas in some cases, it never forms.² From the phase diagram of palladium and nickel, it is prominent that stable IM phase does not form between Pd and Ni.³ The Pd-Ni system is considered to have a combination of solid solutions with no superlattice reflections formed in the Pd-Ni lattice.^{2, 4} Meanwhile, Pd-Ni based alloy compounds are very often used as electrocatalysts in different applications.⁵⁻⁷ The major disadvantages of disordered alloy compounds are the stability of the materials in harsh reaction conditions and non-periodicity of the active sites in the lattice preventing further tuning of the catalyst for a desired reaction.⁸ ⁹ IMCs are thermodynamically more stable, and all elements are ordered periodically in almost all facets which assures the availability of catalytically active sites more than the randomly oriented alloys.^{10, 11} Due to enhanced stability of IMs, the surface vulnerability of IM is lesser than alloys.⁹ This can be enhanced by modifying the system by structurally ordering atoms, which in another way can be interpreted as tuning entropy of the system. The optimum tuning of structural order and entropy can induce the enhancement of catalytic activity towards a selected reaction.¹² Only a few catalysts are reported for mono- or bi- or tri-functional activities in electrochemistry.¹³⁻¹⁸ There is an increased demand of achieving a highly stable multi-functional catalyst which will enhance the economic viability of the material. Any electrochemical reaction has its own criteria for facilitating the rate determining step as per the volcano plot analysis.¹⁹ Fuel cell and water splitting requires oxygen reduction (ORR) and hydrogen evolution (HER) reactions in the cathodic and oxygen evolution (OER) and small organic molecules (like ethanol oxidation (EOR)) in the anodic counterparts, respectively.²⁰⁻²³

H₂, as a green fuel, is of very high demand but the bottleneck for facile hydrogen generation is the anodic reaction, oxygen evolution reaction (OER).²² Whereas this electrochemically generated hydrogen is further used as fuel in fuel cell for proton exchange membrane fuel cells (PEMFCs) and ethanol is utilized as fuel in direct alcohol fuel cells (DAFCs). All these electrochemical reactions have their individual bottlenecks, and each reaction are defined by specific chemical descriptors which are found in different types of catalyst materials. Those challenges for each reaction are discussed and how our material is efficiently exhibiting multiple activities are being lucidly discussed in this entire work. The major challenge for OER is four electrons transfer process for oxidation of singlet state species OH⁻ (or H₂O) to triplet state O₂ molecules which makes it sluggish requiring high overpotential.

Simultaneously, alkaline HER is also sluggish due to the water dissociation process involved in alkali mediated HER. The major concern for ORR is $4e^-$ transfer to O_2 for forming H_2O molecules and not H_2O_2 molecules. Higher electron transfer will lead to generation of high-power density during fuel cell operation.²⁴

Ethanol is an environment-friendly fuel with a very high theoretical energy density of 8030 Wh/Kg and hence can be used as a fuel for transportation and delivery purposes.²⁵ EOR occurs via two mechanism, $4e^-$ transfer incomplete oxidation producing CH_3COOH (or CH_3COO^-) and $12e^-$ transfer complete oxidation forming CO_2 (or CO_3^{2-}).²⁶ More number electrons transferred will generate more power in DAFCs.²⁶ Pd is considered as an EOR active state-of-the-art catalyst for generating acetic acid and carbon dioxide, whereas it is associated with notorious CO poisoning which blocks its active sites.^{19, 23} Attempts are highly required to achieve selectivity of products (majorly CO_2 formation) and to get rid of the CO poisoning effect.²⁷ Efforts have been made to diminish active-site poisoning, product selectivity, and enhanced current density. Reports, such as, strain-generation by core-shell morphology,²⁷ interface engineering,²⁶ P-doping,²⁵ transition metal doped intermetallic and alloys,⁷ are there for attaining the best EOR activity. Our work circles around how entropy tuned orderedness and disorderedness of two metals changes the activity, stability, and selectivity of active sites towards EOR. The generation of a single catalyst overcoming all these hurdles will be highly promising for commercialization during this environmental crisis.

It is calculated that the Gibb's free energy for Pd-Ni alloy formation is lower than that of intermetallic.^{4, 28} In bottom-up approach of nanoparticles synthesis, appearance of superlattice diffraction depends on how the diffusion of the second metal takes place along the specific direction. In solution phase synthesis, different chemicals are used which act as purely solvent, reducing agent and sometimes, morphology directing agent. Oleyl amine has been used for several decades in nanoparticles synthesis and widely known to generate nanoparticles of variegated sizes and shapes.²⁹ One of the exclusive roles of oleyl amine has been extensively studied in this work, which is responsible for the formation of Pd_3Ni , the first ever Pd-Ni based IMC. Other parameters like temperature and time duration have been tuned to observe the gradual generation of Pd_3Ni IM, which is a metastable phase and can be trapped only in certain synthetic conditions.

This work shows the highly tuned synthetic procedure for generation of novel IMC Pd_3Ni having Au_3Co cubic lattice. Pd_3Ni -IM and its disordered structure, named as Pd_3Ni -Al are synthesized via very simple one pot solvothermal technique. It is observed that Pd_3Ni -IM

phase is a metastable phase which is attained at a particular temperature, time duration, and specific amount of oleyl amine during the reaction. Extensive structural analysis is carried out by different characterization techniques like PXRD, TEM, SEM, XAS, XPS, and differential scanning calorimetry (DSC) measurements. Then, the materials were tested for alkali mediated oxygen evolution reaction (OER), ethanol oxidation reaction (EOR), hydrogen evolution reaction (HER), and oxygen reduction reaction (ORR). Pd₃Ni-IM shows tetrafunctional activity, which is exhibiting lower overpotential (220 mV for 10mA/cm² for OER) for all reactions with highly enhanced stability (almost 80,000 cycling HER, >20,000 cycling OER activity, 10,000 cycles for ORR) and faster kinetics (12e⁻ transfer process for EOR) than the disordered structure, Pd₃Ni-Al. Pd₃Ni-IM catalyst is also tested full cell water splitting at industrial conditions of high temperature and in a proton exchange membrane water electrolyser. Enhancement in activity of Pd₃Ni-IM is observed for HER, OER, ORR and EOR which are well explained explicitly in this work. *Operando* studies are performed to understand the real-time evolution of active sites during reaction conditions. Post-electrochemical XPS and XRD are also being measured and analyzed to map the fate of the catalysts after reaction. It has been interestingly analyzed that the pH and potential range during different reactions play a significant role in the phase transition of the ordered catalyst to partially disordered structure with increased entropy of the system. Besides designing this novel IMC, this work performs rigorous electrochemical studies, control experiments, and achieved high activity for four electrochemical reactions in water splitting and fuel cell. This work extensively establishes how a metastable IM is fully stabilized at a specific time, temperature, and optimized chemical interaction with oleyl amine. This phase is exhibiting enhanced activity and stability at all conditions. This mystery is well demonstrated explicitly in this work by extensive experimental and theoretical procedures. Potential and pH dominated phase transition has been well demonstrated in this work.

8.2 Experimental Details

8.2.1 Chemicals and reagents

Palladium acetylacetonate (Pd(acac)₂), nickel acetylacetonate (Ni(acac)₂), cetyltrimethylammonium ammonium bromide (CTAB), oleyl amine (OAm) and octadecyl amine were purchased from Sigma Aldrich. Tetraethylene glycol (TEG) was purchased from Alfa Aesar. The precursors were used without any further purification.

8.2.2 Synthesis of Pd₃Ni-IM and Pd₃Ni-Al

In a typical solvothermal reaction, 0.3 mmol of palladium acetylacetonate (Pd(acac)₂), 0.1 mmol of nickel acetylacetonate (Ni(acac)₂), 75 mg of cetyltrimethylammonium ammonium bromide (CTAB), and 10 mL of oleyl amine were mixed in 15 mL teflon autoclave and stirred for 30 mins. The autoclave was kept at 220 °C and 240 °C for 24 h for synthesizing Pd₃Ni-IM and Pd₃Ni-Al, respectively. The final product was washed several times with 1:1 mixture of hexane and ethanol, and the obtained product was dried and used for further characterization. All the parameters like temperature, time duration, and volume of oleyl amine are varied extensively to study the formation mechanism of the IMC.

8.3 Characterization

8.3.1 Powder x-ray diffraction (PXRD)

PXRD measurements were done at room temperature on a Rigaku Miniflex X-ray diffractometer with a Cu-K_α X-ray source ($\lambda = 1.5406 \text{ \AA}$), equipped with a position-sensitive detector in the angular range of $10^\circ \leq 2\theta \leq 90^\circ$ with the step size 0.02° and a scan rate of 0.5 s/step calibrated against corundum standards. The experimental XRD patterns were compared to the patterns simulated from the data reported in the literature.

8.3.2 Scanning electron microscopy (SEM) and energy dispersive spectrum (EDS)

The SEM measurement was performed using Leica scanning electron microscopy equipped with an energy-dispersive X-ray spectroscopy (EDAX) instrument (Bruker 120 eV EDAX instrument). Data were acquired by using an accelerating voltage of 15 kV, and the typical time taken for data accumulation is 100 s. The elemental analyses were performed using the P/B-ZAF standardless method (where P/B = peak to background model, Z = atomic no. correction factor, A = absorption correction factor, and F = fluorescence factor) for Cu, Ga at multiple areas on the sample coated Si wafer.

8.3.3 Transmission electron microscopy (TEM)

TEM and high-resolution TEM (HRTEM) images, selected area electron diffraction (SAED) patterns were collected using a JEOL 200 TEM instrument. Samples for these measurements were prepared by dropping a small volume of sonicated nanocrystalline powders in ethanol onto a carbon-coated copper grid.

8.3.4 Inductively coupled plasma atomic emission spectroscopy (ICP-OES)

ICP-OES was performed using a Perkin Elmer Optima 7000 DV instrument. The samples were digested in concentrated aqua regia, followed by dilution with distilled water. In

a typical experiment, 2 mg of the sample was dissolved in 1 ml aqua regia and left overnight (12 hrs) for digestion. The digested sample was then diluted to 10 ml volume with deionized water. The solid particles were separated by thorough centrifugation before measurements. We have also performed the ICP-OES for the electrolyte after running the OER reaction.

8.3.5 X-ray photoelectron spectroscopy (XPS)

XPS measurements were carried out using Thermo K-alpha+ spectrometer using micro focused and monochromated Al K α radiation with energy 1486.6 eV. The pass energy for spectral acquisition was kept at 50 eV for individual core-levels. The electron flood gun was utilized for providing charge compensation during data acquisition. Further, the individual core-level spectra were checked for charging using C1s at 284.6 eV as standard and corrected if needed. The peak fitting of the individual core-levels was done using XPSpeak 41 software with a Shirley type background. XPS spectra were measured to study the valence state, chemical composition, and electronic interactions. Ar⁺ sputtering was done for 10 secs each layer for an energy of 2 KeV and high-resolution spectra of Pd 3d, Ge 3d, and Co 2p were performed after each layer etching.

8.3.6 X-ray absorption near edge spectroscopy (XANES) and extended x-ray absorption fine structure (EXAFS):

XANES and EXAFS experiments at 300 K were performed at PETRA III, beamline P64, of DESY, Germany. Measurements of Pt-k edges at ambient pressure were performed in fluorescence as well as transmission mode using gas ionization chambers to monitor the incident and transmitted X-ray intensities. Monochromatic X-rays were obtained using a Si (111) double crystal monochromator. Pellets for the ex-situ measurements were made by homogeneously mixing the sample with an inert cellulose matrix to obtain an X-ray absorption edge jump close to one. Background subtraction, normalization, and alignment of the EXAFS data were performed by ATHENA software. Theoretical XAFS models were constructed and fitted to the experimental data in ARTEMIS.

8.3.7 Differential scanning calorimetry (DSC)

All DSC measurements were done using DSC 3 from Mettler Toledo. The temperature range was used from 423.15 K to 823.15 K and nitrogen gas was used. The temperature was increased at a rate of 0.5K/min to 40K/min.

8.3.8 Electrochemical oxygen evolution Reaction (OER)

All the electrochemical measurements were done in a 3-electrode set-up comprising of a glassy carbon as the working electrode (GCE), graphite rod counter electrode, and

mercury/mercuric oxide electrode (MMO) (for basic media). The catalyst ink was prepared using 1.6 mg catalyst + 0.4 mg Vulcan in 200 μL of mixed solvent (IPA:H₂O = 1:1) + 20 μL of 1 wt.% Nafion used as binder. Five μL of the catalyst ink was drop-casted on the commercial 3 mm GCE. Commercial IrO₂ (Sigma Aldrich) was used for comparison of activity with the reported electrocatalysts. Linear sweep voltammetry (LSV) was recorded for OER at a scan rate of 5 mV s^{-1} at 25 °C. Electrochemical impedance studies were performed in the frequency range from 10 mHz to 100 kHz at different applied DC potentials for different reactions depending on their onset potential values. The electrolyte solution was deaerated by purging N₂ gas into the solution at least for 30 min before each experiment. All the reference electrodes were calibrated with respect to the reversible hydrogen electrode (RHE), using Pt as working and counter electrodes in the respective electrolytes.

8.3.9 Electrochemical oxygen reduction reaction (ORR)

Electrode preparation is done in the same way as OER for ORR, EOR, and HER. Commercial Pt/C (20 wt.%, Sigma Aldrich) were used for comparison of activity since it is the state-of-the-art electrocatalyst. Polarization curves were the anodic sweep of the cyclic voltammograms (CVs) recorded for ORR at a scan rate of 5 mV s^{-1} at 25 °C in potential range of 0.4 V to 1.0 V vs. RHE rotating the RDE at 100, 225, 400, 625, 900, 1225, 1600, 2025, and 2500 rpm. The electrolyte solution was deaerated by purging nitrogen gas into the solution at least for 30 min before each experiment and then N₂ saturated CV was conducted, after which O₂ is being purged for an hour to start taking CVs in ORR conditions. The polarization curves in N₂ and O₂ saturated solutions are taken in 1600 rpm rotating speed of RDE. Accelerated degradation tests of 50,000 cycles were conducted in the potential range of 0.7 V to 1.0 V vs. RHE with scan rate of 50 mV/sec. Electrochemical impedance studies were performed in the frequency range from 10 mHz to 100 kHz at different applied DC potentials for different reactions depending on their onset potential values.

8.3.10 Electrochemical hydrogen evolution reaction (HER)

Commercial Pt/C (20 wt%, Sigma Aldrich) were used for comparison of activity with the reported electrocatalysts. Linear sweep voltammetry (LSV) was recorded for HER at a scan rate of 5 mV s^{-1} at 25 °C. Electrochemical impedance studies were performed in the frequency range from 10 mHz to 100 kHz at different applied DC potentials for different reactions depending on their onset potential values. The electrolyte solution was deaerated by purging nitrogen gas into the solution at least for 30 min before each experiment. All the reference

electrodes were calibrated with respect to the reversible hydrogen electrode (RHE), using Pt as working and counter electrodes in the respective electrolytes.

8.3.11 Electrochemical ethanol oxidation reaction (EOR)

Cyclic voltammetry (CV) was recorded for EOR at a scan rate of 5 mV s⁻¹ at 25 °C. Electrochemical impedance studies were performed in the frequency range from 10 mHz to 100 kHz at different applied DC potentials for different reactions depending on their onset potential values. The electrolyte solution was deaerated by purging nitrogen gas into the solution at least for 30 min before each experiment.

8.3.12 Membrane electrode assembly (MEA) fabrication

Catalyst ink is drop-casted on carbon cloth (CeTech W1S1009, Fuelcellstore) and treated Nafion membrane is sandwiched between catalyst coated carbon substrates and hot-pressed using the hydraulic pressing unit (Boolani Engineering Corporation) at 130 °C for 5 minutes.

8.3.13 Proton exchange membrane water electrolyser

The catalyst coated substrate (CCS) is then tested in proton exchange membrane water electrolyser (RSI-AEM-300, Research Supporters India Pvt. Ltd.) using DI water continuous flow only at the anodic chamber and no electrolyte flow was given in the hydrogen generation side.

8.3.14 In-situ x-ray absorption spectroscopy (XAS)

In-situ XAS was measured using home-made customized cell set up as shown in **Figure 8.1a** under OER conditions. All the experimental details are found in our previous papers.^{21, 22,}

30

8.3.15 In-situ electrochemical Fourier transform infrared spectroscopy (FT-IR)

In-situ electrochemical FT-IR spectroscopic studies were performed using a purged VERTEX FT-IR spectrometer equipped with the A530/P accessory and a mid-band MCT detector. A CaF₂ hemispherical window (F530-8) was used with the working electrode placed 1 mm above the window as the single reflection attenuated total reflection (ATR) accessory for the FTIR study. The in situ experimental set-up is depicted in **Figure 8.1b**. The measurement parameters were 4 cm⁻¹ resolution and 100 scans. This setup enabled the detection of acetate ions, ethanol consumption, and carbonate ions with carbon dioxide peaks during EOR.

8.3.16 In-situ Raman spectroscopy

In situ electrochemical Raman spectroscopic studies were performed using inVia Raman microscope using 532 nm laser with 50x magnification. We have home-customized a cell where 2 ml solution of N₂-purged 0.5M KOH was taken so that a thin film of electrolyte covers on the substrate having the catalyst coated on it. Pt coil and Ag/AgCl were used as counter and reference electrodes, respectively. CA was conducted for 15-20 mins and Raman data was taken at 2 mins each with data acquisition time of 10 secs and using 0.1 % of the power of the laser. Background data was taken with the complete cell setup with electrolyte and without giving the electrode potential.

8.3.17 Differential electrochemical mass spectrometry (DEMS)

Hidden HPR-40 was used for measuring the instantaneous products formed during the ethanol oxidation reaction for both the catalysts, Pd₃Ni-IM and Pd₃Ni-Al. Type cell-A was used where catalyst ink was coated on the glassy carbon electrode. 0.1 M ethanol in 0.1 M KOH was used as the electrolyte which was flowed through the cell by help of a dual-syringe pump. Cyclic voltammetry (CV) was run during which N₂, CO₂, CH₃COOH, CH₃CHO were measured with respect to time. The data has been plotted as mbar of the product w.r.t. time. For HER and OER, same process is being used where electrolyte used in 0.5 M KOH solution.

8.3.18 Computational studies

All the calculations were done within the Density Functional Theory framework implemented in VASP.^{31, 32} Plane-wave augmented pseudopotential³³ was used in conjugation with Perdew-Becke Ernzerhof (PBE)³⁴ approximated exchange and correlation functional. The kinetic energy cut-off for Kohn-Sham orbitals and energy convergence criteria of the electronic self-consistency is chosen as 500 eV and 10⁻⁸ eV, respectively. The Monkhorst-Pack³⁵ mesh k-points of (6 × 6 × 6) were used for cell structure optimization containing 32 atoms. The disordered structure of Pd_{0.75}Ni_{0.25} was generated using the special quasi-random structure (SQS) method implemented in the widely used Alloy Theoretic Automated Toolkit (ATAT) package.^{36, 37} The SQS-generated structure with 32 atoms was used as the computational model for the disordered Pd_{0.75}Ni_{0.25} to compare its phase stability w.r.t ordered Pd₃Ni at different temperatures. The calculations were performed using the methodology described in the previous report.³⁸ Density Functional Perturbation Theory (DFPT) method implemented in VASP was used to calculate the force constants of supercell consisting of 32 atoms, and the phonon frequencies from the force constants were computed using PHONOPY.³⁹ Energy convergence criteria of (10⁻⁸ eV) with 6 × 6 × 6 gamma cantered k-points mesh were used for

computing the force constants. The stability of the considered structures was confirmed by phonon band structures with no imaginary modes in the modeled structures. The thermodynamic properties for Gibbs Free energy calculation were then extracted for phonon eigenvector using PHONOPY. The Free energy change was calculated as: $\Delta G = \Delta H - T (\Delta S_{\text{conf}} + \Delta S_{\text{vib}})$, where ΔH is the enthalpy difference, T is the absolute temperature, ΔS_{conf} , and ΔS_{vib} are the difference of configurational and vibrational entropy between ordered and disordered systems. $\Delta S_{\text{conf}} = k_b \sum x_i \ln x_i$, where k_b and x_i are Boltzmann's constant and the mole fraction of a particular element in an alloy. The adsorption energy (E_{ads}) was calculated as: $E_{\text{ads}} = E_{(\text{surf}+\text{adsor})} - (E_{(\text{surf})} + E_{(\text{adsor})})$ where $E_{(\text{surf}+\text{adsor})}$, $E_{(\text{surf})}$ and $E_{(\text{adsor})}$ are the DFT calculated energy of the surface with the adsorbate, isolated surface, and adsorbate.

8.4 Results & Discussion

8.4.1 Phase confirmation and growth mechanism

The difficulty in synthesizing the IM phase of Pd₃Ni compound is battled with varying different reaction parameters which are time duration, temperature, and concentration of oleyl amine used (**Figure 8.1a, 8.1b and 8.1c, d**). **Figure 8.2a** show the supercell of Pd₃Ni structure (prototype: Au₃Co) with outlined unit cell. The unit cell shows that Ni and Pd atoms occupy the corners and the face centers, respectively. **Figure 8.1b** shows with increasing oleyl amine from 10ml to 12ml, the superlattice diffraction peaks at 2θ values 22.07 ° and 31.31°. for the intermetallic start to appear. Whereas with further increase in OAm amount, there is decrease in peak intensity of (110) w.r.t that of (100) plane.

The periodic arrangements of the planes (110) and (100) are added in **Figure 8.2b** and in **Figure 8.2c**. It shows that a greater number of Ni atoms are occupying in (100) plane than Pd atoms. The relative peak intensity ratios of (100) and (110) are extracted from the PXRD pattern (**Figure 8.1b**) and plotted with respect to amount of OAm in **Figure 8.2d**. To understand the growth of the atomically ordered Pd₃Ni, we computed the thermodynamics stability of both alloy (disordered) and intermetallic (ordered) systems. As already discussed, formation of IM is an enthalpy-driven process. The difference in alloy and IM formation energy (**Figure 8.3a, Tables 8.1-8.4**) suggests that even at low temperatures, alloy formation is more favourable than IM. From the DFT electronic energy calculation with zero-point energy correction, alloy formation is stabilized by 3.78 meV/atom.

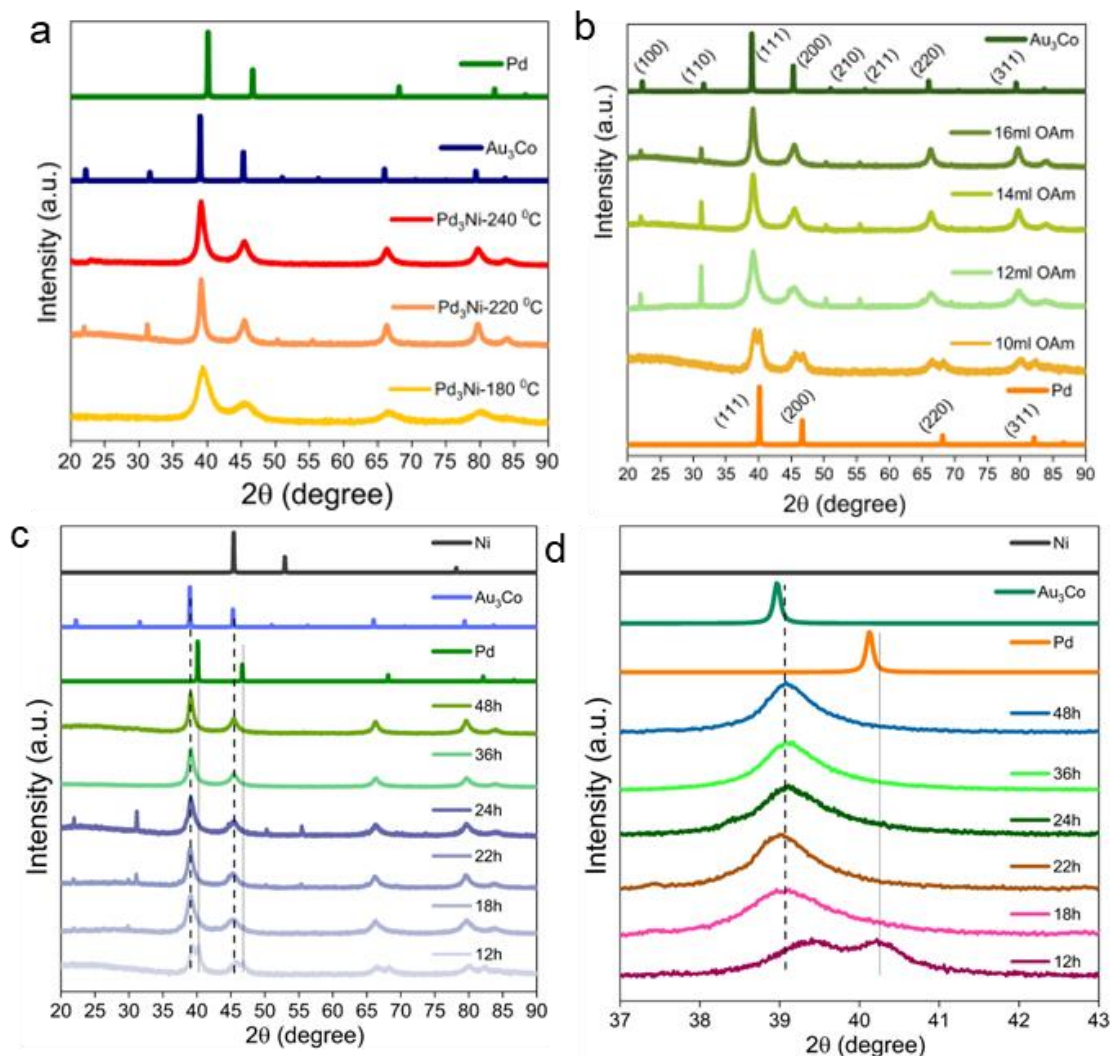


Figure 8.1. PXR D patterns for (a) temperature-controlled, (b) amount of oleyl amine controlled, (c) time-controlled synthesis of Pd₃Ni IM phase. The phase purity was proposed after comparing the simulated patterns of probable structures like Pd and Ni elements. (d) Zoomed in pXR D pattern for Pd₃Ni synthesis with time dependent study.

Table 8.1. Formation energy of Pd₃Ni-IM and Pd₃Ni-Al.

System	Bulk (eV)	Formation energy (eV)/atom
Pd ₃ Ni-IM	-168.154	-5.255
Pd ₃ Ni-Al	-168.307	-5.259

Table 8.2. Energy of stabilization for Ni atom on surface or bulk of both Pd₃Ni-IM and Pd₃Ni-Al.

Element	Surface	Bulk
Ni	-347.237	-347.486

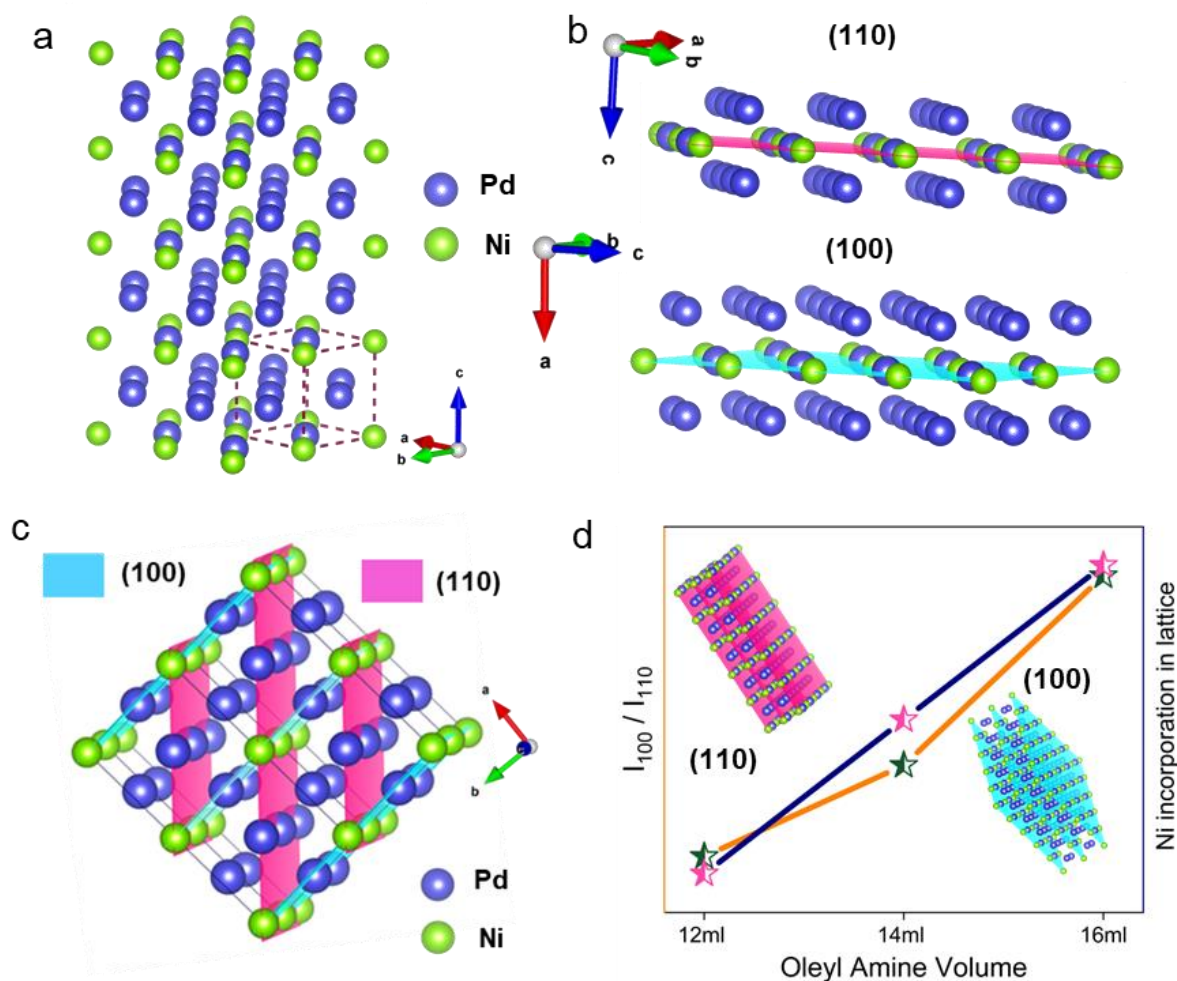


Figure 8.2. (a) The supercell (2*2*4) of Pd₃Ni-IM structure with the unit cell represented as dashed lines. (b) Crystallographic planes (110) and (100) of Pd₃Ni-IM. (c) Super cell of Pd₃Ni intermetallic with (110) and (100) planes drawn. (100) is cyan coloured plane having more Ni atoms and less Pd atoms, and (110) is pink coloured plane having equal number of Pd and Ni atoms. Hence, occupancy of Pd atoms is more in (110) planes. (d) Relative peak intensity ratio of (100) and (110) with increase in OAm amount.

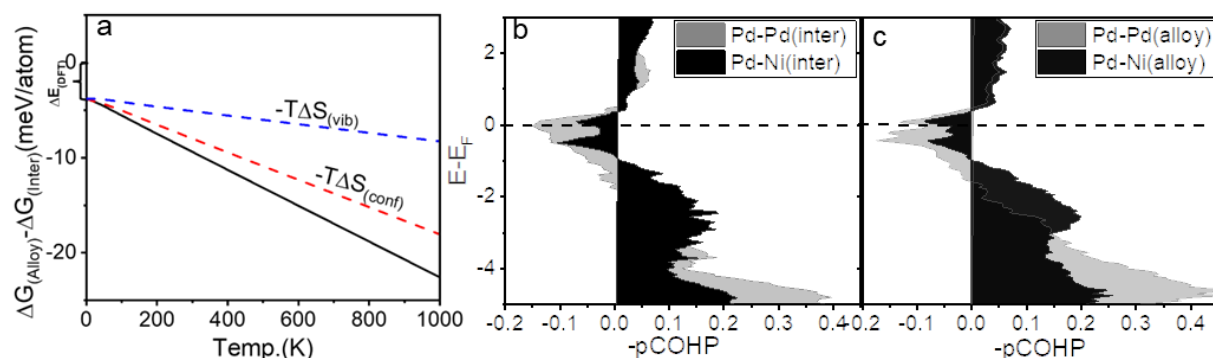


Figure 8.3. (a) The difference in alloy and IM formation energy of Pd₃Ni. COHP curve showing the bonding and antibonding character for Pd-Pd bond and Pd-Ni in (b) Pd₃Ni-Al and (c) Pd₃Ni-IM systems.

Table 8.3. Energy of Pd-N and Ni-N bonds after OAm on Pd and Ni atoms in Pd₃Ni-IM and Pd₃Ni-Al surface.

Pd ₃ Ni	Bonding	E _(ads) (eV)
Alloy	Ni-N	-1.43
	Pd-N	-1.18
Intermetallic	Ni-N	-1.52
	Pd-N	-1.23

Table 8.4. Energy of Pd₃Ni-IM and Pd₃Ni-Al surface before and after adsorption of OAm.

Phase	Before OAm adsorption	After OAm adsorption
Pd ₃ Ni-Al	-353.407 eV	-865.246 eV
Pd ₃ Ni-IM	-352.167 eV	-865.836 eV

This can be explained from the Crystal Orbital Hamilton Population (COHP) curve (**Figure 8.3b, c**) showing that the antibonding character for Pd-Pd bond is a bit higher than in the ordered system. The presence of Ni-Ni bond, which has the highest bond energy among all possible bond pairs, also stabilizes the disordered system. Since we obtained enhancement in IM phase formation with addition of OAm, we performed theoretical calculations for understanding the energetics of OAm addition on surfaces. Firstly, we calculated the adsorption energy of the amine at the surface (111) of the ordered and disordered systems (**Figure 8.4a and 8.4b, c**). It was found that the binding of the amine (-NH₂) group of OAm with the Ni site was better than Pd. And Ni sites on the surface of ordered system showed better adsorption with -NH₂ group than the Ni on the surface of the disordered system.

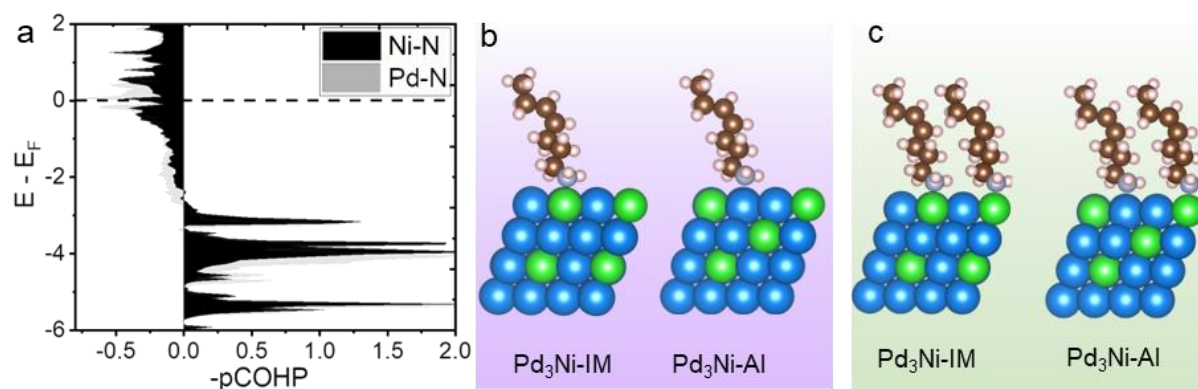


Figure 8.4. (a) The bonding and antibonding character in the N-Pd and N-Ni bonds shown in the COHP curve. Theoretical models of OAm bound on surface atoms of Pd₃Ni-IM and Pd₃Ni-Al at (b) low and (c) high surface coverages.

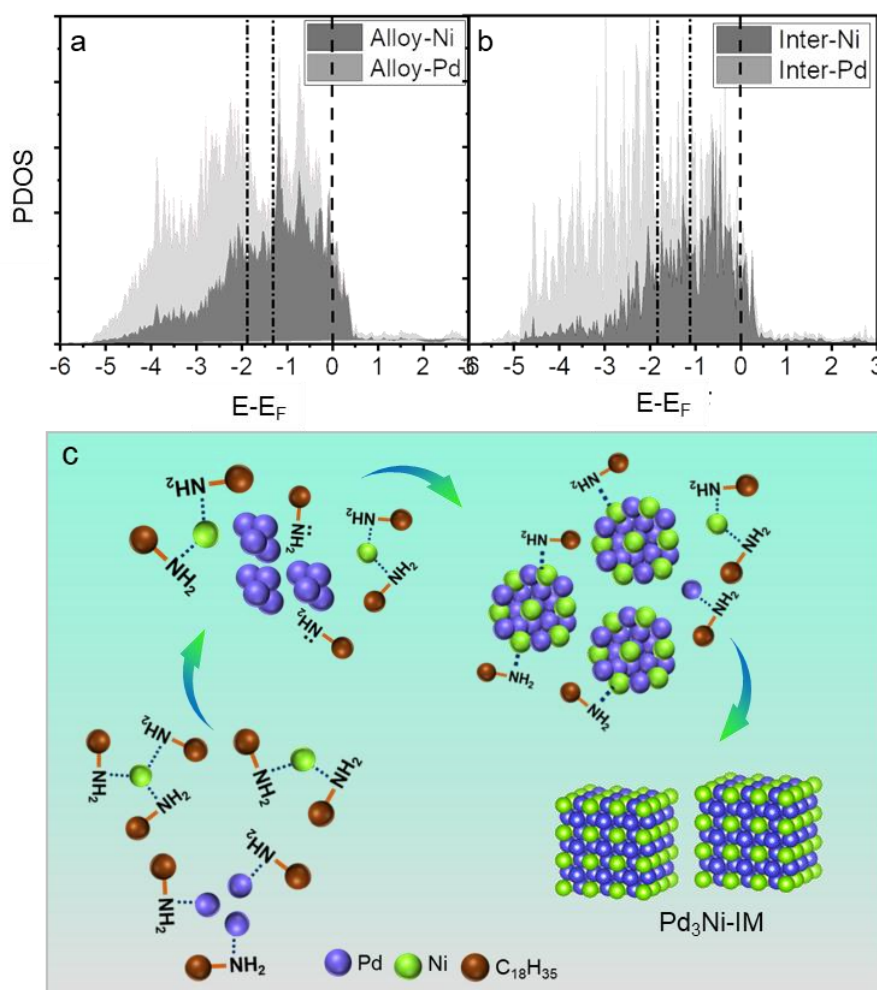


Figure 8.5. PDOS plot for Pd and Ni orbitals of (a) Pd₃Ni-IM and (b) Pd₃Ni-Al. (c) Schematic representing the formation mechanism of Pd₃Ni-IM using OAm.

Understandably, the d-band center of Ni is near to Fermi level than Pd in both cases (**Figure 8.5a, b**). So, the antibonding character in the N-Pd bond (N from Oleyl amine) is higher than N-Ni shown in the COHP curve (**Figure 8.4a**). **Figure 8.5c** schematically presents the formation mechanism of Pd₃Ni-IM phase with higher content of OAm used. **Figure 8.6a** combines the phase formation at different temperatures and time durations from the PXRD patterns in **Figures 8.1a** and **8.1c**. The optimized parameters for IM formation are 16 ml OAm at 220 °C and for 24 hours. PXRD patterns in **Figure 8.6b** shows the formation of alloy (Pd₃Ni-Al) and intermetallic (Pd₃Ni-IM) crystallizing in the Au_{0.75}Co_{0.25} (SG: *Fm* $\bar{3}$ *m*) and Au₃Co (SG: *Pm* $\bar{3}$ *m*) types, respectively.⁴⁰ **Figure 8.6c** shows the SEM images of both phases showing nanoparticles formation and **Figures 8.7(i), 8.7(ii)** and **8.7(iii)** show the TEM and SEM images and elemental mapping of Pd₃Ni-IM and Pd₃Ni-Al, respectively. Both the catalysts exhibit interconnected and aggregated nanoparticles with particle size within 25-30 nm (alloy) and 10 nm (IM). The HRTEM images and SAED pattern show the exposed (111) facets of Pd₃Ni-IM and Pd-alloy.

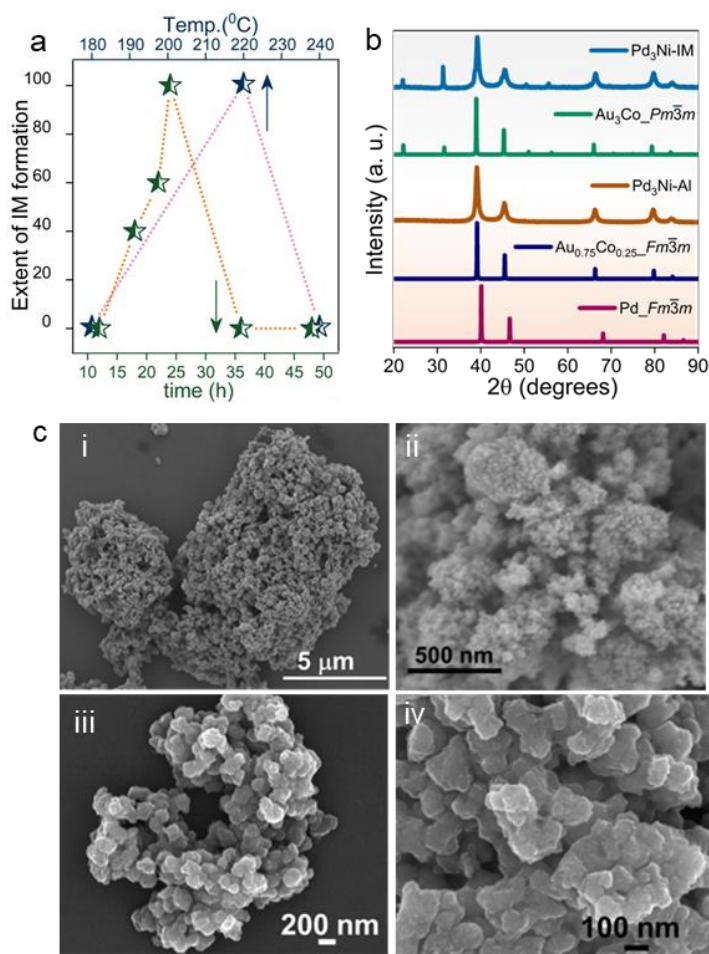


Figure 8.6. (a) Correlation of Pd₃Ni-IM formation from alloy phase by tuning temperature and time duration. (b) Powder X-ray diffraction (PXRD) pattern of Pd₃Ni-alloy and Pd₃Ni-IM with simulated patterns of elemental Pd and Au₃Co intermetallic. (c) SEM images of Pd₃Ni-Al (i) and (ii) and Pd₃Ni-IM (iii) and (iv).

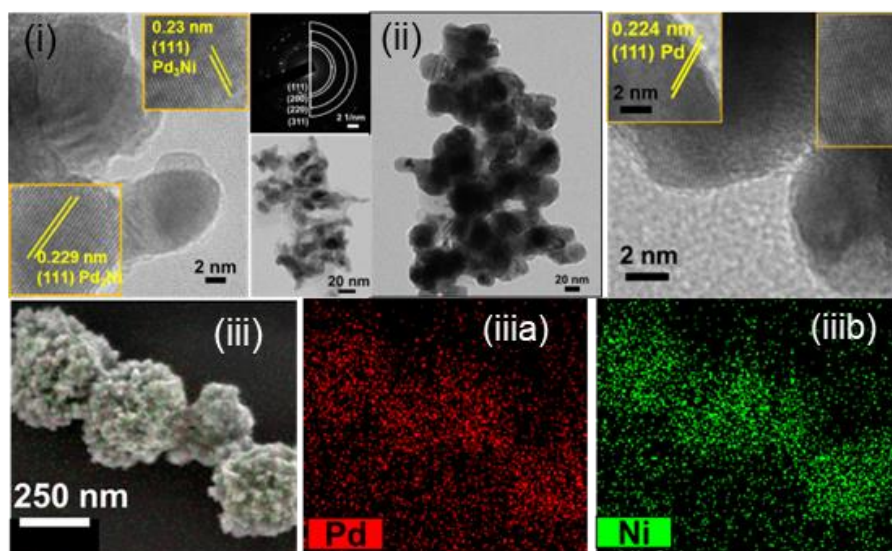


Figure 8.7. (i) Transmission electron microscopic (TEM) and high-resolution TEM (HR-TEM) images of Pd₃Ni-Al catalyst. (j.ii) TEM and HR-TEM images of Pd₃Ni-IM. (j.iii) SEM colour mapping of Pd₃Ni-IM, j(iii.a) and j(iii.b) are showing the Pd and Ni elemental distributions.

8.4.2 Electrochemical results

The catalysts Pd₃Ni-IM and Pd₃Ni-Al are studied extensively for exploring their electrochemical activities and durability for all kinds of energy conversion reactions of fuel cell and water splitting. It is interestingly observed that Pd₃Ni-IM is showing enhancement in its activity for OER, ORR, HER, and EOR with cycling whereas, the alloy counterpart is seen to become less active with more cycling and time (**Figure 8.8-8.11**). Linear sweep voltammograms (LSVs) for OER for Pd₃Ni-IM and Pd₃Ni-Al are compared in **Figure 8.8a** before and after different cycles and compared with the state-of-the-art catalyst IrO₂. Initially, the activity of both catalysts is almost similar whereas with increased cycling there is a crossover of activity, and both the catalysts show better OER activity than IrO₂. In this figure, the peak corresponding to oxidation of Ni is more intense for Pd₃Ni-IM than Pd₃Ni-Al, which indicates that more Ni sites (in metallic state) are exposed on the Pd₃Ni-IM surface which is getting oxidized at a higher rate than the alloy. **Figure 8.8b** show the comparison for OER activities of Pd₃Ni-IM and Pd₃Ni-Al with state-of-the-art catalyst IrO₂. **Figure 8.8c** shows the Tafel slopes for Pd₃Ni-Al, Pd₃Ni-IM, and IrO₂ and **Figure 8.8d** shows the Tafel slope values for Pd₃Ni-Al and Pd₃Ni-IM after 3500 ADT cycles. It is observed that the Tafel slope value for Pd₃Ni-IM decreases substantially (from 85.3 mV/dec to 70.1 mV/dec) after cycling which indicates that the OER kinetics is getting facilitated on surface reconstruction during the OER conditions which is discussed in later sections.

Figure 8.8e and the inset figure portray that with ADT cycling, the OER activity of Pd₃Ni-IM is enhanced accompanied by a left shift of peak maxima for the NiOOH generation peak with industrial level current density.⁴¹ This signifies that the potential requirement for this oxidation is decreasing and becoming more facile with cycling.⁴² Pd₃Ni-IM shows a very low overpotential for 10 mA/cm² of 260 mV for OER which interestingly reduces to 220 mV when ADT cycling is further done. **Figure 8.8f** relates the overpotential for 10 mA/cm² current density and NiOOH formation with increasing ADT cycling. Both follow the same trend signifying that the catalyst is getting better with cycling due to OER-feasible surface reconstruction. **Figure 8.9** shows the chronoamperometry study of Pd₃Ni-IM for 45 hours at 30 mA/cm² current density which exhibit its high durability at harsh conditions. Gradually we explored further the other hand of water splitting reaction, the hydrogen generation activity test for these two catalysts. The HER activity of Pd₃Ni-IM, Pd₃Ni, and 20% Pt/C was tested in 1M KOH after 6000 cycles (**Figure 8.10a**).

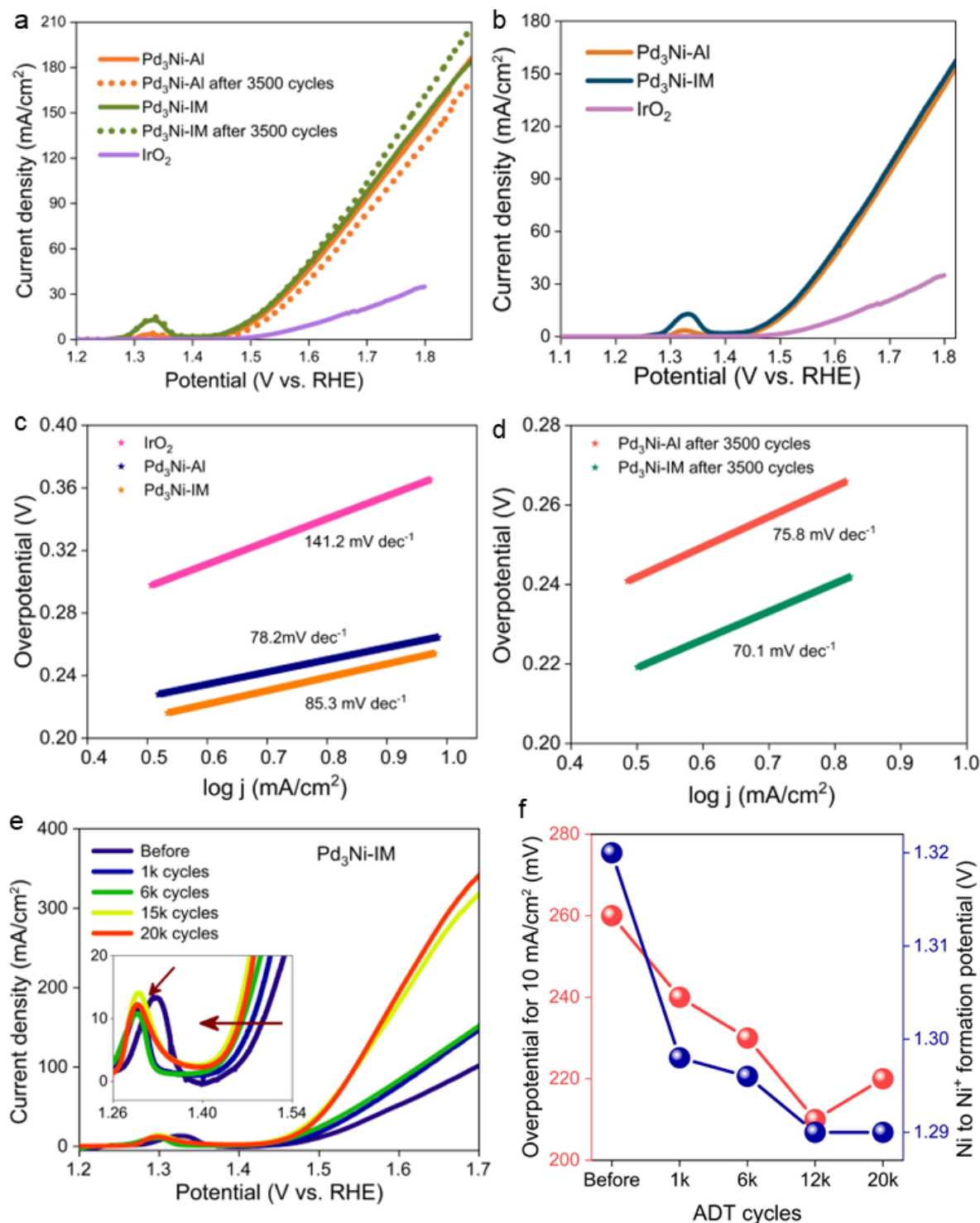


Figure 8.8. (a) Linear Sweep Voltammograms (LSVs) of mediated OER of Pd₃Ni-Al and Pd₃Ni-IM before and after ADT cycles and IrO₂ in 1M KOH solution. (a) LSV comparison for OER activities of Pd₃Ni-IM and Pd₃Ni-Al with state-of-the-art catalyst IrO₂. (b) Tafel plots for Pd₃Ni-Al, Pd₃Ni-IM, and IrO₂. (c) Tafel plots for Pd₃Ni-Al and Pd₃Ni-IM after 3500 ADT cycles. (e) LSVs of Pd₃Ni-IM before and after ADT cycles and inset shows the zoomed in portion of the LSV near the region of oxidation of Ni. (f) Comparison of overpotential and peak position for Ni oxidation hump after different ADT cycles.

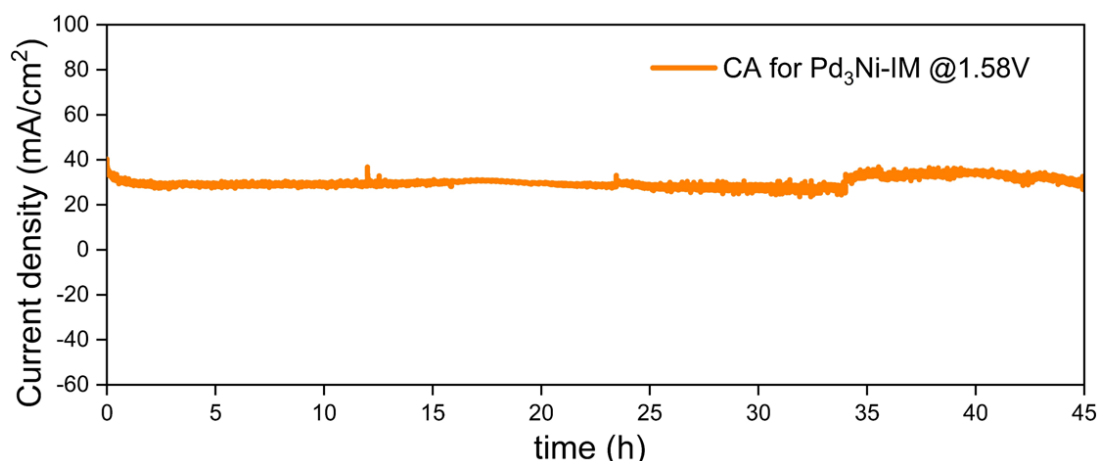


Figure 8.9. Chronoamperometry of Pd₃Ni-IM during OER. Chronoamperometry is performed at a constant potential of for 30 mA/cm² and a stable current is achieved for more than 40 hours.

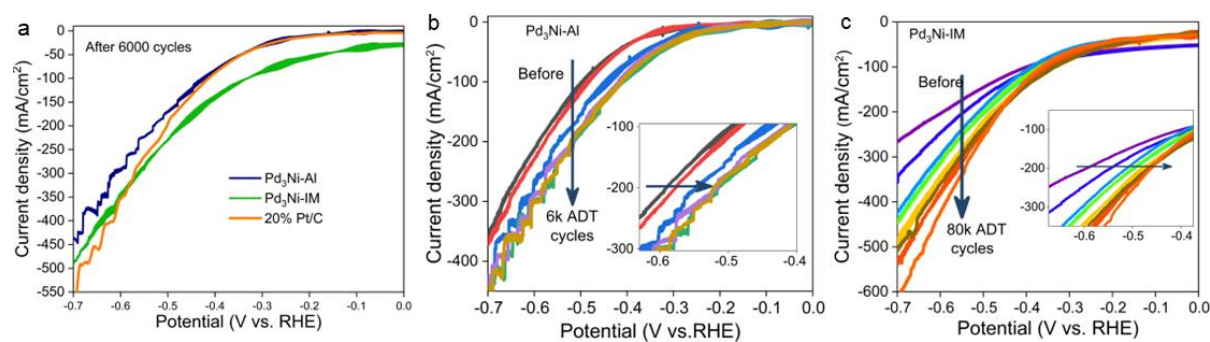


Figure 8.10. (a) LSVs of 1M KOH solution mediated HER of Pd₃Ni-Al, Pd₃Ni-IM, and 20% Pt/C after 6000 ADT cycles. (b) LSVs of HER activity in 1M KOH for Pd₃Ni-Al catalyst after different cycles of ADT. (c) LSVs of 1M KOH mediated HER of Pd₃Ni-IM before and after ADT cycles and inset shows the zoomed in portion of the LSV near the onset of reaction.

The HER activity for Pd₃Ni-Al initially increased and then stabilized after 6000 ADT cycles, as shown in **Figures 8.10b**. Whereas that of Pd₃Ni-IM catalyst keeps on increasing up to 80,000 ADT cycles with industrial level current density, as shown in **Figure 8.10c** (along with the inset figure).²²

We embarked on testing the novel material for fuel cell activity, as well. **Figures 8.11a** and **8.11b** show the LSVs for the ORR activity for Pd₃Ni-IM and ORR activity comparison for both Pd₃Ni-Al and Pd₃Ni-IM, their activity after ADT cycles and 20% Pt/C,²¹ respectively. **Figure 8.11c** shows the ORR activity of Pd₃Ni-Al after different cycles of ADT. It is observed how $E_{1/2}$ (half-wave potential) of Pd₃Ni-IM keeps on increasing and for Pd₃Ni-Al and 20% Pt/C, the activity keeps of decreasing with cycling. It is seen that with 10,000 ADT cycling, both $E_{1/2}$ value and diffusion limited current density increased for Pd₃Ni-IM catalyst which means that both the number of active sites and their inherent efficiency enhanced during cycling.

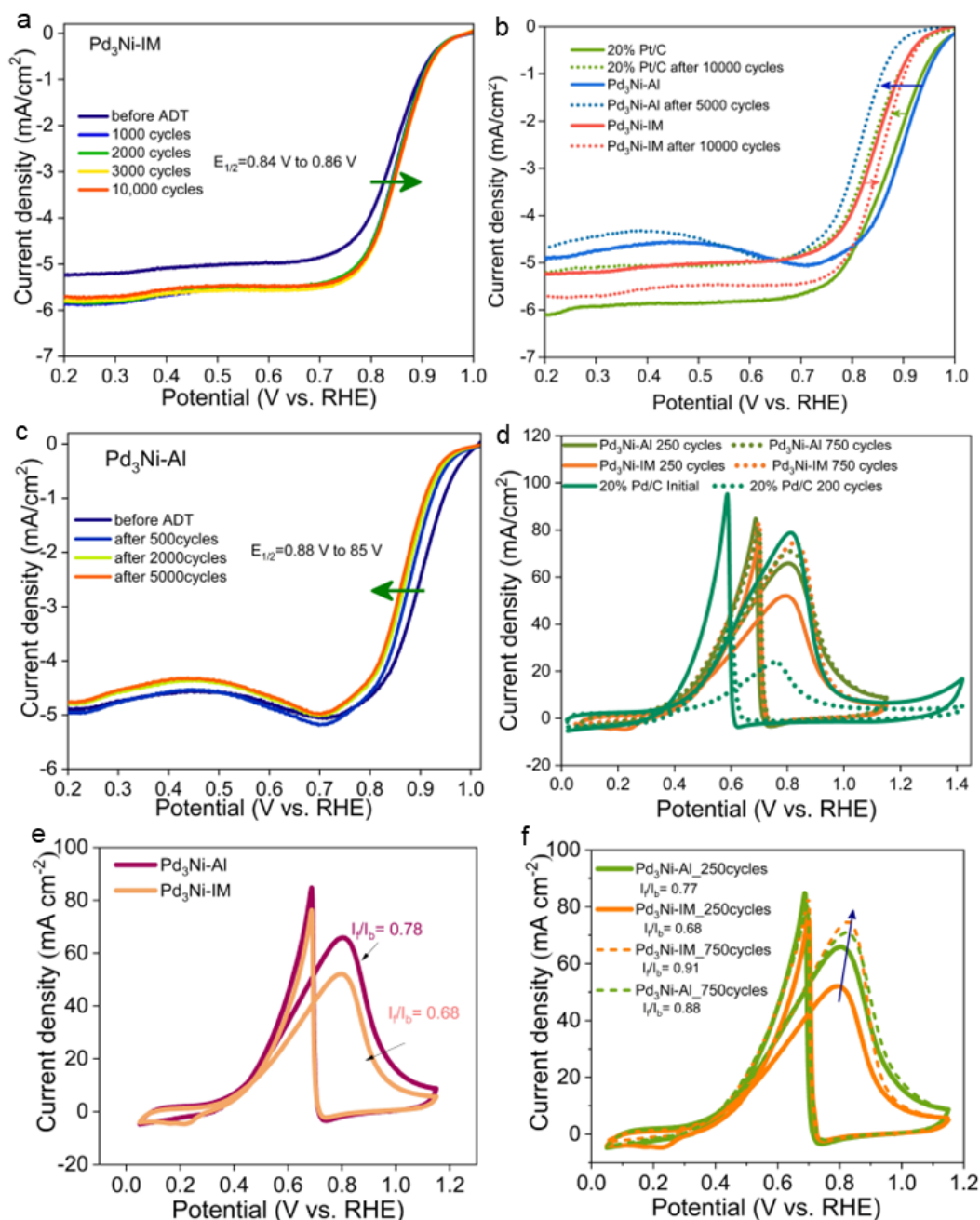


Figure 8.11. (a) LSVs of 0.1M KOH mediated ORR of Pd₃Ni-IM, (b) LSVs of ORR of Pd₃Ni-IM, Pd₃Ni-Al before and after ADT cycles and compared with 20% Pt/C. (c) Comparison of ORR activity of Pd₃Ni-Al catalysts in 0.1M KOH at a rotation speed of 1600 rpm after different cycles of ADT. (d) Cyclic voltammograms of EOR for the catalysts Pd₃Ni-IM and Pd₃Ni-Al and 20% Pd/C before and after different number of cycles in 1M KOH+1M ethanol. (e) Comparison of EOR CVs of Pd₃Ni-IM and Pd₃Ni-Al with 1M ethanol in 1M KOH solution. I_f and I_b are the maximum current density for the forward and backward sweep of the cyclic voltammogram during EOR. (f) CV comparison of Pd₃Ni-IM and Pd₃Ni-Al before and after different cycles and their corresponding change in I_f/I_b ratio.

Whereas for the alloy counterpart, Pd₃Ni-Al there is decrease in both the values which again signify that there is surface passivation which decreases the number of active sites because of Pd exposure (due to OH poisoning) and loss of conductivity due to the presence of

surface Ni-hydroxides (Will be discussed in detail in the subsequent section). Further we checked for the oxidation counterpart of ORR in DAFCs, that is, ethanol oxidation reaction (EOR). **Figure 8.11d** shows the EOR activity of both intermetallic and alloy catalysts showing the enhancement of forward current density for IMC and activity of 20% Pd/C is significantly decreasing with cycling. The ratio of I_f/I_b (I_f = forward current density, I_b = backward current density) for both alloy and IM are shown in **Figure 8.11e, 8.11f**. It is also observed that the ratio of forward to backward current density is improved for the Pd₃Ni-IM which means that the catalyst poisoning effect by CO or CH_x is decreased after cycling of catalyst and thus a reformed surface structure is generated which is enhancing the activity.^{43, 44} This is further explored in in-situ FTIR and DEMS studies in the later part of this paper. **Figure 8.12** is a central schematic representing the efficiency of the tetra-functional material, Pd₃Ni-IM. **Figure 8.13a** shows the schematic of the full cell water splitting in one-compartment cell with 6M KOH as the electrolyte and temperature dependent water splitting was performed. **Figure 8.13b** show that Pd₃Ni-IM catalyst when used as both cathode and anode shows better water splitting activity at room temperature than when 20% Pt/C and IrO₂ are used as cathode and anode, respectively. **Figure 8.13c** shows the LSVs of Pd₃Ni-IM as cathode and anode for water splitting at different industrial temperature conditions. The inset figure clearly shows that the activity of the catalyst in full water splitting enhances with increasing the temperature to 85 °C. We also performed proton exchange membrane (PEM) based water electrolysis using a membrane electrode assembly (MEA) as shown schematically in **Figure 8.14a** and its inset shows the original image. **Figure 8.14b** and **8.14c** show the LSVs and zoomed in LSVs of the water electrolysis of Pd₃Ni-IM catalyst as cathode and anode in a PEM and AEM electrolyser and it is observed that activity of the catalyst is increasing and then stabilizing after some time achieving an industrial level current density when testing is done a high surface area of 9 cm².

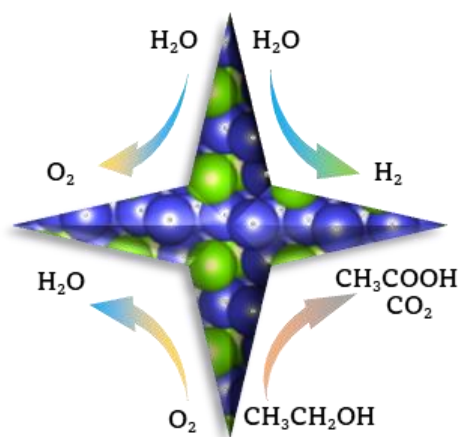


Figure 8.12. Overall schematic of tetra-functionality of Pd₃Ni-IM catalyst.

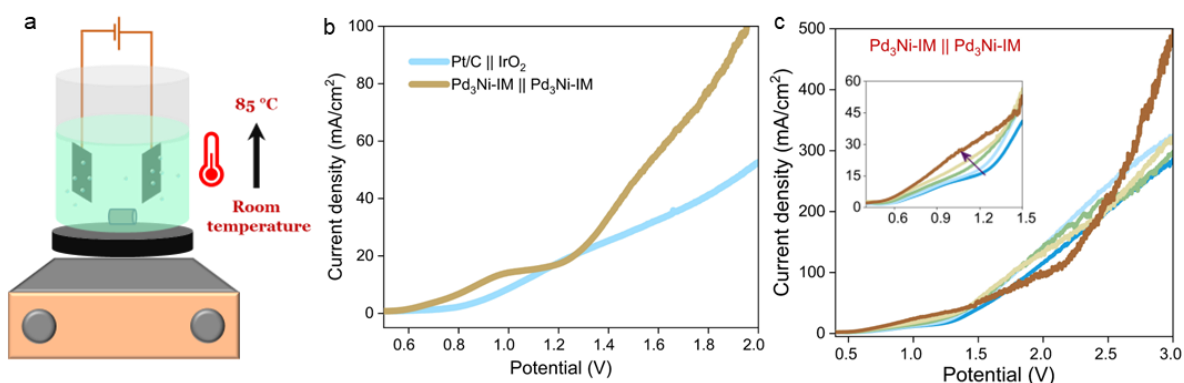


Figure 8.13. (a) Schematic of the one compartment full cell water splitting setup when temperature is varied from room temperature to 85 °C using 6M KOH solution as the electrolyte. (b) LSVs of full cell water splitting in one compartment cell using Pd₃Ni-IM as cathode and anode in one experiment, and standard catalysts, Pt/C and IrO₂ as cathode and anode materials. (c) LSVs for full cell water electrolysis in one compartment cell under different operational temperatures using Pd₃Ni-IM as both cathode and anode using 6M KOH as the electrolyte.

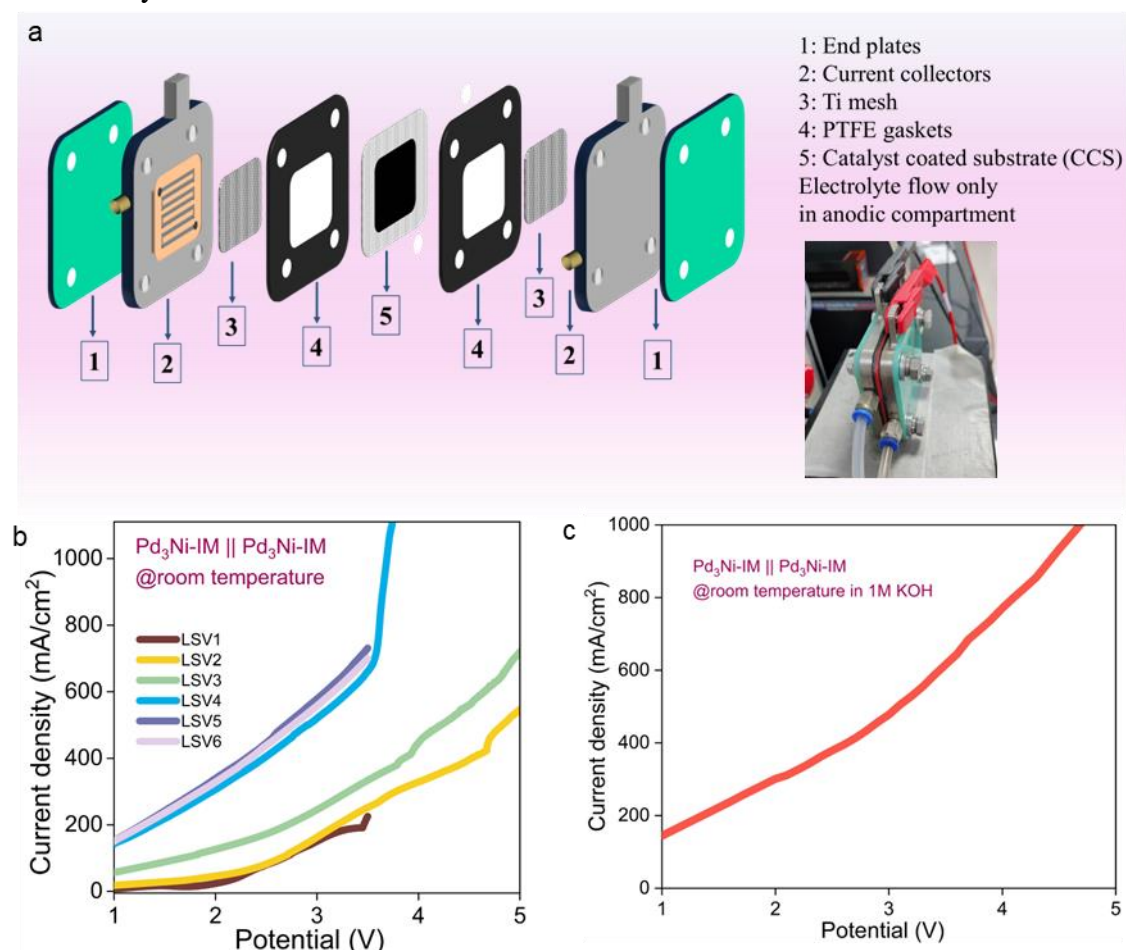


Figure 8.14. (a) Schematic of the full cell stack of the water electrolyser, inset figure is the real image of the electrolyser stack. (b) LSVs of Pd₃Ni-IM catalyst in the electrolyser system where same catalyst is used for both cathode and anode using DI water as the electrolyte. (c) LSVs of Pd₃Ni-IM catalyst in the electrolyser system where same catalyst is used for both cathode and anode using 1 M KOH as the electrolyte.

8.4.3 Structural insights and oxidation state analysis

To delve deep into the structure of this novel ordered phase of Pd₃Ni-IM, ex-situ characterizations of XAS and XPS are done. From the XANES spectra as in **Figure 8.15a**, it is observed that Pd is in metallic state in both alloy and intermetallic counterparts of Pd₃Ni. Pd is in even lesser oxidation state in Pd₃Ni-IM than Pd foil and the sequence of oxidation state of Pd follows the order: Pd₃Ni-IM < Pd foil < Pd₃Ni-Al.^{21, 45} Whereas the oxidation state of Ni in both intermetallic and alloy forms is higher than the Ni foil (**Figure 8.15b**).^{46, 47} The sequence of oxidation state of Ni follows: Ni foil < Pd₃Ni-Al < Pd₃Ni-IM. Charge transfer takes place from Ni to Pd atoms, and this charge transfer is more prominent in Pd₃Ni-IM where Pd is in lowest, and Ni is in highest oxidation state. This observation is also supported from the surface analysis technique, XPS, where Pd is in lower binding energy in Pd₃Ni-IM (335.58 eV) than in Pd₃Ni-Al (335.6 eV), as shown in **Figures 8.15c** and **8.15d**. From Ni 2p XPS spectra (**Figure 8.15e** and **8.15f**), it is seen that Pd₃Ni-Al is surfaced with high content of Ni²⁺ species which is much less in case of Pd₃Ni-IM. Since already mentioned that OAm has a strong binding with the Ni atoms on the surface of Pd₃Ni-IM as compared to Pd₃Ni-Al, free Ni atoms on alloy surface are expected to be oxidized fast as compared to the OAm covered Ni sites in IM. For Pd₃Ni-IM, the ordered nature keeps mostly metallic Ni exposed on the surface. Moreover, as observed theoretically, less anchoring of OAm N atoms with Ni atoms on alloy surface which makes the Ni atoms more prone to oxidation. On the other hand, N-anchored Ni atoms on IM surface are protected from oxidation.⁴⁸

To further check the orderliness of the Pd₃Ni structure, DSC experiments were conducted for both Pd₃Ni-Al and Pd₃Ni-IM. From **Figure 8.16a** it is observed that heat flow peak is observed for Pd₃Ni-IM at higher temperature than the alloy counterpart. This indicates that Pd₃Ni-IM requires more temperature for its phase change than Pd₃Ni-Al. **Figure 8.16b** shows that C_p value for Pd₃Ni-Al is more than that of Pd₃Ni-IM which means the entropy or disorderliness associated with the alloy is much more than that of the IM.^{49, 50} **Figure 8.16c** is the schematic which gives an overview of the direct dependence of entropy and surface Ni oxide where alloy has higher entropy and higher amount of surface oxides than IM. Internal orderliness will dictate the surface bond saturation and will end up in having less tendency to oxidize⁵¹. Thus, it is expected that this structural orderliness will rule the overall catalytic activity since catalysts is a surface and sub-surface phenomenon and it is well explained via in-situ techniques in the following sections.⁵²

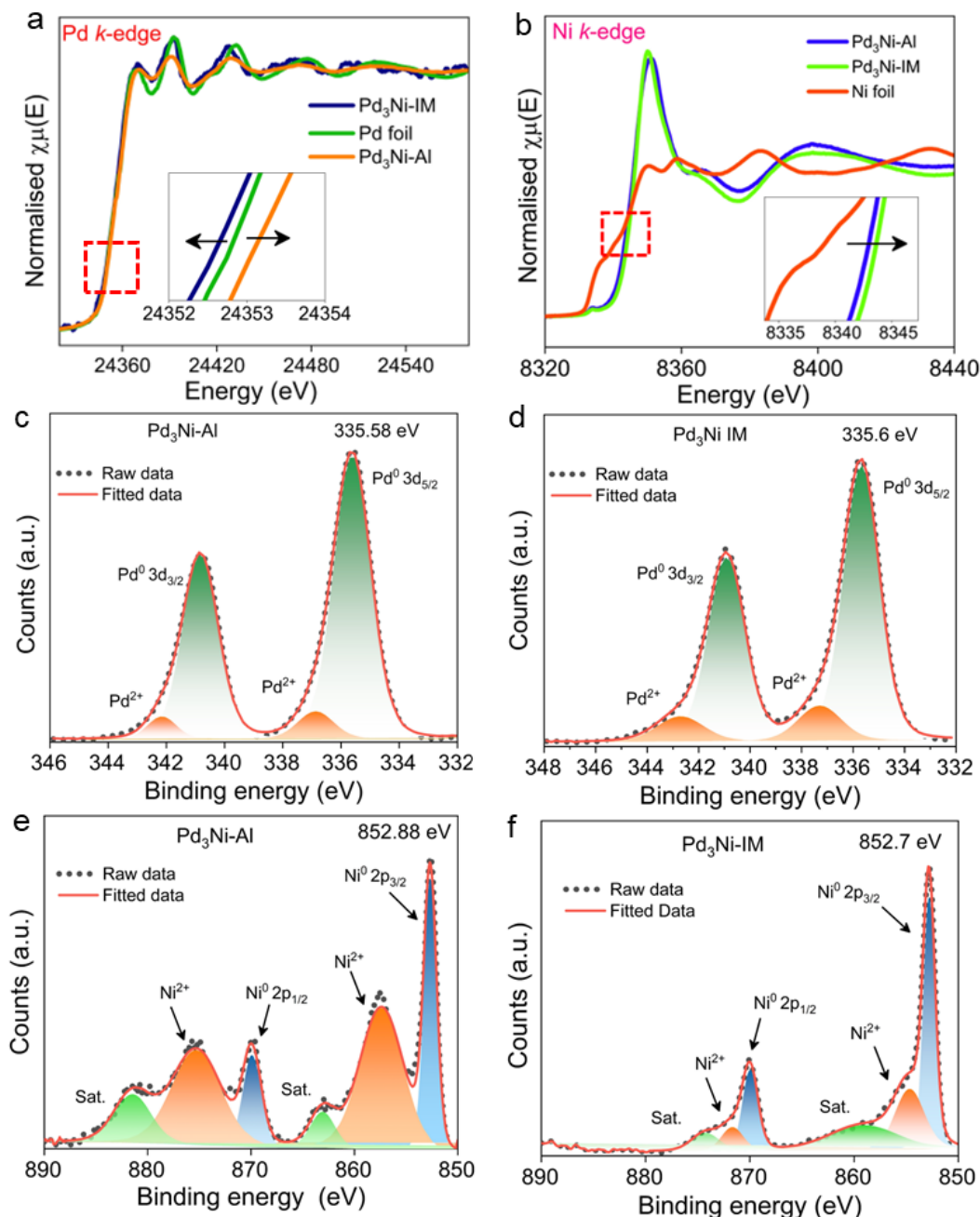


Figure 8.15. (a) X-ray absorption near edge spectra (XANES) of Pd *K*-edge in Pd₃Ni-Al, Pd foil, and Pd₃Ni-IM. (b) XANES of Ni *K*-edge of Pd₃Ni-Al, Pd foil, and Pd₃Ni-IM (c) Pd 3*d* XPS spectrum of Pd₃Ni-Al. (d) Pd 3*d* XPS spectrum of Pd₃Ni-IM. (e) Ni 2*p* XPS spectrum of Pd₃Ni-Al. (f) Ni 2*p* XPS spectrum of Pd₃Ni-IM.

8.4.4 Operando analysis of active species generation

To understand the active sites and their transformation during reaction conditions, we have performed operando and post-electrochemical spectroscopic characterizations for different electrochemical reactions.^{21, 22, 30, 53} Post-OER Ni 2*p* XPS spectra are fitted (**Figure 8.17**), where it is prominent that Ni²⁺ exists along with formed NiOOH for Pd₃Ni-Al catalyst which was already having Ni(OH)₂ before catalysis (**Figure 8.15e**).

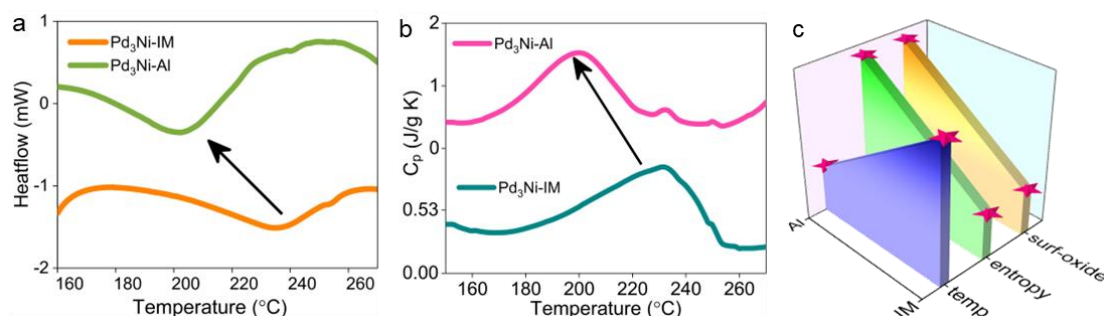


Figure 8.16. (a) Differential scanning calorimetry (DSC) data of heat flow vs. temperature for Pd₃Ni-Al and Pd₃Ni-IM. (b) DSC data of C_p vs. temperature for Pd₃Ni-Al and Pd₃Ni-IM (c) Comparison of temperature for phase change, entropy, and surf-oxide for Pd₃Ni-Al and Pd₃Ni-IM.

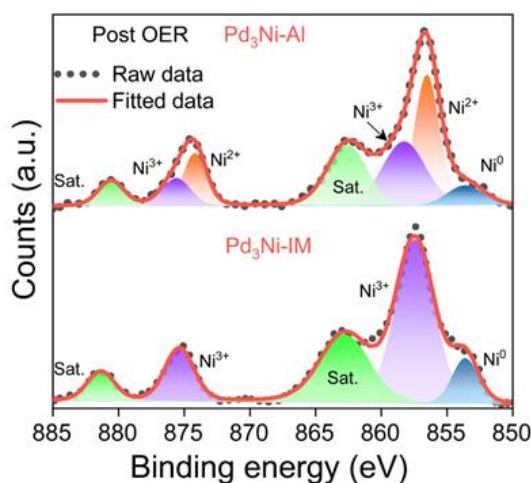


Figure 8.17. Comparison of Ni 2p XPS spectra of Pd₃Ni-Al and Pd₃Ni-IM after alkali mediated OER.

Whereas there is no Ni(OH)₂ on Pd₃Ni-IM catalyst and the surface is purely NiOOH. As already observed in **Figure 8.8e**, Pd₃Ni-IM is exhibiting more intense NiOOH formation peak even after ADT cycles. Due to poor electrical conductivity of Ni(OH)₂, the activity of Pd₃Ni-Al is seen to decrease with time.⁵⁴ Post-OER XPS shows that Ni(OH)₂ is present for Pd₃Ni-Al catalyst which was already present before catalysis. This indicates that after catalysis some of the Ni(OH)₂ got converted into NiOOH and some remained as hydroxide. Ni(OH)₂ is known for poor conductivity which indirectly diminishes the activity of the material over time and cycling. The intercalation of -OH inside the layered Ni(OH)₂ finally converts it to NiOOH. Due to poor electrical conductivity of Ni(OH)₂, full transformation to NiOOH does not occur. On the other hand, in the Pd₃Ni-IM catalyst, surface is not passivated by Ni(OH)₂ and pure metallic Ni is exposed on the surface which under oxidation potential gets leached and that leaching is confirmed from the decrease in the coordination number of Ni from the fitting of Pd K-edge EXAFS data. This leached Ni are in higher oxidation state which forms NiOOH on the surface. Simultaneously, Ni leaching will lead to more OH percolation inside the sub-

surface level which will enhance the NiOOH formation without compromising with the conductivity because of the metallic IM support. Ni³⁺ indicates NiOOH species, which is highly active for OER, which is why, Pd₃Ni-IM is showing very facile OER kinetics and stable high current density up to 20,000 ADT cycles.

To gain further time-resolved information during the reaction, in-situ XAS has been done with home-customized cell setup which is shown as schematic in **Figure 8.1a**. *Operando* XANES spectra of Ni *k*-edge shows that with increasing oxidation potential there is increment in the oxidation state of Ni with right shift of absorption edge (**Figure 8.18a**). *Operando* R-space data also show that with increasing potential there is initial increase in bond length and then again decreased. This initial increase and then decreasing trend is well visible in **Figure 8.18b**. crease in Ni-Pd bond lengths can be ascribed to the leaching of Ni atoms from the sub-surface layers.⁵⁵

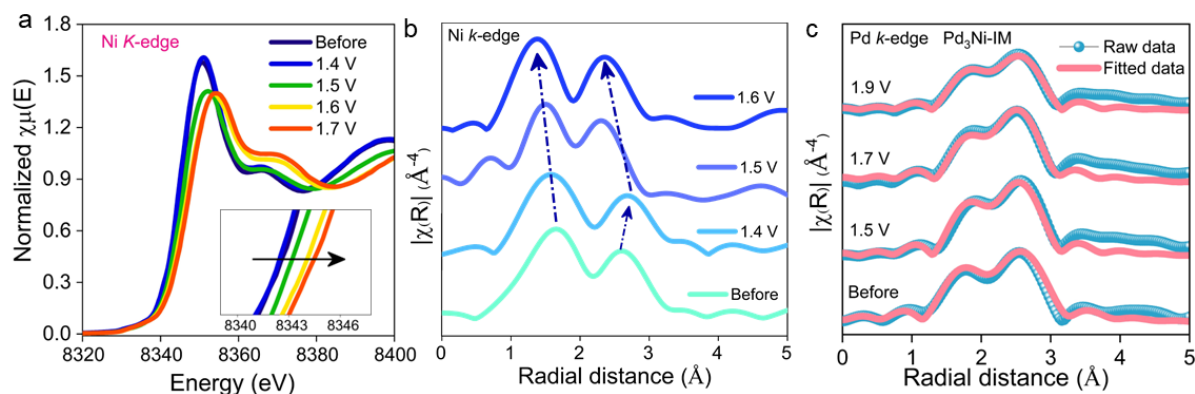


Figure 8.18. (a) Potential-dependent XANES spectra of Ni *K*-edge for Pd₃Ni-IM during OER in 0.5M KOH. Inset shows the zoomed-in absorption edge. (b) Potential-dependent R-space data of Ni *K*-edge for Pd₃Ni-IM during OER in 0.5M KOH. (c) Fitted EXAFS data for Pd *k*-edge at different potential dependent study during OER.

Table 8.5. EXAFS fitting parameters for Pd *k*-edge during in-situ OER studies.

Potential	Path	CN	R	ΔE
Before	Pd-Ni	2.77	2.275	3.900
	Pd-Pd	4.29	2.531	3.900
1.5V	Pd-Ni	2.6	2.267	6.000
	Pd-Pd	4.1	2.505	6.000
1.7V	Pd-Ni	2.1	2.270	4.476
	Pd-Pd	4.1	2.525	4.476
1.9V	Pd-Ni	1.9	2.278	6.396
	Pd-Pd	4.45	2.539	6.396

Whereas the Ni-Ni bond distance is decreasing monotonically due to increasing oxidation state of Ni. To understand if there is any Ni leaching, EXAFS data for Pd *k*-edge during potential dependent study is fitted (fitted plot is in **Figure 8.18c** and parameters are in **Table 8.5**). There is consistent decrease in CN of Ni while sweeping potential from lower to higher oxidation value (CN before reaction is 2.77 and at 1.9V CN is 1.9). To realize the surface chemistry of the catalyst, time- and potential-dependent Raman spectra has been conducted with home customized cell setup which represents that with increasing time (**Figure 8.19a**) and increasing potential (**Figure 8.19b**), the peak intensity corresponding to E_g mode of NiOOH and O-O stretching of active oxygen species are increasing.

The spectra have E_g mode of NiOOH at around 490 cm⁻¹ and the peaks around 900 and 1100 cm⁻¹ corresponding to the O-O stretching mode of free O₂ molecule which further confirms oxygen evolution under that potential with increasing time.⁵⁶⁻⁵⁹ **Figure 8.19c** correlates the decreasing CN and increasing Raman intensity of E_g mode of NiOOH with increasing potential.

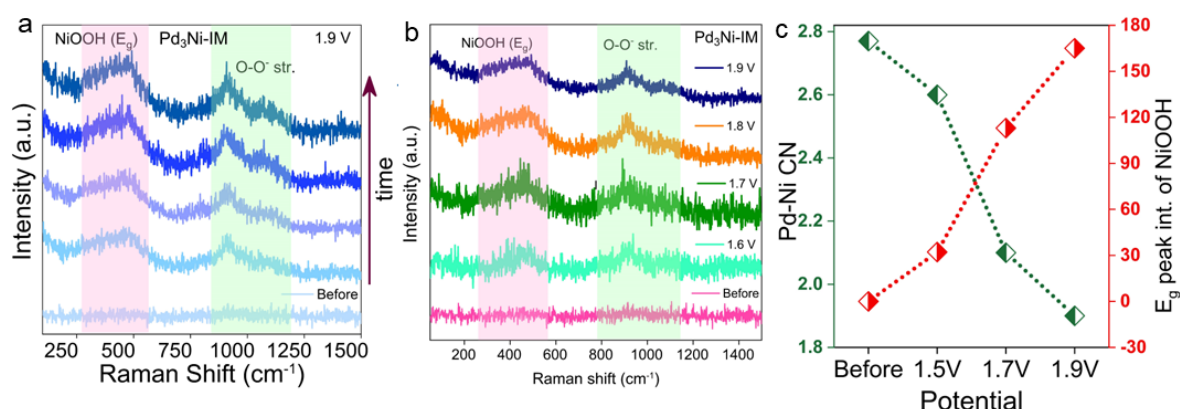


Figure 8.19. (a) In-situ time-dependent Raman spectra for Pd₃Ni-IM during OER in 0.5 M KOH. (b) Potential dependent Raman spectra of Pd₃Ni-IM catalyst during OER activity. (c) Correlation of coordination number of Pd with surrounding Ni atoms and peak intensity of E_g mode of NiOOH in Raman spectra at different potentials.

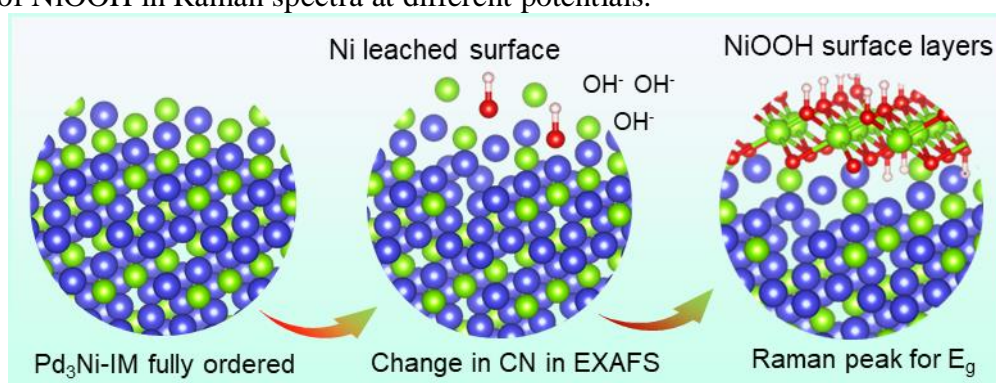


Figure 8.20. Schematic representing how Ni leaches out at oxidation potential from the bulk and forms NiOOH at the surface.

Such a correlation is being represented schematically in **Figure 8.20**.⁶⁰ Due to surface reconstruction with Ni removed from subsurface layers during OER, the intercalation of OH⁻ species inside the sub-surface layers will be more feasible and exhibit faster reaction kinetics. **Figure 8.21a, b** and **8.21c** show the Pd 3d fitted XPS spectra of Pd₃Ni-Al and Pd₃Ni-IM after alkali mediated OER. **Figures 8.22a** and **8.22b** show the Ni 2p XPS spectra of Pd₃Ni-IM and Pd₃Ni-Al before and after alkaline HER, respectively. Negatively charged OH⁻ and dipolar water molecules get easily attracted to the oxide rich Pd₃Ni-Al surface. Water dissociation is the first step for alkaline HER which leads to breaking of O-H bonds of water and thus more OH is generated and adsorbed on the surface which further increases the amount of Ni-hydroxide on alloy surface. On the other hand, some Ni-hydroxides are formed on surface of Pd₃Ni-IM after some time. But there is significant presence of metallic Ni on the surface which establishes that Pd₃Ni-IM has not lost its metallic conducting property and hence keep on activating the surface for HER even till 80,000 ADT cycles. Ni(OH)₂ has poor conductivity due to which it passivates the alloy surface further and the activity degrades after 6000 ADT cycles.

It has been observed that after reaction, the surface metallic Ni has decreased substantially in case of Pd₃Ni-Al whereas it has retained the metallic Ni in Pd₃Ni-IM even after reaction. Existence of metallic Ni on the surface with Ni-hydroxide enhances the HER activity more by facilitated water dissociation step in alkaline HER.¹⁴ **Figure 8.23a, 8.23b** and **8.23c** show the Pd 3d fitted XPS spectra of Pd₃Ni-Al and Pd₃Ni-IM after alkali mediated HER. It is observed from **Figures 8.10** that initially the HER activity of Pd₃Ni-Al is better than Pd₃Ni-IM, which can be attributed to the fact that the reactant molecules H₂O are more attracted to Pd₃Ni-Al because of substantial amounts of Ni²⁺ available (**Figure 8.15e**).^{61, 62} Whereas with time the activity of Pd₃Ni-IM overcomes that the of Pd₃Ni-Al.

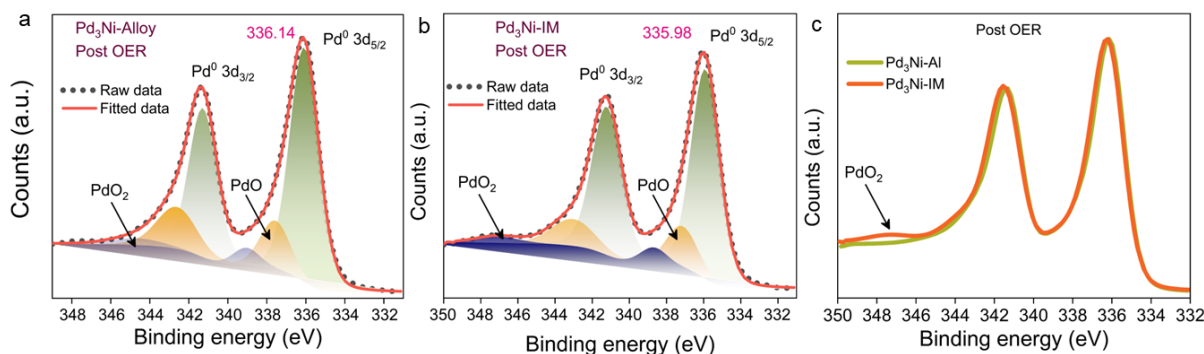


Figure 8.21. Pd 3d fitted XPS spectra after alkaline mediated OER for (a) Pd₃Ni-Al and (b) Pd₃Ni-IM. (c) Comparison of Pd 3d fitted XPS spectra after alkali mediated OER for Pd₃Ni-Al and Pd₃Ni-IM.

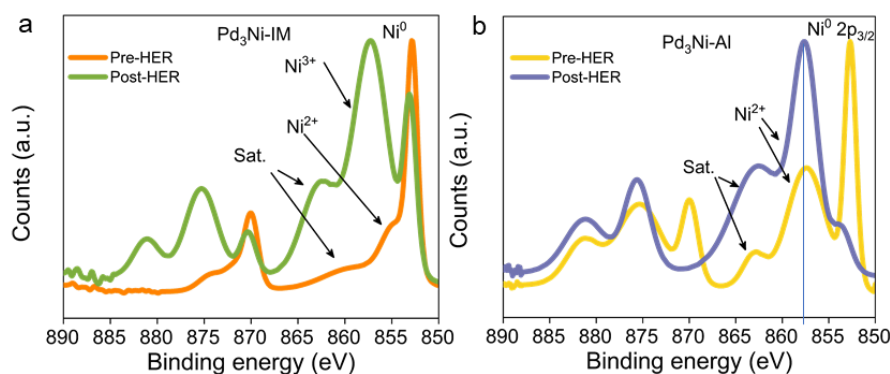


Figure 8.22. Post electrochemical Ni 2p XPS spectra of (a) Pd₃Ni-IM and (b) Pd₃Ni-Al after OER.

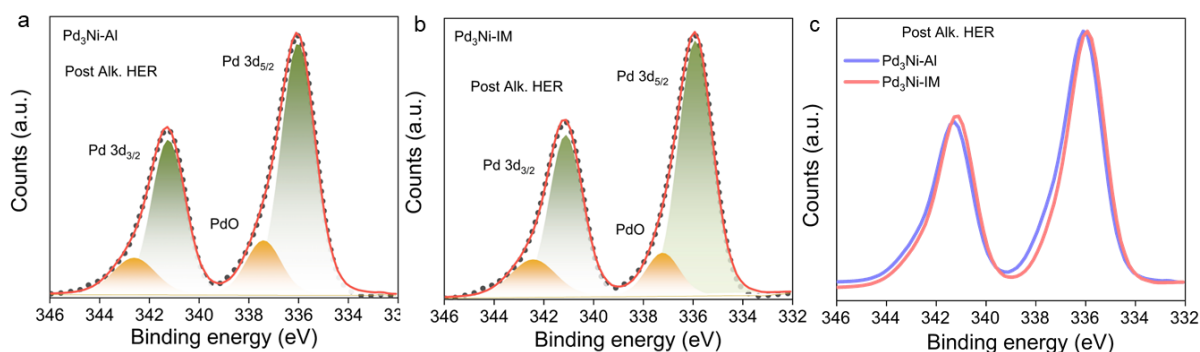


Figure 8.23. Pd 3d fitted XPS spectra after alkali mediated HER for (a) Pd₃Ni-Al and (b) Pd₃Ni-IM. (c) Comparison of Pd 3d fitted XPS spectra after alkaline mediated HER for Pd₃Ni-Al and Pd₃Ni-IM.

Figures 8.10 shows how the current density saturated after 6000 ADT cycles for Pd₃Ni-Al and the current kept on increasing up to 80,000 ADT cycles for Pd₃Ni-IM. The optimized surface of Ni²⁺ (Ni-hydroxide) with Ni⁰ and Pd⁰ metallic states are required to achieve the best alkaline HER activity.

8.4.5 Operando analysis of reaction mechanism and phase transformation

It is observed that Pd-Ni based ordered and disordered phases which have different distribution of Ni atoms in the Pd-coordination significantly affects the product selectivity and activity in longer cycling of EOR. In-situ FTIR study has been done to understand the EOR mechanism using optimized cell setup (**Figure 8.1b**). **Figure 8.24a** shows the potential dependent in-situ FTIR study for Pd₃Ni-IM during EOR. Two peaks at 1434 cm⁻¹ and 1531 cm⁻¹ corresponding to symmetric and asymmetric stretching bands of O-C-O of CH₃COO⁻ ions.²⁷ There is a peak at 1385 cm⁻¹ which corresponds to the absorption peak for CO₃²⁻ ions which signifies formation of CO₂ (in alkaline media) accompanied by small peak at 2352 cm⁻¹ for CO₂. There is a negative peak at 1076 cm⁻¹ corresponding to the C-O stretching vibration of ethanol which denotes the consumption of ethanol during the EOR.²⁷ **Figure 8.24b** and **8.24c** show the zoomed spectra and 3D representation depicting how with increasing time there is

increment in relative peak intensity of carbonate as compared to acetate ions. This observation is correlated with EOR activity data where it has been observed that with increasing the time there is improvement in I_f/I_b ratio (**Figure 8.11d**).

The increased relative peak intensity of carbonate ion which is concluding the enhancement in EOR selectivity in $12e^-$ transfer process with time on $\text{Pd}_3\text{Ni-IM}$ ordered phase. The oxophilic property of Ni has led to enhanced OH adsorption and hence faster oxidation and lesser poisoning.⁶³ Easy desorption of acetic acid for $\text{Pd}_3\text{Ni-Al}$ (disordered phase) is observed at both high and low oxidation potentials. **Figure 8.25a** shows time dependent IR spectra for EOR on $\text{Pd}_3\text{Ni-Al}$ disordered phase which shows only symmetric and asymmetric stretching bands for acetic acid denoting only $4e^-$ transfer process. **Figure 8.25b** shows the 3D representation of the in-situ IR data of $\text{Pd}_3\text{Ni-IM}$ catalyst during EOR showing the emergence broad hump of O-H stretching peak indicating the formation of water. **Figure 8.26** is the schematic representation of EOR on the novel ordered and disordered phases of Pd-Ni based compounds.

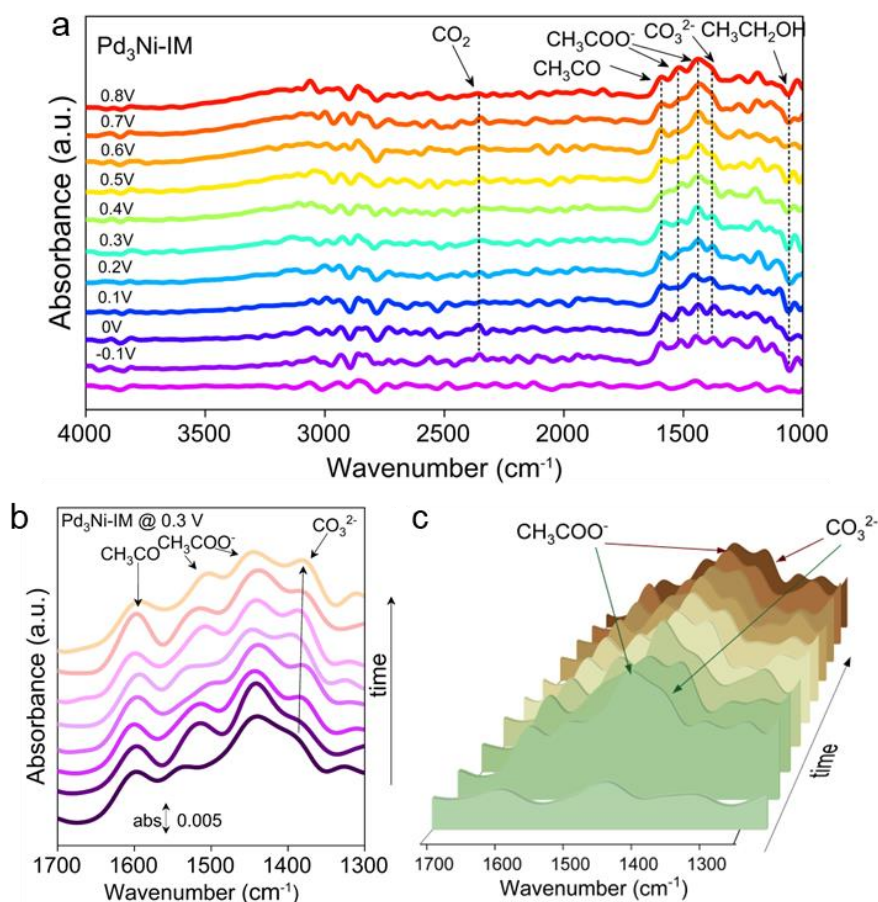


Figure 8.24. (a) Potential dependent FTIR spectra of $\text{Pd}_3\text{Ni-IM}$ catalyst during EOR. (b) Zoomed in and (c) 3D representation of time dependent FTIR spectra of $\text{Pd}_3\text{Ni-IM}$ catalyst during EOR.

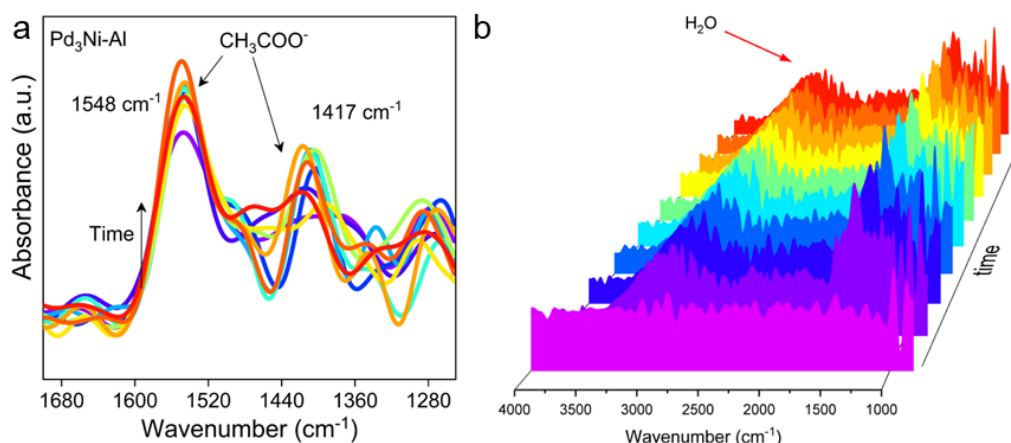


Figure 8.25. (a) (d) Zoomed in representation of time dependent FTIR spectra of Pd₃Ni-Al catalyst during EOR. (b) 3D representation of time-dependent in-situ IR spectra of Pd₃Ni-IM during EOR. The emergence of broad hump around 3000 cm⁻¹ indicates formation of water (O-H stretching frequencies).

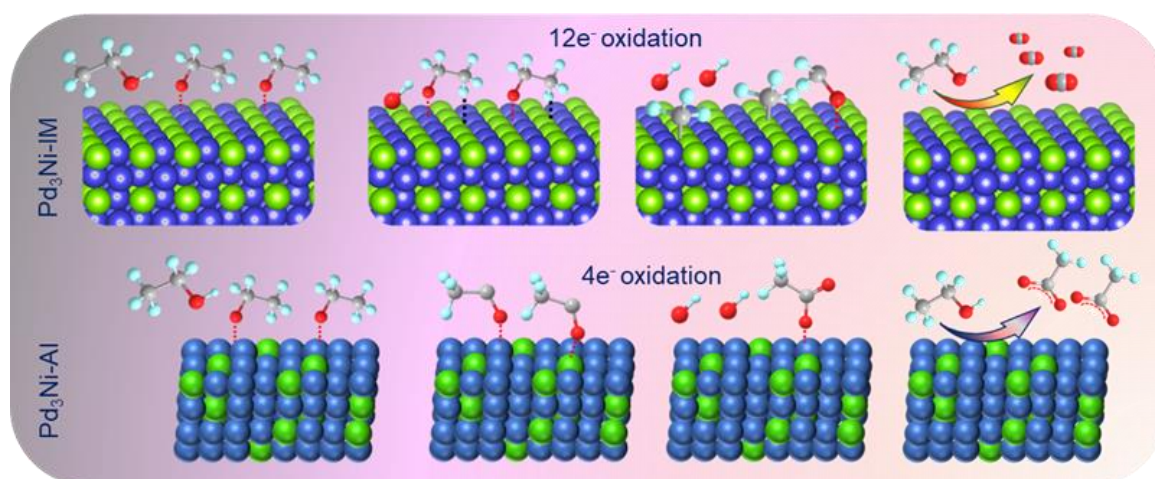


Figure 8.26. Schematic displaying the reaction mechanism on IM catalyst during EOR.

Whereas for Pd₃Ni-IM ordered phase with exposed metallic Ni and Pd atoms stabilizes acetate ions which undergo C-C cleavage and 12e⁻ transfer complete oxidation of ethanol forming carbonate ion and carbon dioxide. Charge polarization at two different atoms (Pd and Ni) help in facile C-C splitting which is absent in alloy phase where no regular arrangement of Pd and Ni are present. Proper *OH adsorption is highly required to oxidise the poisoning CH_x and CO species due to which there is improvement observed in I_f/I_b ratio with further cycling for Pd₃Ni-IM catalyst. Systems with two metals impose bifunctional and electronic effect in enhancing the activity and reducing the catalyst poisoning effect. In ordered phase, the regular arrangement of Pd and Ni atoms have further enhanced the C-C cleavage with periodic charge polarization on the surface of the catalyst. On the other hand, in disordered phase only acetic acid has been observed with no CO₂ formation. The disordered phase is producing majorly acetate ions and no carbonate ions (in alkaline mediated EOR) whereas the ordered phase is

producing both acetate and carbonate and the selectivity towards carbonate is gradually overtaking acetate with increasing time. This observation is further verified by performing mass spectrometric analysis of instantaneous formation of products by differential electrochemical mass spectrometry (DEMS). The schematic of the DEMS setup (type cell A) is shown in **Figure 8.27a**. **Figures 8.27b** and **8.27c** clearly show that there is formation of CO_2 along with CH_3CHO and CH_3COOH in case of $\text{Pd}_3\text{Ni-IM}$ and there is no CO_2 formation in case of $\text{Pd}_3\text{Ni-Al}$ catalyst. This also confirms that 12 electron transfer takes place for $\text{Pd}_3\text{Ni-IM}$ with C-C bond cleavage whereas only 4 electron transfer takes place for $\text{Pd}_3\text{Ni-Al}$. **Figure 8.27d** shows the emergence of H_2 and O_2 during HER and OER of $\text{Pd}_3\text{Ni-IM}$ catalyst.

Figure 8.28a and **8.28b, c** shows the PXRD pattern of $\text{Pd}_3\text{Ni-IM}$ after performing electrochemical reactions at different pH and different reaction potential range. It is observed that $\text{Pd}_3\text{Ni-IM}$ phase remains intact in all reduction potentials for HER and OER.

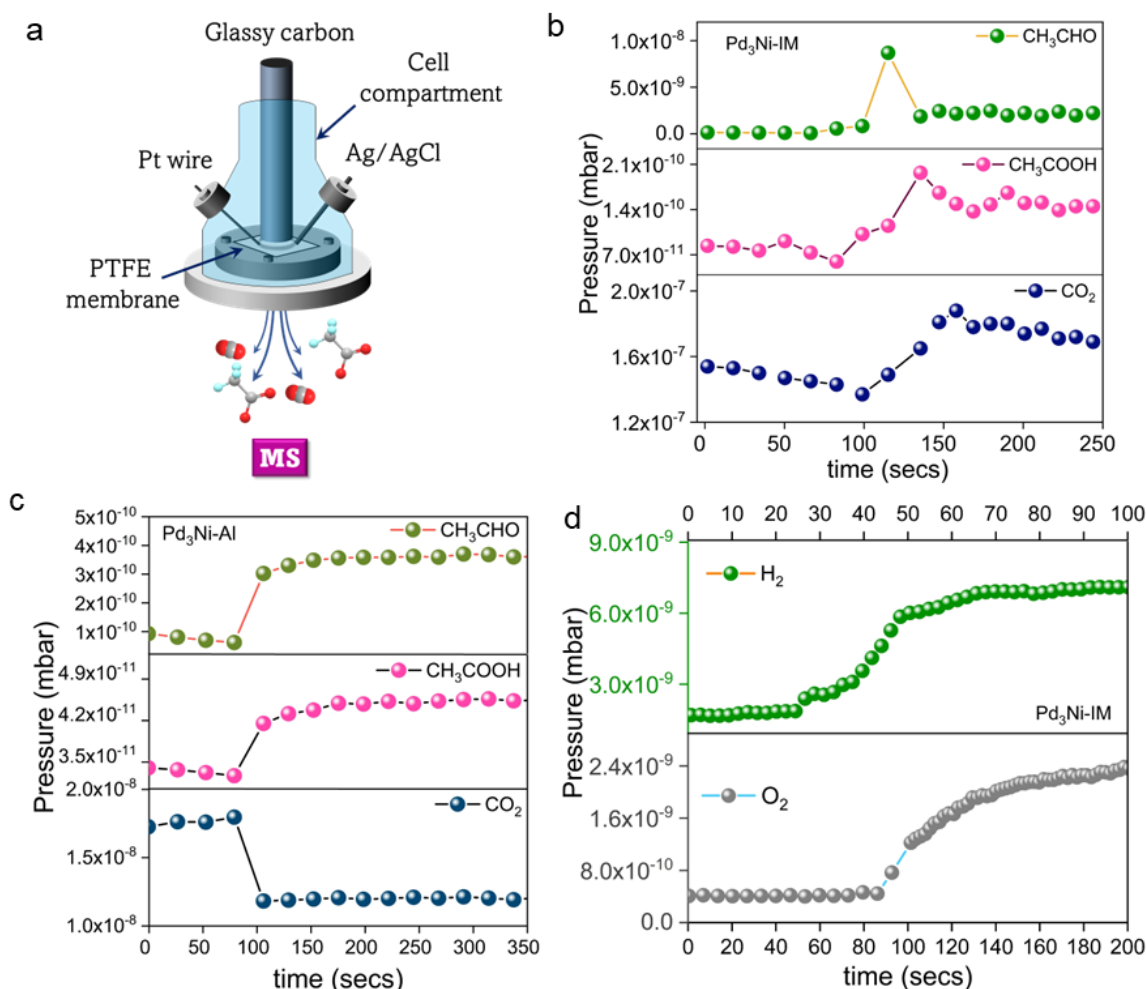


Figure 8.27. (a) Schematic of DEMS cell setup. DEMS spectra of different product evolution with respect to time for (b) $\text{Pd}_3\text{Ni-IM}$ and (c) $\text{Pd}_3\text{Ni-Al}$ during EOR and (d) $\text{Pd}_3\text{Ni-IM}$ during HER and OER.

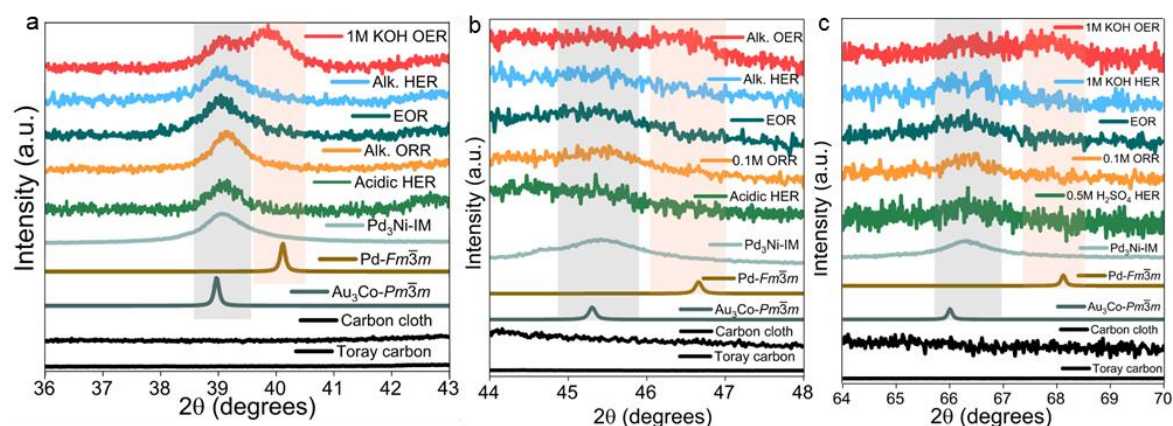


Figure 8.28. (a) Post-HER, OER, ORR, EOR PXRD pattern of Pd₃Ni-IM catalyst. (b, c) Zoomed-in PXRD pattern of Pd₃Ni-IM after different electrochemical reactions. (a) from 2θ value of 44° to 48° (peaks corresponding to (111) and (200) planes). (b) from 2θ value of 64° to 70° (peaks corresponding to (220) plane). Only under the electrochemical conditions of oxygen evolution reaction (higher oxidation potential and higher pH), there is a phase transition partially from IM to alloy of Pd₃Ni-IM catalyst.

Even for EOR at potential below 1.2 V vs. RHE, the ordered Pd₃Ni-IM phase remains intact. Interestingly, during OER, when a higher potential used above 1.2 V vs. RHE, the phase starts transforming to disordered alloy phase.⁶⁴ Conversion to disordered phase indicates increase in entropy and reach a state which will be entropy driven phase. There exists a mixture of both ordered and disordered phase in Pd₃Ni-IM after OER at higher oxidation potential in 1 M KOH. **Figure 8.29** schematically represents how the pH and reaction potential affect the structural orderliness of the Pd₃Ni-IM internal structure. Recollecting the observation from in-situ XAS as in **Figure 8.18c** and **Table 8.5** where the Ni is getting leached and surface restructured as NiOOH, it can be correlated that Ni leached from surface and sub-surface layers which gave a partial disordered structure with increase in entropy near the surface layers. The schematic in **Figure 8.20** can be firmly related to this phenomenon.

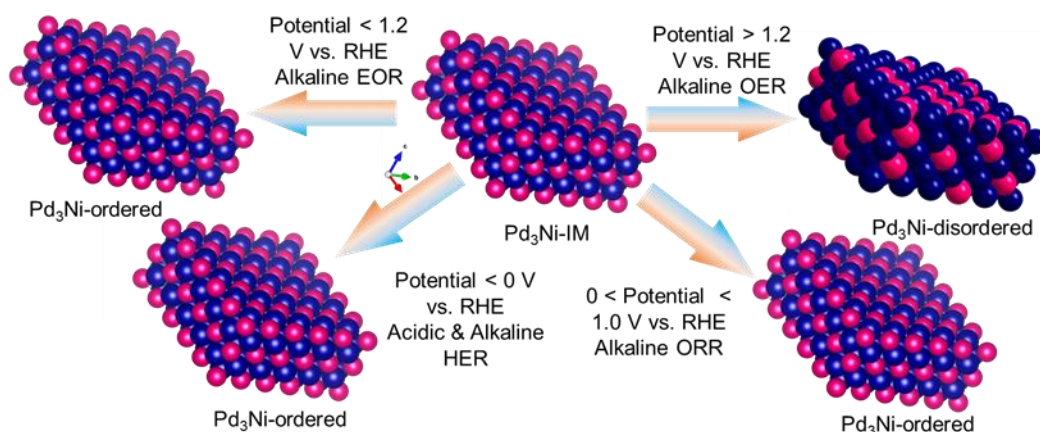


Figure 8.29. Schematic of Potential-dependent and pH dependent phase transformation of Pd₃Ni-IM.

374

We modelled Pd-Ni intermetallics and alloys and performed calculations of equilibrium

structure of Ni and Pd stabilizes OH and H more and water dissociation becomes more feasible on intermetallic than on alloy. Ordered structure in IM will regular patterns of Pd-Ni-Pd-Ni bonds and the amount of Pd-Ni interface will be more in IM than in alloy which has major Pd atoms with random arrangements of Ni in it.

8.5 Conclusion

This work showcases the generation of a novel intermetallic compound of Pd and Ni, Pd₃Ni. To the best of our knowledge, this is the first ordered IM formed with Pd and Ni. Scientific community often finds difficult to stabilize the ordered compounds with two metals in the same group positioned nearby. The ordered compound is compared with a synthesized disordered compound Pd₃Ni-Al of the similar stoichiometry. Extensive characterizations show that charge transfer from Ni atoms to Pd atoms takes place, which is more prominent in the case of Pd₃Ni-IM compared to Pd₃Ni-Al. Orderliness and entropy of the ordered and disordered compounds have been estimated from DSC experiments. High temperature required for phase transformation of Pd₃Ni-IM and high specific heat, C_p value for Pd₃Ni-Al show that Pd₃Ni-IM is more ordered, and the entropy of Pd₃Ni-Al is higher. The surface chemistry and overall conductivity of the intermediate state of the catalyst made the highly ordered structure of Pd₃Ni-IM highly active and selective in HER, OER, ORR, and EOR. Interestingly, the electrochemical activity for Pd₃Ni-IM seem to increase with time and outperforms the activity of Pd₃Ni-Al. To understand the active site generation and reaction kinetics for all reactions of fuel cell and water splitting, in-situ XAS, Raman, in-situ FTIR, and post-electrochemical XPS and XRD are being performed. It is observed from XPS that after alkali-mediated HER and OER, there is a presence of significant amounts of metallic Ni on the surface along with the oxides and oxyhydroxides, for the Pd₃Ni-IM system. This metallic Ni helps in high conductivity and maintains a long-term stability for both HER and OER. Formation of stable NiOOH has been verified from in-situ Raman spectra. Post-electrochemical PXRD pattern finally shows that only KOH mediated OER at potential above 1.2 v vs. RHE triggers the phase transition from ordered to disordered Pd₃Ni lattice. In-situ FTIR during EOR shows IM phase performs 12e⁻ transfer process forming CO₂ whereas alloy forms majorly 4e⁻ oxidized product, acetic acid. Thus, this work showcases the growth mechanism of first ever reported Pd₃Ni intermetallic and how the structure can be tuned to control the structural stability and catalytical performance in a most demanded fuel cell and water splitting reactions. **Table 8.6** shows all the reported Pd-Ni based alloy disordered compounds. **Table 8.7** shows all the reported multifunctional electrocatalysts where it is seen very few works report tetra-functionality, and

Table 8.8 lists all the recent works on intermetallic electrocatalysts, and finally **Table 8.9** shows the comparison of activity of Pd₃Ni-IM with all the state-of-the-art catalysts in each electrochemical test. **Figure 8.31** shows the overall comparison of this novel material with all other Pd-Ni based alloys, A₃B based IMCs, and Pd-M based intermetallic and how this novel Pd₃Ni-IM has been developed for the first time as a tetra-functional electrocatalyst. Ultimately, this catalyst was tested in full cell PEM water electrolyser and high-temperature industrial relevant conditioned AEM electrolysis of water.

Table 8.6. List of A₃B and Pd-Ni based disordered and ordered compounds and their electrochemical functionality.

Sr.no.	Catalysts	IM or Alloy	Functionality	References
1.	Pd ₃ Ni-IM	IM	Tetra-functionality ORR (10,000 cycles) OER (20,000 cycles) EOR (750 cycles) HER (80,000 cycles)	This work
2.	Disordered Pd ₃ Ni, Pd ₄ Ni, Pd ₆ Ni, and Pd ₈ Ni icosahedra	Alloy	ORR (10,000 ADT cycles)	<i>Sci. Adv.</i> 2018 , 4, eaap8817.
3.	rGO supported Pt ₃ Mn	IM	ORR Pt ₃ Mn (5000 cycles)	<i>Angew. Chem. Int. Ed.</i> 2020 , 59, 7857 – 7863
4.	Pt ₃ Fe, Pt ₃ Co, Pt ₃ Zn		ORR Fuel cell studies 10-30k AST cycles	<i>Science</i> , 2021 , 374, 459–464
5.	Pd ₃ Fe	IM	Li-Air battery	<i>J. Am. Chem. Soc.</i> 2015 , 137, 7278–7281
6.	Pd _{0.90} Ni _{0.10} NWs	Alloy	ORR (5000 ADT cycles)	<i>ACS Catal.</i> 2014 , 4, 2544–2555.
7.	Pd ₈₆ Ni ₁₄ /C, Pd ₅₉ Ni ₄₁ /C,	Alloy	EOR (1000 secs)	<i>ACS Appl. Mater. Interfaces</i> 2012 , 4, 4208–4214.
8.	Pt ₃ Co@ML-Pt(NPC ₁₀)	IM	ORR (1,00,000 cycles)	<i>Adv. Mater.</i> , 2023 , 2301310
9.	Pd _{4-x} Ni _x /C (x = 1–3)	Alloy	ORR (7200 secs) FAOR (7200 secs)	<i>ACS Appl. Energy Mater.</i> 2020 , 3, 9285–9295.

10.	PdNi-ECs/GS ₂	Alloy	HER (24 hours durability)	<i>Energy Fuels</i> 2022 , 36, 5910–5919.
11.	NiPd@NF	Alloy	OER (24 hours)	<i>J. of Environ. Chem. Eng.</i> 2022 , 10, 107959
12.	Pt ₃ Sn	IM	ORR (10,000 cycles)	<i>J. Am. Chem. Soc.</i> 2020 , 142, 6, 3231–3239
13.	PdNi ₃ , Pd ₃ Ni, PdNi	Alloy	ORR	<i>Electrochem. Commun.</i> 2022 , 11, 1162–1165
14.	Pd ₈₃ Ni ₁₇ HNS	Alloy	EOR	<i>Angew. Chem. Int. Ed.</i> 2015 , 54, 13101–13105
15.	Pt ₂₅ Cu ₇₅ , Pt ₅₀ Cu ₅₀ , Pt ₇₅ Cu ₂₅	Alloy	ORR	<i>Nature Chem.</i> 2010 , 2, 454–460
16.	Pt ₃ M (M=Ni, Co, Fe, Ti, V)	Alloy	ORR	<i>Nature Mater.</i> 2007 , 6, 241–247

Table 8.7. List of all recently reported multifunctional electrocatalysts with their activity parameters.

Sl. No.	Catalyst	Functionality (F)	F1	F2	F3	F4	Ref.
1.	Pd ₃ Ni-IM	Tetrafunctional	OER (η_{10} = 0.22 V)	Alkaline HER (η_{100} = 0.31 V)	ORR ($E_{1/2}$ = 0.86 V vs. RHE)	EOR (I_p/I_b ratio is 0.91)	This work
2.	NiFe LDH single bond CNT-Co ₃ O ₄ /NC	Tetrafunctional	OER (onset pot. 1.38 V vs. RHE)	Alkaline HER (η_{10} = 0.3 V)	ORR (onset pot. 0.84 V vs. RHE)	eCO ₂ RR (-0.5 mA/cm ² at -0.48 V vs. RHE)	<i>J. Taiwan Inst. Chem. Eng.</i> 2022 , 136, 104397
3.	Co-Ni alloy	Tetrafunctional	OER (η_{10} = 0.25 V)	Alkaline HER (η_{10} = 0.049 V)	ORR ($E_{1/2}$ = 0.86 V vs. RHE)	eCO ₂ RR (-47 mA/cm ² at -1 V vs. RHE)	<i>ACS Appl. Mater. Interfaces</i> , 2020 , 12, 23017–23027
4.	NiCu Bimetallic	Trifunctional	OER (η_{10} = 0.4 V)	Acidic HER (η_{10} = 0.184 V)	ORR ($E_{1/2}$ = 0.80 V vs. RHE)	-	<i>J. Am. Chem. Soc.</i> 2020 , 142, 14688–14701

Decoding Active Sites and Mechanistic Insights for Efficient Electrochemical Water Splitting and Fuel Cell using Transition Metal-based Catalysts

5.	Fe-Co-Ni MOF	Trifunctional	OER (η_{10} = 0.254 V)	Alkaline HER (η_{10} = 0.116 V)	ORR ($E_{1/2}$ = 0.73 V vs. RHE)	-	<i>J. Am. Chem. Soc.</i> 2022 , <i>144</i> , 3411-3428
6.	Co ₂ P/CoNPC	Trifunctional	OER (η_{10} = 0.326 V)	Alkaline HER (η_{10} = 0.130 V)	ORR ($E_{1/2}$ = 0.843 V vs. RHE)	-	<i>Adv. Mater.</i> , 2020 , <i>32</i> , 2003649
7.	NCN-1000-5	Trifunctional	OER (η_{10} = 0.32 V)	Acidic HER (η_{10} = 0.09 V)	ORR ($E_{1/2}$ = 0.82 V vs. RHE)	-	<i>Energy Environ. Sci.</i> , 2019 , <i>12</i> , 322-333

Table 8.8. List of all latest intermetallic compounds in water splitting and fuel cell.

Sl. No.	Catalyst	Activity		Reference
1.	Pd ₃ Ni-IM	OER (η_{10} = 0.22 V) Alkaline HER (η_{100} = 0.31 V) ORR ($E_{1/2}$ = 0.86 V vs. RHE) EOR (I_f/I_b ratio is 0.91)	Tetrafunctional	This work
1.	PtIrFeCoCu HEI	ORR ($E_{1/2}$ = 0.894 V)	Monofunctional	<i>J. Am. Chem. Soc.</i> 2023 , <i>145</i> , 20, 11140–11150
2.	Au-O-PdZn/C	ORR ($E_{1/2}$ ~ 0.92 V)	Monofunctional	<i>ACS Nano</i> 2019 , <i>13</i> , 5, 5968–5974
3.	Mo ₆ Co ₇	HER in 1M KOH (η_{10} = 0.417 V) OER in 1M KOH (η_{10} = 0.427 V)	Bifunctional	<i>Chem. Mater.</i> 2024 , <i>36</i> , 5, 2566–2576
4.	L ₁₀ -Cr-PtFe/C	ORR ($E_{1/2}$ = 0.952 V)	Monofunctional	<i>J. Am. Chem. Soc.</i> 2024 , <i>146</i> , 3, 2033–2042
5.	Pd ₃₁ Bi ₁₂	ORR ($E_{1/2}$ = 0.93 V)	Monofunctional	<i>J. Am. Chem. Soc.</i> 2019 , <i>141</i> , 6, 2342–2347
6.	PdCu-B ₂	Acidic HER (η_{10} = 0.019 V)	Monofunctional	<i>ACS Energy Lett.</i> 2020 , <i>5</i> , 12, 3672–3680
7.	Pd ₃ Pb UPINs/C	ORR ($E_{1/2}$ = 0.908 V)	Monofunctional	<i>Angew. Chem. Int. Ed.</i> 2021 , <i>60</i> , 10942
8.	meso-i-Ga ₁ Pt ₁	ORR ($E_{1/2}$ ~ 0.9 V)	Monofunctional	<i>Angew. Chem. Int. Ed.</i> 2023 , <i>62</i> , e202304420

Table 8.9. List of all state-of-the-art catalysts with Pd₃Ni-IM.

	OER IrO₂	HER (alkaline) 20% Pt/C	ORR 20% Pt/C	EOR 20% Pd/C
Standard	$\eta_{10} = 0.38$ V	$\eta_{100} = 0.41$ V	$E_{1/2} = 0.82$ V vs. RHE after 10000 cycles	I_f/I_b ratio is 0.61 after 200 cycles
Pd₃Ni	$\eta_{10} = 0.22$ V	$\eta_{100} = 0.31$ V	$E_{1/2} = 0.86$ V vs. RHE after 10000 cycles	I_f/I_b ratio is 0.91 after 750 cycles

8.6 References

1. Gumeniuk, R., Chapter 304 - Structural and Physical Properties of Remeika Phases. In *Handbook on the Physics and Chemistry of Rare Earths*, Bünzli, J.-C. G.; Pecharsky, V. K., Eds. Elsevier: 2018; Vol. 54, pp 43-143.
2. Nash, A.; Nash, P., The Ni-Pd (Nickel-Palladium) system. *Bull. alloy phase diagr.* **1984**, 5, 446-450.
3. Bidwell, L. R.; Speiser, R., The relative thermodynamic properties of solid nickel-palladium alloys. *Acta Metall.* **1965**, 13, 61-70.
4. Ghosh, G.; Kantner, C.; Olson, G. B., Thermodynamic modeling of the Pd-X (X=Ag, Co, Fe, Ni) systems. *J. Ph. Equilibria* **1999**, 20, 295-308.
5. Luo, M.; Zhao, Z.; Zhang, Y.; Sun, Y.; Xing, Y.; Lv, F.; Yang, Y.; Zhang, X.; Hwang, S.; Qin, Y.; Ma, J.-Y.; Lin, F.; Su, D.; Lu, G.; Guo, S., PdMo bimetallic for oxygen reduction catalysis. *Nature* **2019**, 574, 81-85.
6. Wang, T.; Chutia, A.; Brett, D. J. L.; Shearing, P. R.; He, G.; Chai, G.; Parkin, I. P., Palladium alloys used as electrocatalysts for the oxygen reduction reaction. *Energy Environ. Sci.* **2021**, 14, 2639-2669.
7. Lee, K.; Kang, S. W.; Lee, S.-U.; Park, K.-H.; Lee, Y. W.; Han, S. W., One-Pot Synthesis of Monodisperse 5 nm Pd-Ni Nanoalloys for Electrocatalytic Ethanol Oxidation. *ACS Appl. Mater. Interfaces* **2012**, 4, 4208-4214.
8. Gamler, J. T. L.; Ashberry, H. M.; Skrabalak, S. E.; Koczkur, K. M., Random Alloyed versus Intermetallic Nanoparticles: A Comparison of Electrocatalytic Performance. *Adv. Mater.* **2018**, 30, 1801563.
9. Antolini, E., Alloy vs. intermetallic compounds: Effect of the ordering on the electrocatalytic activity for oxygen reduction and the stability of low temperature fuel cell catalysts. *Appl. Catal. B: Environ.* **2017**, 217, 201-213.

10. Yan, Y.; Du, J. S.; Gilroy, K. D.; Yang, D.; Xia, Y.; Zhang, H., Intermetallic Nanocrystals: Syntheses and Catalytic Applications. *Adv. Mater.* **2017**, *29*, 1605997.
11. Luo, M.; Sun, Y.; Wang, L.; Guo, S., Tuning Multimetallic Ordered Intermetallic Nanocrystals for Efficient Energy Electrocatalysis. *Adv. Energy Mater.* **2017**, *7*, 1602073.
12. Ma, Y.; Chen, M.; Geng, H.; Dong, H.; Wu, P.; Li, X.; Guan, G.; Wang, T., Synergistically Tuning Electronic Structure of Porous β -Mo₂C Spheres by Co Doping and Mo-Vacancies Defect Engineering for Optimizing Hydrogen Evolution Reaction Activity. *Adv. Funct. Mater.* **2020**, *30*, 2000561.
13. Li, C.; Yuan, Q.; Ni, B.; He, T.; Zhang, S.; Long, Y.; Gu, L.; Wang, X., Dendritic defect-rich palladium–copper–cobalt nanoalloys as robust multifunctional non-platinum electrocatalysts for fuel cells. *Nat. Commun.* **2018**, *9*, 3702.
14. Roy, S.; Bagchi, D.; Dheer, L.; Sarma, S. C.; Rajaji, V.; Narayana, C.; Waghmare, U. V.; Peter, S. C., Mechanistic insights into the promotional effect of Ni substitution in non-noble metal carbides for highly enhanced water splitting. *Appl. Catal. B: Environ.* **2021**, *298*, 120560.
15. Bagchi, D.; Phukan, N.; Sarkar, S.; Das, R.; Ray, B.; Bellare, P.; Ravishankar, N.; Peter, S. C., Ultralow non-noble metal loaded MOF derived bi-functional electrocatalysts for the oxygen evolution and reduction reactions. *J. Mater. Chem. A* **2021**, *9*, 9319-9326.
16. Sarkar, S.; Varghese, M.; Vinod, C. P.; Peter, S. C., Conductive interface promoted bifunctional oxygen reduction/evolution activity in an ultra-low precious metal based hybrid catalyst. *Chem. Commun.* **2021**, *57*, 1951-1954.
17. Ahsan, M. A.; Puente Santiago, A. R.; Hong, Y.; Zhang, N.; Cano, M.; Rodriguez-Castellon, E.; Echegoyen, L.; Sreenivasan, S. T.; Noveron, J. C., Tuning of Trifunctional NiCu Bimetallic Nanoparticles Confined in a Porous Carbon Network with Surface Composition and Local Structural Distortions for the Electrocatalytic Oxygen Reduction, Oxygen and Hydrogen Evolution Reactions. *J. Am. Chem. Soc.* **2020**, *142*, 14688-14701.
18. Zhou, C.; Zhao, S.; Meng, H.; Han, Y.; Jiang, Q.; Wang, B.; Shi, X.; Zhang, W.; Zhang, L.; Zhang, R., RuCoO_x Nanofoam as a High-Performance Trifunctional Electrocatalyst for Rechargeable Zinc–Air Batteries and Water Splitting. *Nano Lett.* **2021**, *21*, 9633-9641.
19. Seh, Z. W.; Kibsgaard, J.; Dickens, C. F.; Chorkendorff, I.; Nørskov, J. K.; Jaramillo, T. F., Combining theory and experiment in electrocatalysis: Insights into materials design. *Science* **2017**, *355*, eaad4998.

20. Chakraborty, S.; Marappa, S.; Agarwal, S.; Bagchi, D.; Rao, A.; Vinod, C. P.; Peter, S. C.; Singh, A.; Eswaramoorthy, M., Improvement in Oxygen Evolution Performance of NiFe Layered Double Hydroxide Grown in the Presence of 1T-Rich MoS₂. *ACS Appl. Mater. Interfaces* **2022**, *14*, 31951-31961.
21. Mondal, S.; Bagchi, D.; Riyaz, M.; Sarkar, S.; Singh, A. K.; Vinod, C. P.; Peter, S. C., In Situ Mechanistic Insights for the Oxygen Reduction Reaction in Chemically Modulated Ordered Intermetallic Catalyst Promoting Complete Electron Transfer. *J. Am. Chem. Soc.* **2022**, *144*, 11859-11869.
22. Mondal, S.; Sarkar, S.; Bagchi, D.; Das, T.; Das, R.; Singh, A. K.; Prasanna, P. K.; Vinod, C. P.; Chakraborty, S.; Peter, S. C., Morphology-Tuned Pt₃Ge Accelerates Water Dissociation to Industrial-Standard Hydrogen Production over a wide pH Range. *Adv. Mater.* **2022**, *34*, 2202294.
23. Ashly, P. C.; Sarkar, S.; Sarma, S. C.; Kaur, K.; Gautam, U. K.; Peter, S. C., Compressive strain induced by multiple phase distribution and atomic ordering in PdCu nanoparticles to enhanced ethanol oxidation reaction performance. *J. Power Sources* **2021**, *506*, 230168.
24. Sarkar, S.; Ramarao, S. D.; Das, T.; Das, R.; Vinod, C. P.; Chakraborty, S.; Peter, S. C., Unveiling the Roles of Lattice Strain and Descriptor Species on Pt-Like Oxygen Reduction Activity in Pd–Bi Catalysts. *ACS Catal.* **2021**, *11*, 800-808.
25. Jiang, R.; Tran, D. T.; McClure, J. P.; Chu, D., A Class of (Pd–Ni–P) Electrocatalysts for the Ethanol Oxidation Reaction in Alkaline Media. *ACS Catal.* **2014**, *4*, 2577-2586.
26. Rizo, R.; Arán-Ais, R. M.; Padgett, E.; Muller, D. A.; Lázaro, M. J.; Solla-Gullón, J.; Feliu, J. M.; Pastor, E.; Abruña, H. D., Pt-Rich_{core}/Sn-Rich_{subsurface}/Pt_{skin} Nanocubes As Highly Active and Stable Electrocatalysts for the Ethanol Oxidation Reaction. *J. Am. Chem. Soc.* **2018**, *140*, 3791-3797.
27. Zhou, X.; Ma, Y.; Ge, Y.; Zhu, S.; Cui, Y.; Chen, B.; Liao, L.; Yun, Q.; He, Z.; Long, H.; Li, L.; Huang, B.; Luo, Q.; Zhai, L.; Wang, X.; Bai, L.; Wang, G.; Guan, Z.; Chen, Y.; Lee, C.-S.; Wang, J.; Ling, C.; Shao, M.; Fan, Z.; Zhang, H., Preparation of Au@Pd Core–Shell Nanorods with fcc-2H-fcc Heterophase for Highly Efficient Electrocatalytic Alcohol Oxidation. *J. Am. Chem. Soc.* **2022**, *144*, 547-555.
28. Nakaya, Y.; Furukawa, S., Catalysis of Alloys: Classification, Principles, and Design for a Variety of Materials and Reactions. *Chem. Rev.* **2023**, *123*, 5859-5947.
29. Chen, Y.; Luo, X.; She, H.; Yue, G. H.; Peng, D. L., Size- and structure-controlled synthesis and characterization of nickel nanoparticles. *J. Nanosci. Nanotechnol.* **2009**, *9*, 5157-63.

30. Bagchi, D.; Raj, J.; Singh, A. K.; Cherevotan, A.; Roy, S.; Manoj, K. S.; Vinod, C. P.; Peter, S. C., Structure-Tailored Surface Oxide on Cu–Ga Intermetallics Enhances CO₂ Reduction Selectivity to Methanol at Ultralow Potential. *Adv. Mater.* **2022**, *34*, 2109426.
31. Kresse, G.; Furthmüller, J., Efficient iterative schemes for ab initio total-energy calculations using a plane-wave basis set. *Phys. Rev. B* **1996**, *54*, 11169-11186.
32. Kresse, G.; Furthmüller, J., Efficiency of ab-initio total energy calculations for metals and semiconductors using a plane-wave basis set. *Comput. Mater. Sci.* **1996**, *6*, 15-50.
33. Blöchl, P. E., Projector augmented-wave method. *Phys. Rev. B* **1994**, *50*, 17953-17979.
34. Perdew, J. P.; Burke, K.; Ernzerhof, M., Generalized Gradient Approximation Made Simple. *Phys. Rev. Lett.* **1996**, *77*, 3865-3868.
35. Monkhorst, H. J.; Pack, J. D., Special points for Brillouin-zone integrations. *Phys. Rev. B* **1976**, *13*, 5188-5192.
36. van de Walle, A.; Tiwary, P.; de Jong, M.; Olmsted, D. L.; Asta, M.; Dick, A.; Shin, D.; Wang, Y.; Chen, L. Q.; Liu, Z. K., Efficient stochastic generation of special quasirandom structures. *Calphad* **2013**, *42*, 13-18.
37. Zunger, A.; Wei, S. H.; Ferreira, L. G.; Bernard, J. E., Special quasirandom structures. *Phys. Rev. Lett.* **1990**, *65*, 353-356.
38. Manzoor, A.; Pandey, S.; Chakraborty, D.; Phillpot, S. R.; Aidhy, D. S., Entropy contributions to phase stability in binary random solid solutions. *npj Computational Materials* **2018**, *4*, 47.
39. Togo, A.; Tanaka, I., First principles phonon calculations in materials science. *Scripta Materialia* **2015**, *108*, 1-5.
40. Okamoto, H.; Massalski, T. B.; Nishizawa, T.; Hasebe, M., The Au-Co (Gold-Cobalt) system. *Bull. alloy phase diagr.* **1985**, *6*, 449-454.
41. Bai, Y.; Wu, Y.; Zhou, X.; Ye, Y.; Nie, K.; Wang, J.; Xie, M.; Zhang, Z.; Liu, Z.; Cheng, T.; Gao, C., Promoting nickel oxidation state transitions in single-layer NiFeB hydroxide nanosheets for efficient oxygen evolution. *Nat. Commun.* **2022**, *13*, 6094.
42. Yang, C.; Fontaine, O.; Tarascon, J.-M.; Grimaud, A., Chemical Recognition of Active Oxygen Species on the Surface of Oxygen Evolution Reaction Electrocatalysts. *Angew. Chem.* **2017**, *129*.
43. Ahmed, M. S.; Jeon, S., Highly Active Graphene-Supported Ni_xPd_{100-x} Binary Alloyed Catalysts for Electro-Oxidation of Ethanol in an Alkaline Media. *ACS Catal.* **2014**, *4*, 1830-1837.

44. Xu, C. W.; Wang, H.; Shen, P. K.; Jiang, S. P., Highly Ordered Pd Nanowire Arrays as Effective Electrocatalysts for Ethanol Oxidation in Direct Alcohol Fuel Cells. *Adv. Mater.* **2007**, *19*, 4256-4259.
45. Feng, G.; Ning, F.; Pan, Y.; Chen, T.; song, J.; Wang, Y.; Zou, R.; Su, D.; Xia, D., Engineering Structurally Ordered High-Entropy Intermetallic Nanoparticles with High-Activity Facets for Oxygen Reduction in Practical Fuel Cells. *J. Am. Chem. Soc.* **2023**, *145*, 11140-11150.
46. Jia, Q.; Zhao, Z.; Cao, L.; Li, J.; Ghoshal, S.; Davies, V.; Stavitski, E.; Attenkofer, K.; Liu, Z.; Li, M.; Duan, X.; Mukerjee, S.; Mueller, T.; Huang, Y., Roles of Mo Surface Dopants in Enhancing the ORR Performance of Octahedral PtNi Nanoparticles. *Nano Lett.* **2018**, *18*, 798-804.
47. Mao, J.; Chen, W.; He, D.; Wan, J.; Pei, J.; Dong, J.; Wang, Y.; An, P.; Jin, Z.; Xing, W.; Tang, H.; Zhuang, Z.; Liang, X.; Huang, Y.; Zhou, G.; Wang, L.; Wang, D.; Li, Y., Design of ultrathin Pt-Mo-Ni nanowire catalysts for ethanol electrooxidation. *Sci. Adv.* **3**, e1603068.
48. Jeong, U.; Teng, X.; Wang, Y.; Yang, H.; Xia, Y., Superparamagnetic Colloids: Controlled Synthesis and Niche Applications. *Adv. Mater.* **2007**, *19*, 33-60.
49. Samanta, B.; Jain, A., Experimental investigation of lattice thermal expansion and specific heat capacity of C₁₅-Cr₂Zr Laves phase intermetallic compound by HTXRD and DSC. *Intermetallics* **2022**, *148*, 107634.
50. Chou, T. H.; Huang, J. C.; Yang, C. H.; Lin, S. K.; Nieh, T. G., Consideration of kinetics on intermetallics formation in solid-solution high entropy alloys. *Acta Mater.* **2020**, *195*, 71-80.
51. Zhang, H.; Pan, J.; Zhou, Q.; Xia, F., Nanometal Thermocatalysts: Transformations, Deactivation, and Mitigation. *Small* **2021**, *17*, 2005771.
52. Somorjai, G. A., Modern Surface Science and Surface Technologies: An Introduction. *Chem. Rev.* **1996**, *96*, 1223-1236.
53. Mondal, S.; Riyaz, M.; Bagchi, D.; Dutta, N.; Singh, A. K.; Vinod, C. P.; Peter, S. C., Distortion-Induced Interfacial Charge Transfer at Single Cobalt Atom Secured on Ordered Intermetallic Surface Enhances Pure Oxygen Production. *ACS Nano* **2023**, *17*, 23169-23180.
54. Shao, D.; Wang, Q.; Yao, X.; Zhou, Y.; Yu, X.-Y., Phase-engineering of nickel hydroxide in the Ni/Ni(OH)₂ interface for efficient hydrogen evolution and hydrazine-assisted water splitting in seawater. *J. Mater. Chem. A* **2022**, *10*, 21848-21855.

55. Yao, Y.; Hu, S.; Chen, W.; Huang, Z.-Q.; Wei, W.; Yao, T.; Liu, R.; Zang, K.; Wang, X.; Wu, G.; Yuan, W.; Yuan, T.; Zhu, B.; Liu, W.; Li, Z.; He, D.; Xue, Z.; Wang, Y.; Zheng, X.; Dong, J.; Chang, C.-R.; Chen, Y.; Hong, X.; Luo, J.; Wei, S.; Li, W.-X.; Strasser, P.; Wu, Y.; Li, Y., Engineering the electronic structure of single atom Ru sites via compressive strain boosts acidic water oxidation electrocatalysis. *Nat. Catal.* **2019**, *2*, 304-313.
56. Trześniewski, B. J.; Diaz-Morales, O.; Vermaas, D. A.; Longo, A.; Bras, W.; Koper, M. T. M.; Smith, W. A., In Situ Observation of Active Oxygen Species in Fe-Containing Ni-Based Oxygen Evolution Catalysts: The Effect of pH on Electrochemical Activity. *J. Am. Chem. Soc.* **2015**, *137*, 15112-15121.
57. Kang, J.; Qiu, X.; Hu, Q.; Zhong, J.; Gao, X.; Huang, R.; Wan, C.; Liu, L.-M.; Duan, X.; Guo, L., Valence oscillation and dynamic active sites in monolayer NiCo hydroxides for water oxidation. *Nat. Catal.* **2021**, *4*, 1050-1058.
58. Lee, W. H.; Han, M. H.; Ko, Y.-J.; Min, B. K.; Chae, K. H.; Oh, H.-S., Electrode reconstruction strategy for oxygen evolution reaction: maintaining Fe-CoOOH phase with intermediate-spin state during electrolysis. *Nat. Commun.* **2022**, *13*, 605.
59. Zhong, M.; Xu, M.; Ren, S.; Li, W.; Wang, C.; Gao, M.; Lu, X., Modulating the electronic structure of Ni(OH)₂ by coupling with low-content Pt for boosting the urea oxidation reaction enables significantly promoted energy-saving hydrogen production. *Energy Environ. Sci.* **2024**.
60. Deng, L.; Hung, S.-F.; Zhao, S.; Zeng, W.-J.; Lin, Z.-Y.; Hu, F.; Xie, Y.; Yin, L.; Li, L.; Peng, S., Unveiling coordination transformation for dynamically enhanced hydrogen evolution catalysis. *Energy Environ. Sci.* **2023**, *16*, 5220-5230.
61. Oshchepkov, A. G.; Braesch, G.; Bonnefont, A.; Savinova, E. R.; Chatenet, M., Recent Advances in the Understanding of Nickel-Based Catalysts for the Oxidation of Hydrogen-Containing Fuels in Alkaline Media. *ACS Catal.* **2020**, *10*, 7043-7068.
62. Vij, V.; Sultan, S.; Harzandi, A. M.; Meena, A.; Tiwari, J. N.; Lee, W.-G.; Yoon, T.; Kim, K. S., Nickel-Based Electrocatalysts for Energy-Related Applications: Oxygen Reduction, Oxygen Evolution, and Hydrogen Evolution Reactions. *ACS Catal.* **2017**, *7*, 7196-7225.
63. Rajamani, A. R.; Ashly, P. C.; Dheer, L.; Sarma, S. C.; Sarkar, S.; Bagchi, D.; Waghmare, U. V.; Peter, S. C., Synergetic Effect of Ni-Substituted Pd₂Ge Ordered Intermetallic Nanocomposites for Efficient Electrooxidation of Ethanol in Alkaline Media. *ACS Appl. Energy Mater.* **2019**, *2*, 7132-7141.

64. Singh, A. K.; Bagchi, D.; Sarkar, S.; Sarma, S. C.; Mumbaraddi, D.; Ramarao, S. D.; Peter, S. C., Optimized Metal Deficiency-Induced Operando Phase Transformation Enhances Charge Polarization Promoting Hydrogen Evolution Reaction. *Chem. Mater.* **2022**.

SUMMARY & FUTURE OUTLOOK

The inspiration of this thesis is to develop cost-effective, stable, and scalable transition metal-based electrocatalysts for the sustainable solution of fossil fuel usage, fuel cell technology with green hydrogen generation. This strategy can be expanded in the broader field of the electrochemistry community to design sustainable catalyst materials for other electrochemical processes as well. A plethora of catalysts were synthesized by various synthesis techniques like high-temperature annealing, hydrogen engineering, solvothermal synthesis, colloidal synthesis, multi-step chemical reduction process, etc. In this work, different solid-state catalyst materials like monometallic, bimetallic, alloy, intermetallic, metal-oxide surface, support based, and morphology tuned catalysts have been properly synthesized. This thesis has also shown tuned synthetic conditions from high-temperature long-duration solution phase synthesis to room temperature, ambient condition, and instantaneous synthesis via electrodeposition. Besides material design and catalytic applications, this thesis is also dedicated in understanding the reactive sites, dynamics of the phase and mechanistic pathway via in-situ spectroscopic and analytical techniques like ATR-FTIR, Raman, XAS, and DEMS, for understanding the reaction kinetics which can help in better enhancement in the field of electrocatalysis. With the help of all these studies, we have not only obtained the idea about the real-time electronic and structural evolution of the catalyst, but we could also be able to identify underlying structure-property relationships which can help to design more efficient catalysts in the future.

The thesis is divided into eight chapters, with Chapter 1 discussing the global environmental issues associated with CO₂ emissions and its probable solutions to overcome these issues. The main source of CO₂ emission comes from fossil fuel combustion which can be sustainably substituted by green technology like fuel cells. The cathodic reaction, oxygen reduction reaction has a very sluggish kinetics with a challenge for 4e⁻ transfer process. Chapters 2 mainly focuses on the discovery of novel nanomaterials as the efficient electrocatalysts for the facile conversion of oxygen gas to water via 4e⁻ reduction process which is the cathodic reaction of a fuel cell. The overall ORR activity is higher than state-of-the-art catalysts 20% Pt/C and undesired 2e⁻ transfer ORR forming hydrogen peroxide (H₂O₂) is diminished in Pt_{0.2}Pd_{1.8}Ge as visible from rotating-ring disk electrode (RRDE) experiment, spectroscopically visualized by *in-situ* Fourier transform infrared (FT-IR) spectroscopy and supported by computational studies. The effect of Pt substitution on Pd has been properly manifested by X-ray absorption spectroscopy (XAS) and X-ray photoelectron spectroscopy

(XPS). The swinging of oxidation state of atomic sites of $\text{Pt}_{0.2}\text{Pd}_{1.8}\text{Ge}$ during reaction is probed by *in-situ* XAS which efficiently enhances $4e^-$ transfer producing extremely low percentage of H_2O_2 . The anodic counterpart of fuel cell deals with green fuel hydrogen oxidation. The gas H_2 is majorly obtained from steam reforming of methane which is not sustainable process and releases CO_2 into the atmosphere. Hence, electrochemical water splitting forms the green hydrogen. The major drawback of facile water electrolysis is sluggish anodic reaction of water splitting, that is, oxygen evolution reaction (OER). Chapters 3-5 discloses efficient OER catalysts with high activity and durability. As chapter 1 deals with Pt substituted Pd_2Ge intermetallic compound, chapter 3 continues with Co substituted Pd_2Ge which forms a ultra-thin layer of CoO on Co substituted Pd_2Ge lattice providing highly efficient OER activity, which is much better than pristine CoO. With the help of powder XRD, XAFS, XPS, and Raman spectroscopic technique, it has been concluded that the core lattice of Pd_2Ge imparts lattice strain and increases the spin density of the surface CoO which ends up in giving industrial level OER activity and stability at a very high current density. The role of the CoO layer in OER has been verified by its selective removal using argon sputtering and conducting OER on the etched catalyst. In-situ X-ray absorption near edge structure (XANES) and extended X-ray absorption fine structure spectroscopy (EXAFS) demonstrate that CoO gets transformed to CoOOH (Co^{3+}) in operando condition with faster charge transfer through Pd atoms in the core Pd_2Ge lattice. In-situ Raman spectroscopy depicts the emergence of a CoOOH phase on applying potential and that the phase is stable with increasing potential and time without getting converted to CoO_2 . Density functional theory (DFT) calculations indicate that the Pd_2Ge lattice induces distortion in the CoO phase and generates unpaired spins in non-magnetic CoOOH system resulting in an increase in OER activity and durability. Differential electrochemical mass spectrometry (DEMS) has been explored to visualize the instantaneous generation of oxygen gas during the onset of the reaction.

In the fourth chapter, the harsh synthetic conditions for solution phase nanoparticles synthesis via solvothermal and colloidal synthesis is being replaced with electrodeposition at room temperature, within 5-10 minutes under ambient conditions. I electrodeposited transition metals Ni, Co, Cu and Fe, amongst which Co gave a highly symmetrical hexagonal flower-like morphology for the first time. The formation mechanism for these hexagonal flowers have been explored via different controlled experiments and this material was tested for electrochemical oxygen evolution reaction (OER) with a very low overpotential of only 170 mV for 100 mA/cm^2 . These Co-flowers were deposited on different substrates like Ni foil, Cu foil, Ni foam,

stainless steel, and carbon paper which reveals the promising flexibility of these highly efficient Co nanoflowers to be commercialized due to being deposited on in-expensive versatile substrates.

The toxicity and expensive property of Co is becoming a concern, and hence decreasing its loading and substitution with non-toxic element like Fe forming CoFe ordered intermetallic structure has been studied in the fifth chapter of the thesis. Multi-walled carbon nanotubes (MWCNTs) with N-doping have been used as a conducting support where Co and Fe is initially forming their nitrides CoN/FeN and finally forming ordered intermetallic CoFe via nitride formation. It has been explored without N-doped MWCNTs, CoFe is not being formed. Nanometric uniform distribution of CoFe intermetallic NPs displayed a very high OER activity. The activity is further increased with just 1% Pt loading on CoFe which generated compressional strain on CoFe IM lattice which enhanced feasible conversion from Co/Fe to CoOOH/FeOOH which is reflected in decreased overpotential for the reaction.

After discussing some efficient OER catalysts, chapter 6 and 7 discloses some highly efficient hydrogen generation (HER) catalysts. The discovery of novel materials for industrial standard hydrogen production is the present need considering the global energy infrastructure. In chapter 6, we introduce a novel electrocatalyst, Pt₃Ge, engineered with a desired crystallographic facet (202) accelerates hydrogen production by water electrolysis and records industrially desired operational stability compared to the commercial catalyst platinum. Pt₃Ge-(202) exhibits low overpotential of 21.7 mV (24.6 mV for Pt/C) and 92 mV for 10 mA/cm² and 200 mA/cm² current density, respectively in 0.5M H₂SO₄. It also exhibits remarkable stability of 15,000 accelerated degradation tests cycles (5000 for Pt/C) and exceptional durability of 500 h (@10 mA/cm²) in acidic media. Pt₃Ge-(202) also displayed low overpotential of 96 mV for 10 mA/cm² current density in the alkaline medium, rationalizing its hydrogen production ability over a wide pH range required commercial operations. Long-term durability (>75 h in alkaline media) with the industrial level current density (>500 mA/cm²) has been demonstrated by utilizing the electrochemical flow reactor. The driving force behind this stupendous performance of Pt₃Ge-(202) has been envisaged by mapping the reaction mechanism, active sites and charge transfer kinetics via controlled electrochemical experiments, ex-situ X-ray photoelectron spectroscopy, in-situ infrared spectroscopy and in-situ X-ray absorption spectroscopy further corroborated by first principles calculations.

One of the important criteria for an electrocatalyst is its economic viability. Volcano plot for HER suggests that Pt is the best catalyst with commercially used catalyst being 20% Pt on

carbon support. Keeping this in mind, chapter 7 has further reduced Pt loading to 10% with non-expensive support of CeO₂. The speciality of CeO₂ is its versatile morphology, switchable Ce (IV)-Ce (III) valency, and inexpensive. I have designed cube and rod CeO₂ morphologies and have incorporated Pt metal in-situ (during CeO₂ formation) and ex-situ (after CeO₂ formation) with different loading percentage which gave the best HER activity for in-situ incorporation of only 10% Pt in CeO₂ cube morphology. This is observed that Pt incorporation with enhanced Pt-CeO₂ is obtained for in-situ in cube and higher interface has provided higher HER. This can be correlated to the H-spillover mechanism during electrochemical HER from Pt to CeO₂ which is highest for cube morphology.

Finally, chapter 8 discloses the Master of all trades! Designing a multifunctional electrocatalyst is of surging demand. This work deals with successful solution phase synthesis of an ordered compound of Pd and Ni, Pd₃Ni, which is assumed to be difficult as almost no adjacent elements in a same group form intermetallic compound. Pd₃Ni is a highly efficient and electrochemically stable material for tetra-functional activity, as in, hydrogen evolution reaction (HER), oxygen evolution reaction (OER), oxygen reduction reaction (ORR), and ethanol oxidation reaction (EOR) which constitutes both fuel cell and water electrolyser. Extensive ex-situ and in-situ characterization has disclosed the robustness of this material and reaction mechanism in different. This material has shown promising activity in proton exchange membrane water electrolyser and high temperature fuel cell. The tuned surface of the intermetallic has enhanced C-C cleavage in ethanol molecules allowing the sluggish 12e⁻ transfer process and have shown very high stability of >80k cycles of alkaline HER. Role of pH and potential has been explored in retaining the ordered phase of the intermetallic. Tetra functionality and its extensive exploration under different reaction conditions have been exhaustively done in this work.

In conclusion, this thesis has succeeded in the development of a variety of transition metal-based electrocatalysts, which are highly efficient electrocatalysts for water splitting and fuel cell. Throughout the thesis, a plethora of fundamental concepts of tuning the catalytic property has been used, like controlling metal-surface oxide, alloying, structural ordering, the role of a single atomic site, the effect of exposed facet, etc. The progress of electrochemical research on water splitting and fuel cell is strongly dependent on the design of efficient catalysts to achieve higher activity, stability, and selectivity towards the desired product. In view of this, the content of this thesis can be used as a handbook for those who are working in this area. Not only the design of the catalyst, the systematic developments of different types of reactors and scaling-up technologies. The standardization and optimization of the various component

involved in the in-situ studies like ATR-FTIR, Raman, XAFS, and DEMS could be beneficial for understanding the real-time picture of the reaction mechanism and the active sites involved in electrochemical HER, OER, ORR, and EOR. Overall, the strategies used in this thesis may be explored for developing highly active and stable sustainable catalysts for the commercial green H₂ generation and integration of hydrogen generation with fuel cell technology which can really find a solution to the global issues related to energy and environment. The overall work in this thesis is schematically represented in the figure below, **Figure 9**.

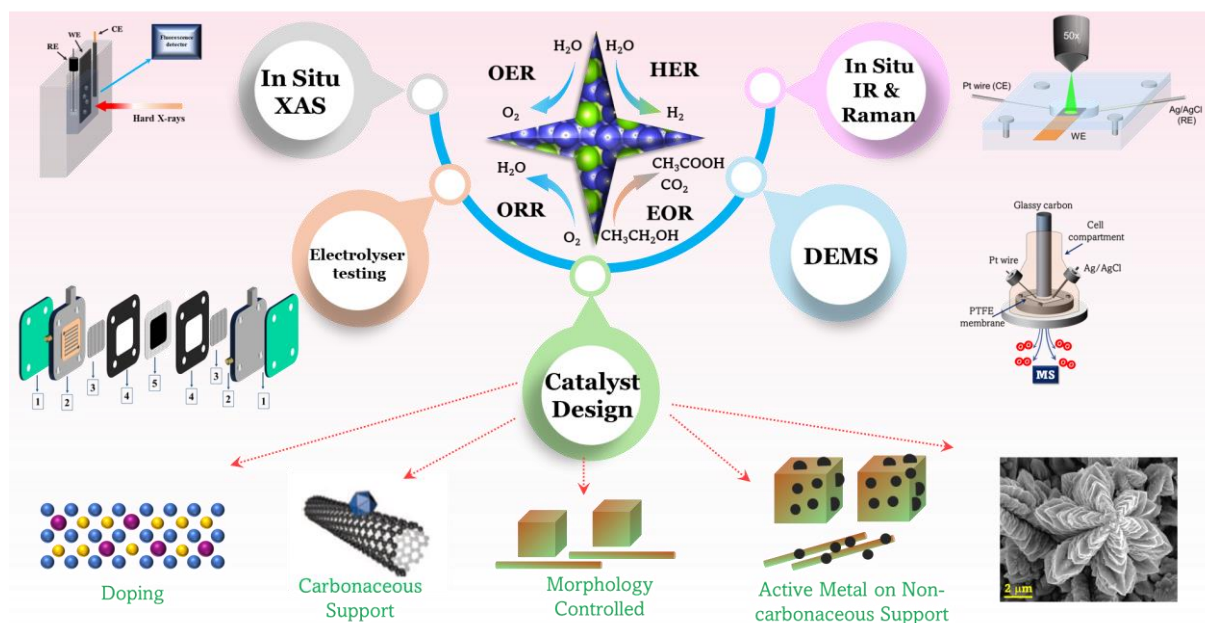


Figure 9. Schematic illustration describing the contents of the thesis.

LIST OF PUBLICATIONS

▪ *Published*

1. *In-Situ* Mechanistic Insights for Oxygen Reduction Reaction in Chemically Modulated Ordered Intermetallic Catalyst Promoting Complete Electron Transfer. **S. Mondal**, D. Bagchi, M. Riyaz, S. Sarkar, A. K. Singh, C. P. Vinod, S. C. Peter. *J. Am. Chem Soc.*, 2022, **144**, 11859–11869.
2. Morphology Tuned Pt₃Ge Accelerates Water Dissociation to Industrial Standard Hydrogen Production in wide pH Range. **S. Mondal**, S. Sarkar, D. Bagchi, T. Das, R. Das, A. K. Singh, P. K. Prasanna, C. P. Vinod, S. Chakraborty and S. C. Peter. *Adv. Mater.*, 2022, 2202294.
3. Distortion-Induced Interfacial Charge Transfer at Single Cobalt Atom Secured on Ordered Intermetallic Surface Enhances Pure Oxygen Production. **S. Mondal**, M. Riyaz, D. Bagchi, N. Dutta, A. K. Singh, C. P. Vinod, S. C. Peter. *ACS Nano*, 2022, **17**, 23169-23180.
4. Nitrogen Doping Induced Structural Distortion in LaMnO₃ Perovskite Nanoparticles Enhances the Bifunctional Activity towards Oxygen Reduction and Oxygen Evolution Reactions. **S. Mondal**, S. Sarkar, M. Riyaz, M. Kar, A. C. Fortuin, S. Vashishth, R. Das, M. Eswaramoorthy, D. Kramer, and S. C. Peter (Just Accepted, *ACS Energy Lett.* 2024, 9, XXX, 3440–3447).
5. A Perspective on Point Source Utilization of CO₂ to Value Added Chemicals via Electrocatalysis. **S. Mondal** and S. C. Peter (*Adv. Mater.* 2024, 2407124).

▪ *Under Review*

1. Unravelling Growth Mechanism of Local Entropy Tailored Intermetallic Pd₃Ni Exhibiting Tetrafunctional Activity in Water Electrolyser and Fuel Cell. **S. Mondal**, S. Sarkar, M. Riyaz, D. Bagchi, R. Burman, N. Dutta, A. K. Singh, S. Das, M. Radhakrishnan and S. C. Peter (under review in *Energy & Environmental Science*).
2. Operando Metal Vacancy Filling in Stable Pd-Sn Intermetallic Catalyst for Enhanced C-C Cleavage in Ethanol Oxidation. P. C. Ashly, **S. Mondal**, D. Goud, D. Bagchi, A. K. Singh, M. Riyaz, S. C. Peter (under review in *Adv. Mater.*).

3. Confining Reaction Intermediates in Oxide Derived Hollow Catalyst Facilitates Selective formation of C_{2+} Alcohols from Carbon Dioxide. N. Dutta, B. Giri, M. Riyaz, S. Midya, D. Bagchi, **S. Mondal**, A. K. Singh, S. Chakraborty, A. K. Singh, and S. C. Peter (Under review in JACS).
4. Dopant-induced simultaneous modification of charge density and C-C coupling sites for efficient CO_2 photoreduction to ethylene. K. Das, S. Chakraborty, S. Kediya, A. K. Singh, R. Das, **S. Mondal**, N. Dutta, C. P. Vinod, and S. C. Peter (under review in Adv. Mater.)

▪ ***Manuscript under preparation***

1. Electrochemically Sculpted Nano-Starflowers Generates Oxygen. **S. Mondal** and S. C. Peter.
2. Non-Metal Anchored Nano-Sized CoFe Intermetallic Formation via Nitride Formation Facilitates Oxygen Generation. **S. Mondal** and S. C. Peter.
3. Reductant-free Sub-nm Pt NPs Anchored on Ceria Support Exploring H-spillover Mechanism in H_2 Generation. **S. Mondal** and S. C. Peter.
4. Fine-Tuning of Intermetallic Nano-Electrocatalysis: Ordered Pd_2Ge as the Paradigm. **S. Mondal** and S. C. Peter.
5. Operando Generated Oxophilic SnO_2 on Ordered $PdSn$ Intermetallic Nanoparticles Enhances Ethanol Oxidation Reaction. P. C. Ashly, U. Roman, **S. Mondal**, and S. C. Peter.

▪ ***Patents:***

1. Provisional Application No.2022410079 99 and PCT/IN2023/050152
2. Provisional Application No. 202141037359
3. Synthesis of hexagonal-flower morphology of transition metals (TM) (Submitted as a patent)

▪ ***Awards:***

1. Secured **64th CSIR** all India Rank in National Eligibility Test (NET, June 2019) conducted by Council of Scientific and Industrial Research, India.
2. Best poster award in the 34th AGM of MRSI and 5th Indian Materials Conclave, 2023 at IIT-BHU.

3. Best Oral Presentation Award in the 11th Asian Conference on Nanoscience and Nanotechnology - AsiaNANO 2024, IIT Madras.
4. Recipient of “**Karnataka DST Nanoscience Fellowship Award 2024**” from Department of Science and Technology, Government of Karnataka and Vision Group on Nanotechnology for advanced studies in Nanoscience and Technology.

About the Author

I was born and raised in Guskara, a small town in West Bengal. I have completed my

B. Sc. at Vivekananda Mahavidyalaya in

Burdwan, and pursued M. Sc. from

Visva-Bharati university, Shantiniketan.

Driven by my passion for science, I pursued

a Ph.D. in Materials Chemistry, where I have

dedicated my doctoral research in applications of room temperature fuel cells

and water splitting which is aimed to achieve a sustainable future. Currently, I

am working on designing catalyst materials and mechanistic investigation for

electrochemical reactions along with theoretical understanding of reaction

pathways. Apart from research, I have an inclination for singing, penning poems

and photography.

